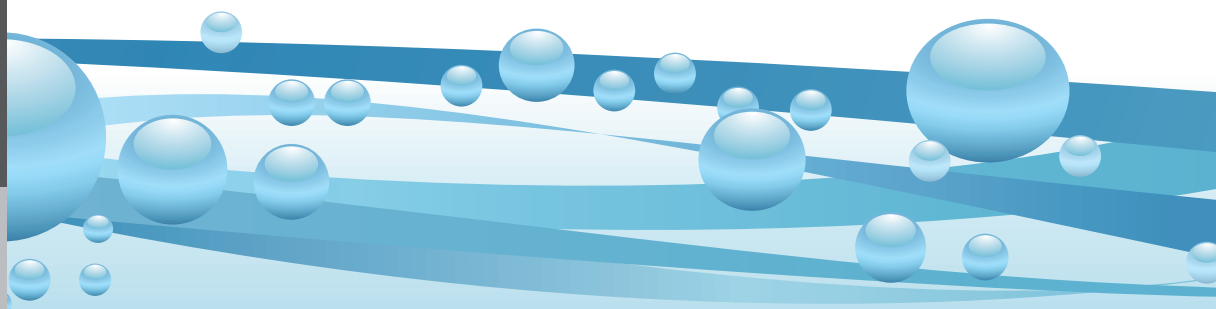

18th

18th World Hydrogen Energy Conference 2010 – WHEC 2010 Proceedings

Parallel Sessions Book 1:
- Fuel Cell Basics
- Fuel Infrastructures

Editors: Detlef Stolten, Thomas Grube

JÜLICH
FORSCHUNGSZENTRUM

Mitglied der Helmholtz-Gemeinschaft

18th World Hydrogen Energy Conference 2010 - WHEC 2010: Parallel Sessions Book 1: Fuel Cell Basics / Fuel Infrastructures

WHEC, May 16.-21. 2010, Essen

Detlef Stolten, Thomas Grube (Eds.)

Institute of Energy Research - Fuel Cells (IEF-3)

Guide to the Online Edition

Forschungszentrum Jülich GmbH, Zentralbibliothek, Verlag

Schriften des Forschungszentrums Jülich / Energy & Environment Vol. 78-1

978-3-89336-651-4 / 1866-1793

FC Fuel Cell Basics

FC.1 Electrochemistry of PEM Fuel Cells

Poster

FC.2 PEM/ HT-PEM Fuel Cells: Electrolytes, Stack Components

Poster

FC.3 Direct Fuel Cells

Poster

FC.4 High-Temperature Fuel CellsDirect Fuel Cells

Poster

FC.5 Advanced Modelling

Poster

HI Fuel Infrastructures

HI.1 Hydrogen Distribution Technologies

Poster

HI.2 Hydrogen Deployment

Poster

HI.3 Fuel Provision for Early Market Applications

Poster

Schriften des Forschungszentrums Jülich
Energy & Environment Volume 78-1

Forschungszentrum Jülich GmbH
Institute of Energy Research (IEF)
Fuel Cells (IEF-3)

18th World Hydrogen Energy Conference 2010 – WHEC 2010

Parallel Sessions Book 1:

- Fuel Cell Basics

- Fuel Infrastructures

Editors: Detlef Stolten, Thomas Grube

Schriften des Forschungszentrums Jülich
Energy & Environment Volume 78-1

ISSN 1866-1793 ISBN 978-3-89336-651-4

Bibliographic information published by the Deutsche Nationalbibliothek.
The Deutsche Nationalbibliothek lists this publication in the Deutsche Nationalbibliografie; detailed bibliographic data are available in the Internet at http://dnb.d-nb.de.

Vol. 78 Set (komplett)
ISBN 978-3-89336-657-6
Editors: Detlef Stolten, Thomas Grube, Bernd Emonts

Publisher and Distributor: Forschungszentrum Jülich GmbH
Zentralbibliothek
52425 Jülich
Phone +49 (0) 24 61 61-53 68 · Fax +49 (0) 24 61 61-61 03
e-mail: zb-publikation@fz-juelich.de
Internet: http://www.fz-juelich.de/zb

Cover Design: Grafische Medien, Forschungszentrum Jülich GmbH

Printer: Grafische Medien, Forschungszentrum Jülich GmbH

Schriften des Forschungszentrums Jülich
Reihe Energy & Environment Volume 78-1

ISSN 1866-1793
ISBN 978-3-89336-651-4

The complete volume ist freely available on the Internet on the Jülicher Open Access Server (JUWEL) at http://www.fz-juelich.de/zb/juwel

Book 1: Fuel Cell Basics | Fuel Infrastructures

Contents

Poster

Preface

Over the past few years, the three major reasons why novel energy technologies will be required in the very next years have become common sense: to mitigate climate change, to secure energy supply, and to foster economic competitiveness. Hydrogen and fuel cells have great potential to meet all three of these societal requirements.

Being at the cutting edge of energy R&D, the government of North Rhine-Westphalia has been supporting hydrogen and fuel cell technologies substantially for many years through the Fuel Cell and Hydrogen Network NRW, by funding research projects, and not the least by hosting the 18th World Hydrogen Energy Conference 2010 in Essen.

Although the 18th WHEC was overshadowed by the consequences of the subprime crisis and the subsequent economic downturn, the number of participants was a record high. More than 1,350 people attended the scientific conference that offered 342 oral presentations in 49 sessions and 183 posters. The technological dimension materialized in an extensive trade fair with 136 exhibitors and a notable share of one third of the presentations being given by industry representatives. Such figures prove that hydrogen and fuel cell technologies are timely and that industry, governments and academia recognize the potential they have of providing viable solutions to the Grand Challenges mentioned above.

In order to ensure that the conference has a long-lasting impact, it was decided to fully document the event in publicly available books. The introductory talks to the sessions are available as full papers in the book entitled Hydrogen and Fuel Cells – Fundamentals, Technology and Applications, edited by D. Stolten and published by Wiley-VCH. These proceedings cover the speeches and technical presentations made on plenary day and the oral presentations and posters in the parallel sessions. They have been published as a set of seven books by the Juelich Research Center.

We gratefully acknowledge the wide-ranging support we had when editing this volume. First of all, we would like to express our gratitude to the authors of the papers in the proceedings who made it possible to promptly publish the talks given in the parallel sessions. Moreover, we are grateful for copy-editing support from the PhD students at the Institute for Fuel Cells in Juelich: Christiane Döll, Ralf Elze, Stefan Hürter, Dennis Krieg, Mirko Kvesić, Fang Liu, Andreas Löhmer, Wiebke Maier, John McIntyre, Florian Scharf, Sebastian Schiebahn, Yong Wang and Christiane Wiethege.

August 2010

Detlef Stolten

Chairman of WHEC 2010

Thomas Grube

Member of the
WHEC 2010 Program Committee

FC Fuel Cell Basics

Electrocatalysis and Catalyst Degradation Challenges in Proton Exchange Membrane Fuel Cells

Hubert A. Gasteiger, Daniel R. Baker, Robert N. Carter, Wenbin Gu, Yuxin Liu, Frederick T. Wagner, and Paul T. Yu

Abstract

After a brief review of the kinetics of the cathodic oxygen reduction and the anodic hydrogen oxidation reaction, a fundamental membrane electrode assembly performance model is outlined, which demonstrates that a 4–10-fold reduced amount of platinum is required for commercially viable large-scale vehicle applications. The various catalyst technology roadmaps to achieve this goal are discussed. With the increasing number of prototype proton exchange membrane fuel cell (PEMFC)-powered vehicles, catalyst durability has also become a strong focus of academic and industrial R&D. Therefore, the key issues of platinum sintering/dissolution under dynamic vehicle operation and of carbon-support corrosion during PEMFC startup/shutdown are reviewed.

On-line In-situ Diagnostics of Processes within PEM Fuel Cells by the Application of a Raman Fiber Technique

Hans Bettermann, **Peter Fischer**, Institut für Physikalische Chemie, Heinrich-Heine-Universität Düsseldorf, Düsseldorf, Germany

1 Introduction

In the recent years various physico-chemical methods have been considered to study fuel cells in operation [1]. These methods dominantly record global electric parameters. Apart global setups, segmented cells have been implied to monitor local parameters as for instance current densities or the distribution of temperatures.

This contribution intends to show how processes within PEM fuel cells can be locally resolved by applying Raman spectroscopy.

A striking advantage of Raman spectroscopy is its unpretentiousness concerning sample design and sample preparation. This enables measurements at hardly accessible locations. Furthermore, the Raman method is less interfered by water. Beside these two general conditions Raman spectroscopy belongs to the few methods that are able to analyze homo-nuclear diatomic gases or mixtures of them quantitatively [2,3]. This later property predestines the application to the pursuance of processes in which hydrogen and oxygen are involved. In the past, Raman spectroscopy has been applied to investigate degradation processes of membrane materials [4] as well as to detect intermediates on SOFC cermet anodes [5, 6].

A common drawback in applying Raman spectroscopy is however the small size of Raman cross sections. This property in general yields only weak light scattering signals especially for measuring trace-like samples as for instance gases in small sample volumes. The lack can be surmounted by using strong light sources, units with high throughputs of light, well chosen optic imaging conditions, and very sensitive detectors.

This contribution presents two experimental setups that make use of such components. The first setup that first demonstrates the feasibility of applying Raman spectroscopy for studying processes inside fuel cells combines a self-constructed Raman microscope with a suitable model fuel cell. The first concept of looking inside the fuel cell was then extended to an approach which allows the simultaneous detection of Raman spectra from seven points of a flow field canal. The issue of this experimental approach is to provide long-time measurements for pursuing local and global processes.

2 Experimental

The selected microscope objective let pass laser light (e.g., 458 nm, 100 mW) into the flow field and collects the generated Raman emission that is then dispersed by a spectrograph and detected by CCD-camera (cooled by liquid nitrogen, kept at -100 C°). A part of the experimental setup is shown in Fig. 1. The setup permits the record of hydrogen, oxygen, nitrogen, liquid water, as well as water vapor.

After proving the detectability of gases within the flow field by Raman spectroscopy, it was verified that the laser excitation does not interfere the fuel cell processes. Possible interferences are the local heating-up of flow field gases and the deterioration of the bipolar plate material by focused laser light. The polypropylene-graphite composite did not show any visual indication of damages after irradiation with intense laser light.

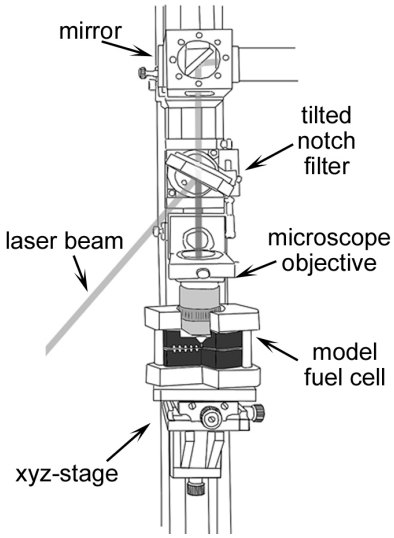

Figure 1: Central part of the Raman microscope setup.

A potential heating-up of gaseous samples can be directly proven by measuring the Raman signals of gaseous water quantitatively. The measurements showed that setting the laser power up to 1 W a temperature increase could not be identified.

The first concept of looking inside the fuel cell was then extended to an approach that allows the simultaneous detection of Raman spectra from several points of a flow field canal (single serpentine). The setup permits the simultaneous record of gas flows, liquid water and water vapor and how those species do change locally during operation. This was realized by a multiple-fiber Raman spectrometer with seven twin fibers. Each excitation fiber directed the laser beam to a specified position of the flow field. The beam of a frequency-doubled thin disk Yb:YAG laser (515 nm, 14 W) was coupled into the excitation fibers (multimode-step-index), respectively, focused by a micro lenses assembly and guided through small holes (1 mm) into the flow field canal. A second fiber attached to each excitation fiber collected the scattered light via the micro lenses and transmitted the Raman emission to the detection unit. The Raman light was again dispersed by a spectrograph and recorded by a CCD-camera. This setup permitted the record of spectra in a few minutes.

The fuel cell was part of a test station that was designed and manufactured by the German Aerospace Center (DLR, Stuttgart, Germany). The test station comprises the control of the humidification, the temperature of the fuel cell and the humidifiers, gas flows and pressures on both the anode and cathode side. Two separate humidifiers externally humidified the gases. The fuel cell was operated in a constant voltage mode. Gas flows were set to the stoichiometric factor of 1.5 for a current density of 1 A cm^{-2}.

3 Results and Discussion

The first setup was used to study membrane damages by Raman microscopy. For this, an artificial hole was manufactured within the Nafion^{TM} membrane by aligning the laser focus onto the MEA surface for a short time. The following Raman spectra exhibited the passage of N_2 and O_2 from the cathode to the anode as well as the generation of water by a catalytic oxidation of H_2 at the rim of the hole. A strong local increase of temperature next to the membrane hole was identified by measuring changes of the intensity distribution of rotational H_2-Raman bands.

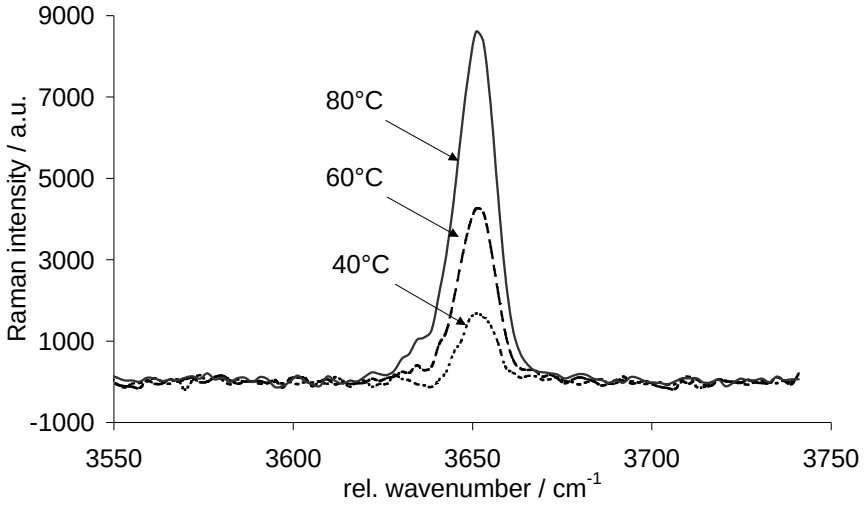

Figure 2: The water vapour signal at different temperatures, Q-branch of the totally symmetric OH stretch mode, centre of signal: 3652 cm^{-1}; excitation wavelength: 477 nm, laser power 1 W, exposure time: 10 min.

Water vapor inside fuel cell canals is more difficult to measure than gases because at low temperatures the mole fraction of gaseous water amounts only few percent of the gas mixture. For this reason, measurements of water vapor at room temperature require stronger laser powers (> 1 W). The Raman signal of water vapour (Q-branch of the totally symmetric OH stretch vibration with highest signal intensity) at different temperatures is presented in Fig. 2.

Detailed information concerning the local conditions of gases especially within the anode canal were achieved by the multi-fiber setup.

The Raman measurements at each measuring point within the anodic flow field exhibited considerable time-dependent fluctuations of hydrogen density. The fluctuations of the H_2 concentrations are addressed to the changing flow conditions inside the flow field as a result of the humidification of the anode. A direct relation between fluctuations of hydrogen density and fluctuations of the cell power could be observed next to the entrance of the anode flow field. Cell power fluctuations occurred after longer operation times. At the end of the anode meander phase shifts between the fluctuations of the hydrogen signal and those of the power signal were observed as an additional result of humidification. Since droplets are moved by

the gas flow, the cross section of the canal is therefore altered locally and the H_2 flow passes several bottlenecks.

Heating the cell at 75 °C, Raman signals of water vapor were observed (Fig. 3). The spectra first revealed an increase of water vapor with increasing canal length.

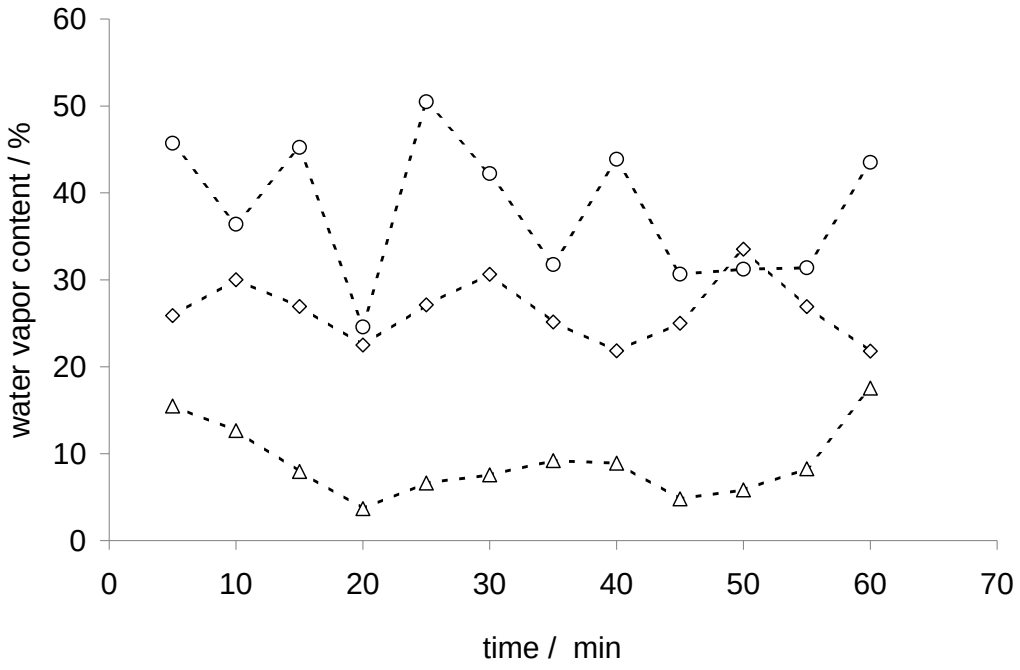

Figure 3: Evolution of the absolute humidity (water vapour signal: 3652 cm^{-1}) as a function of time at three different ports along the anode meander; cell temperature: 75 °C; lower track: port next to the entrance, central track: port close to the center of the canal, upper track: next to the exit of the canal.

This could be directly seen from the average values of water vapor obtained from the selected measuring ports. Time-dependent fluctuations of water vapor did also occur. The local fluctuations of water vapor are obviously coupled to the local condensation of water in almost the same manner as it has been found for the changes of hydrogen concentration.

The spectra also show that the time periods in which changes of water concentration take place become shorter with increasing canal length. Condensation occurs primarily at the end of the meander since the atmosphere of the canal enriches with water vapor. Condensation leads to a temporary contraction of the cross-sectional canal area or its complete blockage. Both obstructions may cause an increase of pressure just in front of the water droplets.

The local Raman spectra were compared with local current density measurements and global impedance spectroscopy. Beside the collection of data for modelling fuel cell processes, the multiple-fiber setup is primarily considered to monitor degradation processes and pre-stages of membrane damages. This project is part of a close cooperation with the DLR (German aero space center, Stuttgart, Germany) and the ZBT (center for fuel cell technology, Duisburg, Germany).

References

[1] Wu, J.; Yuan, X. Z.; Wang, H.; Blanco, M.; Martin, J.J.; Zhang, J. *Int. J. Hydrogen Energy*, **2008**, *33*, 1735-1746.

[2] A. Weber, 1979 *Raman Spectroscopy of Gases and Liquids*, Springer-Verlag, Berlin, Heidelberg, New York, Chap. 2-3

[3] Veirs, D.; Rosenblatt, G. *J. Mol. Spec*. **1987**,*121*, 401-419.

[4] Mattsson, B.; Ericson, H; Torell, L.M.; Sundholm, F. *Electrochim. Acta* **2000**, *45*, 1405-1408.

[5] Pomfret, M.B.; Owrutsky, J.C.; Walker, A.W. *J. Phys. Chem. B*, **2006**, *110*, 17305-17308

[6] Pomfret, M.B.; Owrutsky, J.C.; Walker, A.W. *Anal. Chem*., **2007**, *79*, 2367-2372

Challenge of Non-precious Metal Oxide-Based Cathode for Polymer Electrolyte Fuel Cell

Akimitsu Ishihara, Koichi Matsuzawa, Shigenori Mitsushima, Ken-ichiro Ota,
Yokohama National University, Japan

1 Introduction

Polymer electrolyte fuel cells (PEFCs) are expected to be as power sources for residential cogeneration systems and transportation applications due to their high theoretical energy efficiency and less emission of pollutants. However, PEFCs have some serious problems to be solved for their commercialization. In particular, a large overpotential of the oxygen reduction reaction (ORR) must be reduced in order to obtain higher energy efficiency. A large amount of platinum is generally used as a cathode catalyst in present PEFCs to decrease the overpotential of the ORR. However, Pt is expensive and its resources are limited so that the Pt usage will be limited in the future commercialization of PEFCs. Many researches have been tried to reduce the use of Pt catalyst such as a greater dispersion of Pt particles and/or alloying with transition metals [1, 2]. However, because the dissolution and deposition of highly dispersion Pt particles proceeds during long-term operation [3], the drastic reduction of Pt usage would be difficult. Therefore, the development of a new non-platinum catalyst is strongly required.

We have reported that tungsten carbide with tantalum addition [4], tantalum oxynitride [5-8], zirconium oxide [9, 10], titanium oxide [11], zirconium oxynitride [12, 13], chromium carbonitride [14] and tantalum carbonitride [15] were stable in an acid solution and had a definite catalytic activity for the ORR.

In particular, we found that the partially oxidized $TaC_{0.58}N_{0.42}$ powder had a good catalytic activity for the ORR and the mixture with the carbon black was useful to increase the ORR current [16, 17]. However, the characterization of the specimens and the discussion of the correlation between the physical properties and the catalytic activity for the ORR had not been elucidated yet.

In the present paper, the characterization of the specimens such as the measurement of the ionization potential was performed and the correlation between the physical properties of the specimens and the catalytic activity for the ORR was discussed.

2 Experimental

Tantalum carbonitride (TaC_xN_y) powder was used as a starting material. Ta_2O_5 powder and carbon black were uniformly mixed, and the mixture was heat-treated at 1600 °C under flowing N_2 to make carbonitride. The composition of the TaC_xN_y was controlled by a quantity of the carbon black. In the present study, $TaC_{0.58}N_{0.42}$ powder was used as a starting material.

The $TaC_{0.58}N_{0.42}$ powders were heat-treated at 1000 °C for a holding time from 3 to 32 h under a flow rate of 20 cm^3 min^{-1} of the 2 % - H_2/N_2 gas containing 0.25 % oxygen to obtain

powder specimens with different oxidation state. Crystalline structure of the specimens was analyzed using X-ray diffraction (XRD-6000, SHIMADZU) with Cu Kα radiation. Ionization potential of partially oxidized $TaC_{0.58}N_{0.42}$ was measured using Photoelectron Spectrometer Surface analyzer Model AC-2 (Riken Keiki).

Both TaC and TaN have a same crystalline structure (Rock-Salt type) and form a complete solid solution. The XRD pattern did not change from TaC (JCPDS: 35-0801) to TaN (JCPDS: 32-1283), and an each peak shifts to higher angle with the increase in the nitrogen content, which known as Vegard's law. In the present paper, the compounds with XRD peaks which existed between TaC and TaN were expressed as TaC_xN_y. The peak intensity of the Ta_2O_5 increased with the increase in the holding time of the heat treatment, while the intensity of the TaC_xN_y decreased.

In order to quantify the degree of oxidation of the $TaC_{0.58}N_{0.42}$, the peak intensity at $2\theta = 35°$ of TaC_xN_y (1 0 0), which was expressed as I (TaC_xN_y), and the peak intensity at $2\theta = 28.3°$ of Ta_2O_5 orthorhombic (1 11 0), which was expressed as I (Ta_2O_5), were utilized to calculate the ratio, I (Ta_2O_5)/{I (TaC_xN_y) + I (Ta_2O_5)}. The ratio, I (Ta_2O_5)/{I (TaC_xN_y) + I (Ta_2O_5)}, was designated the degree of the oxidation of the $TaC_{0.58}N_{0.42}$ and expressed as DOO (Degree Of Oxidation).

A partially oxidized specimen was mixed with carbon black (7 wt.-%), Ketjen Black, and the mixed powder (2.8 mg cm^{-2}) was dropped onto a glassy carbon rod ($\Phi = 5.2$ mm). A 0.5 wt.-% Nafion® solution, then, was dropped onto the surface to cover the mixed powder.

All electrochemical experiments were conducted in a three-electrode cell under nitrogen or oxygen atmosphere in 0.1 mol dm^{-3} H_2SO_4 at 30 °C. A reference electrode was a reversible hydrogen electrode (RHE) in the same solution. Cyclic voltammetry (CV) (scan rate: 50 mV s^{-1}, 0.05 - 1.0 V) was performed under nitrogen atmosphere to investigate an electrochemical stability of the specimens. Slow scan voltammetry (SSV) (scan rate: 5 mV s^{-1}, 1.0 - 0.2 V) was performed under nitrogen or oxygen atmosphere to evaluate the catalytic activity for the ORR. A current difference between under O_2 and under N_2 might be due to the oxygen reduction. Therefore, the oxygen reduction current density (i_{ORR}) was defined as the difference in the current densities between under the O_2 atmosphere (i_{O2}) and the N_2 atmosphere (i_{N2}). The current density was based on the geometric surface area of the working electrode. An onset potential for the ORR, E_{ORR}, was defined as the electrode potential at the i_{ORR} = -0.2 μA cm^{-2} to evaluate the catalytic activity for the ORR.

3 Results and Discussion

3.1 Degree of oxidation of $TaC_{0.58}N_{0.42}$

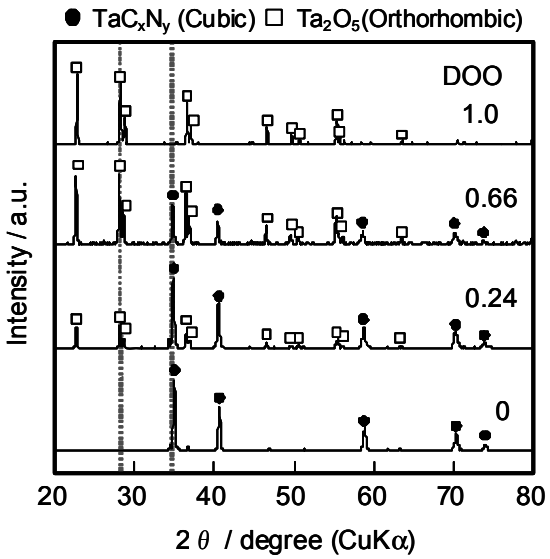

Figure 1: XRD patterns of the powder specimens with the different holding time of heat treatment. The holding time of the upper specimen was longer, and the lowest specimen was the starting material, $TaC_{0.58}N_{0.42}$.

Figure 1 shows the XRD patterns of the powder specimens with the different degree of oxidation (DOO). The DOO of the specimen with no heat treatment was zero, that is, $TaC_{0.58}N_{0.42}$. Although the surface of the $TaC_{0.58}N_{0.42}$ was probably oxidized, no peaks of the Ta_2O_5 were observed because the surface oxide layer was very thin. The DOO of the specimen with completely oxidized was unity, that is, Ta_2O_5. However, this completely oxidized powder was not prepared using the heat treatment in the present paper because of the low oxygen concentration. Therefore, a commercial reagent, Ta_2O_5 (Kojundo Kagaku), was used as the powder with DOO of unity.

3.2 Dependence of the degree of oxidation of $TaC_{0.58}N_{0.42}$ on the catalytic activity for the ORR

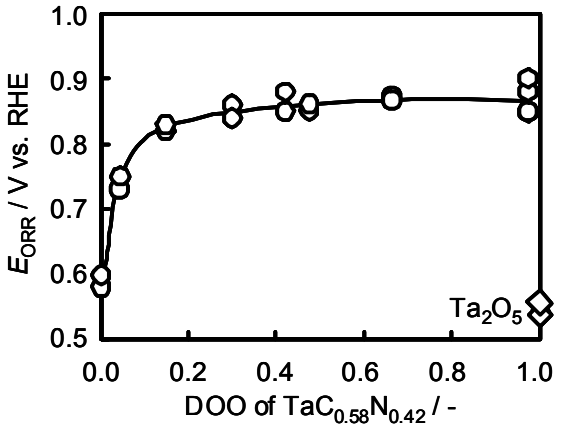

Figure 2: Relationship between the DOO and the E_{ORR}. E_{ORR} was defined as the electrode potential at the i_{ORR} = -0.2 μA cm^{-2}. 0.1 mol dm^{-3} H_2SO_4, 30°C, scan rate = 5 mV s^{-1}.

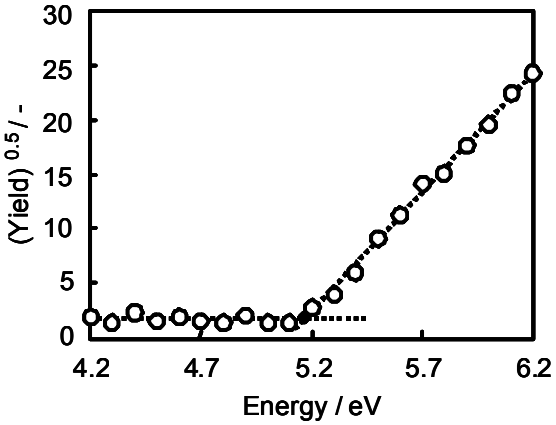

Figure 3: Relationship between the square root of the photoelectric quantum yield $Y^{1/2}$ and the photon energy.

Figure 2 shows the relationship between the DOO and the E_{ORR}. The E_{ORR} abruptly increased with the increasing DOO up to 0.2. Then, the E_{ORR} had high value over 0.85 V above the DOO of 0.3. The maximum of the E_{ORR} is approximately 0.9 V. The starting material (DOO = 0) and the completely oxidized material (DOO = 1) had a poor catalytic activity. This result indicated that an appropriate oxidation of $TaC_{0.58}N_{0.42}$ was essential to obtain the large oxygen reduction current.

3.3 Ionization potential of the partially oxidized $TaC_{0.58}N_{0.42}$

The ionization potential of the specimens was measured using Photoelectron Spectrometer Surface analyzer to discuss the electronic structure of the specimens. Figure 3 shows the relationship between the square root of the photoelectric quantum yield $Y^{1/2}$ and the photon energy, that is, the photoelectron spectra of the partially oxidized $TaC_{0.58}N_{0.42}$ with the DOO

of 0.42. A linear relation was obtained in the range from 5.2 to 6.2 eV. The intersection between the straight line and the background line provided a threshold energy. The threshold energy corresponded to a photoelectric ionization potential. The ionization potential of the partially oxidized $TaC_{0.58}N_{0.42}$ with the DOO of 0.42 was estimated to be 5.10 eV as shown in Figure 3. The highest energy level of electrons in the valence band of Ta_2O_5 is -7.83 ~ -7.93 eV [18], that is, the ionization potential of Ta_2O_5 is 7.83 ~ 7.93 eV. However, the ionization potential of the partially oxidized $TaC_{0.58}N_{0.42}$ with the DOO of 0.42 was 2.7 eV lower than that of Ta_2O_5. The work function of metal Ta was 4.25 eV [19]. For titanium, Henrich et al. investigated the relationship between the work function, that is, the ionization potential, of reduced TiO_2 (1 1 0) and the density of defect states on the surface [20]. They found that the work function decreased with increasing the density of defects. The similar behavior is expected to occur in case of the partially oxidized $TaC_{0.58}N_{0.42}$. Ta_2O_5 had the band gap of 3.9 eV [18]. Lattice defects and impurities introduce localized electron levels in the band gap of metal oxides. Vacancies of oxide ion give donor levels close to the edge level of the conduction band [21]. The conduction band edge level of Ta_2O_5 is -3.93 ~ -4.03 eV [18]. These values are close to the ionization potential of partially oxidized $TaC_{0.58}N_{0.42}$ with the DOO of 0.42. Therefore, the partially oxidized $TaC_{0.58}N_{0.42}$ with the DOO of 0.42 probably had some vacancies of oxide ion.

Figure 4 shows the relationship between the DOO and the ionization potential. The ionization potential of the $TaC_{0.58}N_{0.42}$ was 4.8 eV, and the completely oxidized, commercial Ta_2O_5 had 5.4 eV. The ionization potential of the partially oxidized $TaC_{0.58}N_{0.42}$ powder had almost the same value, 5.2 eV. The ionization potential of pure TaON and Ta_3N_5 were 6.6 and 6.0 eV, respectively [18]. The ionization potentials obtained in the present study were much lower than those of TaON and Ta_3N_5. This low ionization potential suggested that the partially oxidized $TaC_{0.58}N_{0.42}$ had some surface defects. Lattice defects and impurities introduce localized electron levels in the band gap of metal oxides. Vacancies of oxide ion give donor levels close to the edge level of the conduction band. We expected that the partially oxidized $TaC_{0.58}N_{0.42}$ probably had some vacancies of oxide ion.

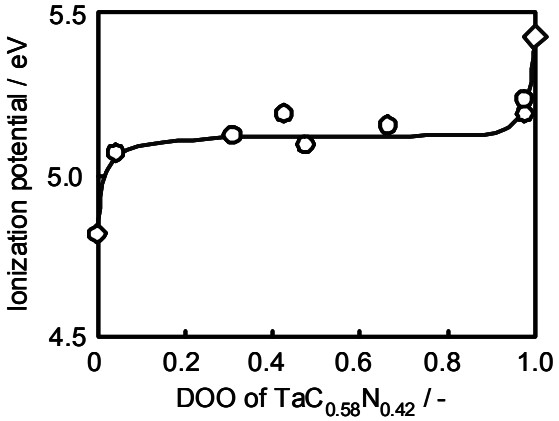

Figure 4: Relationship between the DOO and the ionization potential.

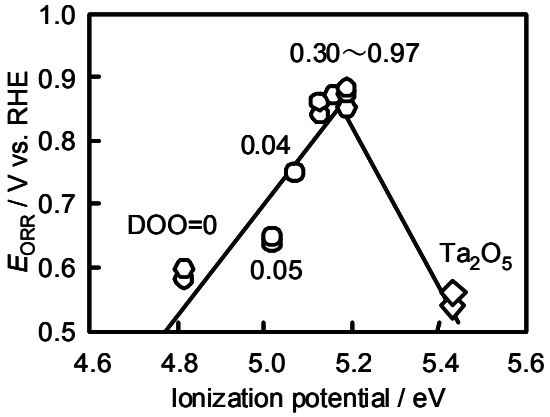

Figure 5: Relationship between the ionization potential and the onset potential of the ORR.

Figure 5 shows the relationship between the ionization potential and the E_{ORR}. The volcano plot was obtained. The adsorption of oxygen molecules on the surface was required as the first step to proceed the ORR. Many researches revealed that the presence of surface defects sites was required to adsorb the oxygen molecules on the surface of the oxides such as TiO_2 (1 1 0), ZnO, NiO (1 0 0), $Ce_xZr_{(1-x)}O_2$, V_2O_5, and MoO_3 [22-27]. The increase in the surface defects on the partially oxidized $TaC_{0.58}N_{0.42}$ yielded the increase in the adsorption sites of oxygen molecules. In addition, the interaction of oxygen with the catalyst surface is essentially important because both the adsorption of oxygen and the desorption of water on the surface is necessary to continue the fluent progress of the ORR. When the interaction of oxygen with the catalyst surface is strong, the desorption of water is restrained. On the other hand, when the interaction of oxygen with the catalyst surface is weak, few adsorption of oxygen molecules proceeds. There might be a most suitable strength of the interaction between the oxygen and the catalyst surface. Metallic Ta atom strongly adsorbed oxygen because of the large adsorption energy of oxygen (887 kJ mol^{-1}) and calculated bond energy of Ta-oxygen atoms (715 kJ mol^{-1}) [28]. In case of Pt, the adsorption energy of oxygen and the calculated bond energy of Pt-oxygen atoms were 280 kJ mol^{-1} and 397 kJ mol^{-1}, respectively [28]. These values of Ta were much larger than those of Pt. As the oxidation of Ta metal proceeded, the interaction of oxygen with Ta of the catalyst surface became weak because the oxide ions attracted the electrons of the highest occupied molecule orbital of Ta to be Ta charged positively. Because the ionization potential was related to the strength between the surface of the specimen and oxygen, the volcano plot shown in Figure 5 suggested that there was a suitable interaction between the surface of the specimen and oxygen. Therefore, the oxidization could control the strength of the interaction between the oxygen and the Ta, and as the interaction became suitable the catalytic activity for the ORR increased.

4 Conclusions

The partially oxidized $TaC_{0.58}N_{0.42}$ was investigated as non-platinum cathode for PEFC. In order to quantify the degree of oxidation, the DOO was defined using the XRD peaks of Ta-CN and Ta_2O_5. The onset potential for the ORR had high value, that is, 0.9 V vs. RHE, at

higher oxidation state of the $TaC_{0.58}N_{0.42}$. We found that the partial oxidation of $TaC_{0.58}N_{0.42}$ was greatly useful to enhance the catalytic activity for the ORR. The volcano plot of the ionization potential vs. the E_{ORR} suggested that there was a suitable interaction between the surface of the partially oxidized $TaC_{0.58}N_{0.42}$ and oxygen.

Acknowledgments

The authors wish to thank A.L.M.T. Corp. for supply of the $TaC_{0.58}N_{0.42}$ and Riken Keiki Co., Ltd. for measurement of the ionization potential. The authors also thank the New Energy and Industrial Technology Development Organization (NEDO) for financial support.

References

[1] T. Toda, H. Igarashi, H. Uchida and M. Watanabe, *J. Elecrtochem. Soc.*, 146, 3750 (1999).

[2] S, Mukerjee, S. Srinirasan, M. P. Soriaga, and J. McBreen, *J. Phys. Chem.*, 99, 4577 (1995).

[3] K. Yasuda, A. Taniguchi, T. Akita, T. Ioroi, and Z. Siroma, *J. Electrochem. Soc.*, 153, A1599 (2006).

[4] K. Lee, A. Ishihara, S. Mitsushima, N. Kamiya, and K. Ota, *Electrochim. Acta*, 9, 3479 (2004).

[5] A. Ishihara, K. Lee, S. Doi, S. Mitsushima, N. Kamiya, M. Hara, K. Domen, K. Fukuda, and K. Ota, *Electrochem. Solid-State Lett*., 8, A201 (2005)

[6] Y. Shibata, A. Ishihara, S. Mitsushima, N. Kamiya, and K. Ota, *Electrochem. Solid-State Lett.*, 10, B43 (2007).

[7] A. Ishihara, S. Doi, S. Mitsushima, and K. Ota, *Electrochim.Acta*, 53, 5442 (2008).

[8] Y. Ohgi, A. Ishihara, Y. Shibata, S. Mitsushima, and K. Ota, *Chem. Lett.*, 37, 608 (2008).

[9] Y. Liu, A. Ishihara, S. Mitsushima, N. Kamiya, and K. Ota, *Electrochem. Solid State Lett*., 8, A400 (2005).

[10] Y. Liu, A. Ishihara, S. Mitsushima, N. Kamiya and K. Ota, *J. Electrochem. Soc.*, 154, B664 (2007).

[11] J.-H. Kim, A. Ishihara, S. Mitsushima, N. Kamiya, and K. Ota, *Electrochim. Acta*, 52, 2492 (2007).

[12] S. Doi, A. Ishihara, S. Mitsushima, N. Kamiya, and K. Ota, *J. Electrochem. Soc.*, 154, B362 (2007).

[13] Y. Maekawa, A. Ishihara, S. Mitsushima, K. Ota, *Electrochem. Solid-State Lett*, 11, B109 (2008).

[14] J.-H. Kim, A. Ishihara, S. Mitsushima, N. Kamiya, and K. Ota, *Chem. Lett.*, 36, 514 (2007).

[15] J.-H. Kim, A. Ishihara, S. Mitsushima, N. Kamiya, and K. Ota, *Electrochemistry*, 75, 166 (2007).

[16] A. Ishihara, Y. Shibata, S. Mitsushima, and K. Ota, *J. Electrochem. Soc.*, 155, B400 (2008).

[17] A. Ishihara, M. Tamura, K. Matsuzawa, S. Mitsushima, and K. Ota, *Elctrochim. Acta*, in press.

[18] W.-J. Chun, A. Ishikawa, H. Fujisawa, T. Takata, J. N. Kondo, M. Hara, M. Kawai, Y. Matsumoto, and K. Domen, *J. Phys. Chem. B*, 107, 1798 (2003).

[19] H. B. Michaelson, *J. Appl. Phys.*, 48, 4729 (1977).

[20] V. E. Henrich, G. Dresselhaus, and H. J. Zeiger, *Phys. Rev. Lett.*, 36, 1335 (1976).

[21] C. Stampfl and A. J. Freeman, *Phys. Rev. B*, 67, 064108 (2003).

[22] J.-M. Pan, B. L. Maschhoff, U. Diebold, and T. E. Madey, *J. Vac. Sci. Technol. A*, 10, 2470 (1992).

[23] A. L. Lisebigler, G. Lu, and J. T. Yates, Jr., *Chem. Rev*. (Washington, D.C.), 95, 735 (1995).

[24] C. Descorme, Y. Madier, and D. Duprez, *J. Catal.*, 196, 167 (2000).

[25] J. M. Blaisdell and A. B. Kunz, *Phys. Rev. B*, 29, 988 (1984).

[26] W. Göpel, *J. Vac. Sci. Technol*., 15, 1298 (1978).

[27] M. Witko and R. Tokarz-Sobieraj, *Catal. Today*, 91–92, 171 (2004).

[28] E. Miyazaki and I. Yasumori, *Surf. Sci.*, 55, 747 (1976).

Relationship between Degradation of Pt/C and Property of Electrolyte for PEFCs

Shigenori Mitsushima, **Kazuki Shinkoda**, **Fumiya Hiraoka**, **Koichi Matsuzawa**, **Ken-ichiro Ota**, Yokohama National University(YNU), Japan

1 Introduction

Polymer electrolyte fuel cells (PEFCs) have started commercialization for small size co-generation systems and fuel cell vehicles because of the high power density, capability of start up from ambient temperature and high energy conversion efficiency. In the present technology, platinum electrocatalyst is essential. However toward real commercialization, precious metal loading should be reduced by one tenth or more because of the limit of natural resources. To reduce precious metal loading with high catalytic activity, higher dispersion technology, alloying and core shell technology have been developed [1-3]. These materials were also required high stability during the system lifetime.

Generally, nano-particle is unstable compared to larger particles, and rated load enhances the degradation of electrocatalyst. There are many reports for the degradation of electrocatalyst for PEFCs. For example, the decrease of electrochemical surface area under potential cycling with small size single cells or three – electrode conventional electrochemical cells, platinum consumption under potential cycling, and dissolution of platinum in acidic medium have been reported. The Ostwald ripening and the sintering model have been proposed as degradation mechanism. However, the degradation mechanism has not been clarified, yet [1, 2, 4-6].

In this study, the electrochemical surface area decrease with various pH electrolytes under various potential patterns has been investigated as a fundamental study to clarify the degradation mechanism and improvement of the durability for PEFCs.

2 Experimental

Pt/C (Tanaka K. K., TEC10E50E) water dispersion was painted on a glassy carbon disk (Tokai carbon, GC-20SS) which was polished to mirror surface. Reference and counter electrodes were reversible hydrogen electrode (RHE) and platinum wire, respectively. Electrolyte was in the concentration range from 0.1 to 1 M (=mol dm^{-3}) of sulfuric acid (Junsei, Analysis grade) or percholoric acid (Merck, Ultrapur). The potential cycle was applied between 0 to 1.2 V vs. RHE. As shown in Fig. 1, 4 types of potential cycling patterns which were triangle waves with 50 mV s^{-1} of sweep rate, rectangular waves with 12 s interval, and the combinations of potential step and sweep were applied for 5000-cycle in nitrogen or oxygen atmosphere. The electrochemical surface area was frequently determined by hydrogen desorption wave of the cyclic voltammogram between 0.05 to 1.2 V vs. RHE during potential cycling under nitrogen atmosphere. After potential cycling, the Pt/C was observed by TEM. The particle diameter was determined from a projection area of a particle to the diameter of a circle. The number of the particle was more than 300.

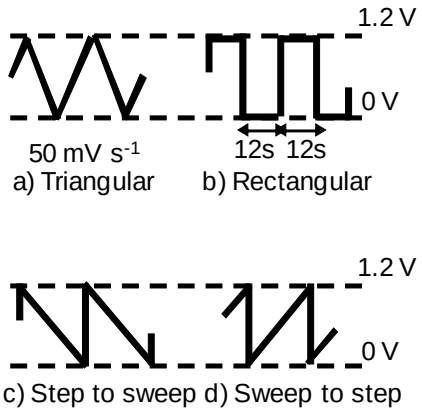

Figure 1: Potential cycling patterns.

3 Results and Discussion

During potential cycling, the shapes of cyclic voltammograms showed normal poly-crystal with small peaks of carbon black support for quinone / hydroquinone, and hydrogen adsorption / desorption and surface oxidation / reduction peaks decreased with potential cycling for all potential patterns. Therefore, the platinum surface did not change to a specific face, and electrochemical surface area was determined by hydrogen desorption charge with 210 $\mu C\ cm^{-2}$.

Figure 2 shows the TEM images Pt/C before and after 5000 triangular potential cycles in various concentration of H_2SO_4 at 25^oC. The platinum particle of the initial Pt/C was uniform diameter, and the particle grew during potential cycling. The particle seems lager diameter and distribute for higher concentration. Figure 3 shows the platinum particle diameter distribution in various concentration of H_2SO_4 under nitrogen atmosphere. The particle size distribution was log-normal distribution, and the medium diameters were 2.4, 4.7, 4.7, and 5.6 nm before and after potential cycling in 0.1, 0.5, and 1M, respectively.

Figure 4 shows the medium diameter of platinum particle as a function of pH. The diameter decreased with the increase of pH for all conditions. Figure 4 a) is for triangular pattern in H_2SO_4 and $HClO_4$ under N_2 or O_2. The difference between N_2 and O_2 atmosphere was not significant. The particle diameter in H_2SO_4 was larger than that in $HClO_4$ at the same pH, and this behaviour was same to the dissolution of Pt in acidic media. Therefore, acidity and solubility would be one of important factor in particle growth process. Figure 4 b) is for rectangular and triangular potential cycling pattern in H_2SO_4 under N_2. The particle diameter of rectangular was ca. 20 % larger than that of triangular, therefore dissolution kinetics would be taken into account for the analysis of the particle growth.

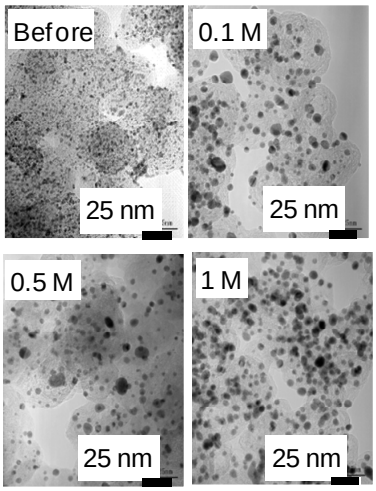

Figure 2: TEM images of Pt/C before and after 5000 triangular potential cycles in various concentration of H_2SO_4 at 25°C.

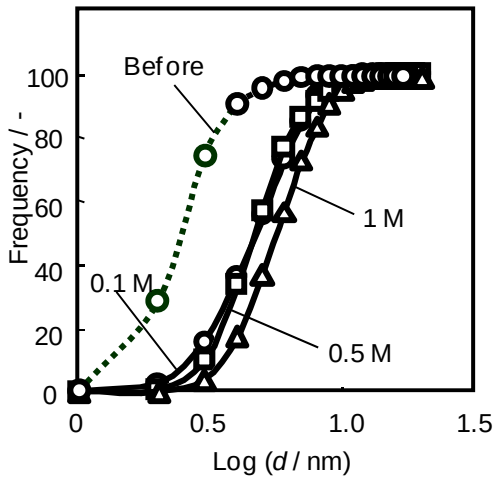

Figure 3: Platinum particle diameter distributions before and after 5000 triangular potential cycles in various concentration of H_2SO_4 at 25°C.

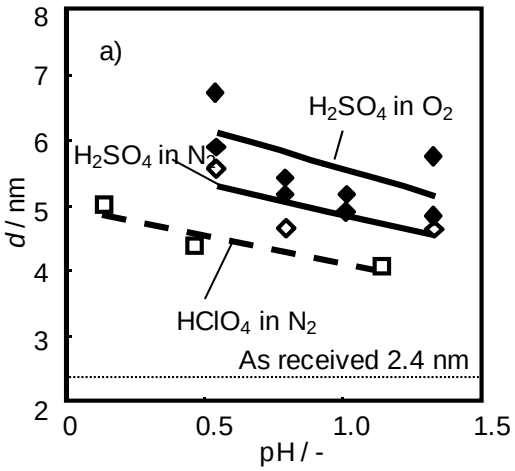

a) Triangular wave in H_2SO4 and $HClO_4$ under O_2 or N_2.

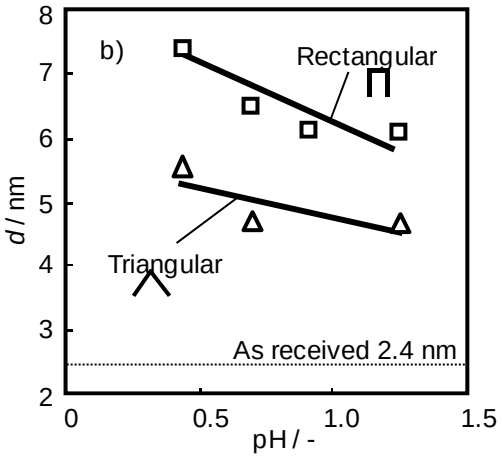

b) Rectangular and triangular potential pattern in H_2SO_4 under N_2.

Figure 4: Medium platinum particle diameter as a function of pH after 5000 potential cycles.

Figure 5 shows the logarithm of normalized electrochemical surface area as a function of the cycling number with the triangular potential pattern in H_2SO_4 under nitrogen atmosphere. The decreases of the surface area were significantly larger for higher concentration of sulfuric acid. Up to 2000 cycles, the surface area decreased with linear relation in this figure, and after 2000 cycles, the surface area decrease rate decreased, especially lower concentration. This behaviour was the same to all other conditions in this study. Here, we analyzed up to 2000^{th} cycle.

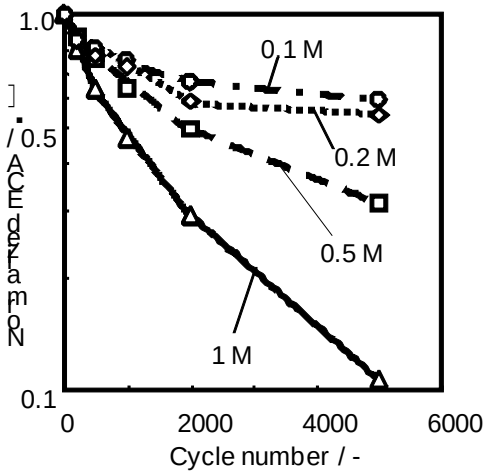

Figure 5: Electrochemical surface area as a function of potential cycling number with triangular potential cycles in various concentration of H_2SO_4 at 25°C

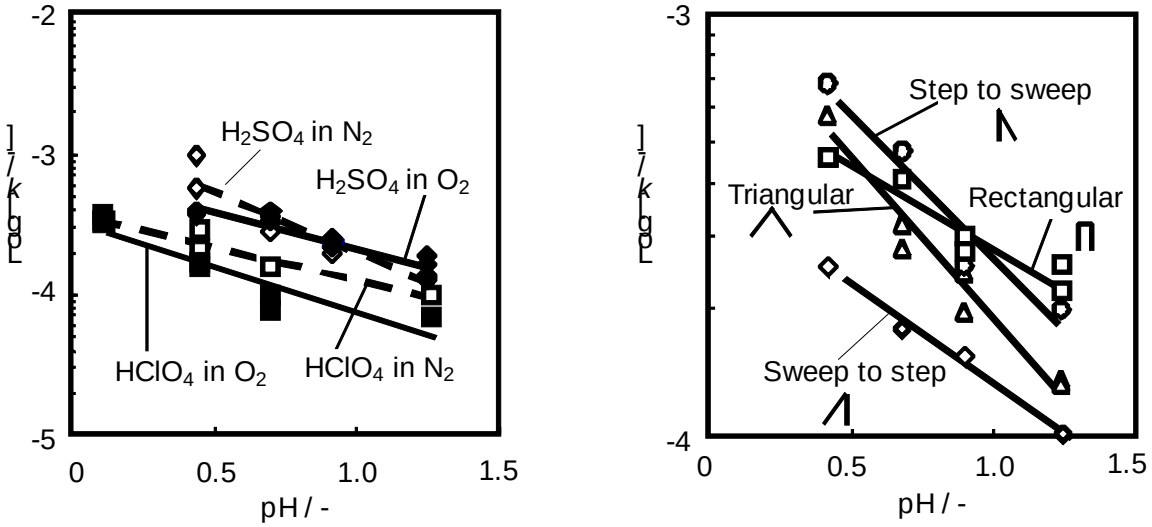

a) Triangular wave in H_2SO4 and $HClO_4$ under O_2 or N_2.

b) Various potential pattern in H_2SO_4 under N_2.

Figure 6: Rate constant of the electrochemical surface area decrease as a function of pH.

If the electrochemical surface area decrease rate is proportional to the electrochemical surface area: *S*, the following equation is obtained.

$$\delta S/\delta n = - k S \quad (1)$$

The *n* and *k* were the cycling number and the rate constant of the surface area decrease, respectively. The rate constants were determined by the slope of Figure 5. Figure 6 shows the rate constant as a function of pH. The rate constants decreased with the increase of pH, which were expected from the particle diameter. Figure 6 a) is the rate for triangular pattern in H_2SO_4 and $HClO_4$ under N_2 or O_2. The difference between N_2 and O_2 was not significant,

and the rate constant in H_2SO_4 was larger than that in $HClO_4$, which would correspond to the particle growth. Figure 6 b) is the rate for various potential cycling pattern in H_2SO_4 under N_2. In the 4 potential cycling patterns, the combination with the sweep oxidation and the step reduction showed the smallest rate constant in all pH. The combination with the step oxidation and the sweep reduction showed the largest rate constant in lower pH region. The dependence of the rate of the triangular pattern on pH was larger than others. Therefore, the kinetics of the simultaneously reactions of oxidation and reduction would affect to these behaviours.

The dissolution reaction follows the acidic dissolution in acid solution under oxidizing atmosphere [5].

$$PtO_2 + H_2O + H^+ = Pt(OH)_3^+ \quad (2)$$

However, the rate determining reaction under potential cycling would not same to the equilibrium. At least, there are 2 kinds of dissolution reactions which are anodic and cathodic processes [4]. Here, we consider the simplest simultaneously reactions of dissolution and protection during anodic and cathodic processes. The reactions and the reaction rate equation might be as follows:

(Anodic)

$$Pt \rightarrow Pt^{4+} + 4e^- \qquad v_{ad} = k_{ad}[Pt^{4+}]^{-1}\exp\left[\{4F(E-E^o_3)\}/(RT)\right] \quad (3)$$

$$Pt + 2H_2O \rightarrow PtO_2 + 4H^+ + 4e^- \qquad v_o = k_{od}[H^+]^{-4}\exp[\{4F(E-E^o_4)\}/(RT)] \quad (4)$$

(Cathodic)

$$PtO_2 + 4H^+ + 2e^- \rightarrow Pt^{2+} + 2H_2O \qquad v_{cd} = k_{cd}[H^+]^4[Pt^{2+}]^{-1}\exp[\{4F(E-E^o_5)\}/(RT)] \quad (5)$$

$$PtO_2 + 4H^+ + 4e^- \rightarrow Pt + 2H_2O \qquad v_r = k_r[H^+]^4\exp[\{4F(E-E^o_6)\}/(RT)] \quad (6)$$

Here, v, E, and E^o_i were the reaction rate, the potential, and the equilibrium potential for each reaction, respectively. The dissolution reactions are equations (3) and (5), and the protection reactions are equations (4) and (6). The protection reaction rates would be lower than that of dissolution reaction, because the protection reactions were more complex than the dissolution reactions. At that time, the step oxidation would enhance the dissolution, because the dissolution amount before the oxidation layer formation would be larger than that of sweep oxidation, and the sweep reduction would enhance the dissolution, because the oxide which was the reactant of the dissolution would be maintained longer time than step reduction during reduction process.

4 Conclusion

In order to clarify degradation mechanism of Pt/C, the electrochemical surface area under potential cycling has been investigated in various conditions. The electrochemical surface area decrease seems to be proportional to the surface area up to 2000 potential cycles, and the rate constant of electrochemical surface area decrease increased with the decrease of pH. The rate constant in H_2SO_4 was larger than that in $HClO_4$. These behaviours were same to the solubility of platinum bulk metal in acidic medium. The rate constant was affected by potential cycling pattern. The rate constant of the combination of sweep oxidation and step reduction was smaller than that of rectangular, triangular, and the combination of step oxidation and sweep reduction. These behaviours could be explained by the kinetics of simultaneously reactions of anodic dissolution and oxide formation, and cathodic dissolution and surface reduction.

Acknowledgement

This study was supported by the project for “Research and Development of Polymer Electrolyte Fuel Cell” from the New Energy and Industrial Technology Development Organization (NEDO).

References

[1] P. J. Ferreira, G. J. La O', Y. Shao-Horn, D. Morgan, R. Makharia, S. Kocha and H. A. Gasteiger, *J. Electrochem. Soc.*, **152**, A2256 (2005).

[2] S. Chen, H. A. Gasteiger, K. Hayakawa, T. Tada and Y. Shao-Horn, *J. Electrochem. Soc.*, **157**, A82 (2010).

[3] S. Koh, N. Hahn, C. Yu and P. Strasser, *J. Electrochem. Soc.*, **155**, B1281 (2008).

[4] S. Mitsushima, S. Kawahara, K. Ota and N. Kamiya, *J. Electrochem. Soc.*, **154**, B153 (2007).

[5] S. Mitsushima, Y. Koizumi, S. Uzuka and K. Ota, *Electrochim. Acta*, **54**, 455 (2008).

[6] S. Kawahara, S. Mitsushima, K. Ota and N. Kamiya, *ECS Trans.*, **3(1)**, 625 (2006).

PEMFC Cathode Catalyst Degradation: Model Study on the Stability and ORR Performance of Pt/C and PtCo/C Electrocatalysts

L.C. Colmenares, Z. Jusys, R.J. Behm, Institute of Surface Chemistry and Catalysis, Ulm University, Germany
M. Lennartz, Umicore – Heterogeneous Catalysts

Alloying of platinum with other transition metals such as Co can improve the oxygen reduction reaction (ORR) activity compared to pure Pt [1-6]. However, the alloyed Pt-based bimetallic catalysts suffer from leaching of non-noble component resulting in changes in the surface composition and a corresponding variation of the ORR performance [7-10]. Therefore, the long-term stability of carbon supported Pt-based cathode catalysts used in polymer electrolyte membrane fuel cells (PEMFCs) for automotive applications is one of most important subjects to be overcome for the commercialization of PEMFCs. Although a fuel cell performance loss is unavoidable, the degradation rate could be minimized based on a better understanding of the underlying mechanisms under relevant operating conditions. The cathode catalyst is exposed to strongly corrosive conditions, which include acidic environment, high O_2 concentration, elevated temperatures and high potentials [11,12]. Under these conditions, the catalyst may loose activity due to a decay of the electrochemical active surface area. This may be caused by a number of different processes such as sintering or migration of the nanoparticles on the carbon support, dissolution of Pt, and corrosion of the carbon support, besides the leaching of the non-noble metal [12]. Depending on the application, the requirements for the fuel cell lifetime vary significantly, ranging from 5000 h for cars to 20000 h for buses and 40000 h of continuous operation in stationary applications [12]. Although the lifetime targets for automobiles are much lower, the cathode catalyst should operate under extremely harsh conditions, such as dynamic cycling under multiple start-up/shut-down cycles [12-15].

Pt-based catalyst – Dissolution of the non-noble metal at cathode operation conditions

The stability of bimetallic Pt electrocatalysts, alloyed with non-noble metal such as Co, is an important issue, which affects the long-term performance of the catalyst. In particular, cathode catalysts which are operating at high potentials where Co leaching could appear. Therefore, the stability of the carbon-supported Pt_3Co (from TKK) catalyst at potentials relevant to cathode operation ($E > 0.5\ V_{RHE}$) was studied and compared with that of a Pt/C catalyst (20 wt. % from E-Tek) as reference. For the evaluation of the potential dependence of the Co dissolution, the potential was cycled (10 cycles at 10 mV s^{-1}) in the supporting electrolyte (0.5 M H_2SO_4) from 0.06 up to 0.5, 0.85 and 1.16 V_{RHE}, respectively.

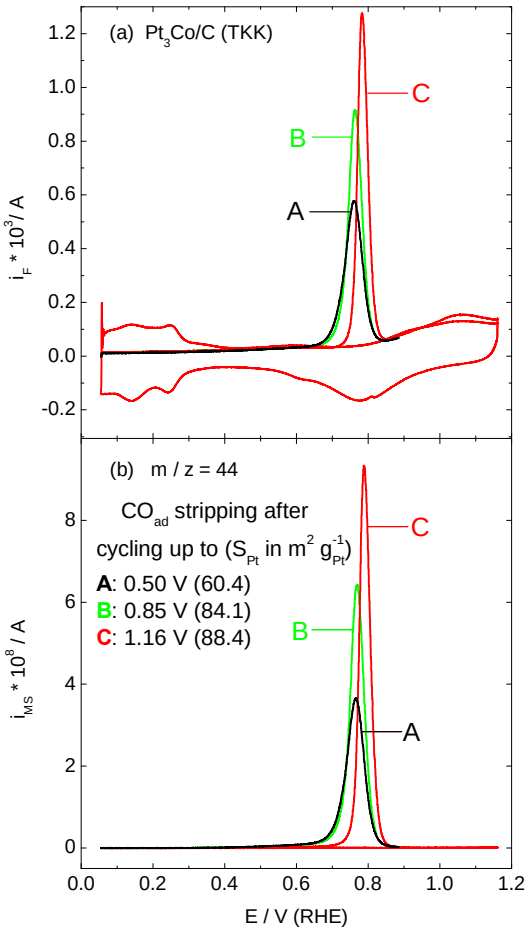

Figure 1: Faradaic (a) and mass spectrometric (b) currents during pre-adsorbed CO_{ad} monolayer strippings on Pt_3Co/C catalyst in 0.5 M H_2SO_4 electrolyte after potential cycling with increasing the upper limit. RT; Pt loading: 70 µg cm^{-2}, Potential scan rate 10 mV s^{-1}, electrolyte flow rate 20 µl s^{-1}.

After each upper potential increment, the active Pt surface area was characterized by pre-adsorbed CO_{ad} monolayer oxidation (CO_{ad} stripping), using a Differential Electrochemical Mass Spectrometry (DEMS) set-up, following simultaneously both the Faradaic current and the mass spectrometric current of CO_2 formation (m/z = 44) [16,17]. Subsequently, a potential cycle was recorded on the CO-free electrode for comparison. The results clearly showed that the active Pt surface area on the Pt_3Co/C catalyst increases when the upper potential is increased to E > 0.5 V_{RHE} (Fig. 1), which can be attributed to the partial dissolution of the non-noble metal from the catalyst surface at high potentials (relevant to cathode operation), resulting in a Pt enrichment with time. In contrast, the active Pt surface on the Pt/C catalyst remained constant after two consecutives CO_{ad} strippings.

Cathode catalyst stability – Accelerated Degradation Test

The resulting change in surface composition, which is especially important for bimetallic catalysts containing a non-noble component, was probed in the ORR activity/selectivity after potential cycling at high scan rate (accelerated degradation test, ADT).

Accelerated degradation testing, as a catalyst aging method for model studies in an electrochemical half-cell, is an attractive alternative for reducing time and costs of the experiment due to the increase in sample throughput, and provides a basis for understanding the origin and mechanism of the fuel cell performance losses. In contrast to real PEMFCs degradation tests, which require prolonged testing periods, ADT tests are relatively fast. In addition, PEMFCs degradation tests are often affected by experimental problems related to catalyst utilization, water management and undefined mass transport conditions.

Catalyst stability and ORR performance as a function of catalyst loading and degradation

In the present study, we have tested the influence of the Pt-loading (70 and 10 μg_{Pt} per geometric surface area) on the relative loss of the active Pt surface area (S_{Pt}) and the ORR activity/selectivity. These issues were investigated on Pt (50 wt. %), heat-treated Pt (50 wt. %) and Pt_3Co carbon supported catalysts. All catalysts were supplied by Umicore AG (Germany). Simulating a dynamic cycling process, the loss of the S_{Pt} (determined by integration of the H-adsorption current after double-layer correction) and the ORR characteristics were investigated by Rotating Ring Disk Electrode (RRDE) measurements.

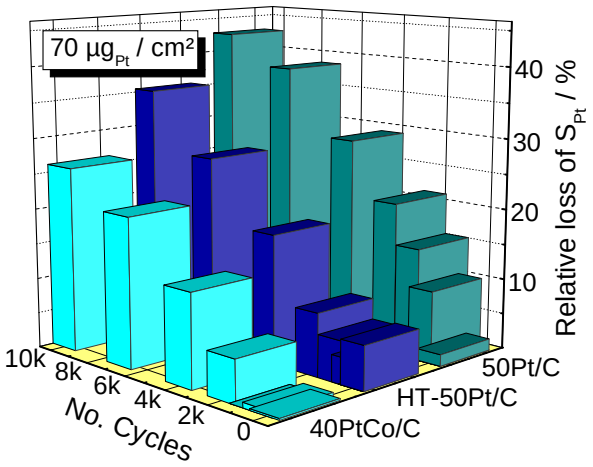

Figure 2: Relative loss of the active Pt surface area as a function of (i) catalyst and (ii) the number of cycles at high potentials (0.5 ↔ 1.1 V_{RHE}). Pt loading: 70 µg cm^{-2}.

ADT treatment consisted of cycling the electrode potential between 0.5 and 1.1 V_{RHE} at 55 °C. After a certain number of cycles, S_{Pt} and the corresponding ORR performance were determined. The mean particle size and particle size distribution for each catalyst were determined before and after the ADT measurements of each specific number of cycles by Transmission Electron Microscopy (TEM) measurements performed at the Institute of Material Science, Technische Universität Darmstadt.

The loss of electrochemical surface area is proportional to the amount of catalyst deposited (or catalyst film thickness), thus the lower the Pt content the higher is the relative loss and vice versa (data not shown). For different catalyst film thicknesses (i.e., Pt loading), the Pt_3Co/C sample always showed less surface area loss than the Pt/C samples. Figure 2

shows the relative S_{Pt} loss for the three catalysts investigated with a Pt loading of 70 μg_{Pt} cm^{-2}.

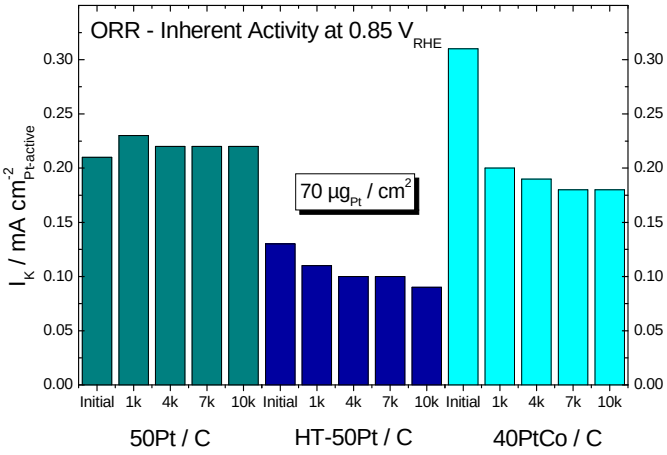

Figure 3: Active Pt surface area normalized ORR kinetic currents at 0.85 V_{RHE} as a function of the catalyst after accelerated degradation test (E cycling: 0.5 ↔ 1.1 V_{RHE}). Potential scan rate: 5 mV s^{-1}. Pt loading: 70 μg_{Pt} cm^{-2}. Temperature: 55 °C. Rotation rate: 1600 rpm.

At high Pt loading, the active Pt surface area normalized ORR kinetic currents showed that the decrease of the S_{Pt} causes negligible changes in the inherent ORR activity (Fig. 3) and selectivity for all tested catalysts. For the low loading Pt catalyst, the Pt particle growth (migration / coalescence; dissolution / agglomeration) results in a significant loss of the electrochemical surface area, accompanied by a reduction of the inherent ORR activity (data not shown) and a significant increases of the hydrogen peroxide production (Fig. 4).

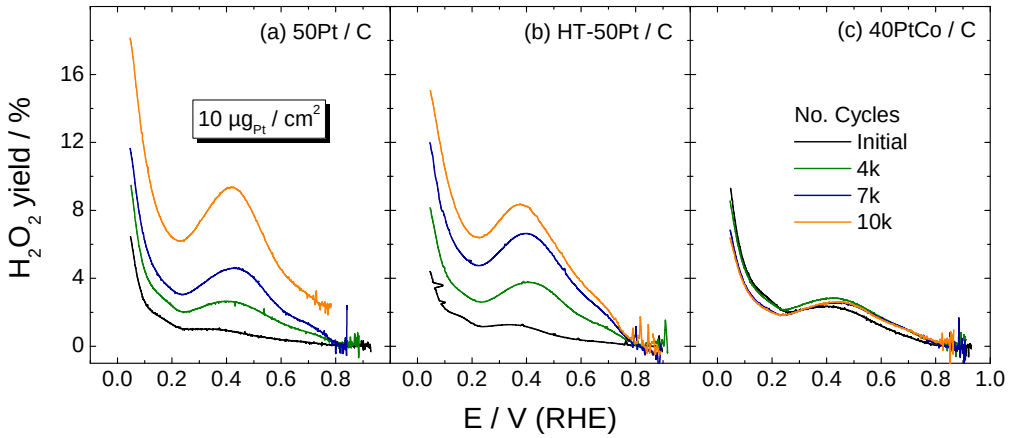

Figure 4: Hydrogen peroxide yields as a function of the applied potential on 50 wt. % Pt/C (a); heat-treated 50 wt. % Pt/C (b) and 40 wt. % Pt in PtCo/C (c) catalysts, after accelerated degradation test. Pt loading: 10 µg per cm^2. Temperature: 55 °C. Rotation rate: 1600 rpm. Potential scan rate: 5 mV s^{-1}.

Here, the long-term degradation of the catalysts layer induces an inhomogeneous Pt distribution. We suggest that this agglomeration increases the H_2O_2 production due to a lower probability of its further reduction to water over Pt-free areas even at potentials relevant for fuel cell cathode operation. The Pt_3Co/C catalyst did not show any significant changes in the H_2O_2 yield at these potentials, although the active surface area decreases considerably as well. Overall, the bimetallic Pt_3Co/C catalyst showed a better long-term stability and less change in the ORR performance than the Pt/C catalysts.

References

[1] S. Mukerjee and S. Srinivasan. *J. Electroanal. Chem.* 357 (1993) 201.

[2] T. Toda, H. Igarashi, H. Uchida, and M. Watanabe. *J. Electrochem. Soc.* 146 (1999) 3750.

[3] U.A. Paulus, A. Wokaun, G.G. Scherer, T.J. Schmidt, V. Stamenkovic, V. Radmilovic, N.M. Markovic, and P.N. Ross. *J. Phys. Chem. B.* 106 (2002) 4181.

[4] V. Stamenkovic, T.J. Schmidt, P.N. Ross, and N. M. Markovic. *J. Phys. Chem. B.* 106 (2002) 11970.

[5] S. Mukerjee and S. Srinivasan, in "*Handbook of Fuel Cells – Fundamental Technology and Applications*", W. Vielstich, A. Lamm, H.A. Gasteiger, (Eds.), Wiley, Chichester, Vol. 2 (2003).

[6] D. Thompsett, in "*Handbook of Fuel Cells – Fundamental Technology and Applications*", W. Vielstich, A. Lamm, H.A. Gasteiger, (Eds.), Wiley, Chichester, Vol. 2 (2003).

[7] M.T. Paffet, J.G. Beery, S. Gottesfeld. *J. Electrochem. Soc.* 135 (1988) 1431.

[8] M. Watanabe, K. Tsurumi, T. Mizukami, T. Nakamura, P. Stonehart. *J.Electrochem. Soc.* 141 (1994) 2659.

[9] T. Toda, H. Igarashi, H. Uchida, and M. Watanabe, *J. Electrochem. Soc*. 145 (1998) 4185.

[10] V.R. Stamenkovic, B.S. Mun, K.J.J. Mayrhofer, P.N. Ross, and N.M. Markovic. J*. Am. Chem. Soc*. 128 (2006) 8813.

[11] L.M. Roen, C.H. Paik, and T.D. Jarvi. *Electrochem. Solid-State Lett.* 7 (2004) A19.

[12] Polymer Electrolyte Fuel Cell Durability. F.N. Büchi, M. Inaba, and T.J. Schmidt, Editors, Springer Science+Business Media (2009).

[13] H.A. Gasteiger, S.S. Kocha, B. Sompalli, and F.T. Wagner. *Appl. Catal. B: Env.* 56 (2005) 9.

[14] P.J. Ferreira, G.J. la O', Y. Shao-Horn, D. Morgan, R. Makharia, S. Kocha and H.A. Gasteiger, *J. Electrochem. Soc.* 152 (2005) A2256.

[15] R. Makharia, S.S. Kocha, P.T. Yu, M.A. Sweikart, W. Gu, F.T. Wagner, H.A. Gasteiger. ECS Transactions, 1 (2006) 3.

[16] Z. Jusys, H. Massong, and H. Baltruschat, J. Electrochem. Soc. 146 (1999) 1093.

[17] Z. Jusys, J. Kaiser, and R.J. Behm, Phys. Chem. Chem. Phys. 3 (2001) 4650.

Fuel Starvation: Irreversible Degradation Mechanisms in PEM Fuel Cells

C.M. Rangel*, R.A. Silva, M.A.Travassos, T.I. Paiva, V.R. Fernandes, LNEG, National Laboratory for Energy and Geology, UPCH Fuel Cells and Hydrogen Unit, Paço do Lumiar, 22 1649-038 Lisboa, Portugal

Abstract

PEM fuel cell operates under very aggressive conditions in both anode and cathode. Failure modes and mechanism in PEM fuel cells include those related to thermal, chemical or mechanical issues that may constrain stability, power and lifetime. In this work, the case of fuel starvation is examined. The anode potential may rise to levels compatible with the oxidization of water. If water is not available, oxidation of the carbon support will accelerate catalyst sintering. Diagnostics methods used for in-situ and ex-situ analysis of PEM fuel cells are selected in order to better categorize irreversible changes of the cell. Electrochemical Impedance Spectroscopy (EIS) is found instrumental in the identification of fuel cell flooding conditions and membrane dehydration associated to mass transport limitations / reactant starvation and protonic conductivity decrease, respectively. Furthermore, it indicates that water electrolysis might happen at the anode. Cross sections of the membrane catalyst and gas diffusion layers examined by scanning electron microscopy indicate electrode thickness reduction as a result of reactions taking place during hydrogen starvation. Catalyst particles are found to migrate outwards and located on carbon backings. Membrane degradation in fuel cell environment is analyzed in terms of the mechanism for fluoride release which is considered an early predictor of membrane degradation.

1 Introduction

The mechanisms of fuel cell degradation are characterised by irreversible changes in the kinetic and transport properties of the cell and presently are not well understood [1-5]. PEM fuel cell operates under very aggressive conditions in both anode and cathode, typically at pH < 1 and with significant levels of water in vapour and liquid phase at temperatures between 60 and 80 °C. Anode catalysts are exposed to a strong reducing H_2 atmosphere whilst the cathode is under strongly oxidizing conditions (high O_2 concentrations and potentials > 0.6 V vs. SHE. Corrosion of both Pt/C catalysts components (catalytic metal and support material) becomes an issue in PEM fuel cells.

Fuel starvation, inadequate fuel supply at the anode, affects the MEA in an irreversible way. Hydrogen is no longer available in sufficient amounts so that the demanded current can be maintained, in this way the anode potential will increase to levels where water electrolysis is possible at the anode ($E^0_{25°C}$ = + 1.23 V vs. SHE).

$$\text{Anode:} \quad 2\,H_2O \rightarrow O_2 + 4\,H^+ + 4\,e^- \qquad (1)$$

* Corresponding author, email: carmen.rangel@lneg.pt

Cathode: $O_2 + 4\ H^+ + 4\ e^- \rightarrow 2\ H_2O$ (2)

For even higher potentials, the carbon in the anode catalyst (Pt/C) will be oxidized in the presence of platinum. Electrochemical oxidation of the carbon is thermodynamically possible above 0.2 V vs. SHE according to reaction (3) providing a supply of protons to support current demand [6].

$C + 2\ H_2O \rightarrow CO_2 + 4\ H^+ + 4\ e^-$ 0.207 V vs. SHE (3)

Oxidation of carbon to carbon monoxide (4) is thermodynamically not favoured according to reaction (5):

$C + H_2O \rightarrow CO + 2\ H^+ + 2\ e^-$ 0.518 V vs. SHE (4)

$CO + H_2O \rightarrow CO_2 + 2\ H^+ + 2\ e^-$ -0.103 V vs. SHE (5)

The reaction affects not only the carbon present in the catalyst but also other carbon components such as the backing layers and eventually the flow field plates [7], leading to a reduction of the carbon content in the catalyst layer with time. As carbon is corroded away, noble metal nanoparticles will be lost from the catalyst layer and migrate to the polymer electrolyte interface or aggregated into larger particles.

In this work, failure modes and mechanism of the membrane-electrode-assembly (MEA) in low power PEM fuel cells are studied stressing the issues that may constrain stability, power and lifetime. Diagnostics methods and tools used include in-situ and ex-situ analysis in order to better categorize irreversible changes in the kinetic and/or transport properties of the cell after fuel cell ageing in extreme testing conditions will be discussed.

2 Experimental

Electrochemical techniques were used in combination with structural and chemical analysis to correlate the performance of the cell with the material properties of the various components and their ageing. Polarization curves were conducted, using a purpose built PEM test station, on a low power PEM fuel cell that uses own designed flow field plates integrated in a series configuration, and a cathode that allows feeding with air, cooling and water removal (a low power consumption air fan in the edge of the cathode manifolds was used providing an excess air stoichiometry condition). Hydrogen was supplied at a pressure of 0.2 bar. Electrochemical impedance spectra were ran using H_2/O_2 (air) gas feeding. A Frequency Response Analyser (model 1250, Solartron) connected to an Electrochemical Interface (model 1286, Solartron) was used to obtain impedance spectra covering a suitable range of frequencies for fuel cell processes.

Post mortem analysis of materials and components degradation, required to enhance understanding of these processes, was undertaken. After cell dismantling, cross sections of MEA samples were observed for morphological and elemental analysis using a Phillips

Scanning Electron Microscope, Model XL 30 FEG, coupled to EDS allowing elemental mapping.

Tests were conducted on 8, 16 and 25 cell stacks. The stack uses an open cathode and own-designed bipolar graphite plates. A low-power consumption air fan in the edge of the cathode manifolds was used, for combined high stoichiometric oxidant supply and stack cooling purposes. After fuel cell ageing in extreme testing conditions by applying a series of pre-defined load cycles, the stack was dismantled and MEAs were analysed. Load duty cycles included open circuit, constant current and full polarization curves in a step by step fashion.

3 Results

8 cell PEM stack

Polarization curves of the fuel cell before and after 1500 h of operation revealed that the maximum power that may be demanded from the fuel cell was reduced in 34%. The polarization curve obtained after cell activation exhibited maximum current densities over 1000 $mAcm^{-2}$. Data were obtained at 500 mbar H_2 relative pressure, room temperature with the air flow rate of 7.56 $Lmin^{-1}$ in a range of currents which varied from nearly zero (near the open circuit potential) to 3 A. The degradation in performance after 1500 h of operation was evident in the activation, ohmic and mass transfer regions of the polarization curve.

The stack degradation analysis comprises observation of catalytic surface layers and MEA cross sections. In the eight cell stack, cells were numbered from 1 to 8 starting from the cell located at hydrogen entry. Surface area seems to be lost with cycling; this was particularly evident for C8.

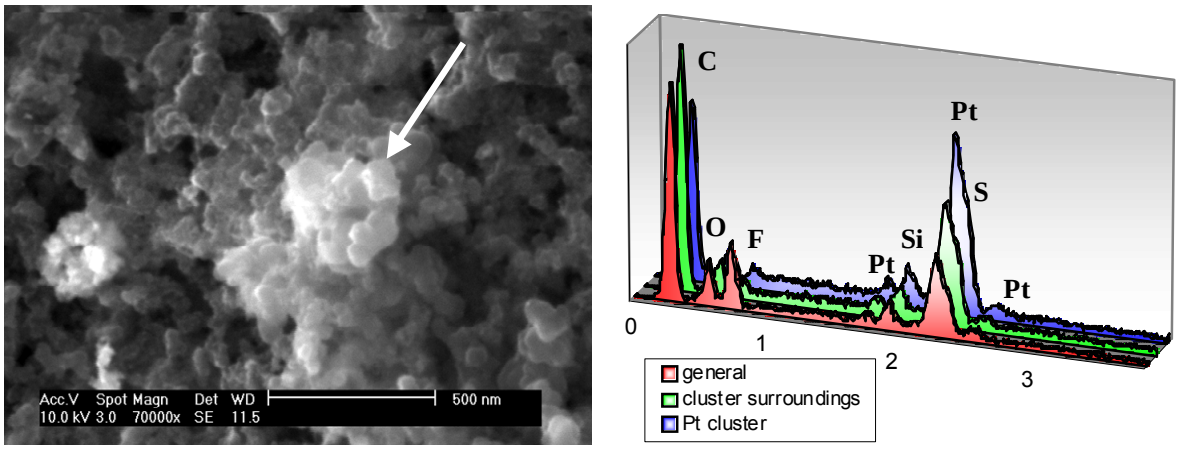

Figure 1: Typical Pt cluster on anodic catalytic layer of C8, as observed by SEM and respective.

Platinum clusterization**,** which is evident in Figure 1a), was also found. EDS analysis was performed on clustered areas, which were shown to be platinum rich. The results obtained on the Pt cluster and its surroundings are presented in figure 1b). A spectra of an area where clusters were not observed is included for comparison. Other degradation features were found upon analysis of the low power PEM fuel cell stack examined in this work after 1500 h

of operation: chemical contamination (Si from piping and sealing gaskets) and debris GDL, electrode thickness variations, cracking and delamination, Pt and F migration; all of which contribute to gradual decrease of output voltage of the stack influencing performance and durability.

16 cell PEM stack

When increasing the number of cells in the stack by 2 regarding the previous situation, polarity reversal was observed in the last cell. While on fixed load, the cell potential values were individually measured showing a dependency on cell position in the stack. Lower values are reported for the farthest cells from hydrogen entry. The potentials values vary from 0.653 V down to 0.492 V, Figure 2a), with the lowest values associated to cells 15 and 16. With continuous operation using a reduced hydrogen flow, an inversion of polarity was observed in the 16th cell of the stack, evident in the potential vs. time plot in Figure 2b), as a result of insufficient hydrogen to reach the last cells. When the incursion into the negative potential values is not to accentuated the phenomenon is partially reversible. Once the phenomenon was made irreversible, the cell was dismantled in order to observe the degradation of the MEA under SEM. The cells images revealed the presence of morphological defects associated to fuel starvation.

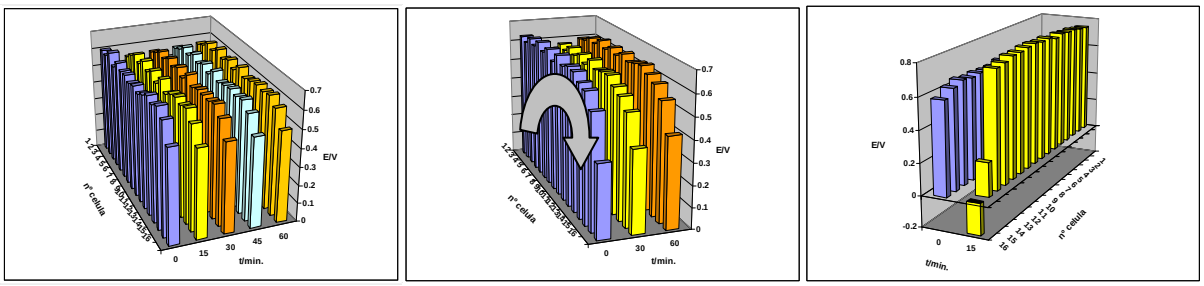

(a) (b) (c)

Figure 2: Cell potential *versus* time for a 15 W fuel cell stack of 16 cells. Data are referred to one hour operation, with measurements every 15 minutes (a); Cell polarity reversal in cell 16th was observed(b); Potential distribution after the full flux of hydrogen was replenished (c). The SEM observations of cross sections were accompanied by EDS mapping for Pt, S and F, corresponding to the 16th cell. The images show delamination at the anode and a striking difference of thickness when compared to the cathode catalyst layer (C), see Figure 3.

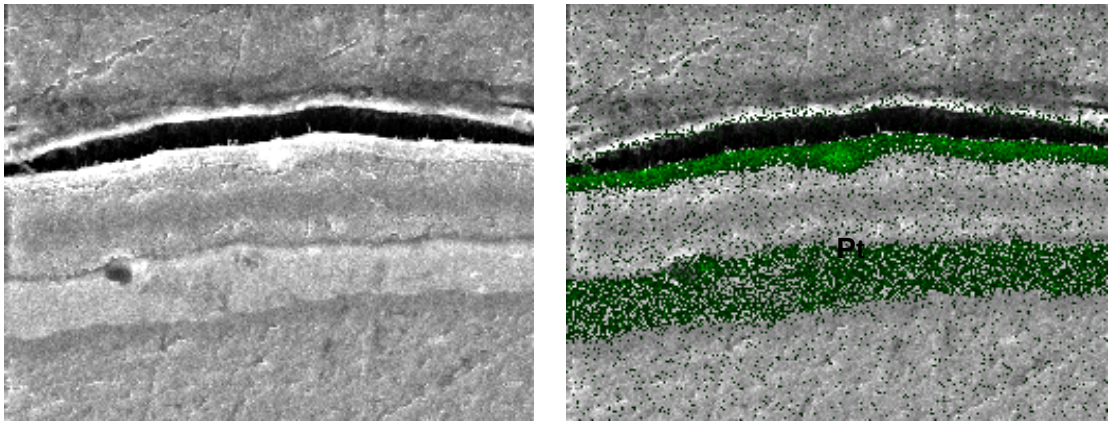

Figure 3: SEM image of cross section of the 16th MEA of the stack showing delamination and elemental mapping for Pt; A = anode, C = cathode and M = membrane (b).

Impedance data, not shown here, were instrumental in identifying membrane resistance increases and transport limitations in affected cells.

25 cell PEM stack

Figure 4 shows that the thickness of the anodic layer of a 25 cell stack is dramatically reduced due to polarity reversal, for the last cells of the stack while the cathode´s is maintained.

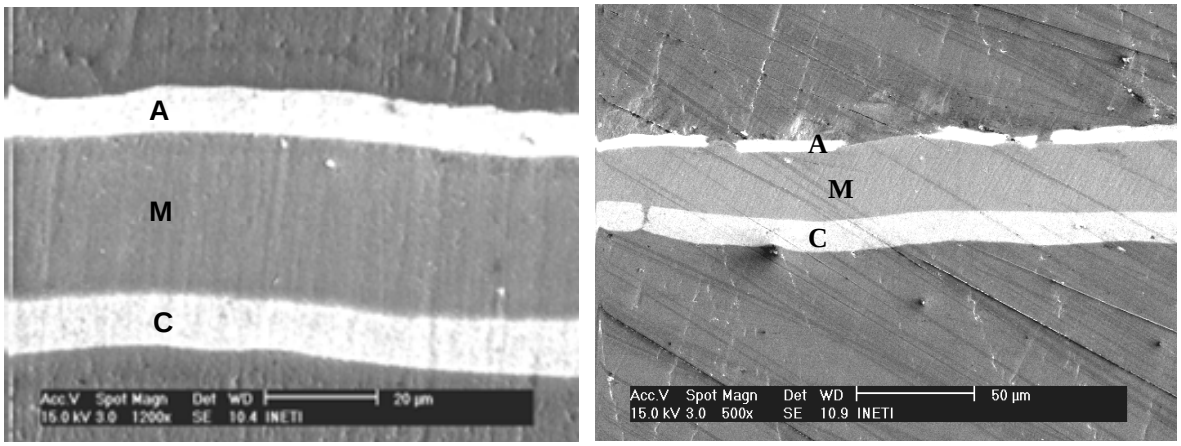

Figure 4: SEM cross section view of the 23rd MEA of a 25 cell stack. Reduction of thickness at anode.

4 Final Remarks

The reduced flow of hydrogen in the fuel stack caused the reversal of polarity of the cells with consequent deterioration of the properties of the stack. Last cells were always affected. Morphological aspects reveal deterioration of peripheral cells with emergence of delamination and varying the thickness of the catalyst layers anodic and cathodic. Furthermore, carbon corrosion and fluoride depletion in the membrane are suggested.

References

[1] Z. Luo, D. Li, H. Tang, M. Pan, R. Ruan, Degradation behavior of membrane-electrode-assembly materials in 10-cell PEMFC stack, *Int. J. Hydrogen Energy* 31 (2006) 1831-1837.

[2] C.M. Rangel, R.A.Silva, T.I.Paiva. PEM Fuel Cells: Materials Ageing Mechanisms and Performance Impact, *J. New Materials for Electroch. Systems* 12 (2009) 119-122.

[3] F. Maillard, M. Chatenet. Ageing Mechanisms of Pt/C Nanoparticles in a PEMFC. Fundamentals and Developments of Fuel Cell Conference 2008, Nancy, France, 2008.

[4] S. Kunda, M. W. Fowler, L. C. Simon, S. Grot. Morphological features (defects) in fuel cell membrane electrode assemblies. *J. Power Sources*, 157, 650 (2006).

[5] S.Kundu, L.C. Simon, M.W Fowler, Polym. Degrad. Stab., 93 (2008) 214-224.

[6] Y.S.-Horn, W. C. Sheng, S. Chen, P. J. Ferreira, E. F. Holby and D. Morgan; Top Catal 46(2007)285305.

[7] W. Schmittinger and A. Vahidi; J. Power Sources 180 (2008) 1–14.

Origin of Diffusion Impedance at the Cathode of a Proton Exchange Membrane Fuel Cell

J. Mainka, G. Maranzana, J. Dillet, S. Didierjean, O. Lottin, LEMTA, Nancy University – CNRS, Nancy, France

Applied to Proton Exchange Membrane Fuel Cell (PEMFC), Electrochemical Impedance Spectroscopy (EIS) allows mainly the identification of the origin of potential losses. However, it can also be used to investigate the electrical properties of the fuel cell components, materials and interfaces, as well as the dependence of their performance on the operating conditions. As far as the diffusion impedance is concerned, one of the most common expressions is that of the finite Warburg element. It is based on simple assumptions: Fick's diffusion of oxygen, surface reaction, and a constant concentration at the gas channel boundary of the diffusion medium. However, as shown experimentally by Schneider et al. [1, 2], the consumption of oxygen along the air channel has a significant influence on the impedance values. Therefore, in order to improve the description of mass transfer, a decreasing oxygen concentration profile along the gas channel can be used as an alternative boundary condition, which leads to a slightly modified expression of the diffusion impedance. Then, starting from experimental spectra, it is possible to identify the impedances appearing in the fuel cell equivalent circuit and consequently, the mass transfer parameters at the cathode (effective diffusion coefficient and equivalent thickness). The values obtained with the usual expression of the Warburg impedance and with that taking account oxygen depletion can be significantly different [3].

1 Electrode Description

The Membrane-Electrode Assemblies (MEA) of PEMFC are complex composite systems made of various media with different physical properties. Thus, a well-adapted geometrical description of their structure is necessary to complete the physico-chemical description of mass transfer and reaction kinetics, all the more so since the limiting layer(s) in term of oxygen diffusion has (have) not been clearly identified yet. There exist different structural models of the electrodes in the literature, like agglomerate models [4-6] where the solid phase is a homogeneous mixture of catalyst (Pt), carbon powder and (possibly) polymer electrolyte forming either cylindrical [7-8] or spherical [9-13] particles. Actually, two descriptions of the solid phase coexist in the literature. In the first case, the agglomerate consists in a mixture of carbon, Pt and electrolyte [4, 7]. The second case corresponds to the description first proposed by Springer [5] and Raistrick [6] where the agglomerate is a mixture of carbon powder and catalyst particles only whereas the electrolyte is assumed to cover the surface of the pores. The catalytic sites are at the interface between the electrolyte and the agglomerates, which corresponds to a surface description of the active layer. Before accessing the active layer, oxygen passes successively through the GDL, through the pores of the electrode, and finally through the thin electrolyte layer coating the carbon and platinum agglomerate. This description is chosen for the interpretation of the impedance spectra.

Since the cathode is the place of water production, the ionic resistance of the well-hydrated polymer can be neglected. The other main hypotheses of the one-dimensional mass transfer model are: the fuel cell is isotherm and isobar, ohmic drops in the active layer and in the GDL are neglected, mass transfer of O_2 and H_2O is assumed to occur only by diffusion in the pores of the active layer and the GDL, water diffusion through the solid phase of the active layer is not considered.

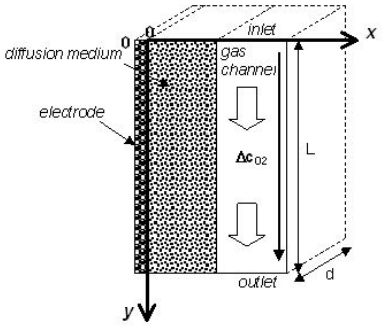

Figure 1: Schematic representation of the pseudo-2D diffusion model. Oxygen concentration variation occurs in the channel between y = 0 and y = L. Oxygen diffusion is considered only in the x-direction, perpendicularly to the electrode surface. The electrode surface is given by *L* × *d*.

In order to take into account the variation in oxygen concentration along the gas channel in the pseudo-2D model (*Figure 1*), three more hypotheses are made: mass transfer resistance in the gas channel is neglected, time variations of the oxygen concentration in the channel are neglected, the Tafel slope *b* is constant between the inlet and the outlet of the air channel.

The faradaic current density $j_f(y)$ and the oxygen concentration $c_{O2}(x,y)$ vary as functions of the y coordinate (Figure 1). *J* is the cell average current density:

$$J = \frac{I}{Ld} = \frac{1}{L}\int_0^L j_f(y)\,dy$$

For convenience, we consider the absolute value of the activation overpotential and the faradaic current density at the cathode: $j_f(y), \eta_{act} > 0$. φ_{O_2} and φ_{H_2O} denote the fluxes in the y direction (in the air channel, in *Mol/s*) while N_{H_2O} and N_{O_2} denote the flux densities in the x direction (in the gas diffusion layer, in *Mol/s/m²*). The molar fluxes of oxygen φ_{O_2} and water φ_{H_2O} in the channel depend also on their y-position. Thus, the molar flux of oxygen $\varphi_{O_2}(y)$ corresponds to that at the inlet of the gas channel minus the amount consumed at the cathode:

$$\varphi_{O2}(y) = \varphi_{02}^{in} - \frac{d\int_0^y j_f(y)\,dy}{4F}$$

Mass transfer along the x direction is assumed to occur only by diffusion, which means that the global molar flux density in x direction $N_{H_2O} + N_{O_2}$ has to be null (Figure 1). This is a particular case that happens when only half of the water produced at the cathode is evacuated toward the air channel ($N_{H_2O} = j_f(y)/4F$), which compensates for the oxygen flux N_{O_2} in the opposite direction[1]. The other half of water produced by the fuel cell as well as the molecules flowing from anode to cathode under the effect of the electro-osmotic drag must diffuse through the membrane under the effect of a concentration gradient. The water flux along the gas channel φ_{H_2O} (in the *y* direction) is a function of *y*, given by:

$$\varphi_{H20}(y) = \varphi_{H20}^{in} + \frac{d\int_0^y j_f(y)dy}{4F}$$

The oxygen molar ratio along the GDL/gas channel interface $(x = \delta)$ is given by:

$$c_{02}(x = \delta, y) = \frac{S_{02} - \frac{d\int_0^y j_f dy}{I}}{S_{02}(1+H)} c_{02}^0$$

Where $S_{02} = \frac{\varphi_{02}^{in}}{I/4F}$ is the oxygen stoichiometric ratio, $H = \frac{\varphi_{H20}^{in}}{\varphi_{02}^{in} + \varphi_{N2}}$ is the absolute inlet humidity and $c_{O2}^0 = \frac{P}{5RT}$ is the inlet concentration of oxygen in dry air.

Strictly speaking, mass transport of oxygen through the pores of the diffusion media in a PEMFC is described by Stefan-Maxwell equations. However, since the binary diffusion coefficients of O_2/H_2O and O_2/N_2 are close to each other, it seems reasonable to use Fick's 1st law. Assuming that the electrochemical reaction takes place only at the active layer/membrane interface (*x = 0*), the 1st Fick's law can be written:

$$N_{O2}(y) = -D_{eff} \left.\frac{\partial c_{O2}}{\partial x}\right|_{\substack{x=0 \\ y}}$$

The diffusion media being porous, it is necessary to use an effective diffusion coefficient D_{eff} taking into account their porosity *ε* and possibly, the presence of Knudsen diffusion. The most common expressions obey Archie's law [14]: $D_{eff} = D\varepsilon^m$, where *m* is an exponent varying between 1.5 and 4. In the case of a *3D* medium, there is a wide consensus for using *m = 3/2*, which corresponds to the differential effective medium approximation introduced by

[1] Note that the question of the validity of the Warburg diffusion impedance in PEM fuel cells does not seem to have been fully addressed yet considering that these operating conditions are not common: the water net drag coefficient can differ significantly from 0.5.

Bruggeman [14-15]. *m = 3/2* is probably appropriate for the active layers, in which the orientation of the solid phase does not follow a privileged direction. In the gas diffusion layers however, the solid phase can be considered as two-dimensional since the carbon fibres are mainly parallel to the electrodes. In this case, the result of the differential effective medium theory is *m = 2* [15]. Knudsen diffusion must be considered in the active layers only, using for instance the Bosanquet formula $\frac{1}{D} = \frac{1}{D_{mol}} + \frac{1}{D^K}$, with $D_i^K = \frac{1}{3} d_{pore} \sqrt{\frac{8RT}{\pi M_i}}$.

Adding a small sinusoidal perturbation $\Delta j_f(y,t)$ to the mean (*DC*) current density $\langle j_f(y) \rangle_t$ makes the oxygen concentration $c_{O2}(x,y,t)$ fluctuating around its steady-state value $\langle c_{02}(x=\delta,y) \rangle_t$ with the same frequency. Solving the diffusion equations with the right boundary conditions allows to express the diffusion impedance as a function of *y*:

$$Z^{2D}_{c02}(y) = R_d^{2D} \frac{\tanh\left(\sqrt{iw\tau_d}\right)}{\sqrt{iw\tau_d}} \text{ with } R_d^{2D} = \frac{b\delta}{4FD_{eff}\langle c_{02}(x=0,y)\rangle_t} \text{ and } \tau_d = \frac{\delta^2}{D_{eff}}.$$

The expression of the pseudo-2D diffusion impedance is close to that of the finite Warburg element. It can be used in the usual Randles equivalent circuit [16] of a whole fuel cell (Figure 2).

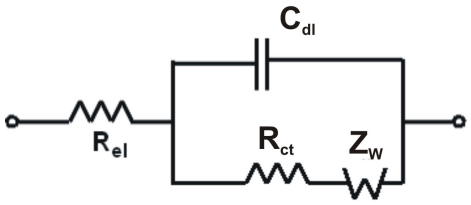

Figure 2: MEA equivalent electrical circuit according to Randles [16].

2 Experimental Setup

The measurements are carried out with a single cell where the current collection is segmented on the cathode side thanks to a set of *18* gold plated brass strips spaced at intervals of *1 mm* (Figure 3). This design makes it possible to perform locally resolved impedance spectroscopy. The current collectors are embedded in a PMMA plate and they delimit a serpentine air channel (of section *0.7 x 1.0 mm²*) on the cathode side of the cell. The hydrogen channel is symmetric to the air channel. The GDL is a *190 µm* thick carbon fibre paper (*Toray™ TGP-H-060*) with a no-compressed porosity $\varepsilon = 0.78$. The MEA (of active area *A = 7.87 cm²*) consists of a PFSA polymer membrane of thickness $\delta_m = 30\ \mu m$ and catalytic layers ($\delta_{cat} \approx 10\ \mu m$) with an average Pt loading of *0.406 mg cm⁻²* at the anode and *0.385 mg cm⁻²* at the cathode. The fuel cell is fed in co and counter-flow (at *1 atm*) by dry hydrogen with a stoichiometric ratio $S_{H2} = 1.2$ and by humidified air with a stoichiometric ratio $S_{air} = 3$. The air is humidified up to about *74 % RH*. All impedance measurements are performed in galvanostatic mode in a frequency range of *0.4 Hz* to *200 Hz* with a peak-to-peak sinusoidal perturbation of *5 %* of the cell current intensity. Global and local impedance

measurements are performed using a passive electronic circuit where each of the 18 brass strips is connected to a *10 m*Ω shunt resistance.

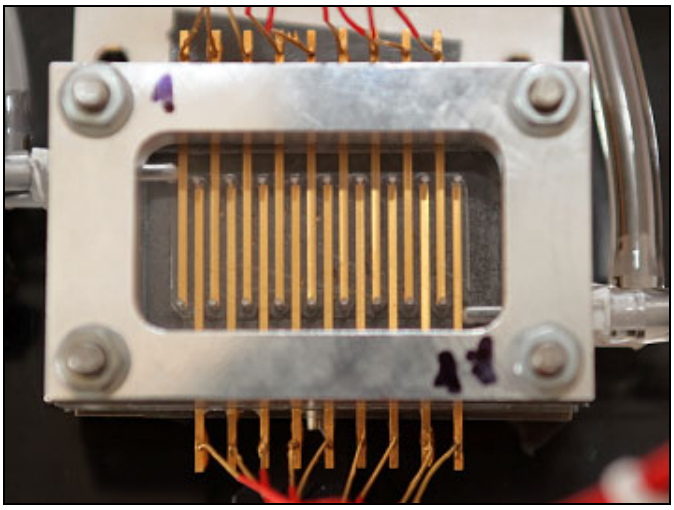

Figure 3: Instrumented cell.

3 Experimental Results

All the results presented below were obtained in identical conditions with a current density fixed to 0.5 Acm^{-2}. Figure 4 shows the local impedance spectra obtained for a gas supply in co-flow (left) and counter-flow (right). The air inlet corresponds to the first segment. In both cases, a second low frequency loop appears progressively along the air channel. This could lead to the conclusion that mass transfer in the GDL or in the active layer becomes limiting but a more detailed analysis carried out after identification of the impedance parameters is necessary. Figure 5 shows the profiles of the diffusion impedance parameters (R_d^{2D}, τ_d) identified starting from the Randles equivalent circuit (Figure 2).

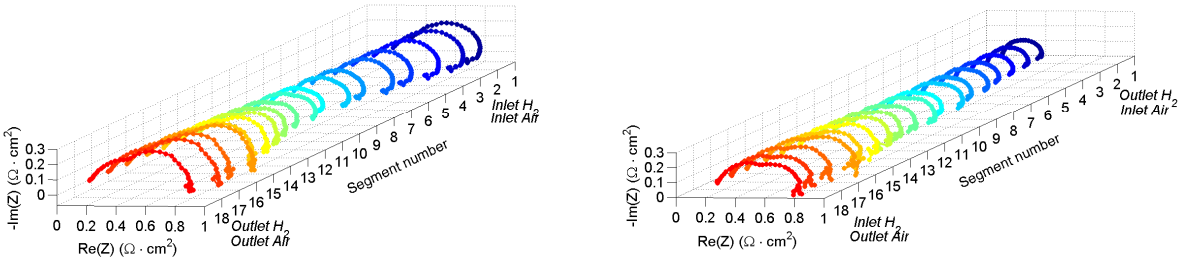

Figure 4: Local impedance spectra in co-flow (left) and counter-flow (right).

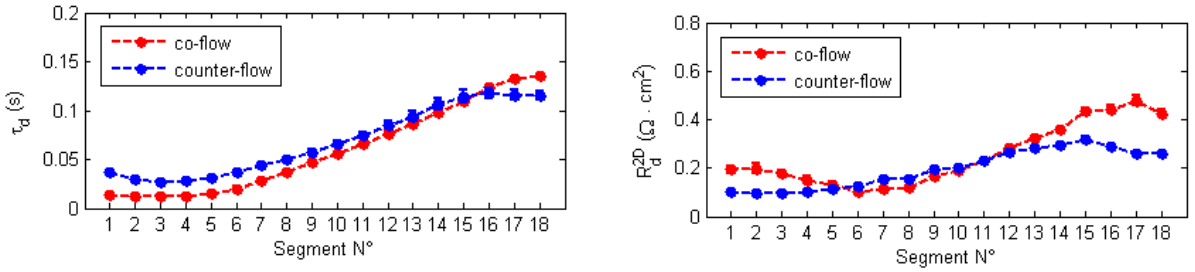

Figure 5: Profiles of the characteristic diffusion time τ_d and the diffusion resistance R_d^{2D}.

The diffusion time τ_d (Figure 5, left) increases progressively along the air channel in co-flow and counter-flow modes. At the air inlet, τ_d is slightly larger in counter-flow than in co-flow, whereas at the channel outlet, the opposite is observed. This difference could be interpreted in term of water content, the air channel inlet being less humidified in co-flow whereas the amount of water is more important near the outlet. The comparison of the profiles of the diffusion resistance R_d^{2D} (Figure 5, right) leads to the similar conclusion but the highest value observed near the air channel inlet in co-flow remains more difficult to explain: one possible interpretation could be that dry conditions reduce oxygen diffusion in the thin electrolyte layer that covers the active sites. However, these tentative conclusions require confirmation.

The values of the diffusion length δ, the effective diffusivity D_{eff}, and the porosity ε can be derived from R_d^{2D} and τ_d. Their profiles are plotted in Figure 6.

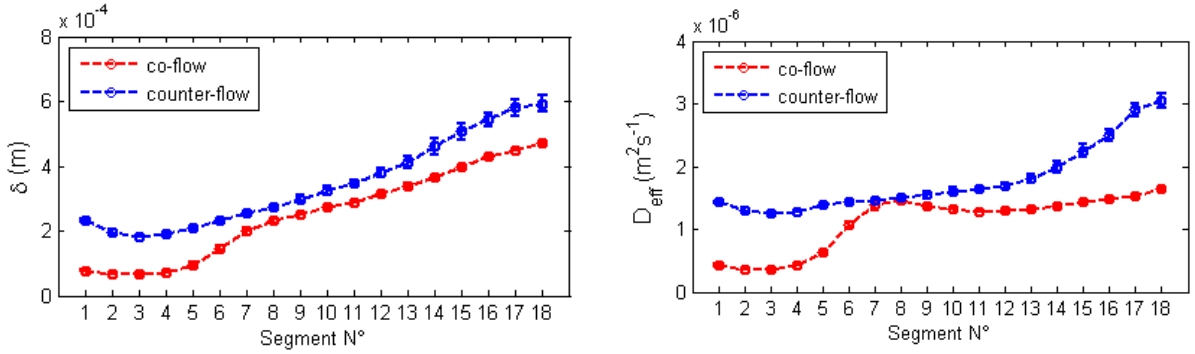

Figure 6: Profiles of the diffusion thickness δ and the effective diffusivity D_{eff} along the air channel.

The diffusion length δ (Figure 6, left) increases continuously along the air channel on co-flow and counter-flow modes but with lower values in the first case. This does not allow any conclusion about the local water content. δ ranges from *77 µm* to *593 µm*, which is far above the typical thickness of catalyst layers (≈ *10 µm*). This suggests that at the limiting media for mass transfer is rather the GDL ($\delta_{GDL} = 190\,\mu m$) but there could be many reasons for the increase in δ along the air channel: 2D diffusion in the GDL below the current collectors, or mass transfer resistance or propagation of the oscillations of oxygen concentration in the channel [1, 2]. As far as the profile of the effective diffusion coefficient is concerned

(Figure 6, right), the increase observed along the air channel seems to be in contradiction with a possible accumulation of liquid water in the pores of the gas diffusion or active layer. However, this increase could also be explained by phenomena occurring upstream in the channel. The numerical values of D_{eff} suggest that if the limiting media were the GDL only or the active layer only, their effective porosity (accounting for the presence of liquid water) would be comprised between 0.2 and 0.6, and 0.2 and 0.35, respectively. Once again, these values do not allow to discriminate between the contribution of the gas diffusion layer and of the active layer to the impedance diffusion. However, the diffusion does not seem to take place in liquid phase, which would yield diffusivities of about $D_{eff} \approx 10^{-11} m^2 s^{-1}$.

4 Conclusion

EIS is frequently used to investigate the origin of the mass transfer impedance in cathode gas diffusion and active layers. However, the expression of a finite Warburg element used for analysing impedance spectra is obtained assuming that the oxygen concentration at the gas channel/gas diffusion layer interface is constant. This hypothesis is much constraining when the gas stoichiometry is low, and it could lead to wrong estimates of mass transfer parameters characterising the diffusion media. An alternative to this expression is proposed: considering gas consumption along the gas channel, which allows furthermore to investigate variations in local impedance spectra and in the diffusion kinetics along the air channel. In this paper, we presented some preliminary results identified from local impedance spectra. They show that oxygen transfer takes place in gaseous phase but they do not allow to discriminate between the contribution of the gas diffusion layer and of the active layer to the impedance diffusion. Furthermore, high values of the diffusion thickness were observed (up to about 3 times the actual GDL thickness). This could be explained either by gas diffusion below the channel rib or by oscillations of the oxygen concentration upstream in the air channel.

References

[1] I.A. Schneider, S.A. Freunberger, D. Kramer, A. Wokaun and G.G. Scherer, J. Electrochem. Society 154 (2007) B383-B388.

[2] I.A. Schneider, D. Kramer, A. Wokaun and G.G. Scherer, J. Electrochem. Society 154 (2007) B770-B782.

[3] J. Mainka, G. Maranzana, J. Dillet, S. Didierjean, O. Lottin, ECS Transactions, Analytical Electrochemistry (General), Volume 19, October 2009.

[4] F. Gloaguen, P. Convert, S. Gamburzev, O. A. Velev and S. Srinivasan, Electrochimica Acta 43 (1998) 3767-3772.

[5] T. E. Springer, I. D. Raistrick, J. Electrochemical Soc. 136 (1989)1594-1603.

[6] I. D. Raistrick, Electrochimica Acta 35 (1990) 1579-1585.

[7] J. Ramousse, J. Deseure, O. Lottin, S. Didierjean, D. Maillet, J. Pow. Sources 145 (2005) 416-427.

[8] M. Bautista, Y. Bultel, P. Ozil, I. Chem. Eng. 82 (2004) 907-917.

[9] N. P. Siegel, M.W. Ellis, D.J. Nelson, M.R. von Spakovsky, J. Pow. Sources 115 (2003) 81-89.

[10] S.J. Lee, S. Mukerjee, J. McBreen, Y.W. Rho, Y.T. Kho, T.H. Lee, Electrochimica Acta, 43 (24) (1998) 3693-3701.

[11] W. Sun, B.A. Peppley, K. Karan, Electrochimica Acta, 50 (2005) 3359-3374.

[12] F. Jaouen, G. Lindbergh, K. Wiezell, J. Electrochemical Soc. 150 (2003) A1711-A1717.

[13] K. Broka, P. Ekdunge, J. App. Electrochemistry, 27(2) (1997) 117–123.

[14] S. Torquato, Random Heterogeneous Materials: Microstructure and Macroscopic Properties, Springer (2002).

[15] H. C. Bruggeman, Berechnung verschiedener Physikalischer Konstanten von heterogenen Substanzen, Ann. Physik (Leipzig) 24, 636-679 (1935).

[16] J.E.B. Randles, Discuss. Faraday Soc., 1, 11 (1947).

Investigating the Impact of Liquid Water in a PEFC by Electrochemical Impedance Spectroscopy

Dietmar Gerteisen, Robert Alink, Fraunhofer Institute for Solar Energy Systems, Germany

1 Introduction

One challenge of a PEFC system is to avoid dehydration of the polymer membrane to ensure a proper protonic conductivity which forces the operating temperature to be below 100°C. This temperature limit dictates the operation of the fuel cell in the range where water also exists in liquid phase. Liquid water in the gas diffusion media and electrode causes mass transport limitations of the reactants, especially at high current densities. Thus, water accumulation has to be avoided. It is reported from many research groups that a micro porous layer (MPL), that is a layer of carbon particles impregnated with PTFE attached to the GDL, improves fuel cell performance [1,2]. The role of the MPL with regard to water transport is discussed contrary in the literature.

Several explanations are given for the measured performance enhancement. For example, Pasaogullari et al. [3] indicated that the MPL enhances the rate of water removal from the catalyst layer (CL) to the cathode gas diffusion layer (GDL), whereas other explanations base on measurements that reveal an increased back diffusion rate of water towards the anode side caused by a water barrier effect of the cathode MPL. Lower electrical contact and thermal resistance is also reported when using a MPL which strongly influences the temperature distribution within the cell and thus also the water management. To get a clearer picture of the MPL influence on water balance, further systematically experimental as well modelling work is required to reveal the mechanism by which the presence of the MPL affects PEM fuel cell performance. Since steady-state polarization measurements are strongly limited in their informative value concerning loss mechanisms, electrochemical impedance spectroscopy (EIS) is a powerful tool that may have the ability to give a closer look into the limiting transport processes.

The aim of this work is to provide a better understanding of the improvement of the mass transport related to the MPL presence. Therefore, a theoretical impedance spectroscopy analysis is conducted. ESEM imaging is used to investigate the wetting properties and liquid water transport of and through the porous media respectively.

2 Modelling Work

The impact and transport of liquid water in the porous media such as GDL, MPL and CL, its coupling with the protonic conductivity of the membrane via the ionomer water content and the kinetics, combined with phase transition is simulated with a 1D dynamic multi-phase agglomerate model. The model assumptions base mainly on a cathode model published in [4], whereas the presented new model is extended by the anode side. A schematic diagram is given in Figure 1.

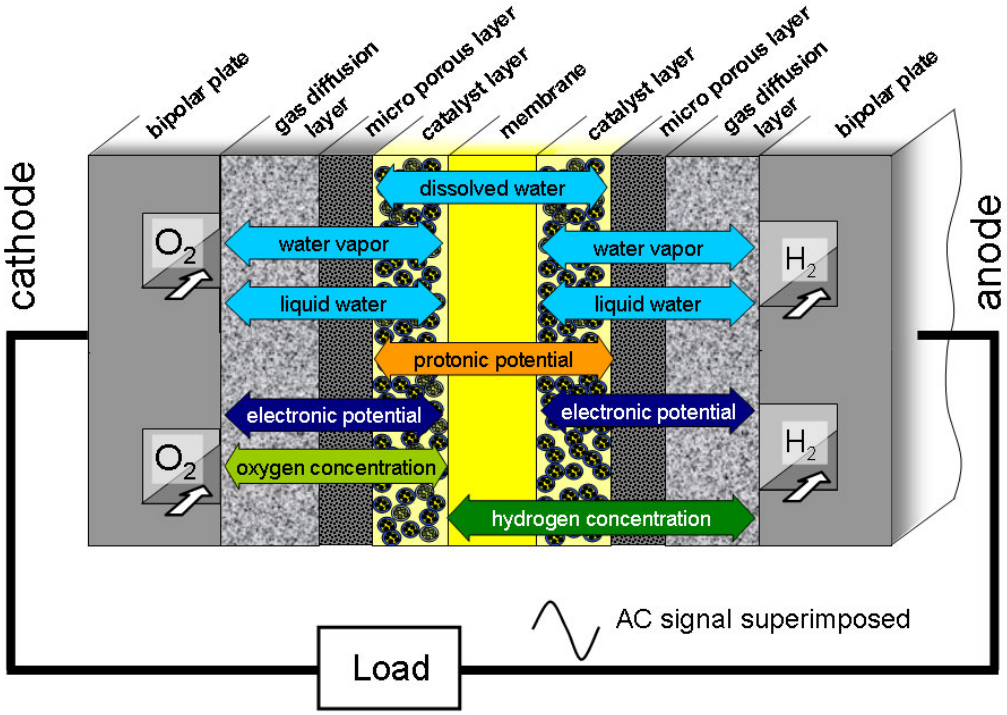

Figure 1: Schematic diagram of the model domains. The arrows depict the domains where the solving variables are defined.

A coupled PDE system describes the interaction of seven solving variables, namely dissolved water, vapour, liquid water, protonic and electronic potential, oxygen and hydrogen concentration. Besides the model parameterization, the interface conditions between the model domains (GDL, MPL, CL, Mem) are the critical input values and thus need specific attention. Regarding the MPL impact it is assumed, that liquid water can penetrate the MPL pores only in case of a certain defined CL saturation. Additionally, the shadowing effect of relatively large droplets at the interface of the coarse GDL structure to the fine micro porous structure of the CL is reduced with a MPL, implemented as a sophisticated functional dependency between oxygen flux und pore saturation.

Figure 2 shows a comparison of two polarization curves simulated with and without MPL at the same operating conditions. The results show an improved cell performance in the high current density range where liquid water is present in case of using a MPL. The liquid water flux towards the cathode GDL is blocked by the MPL as long as the saturation in the CL remains low. This leads to an increased back diffusion to the anode side (see Fig.2 top right). When a defined saturation is reached, water penetrates into the MPL, flows towards the cathode GDL and finally out of the cell.

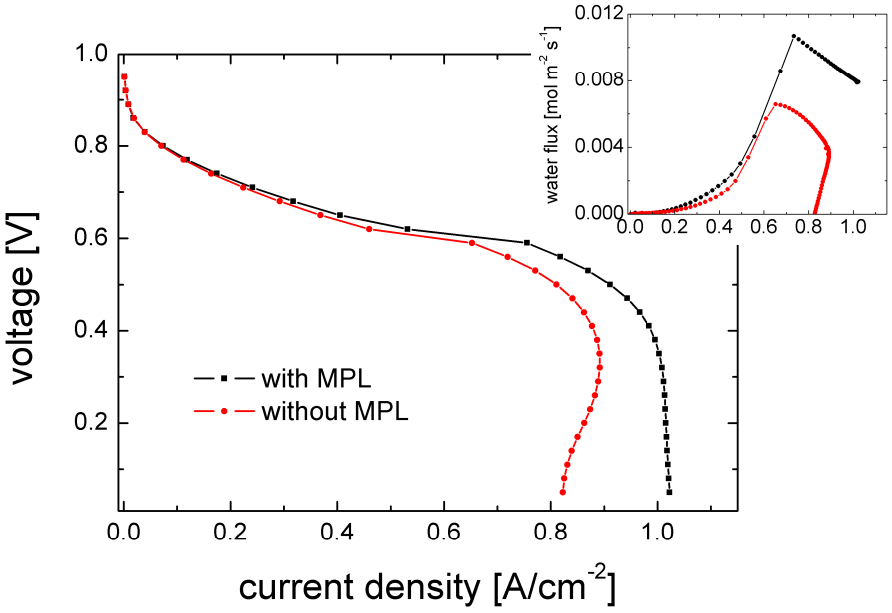

Figure 2: The simulated polarization curve using a MPL shows a higher limiting current density value which can be attributed to a higher water flux toward the anode.

Modifying the boundary condition of the electronic potential by superimposing a small sinusoidal signal ($V_{AC} \cdot \sin(\omega \cdot t)$) with frequency ω and amplitude V_{AC} to the steady-state voltage V_{SS}, the impedance $Z(\omega)$ can be calculated by the Fourier transform of the excitation signal *V(t)* and response signal *i(t)* followed by complex division

$$Z(\omega) = \frac{V(\omega)}{i(\omega)}.$$

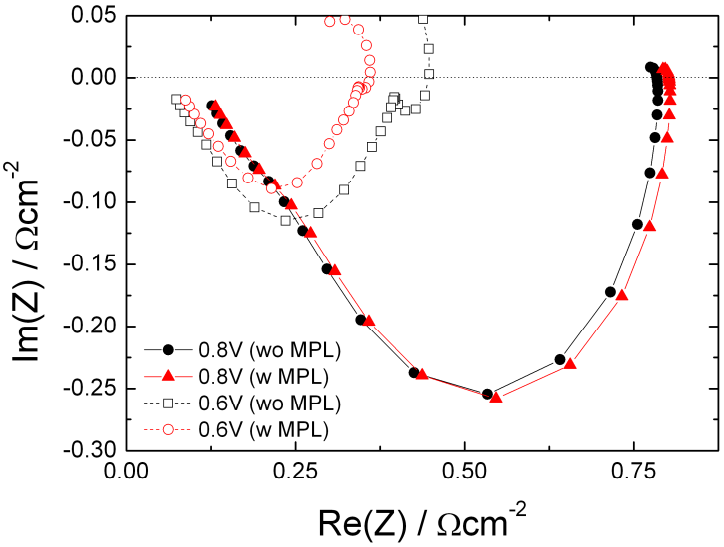

Figure 3: Simulated impedance spectra at 0.8 V and 0.6 V.

Figure 3 shows simulated impedance spectra. At high cell voltage (0.8 V) the spectra are nearly the same. Since no water is present in that operating state, the MPL acts as an additionally oxygen diffusion barrier which can be seen in a small enlarged impedance spectra. At 0.6 V liquid water is present in the porous media. The improved water management by the MPL leads to a smaller impedance arc in the Nyquist plot.

3 ESEM imaging

ESEM imaging is used to analyze the water transport properties of the porous media. By means of condensation experiments the wetting properties such as contact angle and immobile saturation are investigated. Figure 4 shows two identical GDLs from SGL (Sigracet BC 24) lying side by side, one with the MPL-side (left) and one with the GDL-side (right) facing the top. The strong hydrophobic nature of the MPL is clearly visible whereas the GDL side shows areas of contact angle in the range of 90° and below (film formation).

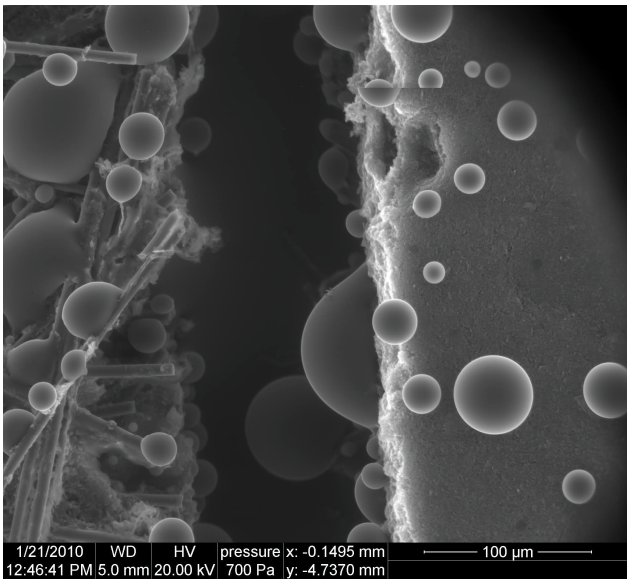

Figure 4: Water droplets on GDL fibers (left) and on MPL surface (right) are shown.

Gerteisen et al. [5] reported a performance enhancement by perforating the GDL. The observations are explained by the positive effect of artificial water transport channels, ‘sucking’ liquid water from their surrounding and finally reducing the overall saturation. This model assumption is now proven by ESEM imaging (see Figure 5), where droplets appear on the side walls of the hole and the water reaches the surface within the hole first.

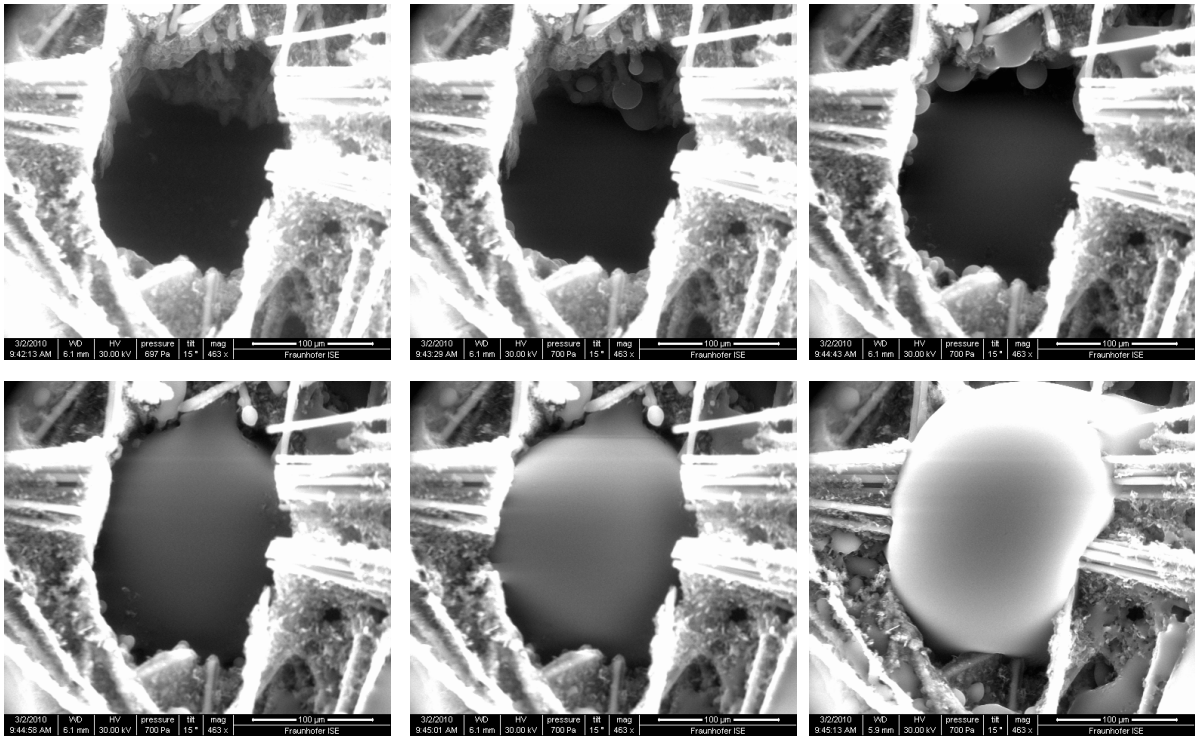

Figure 5: ESEM imaging of water build up in the artificial water transport channel.

4 Conclusion

A new developed multi-phase PEFC model is used to investigate the impact of a micro porous layer on the water management. By means of this model we are able to simulate impedance spectra which help to understand more clearly the water transport mechanism. ESEM imaging is used to analyze the wetting properties of the porous structures and to validate the model assumptions of an improved liquid water transport by providing artificial water transport channels in the GDL [5].

Acknowledgements

The authors would like to thank the Bundesministerium für Bildung und Forschung (BMBF) Germany for the financial support under contract No 03SF0360A (PEM-CA-D).

References

[1] Dai et al., A review on water balance in the membrane electrode assembly of proton exchange membrane fuel cells, International Journal of Hydrogen Energy, 34, (2009), 9461-9478

[2] Li et al., A review of water flooding issues in the proton exchange membrane fuel cell, Journal of Power Sources 178, (2008), 103–117

[3] Pasaogullari et al., Two-phase transport and the role of micro-porous layer in polymer electrolyte fuel cells, Electrochmica Acta, 49(25), (2004), 4359-69

[4] Gerteisen et al., Modeling the phenomena of dehydration and flooding of a polymer electrolyte membrane fuel cell, Journal of Power Sources, 187, (2009), 165-181

[5] Gerteisen et al., Enhancing liquid water transport by laser perforation of a GDL in a PEM fuel cell, Journal of Power Sources, 177, (2008), 348–354

Internal Currents in PEMFC during Start-up or Shut-down

G. Maranzana, O. Lottin, C. Moyne, J. Dillet, A. Lamibrac, J. Mainka, S. Didierjean, LEMTA, Nancy University – CNRS, Nancy, France

Although several working conditions are known to be damaging to Proton Exchange Membrane Fuel cells (PEMFC), their degradation mechanisms are not fully understood yet [1]. For instance, supplying the fuel cell with dry gases can induce a fast degradation of the electrodes [2] but on the other hand, long-time or repeated storage without purging liquid water from the gas channels accelerates the fuel cell aging. Potential cycling [3] or operation under open-circuit conditions [4] are also to be avoided. This paper reports about an experimental and numerical study of the internal currents that occur during fuel cell start-up under open-circuit conditions. Shut-down/start-up cycling results in performance degradation according to Tang et al., Shen et al. and Kim et al. [5-7]. During start-up, hydrogen pushes oxygen, air, or possibly nitrogen that was introduced for purging water toward the outlet so that for a short time depending on various parameters like the flow rate and the channels geometry, a fraction of the anode compartment is filled with hydrogen while the other part is still occupied by the gas initially present. A potential appears at the inlet of the anode but not at the outlet, which generates internal currents under open-circuit conditions. Although these internal currents are scarcely studied, they were modelled by some authors [8-10] and they can be measured using segmented cells [11, 12]. According to Meyer and Darling [9] internal currents can be at the origin of fuel cell performance decay by creating abnormally high potentials at the cathode, causing carbon corrosion. Starting from experimental data measured thanks to a segmented cell, Siroma et al. [11] suggested that the double layer capacitance could play a major role in the origin of reverse currents and high potentials.

1 Experimental Setup

A segmented fuel cell was designed with the objective to reduce as much as possible the high frequency resistance associated with the current collection in order to obtain a good assessment of the magnitude of the internal currents (*figure 1*). Air and hydrogen flow through five *30 cm* parallel straight channels of 0.7×1 mm² in section. On the anode side, the channels are machined in an aluminum plate that is then gold plated. The cathode plate is in polycarbonate (transparent but non conductive) and the channel ribs are made of *15 mm* long, *1 mm* thick gold plated brass strips. They are inserted only between two adjacent channels so that *4×20 = 80* strips were necessary for the five channels. Each strip is electrically isolated from the preceding and following ones (along the *x* axis in *figure 1*) thanks to a small *2.3×1 mm²*, *80 µm* thick Kapton sheet. The main technical difficulty was to obtain a flat contact surface in order to make the contact resistance between the channel ribs and the backing layer as much uniform as possible. This was done by surfacing the channel ribs once they were embedded in the polycarbonate plate. They were then gold plated in a second step. The MEA (*Jonhson-Matthey*) consists of a 30 *µm* thick *Nafion 212* membrane and of catalytic layers with an average Pt loading of 0.4 *mg cm*$^{-2}$ at the anode and cathode.

The active area is $A = 30\ cm^2$. The GDL is a 190 μm thick carbon fibre paper (*Toray TGP-H-060*). The MEA is not segmented. For these experiments, the four adjacent strips are electrically connected outside the cell, which is equivalent to averaging the current intensity along the *y* direction. Thus, twenty wires (one per segment) drive the current towards twenty *5 mΩ* shunt resistors, which voltage drops allow an indirect measurement of the current intensity. Then, all segments are set to the same potential, as shown in the sketch of *figure 2*. The total resistance between the channel ribs and the point where the twenty segments are connected is about *12 mΩ*. The resistance between two consecutive brass strips being of *175 mΩ*, it is reasonable to assume that most of the current produced in a segment actually flows through the corresponding connecting wire instead of the GDL thickness according the plane direction. Numerical data (local current intensities and voltage) are recorded at a frequency of 200 *Hz* and with a 16 *bit* resolution thanks to a *National Instrument SCXI* multiplexer.

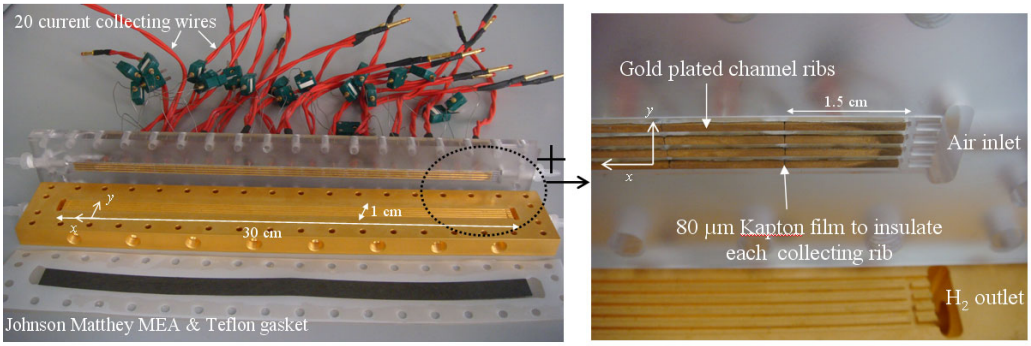

Figure 1: View of the dismantled segmented cell and zoom on the segmented channel ribs.

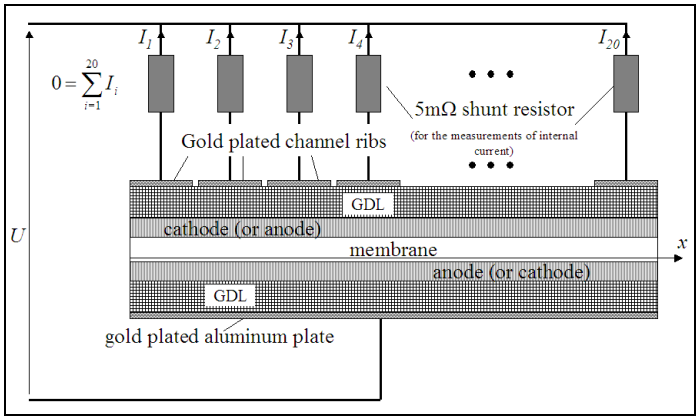

Figure 2: Scheme of the electrical connections.

2 Experimental Results

Several start-up experiments were performed with different values of the hydrogen flow rate, the anode compartment being initially filled with air or nitrogen. Nitrogen was used to study

the effect of a purge after shut-down. The fuel cell was at ambient temperature (22 °C) and air and hydrogen were humidified until saturation using bubblers (also at ambient temperature). The occurrence of internal currents can be seen in *figure 3* with the simultaneous rise of the open circuit potential as functions of time. The hydrogen flow was set to *3 cms*$^{-1}$ and *1 ms*$^{-1}$, which correspond to theoretical values of the current density in steady state of *0.03 Acm*$^{-2}$ and *1 Acm*$^{-2}$ (with a stoichiometry of *1*). The air flow was set to *5 ms*$^{-1}$, which corresponds to a steady state current density of *1 Acm*$^{-2}$ with a stoichiometry of *2*.

The sum of the currents flowing through the twenty segments being null at open circuit, the current that is produced by the first segment is necessarily distributed between the others. Thus, when hydrogen reaches the inlet of the cell the electrical current produced by the first segment flows toward the 19 others so that reverse currents (by reference to the normal fuel cell operation) can be measured. The current produced by the first segment reaches a maximum and then decreases while the hydrogen front is moving forward. Similar current profiles are observed in the other segments but with a lower intensity. Once the hydrogen front has reached the anode outlet, the cell voltage is close to the open circuit voltage and the internal currents have almost entirely disappeared. Their intensity increases with the incoming hydrogen velocity until about *1 ms*$^{-1}$; then, it remains constant whatever the hydrogen velocity, probably because of some imperfections in the experimental setup affecting the time constant of the hydrogen flow. With this fuel cell and in the range of operating conditions we have tested, it can reach a maximum of *1 Acm*$^{-2}$ for positive currents and *0.25 Acm*$^{-2}$ for negative currents.

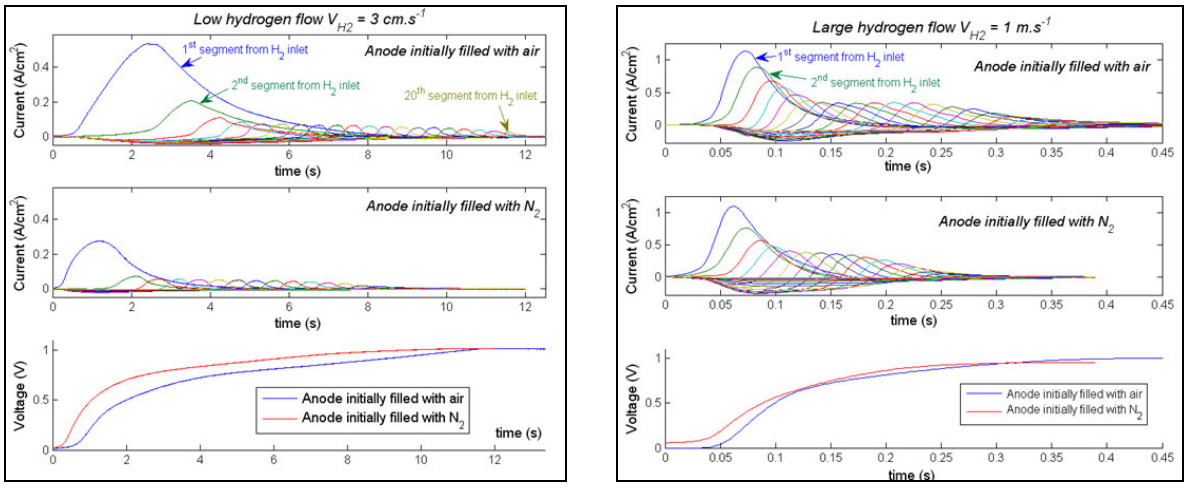

Figure 3: Internal currents and open circuit potential as function of time for two different hydrogen inlet flows and for anode initially filled with air or nitrogen.

The phenomena observed when the gas initially present in the anode compartment is nitrogen or air differ in two points. First, for the lower hydrogen flow rates, the intensity of internal currents is more important with air. The difference is here of the order of 0.2 Acm^{-2}, which cannot be explained by carbon oxidation at the cathode as described in [8-10]: current densities corresponding to carbon oxidation must be of a few mAcm^{-2} [9] only. A more

probable explanation is that the direct oxidation of some hydrogen and oxygen on platinum at the anode improves the hydration of the MEA and raises the local temperature which in turn increases the intensity of internal currents. For the higher hydrogen flow rates, the intensity of internal currents is identical whatever gas is in the anode compartment. This convergence of the magnitude of the internal currents with the hydrogen velocity could be explained either by the imperfections of the experimental setup or by a less significant effect of the MEA hydration mentioned above. The other main difference between air and nitrogen lies in the peak of current density, which happens earlier with nitrogen. Globally, the fuel cell voltage rises also faster with nitrogen. This effect is most probably also linked with the direct oxidation of hydrogen in the presence of oxygen, which slows down the velocity of the hydrogen front in the anode compartment.

3 Modelling

The model presented in the following demonstrates that the occurrence of internal currents can be explained mostly by capacitive effects. Carbon oxidation and other redox mechanisms are considered only via a leakage resistance: redox potentials other than the oxidation of hydrogen are neglected. In order to focus on the main phenomena, the gas initially present in the anode compartment is nitrogen. The case of oxygen is not considered.

For the sake of simplicity, the electrical behaviour of the cell is partially linearized. The basic building block of the model is a generic equivalent circuit of the electrodes which is assumed to be valid whatever the direction of the electrical current (*figure 4*). The electrodes are represented by a double layer capacitance C_{dl} in parallel with a charge transfer resistance R_{tc} and a leakage resistance R_{∞} that accounts for the oxidation of carbon and/or other possible redox phenomena. It is assumed that the value of R_{tc} becomes infinite for negative currents (from anode to cathode) because the voltage maximum value reached during start-up does not allow the electrolysis of water. Moreover, the leakage resistance R_{∞} is neglected when a faradic current exists ($Q_{a,c}>0$): it becomes also infinite. In *figure 4*, the diodes in series with R_{tc} and R_{∞} control their values as functions of the direction of the electrical current. The resistance of the electrolyte and the various contact resistances are accounted for through a single high frequency resistance R_{hf} in series with the anode and the cathode (*figure 5*).

The electrodes as represented in *figure 4* operate following three modes:

- Without hydrogen in the anode compartment, the direction of the electrical current is negative. It flows through the leakage resistance R_{∞} and through the capacitances C_{dlc} and C_{dla} which charge progressively (Q_c, $Q_a < 0$) as the electrical current decreases (in absolute value).
- When hydrogen comes in the anode compartment a voltage E^0 appears between the electrodes and adds to the voltage across to the two partially charged capacitances. The electric current i^k becomes positive and the double layer capacitances C_{dlc} and C_{dla} discharge.
- When the charge of the capacitances becomes null (i.e. when the fuel cell voltage is equal to E^0 or lower) the electrical current i^k becomes a faradic current and it flows through the charge transfer resistances R_{tc} and R_{ta}.

The channel is discretized into *n* segments (*figure 5*) from the inlet (n°*1*) to the outlet (n°*n*). The geometry of the channel and the velocity of hydrogen define a convection time tc_k at which the k^{th} segment is occupied by hydrogen only whereas only nitrogen is present at $t < tc_k$. Air is assumed to be always present in enough quantity in the cathode compartment.

The global equivalent electrical circuit of the fuel cell leads to a system of *3n+1* ordinary differential equations with *3n+1* unknowns. The unknowns are the potential difference between cathode and anode *U*, the current intensity $I^k_{1\le k\le n}$ through the *n* segments, the charge of the *n* cathode capacitances $Q^k_{c\,1\le k\le n}$ and the charge of the *n* anode capacitances $Q^k_{a\,1\le k\le n}$.

$$\begin{cases} U = E^k - R_m I^k - \dfrac{Q_c^k}{C_{dlc}^k} - \dfrac{Q_a^k}{C_{dla}^k} \quad \left(E^k = 0 \text{ if } k > i\right) & 1\le k\le n \\ I^k = \dfrac{dQ_c^k}{dt} + \dfrac{Q_c^k}{R_{tc}^k C_{dlc}^k} = \dfrac{dQ_a^k}{dt} + \dfrac{Q_a^k}{R_{ta}^k C_{dla}^k} \left(R_{ta}^k = R_\infty \text{ if } Q_a^k < 0\right) & 1\le k\le n \\ 0 = \sum_{i=1}^{n} I^i \end{cases}$$

Where E^k stands for the open circuit voltage (in steady state). $E^k = 0\ V$ if $k > i$ and $E^k = E_0$ if $k \le i$. Replacing I^k by its expression (the second equation) in the first and third equations and considering that *U* is constant in all the segments makes it possible to reduce the dimension of the system to 2*n* :

$$\frac{d}{dt}\boldsymbol{Q} = \boldsymbol{M}(t)\boldsymbol{Q} + \boldsymbol{S}(t) \qquad \boldsymbol{Q} = \left(Q_c^1 \cdots Q_c^n \; Q_a^1 \cdots Q_a^n\right)^t$$

Where the remaining unknowns are the charges of the capacitances. $\boldsymbol{M}$ is a $2n\times 2n$ square matrix that is time dependent. The source term $\boldsymbol{S}$ is also time dependent. This system can be easily solved by a Runge-Kutta method but an iterative loop must be used to adjust the location of the hydrogen front by subtracting the consumed quantity - derived from the faradic current - from the total quantity of hydrogen injected. Actually, except in the case of very low hydrogen flowrates, the velocity of the front remains almost constant due to the very low hydrogen consumption. Note that the number of segments used for the simulations (*n = 200*) is much higher than the number of segments in the experimental cell: the numerical results presented below are averaged over *10* consecutive segments. In order to avoid numerical instabilities, it was found convenient to increase linearly E^k with time in the k^{th} segment when $t_{ck} < t < t_{ck+1}$.

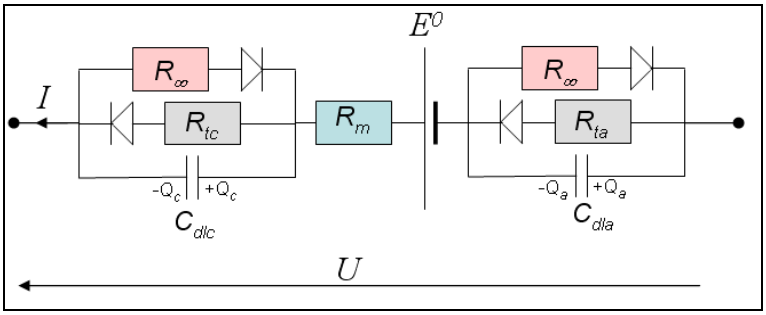

Figure 4: Electrical model of a MEA segment.

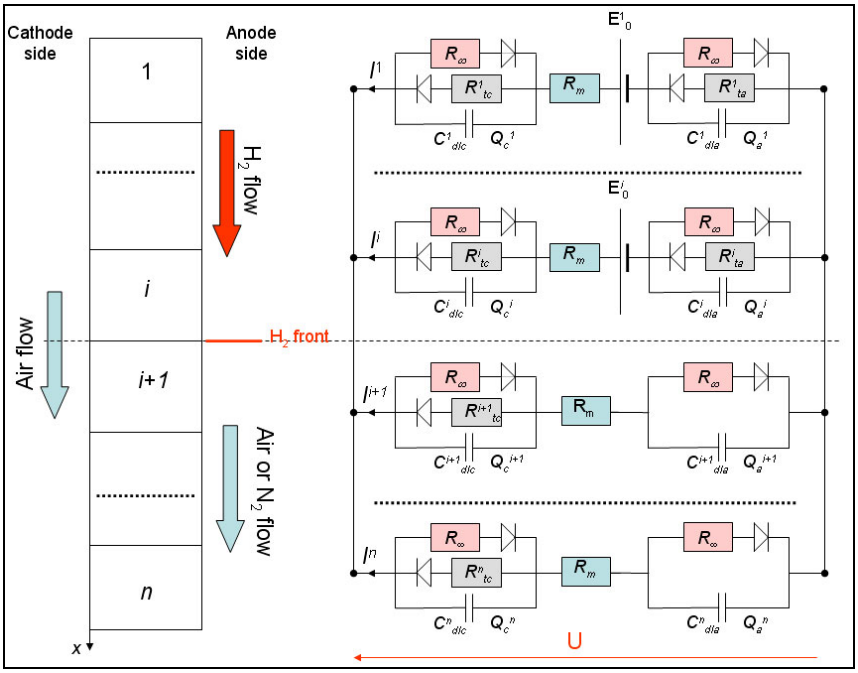

Figure 5: Global equivalent electrical circuit of the fuel cell at time *t* ($t < t_{ci+1}$). The charge transfer resistance R_{tc} at the anode is not represented in the absence of hydrogen because it has no physical meaning.

4 Numerical Results

Figure 6 presents the evolution with time of the internal currents and of the fuel cell voltage as determined by the model with the values of the parameters stated above. The hydrogen flow rate was adjusted so that the inlet velocity corresponds to the experimental values in *figure 3* (*3 cms*$^{-1}$ and *1 ms*$^{-1}$). The experimental (*figure 3*) and numerical results (*figure 6*) are close to each other, at least in qualitative terms. Of course, using constant values for the double layer capacitances, the charge transfer resistances and the leakage resistance is a strong assumption but the model shows that the dominant phenomena are probably linked with the double layer capacitances. Carbon oxidation should occur simultaneously but its contribution to the internal currents is by all appearances negligible.

One can also notice that the model predicts a transient voltage rise over the steady state open circuit voltage ($E_0 = 1\ V$). This voltage rise can be observed experimentally shortly after fuel cell start up: according to these numerical results, it can be explained only by 2D and capacitive effects. However, other phenomena, like hydrogen crossover through the membrane, can show similar effects.

5 Conclusion

Experiments show that the internal currents that occur during PEMFC start-up can reach up to $1\ Acm^{-2}$. This is far more important than the expected order of magnitude of the current densities associated with carbon oxidation, which is only of a few $mAcm^{-2}$. The predominant phenomenon that explains the internal currents is the charge and discharge of the double layer capacitances. A simple model with constant values of the electric parameters yields numerical results close to the experimental ones. It also explains the transient voltage rise (over the steady state open circuit voltage) that is sometimes observed experimentally shortly after the fuel cell start up.

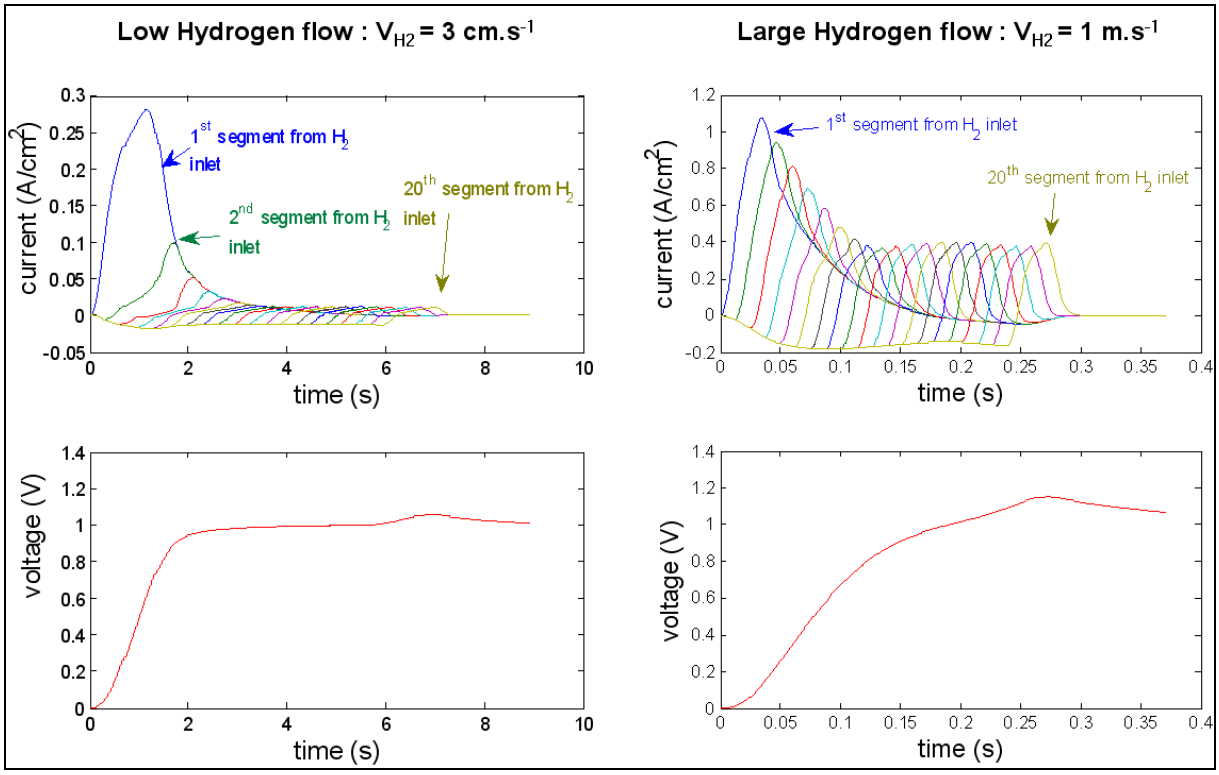

Figure 6: Numerical results obtained with E_0 = 1 V, R_m = 0.4 Ωcm^2, C_{dla} = C_{dlc} = 0.02 Fcm^{-2}, R_∞=1 Ωcm^2, R_{tc} =0.2 Ωcm^2 and R_{ta} = 0.05 Ωcm^2.

References

[1] Y. Shao, G. Yin, Y. Gao, Review: understanding and approaches for the durability issues of Pt-based catalysts for PEM fuel cell, J. Power Sources, 171 (2007) 558-566.

[2] S.D. Knights, K.M. Colbow, J. St-Pierre, D.P.Wilkinson, J. Power Sources, 127 (2004) 127

[3] P. Yu, M. Pemberton, P. Plasse, J. Power Sources 144 (2005) 11.

[4] T. Akita, A. Taniguchi, J. Maekawa, Z. Siroma, K. Tanaka, M. Kohyama, K. Yasuda, J. Power Sources 159 (2006) 461.

[5] H. Tang, Z. Qi, M.Ramani, J.F. Elter, PEM fuel cell cathode carbon corrosion due to the formation of air/fuel boundary at the anode, J. Power Sources, 158 (2006) 1306-1312.

[6] Q. Shen, M.Hou, D.Liang, Z.Zhou, X. Li, Z. Shao, B. Yi, Study on the processes of start-up and shut-down in proton exchange membrane fuel cells, J. Power Sources, 189 (2009), 1114-1119.

[7] J. Kim, J. Lee, Y. Tak, Relationship between carbon corrosion and positive electrode potential in a proton-exchange membrane fuel cell during start/stop operation, J. Power Sources, 192 (2009), 674-678.

[8] C. A. Reiser, L. Bregoli, T. W. Paterson, J. S. Yi, J. D. Yang, M.L. Perry, T.D. Jarvi, A reverse-current decay mechanism for fuel cells, Electrochemical and Solid-State Letters, 8 (6) A273-A276 (2005).

[9] J.P. Meyers, R. Darling, Model of carbon corrosion in PEM fuel cells, J. Electrochemical Society, 153 (8) A1432-A1442 (2006).

[10] N. Takeuchi; T.F. Fuller, Modeling and investigation of design factors and their impact on carbon corrosion of PEMFC electrodes, J. Electrochemical Society, 155 (7) B770-B775 (2008).

[11] Z. Siroma, N. Fujiwara, T. Ioroi, S. Yamazaki, H. Senoh, K. Yasuda, K. Tanimoto, Transient phenomena in a PEMFC during the start-up of gas feeding observed with a 97-fold segmented cell, J. Power Sources, 172 (2007), 155-162.

[12] G. Maranzana, O. Lottin, T. Colinart, S. Chupin, S. Didierjean, A multi-instrumented polymer exchange membrane fuel cell: Observation of the in-plane non-homogeneities, J. Power Sources, 180 (2008), 748-754.

AQUIVION™ – The Short-Side-Chain and Low-EW PFSA for Next Generation PEFCs Expands Production and Utilization

Matthias Gebert, Solvay Solexis, Italy

The new Aquivion™ (formerly “Hyflon Ion”) ionomer product portfolio of Solvay Solexis is introduced. Both membrane and dispersion grades are presented with some of their properties illustrated by analytical results. In addition to the innovative functional ionomer materials Solvay Solexis also provides a variety of other selected functional materials to the emerging commercial MEA market including inert Galden® heat-transfer fluids, advanced Tecnoflon® high-temperature fluoroelastomers for sealings, aqueous Algoflon® PTFE dispersions or tailored film materials for use as membrane sub-gaskets (membrane rims) which are manufactured to order at small or large scale and are customized in terms of polymer choice, film thickness and geometry.

Figure 1: Key data on Solvay Solexis S.p.A. with headquarters in Milan/ Italy.

Figure 1 displays key information of Solvay Solexis, Italian fluoromaterial specialty company and affiliate of the Belgian Solvay Group that emerged from Solvay’s acquisition of Ausimont S.p.A. in 2003. Solvay Solexis manufactures on three continents to provide a broad portfolio of fluoromaterials to a variety of industries and applications that demand the superior performance of fluoromaterials.

AQUIVION™ – Progress within PFSA ionomers

Solvay Solexis focuses on the incorporation of a short-side-chain ionomer in their membrane and dispersion products. Shortening the length of the polymer's side chains results in increased mechanical stability of the polymer; confirmed by stress-strain tests or DSC scans [1]. Such Differential Scanning Calorimetry reveals an increased level of crystallinity for shorter pendant group chains when comparing equal equivalents weight (EW) or ion-exchange capacity (IEC), respectively.

AQUIVION™ – What makes the difference

Shifting physical properties of the PFSA material in the right direction can lead to the desirable progress in PEFC optimization. The repeated requests for "high-temperature membranes" that would enable smaller cooling systems, reduced gas humidification and less active area are answered by Aquivion™ through…

- its higher **thermal stability** thanks to a roughly 40 °C higher softening temperature T_G compared to longer side chains,
- its capability to more strongly **absorb and retain cathode product water** inside the membrane for self-humidification, and
- its cutting-edge **proton conductivity and water mobility** levels, especially when operating PEFCs with gases at low relative humidity.

Exploiting the advantages of the short-side-chain structure and reducing the Equivalent Weight to a satisfactory level are the key choices that provide significant performance improvement of the fuel-cell device.

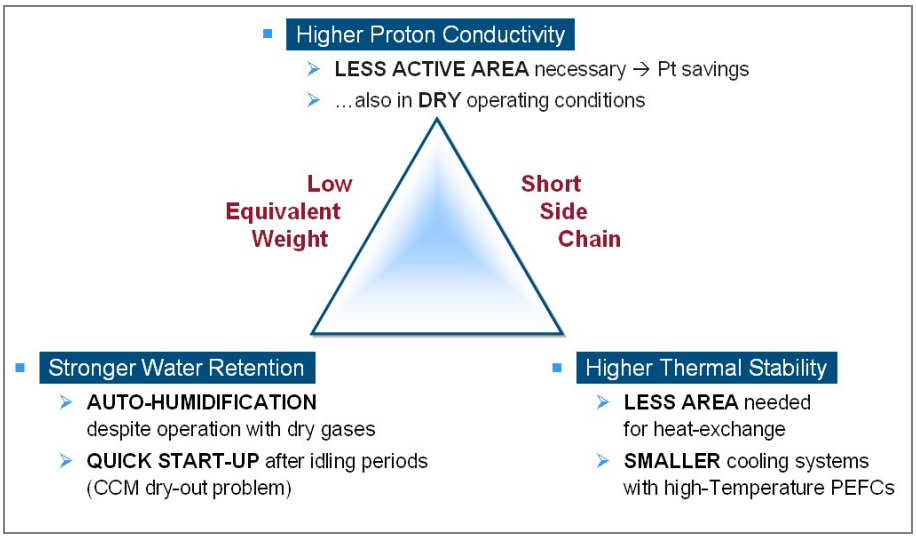

Figure 2: Lower system size and cost via benefits of advanced AQUIVION™ properties.

AQUIVION™ – Exemplified membrane properties

The following three figures describe test results that indicate the physical advantages of Aquivion™ with regard to a high-temperature operation at low reactant pre-humidification.

One exhibits proton conductivity curves of the E79-03S grade at ambient temperature as well as 95 and 120 °C (200 and 250 °F). Even at 95 °C and 20 % rH over 10 mS/cm can be retained as proton conductivity. Absolute values were well reconfirmed by a Round Robin testing within the European Autobrane project (2006-09), see [2] for detailed results of further 12 institutes who screened **Aquivion™ E79-03S** proton conductivity under three pre-defined cell conditions.

The chart on the right illustrates the pronounced effect of superior water retention at 90 °C and quasi dry conditions. Long-side-chain ionomer membranes or baseline Aquivion™ materials such as E87-05S (EW 870, 50 microns) lose cell voltage when lowering reactant pre-humidification. Advanced E79-03S (EW 790, 30 microns) maintain the cell voltage by efficient auto-humidification through absorption and transport of cathode product water.

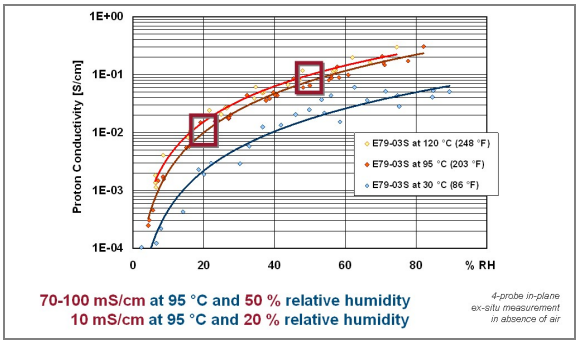

Figure 3: AQUIVION™ E79-03S proton conductivity as a function of rH and T (30 µm).

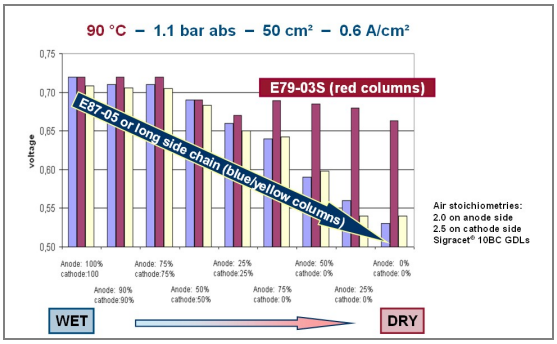

Figure 4: AQUIVION™ E79-03S water retention capability in hot and dry conditions.

The possibility to continuously operate an ionomer membrane at high temperature is limited by its softening temperature. Under fully dry conditions this temperature can be determined as the polymer's alpha-transition peak (for Aquivion™ indicatively between 125 and 140 °C).

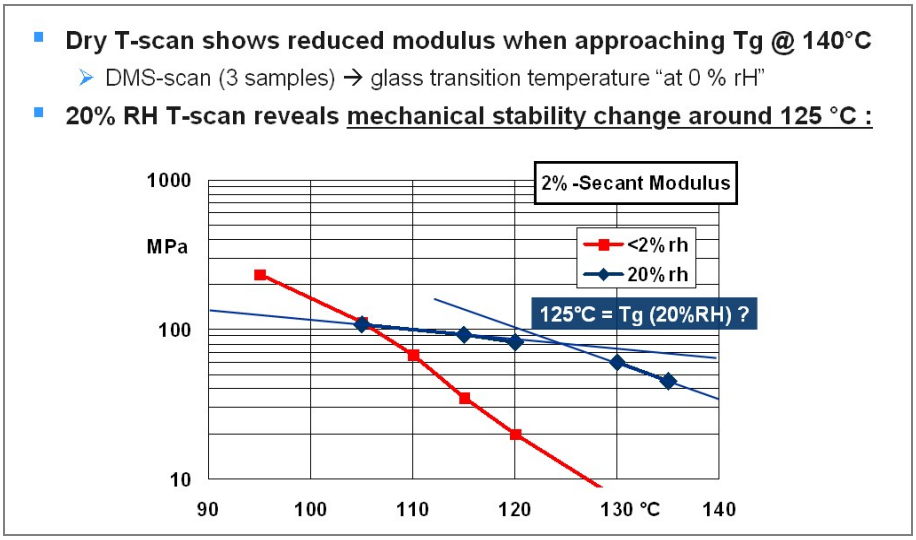

Figure 5: AQUIVION™, Identification of the softening point at 20 % rH.

Validating the situation under partial humidification requires a series of stress-strain tests at fixed rH and various temperatures, as shown by the chart's diamonds. A change in slope of the modulus reduction typically indicates an alternation in the polymer structure; which in case of Aquivion™ can be observed at around 125 °C for measurements at 20 % relative humidity. Lifetime test results are a development criterion of similar importance for the assessment of membrane quality. Solvay Solexis is equipped with several test stations for long-life testing. Selection of suitable combinations of operating conditions and membrane grades will allow simultaneous optimization of both performance and lifetime requirements. More detailed technical discussion of ex-situ and in-situ differences of long- and short-side-chain PFSAs can be found in [3] while [4] and [5] discuss resistance of Aquivion™ against radical attack, again in comparison to LSC PFSAs.

AQUIVION™ – Dispersions

Various grades of Aquivion PFSA ionomer dispersions in different solvent systems do not only provide a powerful raw material for catalyst ink development, but are also essential for other applications such as membrane recasting or treatment of hydrophobic surfaces to impart better water wettability.

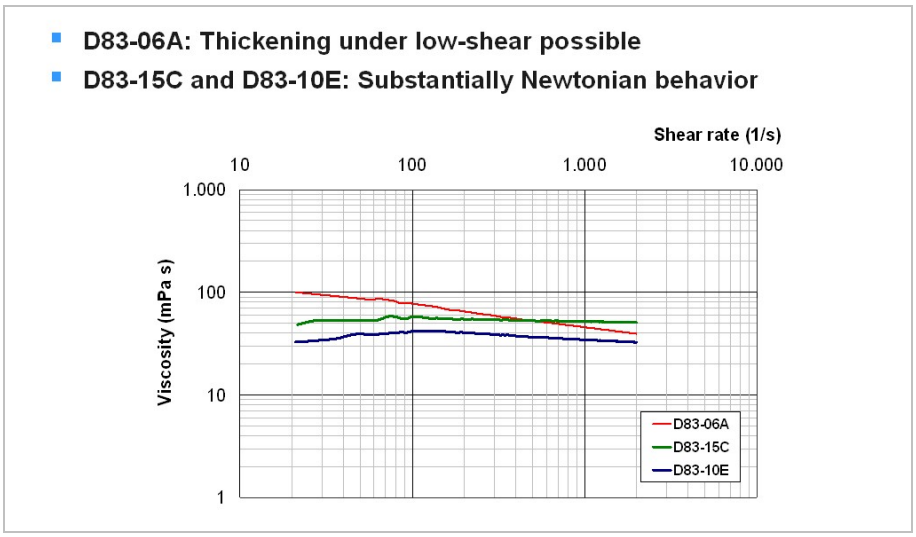

Figure 6: AQUIVION™, Typical rheological curves of various dispersion grades.

Solvent compositions range from predominantly alcoholic (80 % propanol) to virtually aqueous-based. Likewise ionomer concentration can be moderate (6 %) or elevated (20 %). The combination of these two factors – with alcohol acts as a polymer swelling agent – affords different grades with varying rheological behavior, as shown in the graph. Both the absolute viscosity level and its dependency on the shear rate exhibit specific characteristics to adapt the grades to their intended use.

Solvay Solexis supplies all commercial ionomer dispersions worldwide in various containers of 0.5, 5 or 60 liter capacity to both industrial manufacturers and R&D organizations. AQUIVION™ materials are accessible via **solexis.ionomers@solvay.com**. Small-volume samples are dispatched worldwide by the distributor **Ajedium Films LLC** based in Newark,

Delaware (USA). Industrial customers are supplied directly by Solvay Solexis's customer service center CCS in Milan/Italy.

References

[1] A. Ghielmi et al. "Proton exchange membranes based on the short-side-chain perfluorinated ionomer", J. Pow. Sourc. 145(2005) 108-115, Fig. 3.

[2] D. Jones et al. "Progress MEA 2008 : Progress in MEA Components for Medium and High Temperature Polymer Electrolyte Fuel Cells", La Grande Motte, France. September 21-24, 2008. Poster Presentation. (www.progressmea2008.eu)

[3] L. Merlo et al. "Membrane Electrode Assemblies Based on Hyflon® Ion for an Evolving Fuel Cell Technology", Sep. Sci. Techn. 42:13, 2891 – 2908

[4] L. Merlo et al. "Resistance to peroxide degradation of Hyflon® Ion membranes", J. Pow. Sourc. 171(2007) 140-147

[5] S. Schlick et al. "Ranking the Stability of Perfluorinated Membranes Used in Fuel Cells to Attack by Hydroxyl Radicals and the Effect of Ce(III): A Competitive Kinetics Approach Based on Spin Trapping ESR", Macromolecules, 2010, 43 (7), pp 3352–3358

Spatially Resolved Impedance Spectroscopy in PEM Fuel Cells up to 200 °C

Arno Bergmann, **Timo Kurz**, **Dietmar Gerteisen**, **Christopher Hebling**, Fraunhofer Institute for Solar Energy Systems, Freiburg, Germany

1 Introduction

Electrochemical impedance spectroscopy (EIS) is widely used to separate different loss mechanisms in fuel cells due to their different time constants [1]. It is mostly difficult to interpret and valuate the different phenomena by the analysis of the overall current density and cell impedance. Conducting spatially resolved EIS combined with local current density measurements enables the localisation of these different loss mechanisms and degradation phenomena. Additionally the local detection of e.g. fuel starvation or flooding events can help to understand the cell behaviour at critical operating states. Spatially resolved characterisation in combination with electrochemical impedance spectroscopy of conventional PEM fuel cells has been carried out earlier by Hakenjos et al. [2].

The high temperature polymer electrolyte membrane (HTPEM) fuel cell based on phosphoric acid doped polybenzimidazole (PBI) membranes was primarily developed by Wainright et. al. [3] in the middle of the 1990s. Due to several significant advantages they are a promising fuel cell technology and are nowadays receiving growing attention in research. The key advantage is the higher operation temperature of 120 °C to 200 °C compared to conventional low temperature PEM fuel cells based on Nafion® membranes. These operating conditions can be achieved due to a higher chemical and thermal stability of PBI and a proton conducting mechanism that does not require liquid water. The operating temperature leads to a more useful waste heat, a simplified system design due to the easier water management and, above all, to a significantly higher tolerance against catalyst poisons like carbon monoxide [4, 5]. Therefore, the most favourable application for HTPEM fuel cell systems is a combined heat and power (CHP) system in combination with a reformer unit.

In this work, a sophisticated experimental setup for spatially resolved characterisation of conventional and high temperature PEM fuel cells available at the Fraunhofer ISE is described in detail as well as the in-house designed and manufactured test cell. Exemplary some results of spatially resolved measurements are presented to demonstrate the opportunities of the described test facility. The influence of gas stoichiometry on the lateral distribution of current density in a HTPEM fuel cell was investigated at an operating temperature of 160 °C and a cell voltage of 0.5 V. Additionally, impedance spectra at selected cell segments are presented for deeper analysis of the spatial variety of the present processes.

2 Experimental Setup

At the Fraunhofer Institute for Solar Energy Systems ISE a custom-built test bench designed and manufactured by MaterialMates Italia has been installed for the spatially resolved

characterisation of fuel cells. It consists of 50 synchronised potentiostats as well as 50 channel frequency response analyser (FRA) that enables the simultaneous measurement of cell impedance as well as current and voltage at 50 cell segments in potentiostatic and galvanostatic mode, respectively. EIS can be conducted in a frequency range between 0.1 mHz and 20 kHz that offers the opportunity to analyse all loss mechanisms ranging from mass transport problems in the low frequency range and charge transfer losses in the middle frequency range to losses caused by ionic conduction in membrane and catalyst layers impacting at frequencies above 1 kHz.

To reduce the interaction of adjacent cell segments during EIS, even at frequencies up to 10 kHz, the excitation generating potentiostats are hardware-based synchronised. Each FRA measures and analyses the cell response separately and uses a noise-optimised lock-in amplifier. The calculation method of the impedance can be configured freely between highest accuracy and fastest measurement. In addition to the fundamental mode of cell response higher harmonics can be analysed up to 3rd order. This may offer new possibilities to distinguish more precisely between the influence of the present ionic conduction, electrochemical and transport processes in the diffusion layer, micro porous layer and/or catalyst layer. For setting the voltage or current each segment is connected to a separate potentiostat whereas an overall cell current up to 200 A can be handled.

The characterisation of a HTPEM fuel cell was conducted with commercially available MEA sets with an active area of 25 cm^2. The MEA consists of a phosphoric acid doped PBI membrane mounted in a sub-gasket and between two woven gas diffusion electrodes.

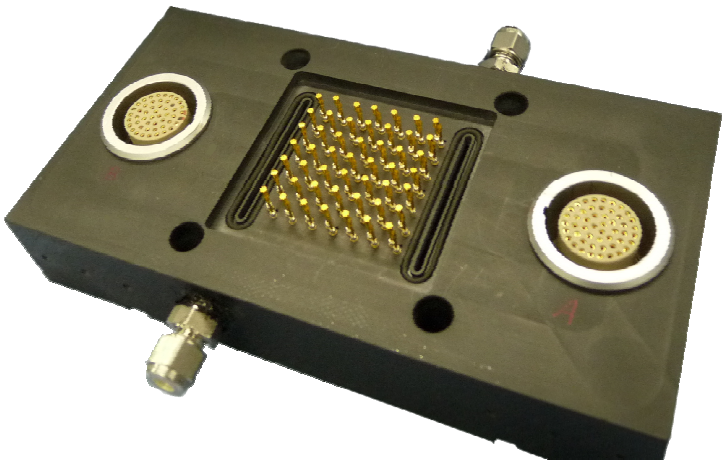

Figure 1: Design of the test cell for characterisation of PEMFCs up to 200°C.

The test cell, shown in Figure 1, is designed and constructed in-house. The key feature is an exchangeable and segmented graphite inlay acting as flowfield which can resist in harsh and acidic environments. Each segment offers an active area of approx. 0.5 cm^2. The design of the segmentation using an exchangeable inlay offers a high flexibility for characterisation of different flowfield geometries in HTPEM fuel cells as well as in conventional PEM fuel cells where the impact of the flowfield design on cell performance and maximum current density is more significant. Electrical contact of the segments is established via gold-coated switch

probes for sensing and current collection and further on via two 50 pin connectors. The connection between the test cell and the potentiostats is realised using extremely low-inductive cables. All components dealing with the segmented side are assembled in a polymer block wherein the gas supply is realised.

While segmenting one side of the cell an unsegmented flowfield is assembled at the other side. Temperature distribution of the cell can be measured at selected cell positions in the cathode flowfield. The test cell is mounted in a laboratory oven providing a homogenous temperature distribution outside the test cell to avoid artificial effects caused by varieties in thermal isolation. All assembled components are designed to resist temperatures up to 200 °C.

Gas flow rate is set using digital massflow controller. Since gas humidifiers are assembled the investigation of the relative humidity of the gases on the cell performance is possible up to a dew point of 60 °C. Data acquisition of temperature measurement and gas flow controlling is realised using LabView.

3 Results

Giving an idea of the characterisation method of combined current mapping and electrochemical impedance spectroscopy in a spatially resolved test cell, earlier results of the characterisation of a HTPEM fuel cell are presented in the following. The measurements were conducted at a cell voltage of 0.5 V and at a temperature of 160 °C. During the measurement the stoichiometry of air was varied between λ_{air} = 1.5 and λ_{air} = 3, while the hydrogen stoichiometry remained constant at λ_{H2} = 1.3.

Figures 2 - 4 show the spatial distribution of current density for selected air stoichiometries. The air flow is oriented along the y-axis, while the hydrogen flows along the x-axis into the cell.

For all stoichiometries the current density shows the same characteristics. Along the air flow the current density shows a steep increase from the gas inlets to the 3rd row of segments over a length of approximately 1 cm. Further on towards the gas outlet the current density decreases with a minor gradient. The segment with the maximal current of each row migrates along the hydrogen flow direction leading to a diagonal arrangement of cell segments 9, 17, 25, and 33. The current density at these segments varies between 288 mAcm^{-2} and 240 mAcm^{-2} at segment 17 and segment 33, respectively. The combination of hydrogen and oxygen concentration coupled with the temperature distribution causes the discovered distribution of current density since the maximal current density is located at the optimal ratio between oxygen and hydrogen concentration at the location of the highest temperature.

Reducing the air stoichiometry does not change the characteristics of the current density distribution but as a result the current density decreases towards the outlet of the cathode channels. This phenomenon is caused by a reduced oxygen concentration due to the current generation along the channel. At segment 33 the current density is reduced from 240 mAcm^{-2} at λ_{air} = 3 to 208 mAcm^{-2} at λ_{air} = 1.5.

Results of the electrochemical impedance spectroscopy are also shown in Figure 2 – 4 for the cell segments 17, 25, and 33. The excitation frequency was varied between 1 kHz and

100 mHz. At high cathodic air flow of λ_{air} = 3 the Nyquist plot of segment 17 near to the gas inlets shows a nearly semicircular RC member-like behaviour. A second arc cannot be seen at the mentioned operating conditions at that cell segment. The shape of the spectra is different for segments 25 and 33 since at both segments a second arc appears at frequencies of several Hz. This indicates a higher mass transfer resistance due to a worse or rather slower gas feed than near the air inlet.

Reducing the air flow leads to significant changes in impedance spectra since both the first and the second arc grow in diameter for all analysed segments. Especially at a cathode stoichiometry of λ_{air} = 1.5 the second arc of the latter segments is remarkably more pronounced which is caused by a stronger diffusion polarisation at lower oxygen concentrations. These results are in agreement with the investigations of Jespersen et. al. who carried out electrochemical impedance spectroscopy in HTPEM fuel cells [6].

The high frequency resistance (HFR) at 1 kHz is approx. 160 mΩcm^2 and does not vary with position and operating conditions at the selected cell segments.

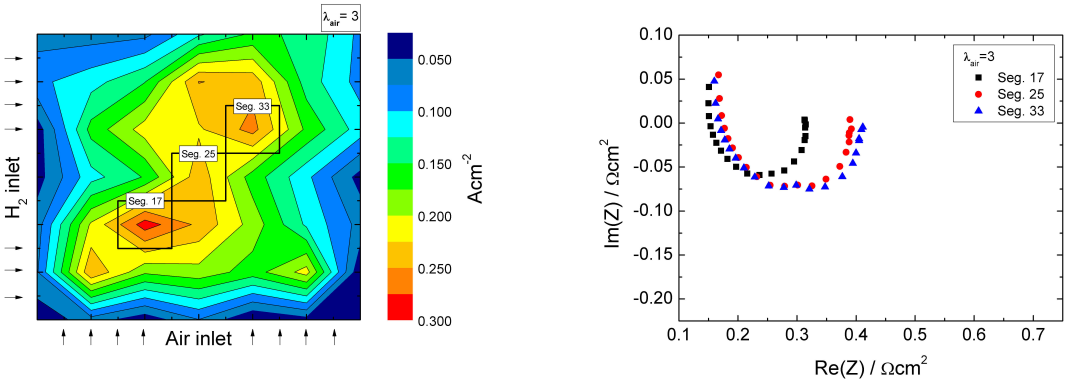

Figure 2: Current density distribution (left) and Nyquist (right) plot of EIS at selected cell segments for a cathode stoichiometry of λ_{air} = 3.

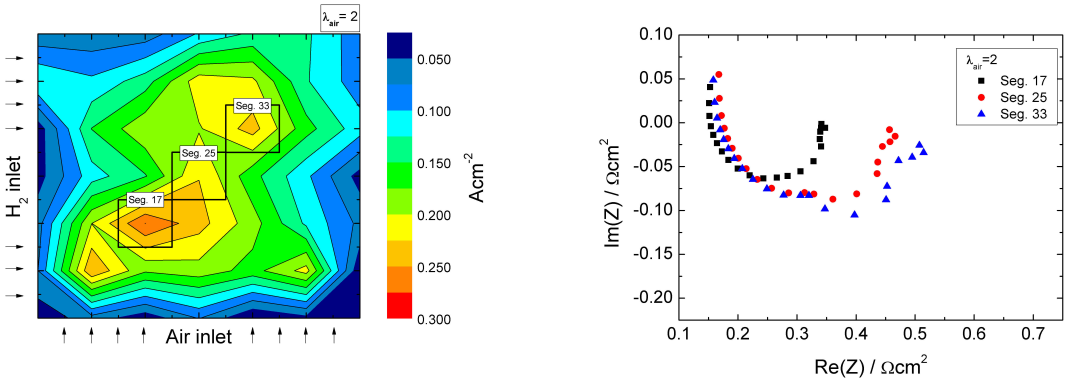

Figure 3: Current density distribution (left) and Nyquist plot (right) of EIS at selected cell segments for a cathode stoichiometry of λ_{air} = 2.

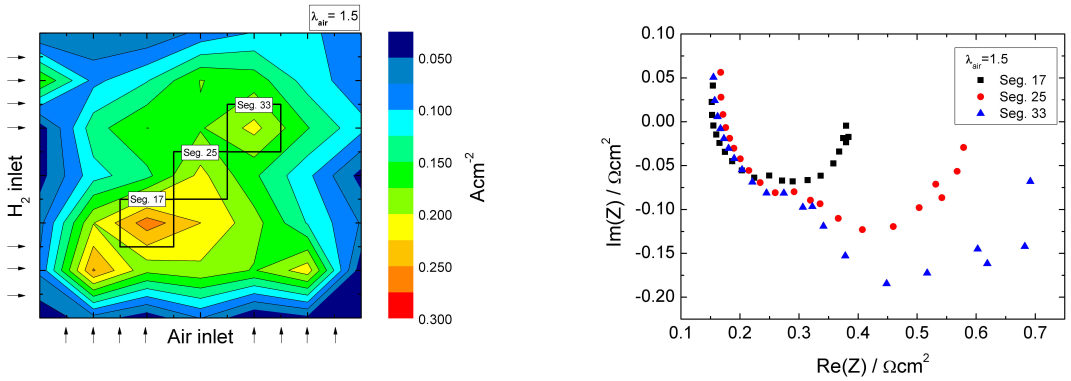

Figure 4: Current density distribution (left) and Nyquist plot (right) of EIS at selected cell segments for a cathode stoichiometry of $\lambda_{air} = 1.5$.

4 Conclusion

In this work, a newly developed, unique 50-channel potentiostat-impedance spectrometer and an in-house designed and manufactured test cell is described in detail. This test facility enables the spatially resolved characterisation of polymer electrolyte membrane fuel cells at temperatures up to 200 °C. Thus, lateral inhomogeneities caused by mass transport losses, membrane dehydration, and catalyst poisoning effects can be investigated at different operating conditions. A sophisticated in-house designed test cell including an exchangeable and segmented flowfield is presented. The cell offers a great flexibility for investigating the influence of different flowfield designs on the conventional as well as high temperature PEM fuel cells.

As an idea of example characterisations which can be conducted with the test bench, the influence of cathodic gas stoichiometry on the spatial distribution of the present processes in a HTPEM fuel cell has been investigated using current density measurements as well as electrochemical impedance spectroscopy. It has been shown that reducing the air flow leads to changes in the spatial distribution of current density and the impedance spectra. More precisely a stronger gradient along the cathodic gas channel appears as well as the Nyquist plot shows more pronounced second arcs at cell segments towards the air outlet. The characteristics of impedance spectra are highly dependent on the position. The HFR does not depend on cathode stoichiometry and does not vary between the investigated segments.

With the presented results it can be concluded that measuring the overall cell impedance might not lead to a complete picture of the processes that determines the fuel cell performance since the impact of lateral inhomogeneities merges the cell response to a non-interpretable spectra. Thus, spatially resolved electrochemical impedance spectroscopy is necessary to achieve a deeper understanding of the present processes in a fuel cell.

References

[1] J. Wu, X. Z. Yuan, H. Wang, M. Blanco, J. J. Martin, J. Zhang, Diagnostic tools in PEM fuel cell research: Part I Electrochemical techniques, *International Journal of Hydrogen Energy*, Volume 33, Issue 6, 2008.

[2] A. Hakenjos and C. Hebling, Spatially resolved measurement of PEM fuel cells, *Journal of Power Sources*, Volume 145, Issue 2, 2005.

[3] J. S. Wainright, J. -T. Wang, D. Weng, R. F. Savinell and M. Litt, Acid-Doped Polybenzimidazoles: A New Polymer Electrolyte, *Journal of the Electrochemical Society*, Volume 142, Issue 7, 1995.

[4] A. Bergmann, D. Gerteisen and T. Kurz, Modelling of CO Poisoning and its Dynamics of HTPEM Fuel Cells, *Fuel Cells*, Volume 10, Issue 2, 2009.

[5] Q. Li, R. He, J.-A. Gao, J. O. Jensen and N. J. Bjerrum, The CO Poisoning Effect in PEMFCs Operational at Temperatures up to 200°C, *Journal of The Electrochemical Society*, Volume 150, Issue 12, 2003.

[6] J. L. Jespersen, E. Schaltz and S. K. Kær, Electrochemical characterization of a polybenzimidazole-based high temperature proton exchange membrane unit cell, *Journal of Power Sources*, Volume 191, Issue 2, 2009.

Computational Modeling of Carbon Corrosion in PEM Fuel Cells

Hans-Wilfried Mindt, ESI-GmbH, Germany
Kunal Jain, ESI US R&D Inc., Huntsville, AL 35806, USA
Ashok Gidwani, CFD Research Corporation, Huntsville, AL 35805, USA
Sanjiv Kumar, Unit Cell Engineering, Ballard Power Systems, Burnaby, BC V5J 5J8, Canada

Proton Exchange Membrane (PEM) Fuel Cells continue to be among the most promising alternative energy devices for automotive as well as stationary applications.

Several modes and mechanisms of degradation of PEM fuel cells, primarily the MEA, have been discussed by de Bruijn et al [1]. Figure 1(B) illustrates the various mechanisms for degradation of electrodes. One such degradation mechanism is the corrosion of carbon supports. Carbon, with an equilibrium potential of 0.207 V at 25 °C, is thermodynamically unstable at typical operating conditions of the fuel cell. Fortunately, slow kinetics allow the use of carbon supports in fuel cells. But, at high electrode potential, the corrosion rate becomes significant. The high potential is mainly caused by mal-distribution of H2. Fuel starvation, or mal-distribution of H2, can also happen due to flooding of the anode or during start-stop cycles, as illustrated in Figure 1 (A).

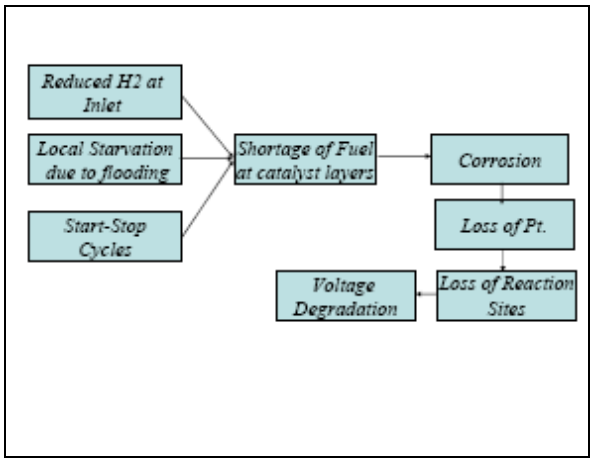

Figure 1 A: Schematic illustrating fuel mal-distribution mode resulting in carbon corrosion.

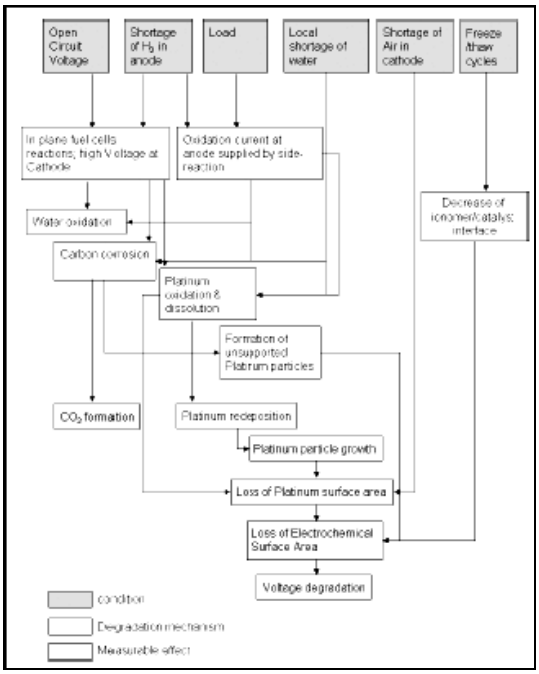

Figure 1 B: Degradation conditions, mechanisms, and effects for electrodes (de Bruijn et al., [1]).

In this work, we numerically study the durability issues of PEM fuel cells due to carbon corrosion in electrodes due to fuel starvation. Understanding of the mechanisms of carbon corrosion and identification of conditions leading to corrosion can help design the operating conditions and guide material development to mitigate the electrode degradation and improve the fuel cell system durability.

The equations governing conservation of mass, momentum, species, and current were solved in a self-consistent manner using a finite volume scheme on arbitrary mesh topology within the framework of the commercial CFD code CFD-ACE+. The details of theory of species transport and electrochemical reactions in porous media, and the mathematical formulation of the conservation equations have been described in detail elsewhere [2,3,9]. Furthermore, species conservations and production/destruction by electrochemical multi-step reactions are considered. Reactants flowing through the pores in a porous solid arrive at the solid catalyst/electrolyte interface by diffusion within the gas pores and the polymer electrolyte. The transfer current is obtained from the Butler-Volmer equation, and has been used in its general form.

1 Model Validation

The developed model was validated against experimental and other model data from the literature. The validation was performed for the cases with and without the carbon corrosion.

1.1 Model Validation for Fuel Cell Operation without Carbon Corrosion

Validation studies were performed against analytical solutions of Newman and Tobias [4] for current through a single porous electrode. Validation was also performed against the experimental data of Ticianelli et al. [5,6]. These studies are reported in detail in our previous publication [2,3] wherein we showed good agreement between the results predicted by our CFD-ACE+ computational model and the analytical/experimental data.

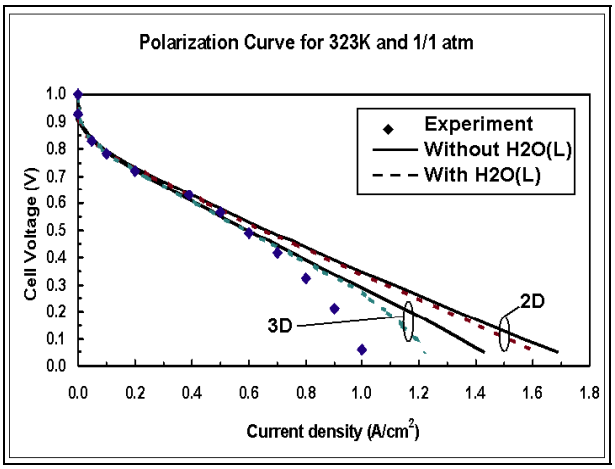

Figure 2: Predicted polarization curve compared against experimental data (Conditions: 323 K, 1 atmosphere pressure and 100 % relative humidity at flow inlet).

Figure 2 presents the polarization curves obtained using two-dimensional and three-dimensional simulations and compares the predicted cell performance with the experimental data. As seen from the polarization curves, at low current densities, there is an excellent match between the computationally predicted data (for both two-dimensional and three-dimensional simulations) and the experimental data. However, as the current density increases, the numerical results overpredict the experimental data, the two dimensional simulation data deviating much more than the three-dimensional simulation prediction. With the inclusion of liquid water formation and transport, the predicted results match better with the experimental data.

1.2 Model Validation for Carbon Corrosion

Carbon corrosion validation studies were performed for air/air polarization for the experimental data reported by UTC-Fuel Cells researchers Meyers and Darling [7]. The channel, GDL, and MEA dimensions and flow rates were same as those in UTC model, and summarized in Table I. The electrochemical reactions and reaction parameters are summarized in Table II. The computational domain with grid is shown in Figure 3. Figure 4 shows polarization curves with air on both electrodes. As explained in Meyers and Darling [7], the current density is negative because current flows through the cell in the direction opposite of normal fuel cell operation. Figure 5 compares the predictions of partial current densities from the current model with the UTC model (Meyers and Darling [7]). The predictions are for air/air case and show excellent match between the two models.

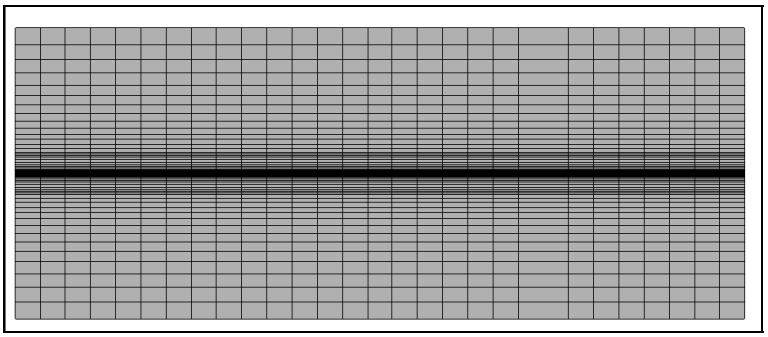

Figure 3: Schematic of the fuel cell with grid distribution. Model scaled in Y by a factor of 100.

Table 1: Channel dimensions and parameters used in this study.

Parameter	*Value*	*Parameter*	*Value*
Length	*711.2 mm*	Fuel Flow Velocity	3.78 m/s
Depth	*0.457 mm*	Air Flow Velocity	10.58 m/s
Width	*1.19 mm*		

Table 2: Electrochemical reactions and parameters used in this study.

Electrochemical Reactions	*Equilibrium Potential*	*Reaction Parameters*	*Value*	*Reaction Parameters*	*Value*
$2H_2 \Rightarrow 4H^+ + 4e^-$	E = 0.0V	$\alpha_{a,H2}$	1	$\alpha_{a,O2}$	0.6
$4H+ + O_2 + 4e^- \Leftrightarrow 2H_2O$	E = 1.2V	$\alpha_{c,H2}$	1	$\alpha_{c,O2}$	1
$C + 2H_2O \Rightarrow CO_2 + 4H^+ + 4e^-$	E = 0.207V			$\alpha_{a,C}$	0.275

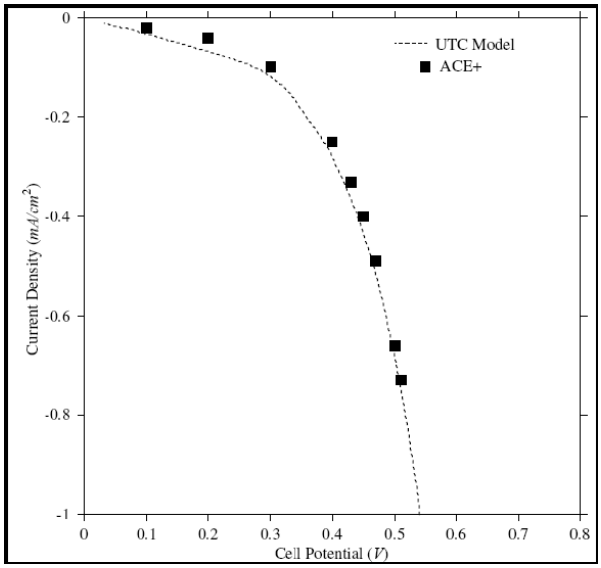

Figure 4: Comparison of air/air polarization data with experimental data reported by Meyers and Darling [7].

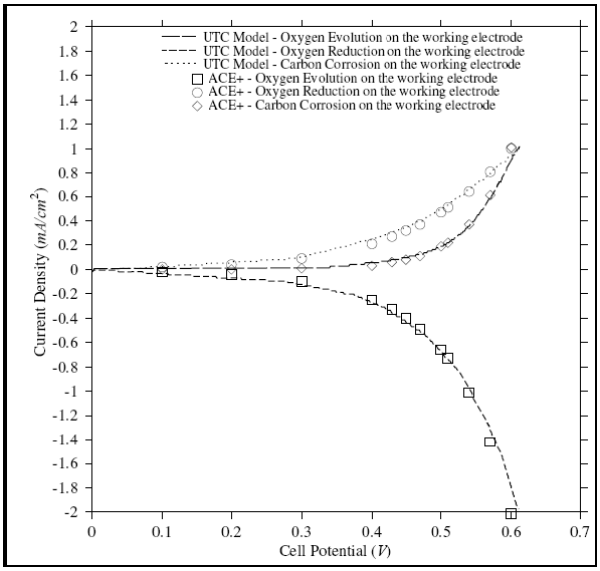

Figure 5: Comparison of partial current densities on the working and counter electrode during air/air polarization curve.

2 Results and Discussion

Having performed model validation, numerical calculations of fuel cell operation under different corrosion conditions were performed in two-dimensional and three-dimensional geometries. The results from these simulations are described in the following subsections.

2.1 Partial starvation due to insufficient hydrogen

This mode of carbon electrode corrosion can occur during start/stop cycles when there is insufficient amount of hydrogen fuel for a brief period of time. We have mimicked this case with a steady state simulation with fuel flow at stoichiometric values less than 1. Figure 6 shows the isocontours of hydrogen mass fraction and corresponding cell potential for three different stoichiometric values for hydrogen. In this case, carbon corrosion reaction is off and the cell is driven with a fixed current density. As seen from the Figure, the fuel concentration decreases as the fuel is consumed downstream. When all the fuel is consumed, the cell potential reverses with electrolysis of water taking place at the working electrode. A transient simulation was performed with carbon corrosion reaction allowed to occur at either electrode.

There was no hydrogen flow in this simulation and air was flown through both channels. A finite number of surface sites for carbon were assumed to be present at the two electrodes. Figure 7 zooms into the catalyst layer and shows the filling of the various carbon sites, C(S), and isocontours of CO2 mass fraction as oxidation of carbon occurs.

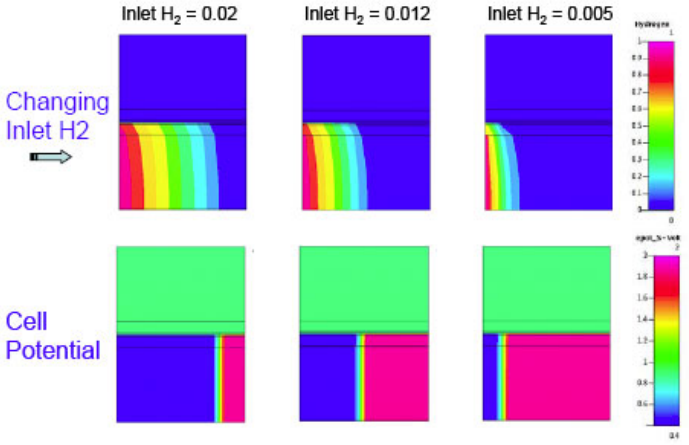

Figure 6: Isocontours of hydrogen mass fraction (normalized) and potential distribution for different stoichiometry values of hydrogen during partial starvation operation; Note: Model scaled in Y by a factor of 100.

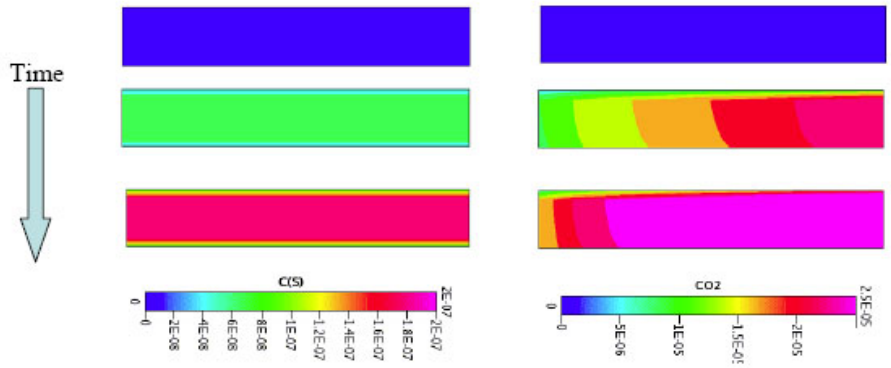

Figure 7: Isocontours of carbon sites (left) and CO2 mass fraction (right) with time illustrating carbon corrosion in the catalyst layer.

2.2 Local starvation

Local starvation of electrode could occur due to localized blocking of catalyst sites by water droplets, which prevents the fuel to reach the active catalyst sites. This situation was mimicked by deactivating the hydrogen oxidation reaction in the blocked region shown in Figure 8. An abrupt decrease in the solid potential is seen where the catalyst site is blocked.

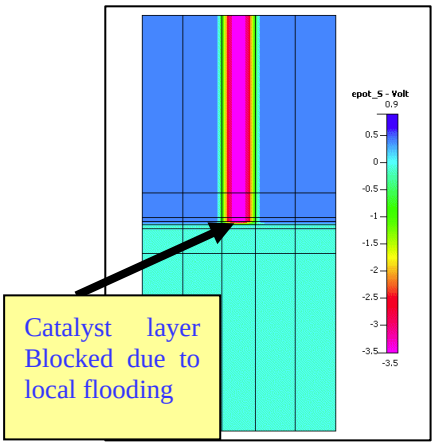

Figure 8: Cell potential distribution during local starvation and carbon corrosion.

2.3 Divided or Dual Cell Reverse-Current Configuration

During start-stop cycles, the fuel electrode may be partially exposed to hydrogen and partially to air. In such a case the region with hydrogen drives the cell while the other half of the cell, which is hydrogen deficient, draws the current and creates the "reversecurrent" conditions. Figure 9(A) depicts the process schematically as it was experimentally demonstrated by Reiser et al. [8] using two electrically connected cells, figure 9(B).

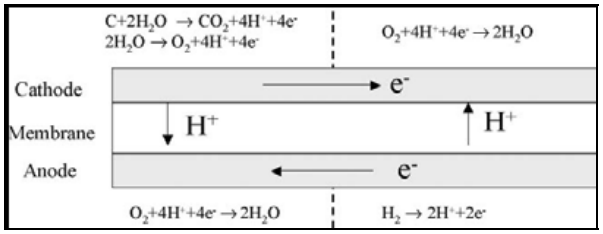

Figure 9 A: Schematic of reverse-current configuration.

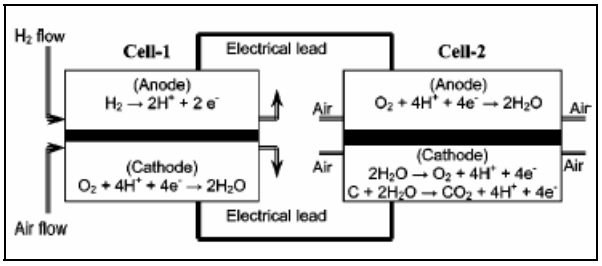

Figure 9 B: Schematic of a dual cell configuration used to simulate the reverse-current condition (Reiser et al.[8])

References

[1] F. A. de Bruijn, V. A. T. Dam, and G. J. M. Janssen, Fuel Cells, 1, 3 (2008).

[2] J. V. Cole and S. Mazumder, J. Electrochem. Soc., 150, A1503 (2003).

[3] J. V. Cole and S. Mazumder, J. Electrochem. Soc., 150, A1510 (2003).

[4] J. S. Newman and C. W. Tobias, J. Electrochem. Soc., 109, 1183 (1962).

[5] E.A. Ticianelli, C. R. Derouin, and S. Srinivasan, J. Electroanal. Chem., 251, (1988).

[6] E.A. Ticianelli, C. R. Derouin, A. Redondo, and S. Srinivasan, J. Electrochem. Soc.,135, 2209 (1988).

[7] J. P. Meyers and R. M. Darling, J. Electrochem. Soc., 153(8), A1432 (2006).

[8] C. A. Reiser, L. Bregoli, T. W. Patterson, J. S. Yi, J. D. Yang, M. L. Perry, and T. D. Jarvi, Electrochemical and Solid-State Letters, 8, A273 (2005).

[9] Ashok Gidwania, Kunal Jainb, Sanjiv Kumarc, and J. Vernon Colea, ECS Transactions, 16(2) 1323-1333 (2008).

Evaluation of Power Performance of Small Free-Breathing Polymer Electrolyte Fuel Cells

Kohei Nakashima, **Tomoya Sawai**, **Ayumu Mitani**, **Soichi Ishihara**, **Yoshio Murakami**, Meijo University, Japan

Abstract

Utilizing commercially-available parts, we constructed a small free-breathing polymer electrolyte fuel cell, with an active area of 4 cm^2 and hole openings in the separator on the cathode side. We then systematically investigated power performance and cell resistance as functions of cell temperature, hydrogen flow rate and cell tilt angle. We thus clarified the power performance at each temperature, hydrogen flow rate and cell tilt angle, and found the optimum operating conditions for higher power performance to current density.

1 Introduction

When used to power portable electronics devices, polymer electrolyte fuel cells need to be small and simple, with minimal auxiliary devices. There are great hopes that portable electronics devices will be powered by free-breathing polymer electrolyte fuel cells (hereafter “free-breathing fuel cells”) needing no auxiliary air circulation devices. The cathode side of these free-breathing fuel cells takes oxygen directly from the surrounding air, using natural convection. Several studies have reported performance evaluations of larger free-breathing fuel cells, with active areas of 6 to 18 cm^2, including Hottinen et al. [1,2], Schmitz et al. [3] and Park et al. [4]. Neponen et al. [5] measured current distribution of free-breathing fuel cell, with an active area of 25 cm^2. However, there have been no full reports evaluating the performance of small free-breathing fuel cells, with active areas of 4 cm^2 or less, applicable to power portable electronics devices. In this study, we investigated the power performance of a small free-breathing fuel cell, without humidifiers on the anode side and without air circulation devices on the cathode side. For the purpose of this study, utilizing commercially-available parts, we constructed a small free-breathing fuel cell with an active area of 4 cm^2 and hole openings in the separator on the cathode side. By controlling our cell temperature and hydrogen flow rate, we examined power performance and cell resistance as functions of cell temperature, hydrogen flow rate and cell tilt angle.

2 Experiment

Figure 1 shows single free-breathing fuel cell with an active area of 4 cm^2. The solid polymer electrolyte membrane was Nafion 112, with a thickness of 54 μm, made by DuPont. The electrodes with gas diffusion layers were carbon paper with a thickness of 0.37 mm, loaded with 1.0 mg/cm^2 platinum, made by Chemix Co., Ltd. The separators, with a thickness of 4.5 mm, were made of carbon with a gas-impermeable treatment, again by Chemix Co., Ltd. The separator on the anode side had a meander channel with a width of 2 mm and a depth of 1 mm. The separator on the cathode side had nine hole openings of 2.8 mm diameter. The

end plates were made of aluminum. We drilled holes of 1 mm and 6 mm diameter, to install a K-type sheathed thermocouple and a cartridge heater, respectively.

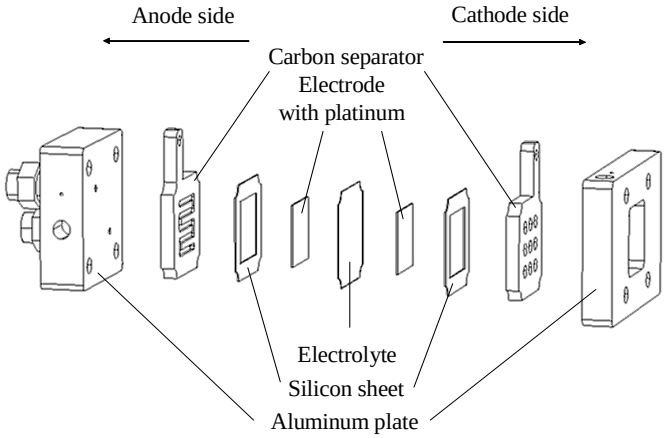

Figure 1: Experimental free-breathing fuel cell.

Figure 2 shows our experimental apparatus. The hydrogen was regulated by a mass flow controller, and then supplied to our free-breathing fuel cell, without humidification. However, only when we were breaking in our cell, we humidified the hydrogen using a humidifier at ambient temperature, before supplying it to our fuel cell. We mounted our fuel cell on a tilt jig, so that we could rotate its center plane between perpendicular to the ground and horizontal. We installed cartridge heaters into the end plates. We connected our fuel cell both to an electric load device (Model PLZ70UA, Kikusui Electronics Corp.) to evaluate cell performance, by measuring polarization and current transients, and to an ohm tester (Model 356E, Tsuruga Electric Corp.) to measure internal resistance of our cell, at a frequency of 10 kHz.

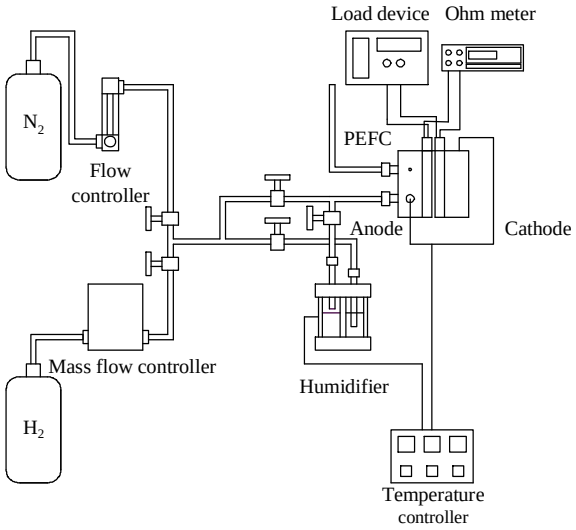

Figure 2: Experimental apparatus.

In our experiments, we set the cell temperature successively at ambient temperature, 30, 40 and 60 °C. We defined the hydrogen supply ratio as the proportion of the supply flow rate to the stoichiometric flow rate at 250 mA/cm^2 (hydrogen 7.0 cm^3/min [normal]). We set this hydrogen supply ratio successively at 1 and 2. Before each measurement, we supplied unhumidified hydrogen of 18.6 cm^3/min [normal] to our cell at ambient temperature, until cell resistance reached 300 mΩ. Then, to break in the cell, we allowed the cell to stabilize at a current density of 2.5 mA/cm^2 for 30 minutes, while supplying the fixed hydrogen with humidification at ambient temperature and setting at the fixed cell temperature. After this break-in, we measured the cell voltage and resistance, while increasing current density in increments of 5 mA/cm^2. Here we averaged two measurements, one immediately after establishing each current density, and one 3 minutes later, for our cell voltage and resistance data. We ran our experiments at an ambient temperature of 22 to 26 °C, and a relative humidity of 35 to 70%.

3 Results and Discussion

Figure 3 shows the effect of cell temperature on cell voltage, power density and resistance, with a hydrogen supply ratio of 1, and with the cell center plane perpendicularly to the ground (i.e. a cell tilt angle of 0°). We see that, at a lower current density, both cell voltage and power density decreased, and cell resistance increased, with increased cell temperature. But at a higher current density, the cell voltage reduction rate at higher cell temperature is less than that at lower cell temperature, and cell resistance has a minimum effect on the cell temperature. The maximum power density also increased with increased cell temperature. It appears that, at a lower current density, the solid polymer electrolyte membrane dries as the cell temperature becomes higher, resulting in an increased resistance to proton conduction, thus reduced cell voltage. On the other hand, it seems that, at a higher current density, the moisture content of the solid polymer electrolyte membrane was maintained by the product water, so the cell voltage reduction rate decreased with higher cell temperature.

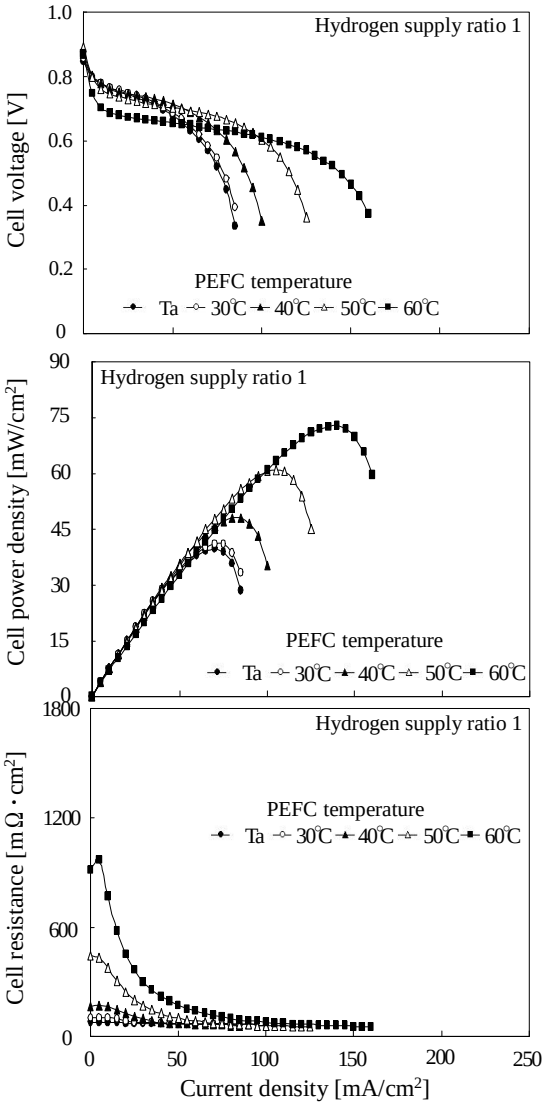

Figure 3: Effect of cell temperature on cell voltage, power density and resistance with hydrogen supply ratio of 1 and cell tilt angle of 0°.

Figure 4 shows the effect of cell temperature on cell voltage, power density and resistance, this time with a hydrogen supply ratio of 2, and again with the cell center plane perpendicularly to the ground (cell tilt angle of 0°). The trend in temperature dependence on cell voltage, power density and resistance vs. current density with this hydrogen supply ratio of 2 is almost the same as that with the previous hydrogen supply ratio of 1. Specifically, at the ambient temperature and a cell temperature of 30 °C, cell voltage, power density and cell resistance with this hydrogen supply ratio of 2, is almost the same as that with the previous hydrogen supply ratio of 1. However, at cell temperatures of 40 °C and above, cell voltage and power density with this hydrogen supply ratio of 2 is lower than that with a hydrogen supply ratio of 1, but the cell resistance with this hydrogen supply ratio of 2 is higher than that with a hydrogen supply ratio of 1. It seems that, with increased hydrogen flow rate and a

higher cell temperature, the solid polymer electrolyte membrane becomes drier, decreasing cell voltage.

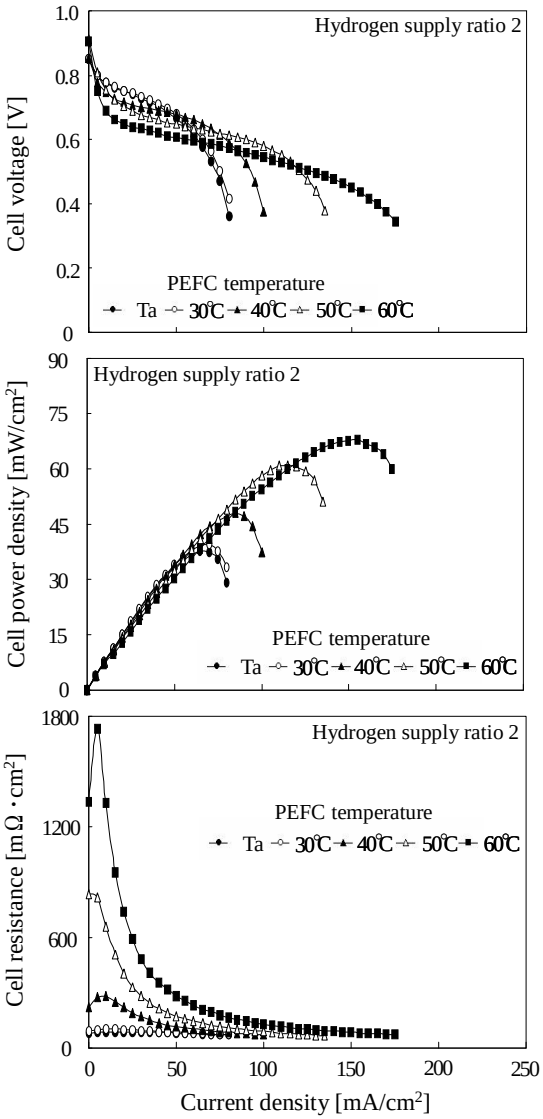

Figure 4: Effect of cell temperature on cell voltage, power density and resistance with hydrogen supply ratio of 2 and cell tilt angle of 0°.

Figure 5 shows the effect of cell tilt angle on cell voltage, power density and resistance, with a hydrogen supply ratio of 1, at ambient temperature. Positive tilt angle represents the cathode inclining upward from the cell center plane perpendicularly to the ground, negative tilt angle represents the cathode declining downward. Both, positive and negative cell tilt angles, have a minimum effect on the cell voltage, power density and resistance. It appears that sufficient air is supplied by natural convection from hole openings in separator to the cathode, even when tilting the cell upwards or downwards.

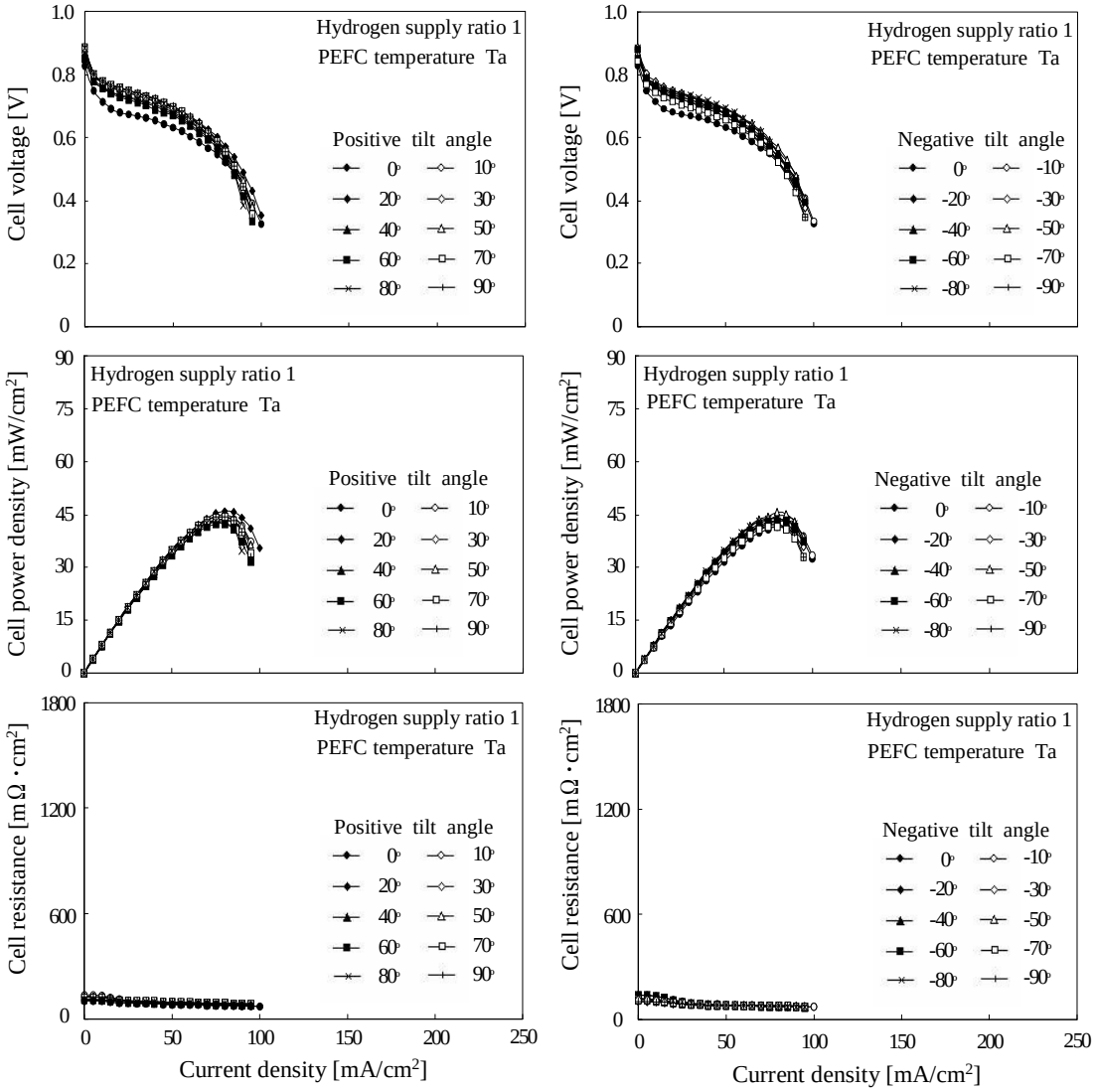

Figure 5: Effect of cell tilt angle on cell voltage, power density and resistance, with a hydrogen supply ratio of 1, at ambient temperature.

4 Conclusion

We constructed a small, free-breathing fuel cell, with an active area of 4 cm^2, and hole openings in separator on the cathode side. We investigated the power performance and cell resistance of this fuel cell, as functions of cell temperature, hydrogen flow rate and cell tilt angle. Our major results follow:

1. At a lower current density, both cell voltage and power density decreased with increased cell temperature. But at a higher current density, the cell voltage reduction rate decreased, and the maximum power density increased, with increased cell temperature.
2. At a higher cell temperature, both cell voltage and power density decreased with increased hydrogen flow rate.

3. Tilting the cell upward or downward has a minimum effect on both cell voltage and power density.

In our future work, we will examine the effect on power performance of the size of the holes in the separator on the cathode side.

Acknowledgements

We would like to thank Chemix Co., Ltd. for their help in producing our small free-breathing fuel cell.

References

[1] T. Hottinen et al., Journal of Power Sources, 129, (2004), 68-72.

[2] T. Hottinen et al., Journal of Power Sources, 138 (2004), 205-210.

[3] A. Schmitz et al., Journal of Power Sources, 118 (2003), 162-171.

[4] S. Park et al., Transactions of the Japan Society of Mechnical Engineers, Series B, 71, 711 (2005), 2808-2815.

[5] M. Noponen et al., Journal of Power Sources, 106 (2002), 304-312

Power Performance of Small Polymer Electrolyte Fuel Cells under Various Humidification Conditions

Kohei Nakashima, **Ayumu Mitani**, **Tomoya Sawai**, **Soichi Ishihara**, **Yoshio Murakami**, Meijo University, Japan

Abstract

To generate stable electricity with a polymer electrolyte fuel cell (PEFC), it is necessary to manage the cell's water content. We constructed a small PEFC with an active area of 4 cm^2, applicable to power portable electronics devices, and then investigated its power performance under various humidification conditions. By controlling the temperature of the PEFC, the humidifiers and the piping, and the hydrogen and air flow rates, we examined the power performance and cell resistance as functions of cell temperature, humidification temperature, and flow rates. We thus clarified optimum humidification conditions for maximum power performance and discovered the relationship between excess air ratio and maximum power.

1 Introduction

In a polymer electrolyte fuel cell (PEFC), hydrogen is supplied to the anode, and oxygen to the cathode. Chemical reactions generate electricity and produce water on the cathode side. Now, because the solid polymer electrolyte membrane between the PEFC electrodes can conduct protons only in the presence of water, almost all PEFCs supply water to the membrane by humidifying their gas feed stream. However, when this feed gas becomes supersaturated and product water accumulates in the PEFC, water flooding occurs in the gas diffusion layer, the catalyst layer, and the gas channel, all resulting in decreased PEFC performance. Such flooding is especially likely in a small PEFC, applicable for powering a portable electronics device, because of its narrow gas channel and lower gas flow rates. Therefore, it is necessary to manage the water content inside the small PEFC to generate stable electricity. Several studies have reported product water under higher humidification conditions in larger PEFCs with active areas of 6 to 104 cm^2, including Konomi & Nakamura [1], Konomi et al. [2], Lu et al. [3], and Yoshikawa et al. [4,5]. However there have been no full reports evaluating power performance and cell resistance of small PEFCs, with active areas of 4 cm^2 or less, under various humidification conditions. In this study, we first constructed a small PEFC with an active area of 4 cm^2. We then systematically examined its power performance and cell resistance as functions of cell temperature, humidification temperature, and hydrogen and air flow rates.

2 Experiment

Fig.1 shows our small PEFC, comprising a solid polymer electrolyte membrane (made of Nafion 112, with a thickness of 54 μm), electrodes with gas diffusion layers (carbon paper, with a thickness of 0.37 mm, loaded with 1.0 mg/cm^2 platinum), gaskets (silicon), separators (carbon with a gas-impermeable treatment, with a thickness of 4.5 mm) and end plates

(aluminum alloy). The separator had a meander channel with a width of 2 mm and depth of 1 mm. Components on the anode side are the same as those on the cathode side.

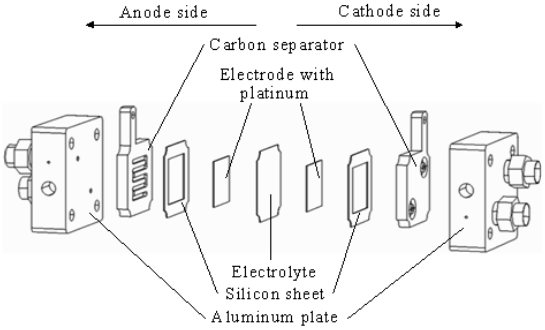

Figure 1: Experimental PEFC.

Fig. 2 shows our experimental apparatus. The hydrogen and air were regulated by mass flow controllers, and then were humidified in separate humidifiers before supplying them to the PEFC. We installed cartridge heaters into the end plates. We wrapped the humidifiers in rubber heaters. We then placed the PEFC, humidifiers, and piping in a thermostatic chamber to control their temperature. We connected the PEFC both to an electric load device (Model PLZ152 with a voltage resolution of 1 mV, Kikusui Electronics Corp.) to evaluate polarization and current transients, and to an ohm tester (Model 356E, Tsuruga Electric Corp.) to measure cell resistance at a frequency of 10 kHz.

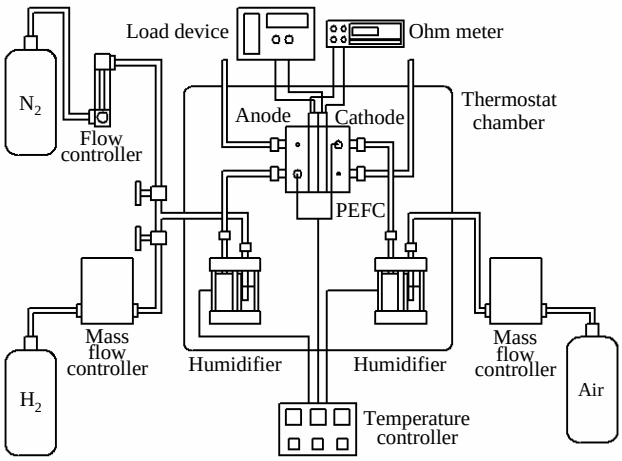

Figure 2: Experimental apparatus.

Table 1 shows our experimental conditions. We define the humidification temperature as the temperature both in water of humidifiers and in the thermostatic chamber. We define the hydrogen and air supply ratios as the proportion of the supply flow rate to the stoichiometric flow rate at 250 mA/cm^2 (hydrogen 7.0 cm^3/min [normal]; air 16.8 cm^3/min [normal]). In our experiment, before each measurement, we allowed the PEFC to stabilize at a current density

of 2.5 mA/cm^2 for 1 hour. We then measured the cell voltage and resistance while increasing current density in increments of 5 mA/cm^2.

Table 1: Conditions.

PEFC	Temperature	60° C	80° C
Hydrogen	Humidification temperature	40, 50, 60° C	60, 70, 80° C
	Supply ratio	1.00	
Air	Humidification temperature	40, 50, 60° C	60, 70, 80° C
	Supply ratio	1.00, 1.25, 1.67, 2.50, 5.00, 10.00	

3 Results and Discussion

Fig. 3 shows the effect of humidification temperature on cell voltage, power density, and resistance, with air supply ratio of 1.25 and 5.00, at cell temperature of 60 °C. Looking first at an air supply ratio of 1.25, and with a current density of 60 mA/cm^2 or less, we see that both cell voltage and power density increased with increased humidification temperature. But when current density exceeds 65 mA/cm^2, both cell voltage and power density are higher at humidification temperature of 50 °C than at 40 °C and 60 °C. Cell voltage dropped extremely at 135 mA/cm^2 at a humidification temperature of 60 °C, but dropped at 230 mA/cm^2 at 40 °C and 50 °C. At lower current densities, cell resistance decreased with increased humidification temperature. But at higher current densities, cell resistance decreased at humidification temperatures of 40 °C and 50 °C, and was similar to that at 60 °C.

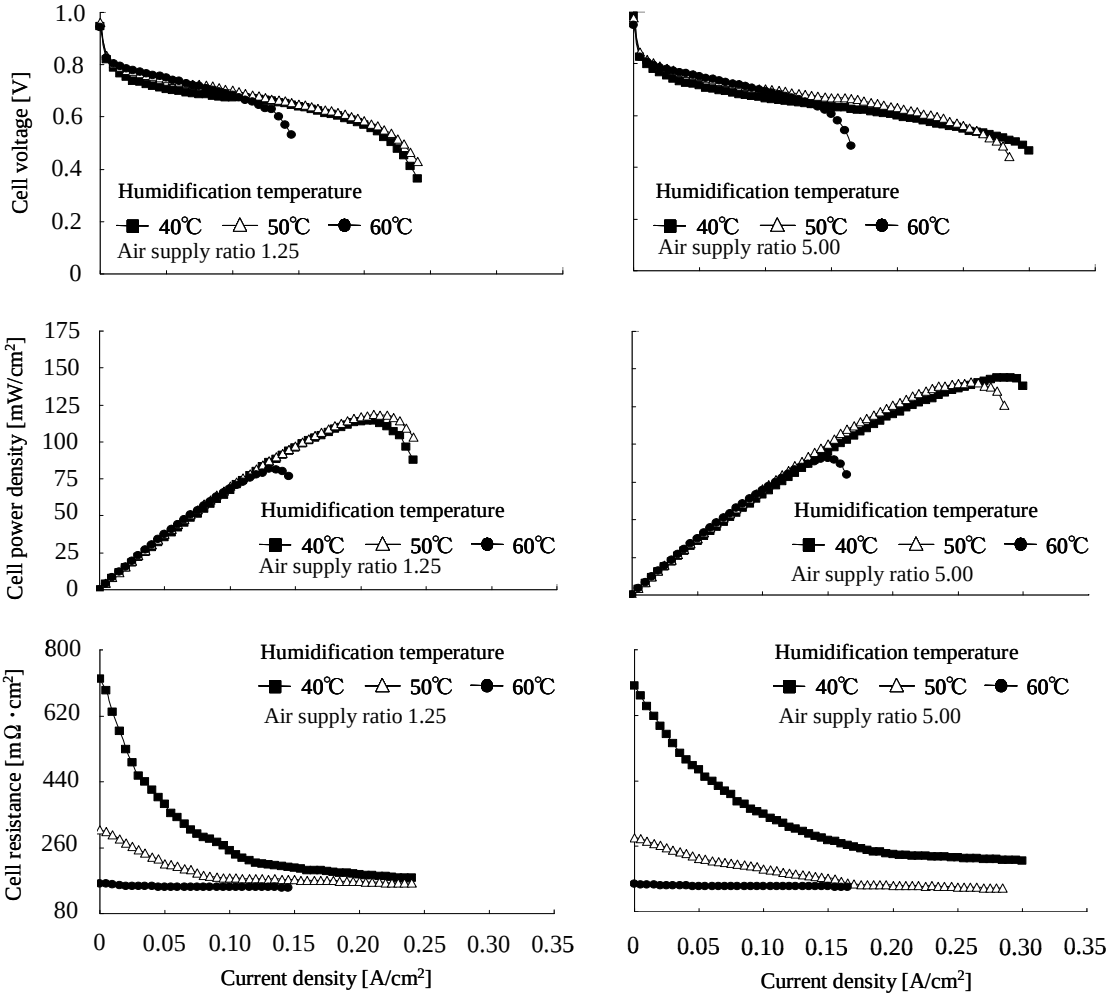

Figure 3: Effect of humidification temperature on cell voltage, power density, and resistance with air supply ratios of 1.25 and 5.00 at cell temperature of 60 °C.

Looking next at an air supply ratio of 5.00, with a current density of 50 mA/cm^2 or less, we see that both cell voltage and power density increased with increased humidification temperature. With current densities between 80 and 260 mA/cm^2, both cell voltage and power density are higher at a humidification temperature of 50 °C than at 40 °C and 60 °C. But when current density exceeds 260 mA/cm^2, both cell voltage and power density are higher at a humidification temperature of 40 °C than at 50 °C. While the cell voltage dropped extremely at 160 mA/cm^2 at a humidification temperature of 60 °C, it dropped at 285 mA/cm^2 at 50 °C, and 305 mA/cm^2 at 40 °C. At lower current densities, cell resistance also decreased with increased humidification temperature. At higher current densities, cell resistance at a humidification temperature of 50 °C fell to almost the same level as that of 60 °C, but cell resistance at 40 °C did not fall to that same 60 °C level. It seems that, at lower current densities, the solid polymer electrolyte membrane dries with a lower humidification temperature, resulting in decreased cell voltage. But as the current density increases, the moisture content on the solid polymer electrolyte membrane is maintained by the product water, so the cell voltage reduction rate decreases with a lower humidification temperature.

Similarly, it appears that at higher current densities water flooding occurs in the gas diffusion layer, or in the catalyst layer in the cathode side, with a higher humidification temperature. This water flooding inhibits reactions and the maximum power density decreases. It seems that, with a higher air supply ratio, it is easier for the product water to drain out, and there is less incidence of water flooding, resulting in increased cell voltage and power density.

Fig. 4 shows the effect of humidification temperature on cell voltage, power density, and resistance, with air supply ratio of 1.25 and 5.00, at cell temperature of 80 °C. Looking first at an air supply ratio of 1.25, with a current density of 105 mA/cm^2 or less, we see that both cell voltage and power density at a humidification temperature of 80 °C are higher than at 60 °C and 70 °C, but cell voltage and power density are similar at 60 °C and 70 °C. With current densities exceeding 110 mA/cm^2, both cell voltage and power density decreased with increased humidification temperature. While the cell voltage dropped extremely at 155 mA/cm^2 at a humidification temperature of 80 °C, it dropped at 230 mA/cm^2 at 70 °C, and 305 mA/cm^2 at 60 °C. At lower current densities, cell resistance decreased with increased humidification temperature. However, at higher current densities, cell resistance at 60 °C and 70 °C did not fall to the 80 °C level.

Looking next at an air supply ratio of 5.00, with a current density of 195 mA/cm^2 or less, we see both cell voltage and power density at a humidification temperature of 80 °C are higher than at 60 °C and 70 °C, and the differences of cell voltage and power density between 80 °C and 60 °C or 70 °C are larger with an air supply ratio of 5.00 than that with the previous air supply ratio of 1.25. Here, with this air supply ratio of 5.00, both cell voltage and power density at 60 °C are similar to those at 70 °C. With current densities exceeding 200 mA/cm^2, both cell voltage and power density decreased with increased humidification temperature. Cell voltage dropped extremely at 205 mA/cm^2 at a humidification temperature of 80 °C, but dropped at 305 mA/cm^2 at 70 °C and at 330 mA/cm^2 at 60 °C. At a humidification temperature of 60 °C, the maximum power density is slightly higher at this air supply ratio of 5.00 than that with the previous air supply ratio of 1.25. At higher current densities, cell resistance at 60 °C and 70 °C with an air supply ratio of 5.00 did not decrease to the level of 80 °C, and was always higher than that with an air supply ratio of 1.25. It seems that, at cell temperature of 80 °C, with decreased humidification temperature, at both lower and higher current densities, the solid polymer electrolyte membrane dries, resulting in no increase to cell voltage and power density.

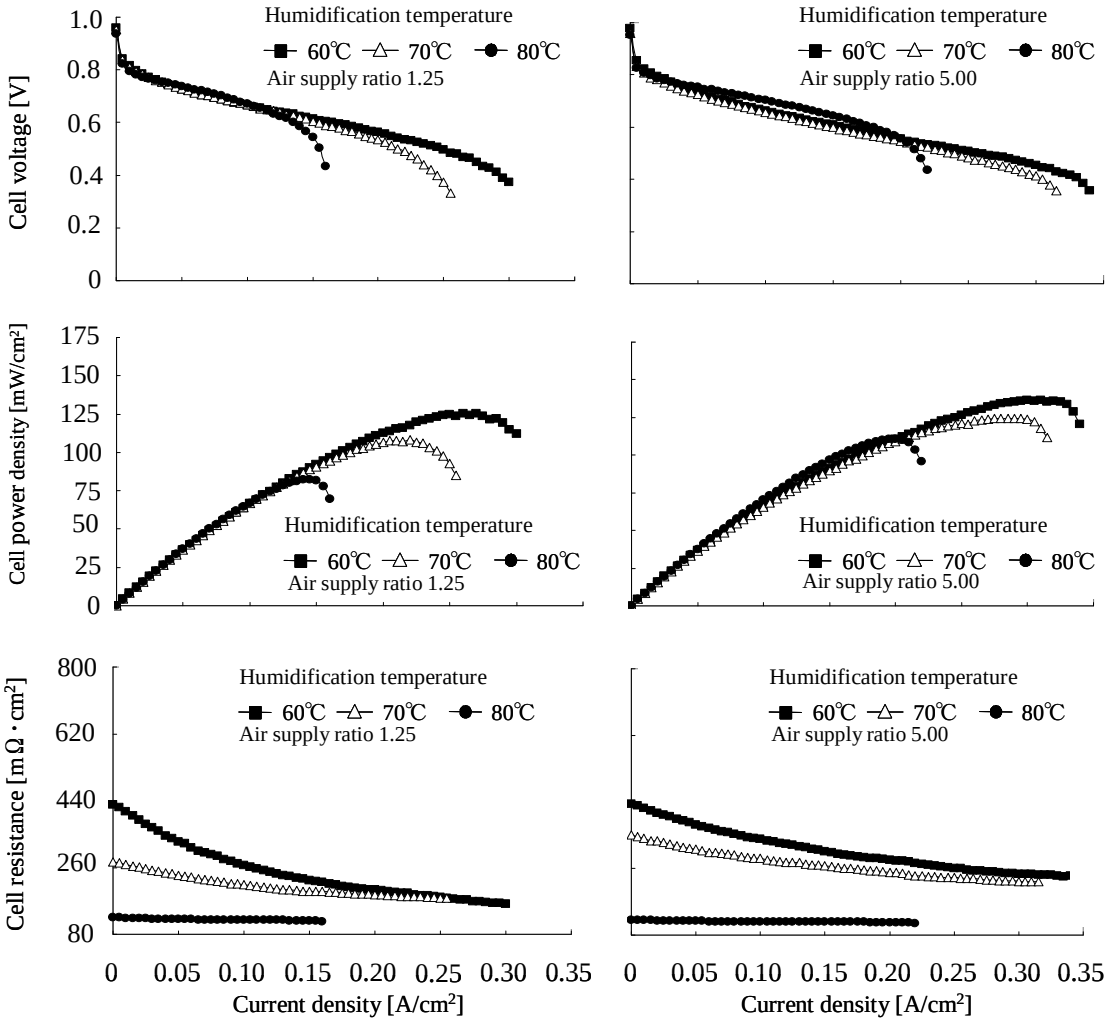

Figure 4: Effect of humidification temperature on cell voltage, power density, and resistance with air supply ratios of 1.25 and 5.00 at cell temperature of 80 °C.

Fig.5 shows the relationship between the excess air ratio and the maximum power density. At cell temperatures of 60 °C and 80 °C, when the humidification temperature increased, the maximum power density decreased. At most humidification temperatures, the maximum power density increased with increased excess air ratio. But at a cell temperature of 60 °C, when the excess air ratio exceeded 5.0, the maximum power density held nearly constant. And at a cell temperature of 80 °C, when the excess air ratio exceeded 2.5, the maximum power density again held nearly constant. Therefore, taking into account the air flow rate supplied in actual operation, the optimum excess air ratio are 5.0 and 2.5, at cell temperatures of 60 °C and 80 °C, respectively.

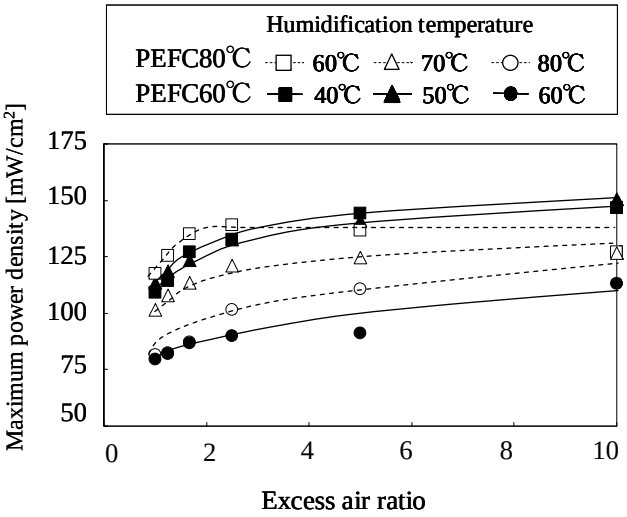

Figure 5: Maximum power density vs. excess air ratio.

4 Conclusion

Utilizing our small PEFC, we investigated its power performance under various humidification conditions. Our major results are as follows:

1. When the humidification temperature increased at lower current densities, or decreased at higher current densities, both cell voltage and power density increased.
2. Maximum power density decreased with increased humidification temperature.
3. Taking into account the air flow rate supplied in actual operation, the optimum excess air ratio is 5.0 at a cell temperature of 60 °C, and 2.5 at 80 °C.

Acknowledgments

We would like to thank Chemix Co., Ltd. for the help in producing the small PEFC.

References

[1] T. Konomi & G. Nakamura, Transactions of the Japan Society of Mechanical Engineers, Series B, 72, 715 (2006), 745-751.

[2] T. Konomi et al., Transactions of the Japan Society of Mechanical Engineers, Series B, 72, 724 (2006), 2978-2983.

[3] G. Lu et al., Journal of Power Sources, 164, (2007), 134-140.

[4] H. Yoshikawa et al., Transactions of the Japan Society of Mechanical Engineers, Series B, 66, 652 (2000), 3218-3225.

[5] H. Yoshikawa et al., Transactions of the Japan Society of Mechanical Engineers, Series B, 67, 653 (2001), 197-202.

High-Temperature PEM Fuel Cells: Electrolytes, Cells, and Stacks

Christoph Wannek

Abstract

Although today, most of the technical requirements which are considered to be relevant before classical (Nafion®-based) low temperature polymer electrolyte membrane (PEM) fuel cells can compete successfully with existing technologies on the market place are already met, at least on the laboratory scale, there are important research efforts to design cells with an operating temperature well above today's 80 °C. Basically, such high-temperature PEM fuel cells could benefit from accelerated electrode kinetics, a simplified system design and a higher tolerance towards impurities in the hydrogen fuel. This paper reviews the stateof-the-art in basic science and industrial development of membranes, electrodes and stacks and points out the main challenges for future development. It first describes various approaches to increase the operating temperature of classical membrane materials up to 120_C, before it focuses on the development of phosphoric acid-doped polybenzimidazoles-type membrane cells that operate at 160–180_C. As the technology readiness levels of alternative electrolytes such as phosphonic acids, ionic liquids, acidic salts and mixed oxides are still very low, they will be described only very briefly.

Development of Low Platinum Catalytic Layers for PEM Fuel Cells

E. R. Savinova, P. S. Ruvinsky, S. N. Pronkin, LMSPC UMR 7515/CNRS-ECPM-University of Strasbourg, France
A. Bonnefont, IC UMR 7177 /CNRS-University of Strasbourg, France

Polymer Electrolyte Membrane Fuel Cells (PEMFC) are considered as promising energy sources for vehicle, portable and stationary applications. However, their commercial use is still limited due to the high cost and insufficient durability. The catalytic layers of the state-of-the-art PEMFCs are multi-component media comprising a carbon-supported Pt or Pt alloy catalyst, accelerating the rates of electrochemical reactions; an ionomer, providing flow of protons through the membrane-electrode-assembly (MEA); and gas- and liquid-filled pores, providing access of the reagents to and the products from the catalyst surface. In this presentation we discuss three different approaches to reduce the platinum metal loadings in a PEMFC. The first approach is related to the optimization of the support material; the second approach deals with the optimization of the catalytic layer architecture, while the third approach is based on the development of non-platinum catalysts for the anode of a PEMFC.

Carbon support materials strongly influence the (i) size and morphology of metal nanoparticles, (ii) catalyst stability, (iii) metal/ionomer contact and catalyst utilization, (iv) mass-transport and (v) water management, and hence are among the key factors affecting the FC performance. The role of carbon materials in the catalytic layers of the PEMFCs has been recently reviewed by Maillard *et al.* [1].

In order to unveil the influence of the carbon support porosity on the fuel cell performance, a set of Pt catalysts supported on carbons of the Sibunit family were prepared. The carbon supports varied in degree of activation and consequently BET surface areas ranging from 22 to 415 m^2g^{-1}. The conventional 20 *wt.* % Pt catalyst supported on Vulcan XC-72 carbon black was used as a reference [2]. Fuel cell tests revealed strong influence of the type of carbon support both on the total and on the Pt mass-normalized currents. The highest mass specific currents are achieved for 30 *wt.* % Pt/Sibunit 20P and 40 *wt.* % Pt/Sibunit 619P with BET surface areas of carbon supports of 292 and 415 m^2g^{-1}, correspondingly. Both of these exceed the activity of 20 *wt.* % Pt/Vulcan XC-72 catalyst, the enhancement factor varying from 4 to 6 depending on whether pure oxygen or air is fed to the cathode. The increased mass specific activities cannot be ascribed to the influence of the carbon support on the metal dispersion which was purposely kept constant and equal to *ca.* 0.3. Analysis of the I-U curves revealed that the improved cell performance is related to the improved mass transport in the cathode layers. The mass transport overvoltages were found to be strongly dependent on the specific surface area and on the texture of the support. This work proves that utilization of novel carbon materials, such as proprietary carbon materials of the Sibunit family, may lead to major improvements in the PEMFC performance, thus allowing to decrease considerably the amount of Pt in the catalytic layers.

We now move to the discussion of the novel catalytic layer architectures for the fuel cell applications. We propose three dimensionally ordered catalytic layers of aligned carbon nano-filaments as the means improve the mass transport, water management and electronic conductivity in the catalytic layer and, ultimately, the effectiveness of the Pt utilization [3]. The arrays of aligned carbon nano-filaments (ACNF) were synthesized by catalytic chemical vapour deposition on TiO_x substrates, obtained via oxidative treatment of either polycrystalline Ti or thin Ti films on Si(100). Figure 1 shows a SEM image of the ACNF. The Pt deposition on the ACNF was utilized to prepare a set of model catalysts, which were investigated in two fuel cell related processes: the oxygen reduction (ORR) and the hydrogen oxidation (HOR) reactions. At this stage the experiments were performed in a conventional three-electrode electrochemical cell in 0.1 M H_2SO_4 electrolyte. The experimental data were compared with the results of mathematical modelling performed for a fast (quasi)reversible and a slow irreversible electrochemical reaction.

For the HOR, high Faradaic current and high effectiveness of the Pt utilization can be obtained for the catalytic layers with high Pt coverage but low Pt loading. The results indicate that for a fast (quasi)reversible electrochemical reaction, such as the HOR, the best performance is provided by an ultra-thin quasi two-dimensional catalytic layer. For the ORR, although the Faradaic current increases with the Pt loading, the effectiveness factor is decreasing with the Pt loading and the thickness of the layer, already for fairly low Pt loadings.

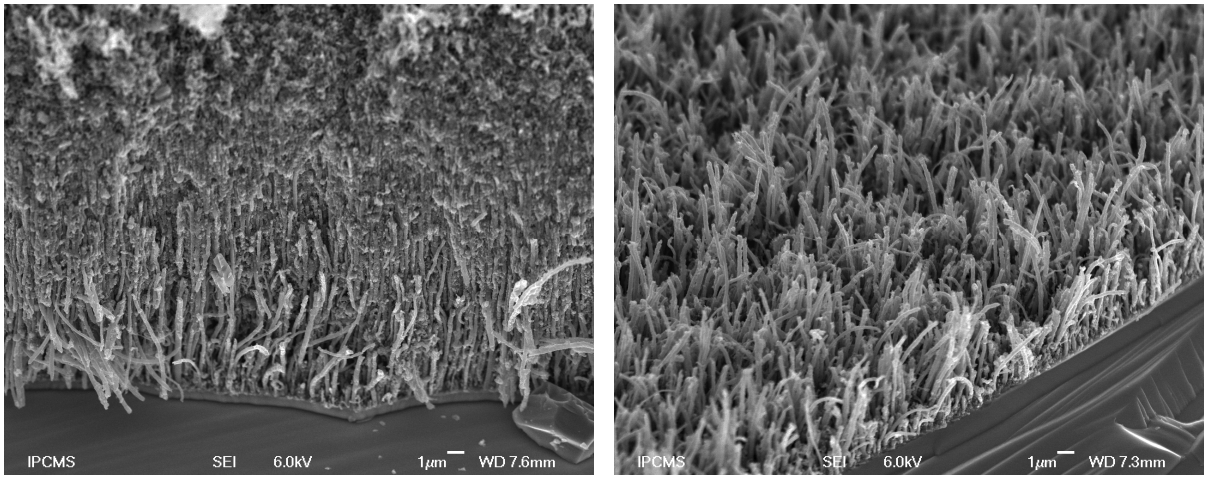

Figure 1: SEM images of ACNF grown on TiO_x/Ti/Si(100) base: an integral ACNF layer (left-hand side), and the bottom part of the ACNF (right-hand side).

The influence of the Thiele modulus (TM) computed as $TM = L\sqrt{\frac{\Gamma_{Pt} k_{ORR}}{D_{O_2} R_{pore}}}$ on the specific activity in the ORR was analyzed. Here L is the height of the layer of ACNF, R_{pore} = 100 nm is the pore radius (estimated as half of the distance between the nearest fiber walls), D_{O2} is the diffusion coefficient of O_2 in the aqueous electrolyte, and k_{ORR} is the electrode potential-dependent kinetic constant.

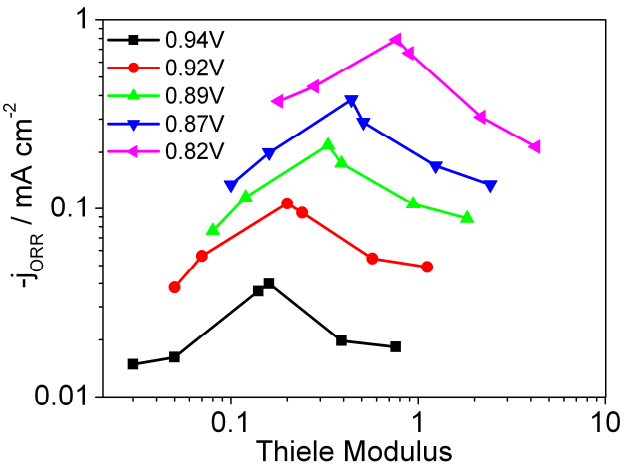

Figure 2: ORR current density extracted from the RDE curves measured in O_2-saturated 0.1 M H_2SO_4 at 30 °C, 5 mV s^{-1} and 1600 rpm at different electrode potentials vs. Thiele modulus. Currents are normalized to the electrochemically active surface area of Pt.

The analysis of the specific activity in the ORR as a function of the Thiele modulus (Figure 2) suggests that the observed decrease of the effectiveness factor at high Thiele moduli is due to the diffusion hindrance in the pores. The drop of the specific activity at low Thiele moduli indicates that ultra-thin catalytic layers may not be advantageous for the ORR. This is attributed to the escape of the H_2O_2 intermediate from the catalytic layer and to the decrease of the effective number of transferred electrons from 4 to 2. Comparison of the specific activities of Pt nanoparticles within Pt/ACNF (d_{Pt} = 4.1 nm) with those of Pt/Vulcan XC-72 (d_{Pt} = 3.7 nm) shows that Pt/ACNF electrodes exhibit factor of 5 higher specific activity at an optimum Pt loading and layer thickness. This observation gives hope that structured catalytic layers may be useful for the future development of highly efficient, low noble metal loading catalytic layers for the PEMFCs. Further studies aimed at the incorporation of Pt/ACNF in the MEA and their utilization in the PEMFCs are in progress. The results will be reported elsewhere.

Finally, we consider the development of non-platinum Pd-Au/C [4] catalysts for the anode of a PEMFC fed with reformate. Palladium-gold particles with varied composition were prepared by Pd electrochemical deposition on Au nanoparticles immobilized on a model carbon support. While the hydrogen oxidation activity of Pd/C [5] and Pd-Au/C [4] catalysts is inferior to that of Pt/C, their CO-tolerance is much superior.

It was found that the decrease of the effective Pd overlayer thickness below *ca.* two monolayers resulted in a two-fold increase of the exchange current density of the hydrogen oxidation reaction and in a significant increase of the CO tolerance (Figure 3). Testing Pd-Au/C catalysts in PEMFCs is now in progress and will be reported elsewhere.

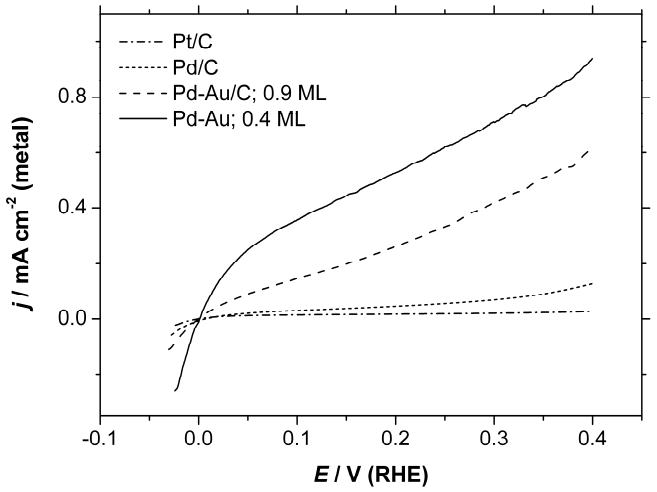

Figure 3: Hydrogen electrooxidation curves on CO-blocked Pd-Au/C surfaces in H_2-saturated 0.1 M H_2SO_4 at 60 °C and 2500 rpm. Currents are normalized to the total metal surface area. The coverage of Au particles with Pd is given in monolayers (ML).

Acknowledgements

ERS gratefully acknowledges all collaborators, students and PostDocs, who contributed to the publications listed below. Financial support from the ANR (Agence National de la Recherche) in the framework of ANR-06-CEXC-004 is gratefully appreciated. P.R. gratefully acknowledges Universite de Strasbourg for the PhD scholarship (Allocation de recherche “Presidence”).

References

[1] F. Maillard, P.A. Simonov, E. R. Savinova, “Carbon materials as supports for fuel cells electrocatalysts” In: Carbon materials for catalysis, Philippe Serp and José Luis Figueiredo, Eds., John Wiley & Sons, 2009, p. 429.

[2] J. Kaiser, P. A. Simonov, V. I. Zaikovskii, L. Jöerissen and E. R. Savinova, J. Applied Electrochemistry 37 (2007) 1429-1437.

[3] P. S. Ruvinskiy, A. Bonnefont, M. Houllé, C. Pham-Huu, and E.R. Savinova, Electrochim. Acta, 55 (2010) 3245-3256.

[4] Pavel S. Ruvinsky, Sergey N. Pronkin, Vladimir I. Zaikovskii, Pierre Bernhardt, and Elena R. Savinova, Phys Chem Chem Phys. 10 (2008) 6665-6676.

[5] S. N. Pronkin, A.Bonnefont, P. S. Ruvinskiy, E. R. Savinova, Electrochim.Acta, 55(2010)3312-3323.

Alternative Electrocatalyst Support Materials for Polymer Electrolyte Fuel Cells: Semiconducting Oxides and Carbon Nanofibers

Kazunari Sasaki, Fumiaki Takasaki, Yusuke Shiratori, Zhiyun Noda, Kyushu University, Japan

1 Introduction

Higher performance and long-term durability of electrocatalysts are essential for polymer electrolyte fuel cells (PEFCs), where electrocatalyst support materials act as a very important role. In this study, as alternatives to the conventional carbon black catalyst support, semiconducting oxides and carbon nanofibers have been applied. Colloidal impregnation procedure was applied to prepare highly-dispersed Pt catalysts on such support materials.

2 Thermochemical Stability of Electrode Materials

Thermochemical calculations were applied to derive pH-potential (Pourbaix) diagrams for almost all elements. Stable substances at 80 °C under the PEFC cathode condition are shown in Fig. 1. Among stable materials in strongly acidic environment at 1.0 V vs. standard hydrogen electrode, we can select elements including Sn, Ti, Nb, Ta, W, and Sb stable under PEFC cathode conditions.

Li	Be											B	C	N	O	F
Li^+	Be^{2+}											H_3BO_3(a)	CO_2(a) CO_2(g)			
Na	Mg											Al	Si	P	S	Cl
Na^+	Mg^{2+}											Al^{3+}	H_2SiO_3(a) (H_4SiO_4)	$H_4P_2O_7$(a)	HSO_4^-	
K	Ca	Sc	Ti	V	Cr	Mn	Fe	Co	Ni	Cu	Zn	Ga	Ge	As	Se	Br
K^+	Ca^{2+}	Sc^{3+}	TiO_2	VO_4^-	Cr^{3+}	Mn^{2+}	Fe^{3+} (Fe_2O_3)	Co^{2+}	Ni^{2+}	Cu^{2+}	Zn^{2+}	Ga^{3+}	GeO_2	$HAsO_4$(a)	H_2SeO_3(a)	
Rb	Sr	Y	Zr	Nb	Mo	Tc	Ru	Rh	Pd	Ag	Cd	In	Sn	Sb	Te	I
Rb^+	Sr^{2+}	Y^{3+}	ZrO^{2+}	Nb_2O_5	MoO_3		RuO_2	RhO_2(g)	PdO_2	Ag^+	Cd^{2+}	In^{3+}	SnO_2	Sb_2O_5	$Te(OH)_3^+$ (H_2TeO_4)	
Cs	Ba		Hf	Ta	W	Re	Os	Ir	Pt	Au	Hg	Tl	Pb	Bi	Po	At
Cs^+	Ba^{2+}		HfO_2	Ta_2O_5	$O_2W(OH)_2$	ReO_4^-	OsO_4(a) (OsO_2)	IrO_2	Pt	Au		Tl^+	Pb^{2+}	Bi_2O_3		

Metal-H_2O system at 80℃

Molality m ($m=10^{-6}$mol/kgH_2O) PH=0

Cathode Eh(vs.SHE)=1.0V

Figure 1: Most stable substances under the typical PEFC cathode condition at 80 °C, derived from pH-potential diagrams thermochemically calculated.

3 Carbon-free Pt Electrocatalysts Supported on SnO_2 for PEFCs

For PEFCs, the electrocatalysts in which Pt nano-particle are homogeneously distributed on carbon black (Pt/C) are widely used. However, fluctuation of cell voltage up to higher potentials can cause oxidation-induced carbon support corrosion especially for cathode

electrocatalysts. Our group has studied the electrocatalysts using oxide supports to solve these issues. Fig. 2 shows FESEM micrograph of the Pt electrocatalyst supported on SnO_2. Pt nano-particles (with ca. 3 nm in diameter) were homogeneously distributed on the support material. Pt/SnO_2 electrocatalyst is relatively stable in the PEFC cathode environment, and has the electrochemical property comparable to Pt/C [1]. Further modification in the electronic conductivity of SnO_2 may be expected by doping with hypervalent (e.g. Nb^{5+}) or hypovalent (e.g. Al^{3+}) ions. In this study, electrocatalysts with different oxide supports including Pt/SnO_2, $Pt/Sn_{0.95}Nb_{0.05}O_2$, $Pt/Sn_{0.98}Nb_{0.02}O_2$ and $Pt/Sn_{0.95}Al_{0.05}O_2$, were prepared and their nanostructure, electrochemical surface area (ECSA) and durability under high potential conditions were evaluated and compared. Voltage cycling up to 10,000 cycles between 0.6 and 1.3 V_{RHE} was applied for the electrocatalysts. Fig. 3 indicates the ECSA of the electrocatalysts as a function of the number of cycles. In comparison with Pt/SnO_2, $Pt/Sn_{0.95}Nb_{0.05}O_2$ and $Pt/Sn_{0.98}Nb_{0.02}O_2$ exhibited larger ECSA in the initial stage. The ECSA of Pt/C rapidly decreased down to nearly zero within 3000 times of voltage cycles. Carbon corrosion and agglomeration of Pt particles would be the main reasons of these phenomena. In contrast, Pt/SnO_2-based electrocatalysts exhibited considerably longer durability compared to Pt/C [2]. Even after 10,000 times of voltage cycles, the carbon-free $Pt/Sn_{0.98}Nb_{0.02}O_2$ electrocatalyst still has sufficient ECSA above 30 m^2g^{-1}.

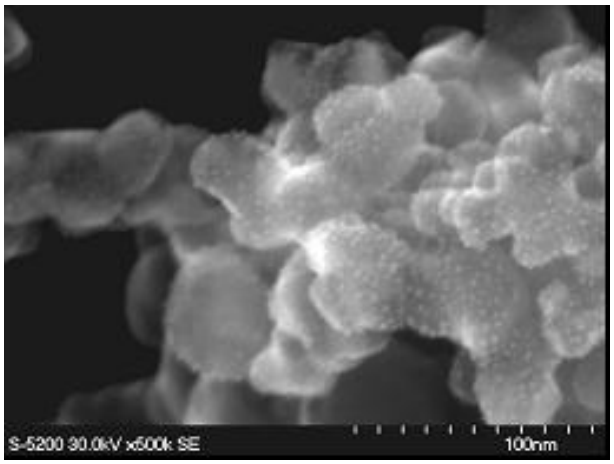

Figure 2: FESEM micrograph of Pt/SnO_2.

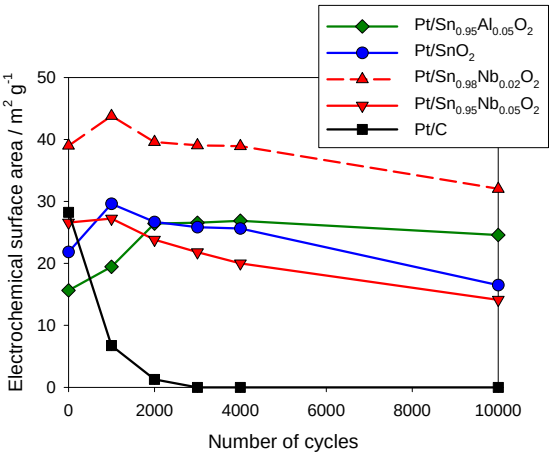

Figure 3: ECSA vs. number of cycles in the potential range between 0.6 and 1.3 V_{RHE}.

These results indicate that SnO_2-based carbon-free electrocatalysts may improve long-term durability of PEFCs against voltage cycling [1-2].

I-V characteristics of single cells with Pt/C or Pt/SnO_2 as the cathode catalyst are shown in Fig. 4, for which the identical preparation procedures and a simple MEA structure (e.g. without MPL) were applied just for comparison. Sufficient performance comparable to that of the conventional cell with Pt/C was achieved using Pt/SnO_2 as a cathode catalyst.

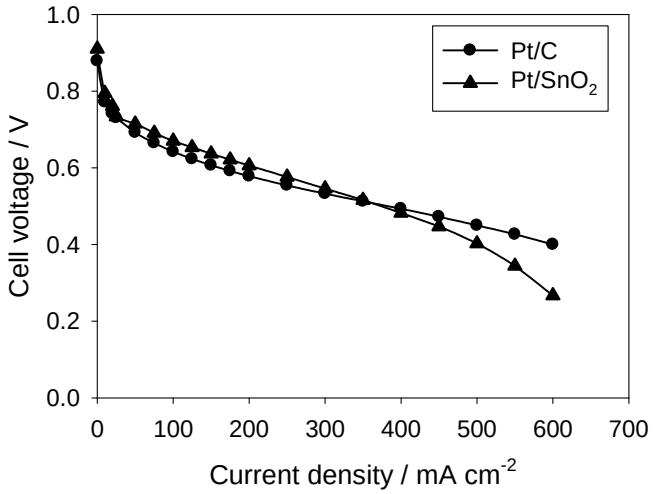

Figure 4: I-V characteristics of a single cell using Pt/SnO_2 as a cathode electrocatalyst, measured at 80 °C. For comparison, I-V characteristics of a cell using Pt/C as a cathode are also shown [1].

4 Pt electrocatalysts Supported on Various Carbon Nanofibers

As the colloidal impregnation was useful to prepare highly-dispersed Pt electrocatalysts on carbon black and other support materials, this procedure was also applied for carbon nanofibers with various crystallographic structures illustrated in Fig. 5. Table 1 shows Pt crystallite size on various carbon nanofibers, determined by XRD. We have found that the colloidal impregnation was suitable for preparing nanocrystalline electrocatalyst particles on various carbon supports.

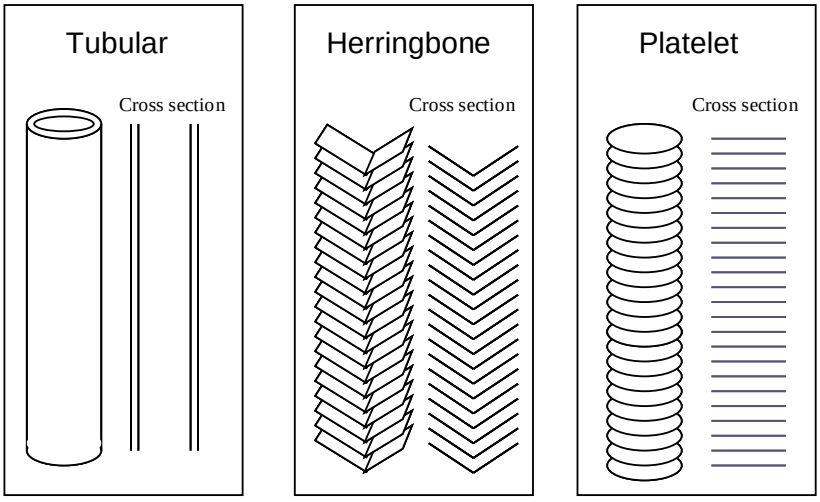

Figure 5: Structures of tubular, herringbone and platelet carbon nanofibers.

FESEM micrograph of Pt electrocatalysts supported on tubular carbon fibers (nanotubes) is shown in Fig. 6. Pt particles were a few nm in diameter, but their distribution was rather

inhomogeneous. It can be considered that high dispersion of Pt catalysts on carbon nanotubes was still difficult even using this colloidal process. Fig. 7 shows FESEM micrograph of Pt electrocatalysts supported on herringbone-type carbon nanofibers, in which their graphene plain is tilted ca. 45° from the fiber direction. It has been found that homogeneity of Pt distribution was improved, whereas no Pt particles existed on some parts of fiber surfaces. Fig. 8 shows FESEM micrograph of Pt electrocatalysts supported on platelet-type carbon fibers. We can clearly find that Pt particles are distributed homogeneously on the surface of this carbon fiber. This impregnation process was also applied to vapour-grown carbon nanofibers (VGCF). We have succeeded to prepare nanocrystalline Pt catalysts on the fibers of this type, as shown in Fig. 9 [3].

Table 1: Pt crystallite size measured by XRD peak broadening.

Carbon support	Crystallite size (nm)
Carbon black (Vulcan)	3.4
CNF-Platelet	3.3
CNF-Herringbone	3.9
CNF-Tubular	3.6
VGCF	5.6

Table 2 shows effective surface area of the Pt electrocatalysts, determined by CV. These well-dispersed Pt electrocatalysts possess comparable effective surface area to the catalyst on the state-of-the-art carbon support (Vulcan). Pt catalysts especially on VGCFs and on herringbone-type fibers exhibit higher effective surface areas. In addition, kinetically-controlled current density of Pt catalysts on VGCFs and on herringbone-type fibers was also higher, compared to that on the other types of carbon fibers. In order to demonstrate the feasibility of Pt electrocatalysts supported on carbon nanofibers, PEFCs were prepared using such electrocatalysts. Fig. 10 shows the cross section of the electrocatalyst layers with VGCF support, exhibiting a typical microstructure with conductive fiber network and open porosity. We have obtained I-V characteristics of such PEFCs at 80 °C, exhibiting a high electrochemical performance, while long-term durability should be controlled and optimized because Pt nanoparticles on such carbon nanofibers tend to agglomerate.

Table 2: Pt effective surface area measured by cyclic voltammetry.

Carbon support	Pt effective surface area / m^2g^{-1}
Carbon black (Vulcan)	52.4
CNF-Platelet	42.7
CNF-Herringbone	56.7
CNF-Tubular	49.7
VGCF	68.3

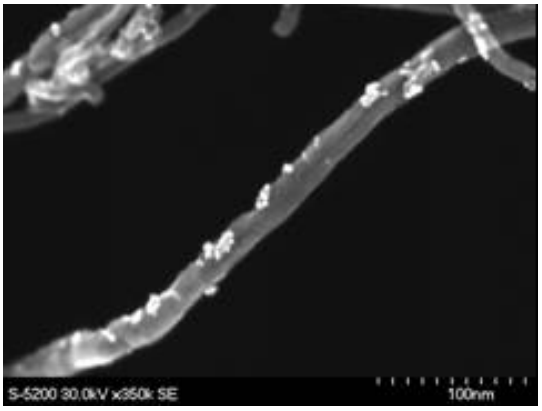

Figure 6: FESEM micrograph of Pt electrocatalysts supported on tubular carbon nanofibers (nanotubes).

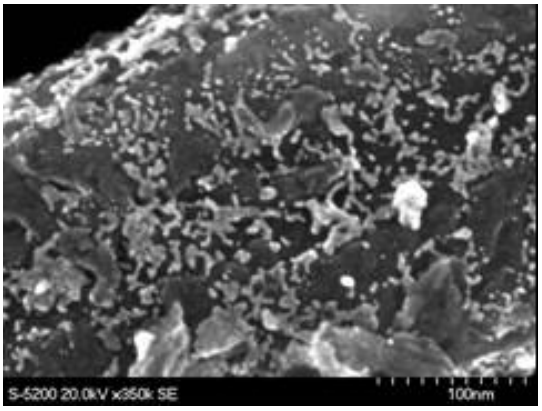

Figure 7: FESEM micrograph of Pt electrocatalysts supported on herringbone-type carbon nanofibers.

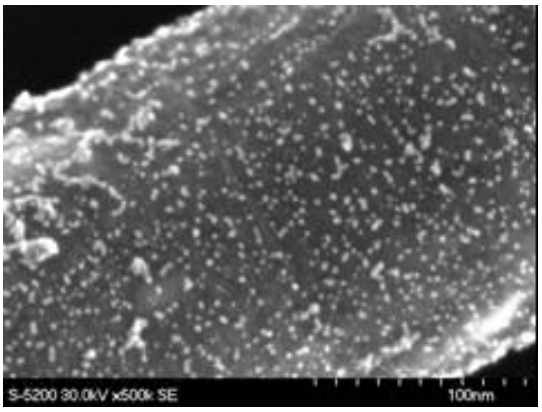

Figure 8: FESEM micrograph of Pt electrocatalysts supported on platelet-type carbon nanofibers.

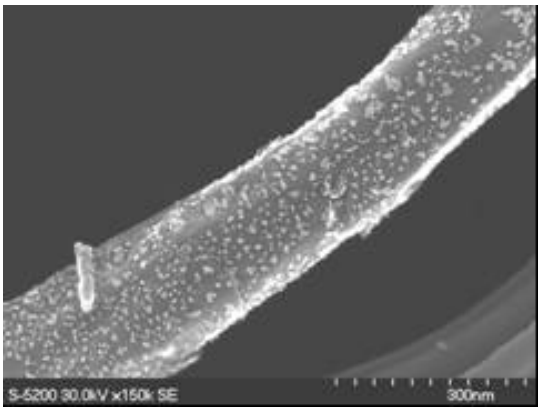

Figure 9: FESEM micrograph of Pt/C (VGCF) electrocatalysts prepared via colloidal impregnation.

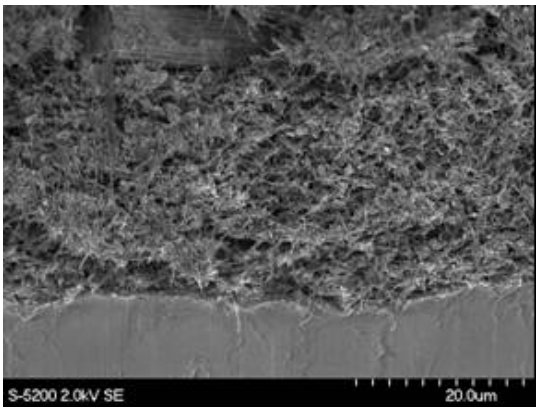

Figure 10: FESEM micrograph of Pt/C (VGCF) porous electrocatalyst layer, with highly-conductive network structure and open porosity.

5 Summary: Electrocatalyst Design from Catalyst Support Materials

Among (semi)conducting oxides, (relatively inexpensive) SnO_2-based oxides exhibit a satisfactory durability against voltage cycling, so that such materials may be applied as alternative catalyst support materials, in order to improve the durability of PEFC systems. Other oxides may be interesting to be tested in a future. Carbon nanofibers are also interesting materials as catalyst supports to prepare electrocatalyst layers with highly-conductive network structure and open porosity, for which the catalyst support stability and the homogeneous dispersion of Pt nanoparticles should be simultaneously optimized.

References

[1] A. Masao, S. Noda, F. Takasaki, K. Ito, and K. Sasaki, *Electrochem. Solid-State Lett.*, **12** (9), (2009).

[2] F. Takasaki, Z. Noda, A. Masao, Y. Shiratori, K. Ito, and K. Sasaki, *ECS Transactions*, **25** (1), 831 (2009).

[3] K. Sasaki, K. Shinya, S. Tanaka, Y. Kawazoe, T. Kuroki, K. Takata, H. Kusaba, and Y. Teraoka, *Mater. Res. Soc. Symp. Proc.* Vol. **835**, 241-46 (2004).

Cell Resistances of ABPBI-Based HT-PEFC-MEAs: Time Dependence and Influence of Operating Parameters

W. Lehnert, K. Wippermann, C. Wannek, Institute of Energy Research - Fuel Cells (IEF-3), Forschungszentrum Jülich GmbH, 52425 Jülich, Germany

Abstract

Time-dependent measurements of cell impedance of a HT-PEFC based on ABPBI were performed at constant frequencies close to the high-frequency (h.f.) intercept of the corresponding Nyquist plots with the real axis. The h.f. impedances approximate the ohmic resistance of the cell and they decrease, when current (140 mA/cm²) is switched on. Steady state values are attained after 10 minutes. *Vice versa*, when current is switched off (OCV), the h.f. impedances instantaneously increase but reach steady state values only after about 1 hour. These values rise with increasing gas flow rates. The results are discussed in terms of hydration/dehydration processes, changing the equilibrium between orthophosphoric and pyrophosphoric acid and thus the conductivity of the electrolyte as well as the mobility of molecules and charge carriers. Impedance spectra were recorded after each time-dependent measurement under OCV conditions. The fit of these impedance data based on an equivalent circuit revealed ohmic resistances corrected by h.f. inductances and low frequency impedances associated with the cathode oxygen exchange reaction. The charge transfer resistances deduced from the low frequency impedances strongly depend on both air and hydrogen flow rates.

1 Introduction

Most of today's high temperature cells (HT-PEFCs) rely on membrane electrode assemblies (MEAs) with phosphoric acid absorbed in PBI (= *poly*(2,2'-(*m*-phenylene)-5,5'-bibenzimidazole) as electrolyte [1]. Recently membranes based on the chemically related ABPBI (= *poly*(2,5-benzimidazole) have emerged as a promising alternative [2-4]. Various aspects of the steady-state cell impedance of HT-PEFCs based on PBI as membrane polymer at different operating conditions have already been reported in the literature (e.g. [5-7]). The influence of water activity on the steady-state conductivity of the electrolyte [8,9] as well as the distribution of phosphoric acid within the membrane electrode assembly (MEA) [10,11] are intensively studied at present. We will not only discuss the influence of several testing parameters on the cell resistance of a MEA based on ABPBI instead of PBI, but we will also turn our attention to its time dependence after changes of the operating conditions.

2 Experimental

MEAs (A = 14.4 cm^2) have been assembled from ABPBI membranes (FuMA-Tech) and gas diffusion electrodes (~1 mg Pt/cm^2) produced in-house which have been impregnated with appropriate amounts of phosphoric acid [4]. They have been characterized in a single cell using pure hydrogen and air at ambient pressure as the reactants. Under these conditions reasonable power densities of ~250 mW/cm^2 are obtained at T = 160 °C [4]. We have

deduced the time-dependent ohmic resistances from impedance measurements using a symmetric two electrode configuration. The experiments were run at a predefined frequency of 5-10 kHz close to the high-frequency intercept of the corresponding Nyquist plots with the real axis. Two hours prior to the beginning of the time dependent measurements during which the current density was changed from j = 0 to 140 mA/cm^2 and *vice versa* at 160 °C the cell was switched to OCV and the hydrogen and air flow rates were changed from $\lambda_{Anode/Cathode}$ = 2/2, to the values used for the respective experiment (λ_{H_2} = 2/4/6, λ_{air} = 2/4/6). In case of OCV measurements, the indicated air and hydrogen stoichiometries refer to the corresponding flow rates at a current density of 140 mA/cm². Additionally, impedance spectra were performed after the end of each time-dependent experiment in a frequency range of 10^{-2} – 10^4 Hz under OCV steady state conditions. The a.c. signal voltage amplitude was always ± 10 mV. The impedance spectra were fitted on basis of an equivalent circuit (see Fig. 2) using the EQUIVCRT 3.0 Software written by B.A. Boukamp [12]. From the fit data, corrected data of the ohmic resistance, R_Ω, could be obtained. In the following, the original impedance values will be denoted as R'_Ω ('ohmic resistance') and the corrected fit data of the ohmic resistance will be indicated as R_Ω. All the impedance measurements were performed with an IM 6 unit of Zahner Elektrik.

3 Results and Discussion

Fig. 1 shows the time dependent behaviour of the 'ohmic resistance', more precisely the high frequency impedance at constant frequency at Im(Z) part of almost zero, for three different air flow rates. The initial values of 250 - 300 mΩcm^2 under OCV conditions drop down within 10 minutes to about 200 mΩcm^2 when a current of 140 mA/cm^2 is switched on. The 'ohmic resistance' reaches steady state values, which shows only a weak dependence on the air flow rate. These results can be explained by the production of water in the cathode, which increases the conductivity of the electrolyte by increasing the amount of free phosphoric acid compared to its less conductive dehydration products (mainly pyrophosphoric acid $H_4P_2O_7$) [13] in the electrodes (especially the cathode) and the membrane. After 3 hours of operation, the current was turned off. The instantaneous increase of the 'ohmic resistances' indicates a more or less reversible hydration / dehydration process. Indeed, it takes the resistances about 1 hour, to reach steady state values during the dehydration process under OCV conditions. A simple explanation for the much faster hydration process is the *in situ* water production at the cathode, compared to the slow removal of water by diffusion processes in case of dehydration process. The steady state values of the 'ohmic resistances' under OCV conditions exhibit a significant increase with rising air flow rate. This effect is even more pronounced if hydrogen flow rate is also enhanced. These results are consistent with the idea of a dehydration process, which should be promoted by increased gas flow rates at both electrodes.

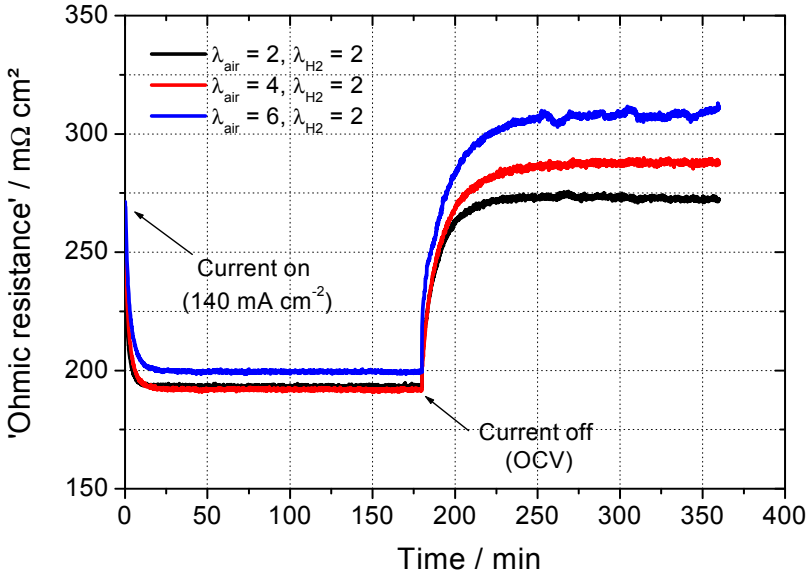

Figure 1: Time dependence of the cell resistance after changing the current density from j = 0 to 140 mA/cm^2 and *vice versa* at 160 °C; Variation of λ_{air} = 2/4/6; λ_{H_2} = 2 (constant).

Besides current density and gas flow rates, cell temperature and humidity of supplied gases should play an important role in the hydration / dehydration process. In future experiments, the influence of these parameters has to be investigated in more detail. First measurements with humidified fuel gas reveal a reversible 10% decrease of the ohmic resistance in presence of 5 vol.% H_2O in H_2 compared to dry hydrogen. This result supports again our reasoning based on a reversible hydration / dehydration process.

After each time dependent measurement, impedance spectra were recorded under OCV conditions in the frequency range of 0.01 Hz to 10 kHz. Fig. 2 shows a Nyquist plot of the MEA impedance at different flow rates of air and hydrogen. The indicated air and hydrogen stoichiometries refer to the corresponding flow rates at a current density of 140 mA/cm². Measured values are marked by closed symbols and fit data are indicated by lines and open symbols. The fit values were obtained by using the equivalent circuit shown in Fig. 2. The measured values and selected fit data are summarized in Table 1.

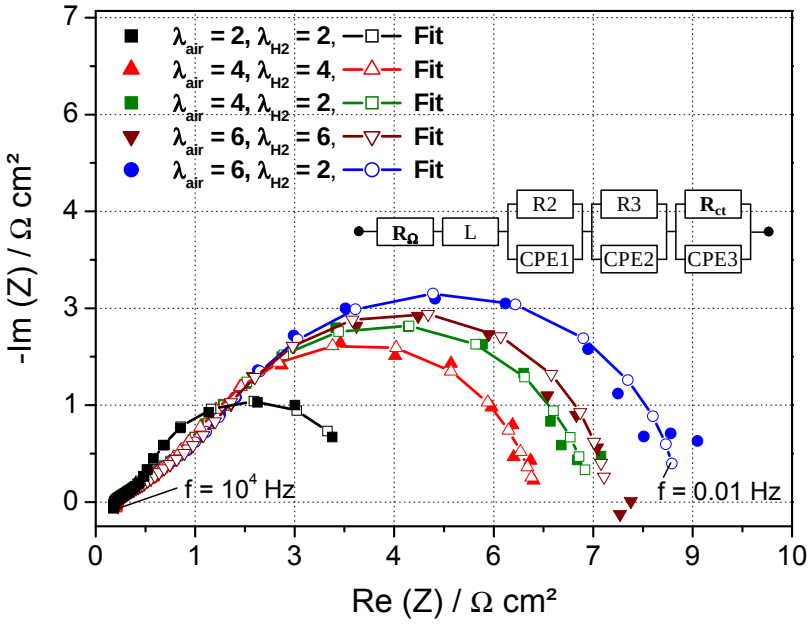

Figure 2: **Nyquist plots of the MEA impedance under OCV conditions; T = 160 °C; Variation of λ_{air} / λ_{H_2}; measured values: closed symbols, fit values: lines and open symbols; frequency range: 10^{-2} – 10^{4} Hz; AC amplitude: 10 mV.**

Table 1: **Ohmic/ charge transfer resistances obtained from impedance measurements (see Figs. 1&2).**

λ_{air} / λ_{H_2}	'Ohmic resistance': Re(Z) @ -Im ≈ 0 / mΩ cm²	Impedance Spectra: Re(Z) @ -Im = 0 / mΩ cm²	Fit of impedance spectra: $R_{\Omega}^{\sim}$ mΩ cm² Fit Code: $R_{\Omega}L(R_2Q_2)(R_3Q_3)(R_{ct}Q_4)$	Fit of impedance spectra: $R_{ct}^{\sim}$ mΩ cm²
2 / 2	272	272	248	3010
4 / 2	289	288	252	4360
4 / 4	306	307	263	4020
6 / 2	311	307	267	6440
6 / 6	333	336	289	5360

In a first approximation, limiting mass transport processes under OCV conditions and limitation of hydrogen reaction rate can be neglected. Under these assumptions, the large semi-arc at medium and low frequencies (see Fig. 2) is mainly attributed to the charge transfer resistance, R_{ct}, of the oxygen exchange reaction. If air flow rate is enhanced (λ=2 to λ=6) at constant hydrogen flow rate (λ=2), R_{ct} increases from 3.0 to 6.4 Ωcm^2 (see Table 1 & Fig. 2). Interestingly, this effect is slightly diminished, if hydrogen flow is also increased, i.e. hydrogen and air stoichiometries are equal: In this case, R_{ct} increases from 3.0 to only

5.4 Ωcm^{-2} (see Table 1 & Fig. 2). On basis of the results presented here, the following tentative explanation may be given: If air flow rate is increased, the water content of the MEA decreases and the amount of pyrophosphoric acid in the equilibrium between $2\ H_3PO_4 \leftrightarrow H_4P_2O_7 + H_2O(g)$ increases. For this reason, the proton conductivity of the MEA decreases, causing a decrease of catalytic activity especially in the outer part of the cathode. Because the solubility of oxygen in H_3PO_4 is much lower than in water [14], the oxygen concentration nearby the platinum catalyst decreases, in spite of the higher air flow rate. Both effects decrease the exchange current density of the oxygen equilibrium reaction and thus increase the charge transfer resistance, R_{ct}, as observed. By increasing the hydrogen flow rate, more hydrogen permeates from the anode through the membrane to the cathode. Although hydrogen 'consumes' a part of the oxygen which is present at the cathode, the increased formation of water causes a much better solubility of oxygen and a more thorough wetting of the inner surface of catalyst layer, leading to an enhanced oxygen concentration respectively a higher activity of the cathode. Hence, the exchange current density of the oxygen equilibrium reaction increases and R_{ct} decreases.

4 Conclusions

It turns out, that time dependent measurements of cell impedance at different operating conditions are crucial since they provide a valuable insight into the hydration / dehydration processes of HT-PEFCs. We attribute the fact that high water production by the fuel cell reaction, high water insertion, and its low removal by the gas flows (i.e. the water content in the cell) lowers the ohmic resistance to the increasing amount of mobile H_3PO_4 in the electrolyte. The hydration process is fast because of the water production inside the cathode, compared to the slow removal of water by diffusion processes through the gas diffusion layer into the channel. In general, ohmic resistances become small when (a) the current density is increased, (b) the gas flows are reduced, (c) the cell is run at elevated temperatures, and (d) when the fuel gas is humidified. Furthermore, the hydration / dehydration processes are believed to influence the local distribution of free phosphoric acid in the cell and thus local physico-chemical properties of the HT-PEFC, like proton conductivity, oxygen gas solubility, and inner active surface of the electrodes. For future studies, it is therefore important to investigate the local distribution and composition of the phosphoric acid electrolyte depending on the operation conditions of HT-PEFC in more detail.

References

[1] J. Mader, L. Xiao, T.J. Schmidt and B.C. Benicewicz, *Adv. Polym. Sci.*, 216 (2008) 63-124.

[2] J.A. Asensio and P. Gómez-Romero, *Fuel Cells*, 5 (2005) 336-343.

[3] C. Wannek, B. Kohnen, H.-F. Oetjen, H. Lippert and J. Mergel, *Fuel Cells*, 8 (2008) 87-95.

[4] C. Wannek, W. Lehnert and J. Mergel, *J. Power Sources*, 192 (2009) 258-266

[5] N.H. Jalani, M. Ramani, K. Ohlsson, S. Buelte, G. Pacifico, R. Pollard, R. Staudt and R. Datta, *J. Power Sources*, 160 (2006) 1096-1103.

[6] Y. Tang, J. Zhang, C. Song and J. Zhang, *Electrochem. Solid-State Lett.*, 10 (2007) B142-B146.

[7] J. Lobato, P. Canizares, M.A. Rodrigo and J.J. Linares, *Electrochim. Acta*, 52 (2007) 3910-3920.

[8] M.K. Daletou, J.K. Kallitsis, G. Voyiatzis and S.G. Neophytides, *J. Membrane Sci.* 326 (2009) 76-83.

[9] A. Schechter, R.F. Savinell, J.S. Wainright and D. Ray, *J. Electrochem. Soc*. 156 (2009) B283-B290.

[10] K. Kwon, T.Y. Kim, D.Y. Yoo, S.-G. Hong and J.O. Park, *J. Power Sources* 188 (2009) 463-467.

[11] C. Wannek, I. Konradi, J. Mergel, W. Lehnert, *Int. J. Hydrogen Energy*, in press

[12] B.A. Boukamp, *Equivalent Circuit, Internal Report CT89/214/128,* University of Twente, 1989

[13] Z. Liu, J.S. Wainright, M.H. Litt and R.F. Savinell, *Electrochim. Acta* 51 (2006) 3914-3923.

[14] K. Klinedinst, J.A.S. Bett, J. MacDonald and P. Stonehart, *J. Electroanal. Chem.* 57 (1974) 281-289.

Ongoing Efforts Addressing Degradation of High Temperature PEMFC

Jens Oluf Jensen, Qingfeng Li, Chao Pan, Niels J. Bjerrum, Department of Chemistry, Technical University of Denmark, Denmark
Hans Christian Rudbeck, Thomas Steenberg, Danish Power Systems ApS, Denmark

1 High Temperature PEM Fuel Cells

Proton exchange membrane fuel cells (PEMFC) for operation at temperatures above 100 °C have in recent years attracted increased attention as an alternative to conventional PEMFC based on humidified perfluorosulphonic acid membranes [1]. The reasons for aiming at a higher working temperature are increased tolerance to fuel impurities like carbon monoxide [2], the absence of liquid water, higher value of excess heat [3] and higher temperature gradients for cooling, which all lead to simpler and less costly system architecture. In order to operate the cell at temperatures over 100 °C electrolyte membranes less dependent of high water content must be developed and applied. There have been many attempts to develop such high temperature membrane materials (as reviewed [4]) and the most successful one is the phosphoric acid doped polybenzimidazole (PBI) membrane originally invented in the nineties at Case Western Reserve University [5]. There are many variants of PBI and the most common is poly (2,2´-*m*-(phenylene)-5,5´-bibenzimidazole) also called *meta*-PBI, *m*-PBI or often simply PBI (see Figure 1). The polymer itself is not a proton conductor, but when doped with a significant amount of phosphoric acid it gains conductivity comparable to the perfluorosulphonic acids traditionally used in PEMFC. However, one important difference is that the conductivity is still high if the cell is operated without humidification and the cells can be operated at higher temperature.

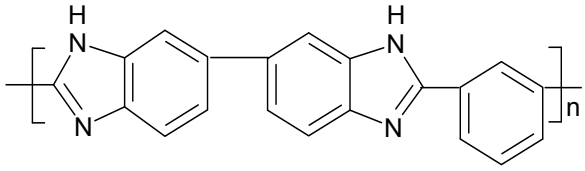

Figure 1: PBI, poly (2,2´-*m*-(phenylene)-5,5´-bibenzimidazole).

2 State-of-the-art for Lifetime and Degradation of High Temperature PEMFC

The high temperature PEMFC (HT-PEMFC) system has reached a state of development where durability becomes a key issue. The PBI based PEMFC can be seen as a hybrid between the conventional PEMFC and the phosphoric acid fuel cell (PAFC) because it has a membrane as well as phosphoric acid in the electrolyte. The electrodes are similar in all three cases with the catalysts being platinum on carbon. It can therefore be expected that

many of the degradation mechanisms known from both PEMFC and PAFC will be found with the PBI based HT-PEMFC. The literature on HT-PEMFC degradation is still limited but growing. The authors group published early durability results at different temperatures in 2003 [6]. The experiments (Figure 2) indicated that performance was most stable at temperatures of 150 °C or lower while a fast performance decay was seen at temperatures of 180 and 200 °C. Selected durability results reported are collected in Table 1. It shows that the longest lifetimes are demonstrated at 150 – 160 °C.

Different lifetime targets are set for different applications and by different authorities or stakeholders, but it is normally considered fair to say that for stationary applications like combined heat and power production it is over 40,000 hours at constant load with only few start-ups. For vehicles, only 5,000 hours should do, but at dynamic load and with multiple start-ups.

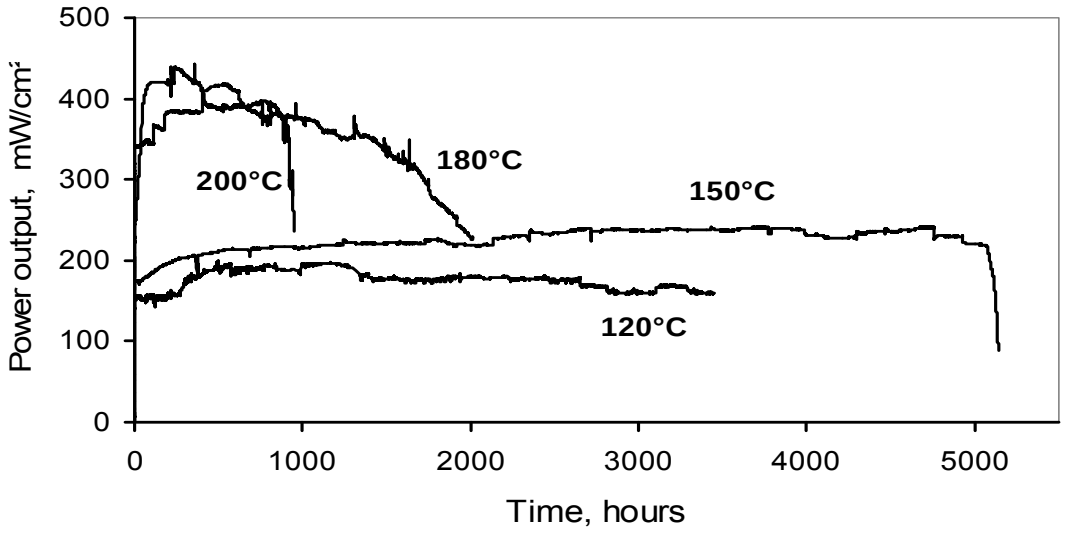

Figure 2: Early durability results. Constant voltage: 0.5 V, Pt loading: 0.5 mg cm^{-2}, reactants: H_2/O_2 at 1/1 bara, electrode area: 4 cm^2. Re-plotted after [6].

Table 1: Selected single cell lifetime results from the literature. Some experiments proceeded after the hours listed. Most reported experiments have been carried out at 150 – 160 °C, and the most commonly used cell is Celtec-P 1000 from BASF.

Temperature	Lifetime	Degradation	Cell from
80 °C	1,000-1,500 h	14-45 μVh^{-1}	Benicewich, modified PBI
120 °C	3,500-13,000 h	6.3-? μVh^{-1}	DTU, BASF (longest)
150 °C	5,000-10,000 h	n.a.	Fumatech, ABPBI (longest)
160 °C	5,000-18,000 h	5-25 μVh^{-1}	Jülich or BASF (longest)
180 °C	2,000 h	26-? μVh^{-1}	BASF or DTU
200 °C	1,000 h	n.a.	DTU

3 Failure Modes

A PEMFC is a complex structure with multiple internal functionalities and it is obvious that many things can go wrong. A substantial review is given by Borup et al. [7]. Degradation is often described externally as a voltage decay rate (μVh^{-1}) at constant current load. From this, extrapolations to lifetimes are sometimes made, but in many case another failure mode like membrane collapse becomes the limiting factor. The gradual decay is often assigned to catalyst coarsening or corrosion and catalyst substrate corrosion. Membrane failure can be due to mechanical stress or chemical attack in the form of oxidation. In the HT-PEM system acid loss seems not to be as big a problem as in PAFC. This is probably because the long term experiments are carried out at 150 – 160 °C which is significantly lower than for PAFC (~200 °C). In the following examples of results with membrane oxidation and catalyst degradation from the authors group are given.

4 Oxidative Degradation of the PBI Membrane

A well known test for oxidative stability of polymers is the Fenton test in which the membrane is kept in a solution of H_2O_2 and Fe^{2+}/Fe^{3+} ions. It is debated to which extent the test is relevant or too harsh. In this work it is seen as an accelerated test that will show relative stability of selected polymers. The Figures 3 to 6 show oxidation results of different polymers as explained in the figure texts. Nafion is included for comparison. It is common knowledge that hydrocarbon polymers are more sensitive to oxidation than per-fluorinated polymers.

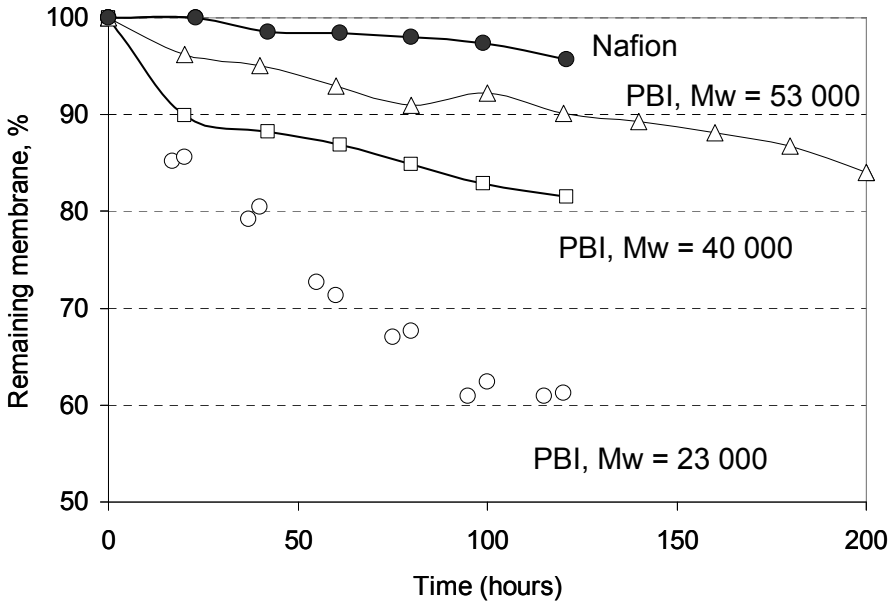

Figure 3: Fenton oxidative testing of Nafion and PBI with different molecular weights as indicated. The experiment indicates a strong dependency on molecular weights.

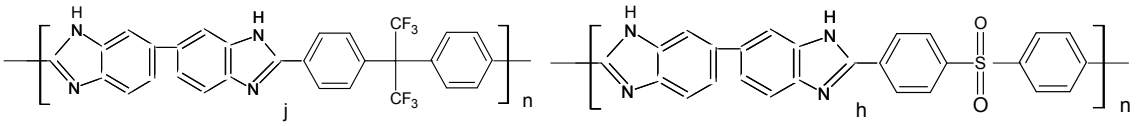

Figure 4: Structures of F_6-PBI (left) and SO_2-PBI (right) [8].

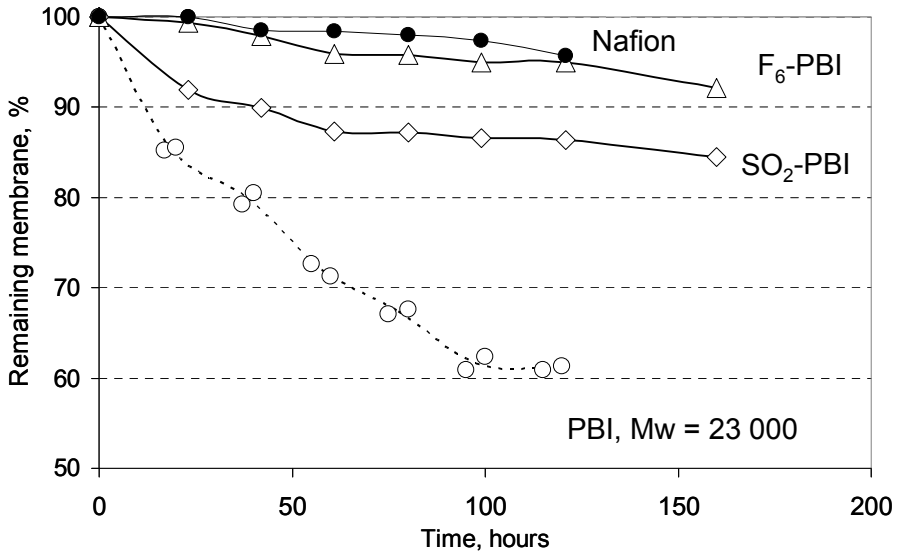

Figure 5: Fenton oxidative testing of Nafion, F_6-PBI and SO_2-PBI (see Figure 4).

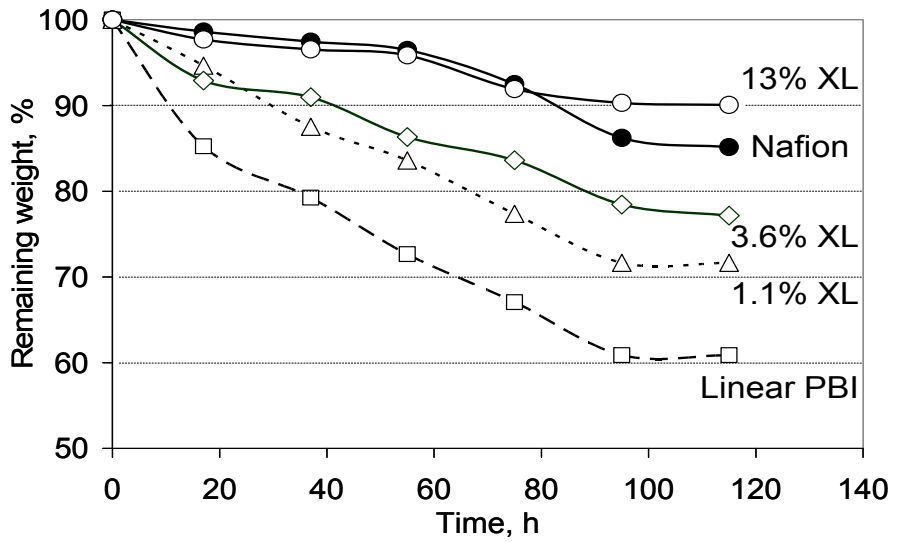

Figure 6: Fenton oxidative testing of PBI cross-linked to different extents by *p*-xylene dibromide [9].

It can be concluded that it is possible to increase the lifetime of the polymers in H_2O_2. However, the dependency on molecular weight seen in Figure 3 was somewhat unexpected since the chemistry of the polymer is unchanged. It points in the direction of endpoint attack, but there is no solid conclusion yet. A spectroscopic study is in progress by the authors group. The results on modified PBI are also promising, but they don't show whether the improvement is due to the chemical modification or simply the molecular weight.

5 Carbon Support Oxidation

A series of accelerated carbon oxidation tests were performed on the carbon supported catalyst by voltage cycling. The voltage was cycled between 0.9 and 1.2 V, 3 min per cycle for 17 hours. After a rest period of 6 – 7 hours at 0.5 V a polarization curve was measured. In Figure 7 the performance at 0.5 V is plotted as a function of potential cycles. It can be seen that the standard catalyst support materials, Vulcan XC 72R and Ketjen black as well as HISPEC and Ensaco are most seriously affected, while the graphitized Vulcan XC 72R degrade much slower. The longest lasting candidate is a special corrosion resistant catalyst from Johnson Matthey. There was no detailed information on it available. In all cases the degradation was understood as a loss of active area. This can be caused by detachment due to the support corrosion, but platinum particle growth was also seen by line broadening in X-ray diffraction.

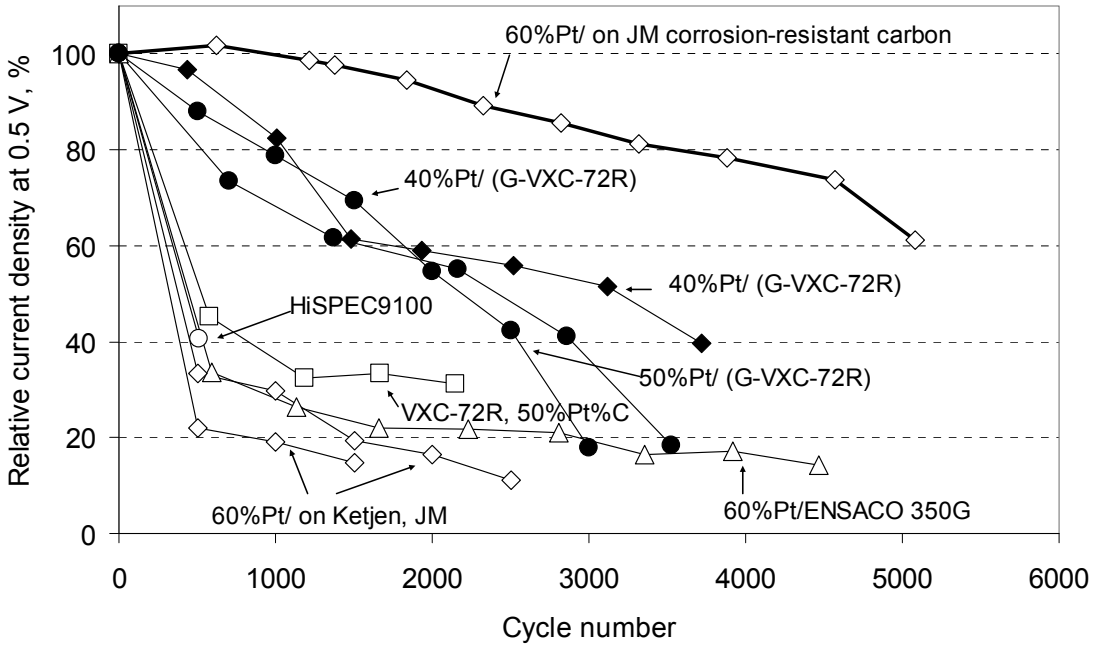

Figure 7: Results of potential cycling of Pt catalysts on different carbon supports. Open markers refer to standard supports (Vulcan XC 72R, Ketjen black and trademarks). Filled markers are Pt on partially graphitized Vulcan XC 72R. The uppermost curve with thick line is for a special Johnson-Matthey product.

References

[1] Q. Li, J. O. Jensen, R. F. Savinell and N. J. Bjerrum. Prog. Polymer Sci. 34, 449-477 (2009).

[2] Q. Li, R. He, J. Gao, J. O. Jensen and N. J. Bjerrum. J. Electrochem. Soc. 150, A1599-A1605 (2003).

[3] J. O. Jensen, Q. Li, et al. Int. J. Hydrogen Energy 32, 1567– 1571 (2007)

[4] Q. Li, R. He, J. O. Jensen and N. J. Bjerrum. Chem. Mater. 15, 4896-4915 (2003)

[5] J. S. Wainright, J.-T. Wang, D. Weng, R. F. Savinell, M. Litt.J. Electrochem. Soc. 142, L121(1995)

[6] Q. Li, J. O. Jensen et al. Recent Res. Dev. Electrochem. 6, 1-26. (2003).

[7] R. Borup et al. Chem. Rev. 107, 3904-3951 (2007).

[8] Q. Li, H. C. Rudbeck et al. J. Membrane Sci. 347, 260–270 (2010).

[9] Q. Li, C. Pan, J. O. Jensen, P. Noyé and N. J. Bjerrum. Chem. Mater. 19, 350 (2007).

Characterization of Membranes for Fuel Cell Applications: Challenges in Translating Ex-situ Properties into In-situ Performance

Oliver Conradi, 3M Fuel Cell Components Program, Neuss, Germany

1 Introduction

For automotive or stationary applications of PEM fuel cells several advantages result by operating under elevated temperature (> 100 °C) and low relative humidity (< 35 %) conditions, such as more efficient heat and water management, higher reaction rates and improved tolerance against catalyst poisoning. However, under these conditions dehydration and degradation of state-of-the-art PFSA membranes result in an enhanced loss of conductivity and cell performance. For this reason novel membrane concepts (e.g. composite membranes with inorganic additives) as well as more specific and reliable test schemes are needed to reflect the fuel cell operation under hot and dry conditions.

This paper addresses different material concepts with respect to low rH / high temperature conditions. Furthermore specific considerations from an MEA manufacturer's perspective in applying characterisation techniques, designing efficient test protocols to identify membrane materials with improved properties and translating ex-situ data into in-situ performance will be discussed.

An integrated test scheme for composite membranes can be subdivided in ex-situ and in-situ experiments.

(a) Determination of intrinsic membrane properties in ex-situ experiments such as ionic conductivity by impedance spectroscopy (EIS), mechanical properties by dynamic mechanical thermal analysis (DMTA) under humidity cycling protocols, accelerated aging by Fenton's Test, electrochemical stability and mobility of inorganic additives by cyclic voltammetry.

The data from those tests supports the screening of membrane materials and suitable candidates are identified for more complex in-situ experiments.

(b) In-situ experiments with membrane-electrode-assemblies in a single test cell are standard protocols to test performance as against reference MEAs (e.g. based on a design with a catalyst coated GDL), protocols reflecting hot and dry operating conditions to gather performance data relative to standard materials and specific protocols aiming at accelerated aging. To investigate membrane specific failure modes in-situ experiments have to be accompanied by several diagnostic tools, such as cyclic or linear sweep voltammetry to measure hydrogen crossover, electrical shorts and stability of inorganic additives. Hydrogen pump can be used to monitor DC membrane resistance.

Lifetime and durability are critical issues in fuel cell systems. In useful lifetimes the membrane-electrode-assembly (MEA) is the most limiting component of such systems. In order to develop materials with enhanced lifetime and better durability a sound understanding of failure modes such as membrane thinning and catalyst degradation during

fuel cell operation is needed. Hence the application of accelerated aging tests and life time models are important tools in the development of membrane-electrode-assemblies.

2 Membrane Concepts

The state-of-the-art proton exchange membrane (PEM) materials for fuel cells are based on perfluorinated sulfonic acids (PFSA). The limitation to operate those PFSA-based PEM-fuel cells under low relative humidity or even without external humidification is mainly based on the fact that proton conductivity of the membrane will decrease significantly. That restriction is the main driver for developing novel membrane materials. Besides conductivity those materials have to fulfil various other properties:

- high proton conductivity
- low electrical conductivity
- low H_2 and O_2 crossover, but high enough oxygen solubility to allow good cathode ORR reaction
- good water permeability / diffusivity
- oxidative and hydrolytic stability
- mechanical integrity and dimensional stability

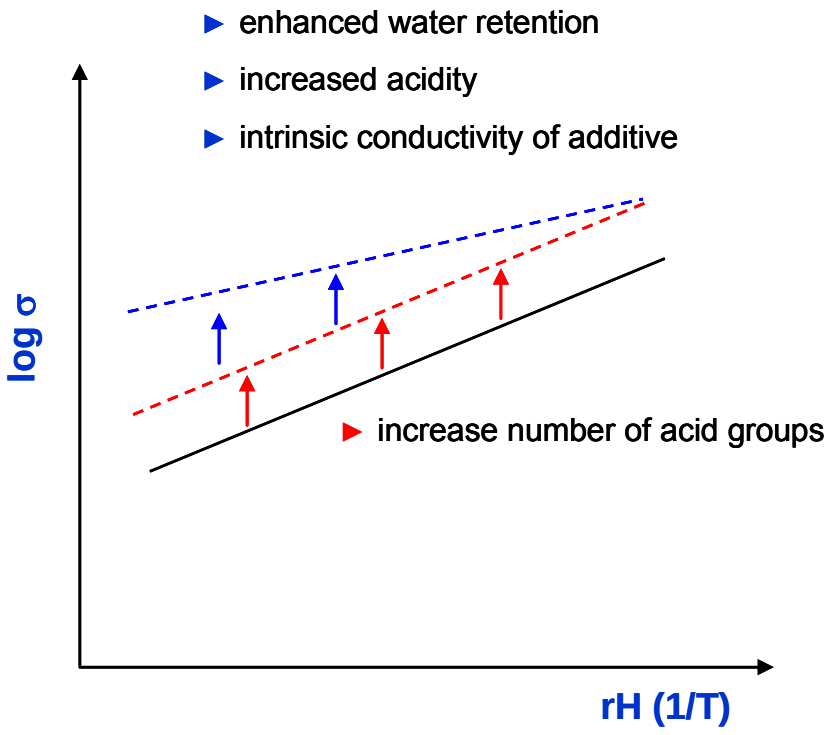

Figure 1: Influence of different material approaches on proton conductivity.

The scheme in Figure 1 shows how different material concepts could address an increase in proton conductivity as a function of relative humidity (or inverse temperature at constant dew point). Increasing the number of acid groups - reducing the equivalent weight at a given

molecular weight - would shift the proton conductivity to higher values however with the same sensitivity towards relative humidity expressed by the slope of the plot. By enhancing water retention and / or increasing the acid strength also the slope of the σ-rH-characteristic could be addressed.

Reducing the equivalent weight at a given molecular weight however will be accompanied with a lower degree of crystallinity and the membrane will compromise in its mechanical properties and integrity. The solubility increases with lower equivalent weight where the crystallity goes to zero and many mechanical properties parallel this effect. The experimental data in Figure 2 shows the proton conductivity for two different humidity conditions (T = 80 °C, DP = 80 °C and T = 120 °C, DP = 80 °C) as a function of equivalent weight.

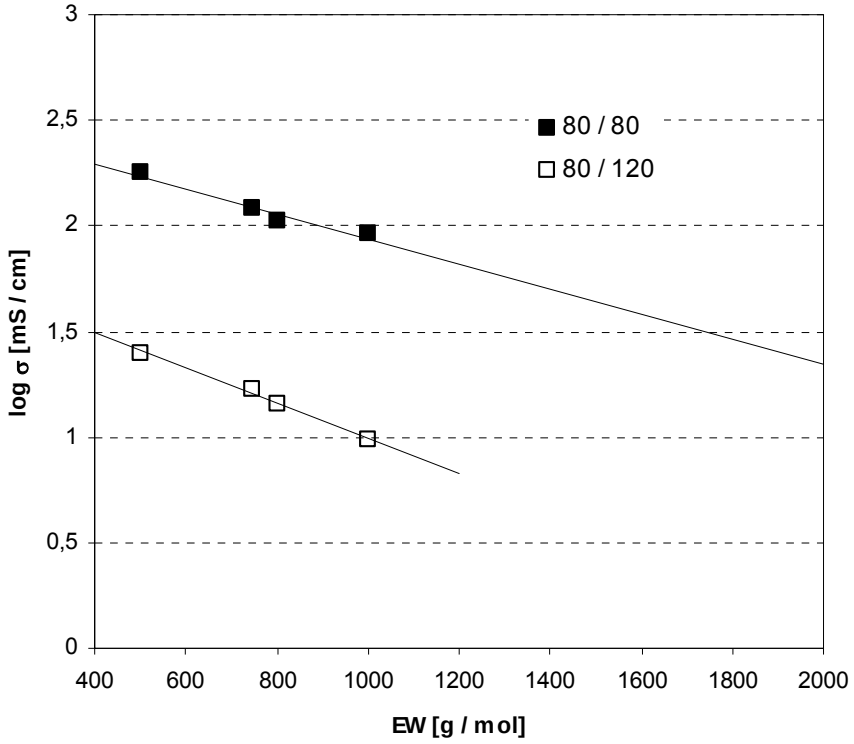

Figure 2: Proton conductivity for PFSA-based membranes as a function of equivalent weight (EW).

References

[1] S. Holdcroft et al., J. Power Sources 160 (2006) 872-891

[2] V. Ramani et al., J. Membrane Science 232 (2004) 31-44

[3] Jiang et al., Electrochem. Comm. 9 (2007) 2003-2008

[4] Datta et al., J. Electrochem. Soc. 152 (2005) 316-325

[5] Li et al., Chem. Mater. 15 (2003) 4896-4915

[6] D. Schiraldi, J. of Macromolecular Science 46 (2006), 315-327

Experience in Stack Development for High Temperature PEM Fuel Cells

P. Beckhaus, J. Burfeind, G. Bandlamudi, A. Heinzel, Zentrum für BrennstoffzellenTechnik ZBT GmbH, Germany

1 Introduction

High temperature PEM fuel cells (HT PEMFCs) offer tremendous flexibility when used as energy converters in stationary as well as mobile power devices. Coupling HT PEMFC stacks with fuel processors which use liquid as well as gaseous fuels to generate hydrogen rich gas is a promising prospect which paves the way for a possible hydrogen economy. One core challenge of the integration of these membranes operated at approx. 160 °C is the realization of stable and producible fuel cell stacks.

Within several research projects various innovative stack designs with different active areas (28 cm^2, 50 cm^2 and 200 cm^2) have been developed, constructed and operated at ZBT. Realized solutions for cooling structures, fuel channels, gasket technologies and the stack assembly are derived from these experiences. Furthermore operational results of these stacks and system solutions are being summarized.

2 High Temperature PEM

High temperature PEM fuel cells (HT PEM) can be operated in the temperature range between 130 °C and 200 °C and offer a number of potential advantages compared to low temperature PEM fuel cells (LT PEM), e.g., high CO tolerance, no need for humidification of reactant gases, and simplified heat management of the fuel cell system. The fuel cell research centre ZBT GmbH ("Zentrum für BrennstoffzellenTechnik") has started development work for small scale HT PEM fuel cell stacks in 2004, based on commercially available MEAs (Membrane Electrode Assemblies) of different suppliers. This technology offers a variety of potential advantages such as simplified system management, water management and adaptability to fuel reformers.

Comparing the efficiencies of the single fuel cell of a LT PEM and a HT PEM surely the HT PEM shows a slightly poorer performance. Neither the voltage stability nor the maximal current densities today reach the values of the classical PEM technology. Nevertheless comparing full system efficiencies of reformer based systems the HT PEM proves a better performance and offers the reduction of significant system components such as gas purification and humidification and in parallel an increase of operational stability of the fuel cell stack and the overall system.

But integration of a HT PEM MEA into a long term stable fuel cell stack environment and integration of this stack into a complete working system is yet another challenge. Identification of stack and system materials is a critical issue as long term and even short term operation of fuel cell stacks have proven [1]. This results in high material costs for the components of the fuel cell stack, namely MEA, bipolar plate, gasket and also the endplate

setup, all have to stand the high temperatures as well as the complex electrochemical and chemical cell environment.

3 First Approaches in HT PEM Fuel Cell Stack Construction and Operation

Starting 2004 ZBT has constructed first single cells and fuel cell stacks based HT PEM MEAs which at that time had been provided by PEMEAS GmbH, now BASF Fuel Cell GmbH. Based on the well proven LT PEM fuel cell stack design a 50 cm^2 approach was chosen, using milled graphite bipolar plates and foamed gaskets. As results of stack manufacture as well as cell and stack operation it became obvious that not only the temperature stability of the used materials is critical. A single cell was operated for 3000 hrs showing a good performance in principle but still a significant voltage decrease. In post mortem analysis the cell components were analysed, the bipolar plates surface deterioration was negligible, no cracks were to be identified and the electrical conductivity as well as the gas tightness was still comparable to the starting point. Also the MEA did not show any visible changes. Surprisingly a significant part of the increased cell resistance was identified to be caused by the gold plated copper current collectors: The gold plating was diffused during the high temperature operation resulting in conductivity deterioration. During cell operation furthermore the product water was analysed, here carbon particles were found to be usually < 1 mg/litre, Pt particles were found to be < 0,003 mg/litre and traces of phosphoric acid were found at 0,2 µg/m^2/s (peak: 0,44 µg/m^2/s).

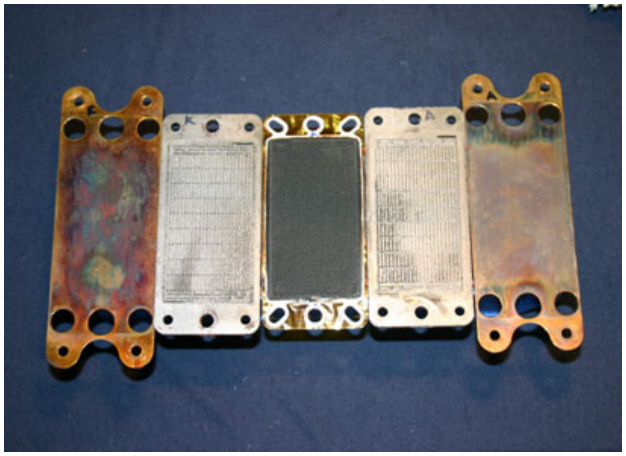

Figure 1: Single cell components after 3000 hrs of operation.

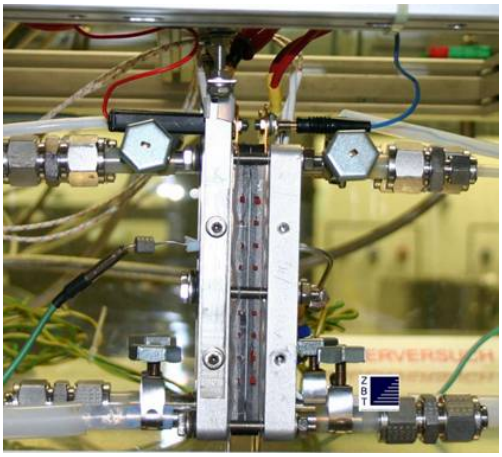

Figure 2: 50 cm^2 single cell (2006).

As result of the experience of this and other experiments also with respect to operation regimes, short and long stacks were to be manufactured and operated. A first milestone was the realization of a 12 cell stack which was constructed for the Boreskow Institute of catalysis in Novosibirsk (BIC). This stack was manufactured and proved a comparable performance even under different media supply at ZBT and BIC. Even after laboratory and development use, long storage times (about 1 year) and further transportation still very stable performance was reported.

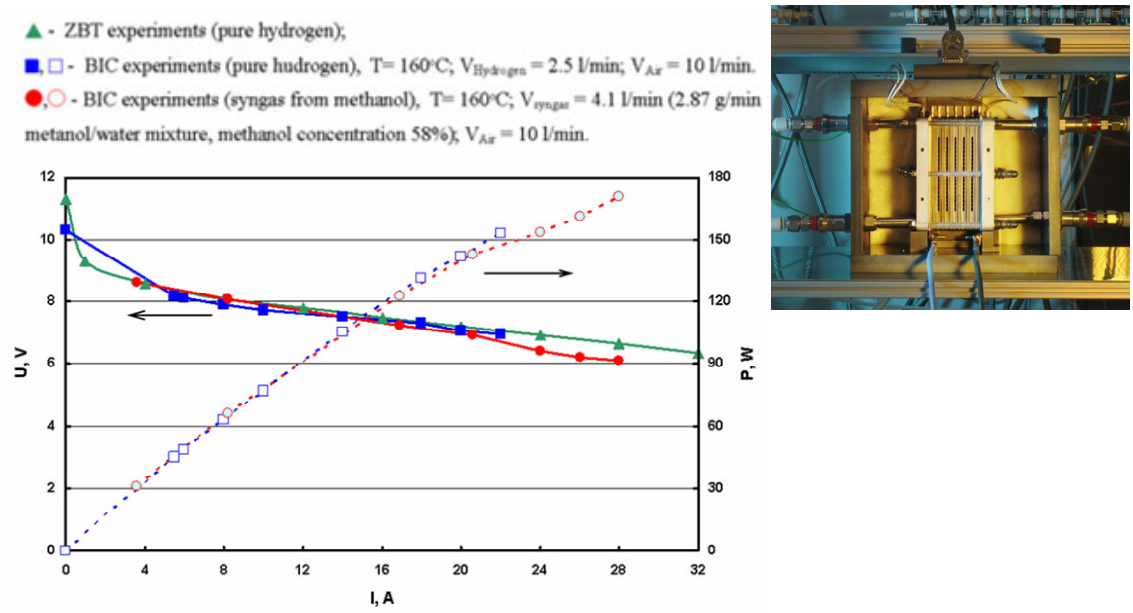

Figure 3: 12 cell stack operation at different test setups and feeding gases.

4 Micro Fuel Cell Stack

On the basis of the described pre-work in 2006 a joint research project was initiated to design and construct a compact 140 W_{el} HT PEM fuel cell stack to be integrated into a methanol reformer setup [2]. The aim of the overall project was the development of an efficient and robust portable power generation device applying methanol as fuel with an electrical net power output of 100 W_{el}. ZBT for this purpose has developed a 24 cell air cooled compact, lightweight HT PEM-stack. Different flow-field geometries were designed and optimized regarding pressure drop and performance, active area of the cell geometry was 27,6 cm^2. During the project a concept for HT PEM suitable gaskets was developed based on injection moulded FKM materials. Finally the stack was coupled to a methanol reformer and both integrated into system environment. In co-operation with project partners a system control concept was developed and integrated into the test stand control system. Laboratory equipment was replaced by low cost peripheral components stepwise and automated operation of the system was established. A coupled reformer HT PEM stack system could thereby be demonstrated.

The main new approach for the stack development was using single peace bipolar plates with external cooling fins. Instead of the classical approach of two bipolar half plates integrating cooling structures on the back side of the active area of a fuel cell, the approach utilizes the good thermal conductivity of the bulky graphite compound material (Schunk FU4369). The generated heat is transferred to the cooling fins. By alternating the position of the fins an effective cooling is secured. Simulations using multiphysics software COMSOL [3,4] have first been used to verify the concept which has finally also been approved by real stack and system performance tests. The fin technology was also successfully used for the heating process at stack start-up: exhaust gas and hot air was blown past the stack and the fins resulting in start up times of approx. 15 min for the fuel cell stack.

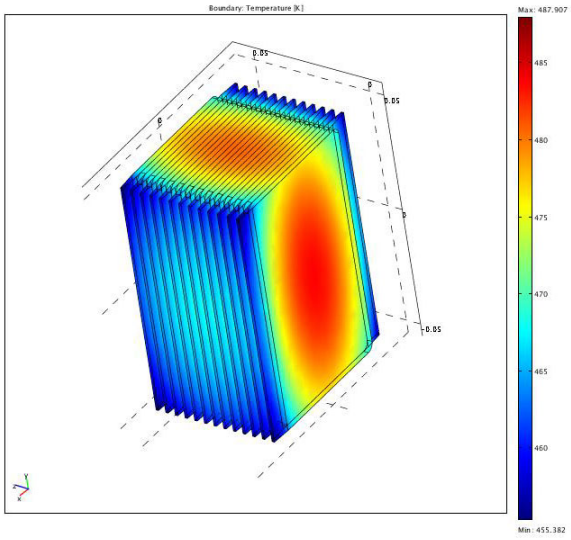

Figure 4: Simulation of the temperature profile using external cooling fins and moderate air flows.

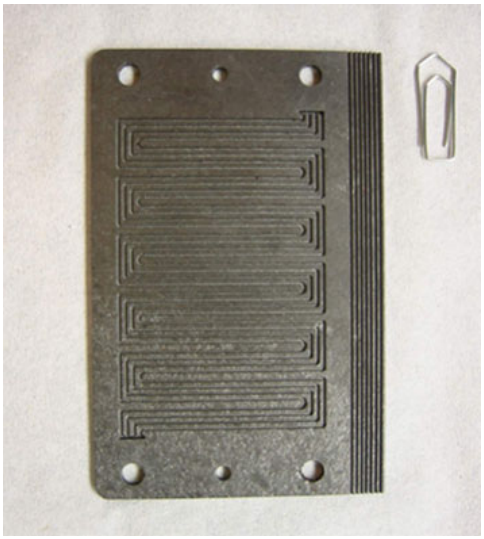

Figure 5: 27,6 cm^2 active area bipolar plate based with cooling fins.

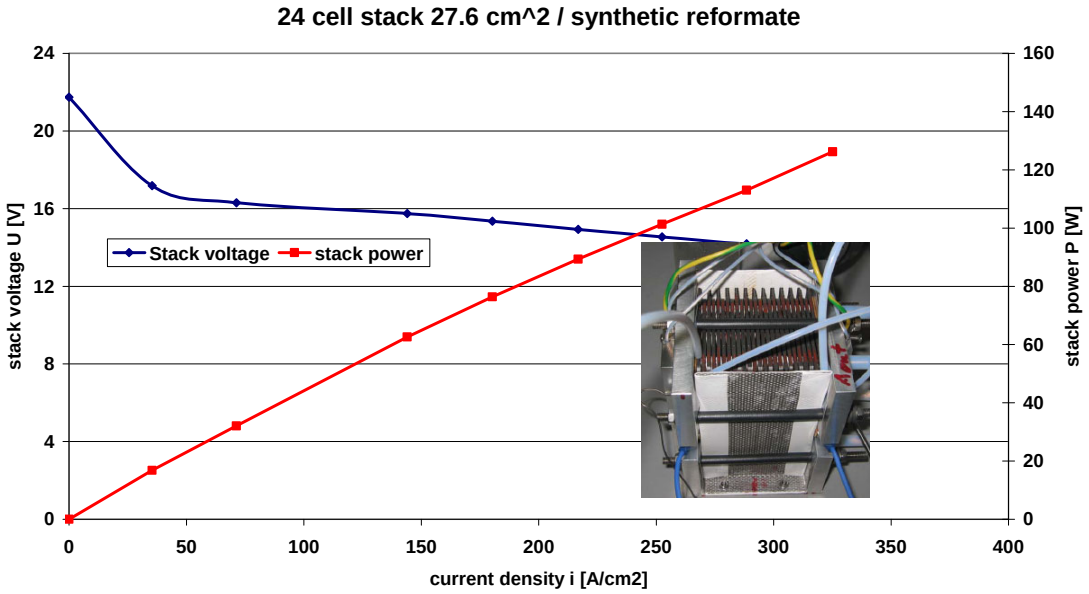

Figure 6: Performance curves of 24 cell stack / 27.6 cm^2.

5 Air Cooling versus Liquid Cooling

As described above air cooling of HT PEM fuel cell stacks is suitable using internal cooling structures or external cooling fins. The external concept was adapted again to the standard 50 cm^2 stack design and HT PEM fuel cell stacks have been constructed for industrial partners based on different commercial MEA. The stack concept thereby has proven to be functional also for power ranges up to at least 500 Watt.

Furthermore special applications demand the liquid cooling for efficient heat integration into the applications. Fuel cell stacks with liquid cooling have been designed and demonstrated with additional inserted cooling plates [5]. As it is necessary to keep cooling media suitable for operation at 160 °C (e.g. thermo oil) strictly away from the MEA an approach based on laser sintered metallic heat exchanger plates was chosen. By laser sintering three dimensional components can be produced integrating cooling channels; every fifth bipolar plate one cooling plate has to be integrated additionally into the stack. The concept has been proven to be suitable for heat integration topics regarding HT PEM fuel cell stacks. Nevertheless the effort for producing the cooling plates and the parallel connection of the plates to the cooling circuit is high. A single port solution transferring the cooling media through the fuel cell stack would be more beneficial. As gaskets do not guarantee a full tightness against cooling oils alternative cooling media have to be identified to realize low cost liquid cooled HT PEM stacks.

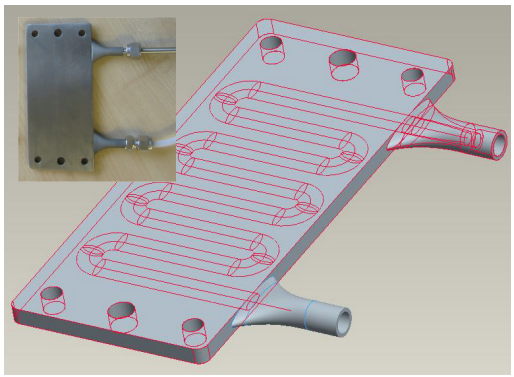

Figure 7: Laser sinter cooling plate (3D design).

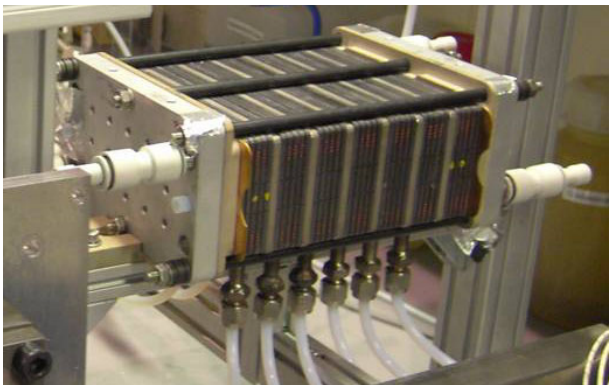

Figure 8: Cooling plates integrated into 50 cm^2 (active) 28 cell fuel cell stack.

6 Conclusion

High temperature Membrane Electrode Assemblies (MEA) do have high benefit for fuel cell applications. Systems either powered by pure hydrogen or by hydrocarbons via reforming processes do run more stable operated at higher temperatures. But the integration of the MEA in fuel cell stacks demands high efforts regarding materials to be used for gaskets, bipolar plates and most other stack and system components. As the operating temperature is high air cooling is suitable even at extreme outside temperatures but increases the effort for start-up-heat integration. Liquid cooling is still a challenging topic as no contact between cooling media and MEA is acceptable.

Acknowledgement

Parts of this work have been funded by the European Funds for Regional Development and the Region of North Rhine-Westphalia, other parts have been performed within the project “MicroPower / 03X3511G” financed by the “Bundesministerium für Bildung und Forschung” and the project “Entwicklung eines portablen Hochtemperatur-PEM-Brennstoffzellensystems mit thermisch integriertem Metallhydridspeicher / 247 ZN” financed by “Bundesminsterium für

Wirtschaft und Technologie" within the programme "Industrielle Gemeinschaftsforschung, IGF".

References

[1] George C. Bandlamudi, et al.: Chemical and mechanical stability of HT PEM fuel cell components - Proceedings of Fundamentals and Developments of Fuel Cell Conference 2008, Nancy, France, 10.-12.12.2008

[2] G. Kolb, K.-P. Schelhaas, M. Wichert, J. Burfeind, C. Heßke, G. Bandlamudi: Entwicklung eines mikrostrukturierten Methanolreformers gekoppelt mit einer Hochtemperatur-PEM Brennstoffzelle - Chemie Ingenieur Technik - CIT - Volume 81 Issue 5 (May, 2009) (Special Issue: Brennstoffzellen und Wasserstofftechnologie)

[3] Christian Siegel, et al.: Large Scale 3D Flow Distribution Analysis in HTPEM Fuel Cells - Proceedings of the European COMSOL Conference 2009, 14-16. Oct. 2009, Milan, Italy.

[4] Christian Siegel, et al.: Modeling Polybenzimidazole/ Phosphoric Acid Membrane Behaviour in a HTPEM Fuel Cell" - Proceedings of European COMSOL Conference 4.-6.11.2008 - Hannover

[5] R. Urbanczyk, et al.: HT-PEM Fuel Cell System with integrated complex hydride storage tank - Proceedings of WHEC 2010, Essen, Germany (Poster Presentation / Session Metal Hydrides/No. HS.2a)

Validation of a HTPEMFC Stack for CHP Applications

S. Pasupathi, Ø. Ulleberg, HySA Systems, SAIAMC, University of the Western Cape, South Africa
P. Bujlo, HySA Systems, SAIAMC, University of the Western Cape, South Africa and Electrotechnical Institute Wroclaw Division, Poland
J. Scholta, Centre for Solar Energy and Hydrogen Research (ZSW), Germany

Abstract

Fuel cell systems are very attractive for stationary co-generation applications as they can produce heat and electricity efficiently in a decentralized and environmentally friendly manner. PEMFC stacks operating at temperatures above 120 °C, specifically in the range of 140-180 °C, are ideal for co-generation purposes.

In this study, preliminary results from a HTPEMFC stack designed for CHP applications is presented and discussed. A short, five-cell, HT-PEMFC stack was assembled with Celtec–P-2100 MEAs and validated in terms of electrical performance. The stack was operated with hydrogen and air at 160 °C and the utilization curves for anode and cathode were recorded for a wide range of gas utilization at a current density of 0.52 A/cm^2. The current voltage characteristic was measured at optimal utilization values at 160 °C. A 1 kW stack is assembled and is currently being validated for its performance under various operating conditions for use in CHP applications.

1 Introduction

A domestic combined heat and power (CHP) system, which is a replacement for conventional heating boilers, providing both heat and power is attracting considerable commercial interest. Among the competing technologies, fuel cells offer significant advantages and in fact fuel cell technology is ideal for CHP generation as it offers high fuel efficiency together with very low environmental impact [1, 2]. Fuel cells in the range of 3 - 5 kW are appropriate for residential applications as it will be sufficient to cater for all the energy needs of a family. Among fuel cells, PEMFC, SOFC, AFC and PAFC have been regarded as potential candidates for CHP applications with PEMFC and SOFC at the forefront [2]. Recent developments in PEMFC technology, the HTPEMFC (operating above 120 °C) has increased the potential of this technology for CHP applications.

Development of HTPEMFC based CHP systems is part of the HySA Programme, a national hydrogen and fuel cell technology strategy in South Africa. In this paper, the work carried out by one of the three competence centres, HySA Systems, on the development of HTPEMFC stacks for CHP systems is presented. A five-cell short stack and a 1 kW stack was assembled and tested for gas utilization and performance. Currently experiments are underway to evaluate the performance in terms of electrical, thermal and combined efficiencies. Preliminary results on the gas utilization and performance of the stack is presented and discussed.

2 Experimental

The experimental part of the work consists of two stages, namely the HT PEM fuel cell stack assembly and stack testing.

2.1 Stack assembly

In the construction of the HTPEMFC stack, the Celtec –P-2100 MEAs delivered by BASF were used. The thickness of the MEA was 884 µm and the active area of electrodes was 96.04 cm^2. The graphite bipolar plates with serpentine flow patterns were used to supply reactant gases to the electrodes. Silver coated current collectors were used to minimize contact resistance bipolar plates. An oil based external cooling/heating system was applied to avoid possible leaks during internal cooling which might cause MEA damage. The four pipes mounted on two sides of the stack allowed appropriate heating and cooling, ensuring a homogeneous temperature distribution along the bipolar plates. More detailed description of the external cooling system used is available elsewhere [3]. A picture showing the stack installed on the test bench is shown in Fig. 1.

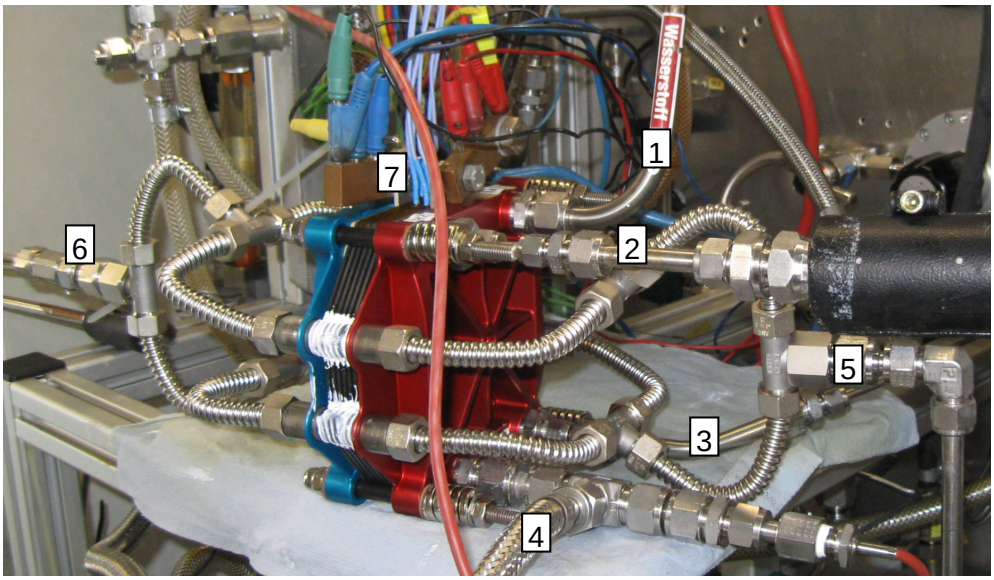

Figure 1: The view of 5-cell HT-PEMFC installed on the test stand. 1-Anode inlet, 2-Cathode inlet, 3-Anode exhaust, 4-Cathode exhaust, 5-Cooling/heating system inlet, 6-Cooling/heating system outlet, 7-Electrical connections.

2.2 Testing station

The performance tests of the stack were performed with the aid of testing station developed and available at ZSW. The testing station allowed control of all parameters, having influence on performance of the stack. More detailed description of the test bench is available elsewhere [4].

In addition to the standard test bench layout the high temperature circulator was used for the stack temperature control. The thermal oil was used in the high temperature system to heat up the stack to operation temperature at the start up and maintain proper temperature during

stack operation. Moreover, data were recorded with the aid of test stand built in data logging system and Yokogawa Data Acquisition Station. The latter was used to record single cell voltage and air outlet temperature.

2.3 Stack testing

The stack was evaluated in a test stand which allowed precise control of all the parameters expected to influence its performance. A detailed description of the test stand can be found elsewhere [4]. An AC Milliohmmeter was used to measure high frequency resistance at a frequency of 1 kHz which corresponds to the stack resistance closely related to water management and cell construction [5]. The stack was tested using pure hydrogen as a fuel that was supplied to the anode and air that was supplied to the cathode. Non-humidified gases at ambient pressure were supplied to both electrodes. Only air was preheated up to 100 °C before entering the stack. The nominal operation temperature of the stack was set to 160 °C. The utilization curves were recorded for various cathode and anode utilization levels. The cathode utilization curve was measured at cathode utilization level from 50% to 85% while anode utilization curve was recorded from 80% to 100% utilization range. Cathode utilization was changed at 5% steps while the anode was initially changed at 5% steps and 2% steps for utilization levels higher than 90%. The polarization curve was then recorded at the nominal temperature and at 80% and 50% utilization level for anode and cathode respectively. A stabilization time of five minutes was applied for each utilization point for cathode utilization curve measurements and six minutes stabilization time for anode utilization curve measurements.

3 Results and Discussion

In this section of the paper preliminary testing results performed on a 5 cell HT-PEMFC are presented and discussed.

3.1 Gas utilization curves

The utilization curves of the stack were measured for the anode and cathode separately at 0.52 A/cm^2. When the cathode utilization curve was measured, the anode utilization was kept constant at 80%. When the anode utilization curve was measured, the cathode utilization level was kept constant at 50%. The single cell voltages for each cell, as well as high frequency resistance of the stack, were recorded during measurements. The average voltage value and resistances are shown in the Fig. 2 (a) and (b), for cathode and anode respectively.

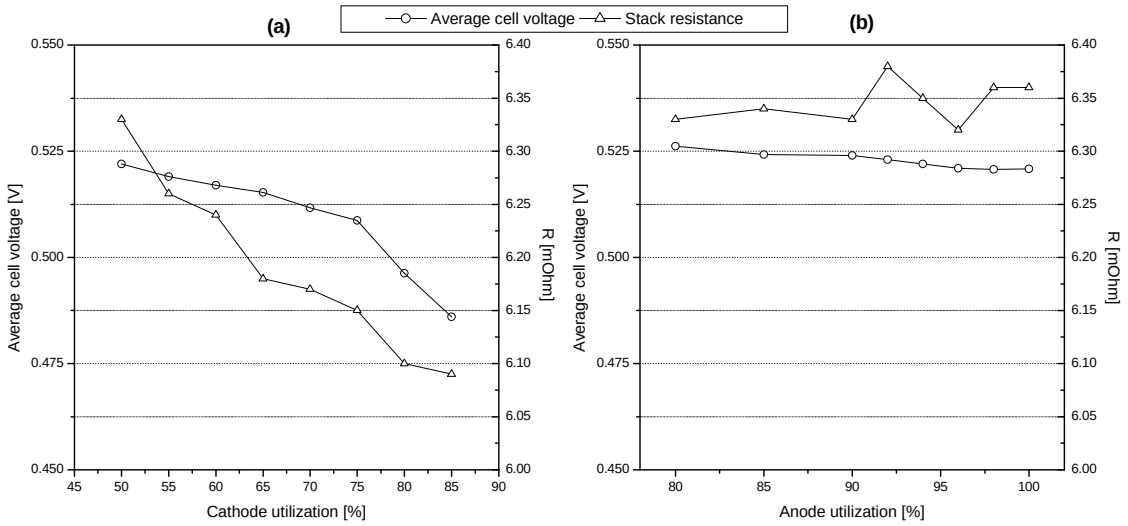

Figure 2: The cathode (a) and anode (b) utilization curves.

The initial value for high frequency resistance in both cases was about 6.33 Ohms. In Fig.2 (a), it is seen that the average voltage starts to drop for each point of utilization for utilizations from 50% to 75% and the slope is steeper for utilizations above 75%. This allows us to conclude that for cathode utilization higher than 75%, mass transport effect starts to have a significant influence on the stack or average cell voltage. Further, the reason that no increase in high frequency resistance was noted during the above measurements shows that the drop in the voltage with increasing utilization value is due to mass transport limitations. For the following measurements the cathode utilization value was set to at 50%. The change of anode utilization (Fig. 2 (b)) on average cell voltage is not very influential on electrical parameters although the average cell voltage decreases with increasing utilization level from 80% to 100%. The changes in high frequency resistance are negligible. For the following measurements the value of 80% anode utilization was used.

3.2 Polarization curve

The polarization curve of the stack was measured for the average single cell voltage ranging from 700 mV to 500 mV. The OCV was measured only for a few seconds to avoid degradation mechanisms to occur. A constant current was drawn during the measurements. For high currents, from 10 A to 60 A, a 5 A step with 2 minutes stabilization time was applied and for low currents, below 10 A, 2 A steps with the same stabilization time were used. The stack temperature during measurement was set to 160 °C. The anode and cathode utilization was 80% and 50% respectively. The minimum flow rates of the gases were kept at a value that is required by the stack to generate 0.2 Acm^{-2}. In parallel to current and voltage measurements the high frequency resistance of the stack was measured and data is displayed in the Fig.3.

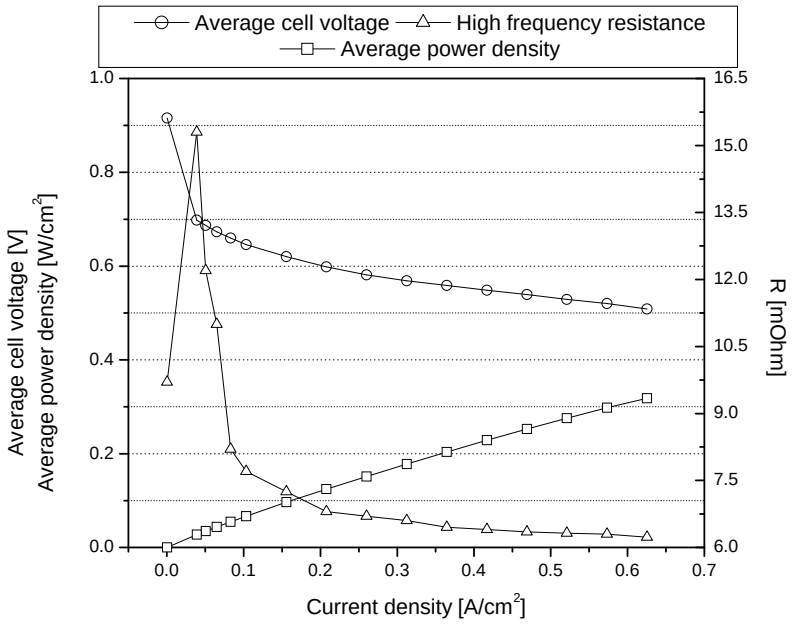

Figure 3: The polarisation curve of the 5 cell HT-PEM stack with active area of 96 cm².

A stable stack performance was recorded during the measurements of the polarization curve. It was possible to generate more than 0.3 W/cm^2 at current densities higher than 0.6 A/cm^2 and average cell voltage of 0.5 V. A total stack power of 150 W was generated at 0.625 A/cm^2 and 0.5 V average cell voltage. A sharp increase in the high frequency resistance was noted when the load was applied to the stack i.e., when the voltage was changed from OCV to 700 mV, most likely due to the internal membrane resistance expected at those voltages. The high frequency resistance decreased with increasing current density from the initial value of 15 Ohms (at 700 mV) to 6.33 Ohms (at 500 mV).

A 1 kW stack has been built using similar components and stack design, and performance of the stack is currently being evaluated with respect to electrical and thermal output.

4 Conclusion

A HT-PEMFC short stack was assembled based on BASF Celtec – P-2100 MEAs. In the construction and evaluation of the stack, an external thermal oil based cooling system was applied. Experiments showed that the optimal anode and cathode utilization of gases was 80% and 50% respectively. The electrical power density generated by the stack reached 0.31 W/cm^2, and an overall power output of 150 W was measured at 0.625 A/cm^2 and 0.5 V of average cell voltage. Further test on extended version, up to 1 kW power fuel cell stack construction is underway with the aim to validate the stack for CHP applications in terms of both thermal and electrical and combined efficiency.

Acknowledgements

This work is supported by the HySA Programme (project KP1-S03), Department of Science and Technology, South Africa.

References

[1] A.D. Hawkes and M. A. Leach. “On policy instruments for support of micro combined heat and power”. Energy Policy. 36 (2008) 2973-2982.

[2] H. I. Onovwiona and V. I. Ugursal. “Residential cogeneration systems: review of the current technology”. Renew. Sust. Energ. Rev., 10 (2006) 389-431.

[3] J. Scholta, M. Messerschmidt, L. Jorissen, Ch. Hartnig, “Externally cooled high temperature polymer electrolyte membrane fuel cell stack”. J. Power Sources 190 (2009) 83–85.

[4] M. Purmann, "Optimization of operating conditions of PEM fuel cells, taking into account the electrical and overall efficiency at different load requirements and operating parameters". Otto-von-Guericke University - Magdeburg, Faculty of Electrical Engineering and Information Technology, Inst of Electrical Energy Systems, Dissemination.

[5] J. Scholta, F. Haussler, W. Zhang, L. Kuppers, L. Jorissen, W. Lehnert, “Development of a stack having an optimized flow field structure with low cross transport effects”. J. Power Sources 155 (2006) 60–65.

Modular Fuel Cell System

Michael Brodmann, **Martin Greda**, University of Applied Sciences Gelsenkirchen, Germany

1 Introduction

The modular fuel cell system is a newly developed concept for self-sustaining energy supply of small consumers in the range up to 300 W.

The main goal of the implementation was to design and provide effective and low-cost PEM fuel cell stacks which are hydrogen supplied and its balance-of-plant (BoP) components.

The system is scalable, built in 30 W increments, in order to cover all power categories up to 300 Watts.

Great importance was attached to the construction of an insensitive and robust system, because the portable system should be able to operate under a variety of environmental conditions.

The modular fuel cell system consists of a modular fuel cell stack, a modular designed electronic circuit board and a customizable BoP according to the total power/ overall performance.

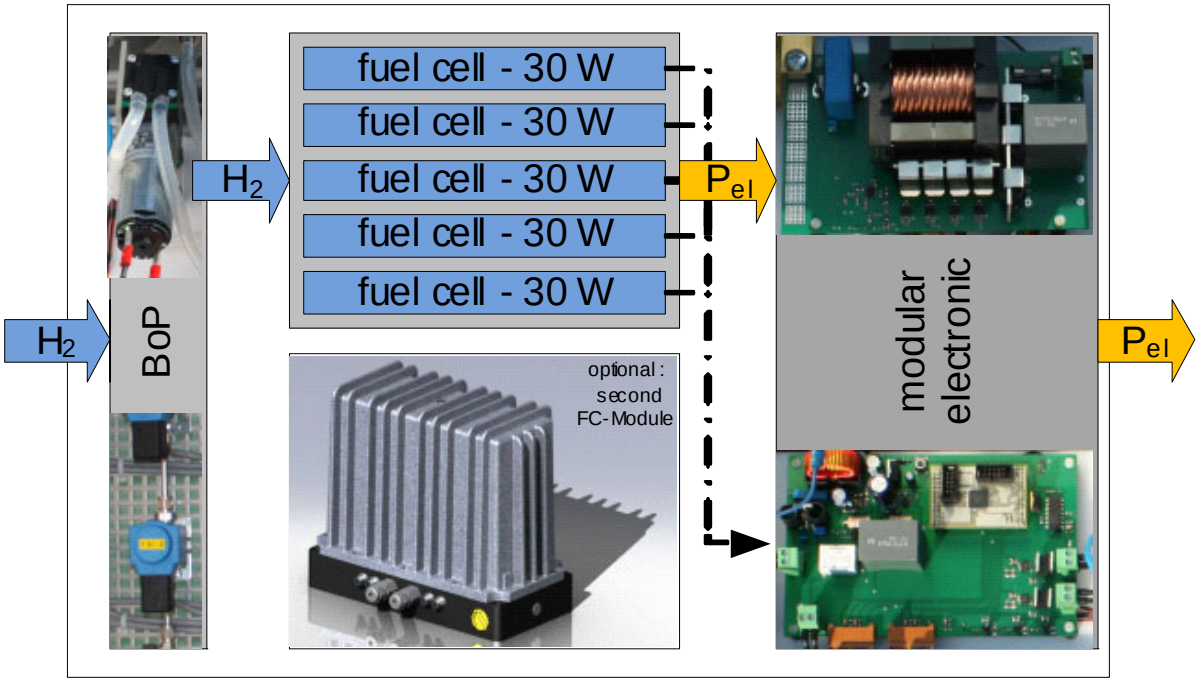

Figure 1: The modular fuel cell system.

2 The Modular Fuel Cell Stack

The modular fuel cell stack distinguishes itself from a standard fuel cell stack in two important features:

1. the design of the fuel cells based on metal pole plates and
2. the hydraulic compression of the fuel cell.

The advantages of point 1 are obvious, metal pole plates are more robust than graphitic pole plates. In addition, the pole plates can be quickly molded by a molding press, which leads to a low cost fabrication.

Figure 2: Section through a mono-cell.

Figure 2 shows the smallest unit of the modular fuel cell stacks, the mono-cell (the fuel cell itself) consisting of two metal pole plates with integrated membrane-electrode assembly.

This stack structure with parallel gas supply route and hydraulic compression has the advantage of been able to remove a damaged fuel cell quickly from the stack with minimal effort and without damaging the other units.

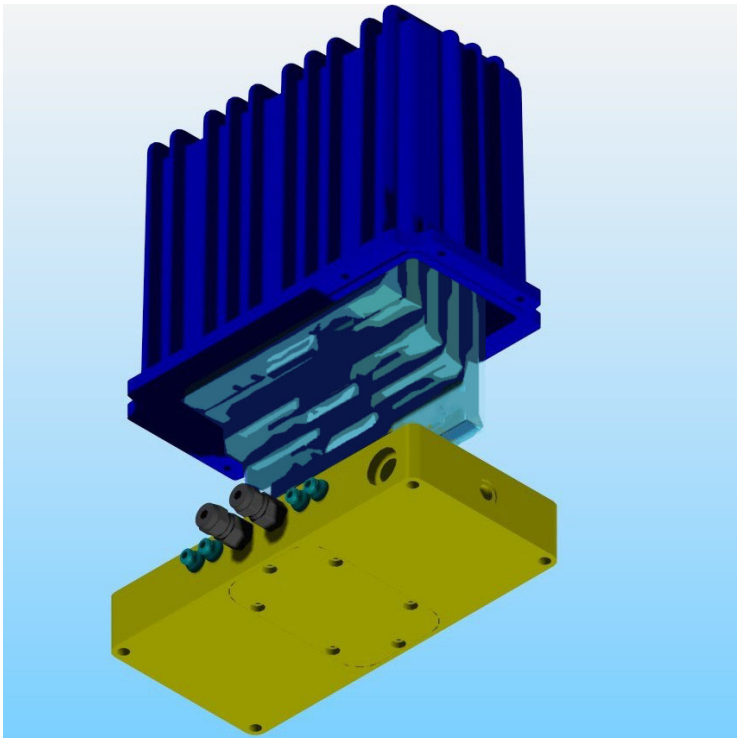

Figure 3: Schematic representation of the modular fuel cell stacks.

In conventional fuel cell stacks an exchange of the fuel cell is often not possible because the plates are pressed or bonded with each other what leads to damage while disassembling.

In the case of the modular fuel cell system the replacement of one cell is quite simply.

For the structure of the modular stacks, see Figure 3.

In order to perform a cell switch, the housing has to be relieve, which is easily done via a simple screw mechanism.

Subsequently, the cover can be removed and the cell can be easily replaced. Evan a non-specialist is able to replace a faulty fuel cell within minutes. The information regarding which cell has to be changed is displayed by the electronic circuit board!

3 The BoP

There are a variety of components such as valves, pumps etc. offered at the market, suitable for operation with hydrogen. However, the selection and integration of corresponding components are still a challenge.

Great deal of importance was attached to the high availability of the BoP, which are applied in modular fuel cell systems and the system efficiency optimization.

Since the fuel cell stack is scalable, BoP of the system has to be adapted depending on the system output power.

The appropriate platform for an individual adjustment is realized by standardized housing and mounting fixtures.

4 The Modular Electronic Circuit Board

In order to supply a load with electrical energy efficiently, an electronic circuit board is required in addition to the fuel cell BoP, which has to provide a stable output voltage by an optimized efficiency.

Especially for this purpose, a two-stage DC / DC converter was designed. It is possible to operate a second fuel cell stack in addition to the main stack at the entrance of the DC / DC converter. The second-stage of the switched power amplifier offers an efficient increase of the DC voltage to output voltage level, as well as electrical galvanic separation.

The output voltage of the DC / DC Converter is, by the way, adjustable to the needs of the load.

In addition, the galvanic separation allows switching the output of a further modular fuel cell system in series, thus doubling the output voltage is possible.

It is also apparent that great value was attached to a high degree of modularity and flexibility while designing the system.

Another essential element is the control board, which constitutes the controlling “heart” of the whole system. Especially for this purpose a microcontroller board was developed. This board has high power outputs for the BoP, such as the pumps and the magnetic valves. All the control and automation interventions are initiated by the microcontroller.

In addition, the control unit supervises the fuel cell stack, for example, individual cell voltages are continuously read. Thus, the real functions of the fuel cell are monitored and if

necessary, a message will be displayed. Finally, on this board the monitoring as well as the communication with the external monitoring point are possible. In this way an online monitoring is possible for a given network connection or GSM.

References

Michael Brodmann, Achim Edelmann, *Modular Designed Robust Fuel Cell Stack*. In proceedings: 9th Annual Meeting of the Fuel Cell and Hydrogen Network NRW, Düsseldorf, 10.12.2009

Preparation and Characterization of Nafion/ Titanium Dioxide Nanocomposite Membranes for Proton Exchange Membrane Fuel Cells

Inci Eroglu, **Yılser Devrim**, **Serdar Erkan**, Middle East Technical University Dept. of Chemical Engineering, Ankara, Turkey
Nurcan Bac, Yeditepe University Dept. of Chemical Engineering Istanbul, Turkey

Abstract

In the present study, Nafion/Titanium dioxide (TiO_2) nanocomposite membranes for use in proton exchange membrane fuel cells (PEMFC) were investigated. Nafion/TiO_2 membranes were prepared using the recasting procedure. The composite membranes have been characterized by thermal analysis, XRD, SEM, proton conductivity measurements and single cell performance. Thermal analysis results showed that the composite membranes have good thermal properties. The introduction of the inorganic filler supplies the composite membrane with a good thermal resistance. The physico-chemical properties studied by means of scanning electron microscopy (SEM) and X-ray diffraction (XRD) techniques have proved the uniform and homogeneous distribution of TiO_2 and the consequent enhancement of crystalline character of these membranes. The energy dispersive spectra (EDS) analysis indicated that the distribution of Ti element on the surface of the composite membrane was uniform. Performances of fabricated Membrane electrode assembly (MEA)'s measured via the PEMFC test station built at METU Fuel Cell Technology Laboratory. A single cell with a 5 cm^2 active area was used in the experiments. These results should be conducive to the preparation of membranes suitable for PEMFC. We believe that Nafion/TiO_2 nano composite membranes have good prospects for use in PEMFC.

1 Experimental

1.1 Membrane preparation

Nafion/TiO_2 composite membranes were prepared using the recasting method [1]. Nafion solution (15 wt.%) was evaporated at 60^{o}C until a dry residue was obtained. The residual Nafion resin was redissolved in a desired amount of DMAc to form a solution containing 5 wt. % of Nafion. TiO_2 powder was added and dispersed in an ultrasonic bath. The resulting mixture was cast onto a Petri dish and the solvent was evaporated at 80^{o}C. The membrane was removed from the Petri dish by wetting with de-ionized water. The membrane thickness around 80 µm was obtained from 10 wt. % TiO_2 loading. A recast Nafion membrane was also prepared with the same procedure for comparative study. All membranes were stored in deionized water before any test was performed. Before MEA preparation the membrane was treated by boiling in H_2SO_4 solution (0.5M) about one hour and washing in DI water for half an hour.

MEAs were prepared by spraying catalyst ink onto the gas diffusion layers (GDL 31 BC, SGL Carbon Germany) [2]. The catalyst ink was sprayed until the desired catalyst loading (0.4 mg

Pt/cm2 for both anode and cathode sides) was achieved. After spraying the catalyst ink onto the GDL's, MEA was prepared by pressing these GDL's onto the treated membrane at 130^0C, 688 N cm-2 for 3 min. Performances of fabricated MEA's were measured via the PEMFC test station built at METU Fuel Cell Technology Laboratory. A single cell PEMFC (Electrochem FC05-01SP-REF) with a 5 cm^2 active area was used in the experiments.

1.2 Characterization

The composite membranes have been characterized by thermogravimetric analysis (TGA), scanning electron microscopy (SEM), X-ray diffraction (XRD) and single cell performance. The energy dispersive spectra (EDS) analysis indicated that the distribution of Ti element on the surface of the composite membrane was uniform. Performances of fabricated MEA's were measured via the PEMFC test station built at METU Fuel Cell Technology Laboratory. The membranes were tested in a single cell with a 5 cm^2 active area operating at 70 °C to 120°C.

2 Results

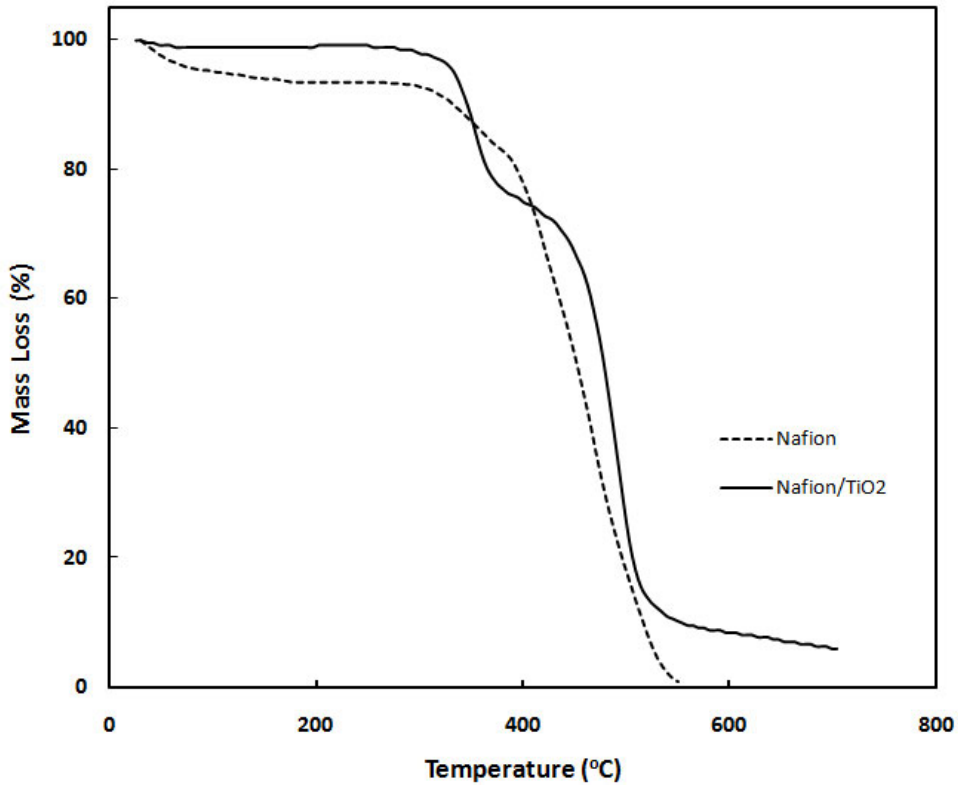

Figure1: TGA curve of Nafion and Nafion/TiO_2.

Thermal analysis results showed that the composite membranes have good thermal properties. The introduction of the TiO_2 supplies the composite membrane with a good thermal resistance (Figure 1). There is three derivative weight loss peaks for Nafion around 50^oC – 200^oC, 200^oC –400^oC, and 400^oC –550^oC. Initial weight loss is due to residual water. The next peak is attributed to the decomposition of the -SO_3H groups and the final peak is assigned to the degradation of the polymer main chain. Nafion/TiO_2 composite membranes

have good thermal stability. The results indicates that addition of inorganic TiO_2 do not change the thermal stability of Nafion. The decrease of the degradation temperature observed in the Nafion/TiO_2 composites has been associated with a catalytic effect of titania and chemical interaction between the acid groups in Nafion and the surface of the TiO_2 particles [3,4].

The physico-chemical properties studied by means of scanning electron microscopy (SEM) and X-ray diffraction (XRD) techniques have proved the uniform and homogeneous distribution of TiO_2 and the consequent enhancement of crystalline character of these membranes.

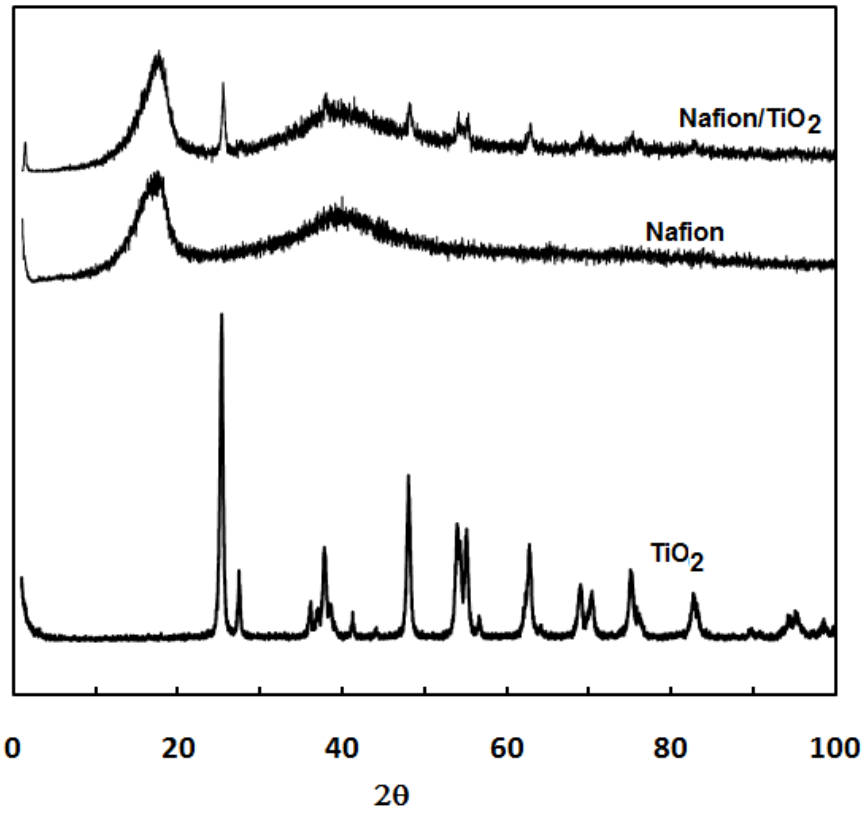

Figure 2: XRD patterns of Nafion, TiO_2 and Nafion/TiO_2.

As seen from Figure 2. the crystallinity of the composite membrane increases when 10 wt% TiO_2 is incorporated into membrane. The increase in crystallinity suggests that the interface adhesion is strong between inorganic additives and organic polymer structure due to the structural modification [5,6].

SEM analysis has proved the uniform and homogeneous distribution of TiO_2 (Figure 3). The energy dispersive spectra (EDS) analysis indicated that the distribution of Ti element on the surface of the composite membrane was uniform.

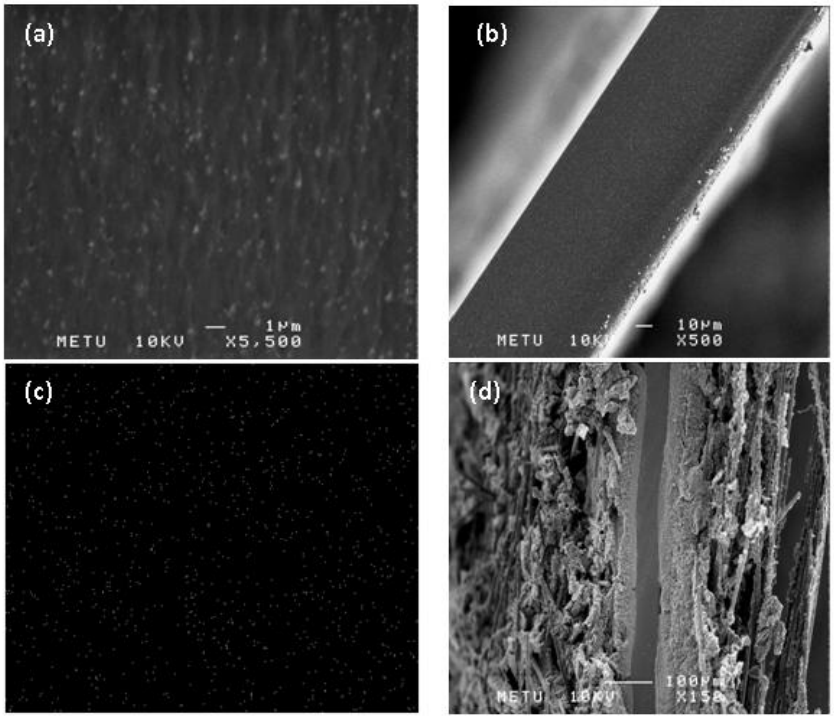

Figure 3: SEM images of a) Nafion/TiO_2, b) cross section of Nafion/TiO_2, c)Ti distribution by EDS, d) cross section of MEA prepared by Nafion/TiO_2.

Figure 4 and 5 illustrate the polarization curves obtained at different cell temperatures for the membrane electrode assemblies (MEAs) prepared with Nafion and Nafion/TiO_2 composite membrane. The maximum power reached for the cell constructed with Nafion/TiO_2 composite membranes is 0.266, 0.218 and 0.18 W/cm^2 for the cell operating temperatures of 80, 85 and 90^oC, respectively. The maximum power density measured for the cell constructed with Nafion/TiO_2 composite membrane is more than the cell constructed with Nafion membrane. Single fuel cell tests performed at different operating temperatures indicated that Nafion/TiO_2 composite membrane is more stable and also performed better than Nafion membranes.

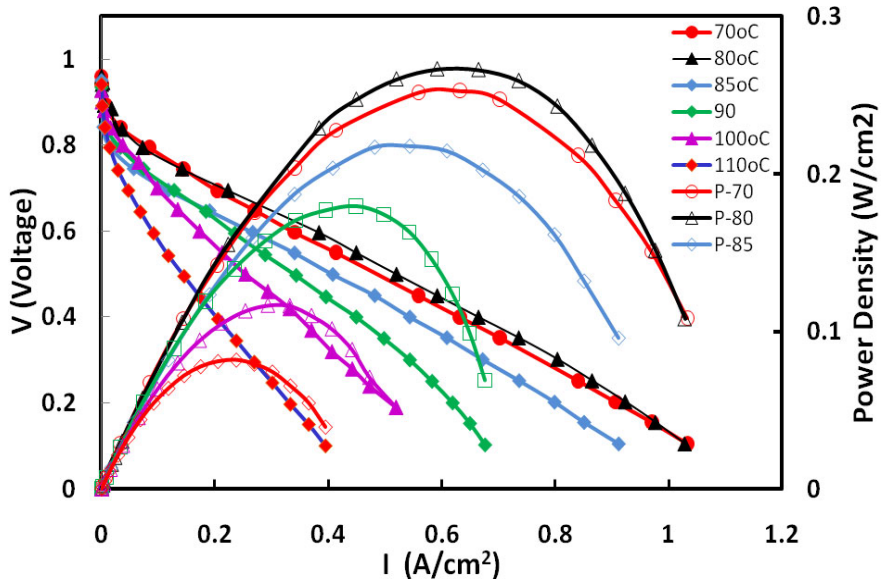

Figure 4: VI curve of Nafion/TiO_2 composite membranes at different temperature.

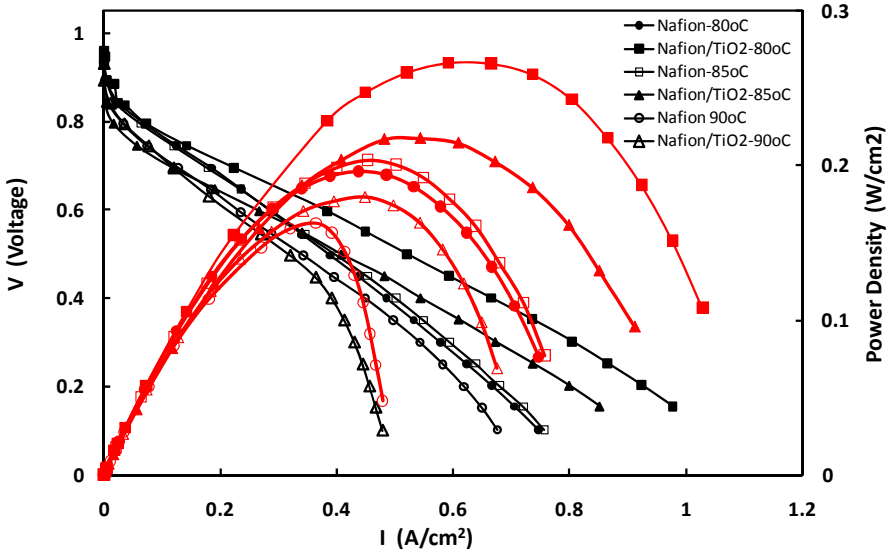

Figure 5: VI curve of Nafion and Nafion/TiO_2 composite membranes.

3 Conclusion

Nafion/TiO_2 composite membranes prepared with TiO_2 nanoparticles exhibit 30% higher power density compared to Nafion membranes. The maximum power density achieved is 0.266 W/cm^2 at 80^{o}C for composite membranes. Uniform distribution of TiO_2 nanoparticles in Nafion enhances the thermal stability of Nafion membranes. Although the power density

decreases with increasing temperature above 80^{o}C, the composite membranes resist up to 110^{o}C in PEMFC. These results should be conducive to the preparation of new membranes suitable for PEMFC.

References

[1] Chen, S.Y., Han, C.C. Tsai, C.H., Huang, J., Chen-Yang, Y.W. Effect of morphological properties of ionic liquid-templated mesoporous anatase TiO2 on performance of PEMFC with Nafion/TiO2 composite membrane at elevated temperature and low relative humidity. Journal of Power Sources 2007; 171: 363–372.

[2] Bayrakçeken A., Erkan S., Türker L., Eroglu I. Effects of membrane electrode assembly components on proton exchange membrane fuel cell performance. Int J Hydrogen Energy 2008; 33(1): 165-170.

[3] Adjemian K.T., Dominey R, Krishnan L, Ota H, Majsztrik P, Zhang T, et al. Function and characterization of metal oxidenaflon composite membranes for elevated-temperature H-2/O-2 PEM fuel cells. Chem Mater. 2006;18: 2238–48.

[4] Patil, Y., Mauritz, K.A.,Durability Enhancement of Nafion Fuel Cell Membranes Via in Situ Sol-Gel Derived Titanium Dioxide Reinforcement. Journal of Applied Polymer Science 2009; 113: 3269-3278.

[5] Devrim Y., Erkan S., Baç N, Eroglu I. Preparation and characterization of sulfonated polysulfone/titanium dioxide composite membranes for proton exchange membrane fuel cells. Int J Hydrogen Energy 2009; 34: 3467-75.

[6] Nam, S., Lee, K.H., Kang, Y., Park S.M., Lee, J. W., Organic-Inorganic Nanocomposite Membranes as High Temperature Proton Exchange Membranes for a Direct Dimethyl Ether Fuel Cell Application, Separation Science and Technology 2007; 13: 2927 – 2945.

CarbonNanoTubes (CNT) in Bipolar Plates for PEM Fuel Cell Applications

M. Grundler, T. Derieth, P. Beckhaus, A. Heinzel, Centre for Fuel Cell Technology ZBT GmbH, Germany

Abstract

Using standard mass production techniques for the fabrication of fuel cell components, such as bipolar plates, is a main issue for the commercialisation of PEM fuel cell systems. Bipolar plates contribute significantly to the cost structure of PEM stacks. In an upcoming fuel cell market a large number of bipolar plates with specific high-quality standards will be needed. At the Centre for Fuel Cell Technology (ZBT) together with the University of Duisburg-Essen fuel cell stacks based on injection moulded bipolar plates have been developed and demonstrated successfully [1]. This paper focuses on the interactions between carbon filling materials (graphite, carbon black and carbon nanotubes (CNT)) in compound based bipolar plates and especially the potential of CNTs, which were used in bipolar plates for the first time. The entire value added chain based on the feedstock, the compounding and injection moulding process, the component bipolar plate, up to the operation of a PEM single fuel cell stack with CNT-based bipolar plates is disclosed.

1 Introduction

Besides the membrane-electrode-assemblies (MEA) and the gas-diffusion-layers, the bipolar plates constitute the most important element of a PEM fuel cell stack with manifold functions. Bipolar plates work as both electrical and thermal conductive plate between the active cells. They separate the reactant gases and distribute them on each side over the whole active area of the MEA. Finally, they serve as structural element distributing mechanical forces. An important require of property of bipolar plates is their chemical resistance to the operation conditions inside a fuel cell stack. In essence, the bipolar plate material used for low temperature PEM-FCs has to endure a steady electrical potential, a wet environment of pure water, a low pH-value and temperatures of about 80 °C [2].

One way to fulfil all the requirements for bipolar plates combined with the possibility of mass production leads to carbon filled polymer materials for bipolar plates. The development of such compound materials is focused in various of investigations [3,4]. The polymeric matrix allows usage of conventional processing methods such as extrusion for the production of compounds and the further processing to bipolar plates via injection moulding. One main requirement of bipolar plates is a good electrical and thermal conductivity. In order to achieve adequate conductivities for the bipolar plates the (therefore used) compound material normally consist of a polymer which functions as a binding matrix, and a high load (ca. 80 wt%) of carbon-based electrically and thermally conductive filling materials such as graphite and carbon blacks [5]. In the recent years carbon nanotubes seem to be another promising filler material due to their favourable electrical and mechanical properties [6]. Carbon nanotubes have the potential to improve the properties of such highly filled

compounds when used in combination with other filler materials. CNTs generally form large agglomerates and the biggest challenge is to disentangle and to disperse the CNT-agglomerates during the process of melt-compounding. To incorporate the CNT homogenously distributed into a polymeric matrix is necessary to achieve high conductivities of such materials even at low CNT content. This plays a key role to transfer the unique properties of CNTs into compound materials. The production of such high filled compound materials can be done by using a kneader or an extruder. In a following step the compound materials are used to produce bipolar plates by injection moulding or compression moulding.

The first objective of this work has been the determination of the influence of different carbon filling materials, especially CNTs, in a polymeric matrix regarding the production process. The second aim focuses on the final properties such as electrical conductivities of injection moulded samples. Finally the effect of this carbon fillers on the performance of a single PEM fuel cell stack has been investigated. The intention of this study is the development of new CNT-based compound materials with improved properties in comparison to carbon black compounds for bipolar plates.

2 Experimental

2.1 Compounding of high filled polymeric materials

As mentioned before a high content of carbon filling materials has to be incorporated into a polymeric matrix to achieve good conductivities. Therefore five highly filled polymer compounds have been processed in a small compounder (kneader, Thermo Scientific Rheomix 3000p) under similar process conditions for benchmarking. Within the scope of this investigation, all compounds have been produced with a similar filling load of 87 wt% to ensure processability and comparability. To explore the interacting dependencies between the filling materials graphite and carbon black or CNTs the following binary and hybrid compounds have been investigated:

- binary compound: graphite (87 wt%) in polypropylene
- hybrid compounds: graphite (84,5 wt%) with a secondary filling material; carbon black (2,5 wt%) or CNTs (2,5 wt%) in polypropylene
- hybrid compounds: graphite (82 wt%) with a secondary filling material; carbon black (5 wt%) or CNTs (5 wt%) in polypropylene

2.2 Injection moulding of samples und bipolar plates

In general ZBT has chosen the injection moulding technique as a standard production method to manufacture bipolar plates in a one-step process with process cycle times below 18 seconds (Kraus Maffei, Germany, F_{max}=3000 KN, p_{max}=350 MPa). The injection moulding of such high filled compound materials is not trivial because of the high melt viscosities of the compounds. Nevertheless it is possible to produce bipolar plates for usage in PEM fuel cells by injection moulding. To achieve a reproducible and fast characterisation of different compound materials, small unstructured plates (diameter = 30 mm, thickness = 2 mm) were injection moulded on a small piston injection moulding machine (Thermo Scientific HAAKE MiniJetII, p_{max} = 120 Mpa).

2.3 Measurement of electrical conductivity

For measurement of through plane electrical conductivity a four pole measurement apparatus is used. The injection moulded samples were placed between two gas diffusion layers (W.L. Gore & Associates GmbH) which are fixed on gold plated stainless steel stamps integrated in a hydraulic press. The measurements were performed under pressure to simulate the operating conditions of a PEM fuel cell. A pressure of 2 Mpa and a current of 500, 1.000, 1.500 and 2.000 mA (Wenking HP 96-20) was applied and the resulting voltage recorded.

2.4 Analysis of internal material structures

Images from scanning electron microscope (field emission-SEM) (Leo 1530 Gemini) give an idea about the internal structure and dispersion of nano particles between graphite flakes at injection moulded compound materials. For SEM measurements, the plates were broken in liquid nitrogen to prevent thermal deformations. The plate samples were placed in the sample holder, vacuum was applied and SEM images were taken from the broken surface (cross sectional direction).

3 Results and Discussion

3.1 Compounding

The addition of a secondary nanometer sized filling material, especially of carbon blacks, adversely affects the processability of the compound material during extrusion because of high surface and abrasive behaviour. A suitable indicator to describe the melt-viscosity of the compounds is the measured torque during the compounding process and the resulting melt temperature. The higher the torque the higher is the melt viscosity, keeping in mind that a lower melt-viscosity facilitates injection moulding of bipolar plates. The following figures show the obtained torques and temperatures during compounding of the five highly filled materials.

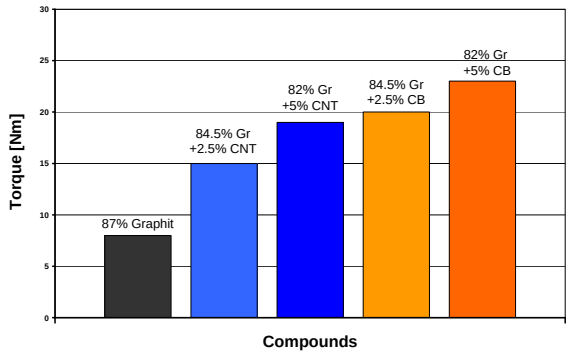

Figure 1: Torque during compounding.

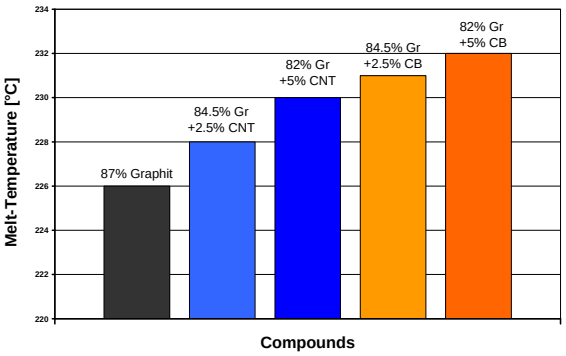

Figure 2: Recorded melt temperature.

As aforementioned the binary graphite/polymer compound shows the lowest torque during compounding. The addition of carbon blacks (CB) or CNTs in hybrid compounds significantly increases the torque and thus the melt temperature. But it can be seen that CNT-based compounds reveal a lower torque-value when compared to their carbon black based

counterparts. CNTs tend to be less abrasive than carbon blacks and this induces a lower melt viscosity.

3.2 Electrical conductivity

The following graph shows the area specific volume resistivity of the five investigated compounds, measured at injection moulded material samples.

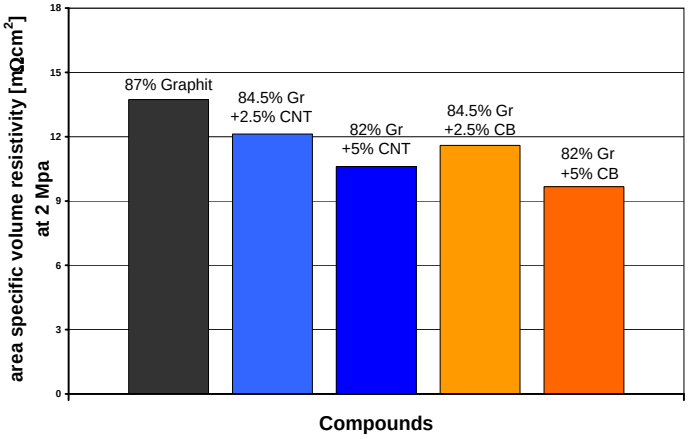

Figure 3: Electrical resistivity.

Figure 4: Injection moulded samples.

The experimental results show that the combination of graphite with carbon blacks or CNTs exhibits a positive effect and leads to lower volume resistivities. It can be seen that there is no significant difference in electrical conductivity between carbon black and CNT filled compound based plates at equal filling content. The addition of the nanometer sized carbon blacks or CNTs forms further conductive bridges through the insulating polymer matrix between the micro sized graphite flakes. Figure 5 and Figure 6 show schematically the differences between binary and hybrid compounds.

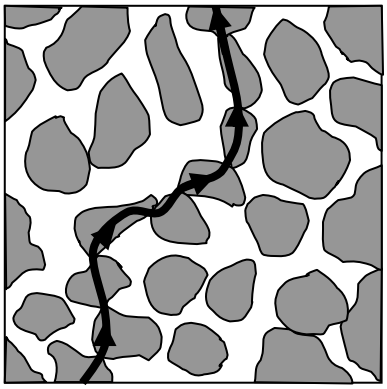

Figure 5: Scheme of a binary system (graphite flakes in a polymer).

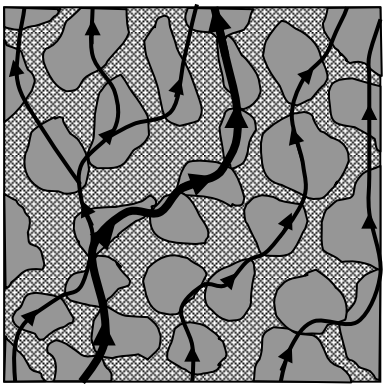

Figure 6: Scheme of a hybrid system (graphite + CB or CNTs in a polymer).

This assumption can be approved by images from scanning electron microscope which give an idea about the internal structure and dispersion of nano particles between graphite flakes at the injection moulded compound materials.

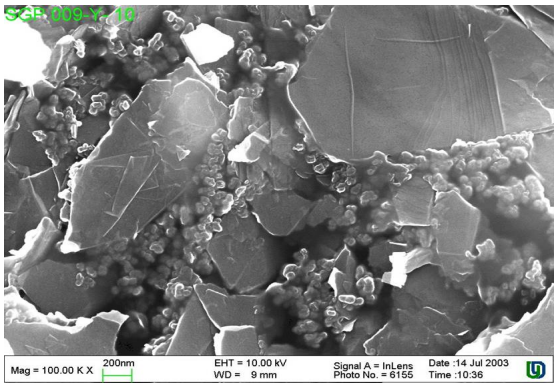

Figure 7: Carbon black between graphite.

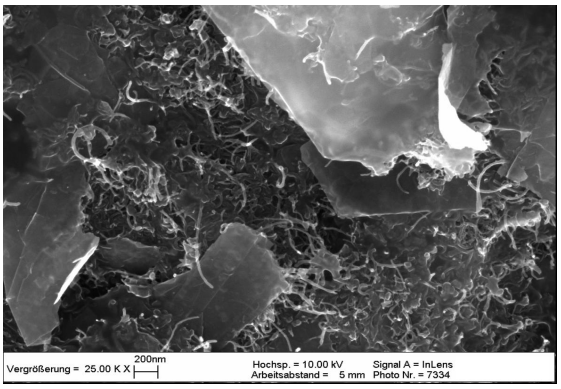

Figure 8: CNTs between graphite flakes.

3.3 Injection moulding and single fuel cell test

Based on the mentioned positive effects of compound material with CNTs, first CNT-based bipolar plates have been injection moulded with a cycle time of 18 seconds for one bipolar plate (Figure 9). Differences in bipolar plate quality in comparison with carbon black based bipolar plates could not be observed so far. A fully automated removal from the bipolar plates out of the injection moulding tool is ensured by robots, to prevent the operator from eventually occurring expositions with CNTs.

A first single fuel cell stack with injection moulded CNT-based bipolar plates has been assembled and the performance has been tested. This first test has been carried out to analyse the appropriateness of CNT-based bipolar plates in principle. It could be observed that CNT-based bipolar plates do function as well as carbon black based bipolar plates in a PEM fuel cell. No significant difference in the cell performance could be observed.

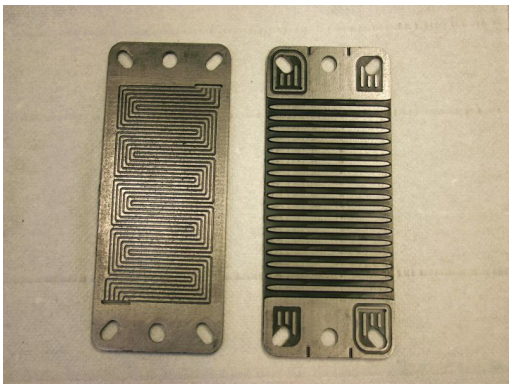

Figure 9: Injection moulded CNT based bipolar plates.

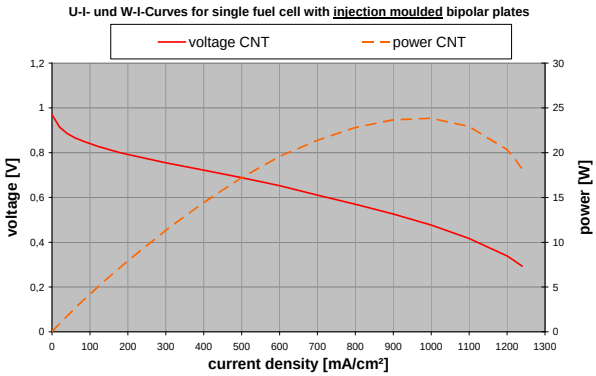

Figure 10: Polarisation-curves for a single fuel cell stack with CNT-based bipolar plates.

4 Conclusion

The combination of nano sized (CNTs) and micro sized (graphite) filling particles in hybrid compounds is chosen as the next step towards optimized bipolar plates for PEM fuel cells. It turned out that CNTs tend to be less abrasive than carbon blacks and this leads to a lower melt viscosity which is required and helpful for the injection moulding process to bipolar plates. Furthermore CNTs do function as bridging particles between the other filling component graphite and this leads to a significantly improved conductivity. Due to their favourable electrical and mechanical properties carbon nanotubes are most probably a promising filling material. There is still a need for more investigations to utilize the unique properties of CNTs in hybrid compounds. Nevertheless, first CNT-based bipolar plates were successfully produced and tested in single fuel cell stacks.

Acknowledgment

Parts of this work have been funded by the European Commission through the Sixth Framework Programme for Research and Development within the project SAPHIR and the German Federal Ministry of Education and Research (BMBF) within the Innovation Alliance Inno.CNT project CarboPlate, BMBF 03X0048A.

References

[1] C. Kreuz, Spritzgießtechnische Verarbeitung hochgefüllter Graphit-Compounds zu Bipolarplatten für PEM-Brennstoffzellen, Dissertation, Universität Duisburg-Essen, 2007.

[2] K. Roßberg, V. Trapp, in: W. Vielstich, H. A. Gasteiger, A. Lamm (Eds.), Handbook of Fuel Cells-Fundamentals, Technology and Applications, vol. 3: Fuel Cell Technology and Applications, Wiley & Sons, New York, pp 308-314, 2003.

[3] J. Huang, D. G. Baird, J. E. McGrath, Development of fuel cell bipolar plates from graphite filled wet-lay thermoplastic composite materials, Journal of Power Sources 150, 110 (2005).

[4] N. Kazuya, I. Hitoshi, N. Hideyuki, Effect of particle size of graphite on electrical conductivity of graphite/polymer composites, Composites Interfaces, Vol. 6, No.5, 483 (1999).

[5] D. Buswick, M. Wilson, US Patent 6248467, 2001.

[6] R. Socher, B. Krause, P. Pötschke, S. Hermasch, R. Wursche, Nanocomposites of PA12 with CNT: Influence of matrix properties and the use of mixed filler systems containing CB, 4th International Conference on Carbon Based Nanocomposites, 2009.

Multilayered Proton-Electron Conductive Polymer Membrane for Fuel Cells

J. Hodakovska, **G. Chikvaidze**, **J. Kleperis**, Institute of Solid State Physics of University of Latvia, Latvia

1 Introduction

What we don't need is a polluting carbon based energy policy that exists simply because the supply side wants it that way. We really can't justify trashing the planet by burning carbon just because it is available. The Wind-Solar-Hydrogen Economy is achievable now. What we need is to improve hydrogen production, storage, transportation and usage methods. Very important for most of European countries is question about electricity generation power - an energy policy for future must be oriented to local renewables and clean generation technologies at amounts to satisfy self sufficiency.

Fundamental problem needs closer attention is the method of getting energy back from the hydrogen. One of the possibilities is direct burning, which is attractive because internal combustion engines can be transformed easy for hydrogen fuel. Nevertheless combustion engines have small efficiencies and great exhausts – nitrogen oxides, when hydrogen is burnt in air. As another way for regaining energy from hydrogen, the fuel cells are named, because of theoretically possible high energy recovery value [1]. One type of fuel cells is polymer electrolyte fuel cell. Advantages of this technology is comparably low working temperatures (typically till 100°C), which makes it interesting for application in portable devices and transport (bikes, cars, vehicles) [2].

Developing polymer membrane fuel cells one has to deal with several main topics: membrane itself, membrane-electrode assembly, catalyst etc. Our research group decided to elaborate advanced composite membranes for low temperature fuel cells, based on already well-known material – sulfonated poly(ether-ether-ketone) (SPEEK). As the second material polyaniline (PANI) was chosen as a electron conductive material, which also can reduce platinum load according to H.Gharibi *et.al*. [3]

2 Experimental

SPEEK was prepared from poly(ether-ether-ketone) (PEEK) supplied by Aldrich. The sulphonated SPEEK ionomers were synthesized using original and simple method [4]. Homogeneous proton-conducting membranes were developed from the obtained SPEEK by solvent casting method. Our idea is to make composite electron/proton conducting membrane from available non-expensive polymers - SPEEK and electron conducting material polyaniline (PANI). For synthesis we used PANI in non-conductive form (emeraldine base) with molecular weight of 60000 g mol^{-1}, supplied by Aldrich. Physical and chemical properties of separate polymers SPEEK and polyaniline (PANI) and SPEEK/PANI membrane were analysed.

The membranes were characterized by FTIR to confirm sulfonation [5]. FTIR spectra for both poly(ether-ether-ketone) (PEEK) and SPEEK were measured with a Bruker EQUINOX 55 spectrometer equipped with Praying Mantis TM (DDR) accessory designed for examining samples by diffuse reflection spectroscopy. The spectra were measured in transmittance mode and in DDR mode over a wave number range of 7000-400 cm^{-1} with resolution of 1 cm^{-1}. Thermogravimetric (TG) and differential thermal analysis (DTA) were performed with SHIMADZU DTG-60 instrument in Ar atmosphere (Ar 5.0 from AGA Ltd.) with flow 50 ml/min in temperature range from room temperature (RT) till 350 °C with heating rate 10 deg/min.

3 Results and Discussion

For wave number between 1700 and 500 cm^{-1} some changes indicate successful sulfonation. The peak at around 1500 cm^{-1}, which corresponds to C-C bond, splits into two (1470 cm^{-1} and 1493 cm^{-1}) in SPEEK sample due to hydrogen replacement with SO_3H group (marked with 1, Fig.1). Also new peaks appear due to sulphur and oxygen bonds (e.g. S=O bond at 1022 cm^{-1}; O=S=O symmetrical and asymmetrical stretching vibrations at 1080 cm^{-1} un 1250 cm^{-1} accordingly) (2 and 3, Fig.1).

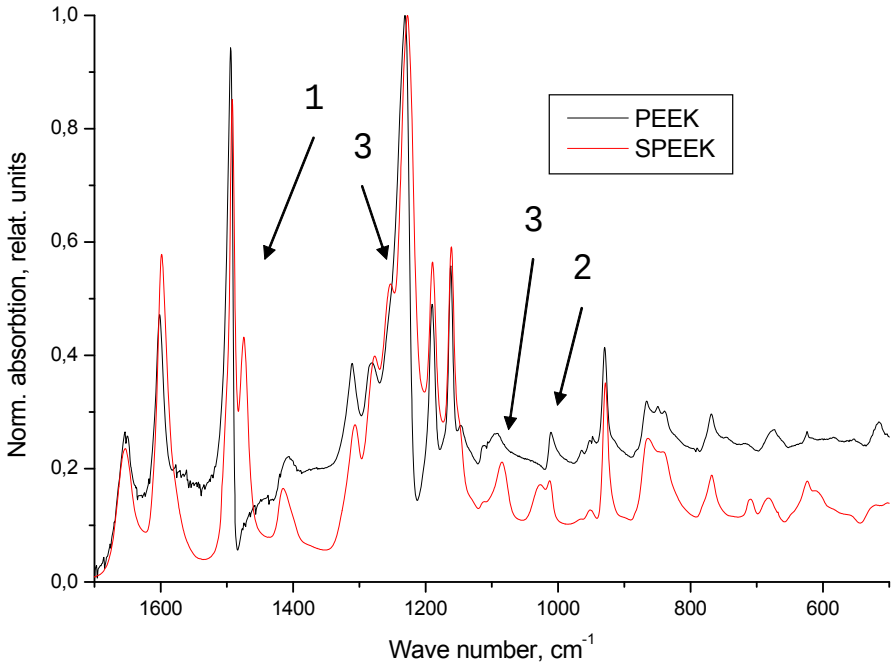

Figure 1: Spectrum of poly(ether-ether-ketone) and sulfonated poly(ether-ether-ketone).

New synthesized SPEEK membrane was compared with Nafion membrane with a help of thermogravimetric (TG) analysis. Fully hydrated samples were used for TG measurements. As it is seen from obtained results (Fig. 2), in region around 100 °C, which corresponds to water loss, the higher temperature is necessary for our SPEEK material to lose the water. Conclusion is that SPEEK membrane indicates better behaviour comparing with Nafion of membrane in case of reaching higher end of working temperature range (Fig.2).

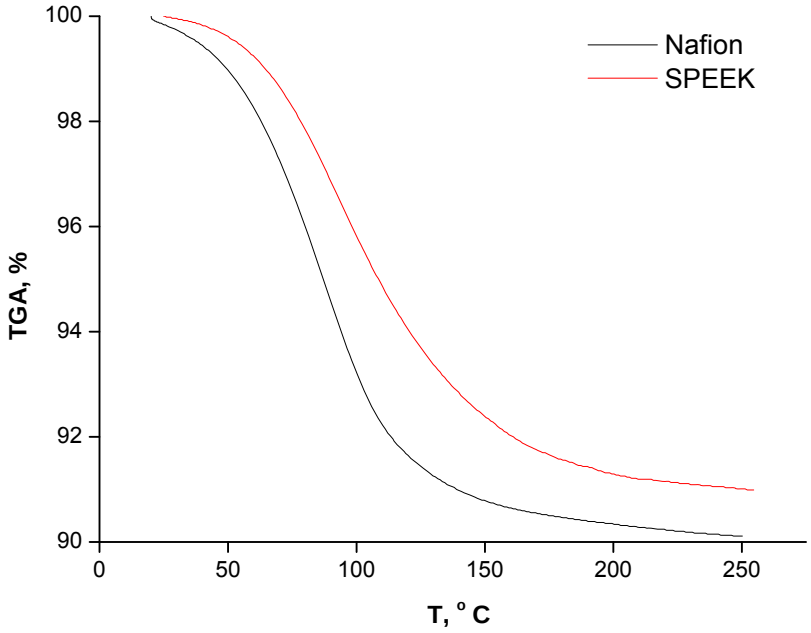

Figure 2: Thermogravimetric measurements in a region from root temperature till 250°C for new synthesized SPEEK and Nafion membranes.

The proton conductivities of our SPEEK membranes were found to be excellent in the order of 10^{-2} S/cm in the fully hydrated condition at room temperature. Testing samples in temperature range till 90°C, the steady grows was observed, reaching values around 50 mS/cm (Fig.3).

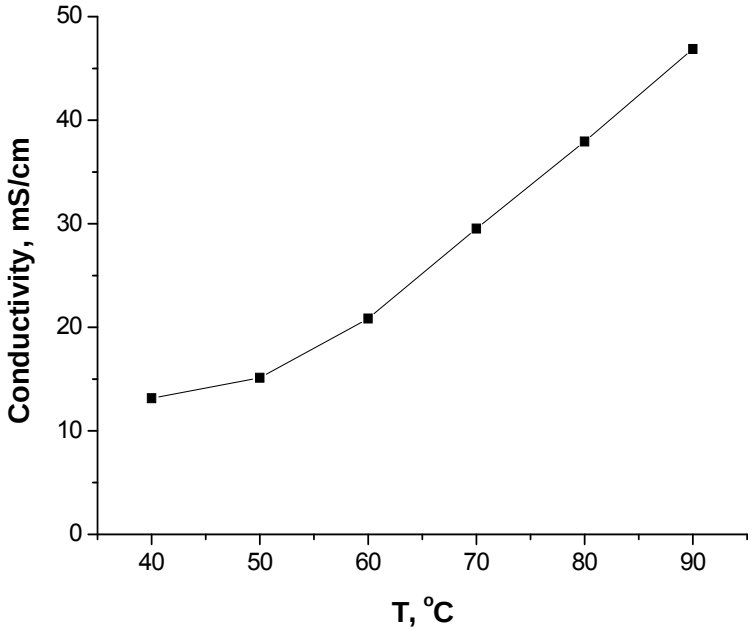

Figure 3: Conductivity measurements for new synthesized SPEEK polymer membrane.

The most important parameter for membranes is proton conductivity, and measured values showed (Figure 4), that for composite membrane with 10 wt% PANI the conductivity decreased significantly (3-4 times depending from temperature region).

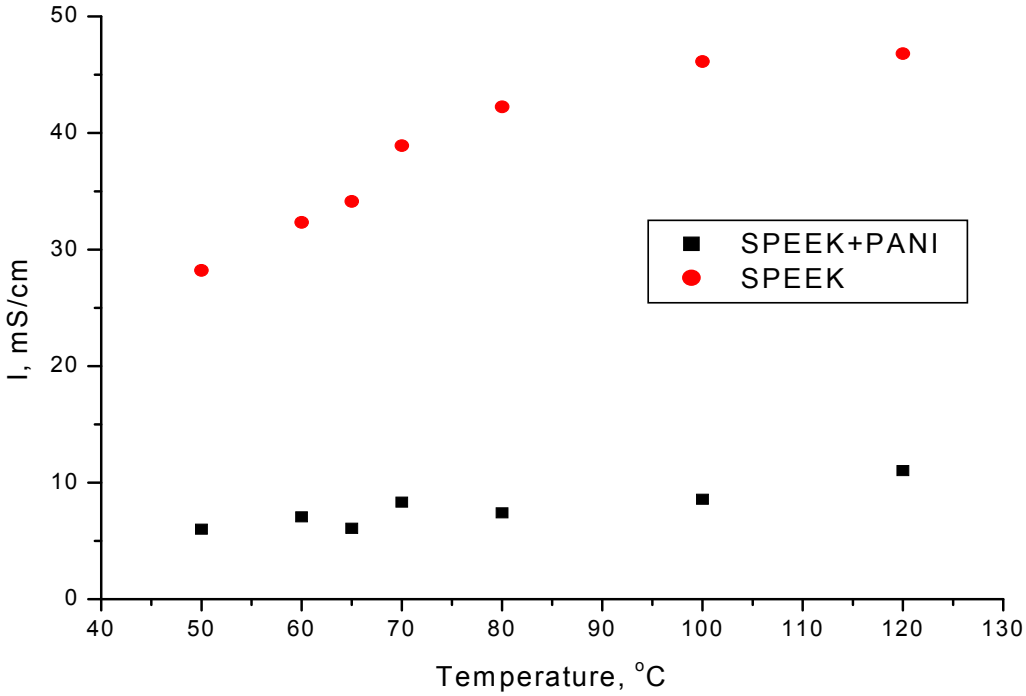

Figure 4: Conductivity measurements for SPEEK and SPEEK with 10 wt% PANI.

One of the possible reason for significant conductivity decrease could be the possibility of SPEEK polymer to play the doping role in PANI polymer. This process decreases the number of SO_3H groups, which are responsible for proton conductivity in membrane. To increase the proton conductivity, another doping polymer could be used, e.g. some acid. As it was seen from preliminary impedance spectra of composite SPEEK/PANI membrane, an electronic conductivity is found to be insignificant. It would be suggested that PANI transformation to electron conductive form also would increase the conductivity of composite membrane. Adding a doping would result in next two processes. Firstly, PANI will transform to electron conductive form, allowing reaching our goal of developing material with both types of conductivity. Secondly, doping will increase proton conductivity, because SPEEK partly reacts with PANI and acts as doping, at the same time decreasing proton conductivity.

Acknowledgements

We thank the Latvian National Research Program in Energetics and one from us (JH) would like to thank ESF (European Social Fund) for financial support in researches. We acknowledge the technical assistance of H.Luo for membrane synthesis and G.Vaivars for consultations.

References

[1] Zhao T.S., Kreuer K.-D., Trung van Nguyen (2007) Advances in Fuel Cells, Elsevier

[2] Barbir F. (2005) PEM Fuel Cells. Theory and Practice, Elsevier Academic Press

[3] Gharibi H., Zhiani M., Mirzaie R.A., Kheirmand M., Entezami A.A., Kakaei K., Javaheri M. “Investigation of polyaniline impregnation on the performance of gas diffusion electrode (GDE) in PEMFC using binary of Nafion and polyaniline nanofibers”, Journal of Power Sources 157, 2006, 703-708

[4] Patent LV13960

[5] Samms, S.R., S. Wasmus, and R.F. Savinell, Thermal Stability of Proton Conducting Acid Doped Polybenzimidazole in Simulated Fuel Cell Environments. Journal of The Electrochemical Society, 2005. 143: p. 1225

A Compact, Open-cathode HTPEM Fuel Cell Module for Portable Applications

Timo Kurz, Julian Keller, Fraunhofer Institute for Solar Energy Systems, Germany

1 Introduction

High Temperature PEM fuel cells based on a phosphoric acid doped polybenzimidazole (PBI) membrane are a relatively young technology compared to standard PEM fuel cells. The main advantage of this cell type is the operating temperature above the boiling point of water, leading to a simplified water management and to a strongly increased CO tolerance. Because of this higher CO tolerance and a higher usable temperature level, they are considered to be a promising technology for CHP systems.

Besides CHP systems, HTPEM fuel cells offer new possibilities also for other applications: Due to the absence of liquid water, they show a more stable operation, especially at high current density. Because the membrane is conductive in dry conditions, the cell can be operated with high, non-humidified air flow by using simple flow field geometry. This leads to the possibility of an open cathode design that acts as both the air supply and the cooling channel.

This work presents the development and characterisation of a stack module for portable applications in the range of some 100 W. The aim was to develop a small and compact system with few components and stable operation.

2 Stack Design and Housing

To realise a system with few additional components, a stack concept with open cathode has been designed: The cathode air is used also as coolant, so only one fan or air pump is needed. PBI membranes need no humidification and therefore high flow rates can be used without damaging the cells.

With high flow rates, the pressure drop in the cathode flow field has to be as small as possible to enable a standard fan for the air supply. To achieve this, simple parallel channels could be used.

On the other hand, high flow rates of cool air can lead to a strong temperature gradient along the channel. To reduce this, single serpentines have been used in the air flow field. The resulting temperature distribution at inlet and outlet is analysed in section 3.

To validate this system concept, a 5-cell test short-stack including complete housing and connectors has been developed. Figure 1 shows a cross section of this module with the air path in the housing and the flow field design. In front of the stack inlet, a heating wire is inserted to heat up the inlet air during start-up. The stack is fully enclosed in the housing with glass wool for thermal insulation. The box can be closed on inlet and outlet to avoid moisture absorption after shutdown that can be critical for membrane degradation. Gas supply and electrical connectors for load and heating are attached. Table 1 shows an overview of stack and module properties:

Table 1: Module characteristics.

Module dimensions	240 x 120 x 100 mm
Module weight	2.2 kg
Heating	electrical, 100 W / 12V
Cell number	5
Cell active area	31.4 cm²
Stack nominal power	45 W @ 15 A
Stack max. power	> 90 W
Hydrogen supply	dead end or recirculation with purging
Air supply	open cathode, up to 50 slpm

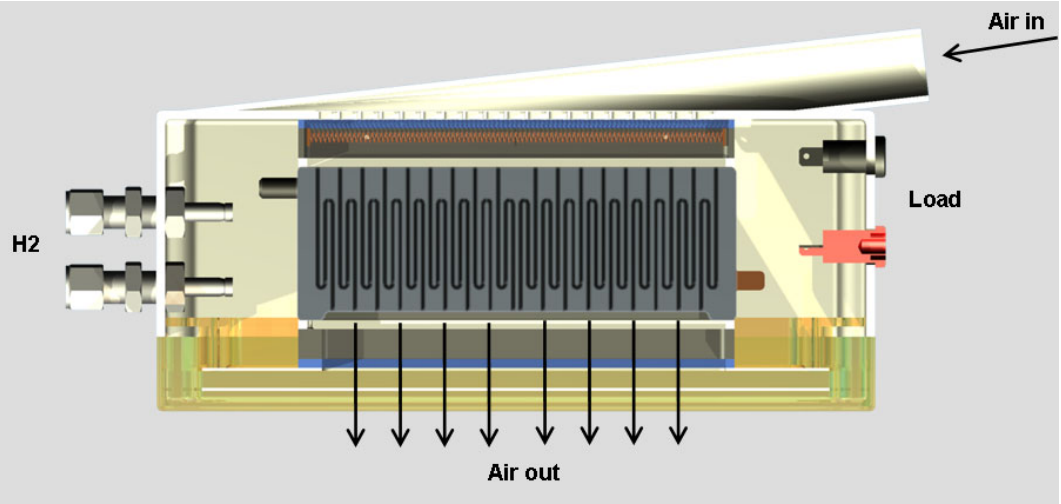

Figure 1: Cross section of the stack module.

3 Results and Discussion

During operation, temperature distribution has been measured with 16 type-K thermocouples attached to the stack: 6 near the serpentines at the inlet and 8 near the outlet. These sensors provide a complete picture of the temperature distribution in plane as well as from top to bottom. Figure 2 shows the location of the thermocouples. They measure the bipolar plate temperature near the channel without blocking the channels.

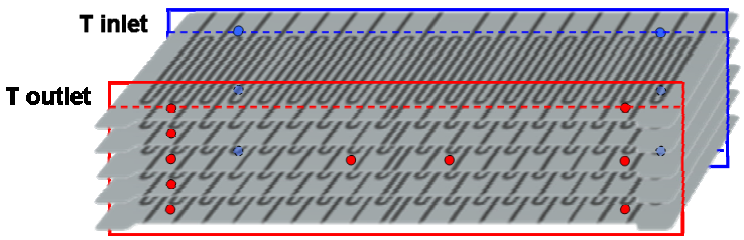

Figure 2: Schematic view of the location of the thermocouples in the stack.

3.1 Start-up

Figure 3 shows the average stack temperature during heating at start-up. The stack is heated only by air passing the heating wire. Heating is switched on at 950 s. The stack temperature rises and reaches 120 °C at 1950 s. From this moment on, the stack is switched on and reaches nominal power (15 A, 0.6 V_{cell}) at 2090 s. The nominal working temperature, 160 °C, is reached at 3450s.

In this configuration, it needs 100 kJ electrical energy and 16:40 min for heating this system up to starting temperature. This consumption / time can be further optimised by lowering the possible starting temperature (with more stable membranes), increasing the stack-to-system-weight-ratio using a bigger stack (30 instead of 5 cells) or by an improved heat transfer to the incoming air.

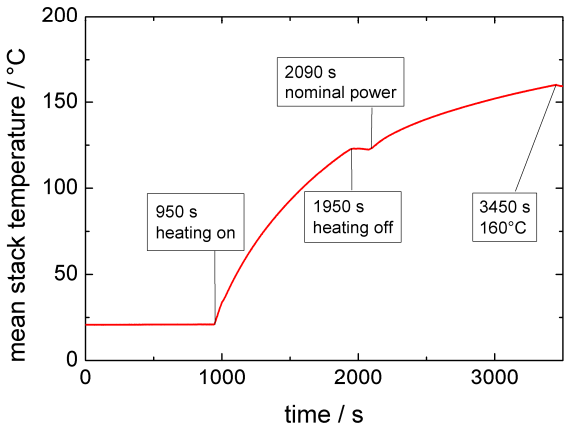

Figure 3: Mean stack temperature during a standard heating procedure. In the first period, the stack is heated only electrical (@ 100 W). After reaching 120 °C, the stack is started and operated at 15 A.

3.2 Operation

Figure 4 shows polarisation curves of the stack in galvanostatic mode at different mean stack temperatures. The temperature has been controlled only by cathode air flow. Hence, stoichiometry during this measurement varies in a wide range from $\lambda = 3$ (high temperature, low current) to $\lambda = 15$ (low temperature, high current).

The stack shows excellent characteristics, (608 mV_{cell} / 500 $mAcm^{-2}$ at 160 °C) and as expected a slightly increasing voltage with increasing temperature (570 mV at 130 °C up to 618 mV at 170 °C).

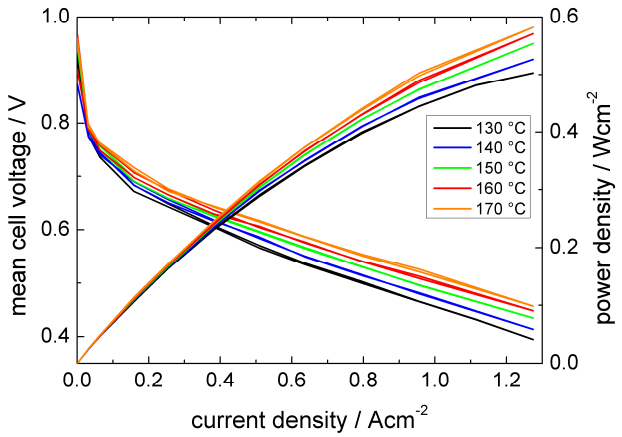

Figure 4: Polarization curves of the stack at different mean temperatures at λ_{H2} = 1.5. Oxygen stoichiometry varies between 3 and 15 due to temperature control by cathode air.

3.3 Temperature distribution

Figures 5 and 6 show the temperature distribution in the left side of the stack (see figure 2) at two different operation points; at nominal operation (15 A, 11 slpm, filled symbols) and at high power operation (30 A, 35 slpm, hollow symbols).

Figure 5 shows temperature variation from top to bottom; temperatures at the outlet (red) are slightly higher than at the inlet (blue) due to the cool inlet air. The difference is larger at higher air flow due to a higher cooling rate: At 30 A, the maximum difference is 8.6 °C, and it is only 5 °C at 15 A. The temperatures show an increase from top to bottom cell, this can be due to an inhomogeneous inflow and/or due to less insulation material on top.

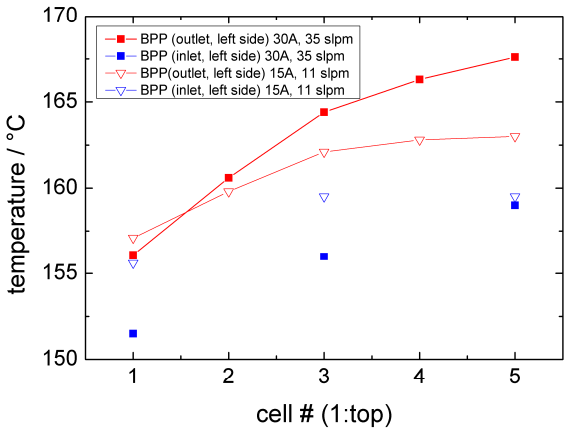

Figure 5: Temperature distribution during operation at 160 °C on the left side of the stack from top (1) to bottom (5). The plots show the difference between inlet (blue) and outlet (red) and between the operation at 30 A / 35 slpm (filled) and 15 A / 11 slpm (unfilled symbols).

Figure 6 shows the variation from left to right in the cathodic bipolar plate of cell 3. The temperature distribution is nearly symmetric, indicating good inflow geometry in this direction (see figure 1, top). The highest difference between left and right side is 3.7 °C at the inlet (at 30 A). The outlet temperatures show higher values in the middle of the cell. This can be explained by heat losses through the side faces of the stack. As also seen in figure 5, temperature variation between inlet and outlet increases at higher air flow rate. The maximum difference is here 10.4 °C on the right side.

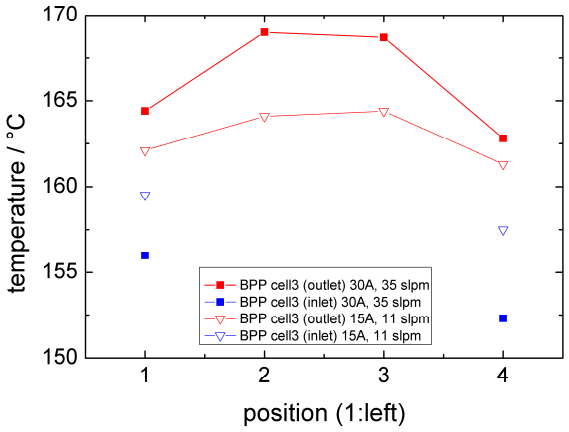

Figure 6: Temperature distribution during operation at 160 °C in BPP 3 at inlet (blue) and outlet (red) from left to right. The air flow comes from the right side (see figure 1). The plots show the difference between the operation at 30 A / 35 slpm (filled) and 15 A / 11 slpm (unfilled symbols).

4 Conclusions

A compact fuel cell module for small portable systems has been presented. It consists of a HTPEM fuel cell short-stack with open cathode that can be operated with a controllable fan only (besides the fuel connection). Thermal insulation, gas and electrical connectors as well as electrical heating are integrated.

Polarisation and temperature measurements have been performed. They show that electrical heating only by heating the inlet air is possible and leads to a heating time of < 17 min. In operation, the stack shows an excellent power characteristics and small temperature variation even at high flow rates of ambient air due to a specific designed flow field. In high power mode (high air flow), the maximum temperature difference (at 160 °C mean temperature) is 17.5 °C, and it is only 8.8 °C at nominal power operation. These results show that this stack module concept with open cathode works excellent and leads to a simple system design, ready to be scaled up to higher cell numbers.

Acknowledgements

This work was partially supported by the Scholarship Programme of the German Federal Environmental Foundation DBU (Deutsche Bundesstiftung Umwelt).

Application Segmented Cell for In-situ Detection and Controlling the Stability of PEM Fuel Cell

Rui Lin, Jian Xin Ma, Clean Energy Automotive Engineering Center, School of Automotive Studies, Tongji University, Shanghai, 201804 China
Heinz Sander, Erich Gülzow, Andreas K. Friedrich, Electrochemical Energy Technology, Institute of Technical Thermodynamics, German Aerospace Center, Stuttgart, 70569 Germany

Water plays a critical role on the PEMFC performance, stability and lifetime. On one hand, water is needed to guarantee good proton conductivity of the membrane and active layers; on the other hand, the presence and accumulation of liquid water in the flow-field channels and/or electrodes gas porosities resulted in flooding of the electrodes [1-5]. A subtle equilibrium has to be controlled between membrane drying and liquid water flooding to prevent degradation and guarantee a stable performance of fuel cell.

At DLR, printed circuit boards (PCBs) with segments and internal measurement resistances have been developed to measure current density distributions both of single cells as well as stacks [5, 6]. Through investigation of current density distributions, the correlations between the current activities and humidity of fuel cell would be found. In the present work, we applied the segmented cell to find the correlations between the current instabilities and humidity of fuel cell. Thus, the countermeasure for optimization of water management of fuel cells would be found. Through controlling the humidity of anode (RHa) and cathode (RHc), the stability and performance of fuel cell would be improved.

Fig.1 shows the performance of PEM fuel cell at potentiostatic operation conditions at 80 °C. The humidification temperature of fuel cell is also set at 80 °C. Time-dependent oscillations of current would also appear. It is due to less water was produced and transported by electro-osmotic drag. Water electro-osmotic drag or low humidity operation caused a positive spike in cell current with respect to a stationary value, which may indicate a temporary improved performance. Increasing the humidity of anode and/or cathode to the optimal condition (increasing the humidification temperature to 85 °C in this case), the performance would improve and become stable. Furthermore, it was found if the humidity of the cell went back to the starting unfavourable condition, the performance became unstable again. Through controlling the humidity of fuel cell, the stability of that could be efficiently improved. The performance is reversible if adverse humidity conditions are temporarily applied. Similar phenomenon would be found at higher temperature (120 °C, Fig.1). The performance irreversibly changed when the humidity conditions of the fuel cell was modified. In this case, returning to favourable humidity conditions made the performance stable but an irreversible degradation associated with the adverse humidity conditions was observed. It may be due to the severe drying conditions, which caused irreversible membrane degradations.

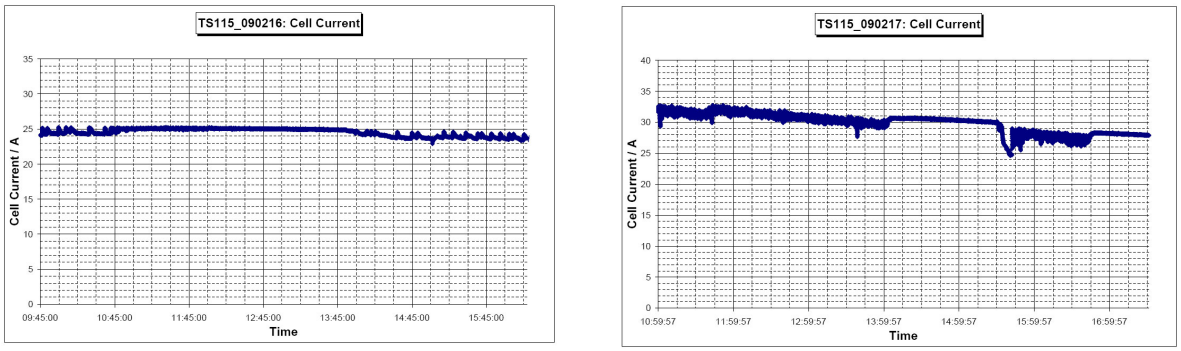

Figure 1: Improvement the stability of fuel cell at 80 °C (on the left side) and 120 °C (on the right side) by adapting humidity and observed irreversible degradation.

The stability of the fuel cell system was also dependent on the forced cell voltage, which was shown in Fig. 2. The cell was operated at 100 °C. At 700 mV, current was at lower value and no current peaks appeared (not shown in the figure). At 600 mV, the current showed variations in the range of 5 minutes. Decreasing the voltage to 500 mV, the current became unstable and the performance changed from the top to the bottom in less than one minute. It was apparently that water balance of the cell was affected by the forced voltage. The amplitude and the frequency of current peaks compared to the reference value were affected by the cell voltage. The lower the forced voltage, the higher rate of water would be produced. So it was difficult to stabilize the performance at higher current densities and fast change of performance would occur, which led to a higher fluctuation of current frequency.

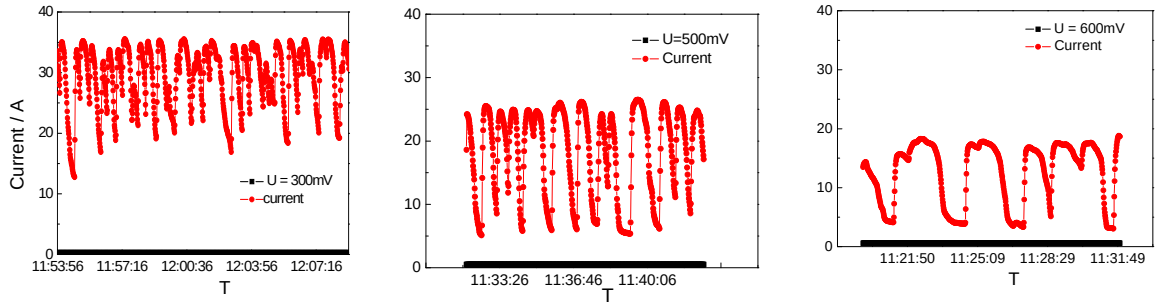

Figure 2: Frequency of current peaks increased with voltage decreased (under potentio-static state). T cell = T humidification air = T humidification H_2= 100 °C; Pair = PH_2 = 2 bar.

Fig. 3a was the mapping of current density distributions at different stages (baseline or peak top) of the positive spike of the current. At different stages of current, the contour plot of current density distribution was similar (Fig. 3b). In the case of operating conditions where water flooding was expected, negative spikes in cell current compared to the stationary reference value was observed (Fig. 4a). The contour of current density distribution during the negative spike in cell current was much different to the one before and after the negative spike in cell current (Fig. 4b). In different stages of negative spikes of current, their current

density distributions differed greatly. It might be due to the case that the flooding of water in the channel occurred and the liquid water accumulated in different location of the flow field, which would greatly affect the local current density distribution. When the operating conditions allow the liquid water to accumulate to some extent, severe water flooding occurred. The gas flow path would be temporarily blocked, giving rise to a negative spike in cell current [4]. The periodic build-up and removal of liquid water in the cell caused the observed fluctuations in cell performance. It was also found that at the stage current peaks up or current peaks down, the homogeneity of current density was less than the one at the stationary reference.

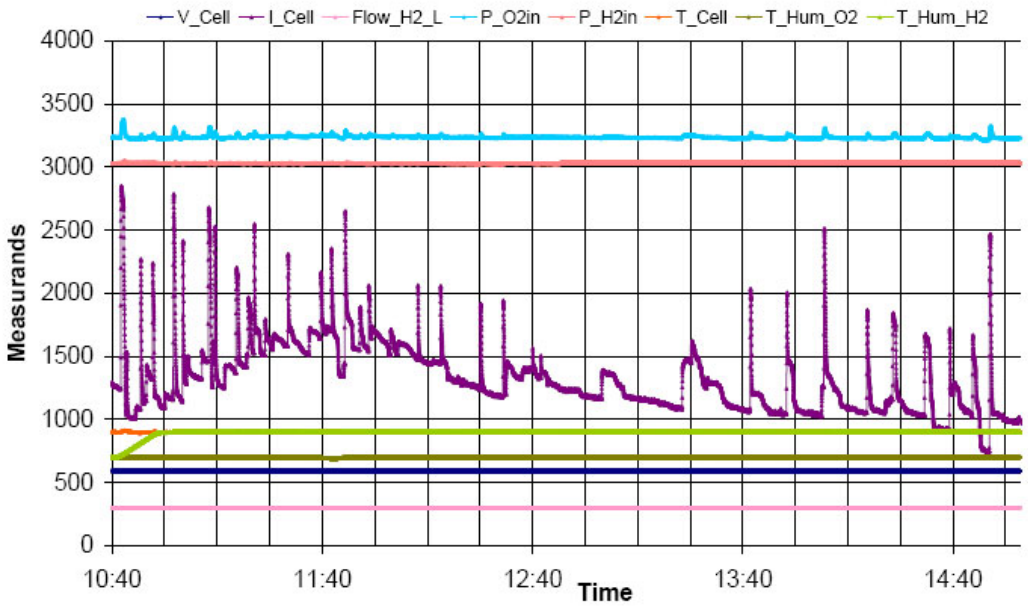

Figure 3a: Overview of operation parameters for the current peaks up.

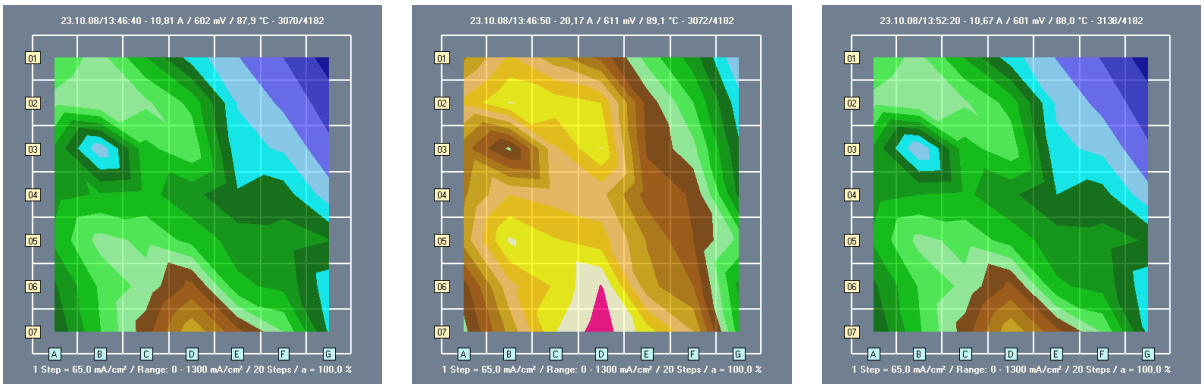

Figure 3b: Current density distribution of PEM fuel cell, before, during and after current peaks up.

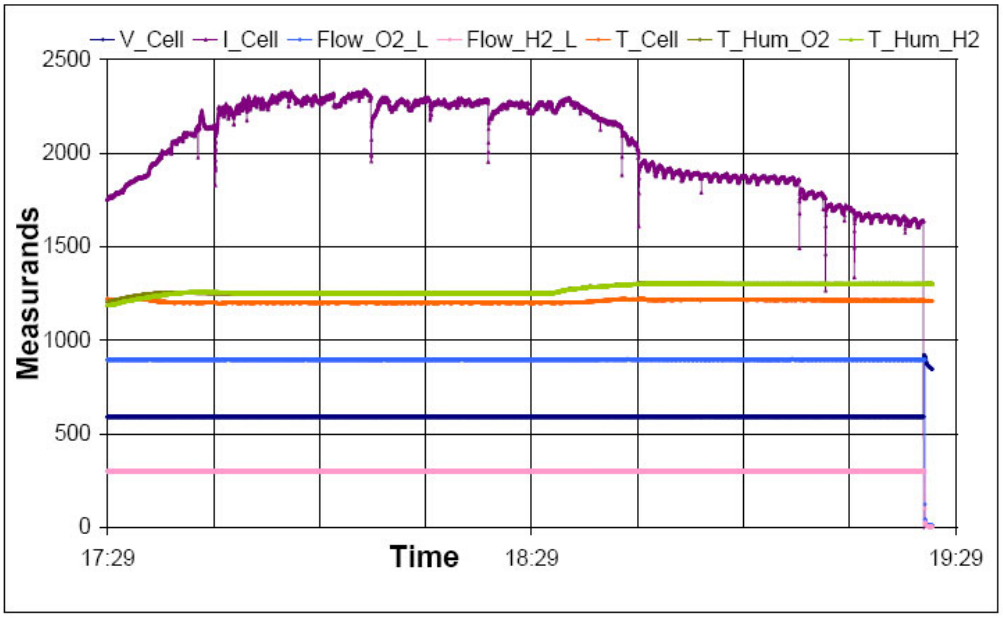

Figure 4a: Overview of operation parameters for the current peaks down.

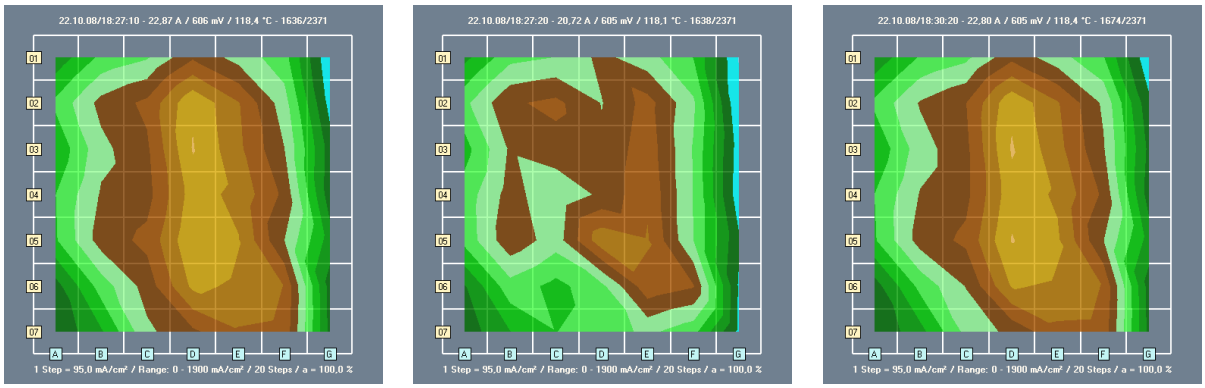

Figure 4b: Current density distribution of PEM fuel cell, before, during and after current peaks down.

In a summary, in certain operating conditions, the time-dependent oscillation of current (potentio-static state) at fixed voltage would appear. The periodic build-up and removal of liquid water in the cell caused fluctuation of the cell performance (positive or negative spike of current compared to the stationary value), causing unstable, unreliable and inconsistent cell performance. In the present work, we applied in-situ segmented cell technology to detect the current density distributions of fuel cell and thus found the correlation of that with the humidity of fuel cell. Controlling the humidity of fuel cell, the stability of fuel cell would be efficiently improved.

The stability of the fuel cell system was also dependent on the input voltage. The amplitude and the frequency of current peaks up are affected by the applied of voltage.

The current density distribution maps were similar in different stages of the spike up of current. But during the flooding stage, their current density distributions differed greatly. This behaviour was interpreted as indicating flooding in different locations of the flow field.

References

[1] Effects of hydrophobic polymer content in GDL on power performance of a PEM fuel cell, Chan Lim, C.Y. Wang, Electrochimica Acta 49 (2004) 4149-4156

[2] A review on PEM voltage degradation associated with water management: Impacts, influent factors and characterization, N. Yousfi-Steiner, Ph. Moc otéguy, D. Candusso, D. Hissel, A. Hernandez, A. Aslanides, J Power Sources 183 (2008) 260–274.

[3] J. Zawodzinski, C. Derouin, S. Radzinski, R.J. Sherman, V.T. Smith, T.E.Springer, S. Gottesfeld, J. Electrochem. Soc. 140 (1993) 1041.

[4] H. Li, Y.H. Tang, Z. W. Wang, Z. Shi, S. H. Wu, D. T. Song, J. L. Zhang, K. Faith, J. J. Zhang, H. J. Wang, Z. S. Liu, R. A. Abouatallah, A. Mazza, J Power Sources, 178 (2008) 103-117.

[5] Transient analysis of polymer electrolyte fuel cells, Y. Wang, C.Y. Wang, Electrochimica Acta 50 (2005) 1307-1315.

[6] Diagnostic tools for in-situ and ex-situ investigations of fuel cells and components at the German Aerospace Center, M. Schulze, E. Gulzow, K. A. Friedrich, P. Metzger, G. Schiller, ECS Transactions, 5(2007) 49-60.

Analysis of the Influence of a Filter for Traffic-related Gaseous and Particulate Contaminants on PEMFC

U. Misz, **J. Burfeind**, **P. Beckhaus**, **A. Heinzel**, Zentrum für BrennstoffzellenTechnik ZBT GmbH, Germany

1 Introduction

An important subject to increase the lifetime of PEM fuel cells is purity of the in-coming gases. Especially cathode air must be very clean. Impurities in the air can contaminate the catalyst, electrolyte or GDL [1, 2].

Degradation can be reduced by using a cathode air filter. Research about effects of contaminants on fuel cells has been carried out [3]. CO, NO_2, NH_3 and SO_2 have been fed consecutively to the fuel cell in ppm ranges with and without a fuel cell cathode filter. Results show that CO removal is not necessary as it is converted with O_2 to CO_2. But the used concentrations of the other corrosive gases significantly harmed the single fuel cell within the timeframe of only an hour.

Unlike the tests without filter voltage curves of the fuel cell by using a cathode air filter remain at a constant level and don't even fall over a longer period of contamination. However solely NO_2 is leading to a significant decrease in cell voltage over time. The filter used in this experiment is not effectively removing NO_x from air.

Further tests with particles and real depleted diesel exhaust gas have been conducted. The results have revealed that available filters can't separate a typical traffic-related contaminant mix effectively from incoming air.

2 Cell Degradation without Cathode Air Filter

Research about corrosive gases at road traffic areas in Germany and their effects on fuel cells has been done [3]. First CO, NO_2, NH_3 and SO_2 have been conducted through the fuel cell in a ppm range without an upstream filter. The test parameters at all experiments were identical to get comparable results. Cell temperature was 55 °C and the cathode gas was not humidified. A constant current density of 800 mA/cm² was adjusted.

A water cooled single cell was manufactured and integrated in a special test stand for corrosive gases. New MEAs were assembled for each measurement with a different corrosive gas. Fig. 1.1 shows the results without any filter materials. The used single cell is seen in Fig. 1.2.

Results show that CO filtering is not necessary as it does not affect fuel cell performance and is likely converted with O_2 to CO_2. But the used concentrations of the other corrosive gases significantly harmed the single fuel cell within one hour. After NO_2-poisonning the cell performance can be recovered completely, by running the cell with pure NO_2 free air for several hours. In a following test the single cell was fed with only 1 ppm NO_2. A voltage loss of 4 % could be seen within the first 10 minutes. After 220 minutes the cell performance declined by 10 % (Fig. 2.1).

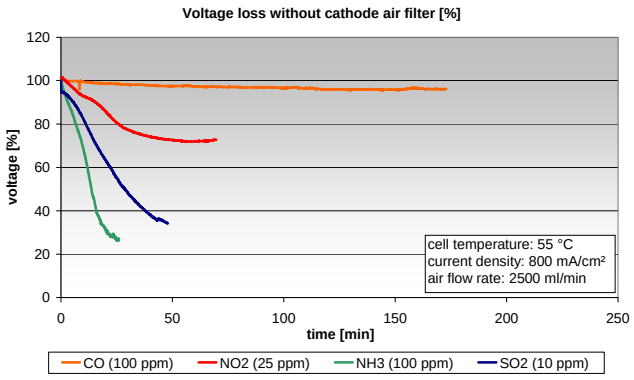

Figure 1.1: Voltage loss without a cathode air filter [%].

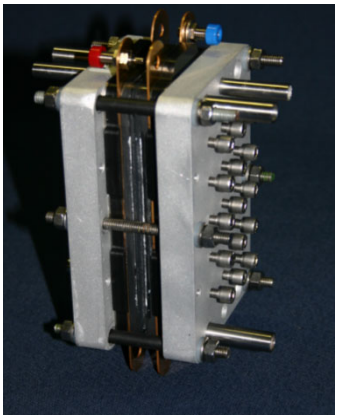

Figure 1.2: Water cooled single cell.

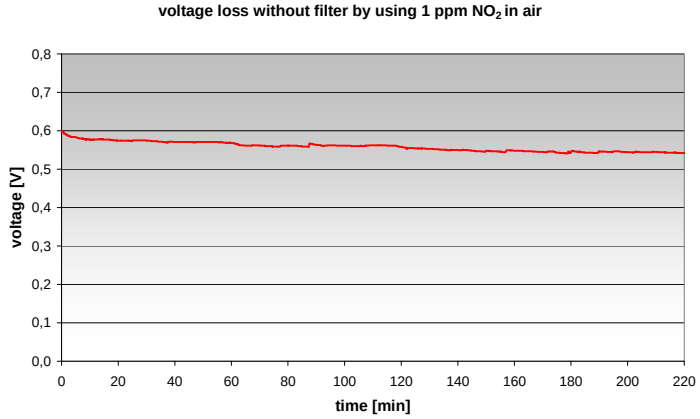

- 10 % voltage loss within 220 minutes
- 4 % voltage loss within only 10 minutes
- Reversible process

Figure 2.1: Voltage loss without a cathode air filter by using 1 ppm NO_2.

3 Cell Degradation with Cathode Air Filter

In a second experimental series a filter system was used for the cathode feed. The filter consisted of activated carbon layers and ion exchanger layers. The concentrations of the corrosive gases were the same as in Fig. 1.1.

Fig. 3.1 pictures the results with filtered cathode air. The voltage curves of the fuel cell with a cathode air filter are at a constant high level and don't fall over a longer period. However NO_2 is leading to a significant decrease in cell voltage over time. The filter used in this experiment is not effectively removing NO_x from air.

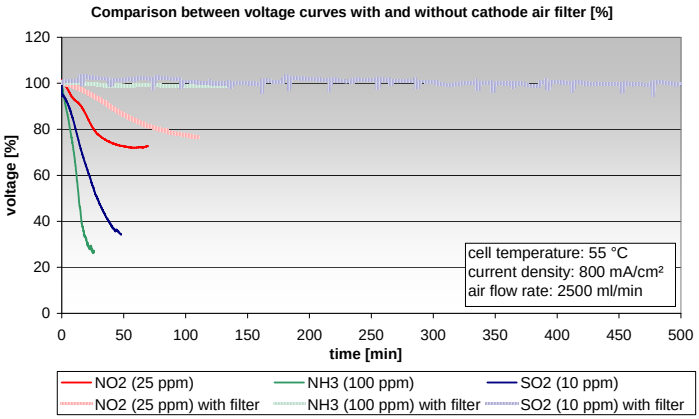

Figure 3.1: Voltage loss without a cathode air filter [%].

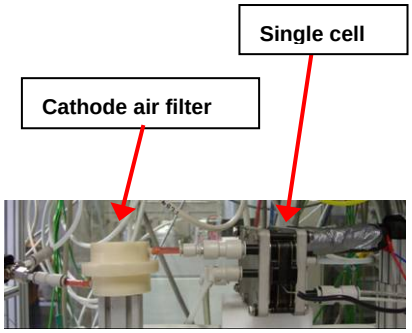

Figure 3.2: Filter with single cell.

4 Separation of NO_x

A further test series was made to analyse the filter efficiency of different materials for NO_x. The used filters were a column packed with activated carbon (potassium carbonate (K_2CO_3)) granules, a column packed with polyphenylene sulphide (PPS) granules and a filter consisting of Ion exchanger layers as well as activated carbon filter layers used in the experiment before [4]. Fig. 4.1 shows the results of a few tests with different filter materials.

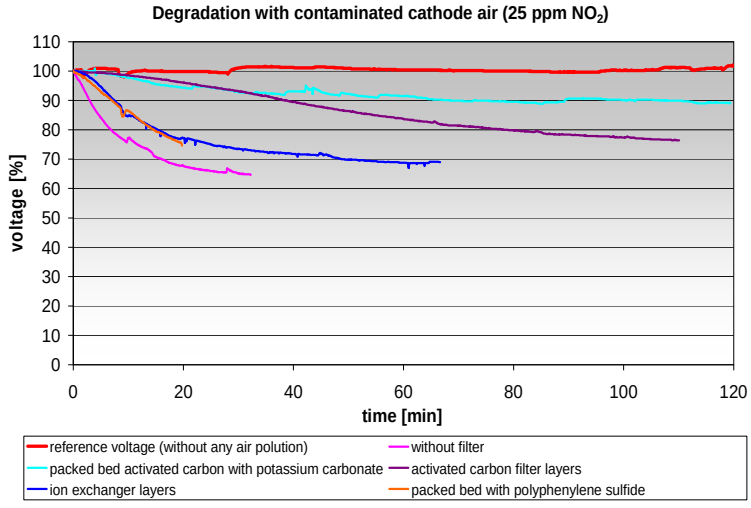

Figure 4.1: Voltage loss without a cathode air filter [%].

Figure 4.2: Activated Carbon.

According to the state of technology neither an air cathode filter nor a catalyst are able to separate NO_x from the cathode gas flow of PEM fuel cells adequately.

5 Analyzing the Effect Gas Mixtures on the Fuel Cell

In a final experiment the effect of a gas mixture on the fuel cell was analysed. A test stand with a real diesel engine at the partner institute IUTA was used. The diesel exhaust gas was

analysed and depleted to a defined degree. A 5-cell water cooled stack was fed with the diluted diesel exhaust gas at a ratio of 1:70 in air. This exhaust gas contained 0,9 ppm SO_2, 7,9 ppm CO, 7,5 ppm NO and less than 1 ppm NO_2. In addition soot particles are parts of the engine generated diesel exhaust gas. But former experiments with soot particles have shown that these particles don't contaminate the fuel cell. The tests were realized with and without a filter system (Fig. 5.1).

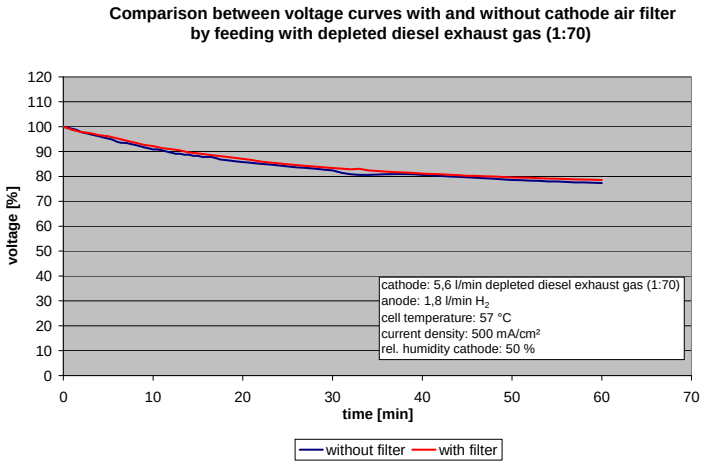

Figure 5.1: Voltage loss by using depleted diesel exhaust gas [%].

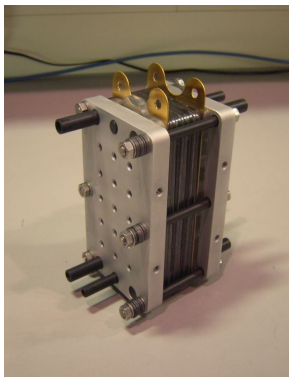

Figure 5.2: 5-cell-stack.

The voltage loss by using a filter is nearly identical to the voltage loss without any filter system. A voltage drop up to 20 % within one hour caused by the Diesel exhaust gas could be seen. But after charging with neat air the PEMFC is recovered completely, despite the presence of SO_2 in the diesel exhaust gas. Normally SO_2 leads to irreversible cell damage. So it is presumed that the presence of nitrogen-containing groups suppress the adsorption of SO_2 on the catalyst layer. The kinetic of the reversible NO_x absorption could be faster then the irreversible SO_2 absorption, so no irreversible performance lost could be detected. More experiments with mixed gases are necessary.

6 Conclusion

Experiments have shown that a cathode air filter can increase the lifetime of a PEM fuel cell except the degradation due to NO_2 which is fortunately a reversible effect. Further tests are mandatory. So a new project has been started in January 2010 which will deal with investigations on the damage mechanisms. Electrochemical Impedance Measurements (EIS) will be one of the methods to be applied [5]. Furthermore tests with different types of particles will follow.

Acknowledgement

Thanks to "Verein für Energie und Umwelttechnik e.V." for sponsoring this project (15079N) with allocated funds from "Bundesministerium für Wirtschaft und Technologie (BMWi)"

through „Arbeitsgemeinschaft industrieller Forschungsvereinigungen "Otto-von-Guericke" e.V. (AiF)“.

References

[1] Schmittinger, W.; Vahidi, A.: “A review of the main parameters influencing long-term performance and durability of PEM fuel cells” Department of Mechanical Engineering, Clemson University, Clemson, SC 29634-0921, USA, January 2008.

[2] Burfeind, J. ; Heinzel, A. (2005): Untersuchung von Luftschadstoffen auf die Leistungsfähigkeit von Brennstoffzellensystemen, ZBT Januar 2005.

[3] http://www.lua.nrw.de/, Landesumweltamt Nordrhein-Westfalen.

[4] Schleicher, Frrank, Eschway, Eysmondt (1995): WIPO Patent Application WO/1995/033682 “PROCESS AND FILTER FOR PRODUCING NO2-FREE NITROGEN MONOXIDE WITH SULPHUROUS POLYMERS”

[5] Kuhn, Holger. Dissertation (2006) TU Karlsruhe: „In-Situ Charakterisierung von Polymer-Elektrolyt Brennstoffzellen mittels Elektrochemischer Impedanz-spektroskopie, 2006, TU Karlsruhe“

Soft Switching PWM Isolated Boost Converter for Fuel cell Application

Majid Rezaei, Isfahan Subsea R&D Institute, Iran

Abstract

In this paper a new soft switching isolated boost type converter is introduced for fuel cell applications. In this converter zero voltage switching condition is achieved for the main switches and the auxiliary circuit is also soft switched. Also, the converter control circuit is simple PWM. Due to achieved soft switching condition, the converter can operate at high powers which make it suitable for fuel cell applications. Also, due to high voltage gain of the converter and isolation between input and output sources, the converter is a proper choice for the interface of fuel cell and inverters. Furthermore, the input current of the converter (current drained from the fuel cell) is almost constant since it is a boost type converter. The converter is analyzed and the simulation results presented confirm the validity of theoretical analysis.

1 Introduction

Boost type converters are vastly used as the interface circuit for solar cells, batteries and fuel cell since their input current is almost constant. Also boost type isolated converters can provide high voltage gain because in these converters the total converter gain is the multiply of boost stage gain and transformer voltage gain. Therefore, these converters are suitable solutions to boost the low output voltage of solar cells, batteries and fuel cells to provide high DC voltage for the inverter stage.

In isolated boost converters usually high voltage stress and high switching losses are applied to the switches due to converter leakage inductance. Therefore, the efficiency of these converters considerably decreases and also due to voltage spikes on the converter switch, switches with high voltage rating should be used. RCD snubbers and clamps can be used to reduce switching losses and to limit voltage spikes across the switch. However, RCD snubbers and clamps increase the total converter loss and further reduce the converter efficiency.

Lossless snubbers are another solution to limit the voltage spikes and to reduce the switching losses and also to increase efficiency [1-8]. Several lossless snubbers are previously introduced for boost converters in [6-7]. But, in these converters additional current stress is applied on the main switches. In the converter introduced in [8], a lossless snubber is introduced for current fed converters which is applied in the secondary side of transformer. This lossless snubber can reduce switching losses, but it is unable to limit the voltage spikes across the switches. Therefore, for practical implementation, a RCD clamp is also required in the transformer primary side.

In this paper, a new soft switching boost converter is introduced which does not suffer from the above mentioned disadvantages. This converter is introduced and analyzed in the

second section. Simulation results are presented in the third section using PSpice software. Therefore, the simulation results are with the actual model of semiconductor devices. Also, leakage inductance of transformers is considered for the simulation purpose to verify the effectiveness of applied soft switching auxiliary circuit.

2 Converter Analysis

The proposed converter is shown in Fig. 1. S_1 and S_2 are converter main switches and unidirectional switches S_{a1} and S_{a2} are the converter auxiliary switches. Before the first mode, it is assumed that S_1 and D_1 are conducting and all other semiconductor devices are off. Also, the transformer magnetizing inductance current, input inductor current and capacitor C voltage can be assumed constant and equal I_m, I_{in} and V_c, respectively. According to Fig. 1 the converter main transformer turns ratio is 1:n and coupled inductors L_{a1}, L_{a2} and L_{a3} turns ratio is 1:1:m.

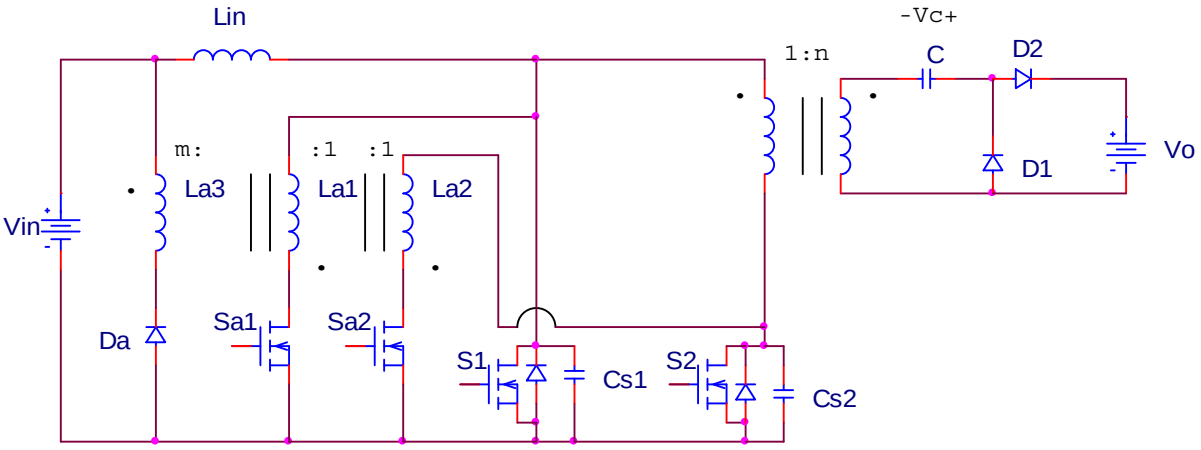

Figure 1: Proposed soft switching isolated boost converter.

Assuming all semiconductor devices ideal, the converter operating modes are as following:

Mode 1: By turning the S_{a2} on, this mode begins. By turning this switch on, V_c/n is placed across L_{a2} and its current increases linearly to I_m and S_1 current decreases to I_{in}-I_m. Thus, S_{a2} turn on is zero current switching.

Mode 2: In this mode a resonance starts between C_{s2} and L_{a2} and C_{s2} completely discharges. L_{a2} current during this mode and at the end of this mode are:

$$I_{La2} = I_m + \frac{V_C}{nZ_2}\sin(\omega_2(t)) \tag{1}$$

$$I_{La2} = I_m + \frac{V_C}{nZ_2} = I_2 \tag{2}$$

where:

$$\omega_2 = \frac{1}{\sqrt{L_{a2}C_{S2}}} \tag{3}$$

$$Z_2 = \sqrt{\frac{L_{a2}}{C_{S2}}} \tag{4}$$

Mode 3: L_{a2} current runs through the body diode of S_2. S_2 can be turned on under zero voltage switching. L_{a2} current remains constant until S_{a2} is turned off.

Mode 4: S_1 is turned off and the difference of input inductor current and I_m charges C_{s1} up to $(V_0\text{-}V_c)/n$. Thus, S_1 turn off is under zero voltage switching. C_{s1} voltage equation during this mode is:

$$V_{C_{S1}} = \frac{(I_{in} - I_m).t}{C_{S1}} \tag{5}$$

Mode 5: The difference of input current and L_{a2} current runs through S_2.

Mode 6: S_{a2} is turned off and L_{a2} current runs through L_{a3} and D_a. Thus, the voltage across S_{a2} is equal $V_{in}/_m$. By selecting relatively large value for m, S_{a2} turns off under almost zero voltage switching. At the end of this mode D_a current becomes zero. L_{a3} current at the beginning of this mode is I_2/m. Thus, L_{a3} current equation during this mode is:

$$I_{La3} = \frac{I_2}{m} - \frac{V_{in}t}{L_{a3}} \tag{6}$$

Mode 7: In this mode I_{in} runs through S_2. Also D_2 is conducting in this mode.

Mode 8: This mode begins by turning S_{a1} on. Thus, $(V_0\text{-}V_c)/n$ is placed across and L_{a1} current linearly increases to $I_{in}\text{-}I_m$ and S_2 current decreases to I_m.

Mode 9: In this mode, C_{s1} discharges in a resonance with L_{a1}. Thus, L_{a1} current equation during this mode and its value at the end of this mode are:

$$I_{La1} = I_m + \frac{V_0 - V_C}{nZ_1}\sin(\omega_1(t)) \tag{7}$$

$$I_{La1} = I_m + \frac{V_0 - V_C}{nZ_1} = \frac{I_1}{m} \tag{8}$$

where:

$$\omega_1 = \frac{1}{\sqrt{L_{a1}C_{S1}}} \tag{9}$$

$$Z_2 = \sqrt{\frac{L_{a1}}{C_{S1}}} \tag{10}$$

Mode 10: In this mode L_{a1} current is constant and runs through body diode of S_1. During this mode S_1 can be turned on under zero voltage switching. L_{a1} current remains constant until S_{a1} is turned off.

Mode 11: This mode starts by turning S_2 off and C_{s1} is charged up to V_c/n with constant current I_m. Therefore, S_2 turn off is zero voltage switching. C_{s2} voltage equation during this mode is:

$$V_{C_{S2}} = \frac{I_m.t}{C_{S2}} \tag{11}$$

Mode 12: The difference of input current and L_{a1} current runs through S_1.

Mode 13: This mode begins with turning S_{a1} off and thus, L_{a1} current runs through L_{a3}. Therefore, V_{in}/m is placed across S_{a1} and by choosing relatively large value for m, S_{a1} turn off is almost zero voltage switching. At the end of this mode D_a current becomes zero. L_{a3} current at the beginning of this mode is I_1/m. Thus, L_{a3} current equation during this mode is:

$$I_{La3} = \frac{I_1}{m} - \frac{V_{in}t}{L_{a3}} \tag{12}$$

Mode 14: In this mode S_1 and D_1 are on and all other semiconductor devices are off.

The converter theoretical waveforms are shown in Fig. 2. Since the waveforms of S_1 and S_2 and also the waveforms of S_{a1} and S_{a2} are similar, only theoretical waveforms of S_2 and S_{a2} are presented. The main converter can be designed like its hard switching counterpart [9]. Designing the auxiliary circuit of the converter is simple. C_{s1} and C_{s2} are the snubber capacitors of S_1 and S_2 and these capacitors are designed similar to any turn off snubber. Also, L_{a1} and L_{a2} are the turn on snubber off S_{a1} and S_{a2} accordingly and these inductors can be designed like any turn on snubber inductor. It is desirable to choose large value for m. However, this will result in large values of L_{a3}. Therefore, in mode 6 and 13, L_{a3} current won't reach zero before turning the auxiliary switches on again. Thus, the only limitation on m is the duration of modes 6 and 13.

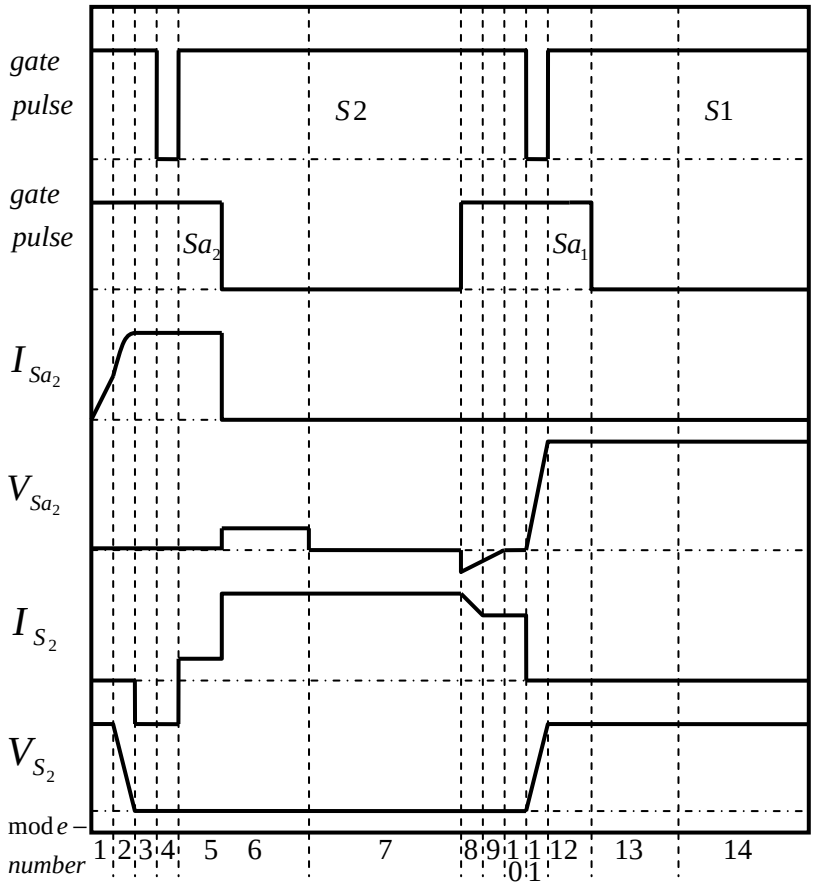

Figure 2: Theoretical waveforms of the converter.

3 Simulation Results

A 200 W prototype converter is simulated with PSpice software. The converter input voltage is 48 V and its output voltage is 400 V. The converter switching frequency is 100 kHz. For the converter main switches IRF740 model is used and for the converter auxiliary switches IRGBC20F model is used. The converter operating duty cycle is selected 0.5 and therefore the main converter approximately provides voltage gain of 4. Also, the converter transformer provides a voltage gain of 2.5 nF capacitors are used for C_{s1} and C_{s2}. Also, 4 uH inductors are applied for L_{a1} and L_{a2} and 100 uH inductor is also applied for L_{a3}. 1 uH inductor is added in series with the transformer for the leakage inductance. Also, 0.1 uH inductors are added in series with L_{a1} and L_{a2} for their leakage inductances. A 200 uH inductor is used for the input filter inductor and a 50 nF capacitor is used for the output filter capacitor. A 0.1 uF capacitor is used for C. MUR460 model is used for diodes. The converter simulation results are presented in Fig. 3. The simulation results confirm the validity of theoretical analysis presented. Also, it can be observed from the simulation results that snubber capacitor has limited the voltage spikes due to transformer leakage inductance which is observable in hard switching isolated DC-DC converters.

The simulation results show that the efficiency of soft switching converter is approximately 88.5% while the efficiency of hard switching counterpart is approximately 83%.

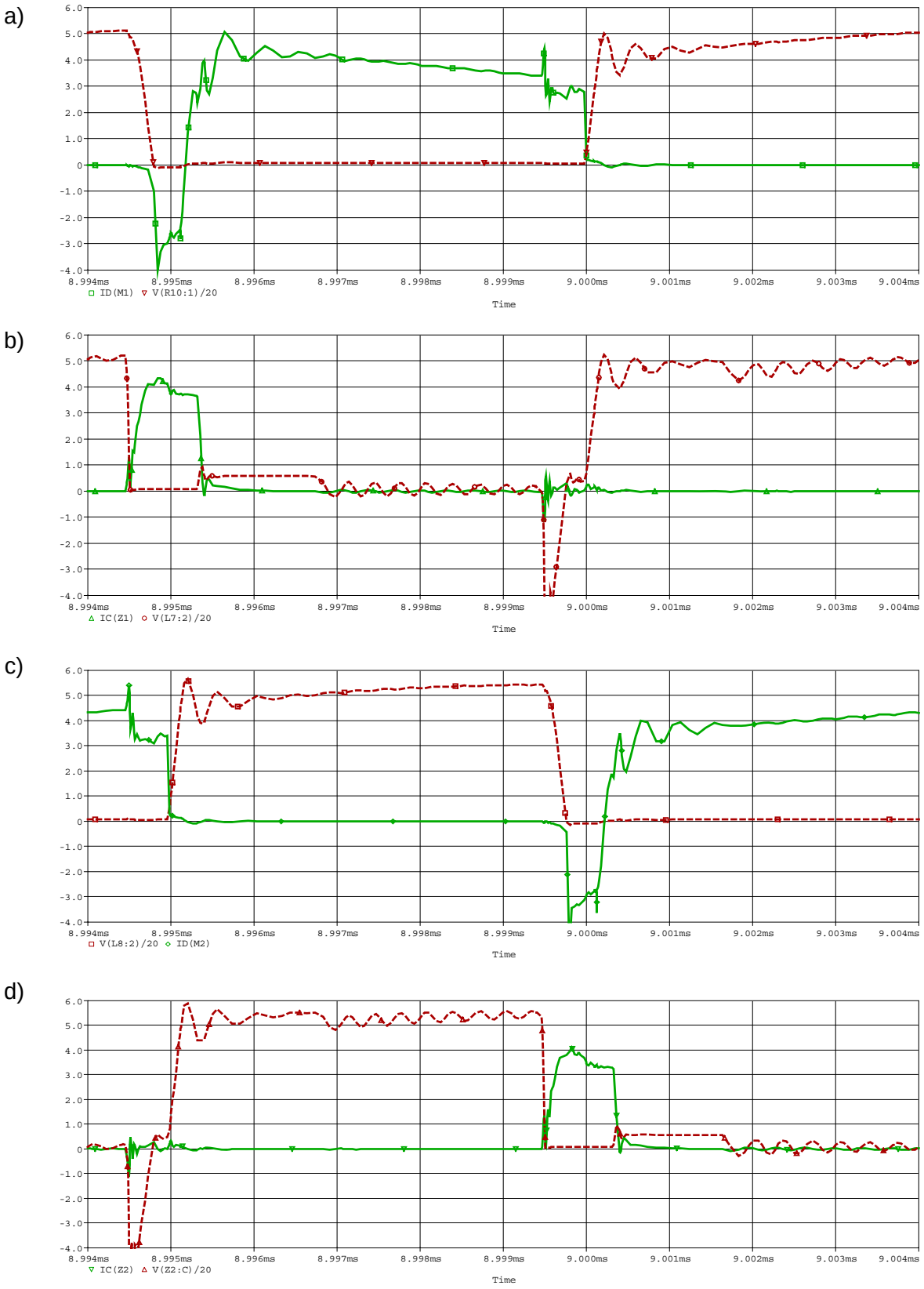

Figure 3: Voltage (broken line) and current (continues line) of (a) S2 (b) Sa2 (c) S1 (d) Sa1. (vertical scale is 20 V/div or 5 A/div and time scale is 1 us/div).

4 Conclusions

In this paper a soft switching boost type converter is introduced and analyzed. In this converter zero voltage switching condition is achieved for main switches. Also, the auxiliary switches are soft switched. Simulation results presented justify the theoretical analysis and the effectiveness of the introduced method.

References

[1] Y.K. Lo and J.Y. Lin. 2007. Active Clamping ZVS Flyback Converter Employing Two Transformers. *IEEE Trans. On Power Electron*22(6): 2416- 2423.

[2] E. Adib, H. Farzanehfard.2008.Family of zero-current transition PWM converters. *IEEE Trans. on Ind. Electron*55(8): 3055-3063.

[3] E. Adib, H. Farzanehfard.2008.Family of isolated zero voltage transition PWM converters.*IET Power Electron*1(1): 144-153.

[4] N. Lakshminarasamma, V. Ramanarayanan.2007.A family of auxiliary switch ZVS-PWM DC-DC converters with coupled inductor. *IEEE Trans. on Power Electron*22(5): 2008-2017.

[5] P. Das, G. Moschopoulos.2007.A zero-current-transition converter with reduced auxiliary circuit losses.IEEE Trans. on Power Electron22(4): 1464-1471.

[6] R. watson, F.C. Lee.1996.A Soft-Switched Full-Bridge Boost Converter employing an active clamp circuit. *IEEE PESC conference*: 1948 – 1954.

[7] S.K. Han, H.K. Yoon, G.W. Moon, M.J. Youn, Y.H. Kim, K.H. Lee.2005.A new active clamping zero voltage switching PWM current fed half bridge converter. *IEEE Trans. on Power Electron*20(6): 1271-1279.

[8] J.G. Cho, C.H. Jeong, H.S. Lee, G.H. Rim.1998.Novel zero voltage transition current fed full bridge PWM converter for single stage power factor correction.*IEEE Trans. on Power Electron*13(6): 1005-1012.

[9] P. Mantovaneli, I. Barbi.1996.A new current fed, isolated PWM DC-DC converter. *IEEE Trans. on Power Electron*11(3): 431-438.

Optimization of Thermal Management in High Temperature Fuel Cells

Julia Varfolomeeva, **Claas Mueller**, **Holger Reinecke**, IMTEK, Laboratory for Process Technology, University of Freiburg, Georges-Koehler-Allee 103, 79110 Freiburg, Germany

1 Introduction

Having numerous advantages over low temperature fuels cells, like a low CO-sensitivity and the absence of a complex water management, high temperature fuel cells still have to deal with one major challenge – a high output of lost heat. To prevent the fuel cell from a breakdown due to overheating, the lost heat needs to be properly dissipated and therefore makes high demands on the thermal management. The nowadays solutions, like water or air cooling, often have a large sized setup due to components like cooling fans, pumps and additional radiators which also make it difficult to control the heat dissipation. Also, the low thermal conductivity of these systems makes the heat dissipating process slow and therefore less effective. An improvement in the modern heat dissipating techniques, for example through the implementation of heat pipes, is essential and therefore the subject of the present work.

2 Heat Pipes as a Heat Dissipating Solution

Heat pipes are known to have a high thermal conductivity being space saving at the same time. They are usually known to be tubular shaped and are used for CPU-cooling or dissipating the heat in pipeline systems. Reducing the heat pipe dimensions combined with novel shapes gives the possibility to implement heat pipes in other systems like the high temperature fuel cells. Three different types of heat pipes are presented in this work including possibilities of their implementation in a high temperature fuel cell and the evaluation of their thermal conductivity.

Figure 1 shows the three heat pipe layouts. ***Figure 1a)*** shows a directly integrated assembly of four silicon heat pipes. It consists of two silicon plates (one of which containing the flowfield pattern on top) with groove shaped heat pipe structures (smaller image) which are bonded together. An opening close to the wafer frame is used for filling the working fluid inside the heat pipe and is sealed at the end of the filling process. ***Figure 1b)*** and ***c)*** show two layouts of graphite-heat pipe systems including commercialized copper heat pipes (round/flat). The graphite plates can easily be structured with a flowfield pattern on the outer side. In all three cases, the area of the flowfield was 2 cm x 5 cm.

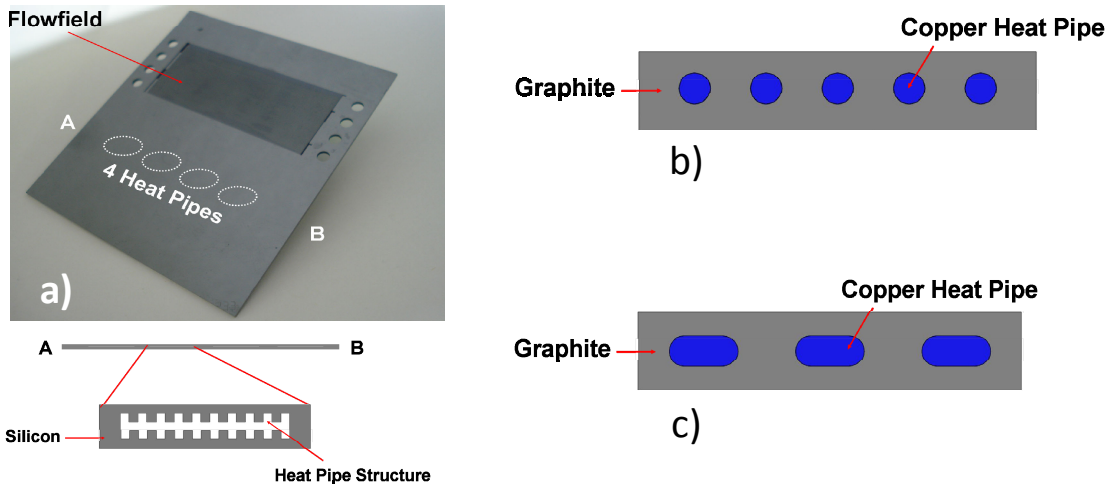

Figure 1: **a) Silicon flowfield-integrated heat pipes, b) round copper heat pipes and c) flat copper heat pipes.**

3 Simulation

An effective dissipation of heat in the fuel cell is strongly affected by the density of implemented heat pipes. The higher the density, the smaller the temperature peaks between the single elements. In case of silicon heat pipes this problem is solved through a maximum heat pipe density. In the case of round and flat copper heat pipes (***Figure 1b)*** and ***c)***) the temperature profile in the graphite plate cross section in dependence of the number of required copper heat pipes was calculated through a simulation. The maximum number of heat pipes was limited by the flowfield and the heat pipe width (3 mm for round heat pipes and 6 mm for flat heat pipes). The simulated temperature profiles are shown in ***Figure 2***.

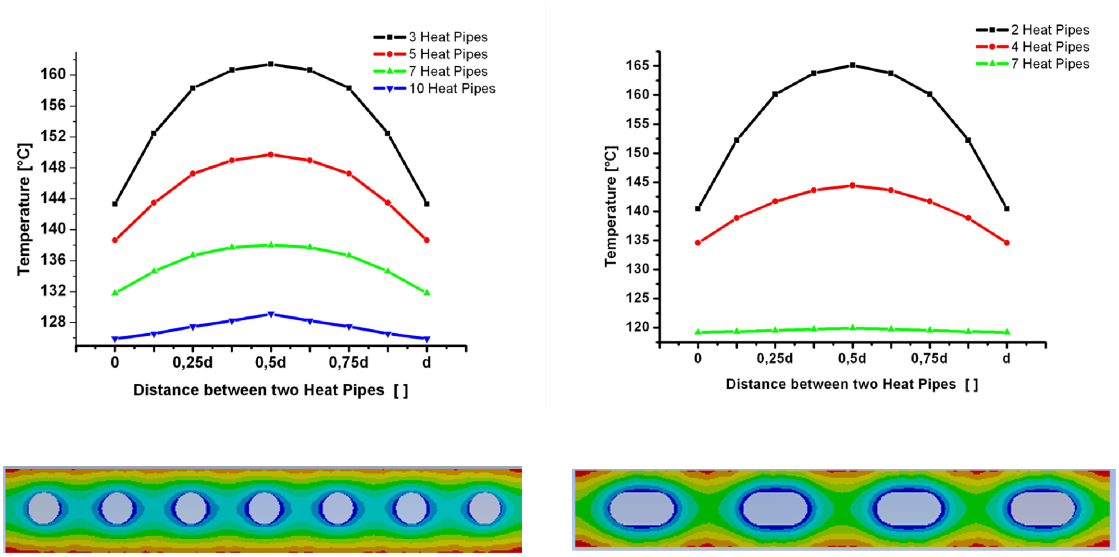

Figure 2: **Temperature distribution between single heat pipes in dependence of the heat pipe number in the graphite plate.**

To prevent the graphite surface from overheating, the temperature difference should not overrun the value of 10 °C. According to the simulation results, this is the case for 7 round and 4 flat heat pipes of the named dimensions.

4 Thermal conductivity

The thermal conductivity λ is an important parameter in order to compare the efficiency of single heat pipe types. Due to a high complexity of the measurement of λ, the calculation was done indirectly through a comparison of heat pipes with a silicon plate/copper bar of the same dimensions and a known thermal conductivity.

In the case of silicon heat pipes, the silicon plate with integrated heat pipes (filled and unfilled) and a solid silicon plate were heated on one end using a hot plate (temperature range: 100 – 170 °C) and cooled on the other end (PC-fan) and the temperature profile at defined measuring points (***Figure 3***) was measured with an infrared temperature measurement device.

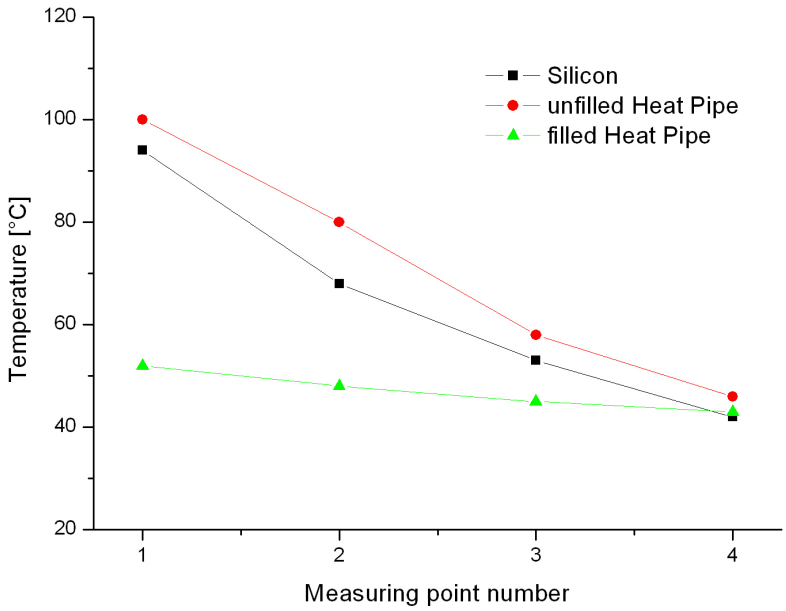

Figure 3: Temperature profile along a filled/unfilled silicon heat pipe compared to a solid silicon plate at a hotplate temperature of 170 °C.

Assuming a nearly equal heat input and having the same dimensions, the relationship of the unknown thermal conductivity λ_1 and the known thermal conductivity λ_2 is:

$$\frac{\lambda_1}{\lambda_2} = \frac{\Delta T_2}{\Delta T_1} .$$

As expected, the temperature profile of the heat pipe has a considerably smaller gradient than plain silicon and the unfilled heat pipe. Using the upper equation, the thermal conductivity of the heat pipe $\lambda_{Si\text{-}HP}$ results in:

$$\lambda_{SiHP} = \frac{\Delta T_{Si}}{\Delta T_{SiHP}} \lambda_{Si} \approx 1200 \frac{W}{mK}$$

The previously determined influences from the environment result in a decrease of λ of approximately 15-20%. Accordingly, the value of $\lambda_{Si\text{-}HP}$ including the environmental influences is ca. 1400 $\frac{W}{mK}$.

Similar to silicon heat pipes, the temperature profile along copper heat pipes was measured. Round copper heat pipes were therefore integrated in a graphite bipolar plate (***Figure 4a)***) and the determination of their thermal conductivity resulted from a comparison with a graphite/copper plate of same dimensions (725 W/mK, ***Figure 4b)***).

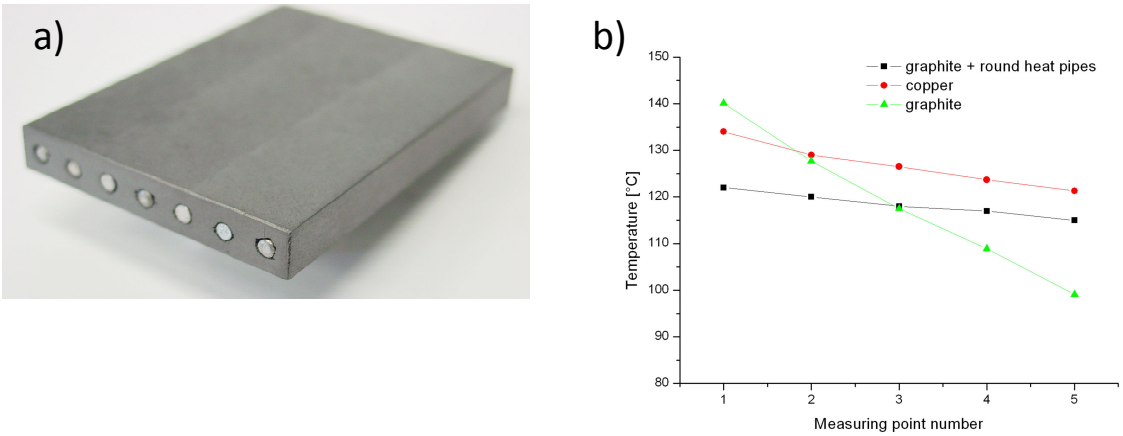

Figure 4: a) Graphite bipolar plate with integrated round copper heat pipes, b) temperature profiles of graphite+heat pipes, graphite and copper at a hotplate temperature of 170 °C.

In the case of flat copper heat pipes, the temperature profile was measured directly on the heat pipe surface due to its flatness and compared with a solid copper bar. The six measuring points were arranged along the centre line of the heat pipe and at the same intervals. The two outer points were arranged as close as possible to the hotplate/PC-fan. ***Figure 5a)*** shows the temperature profiles (at a hotplate temperature of 100 °C, 110 °C, 120 °C, 140 °C, 160 °C and 170 °C) along the heat pipe (mean value of 20 heat pipes) and the copper bar and the temperature difference between the outer points in dependence of the hotplate temperature (***Figure 5b)***, 3 heat pipes compared to 3 copper bars).

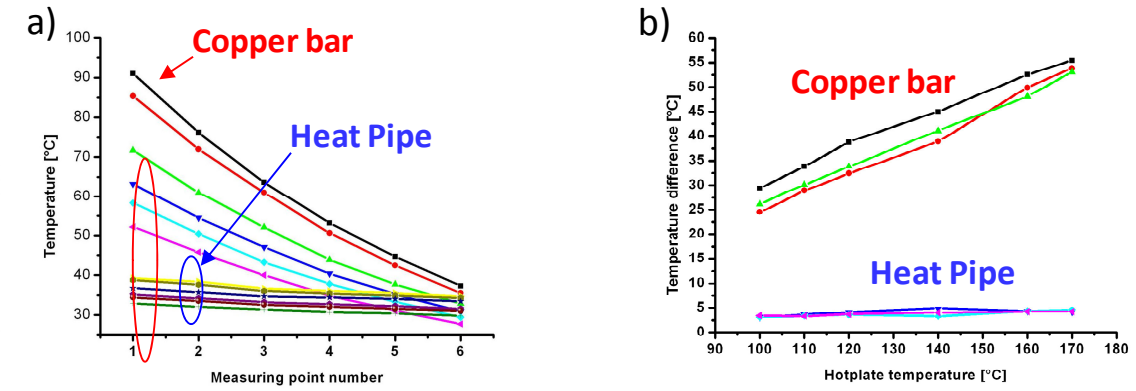

Figure 5: a) Temperature profile along a heat pipe and b) temperature difference between the outer measuring points.

Compared to the results of the copper bar, the temperature gradient of the heat pipe is extremely small and has a temperature difference between the outer measurement points of < 5 °C. The thermal conductivity of flat copper heat pipes can results in 36000 W/mK (including environmental influences).

5 Experimental setup

A model of the experimental setup including two flat copper heat pipes (with a width of 24 mm) and a high temperature fuel cell is shown in ***Figure 6***.

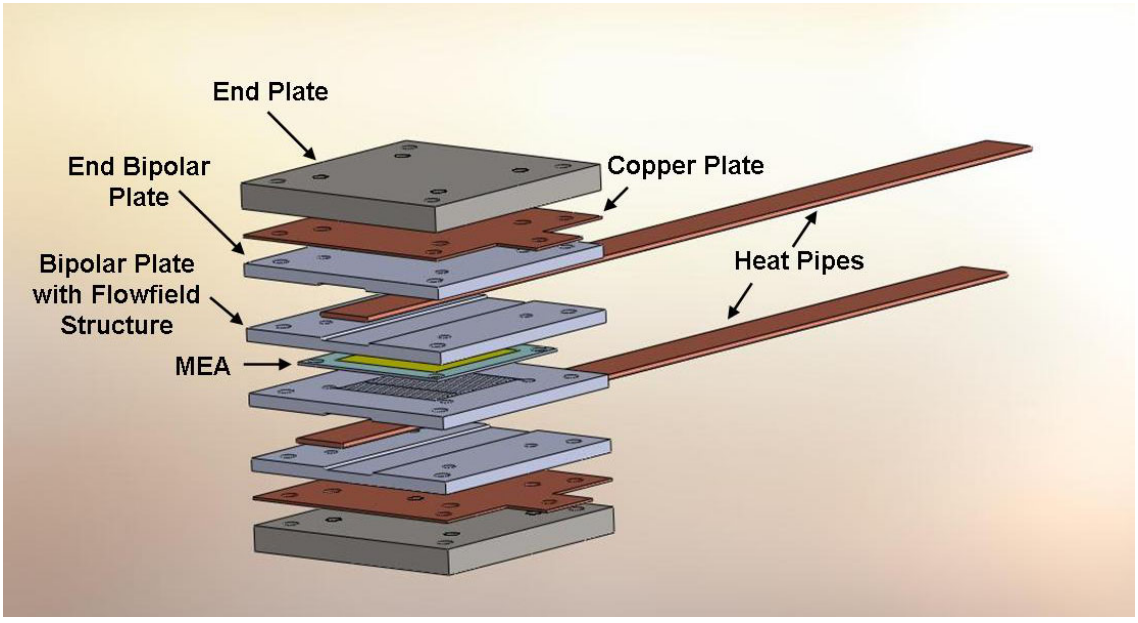

Figure 6: Model of the experimental setup with two flat copper heat pipes.

The model is symmetrical with the membrane electrode assembly (MEA) in the centre. The supply of hydrogen and oxygen, as well as the evacuation of the resulting water vapour and the unused hydrogen, occurs through the two end plates (stainless steel). The two inner

bipolar plates (BPP) contain a rectangular groove shaped flowfield structure and the MEA between them, where the hydrogen is split in protons and electrons. To dissipate properly the generated lost heat, a heat pipe is adjoined directly on the outer side of the inner bipolar plate, opposite to the flowfield structure and closed with a second bipolar plate. Finally, the assembly contains two thin copper plates for electrical contacting. This model can easily be expanded to a stack by simply repeating the MEA-BPP-unit.

Figure 7 shows the experimental setup consisting of one cell with an active area of 25 cm^2, including fuel inlets, water vapour/unused hydrogen outlets and an ohmic resistance.

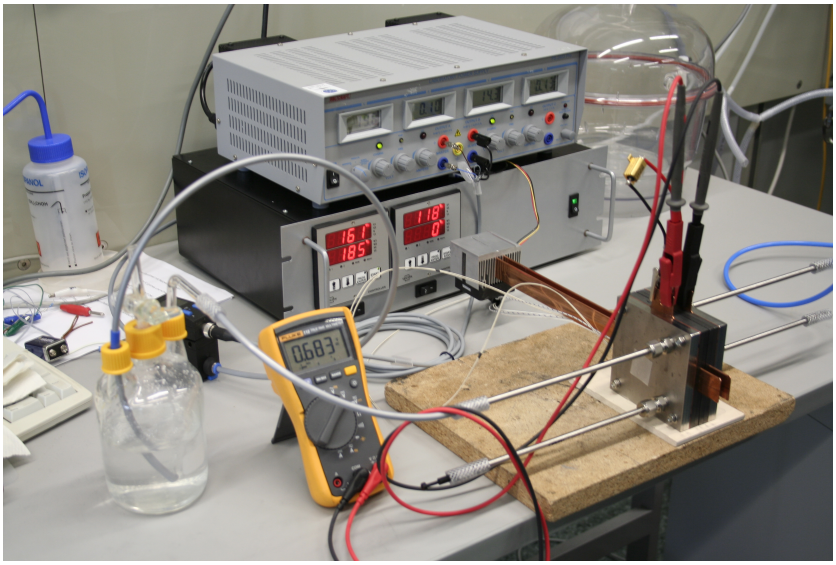

Figure 7: Integration of flat copper heat pipes in a high temperature fuel cell.

Using an external heat source and two flat copper heat pipes, the high temperature fuel cell was heated to a temperature of 135 °C. During the operation, the produced lost heat could successfully be conducted from the fuel cell using the heat pipes and hence be maintained at a constant operating temperature level. During the operating time of several hours a power density of 328 $mW/cm^2$was measured.

The effectively accomplished heat supply, as well as the lost heat dissipation has proven a successful functionality of the heat pipes.

6 Conclusions

A novel possibility of dissipating heat in high temperature fuel cells by the implementation of heat pipes was presented in this work. Three different heat pipe types were shown: a silicon heat pipe and two different copper heat pipes. The silicon heat pipe features its extremely high integrity into a fuel cell, its compact size and a high thermal conductivity, which is more than three times larger then the thermal conductivity of copper. The round and flat copper heat pipes could easily be integrated in a fuel cell by being placed inside a drilled hole of one bipolar plate or in a cavity between two bipolar plates. Especially the flat copper heat pipes have shown excellent results in thermal conductivity, which was 120 times as big as the thermal conductivity of copper. All three heat pipe types featured a remarkable temperature

homogeneity over their length, which is essential for dissipating high amounts of lost heat in the high temperature fuel cell. An experimental investigation has proven the excellent functionality of heat pipes as a heat dissipating solution, by successfully conducting the start-up heat towards the fuel cell as well as discharging the lost heat from the fuel cell during its operation.

Current Status of and Recent Developments in Direct Liquid Fuel Cells

Jürgen Mergel, Andreas Glüsen, and Christoph Wannek

Abstract

Direct liquid fuel cells, such as the direct methanol fuel cell (DMFC) or the direct ethanol fuel cell (DEFC), convert liquid fuel directly into electric current. In comparison to fuel cell systems that operate with pure hydrogen or hydrogen-rich gases from reforming processes, the fuel in the DMFC is supplied directly via liquid methanol. Apart from the very high energy density of methanol, the DMFC is characterized by easy handling and trouble-free refueling. As the reforming step is by-passed in direct fuel cells, compensation in the form of higher overvoltages (i.e. electrochemical losses) is acceptable. Despite the resulting moderate power densities, direct fuel cells are more attractive for a variety of applications in the low to medium power range than PEM fuel cells powered by hydrogen. Examples of their use include replacement of batteries in portable applications and for light traction, as there is no need for the relatively expensive and time-consuming charging of batteries or for a spare battery for multipleshift operation. Furthermore, the high energy density of the liquid energy carrier permits much longer operating times than batteries or fuel cell systems based on hydrogen. This paper outlines the level of development of different direct liquid fuel cells based on current research findings and trends.

Conditions for Autonomy of a DMFC System

Federico Zenith, **Ulrike Krewer**, Max Planck Institute for Dynamics of Complex Technical Systems, Germany

1 Motivation

Methanol-powered fuel-cell systems have a great potential for portable power in comparison to today's ubiquitous lithium-ion batteries: the energy density of methanol is over 15 times that of Li-ion batteries on volume basis, and over 40 times on mass basis (Li-ion energy densities: ~1 J/mm³ and ~0.5 J/mg (Tarascon and Armand, 2001). Methanol energy densities: 17.36 J/mm³ and 21.92 J/mg (Perry and Green, 1997)).

Direct methanol fuel cells (DMFC) convert methanol directly into electricity; while the overall efficiency of present systems may not be impressive (~20%), the high energy density of methanol more than offsets these losses.

Compared to a Li-ion battery pack, a DMFC system requires a "dead weight" to process methanol into electricity, i.e. the fuel-cell stack itself, separators, mixers and coolers. Therefore, DMFC, compared to Li-ion batteries, have more of an advantage at low power-to-energy ratios, i.e. for applications required to run independently for a long time.

DMFC systems are already available in fire-surveillance cameras, as mobile power supply for recreational vehicles, and portable power supply for military applications.

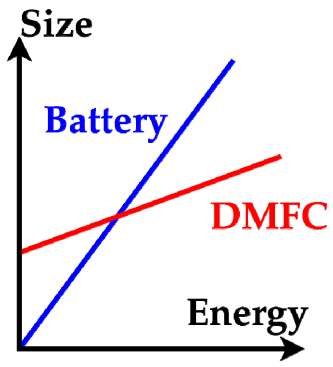

Figure 1: Energy density of DMFCs and batteries.

2 DMFC Reference System

DMFC systems can be divided up in two groups: *passive* systems, in which reactant transport is obtained by physical phenomena such as capillary pressure (Zhao et al., 2009), and *active* systems, in which the flows are driven by pumps, blowers or compressors.

Active systems are more flexible, can react better to changing environmental conditions and are more efficient, but require a larger dead weight for their ancillary units; therefore, passive systems are preferred for smaller-size applications such as mobile phones, whereas active systems are more appropriate for laptop computers or portable power sources.

The modelled system is an active one, in which all units perform a single task without any integration (the exception being the fuel-cell stack itself). The system operates at atmospheric pressure, and is referred to as the *reference* system.

The stack's anodic side operates on a lean methanol solution (~1M), pumped from a mixing tank. The solution is cooled after passing through the stack and the carbon dioxide produced by the reaction is then separated. The liquid phase returns to the mixer, completing the *anodic loop*. The stack's cathodic side is fed by environment air, which is pushed through the system by an inlet blower. The cathodic outlet is then cooled by a heat exchanger and any condensed water is recovered to the mixer. The neat methanol is pumped directly into the mixer.

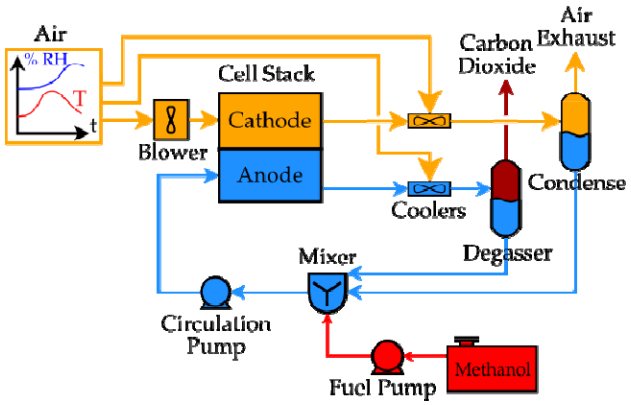

Figure 2: The reference DMFC system.

The fuel-cell stack includes several phenomena, the most important of which are:

- The anodic reaction, in which methanol and water are consumed to produce protons, electrons and waste carbon dioxide;
- The cathodic reaction, in which protons, electrons and oxygen produce water;
- The methanol cross-over, caused by diffusion of methanol through the membrane;
- The water drag, caused by the hydration of protons migrating to the cathode;
- Voltage is not modelled in full detail, but rather with a Thévenin approximation (i.e. voltage generator and a resistance), which is more appropriate for our purposes.

Separators perform an ideal separation of two phases. Coolers are assumed to be controlled so that it is possible to set their process outlet temperature, within physical bounds. The mixer is the only unit with a mass hold-up, since it is assumed to store a much larger quantity of solution than all other units. Both the fuel-cell stack and the mixer have an energy hold-up, though the stack considers only the heat capacity of the plates.

The resulting dynamic model is appropriate for bandwidths in the order of magnitude of several minutes or slower.

3 Dynamics and Control of DMFC Systems

The system model described in the previous section has been analysed for stability and controllability. The main dynamic variables are that of solution volume, methanol con-

centration, mixer temperature in the anodic loop, oxygen partial pressure in the cathode, and fuel-cell temperature.

All dynamic modes are stable, with the important exception of solution volume, which is *metastable* and slowly drifts away from its nominal value. Simulations indicate that this reduction can be as slow as 1 cm^3 every several hours for portable systems, which makes the issue difficult to notice in laboratory test runs. To make a commercial system viable, however, solution volume must be controlled so that it is maintained to an acceptable value: to control a metastable dynamics, feedback control and some measurement of solution volume are mandatory.

The adopted control strategy was to use a set of single-input, single-output controllers (decoupled control), with one controller for each dynamics. The resulting layout included (Zenith and Krewer, 2010):

- Feedforward stoichiometry (λ) control for both cathode and anode inflow;
- Feedback PI control of the anodic cooler to set stack temperature;
- Feedback P control, with gain scheduling, of the cathodic cooler to stabilise the solution volume;
- Feedforward control of neat-methanol inflow to the mixer, to compensate consumption by reaction and cross-over.

The simulations and experimental runs indicated that the overall control system is sound, and that interactions among the control loops are limited; the only significant one, which is the interaction between the control loops of stack temperature and methanol concentration, does not lead to instability under broad conditions.

4 Autonomy and Feasibility Envelope

Given that it is possible to control a DMFC system such as the proposed one, it remains to be seen in which conditions this is at all feasible. The most critical variable is the water content in the solution: water is removed from the anodic side of the stack, mostly by the electro-osmotic drag, and must be recovered by the condenser on the cathodic side. The ability of a DMFC system to maintain its water content is termed *autonomy*.

Since the minimum achievable condenser temperature is limited by the environment temperature, it can be imagined that there are conditions in which it will not be possible to recover the necessary amount of water if environment temperature is too high.

Indeed, a steady-state analysis based on material balances shows that the autonomy of a DMFC system depends on a surprisingly small set of variables (Zenith et al., 2010):

- Cathodic reactant excess ratio (the cathodic λ);
- Environmental humidity;
- Condenser temperature.

It is worth remarking that autonomy does not depend on any of the following:

- Current, voltage or other electrochemical variables;
- Concentration, stack temperature, anodic flow rate, or other operating conditions;
- Any cell parameter, such as those describing methanol cross-over, electro-osmotic drag, number or size of cells.

Autonomy of DMFC systems can therefore be determined in very general terms, for any DMFC system configured as our reference system (or systems with different configuration but leading to the same mass balances). One solution of the autonomy relationship is presented in figure 3.

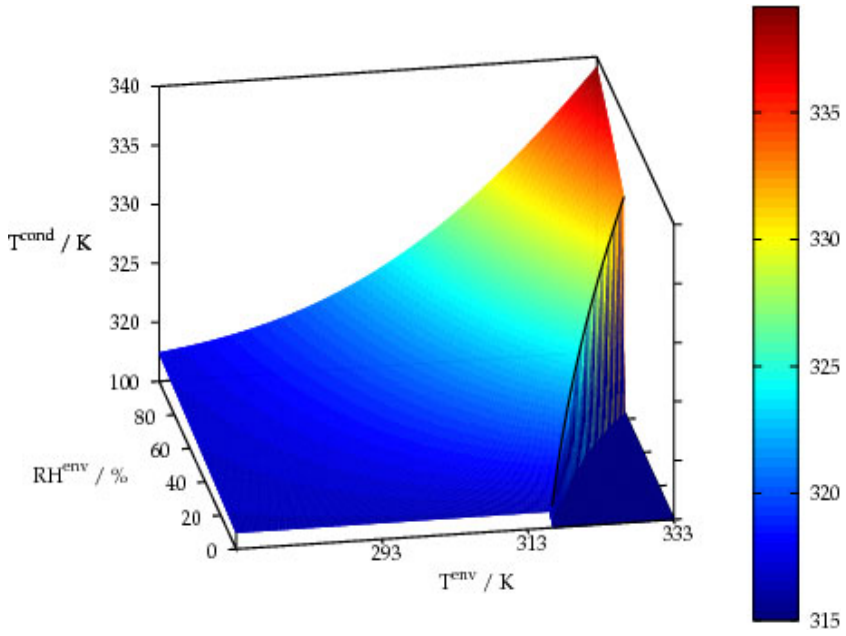

Figure 3: The value of T^{cond} represents the autonomy relationship; the sharp drop on the right is the edge of the feasibility envelope. The plot is for $\lambda = 3$.

The set of environmental conditions (humidity and temperature) allowing operation of DMFC systems is termed the *feasibility envelope*. If necessary, this envelope can be extended by diluting the methanol reservoir with water, an approach taken in some prototypes produced by the industry; calculations, however, show that this approach does not improve autonomy significantly, and has the price of reducing the DMFC's main advantage, i.e. energy density.

Extending the envelope by means of system pressurisation seems a more promising approach, even though pressurisation is known to reduce system efficiency and should be avoided whenever possible. Specularly, operation at pressures lower than one standard atmosphere (for example in high altitude) results in a significantly tighter feasibility envelope.

5 Determination of Cross-Over Parameters

The proposed DMFC system contains three feedforward control systems to set cathodic, anodic, and neat-methanol inflows. The autonomy criterion was derived assuming this control is perfectly implemented. All these feedforward control laws have to compensate for the cross-over, whose estimation is therefore of critical importance.

To estimate the cross-over, the system was run on a slightly modified configuration: the neat methanol was injected directly on-line between the mixer and the fuel cell, and the concentration downstream of the mixing point was measured by a sensor. The neat-methanol inflow was then set by a PI feedback controller, that maintained an inlet concentration of 1 M with a standard deviation of 2.5%.

Maintaining the stack temperature at 60 °C and the anodic cooler's at 40 °C, the cross-over was estimated by setting several currents in the interval between open circuit and 2300 A/m^2 and measuring the inflow of neat methanol set by the concentration feedback controller. When the steady state is reached, the resulting neat-methanol inflow is the steady-state sum of methanol lost to anodic reaction, cross-over and anodic separator (the last one being a negligible term).

The cross-over model was validated by nonlinear model fitting. The two parameters used to estimate cross-over could be estimated with good precision, indicating that feedforward control is realistic.

The two parameters are the mass-transport coefficients from the anodic bulk to the membrane (k_m) and from the anodic side of the membrane to the cathodic one (k_x), the latter being relevant for crossed-over methanol only.

Table 1: Estimates for mass-transport coefficients at 60°C, 1 M.

Parameters	Estimation	Standard deviation
k_m	8.00 µm/s	2.3 %
k_x	1.98 µm/s	1.8 %

In further work, the cross-over will be estimated for other stack temperatures and methanol concentrations, in order to enable feed forward control in real systems, where these variables may change.

References

[1] Perry, R. H. & Green, D. W. (ed.): Perry's Chemical Engineers' Handbook, 1997.

[2] Tarascon, J. & Armand, M.: Issues and challenges facing rechargeable lithium batteries, Nature, 2001, 414, 359-367.

[3] Zenith, F. & Krewer, U.: Modelling, Dynamics and Control of a Portable DMFC System, Journal of Process Control, 2010, 20, 630-642.

[4] Zenith, F., Weinzierl, C. & Krewer, U.: Model-Based Analysis of the Feasibility Envelope for Autonomous Operation of a Portable Direct Methanol Fuel-Cell System, Chemical Engineering Science, 2010, 65, 4411-4419.

[5] Zhao, T. S., Chen, R., Yang, W. W. & Xu, C.: Small Direct Methanol Fuel Cells with Passive Supply of Reactants, Journal of Power Sources, 2009, 191, 185-202.

Direct Converting Low Temperature Bio-Ethanol Fuel Cells

C. Cremers*, **D. Bayer**, **J. Meier**, **F. Jung**, **B. Kintzel**, **J. Tübke**, Fraunhofer Institute for Chemical Technology ICT, Department for Applied Electrochemistry, Joseph-von-Fraunhofer-Str. 7, 76327 Pfinztal, Germany

1 Introduction

Bio-ethanol is a renewable fuel with low CO_2 emissions. However, as its production conflicts with the production of food, it will not become abundantly available. A sustainable use therefore requires high efficiency. Fuel cells can deliver the required efficiency in producing electricity from bio-ethanol, in particular when direct conversion is possible. In low temperature fuel cells, which are suitable for a number of applications, conversion of ethanol is often hindered, leading to an incomplete oxidation of the fuel. As this incomplete oxidation reduces the conversion efficiency and can result in the formation of undesired by-products such as acetaldehyde, it should be avoided. Optimisation of the catalyst and the electrode layers is therefore required in order to use ethanol in low temperature direct ethanol fuel cells. This optimisation needs to be carried out separately for all fuel cell technologies of interest. Currently available fuel cell technologies of interest are low-temperature proton exchange membrane fuel cells LT-PEMFC, alkaline anion exchange membrane fuel cells AEMFC and high-temperature proton exchange membrane fuel cells HT-PEMFC. Within this project, the electrochemical behaviour of ethanol at platinum electrodes at ambient temperature was investigated in both acidic and alkaline environments, employing standard electrochemical techniques such as cyclic voltammetry (CV), chronoamperometry (CA) and differential electrochemical mass spectrometry (DEMS). Additional tests were carried out for the oxidation of acetaldehyde as a known intermediate. Furthermore development of LT-PEMFC electrodes and membrane electrode assemblies was performed, allowing for the stable operation of a DEFC at ambient temperature with passive air supply. Additional tests on AEM-DEFC showed the high potential of this technology.

2 Electrochemical Behaviour of Ethanol

Electrochemical reactions are often hampered by adsorbates formed from the substrate which bind too strongly to the surface to be easily removed. In the case of the ethanol oxidation reaction, in order to find such adsorbates and determine their nature, stripping measurements were performed in a flow-through DEMS cell. For these measurements the electrode surface was cleaned by repeatedly cycling the potential of the electrode in neat electrolyte solution between the hydrogen and oxygen evolution potential until a stable base CV was observed. Subsequently the electrode potential is set to the desired adsorption potential and ethanol in electrolyte solution is admitted to the cell during the adsorption period. Finally the electrolyte is replaced by neat electrolyte again, and after all ethanol

* Corresponding author, email: carsten.cremers@ict.fraunhofer.de

signals have disappeared from the MS the electrode potential is cycled starting either in the anodic or the cathodic direction. In the case of the stripping of ethanol adsorbed from acidic solution, a number of studies can be found in literature[1-3]. In this project the results were compared to those for ethanol adsorption from alkaline solution. Comparable behaviour was observed. Adsorbing ethanol onto a cleaned polycrystalline platinum surface leads to the formation of two types of adsorbates differing in their desorption potentials during the anodic sweep of the stripping cycle. As can be seen from Figure 1 two oxidation peaks at about 0.6 V vs. RHE and 1.1 V vs. RHE, respectively are observed during the stripping of ethanol adsorbates, both giving CO_2 as the product.

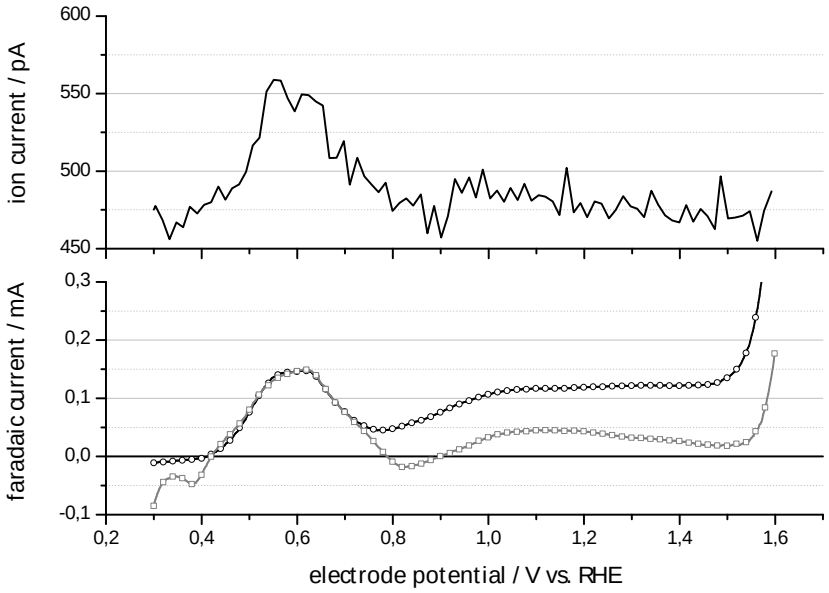

Figure 1: Oxidation of adsorbed ethanol at platinum in 0.1 M KOH: Mass spectrometric ion current m/z 44, first anodic potential sweep (black line), Faradaic current, first anodic potential sweep (black circles), difference between the Faradaic current of the first and second anodic potential sweep (grey squares). Adsorption potential 0.3 V vs. RHE, adsorption time 5 minutes, scan rate 10 mV s^{-1}.

However, if the stripping cycle is started in the cathodic instead of the anodic direction, the result differs significantly. Now in the low potential region the additional formation of methane is observed. The oxidation peak at about 0.6 V vs. RHE remains mainly unchanged whereas the oxidation peak at about 1.1 V vs. RHE has disappeared (cf. Figure 2).

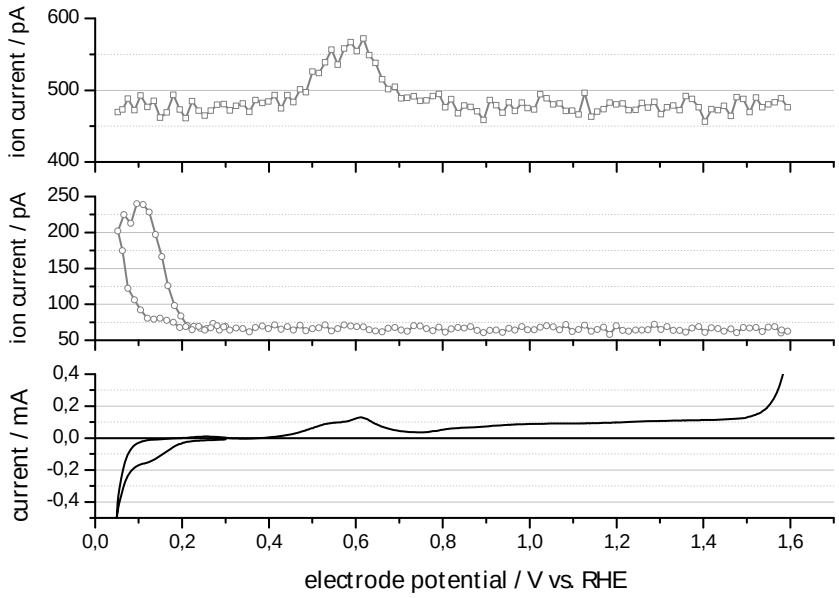

Figure 2: Cathodically started stripping of ethanol adsorbates in 0.1 M KOH at platinum: mass spectrometric signal for carbon dioxide (m/z 44, grey squares), mass spectrometric signal for methane (m/z 15, grey circles) and Faradaic current of the first potential sweep (black line). Adsorption potential 0.3 V vs. RHE, adsorption time 5 minutes, scan rate 10 mV s^{-1}.

It was further found that the stripping of CO under these conditions yields a single oxidation peak at about 0.6 V vs. RHE independent of the starting direction of the stripping cycle. Thus it can be concluded that the products formed by the adsorption of ethanol are CO_{ads} and $CH_{x,ads}$. The splitting of the C-C bond is therefore not hindered at a clean platinum surface, in agreement with the results found in literature for the acidic environment. However, in both cases the product composition changes in presence of bulk ethanol. This can be attributed to the poisoning of the electrode surface. The products released are acetaldehyde, acetic acid and ethyl acetate, both in the acidic and the alkaline environment. In the acidic environment the use of PtSn instead of Pt electrodes decreases the on-set potential for aldehyde formation but does not support the further oxidation of the acetaldehyde (cf. Figure 3 left) in agreement with literature[4]. However, it could be shown, that PtRu catalysts support the oxidation of acetaldehyde to carbon dioxide (cf. Figure 3 right).

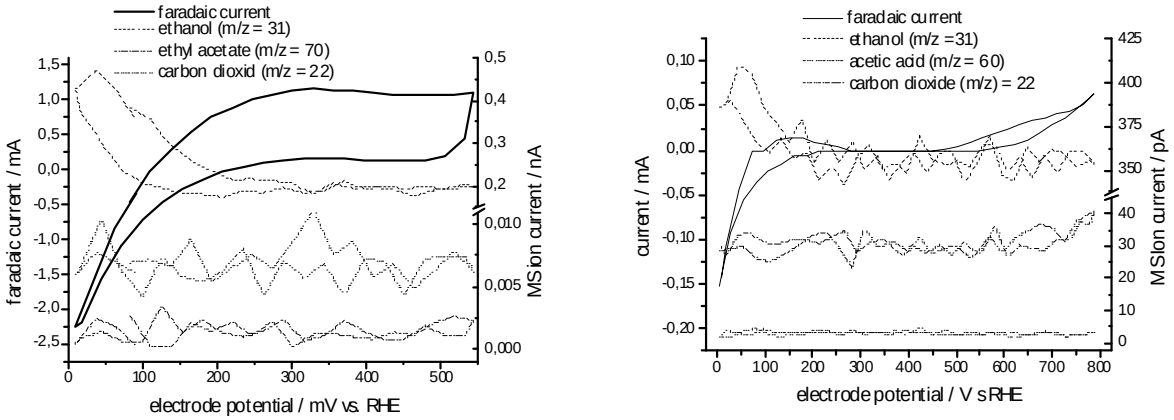

Figure 3: MSCV of a platinum tin (3:1) electrode (left and a platinum ruthenium (3:19 electrode (right) in 0.1M acetaldehyde, 0.5 M sulfuric acid solution, CV (straight), ethanol (dashed), ethyl acetate (dash-dot) and carbon dioxide (dotted). MSCV was recorded at ambient temperature with a scan rate of 20 mVs^{-1}.

In an alkaline environment the use of a palladium instead of a platinum catalyst can strongly increase the achievable current densities (cf. Figure 4).

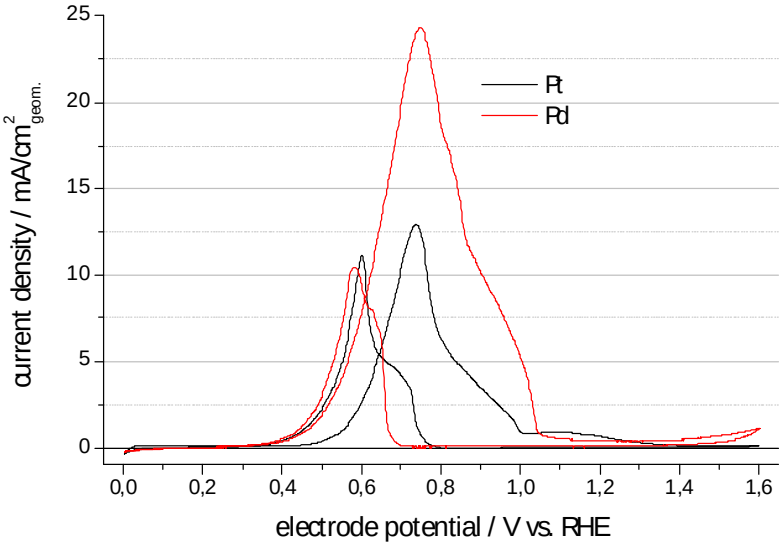

Figure 4: Cyclic voltammograms of ethanol oxidation in 1M ethanol, 0.1M KOH solution at a platinum and a palladium electrode, respectively.

Also some non-noble metals are active for ethanol oxidation under alkaline conditions (cf Figure 5). Details on the electrochemical investigations can be found in some recent publications[5-8].

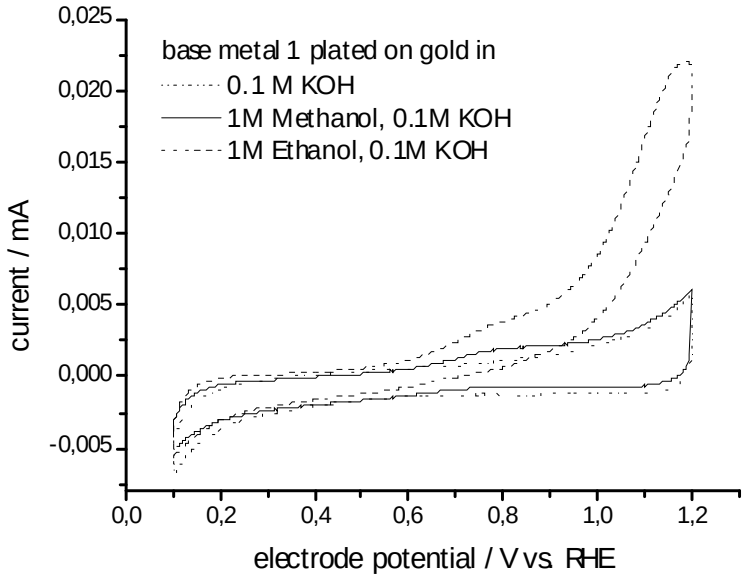

Figure 5: Activity of a base metal electrode for the oxidation of ethanol and methanol in KOH solution at ambient temperature.

3 Membrane Electrode Assemblies and Single Cell Results

Using the findings that PtRu, in contrast to PtSn, can catalyse the oxidation of intermediately formed acetaldehyde, a concept for an electrode layer containing both catalysts was developed. It was shown that the use of mixed anodes does increase the performance of the cell compared to cells that use only PtSn catalyst at the same catalyst loading (cf. Figure 6) and that the yield of carbon dioxide is increased even at a decreased catalyst loading (cf. Figure 7).

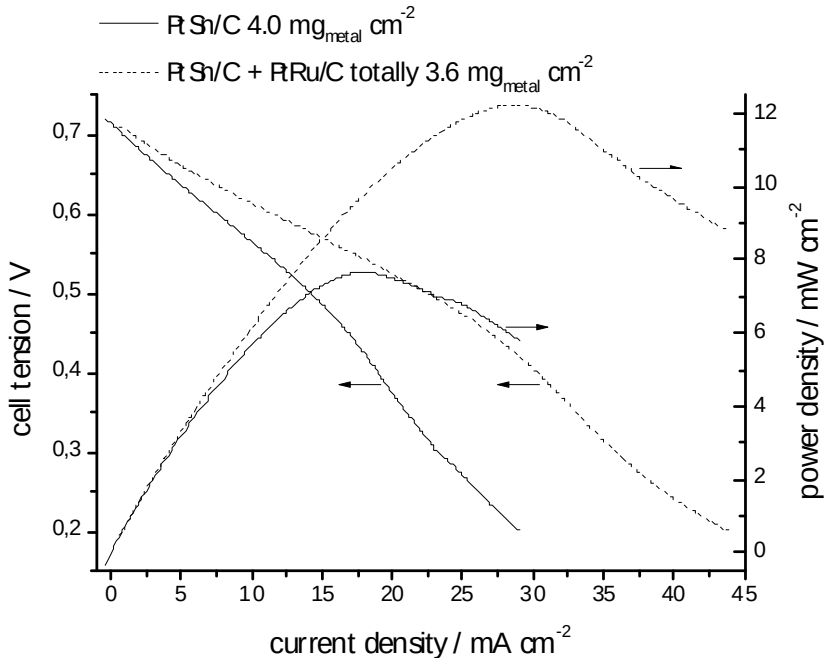

Figure 6: i-V and i-p properties of two different DEFC MEAs, with either Pt_3Sn/C or a mixture of Pt_3Sn/C and PtRu/C as anode layer, recorded at 50 °C, anode feed 1.5 ml/min 1 M ethanol solution, cathode feed 1 l/min synthetic air, scan rate 1 mVs^{-1}.

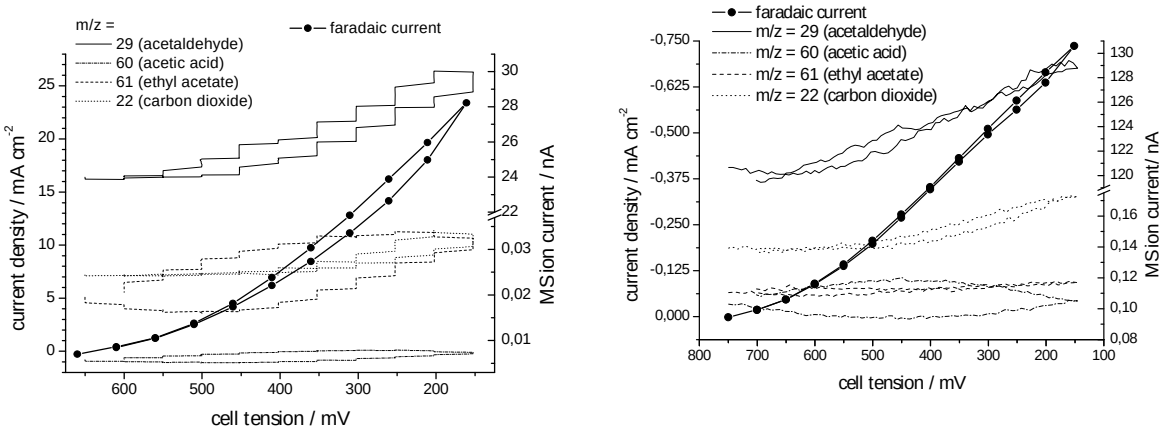

Figure 7: U-I curve and online MS-data for ethanol conversion in a DEFC with Pt_3Sn/C anode with 3.4 mg_{metal}/cm^2 (left) and DEFC with mixed Pt_3Sn/C and PtRu/C anode with 1.8 mg_{metal}/cm^2 (right) recorded at 40 °C, 2.0 ml/min 1 M ethanol.

This approach is protected by German patent 10 2007 031 526 with worldwide patents pending.

Combining this approach with a new sPEEK based mixed matrix membrane developed by Fraunhofer IGB[9, 10] results in membrane electrode assemblies able to operate at close to ambient temperature with low cathode airflow rates[11] (cf. Figure 8)

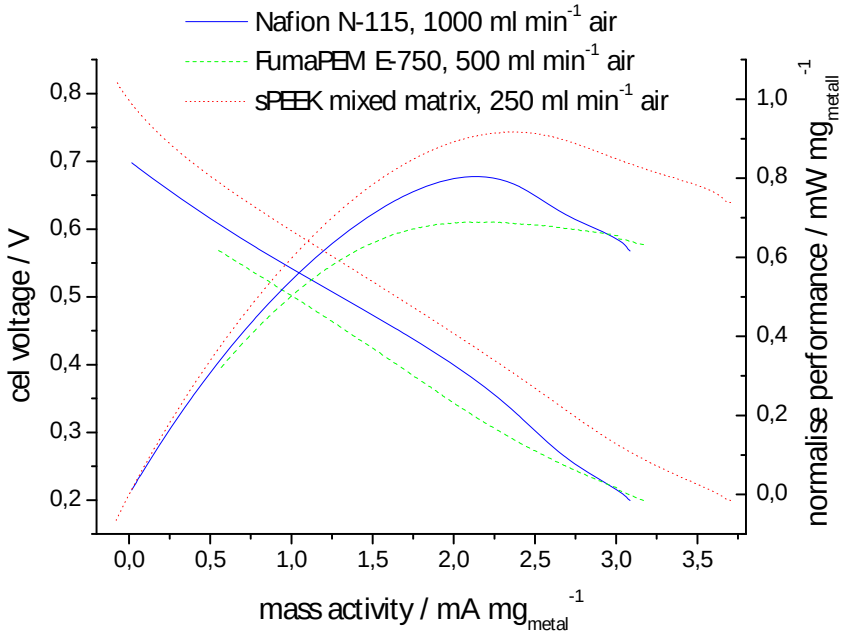

Figure 8: Comparison of the catalyst mass normalized performance values of MEAs with three different types of electrolyte at 30 °C. Air flow is set to the minimum useful value with the respective membrane.

These cells operate very stably, however their performance is more suitable for small power applications, such as small portable appliances or remote sensors. The performance can be increased using alkaline fuel cells (cf. Figure 9). Using commercially available materials, power densities of > 100 mW cm^{-2} were achieved at 50 °C without cell optimisation.

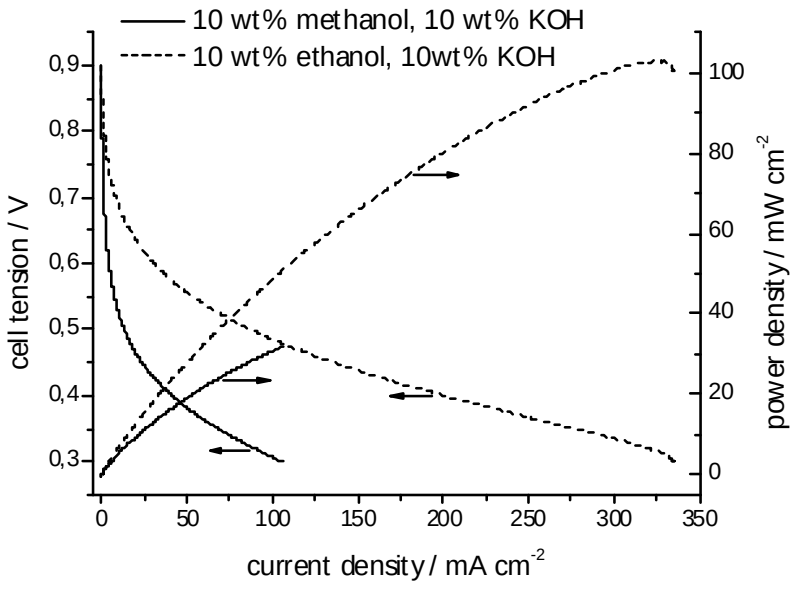

Figure 9: i-V curves of an AEM based DAFC with fumatech Fumasep membrane and Acta Hypermec electrodes operated at 50 °C and with synthetic air as oxidant. Fuel was either methanol or ethanol.

The alternative way to increase power densities could be an increase of the operating temperature. So it could be shown that the performance of Nafion® based DEFC is increased significantly by increasing the operating temperature to 80 °C.

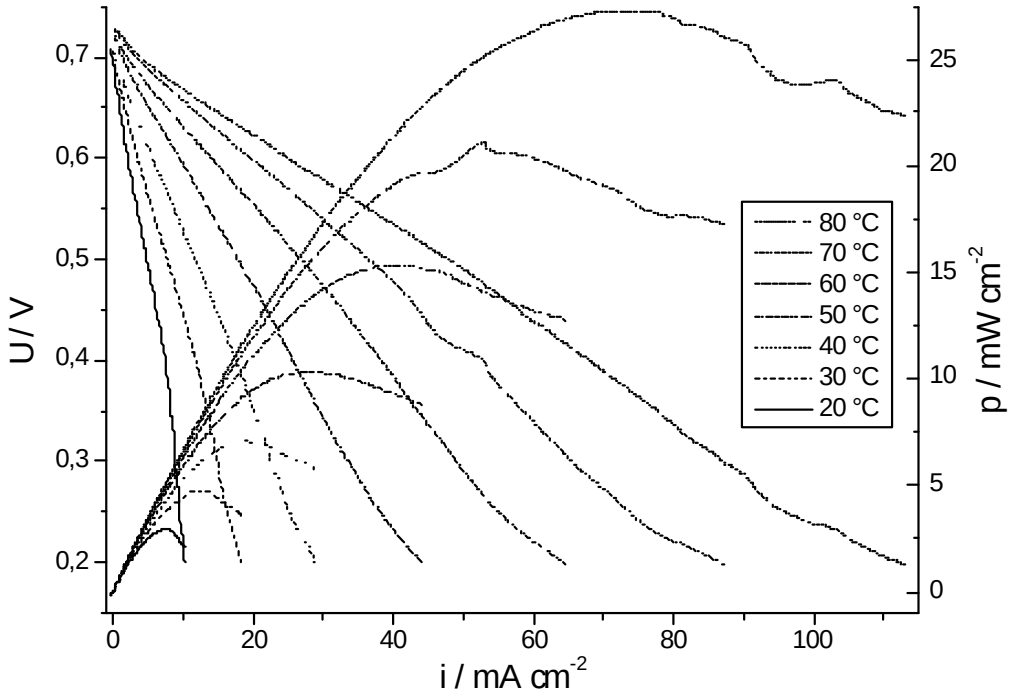

Figure 10: I-V curves of a DEFC MEA with Nafion N-115 electrolyte, PtCo/C cathode with 2.3 mg cm^{-2} loading and a mixed PtSn/C PtRu/C anode with 3.6 mg cm^{-2} loading, operated with 1 M ethanol at 1.5 ml min^{-1} and air at 1000 $mlmin^{-1}$.

A further increase of the operating temperature could therefore be a suitable option. First reports in literature on DEFC using either PBI/H_2SO_4 MEA[12] or PBI/KOH MEA[13] are quite encouraging.

4 Conclusions

The results show that the splitting of the C-C bond in ethanol is only hindered by the poisoning of the catalysts. An optimization of the catalyst to avoid the poisoning effects should be possible. As the oxidation the adsorbed CO_{ads} and $CH_{x,ads}$ species requires the availability of oxygen at the catalyst surface working at high pH levels will be beneficial as the oxygen availability increases with the pH. Alternatively, further increasing the reaction temperature should also help to avoid electrode poisoning. Thus DEFC in the kW power scale should be feasible.

References

[1] T. Iwasita and E. Pastor, Electrochimica Acta 39 (4), 531-537 (1994).

[2] U. Schmiemann, U. Müller and H. Baltruschat, Electrochimica Acta 40 (1), 99-107 (1995).

[3] H. Wang, Z. Jusys and R. J. Behm, Fuel Cells 4 (1-2), 113-125 (2004).

[4] S. Rousseau, C. Coutanceau, C. Lamy and J. M. Leger, Journal of Power Sources 158 (1), 18-24 (2006).

[5] C. Cremers, D. Bayer, J. O. Meier, S. Berenger, B. Kintzel, M. Joos and J. Tubke, ECS Transactions 25 (13), 27-37 (2010).

[6] C. Cremers, D. Bayer, B. Kintzel, M. Joos, F. Jung, M. Krausa and J. Tubke, in *Proton Exchange Membrane Fuel Cells 8, Pts 1 and 2*, edited by T. Fuller, K. Shinohara, V. Ramani, P. Shirvanian, H. Uchida, S. Cleghorn, M. Inaba, S. Mitsushima, P. Strasser, H. Nakagawa, H. A. Gasteiger, T. Zawodzinski and C. Lamy (2008), Vol. 16, pp. 1263-1273.

[7] D. Bayer, C. Cremers, H. Baltruschat and J. Tubke, ECS Transactions 25 (13), 85-93 (2010).

[8] D. Bayer, S. Berenger, C. Cremers and J. Tubke, ECS Transactions 25 (13), 95-103 (2010).

[9] K. S. Roelofs, A. Kampa, T. Hirth and T. Schiestel, Journal of Applied Polymer Science 111 (6), 2998-3009 (2009).

[10] K. S. Roelofs, T. Hirth and T. Schiestel, Journal of Membrane Science 346 (1-2), 215-226 (2010).

[11] C. Cremers, F. Jung, B. Kintzel, K. Roelofs, T. Schiestel and J. Tubke, ECS Transactions 25 (1), 1685-1695 (2009).

[12] J. Lobato, P. Canizares, M. A. Rodrigo and J. J. Linares, Fuel Cells 9 (5), 597-604 (2009).

[13] H. Y. Hou, G. Q. Sun, R. H. He, Z. M. Wu and B. Y. Sun, Journal of Power Sources 182 (1), 95-99 (2008).

Effect of the Impurities in Methanol Fuel on the Performance of MEA for Direct Methanol Fuel Cell

Dong-Hyun Peck, **Young-Chul Park**, **Byung-Rok Lee**, **Doo-Hwan Jung**,
Fuel Cell Research Center, Korea Institute of Energy Research (KIER), Daejeon, Korea

1 Introduction

The impurities in the methanol fuel that is used for direct methanol fuel cell (DMFC) could greatly affect the performance of membrane electrode assemblies (MEA). The most common impurities in the commercial methanol fuel are mainly ethanol, acetone, acetaldehyde, or ammonia. In this study, the effect of impurities in methanol fuel was investigated on the performance of MEA. We will propose the optimum compositions and limit concentration of impurities in methanol fuel for high performance of MEA for DMFC.

2 Experimental

The effect of impurities in the methanol fuel was evaluated using the 6 different kinds of commercial methanol fuels (methanol W, A, B, C, D, and E), as listed in Table 1.

The MEA was fabricated using commercial Nafion 115 as a membrane, PtRu/C (HISPEC 12100, Johnson Matthey Fuel Cells) as an anode catalyst, and Pt/C (HISPEC 13100, Johnson Matthey Fuel Cells) as a cathode catalyst. A single cell with active electrode area of 9.0 cm^2 was tested using an electrochemical test system (Won-A Tech., Korea). The changes of voltage/power density of the cells during the supply of methanol fuel with different commercial methanol were performed at 60^oC and constant operating current of 1.35 A (150 mW cm^{-2}) under ambient pressure. A solution of 1M methanol solution was fed into the anode at a flow rate of 2 cc min^{-1} and air was supplied into the cathode at a flow rate of 400 cc mim^{-1}. The anode polarization of the cells was also measured under the same conditions as those of a single cell test, except that hydrogen (H_2) gas was supplied to the cathode at a flow rate of 10 ml min^{-1} in order to make a dynamic hydrogen electrode (DHE).

Impedance spectra of the single cells during an electrochemical reaction at 60^oC and galvanostatic operation of 1.35 A (150 mW cm^{-2}) were observed using an electrochemical analysis instrument (Zahner, IM6&IM6eX, Germany). Cyclic voltammograms (CV) test was measured in the three electrodes, and the scan rate of the CV was 1 mV s^{-1}. A glassy carbon disk (1 cm^2) with electrocatalysts is used as working electrode, Pt mesh as counter-electrode, and Ag/AgCl electrode as reference. 0.5 M H_2SO_4 and 1 M methanol solution were served as electrolytes for the CV test and N_2 was bubbled into the electrolytes during the experiment.

Table 1: Property table of commercial methanol (methanol W, A, B, C, D, and E).

Methanol Matter	Methanol W	Methanol A	Methanol B	Methanol C	Methanol D	Methanol E
Water (%)	max. 0	max. 0.2	max. 0.01	max. 0.1	max. 0.2	max. 0.2
Non-volatile matters (%)	max. 0	max. 0.001	max. 0.001	max. 0.001	max. 0.001	max. 0.001
Acid (as CH_3COOH) (%)	max. 0	max. 0.003	max. 0	max. 0	max. 0.003	max. 0.003
Alkali (as NH_3) (%)	max. 0	max. 0.0003	max. 0	max. 0	max. 0.0003	max. 0.0003
Acetone, Aldehydes (as C_2H_5OH) (%)	max. 0	max. 0.003	max. 0.001	max. 0.001	max. 0.003	-
Assay (by G.C) (%)	min. 99.9	min. 99.8	min. 99.8	min. 99.8	min. 99.8	min. 99.5

3 Results

The changes of voltage/power density of the cells during the supply of methanol fuel with different commercial methanol are shown in Fig. 1. MEA 1 was constantly supplied with methanol W, whereas MEA 2 was supplied with different methanol listed in Table 1 for the period of 24 h. A solution of 1 M Methanol of MEA 2 was replaced as the following order; methanol W → methanol A (A sector) → methanol W → methanol B (B sector) → methanol W → methanol C (C sector) → methanol W → methanol D (D sector) → methanol W → methanol E (E sector) → methanol W. As shown in Fig. 1, when MEA 2 was supplied with methanol A, the performance of the cell was abruptly decreased as compared with the other methanol solution. The cell supplied with methanol A showed the performance loss of about 10 mW cm^{-2}. When MEA 2 Also was supplied with methanol E, the performance of the cell was slightly fluctuated. These results indicate that a methanol solution supplied into a DMFC cell could affect the performance and durability of the cell.

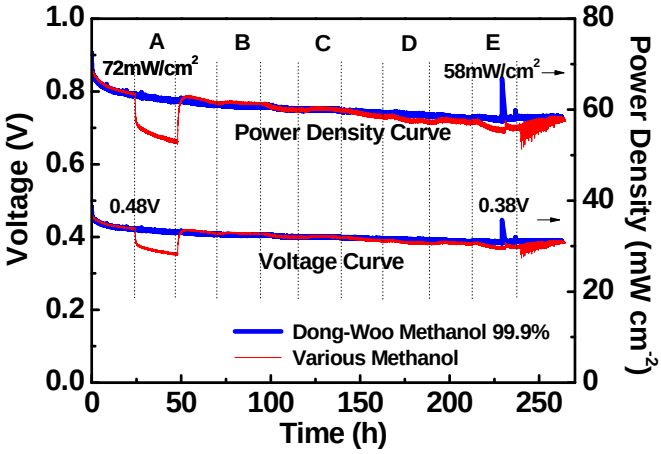

Figure 1: Changes of voltage/power density of the cells during the supply of methanol fuel with different commercial methanol (operating current: 1.35 A (150 mW cm^{-2})).

Such results appear to be proved from anode polarization curve of the cells (Fig. 2) and impedance analysis (Fig. 3). Fig. 2 shows anode polarization curves of the cell supplied with methanol W and methanol A. It was found that anode overpotential loss of the cell supplied with methanol A was higher than that of the cell supplied with methanol W (Fig. 2). In addition, as presented in Fig. 3, charge transport resistance of the cell supplied with methanol A was higher than that of the cell supplied with methanol W. These results indicate that methanol A supplied into a DMFC cell adversely affected electrochemical reactions on the anode electrode. Assumedly, it appears to be ascribed to impurities in commercial methanol A.

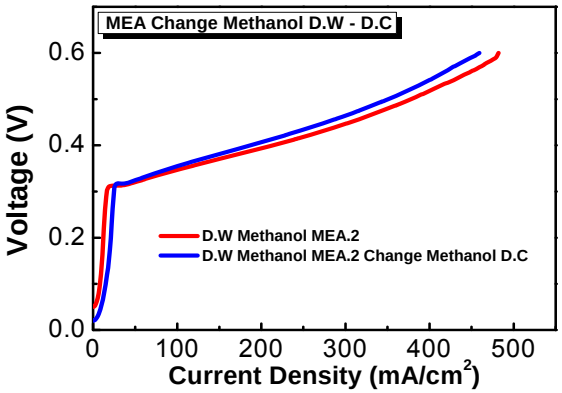

Figure 2: Anode polarization curves of the cell during the supply of methanol fuel with methanol W and methanol A.

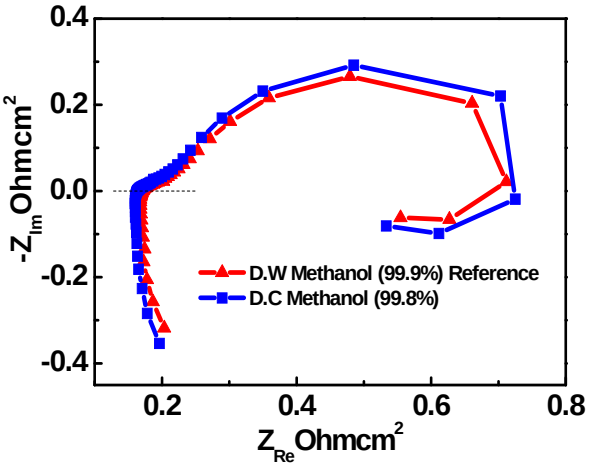

Figure 3: Anode impedance spectra of the cell during the supply of methanol fuel with methanol W and methanol A.

According to Table 1, commercial Methanol A, which showed higher performance loss than the other methanol, includes impurities such as ethanol, acetone, acetaldehydes and ammonia. Therefore, to examine effects on the performance of cells of these impurities in methanol fuel, the following study was performed with methanol fuel adding ethanol, acetone, acetaldehydes, and ammonia of 0.5 wt% to standard methanol W, as presented in Fig. 4. Methanol fuel including different impurities (0.5 wt%) was replaced as the following order; methanol W → methanol W + ethanol (A sector) → methanol W → methanol W + acetaldehyde(B sector) → methanol W → methanol W + acetone(C sector) → methanol W → methanol W + NH_3 solution(D sector) → methanol W.

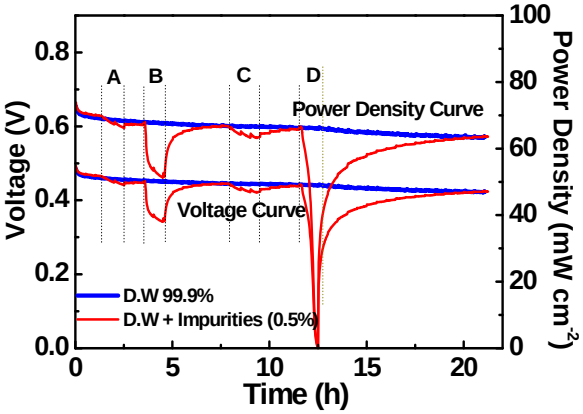

Figure 4: **Changes of voltage/power density of the cell with impurity (0.5 wt%) in methanol fuel with methanol W.**

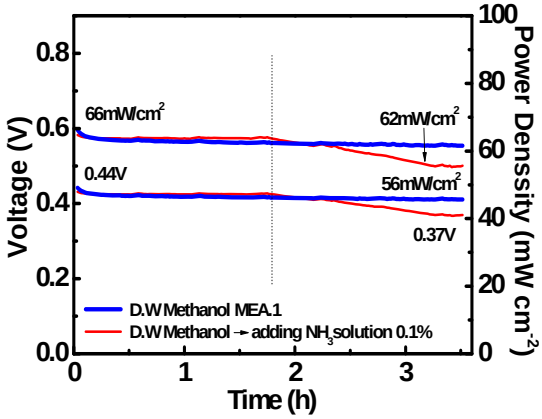

Figure 5: **Changes of voltage/power density of the cell with ammonia in methanol fuel with methanol W (impurities: 0.1 wt%).**

As shown in Fig. 4, when methanol fuel including ethanol or acetone as an impurity was supplied into the cell, the cell voltage slightly dropped from 0.47 V to 0.45 V and 0.44 V, respectively. In contrast, when methanol fuel including acetaldehyde or ammonia was supplied into the cell, the cell voltage significantly dropped from 0.45 V to 0.35 V and 0.0015 V, respectively. Especially, ammonia as an impurity in methanol fuel made the cell severely damaged. However, it should be noted that these impurities did not bring about irreversible performance losses of the cell. Although voltage recovery rate of the cell varied with a kind of impurity, the cell was finally recovered to a normal voltage by supplying methanol W, which includes less impurity.

Fig. 5, Fig. 6 and Fig. 7 exhibit change of voltage/power density of the cells according to concentration of ammonia (Fig. 5: 0.1 wt%, Fig. 6: 0.05 wt%, Fig. 7: 0.01 wt%) in methanol fuel. When methanol fuel including ammonia of 0.1 and 0.05 wt% was supplied into the cell, the cell voltage dropped from 0.44 V to 0.37 V and 0.39 V, respectively (Fig. 5 and 6). On the other hand, when methanol fuel including ammonia of 0.01 wt% was supplied into the cell, the cell voltage did not drop, as shown in Fig. 7. This indicates that the performance of the cell was affected by concentration of ammonia in methanol fuel. These results present that concentration of ammonia in methanol fuel is below 0.01 wt% to avoid the performance degradation by supplied methanol fuel.

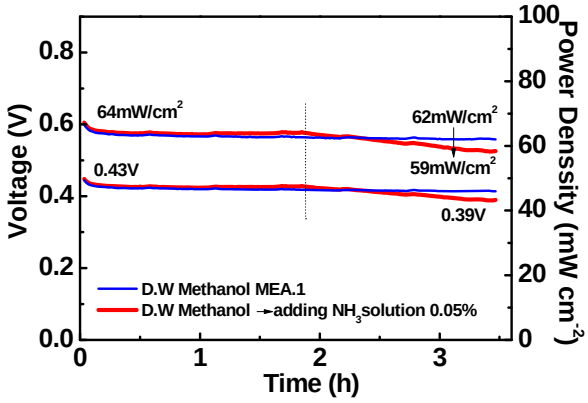

Figure 6: Changes of voltage/power density of the cell with ammonia in methanol fuel with methanol W (Impurities: 0.05 wt%).

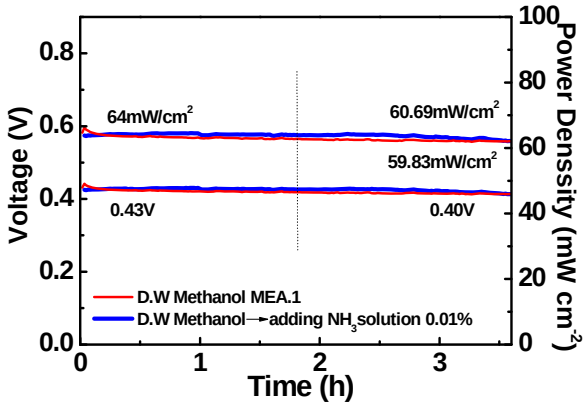

Figure 7: Changes of voltage/power density of the cell with ammonia in methanol fuel with methanol W (Impurities: 0.01 wt%).

To investigate change of electro-activity of the anode catalyst (PtRu/C, HISPEC 12100, Johnson Matthey Fuel Cells) according to the concentration of ammonia in methanol fuel, cyclic voltammetry of the anode catalyst was measured in 0.5 M H2SO4 and 1M methanol solution including ammonia of 0.5 and 0.05 wt%. From cyclic voltammetry of Fig. 8, it was found that as concentration of ammonia increased, oxidation current of methanol gradually decreased. This result indicates that as concentration of ammonia increased, electro-activity of the anode catalyst decreased.

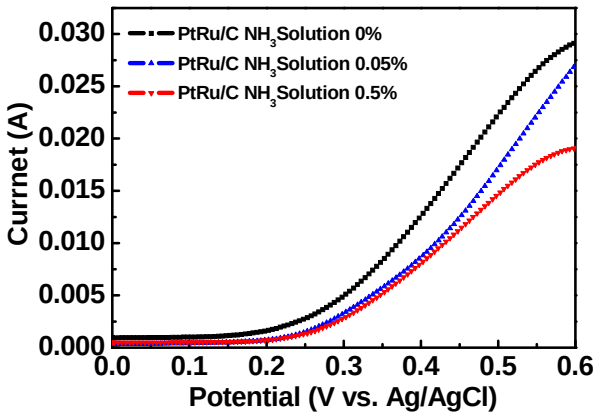

Figure 8: Cyclic voltammetry in methanol fuel with the concentration of ammonia (0.05 wt% and 0.5 wt%)

4 Conclusion

In this study, the effect of impurities in methanol fuel was investigated on the performance of MEA for DMFC. The methanol solution with commercial methanol A was supplied into the DMFC cell, the performance of the cell was decreased

compared with the other methanol solution. When methanol E was supplied into the cell, the performance of the cell was slightly fluctuated. According to the anode polarization curves and impedance spectra, anode overpotential loss and charge transport resistance of the cell supplied with methanol A was higher than that of the cell supplied with methanol W.

The methanol fuel including acetaldehydes or ammonia as an impurity was supplied into the cell, the cell voltage significantly dropped from 0.45 V to 0.35 V and 0.0015 V, respectively. Especially, ammonia in methanol fuel made the cell severely damaged. The performance of the cell was directly affected by concentration of ammonia in methanol fuel. This study present that concentration of ammonia in methanol fuel is below 0.01 wt% in order to avoid the performance degradation by supplied methanol fuel. However, it should be noted that these impurities did not bring about irreversible performance losses of the cell. From the results of cyclic voltammetry, it was found that as concentration of ammonia impurity increased, electro-activity of the anode catalyst decreased.

References

[1] M. Funk, Methanol fuel quality specification study for proton exchange membrane fuel cells", Final report, XCELLSIS, Feb. 2002.

[2] X. Zhao, G. Sun, L. Jiang, W. Chen, S. Tang, B. Zhou, and Q. Xin, "Effects of chloride anion as a potential fuel impurity on DMFC performance", Electrochmical and Solid-State Letters, 8(3) A149-A151 (2005)

[3] Recent Progress in micro fuel cells, T. Yoshida, NTS , Tokyo, 2008

[4] Y. Nishimura, I. Nagai, M. Matsuyama, M. Yamane, M. Yanagida, Y. Miyazaki, "Current Status in Fundamental Research for the Development of Standards for Advanced Application of Fuel Cells", 2008 Fuel Cell Seminar, Phoenix, AZ, Oct. 27-30 2008, GHT35a-13.

[5] Y. Nishimura, K. Mastuyama, M. Ishii, T. Ota, M. Yamamoto, M. Yanagida, I. Nagai, Y. Miyazaki, "Influences of fuel impurities on the performance of direct methanol fuel cells", The 14th Fuel Cell Symposium Proceedings (Japan), pp. 262-264 (2007).

[6] Y. Nishimura, K. Mastuyama, M. Yamamoto, M. Yanagida, I. Nagai, Y. Miyazaki, "Effects of impurities in the fuel on the output performance of DMFC", Fuel Cells (Japanese journal), 7(1), p.60 (2007).

Manufacturing Technologies for Direct Methanol Fuel Cells (DMFCs)

Andreas Glüsen, **Martin Müller**, **Nicola Kimiaie**, **Irene Konradi**, **Jürgen Mergel**, **Detlef Stolten**, Institute of Energy Research – IEF-3: Fuel Cells, Forschungszentrum Jülich, Germany

1 Introduction

Fuel cell research is focussing on increasing power density and lifetime and reducing costs of the whole fuel cell system [1]. In order to reach these aims, it is necessary to develop appropriately designed components outgoing from high quality materials, a suitable manufacturing process and a well balanced system.

To make use of the advantages that can be obtained by developing production technology, we are mainly improving the coating and assembling techniques for polymer electrolyte fuel cells, especially Direct Methanol Fuel Cells (DMFCs). Coating is used for making fuel cell electrodes as well as highly conductive contacts. Assembling is used to join larger components like membrane electrode assemblies (MEAs) and bipolar units consisting of flow fields and the separator plate, as well as entire stacks.

On the one hand a reproducible manufacturing process is required to study fine differences in fuel cell performance affected by new materials or new designs. On the other hand a change in each parameter of the manufacturing process itself can change product properties and therefore affect fuel cell performance.

As a result, gas diffusion electrodes (GDEs) are now produced automatically in square-meter batches, the hot-pressing of MEAs is a fully automated process and by pre-assembling the number of parts that have to be assembled in a stack was reduced by a factor of 10. These achievements make DMFC manufacturing more reproducible and less error-prone. All these and further developments of manufacturing technology are necessary to make DMFCs ready for the market.

2 Coating Technology

An important manufacturing step for Direct Methanol Fuel Cells is the preparation of fuel cell electrodes by coating techniques. It is our aim to understand and, in a later step, to take advantage of the influence of coating technology on electrode properties. For our new pilot production facility, built in 2008/2009 (see below), we chose complementary coating techniques in order to allow comparing different techniques for electrode preparation as well as different ways to integrate the catalyst layer into the membrane electrode assembly (MEA). The electrodes can be prepared onto a gas diffusion layer (GDL) to form a gas diffusion electrode (GDE) or onto a membrane to form a catalyst coated membrane (CCM) [2]. A catalyst layer can be made in one coating step or by coating several thin layers on top of each other. The coating techniques available in Jülich are knife-coating, slot-coating and screen-printing.

2.1 GDE-manufacture by knife-coating

In the past 8 years manual small-scale manufacturing of GDEs was transferred in Jülich to a continuous roll-to-roll knife coating process. GDLs and GDEs are now routinely manufactured in widths of up to 45 cm and a maximum continuous length of 45 meters. For the manufacture of a 90-cell DMFC stack in the kW-class for use in a horizontal order picker in 2009, 30 meters of GDL were continuously manufactured and used as the substrate for the manufacture of GDEs in 5 batches. Batch-size for GDEs was limited because of the high cost of noble metal catalyst and the resulting high economic risk in case of an (improbable) failure of a coating batch. GDL manufacture was made by coating a layer consisting of PTFE (40%) and carbon black (60%) onto teflonized carbon fabric. Dry coating weight was 3.7 mg/cm² with a standard deviation of 0.3 mg/cm² as determined from 80 samples of 20 cm² taken at various positions along the length and the width of the GDL. The standard deviation was approximately the same when comparing samples taken at one lateral position along the length of the GDL and for samples taken at one longitudinal position across the GDL. On top of this GDL the catalyst layers were coated with an average noble metal loading of 2.2 mg/cm² (cathodes) and 2.3 mg/cm² (anodes) and a standard deviation of 0.1 mg/cm² in both cases. Due to this good reproducibility the performance of the individual cells in a 90-cell DMFC stack is very homogeneous as can be seen in Figure 1. Lower cell voltages in the first and the last cell are probably due to thermal loss through the end-plates.

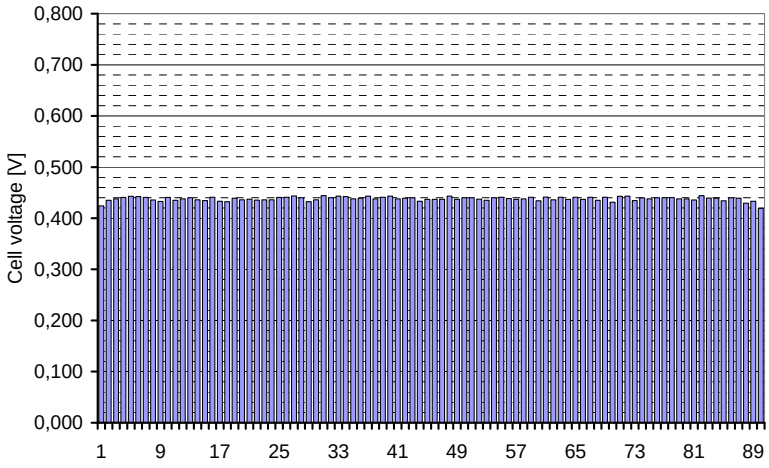

Figure 1: Cell voltage distribution in a 90 cell DMFC stack at a current density of 0.16 A/cm², 70 °C and high air flow rates.

2.2 Advanced coating equipment

In order to further optimize coating technology, a new coating facility was set up in Jülich in 2008 and 2009. In the new coating facility equipment for knife coating, for slot coating and for screen-printing is available. A flexible roll-to-roll coating machine is available for knife coating and slot coating. It has been constructed by Coatema under the brand-name Click & Coat [3]. It consists of several individual modules, which can be combined to a coating machine as required for a specific coating task. Figure 2 shows a coating machine made by combining

several different modules. Figure 3 shows schematically how the machine can be modified to compare different manufacturing processes. While the final production process for GDEs will contain coating and several processing steps, for example drying, sintering and calendering, it may be useful to find out, how the individual process steps can best be combined. For example, it can be studied by changing the machine setup if calendering is more effective before or after sintering. A simpler machine can be combined to just study the basic process consisting of coating and drying. The resulting raw electrode can then be fed into another setup to study and optimize one individual process step. Another roll-to-roll coating machine is specifically designed for slot-coating both sides of a membrane at the same time. This will allow continuous manufacture of CCMs. Single-sided slot-coating is also possible with this machine and will be used for coating membranes as well as decal substrates. Screen printing is done with a standard screen printer as routinely used in the electronics industry.

Figure 2: Flexible coating machine made up of several modules.

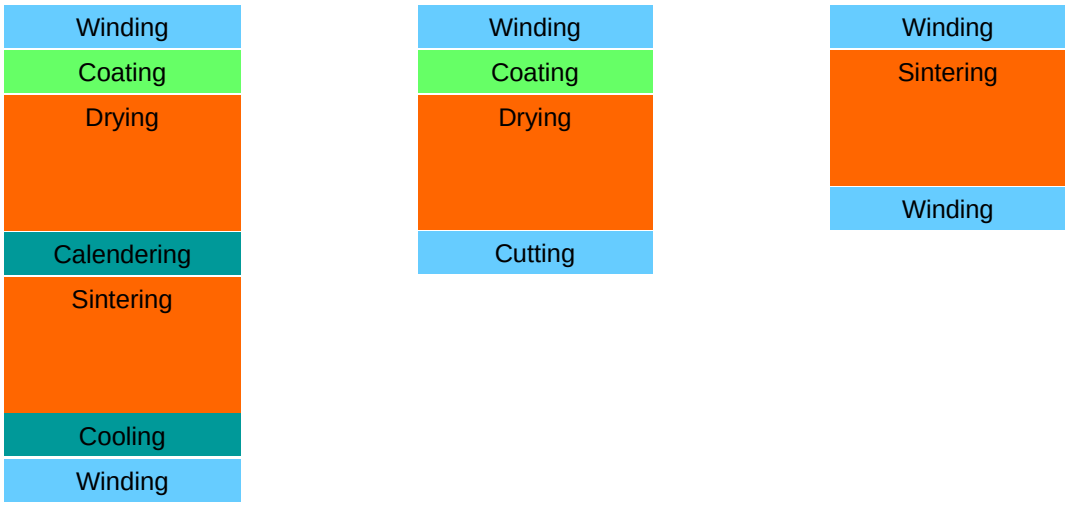

Figure 3: Schematic representation of different machine setups; left: complex machine for coating and several post-processing steps, middle: simple coating machine, right: machine for studying one processing step (here: sintering).

2.3 Substrate for electrode preparation

When electrodes are made by coating onto a GDL (GDE-route), coating is usually easy because the substrate is mechanically and dimensionally relatively stable. All coating techniques are suitable for this route and it is therefore this route that is currently used for all large scale manufacturing projects in Jülich. Coating onto membrane is more difficult, because many membranes are not as stable as the GDLs and because membranes tend to swell during the coating process due to the solvent used in the catalyst ink. These problems can best be avoided by using the screen-printing technique. During the printing process the screen is pressed onto the substrate by the squeegee. This results in a flat substrate during coating even if swelling occurs. An alternative is to coat and dry the catalyst layer on a so called decal substrate and transfer the catalyst layer to the membrane by hot-pressing.

2.4 Coating techniques

Different coating techniques can be used to make catalyst layers from a catalyst ink and they all have their specific advantages and disadvantages. Therefore it is necessary to compare different coating techniques in order to use the best technique for each coating application. The techniques differ in the geometries that can be coated and in the influence the substrate has on the coating result. A general differentiation is between a continuous process where the substrate is passed from roll to roll through the coating equipment and a discontinuous process where individual sheets of substrate are coated one after the other.

Knife coating and slot coating are continuous processes whereas screen-printing is a discontinuous process. The amount of catalyst ink applied in the knife coating process is controlled by the distance of the coating knife and the substrate. The porosity of the substrate, however, leads to an additional amount of ink that penetrates into the substrate. In the slot coating process in contrast, the amount of catalyst applied to the substrate is controlled by a metering pump and independent of the substrate. In both cases the coating amount can be varied continuously. The screen used for screen-printing determines the amount of catalyst ink applied to the substrate. For each variation of the amount of catalyst ink, a different screen has to be made.

3 Assembling

The fabrication of fuel cells and their components can be broken down into a number of assembly steps. The monitoring and verification of material flows and the associated documentation are crucial processes in all assembly steps. The DMFC stacks in the kW range developed at IEF-3 have an active cell area of 315 cm^2 and mainly consist of graphite bipolar plates. For stacks with lower power output stainless steel or other alloys were also tested. In this article the focus is on the assembling process of the graphite material. The assembling of these stacks is consisting of different production steps:

- Manufacturing of the structures by punch cutting and laser or water beam cutting
- Pre-assembly of membrane electrode assemblies (MEAs)
- Pre-assembly of bipolar units outside the stack
- Robot assisted stacking of bipolar units and MEAs

- Mechanical fastening of the stack
- Installation of faceplates

3.1 Membrane electrode assemblies

Outgoing from coated substrates the membrane electrode assemblies (MEAs) were built up. This is done under a temperature of 130 °C and a defined pressure [4] in a hot pressing module. The process is fully automated so that reproducibility can be guaranteed. Figure 4 shows on the left hand the subcomponents of the MEA: Membrane, anodic and cathodic GDE and stabilizing frames. On the right hand the robot assisted supply of the MEA components into the hot pressing module is shown, next to the hot pressing module is a further press module for cooling the components from 130 °C down to environmental temperature. During the pressing process the parameters temperature, pressure and distance between the hardboards are electronically logged.

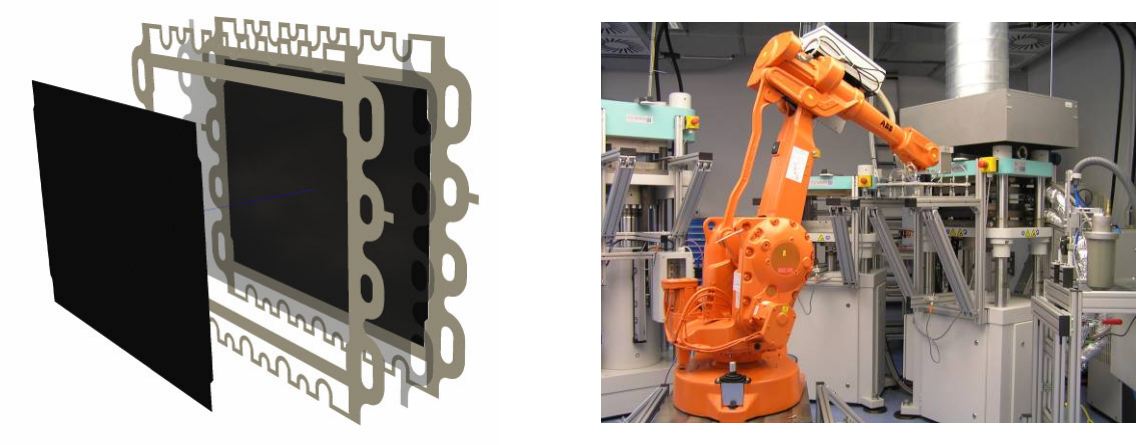

Figure 4: MEA setup and robot assisted MEA production.

The challenge is in handling the flexible electrodes and the flexible membrane under moisture expansion. During this assembling step the very flexible structures of the membrane and the electrodes are transformed in the frame stabilized MEA structure that is easy to handle. After the assembling process the MEAs are ready for stack integration and electrochemical tests.

3.2 Pre-assembly of bipolar units

To produce stacks with a homogeneous media distribution and an even cell voltage distribution it is necessary that the manufacturing tolerances are not affected by the assembly process itself. This is difficult especially if flexible materials like expanded graphite are used. The bipolar units used in DMFC stacks developed at IEF-3 consist among other things of three different expanded graphite layers. By building up the bipolar unit in layers it is possible to adapt the material properties better to the functional demands of each layer. The bipolar unit consists of the flexible cathodic flow field, the firm separator plate, the flexible anodic flow field, centering bolts and a very flexible wick (Figure 5).

One way to achieve a precise and reproducible bipolar unit is to fix these subcomponents with adhesives in a pre-assembling process. With a special adhesive that is stable under the anodic and cathodic conditions and which releases no ionic or organic impurities the different parts of the bipolar unit get bonded.

Pre-assembling of the bipolar unit reduces the number of parts by a factor of eight during the stack assembling process. Compared with using three flexible layers the assembly of the bipolar unit allows to control the manufacturing tolerances before the stack assembly.

The pre-assembling of the bipolar unit is done automatically by a robot technology. The adhesive is deposited on the components by a robot based sprayer. After the deposition of the adhesive the components of the bipolar unit are stacked by the robot (Figure 5). Finally the parts get bonded under pressure and temperature inside the hot pressing module.

The repeat accuracy of the robot is 0.06 mm. Compared with a manual assembly this is very accurate. Furthermore the robot system is flexible so that different tools like vacuum gripper, dispenser and sprayer can be used. A quick release tooling system allows different tools to be connected to the robot with a change-over time of only a few seconds, whereby the robot grips the required tool itself.

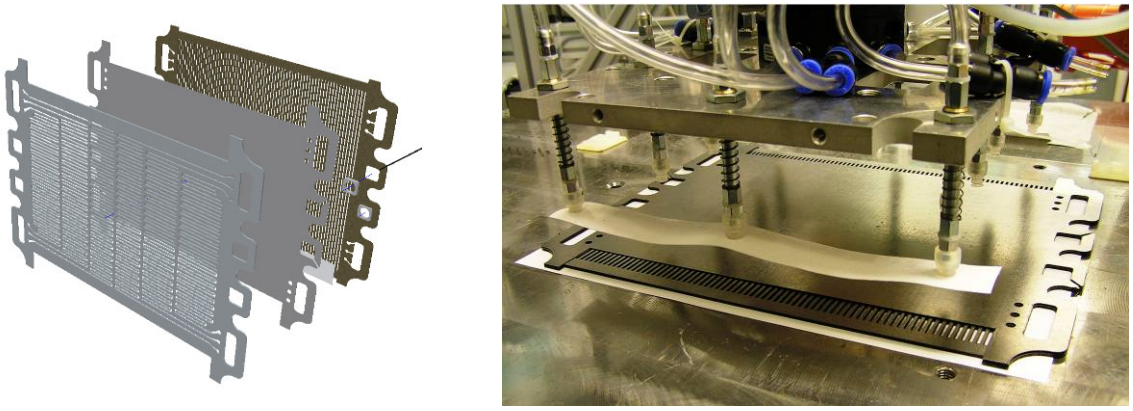

Figure 5: Bipolar unit setup and robot assisted assembly of wick.

3.3 Quality assurance

To know if a different cell performance is affected by a new design or different manufacturing techniques it is necessary to control the manufacturing tolerances of each component of the stack. It is essential that the dimensional compliance is verified in order to reveal possible errors as early as possible.

In contrast to standard components, which have a limited number of characteristic dimensions, a topographic profile of large surfaces must be created for fuel cells. This can be done with the aid of a non-contact 3D laser measurement system and the corresponding analysis software (see Figure 6). Measurement accuracies up to 0.01 µm can be achieved.

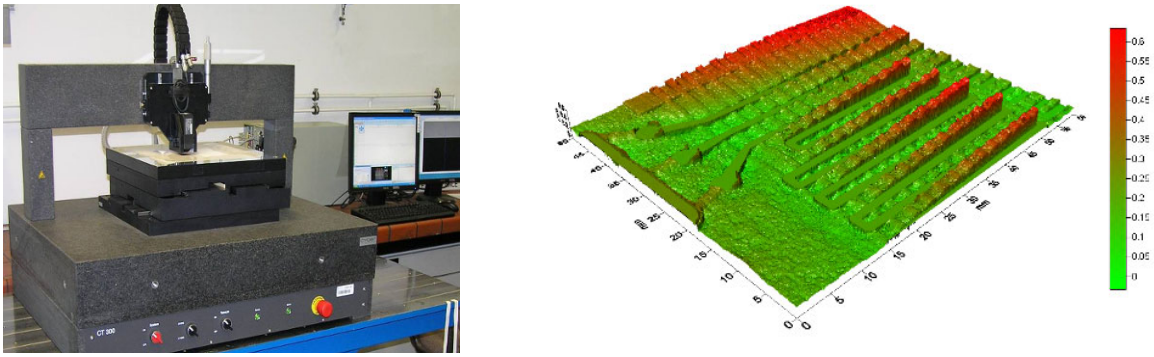

Figure 6: Laser scan device and results of bipolar unit scanning.

3.4 Stack assembling

After all components have passed preassembling and quality control the stack can be built up. Figure 7 shows on the left hand a 90-cell stack built up in 2009 and on the right hand a polarization plot of the same stack at an operating temperature of 70 °C and a methanol concentration in the anodic loop of one mole per litre. This stack is a result of a government-funded project with the aim of introducing DMFC technology into horizontal order pickers. After the first electrochemical tests the stack was integrated into a DMFC system that fits into a horizontal order picker for a 3,000 h duration test [5].

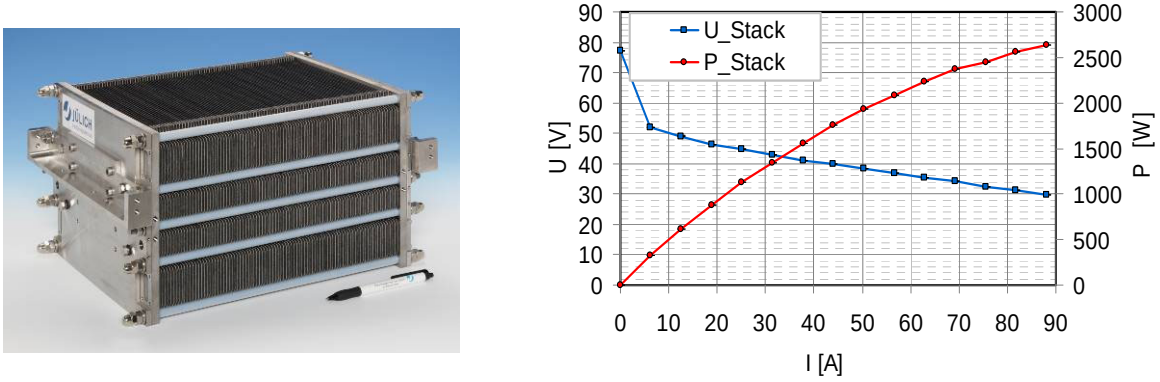

Figure 7: 90-cell DMFC stack and polarization plot.

References

[1] J. Mergel, A. Glüsen, C. Wannek: „Current Status of and Recent Developments in Direct Liquid Fuel Cells“ p. 41ff in D. Stolten (ed.) “Hydrogen and Fuel Cells” Wiley VCH, Weinheim 2010

[2] Q. Mao, G. Q. Sun, S. L. Wang, H. Sun, G. X. Wang, Y. Gao, A. W. Ye, Y. Tian, Q. Xin: „Comparative studies of configurations and preparation methods for direct methanol fuel cell electrodes”, *Electrochimica Acta* 52, 6763 (2007)

[3] T. Kolbusch, A. Glüsen, J. Mergel: „Manufacturing Processes for Gas-Diffusion Electrodes for Polymer Electrolyte Fuel Cells", Presented at World Hydrogen Energy Conference WHEC 2010 Essen: 16.05.2010 – 21.05.2010 and Chapter in this book

[4] A. S. Aricò, P. Cretì, P. L. Antonucci, J. Cho, H. Kim, V. Antonucci: "Optimization of operating parameters of a direct methanol fuel cell and physico-chemical investigation of catalyst-electrolyte interface" *Electrochimica Acta* 43, 3719 (1998)

[5] H. Jansen, M. Hehemann, J. Mergel, D. Stolten: „System technology aspects for light traction applications of direct methanol fuel cells", Presented at World Hydrogen Energy Conference WHEC 2010 Essen: 16.05.2010 – 21.05.2010 and Chapter in this book

Applying Methanol Vapor in Passive Planar DMFC as Micro Power Sources

Xiaohui Tian, **Thomas Jungmann**, **Georgios Sandris**, **Christopher Hebling**, Fraunhofer Institute for Solar Energy Systems, Freiburg, Germany

1 Introduction

The today's personal electronic devices challenge the power sources more strongly due to the enhanced features of the devices which consume much more energy than before. For example, the electrocardiography (ECG) device as demonstrator shown in this work can only work for approx. 24 hours with one piece of normal AA battery. This gives patients and doctors inconvenience for a long-term and non-Stop monitoring as well as data recording. Beside high capacity batteries like Li-ion battery the fuel cells, especially direct methanol fuel cells (DMFCs), seem to be suitable potential solution for replacing the conventional batteries because of the high energy density of liquid methanol, easy recharging and handling [1].

However, the special characteristics of DMFC, methanol crossover, determines that only diluted methanol solution (normally 1 – 2 mol/l) could be used in DMFC and in the most cases pumps, valves or other side equipments are needed. This increases the complexity of BOP (Balance of Plant) and therefore reduces the system efficiency [2-5].

In this work a unique planar DMFC system designed as micro power sources with fully passive operation is introduced. The specialty is to use methanol vapor passively at anode side under methanol boiling point which is realized by a phase separation membrane as the evaporator. The air-breathing cathode allows oxygen to enter fuel cell by natural diffusion. Based on the previous studies [6,7] the DMFC fed with methanol vapor (vDMFC) shows more advantages than the traditional liquid DMFC. The gaseous reactant has better reaction kinetics than liquid feed. The single gas phase inside fuel cell reduces the mass transport problem, for instance, no more block of methanol to catalyst layer by produced CO_2 bubbles. Using high concentrated or even pure methanol becomes possible because no liquid methanol directly touch the anode catalyst layer, but only methanol vapor. Therefore, the methanol crossover problem is not as big as liquid DMFC. As consequence the energy density can be greatly increased. The passive delivery means no active devices like pumps etc. needed so that the vDMFC system could be constructed with very compact design and light weight which is suitable for the portable applications.

2 Working principle of vapor fed DMFC (vDMFC)

One of the core components in vDMFC is the phase separation membrane (PS-membrane) working as passive evaporator shown in Fig. 1. The PS-membrane is a polymer-based fine porous layer covered with very thin silicon film on one side. The liquid methanol can not directly go through this PS-membrane, but is first absorbed on the silicon side, then diffuses through the membrane to the other side and is desorbed as vapor phase from the other side. This absorption / desorption process realizes methanol change from liquid phase to vapor phase. The PS-membrane can also prevent overload of liquid (pure) methanol to the anode

which can cause overheating by enormous methanol crossover. So this membrane can also work as self-regulator.

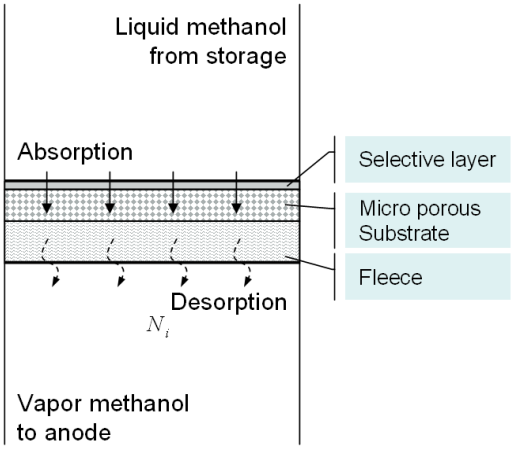

Figure 1: Schematic representation of phase separation membrane which consists of 3 layers: Selective silicon layer, micro porous substrate and fleece.

The pure methanol is used in this work without extra water supply. The water required for anodic reaction comes from ambient humidity. The water vapor from the air diffuses from cathode side through the membrane to the anode to start the reaction. Once the reaction is activated, the more water will be produced at the cathode side and go back to the anode by back-diffusion.

3 Characterization of vDMFC-operation

To evidence that water vapor in the air with normal relative humidity (rH) is sufficient for activating the reaction, an “air-box” with closed and defined volume was constructed for testing condition change affected by the open cathode. Several sensors were integrated in the “air-box” to measure the environmental parameters such as concentration of oxygen, methanol, rH, temperature, pressure and so on. Fig. 2 shows a typical measurement curves recorded during the vDMFC working in the “air-box”. During the first several minutes the rH (green line) in the box reduced quickly from 50% to 45% and then kept increasing up to 70%. This evidences that the water is consumed from the environment to activate the reaction and then produced from the reaction. The temperature (black line) rise from room temperature 25°C to 33°C and oxygen concentration (blue line) decrease confirm the reaction taking place. The methanol concentration (red line) in the box at the cathode side was recorded about 16 times higher than that at beginning which means methanol crossover still existed with methanol vapor feed at anode, but acceptable with 100% methanol in the anode tank.

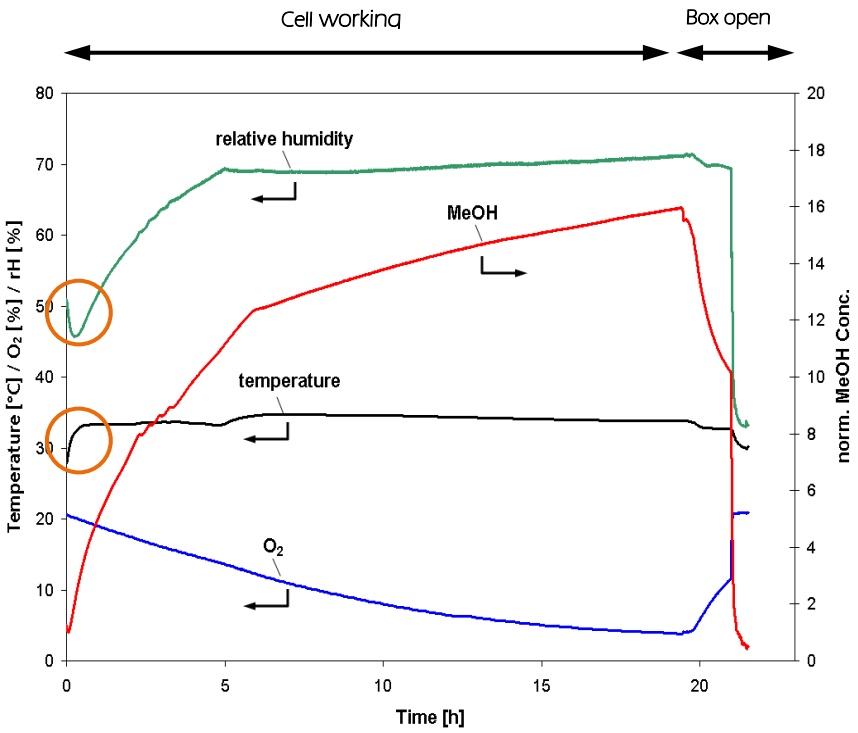

Figure 2: Measurement curves of environmental parameters recorded in the „air-box“ during the vDMFC working. Cathode side faces into box. Anode side is coupled with methanol tank containing pure methanol. Experiment was conducted at room temperature without heating device.

Several measurements were carried out with vapor and liquid methanol solution in the test cell setup described in [5] which was fully passive operated and temperature controlled. A comparison result is shown in Fig.3. At 50°C and passive operation the vDMFC yields over 20 mW / cm² which is higher than 0.5 M and 1 M liquid methanol DMFC.

A number of MEAs designed for vDMFC were screened in the test cell setup at 30°C and 50°C, respectively. The maximal power densities of each MEA are summarized in Fig.4. Most of the MEAs work at high temperature well with about 20 mW / cm² or more. At lower temperature the produced power densities are generally much lower than that at 50°C due to the worse reaction kinetics and less methanol vapor evaporation.

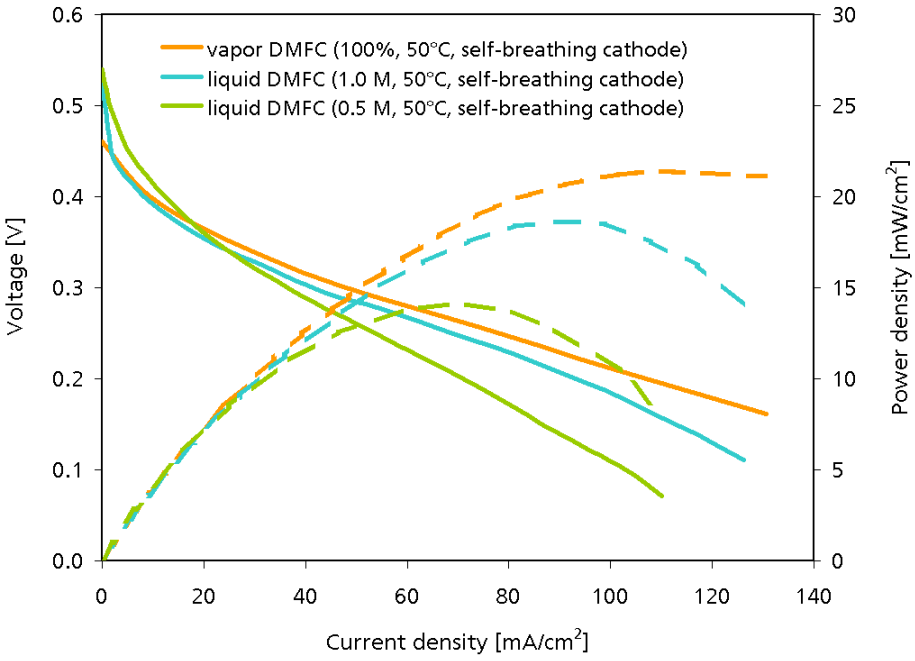

Figure 3: Comparison of cell performance of vDMFC (100% methanol) and liquid DMFC (0.5 M / 1 M) at the same condition.

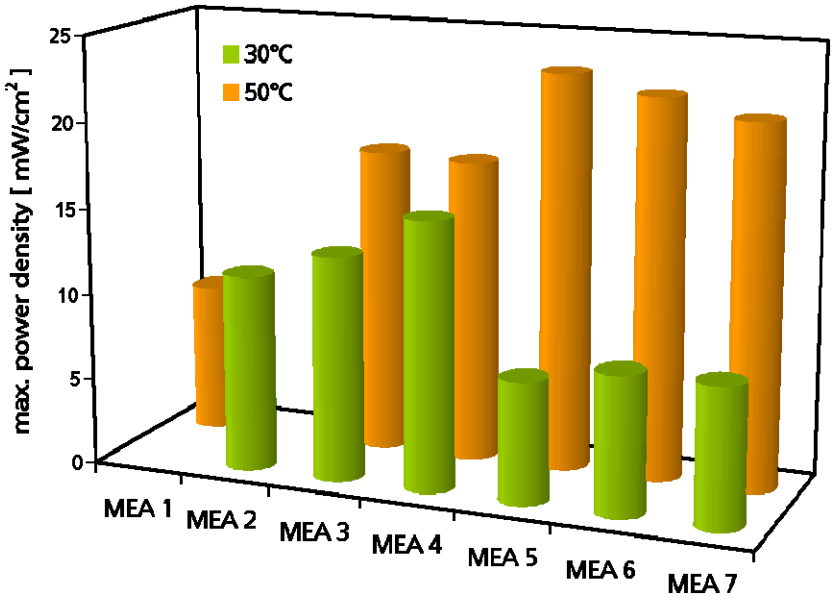

Figure 4: Summary of max. power densities of different MEAs in vDMFC at 30°C and 50°C.

4 Realization of vDMFC-prototype

The cross-section illustration of a vDMFC module is shown in Fig.5 (a) which includes CO_2 absorber, methanol tank and vDMFC. The methanol vapor and produced CO_2 can enter or get out of the cell through the separated channels. Because the single vDMFC has a very

low working voltage, in the final demonstrator a 4-cell system with series connection was designed for a high total voltage as shown in Fig.5 (b). The size of the planar vDMFC is 47x75x4 mm and the whole system is 15 mm thick. In the methanol tank min. 6 ml Methanol can be stored and delivered passively into anode independent of position. The entire system can deliver about 50 mW so far.

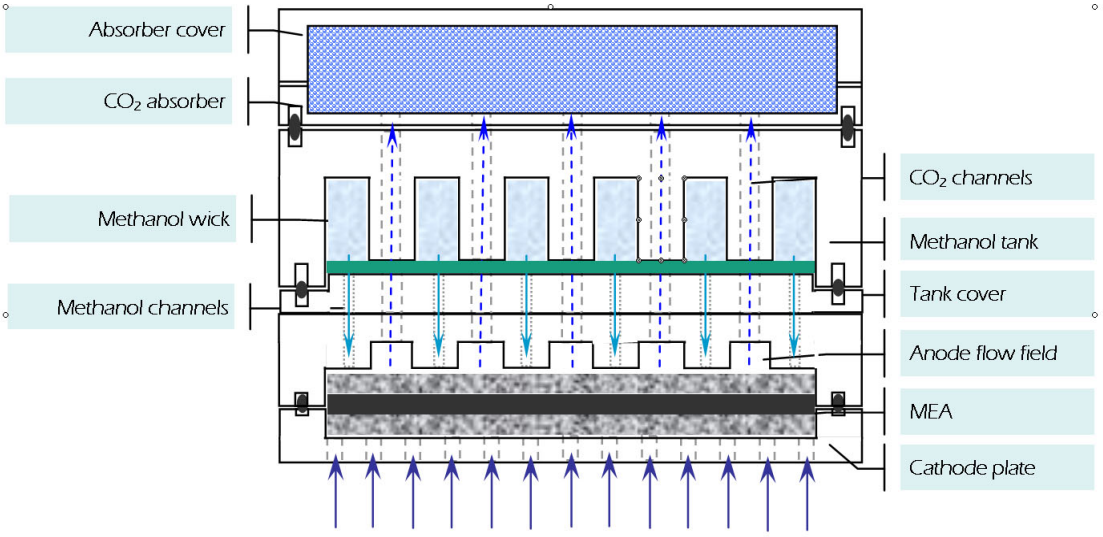

a)

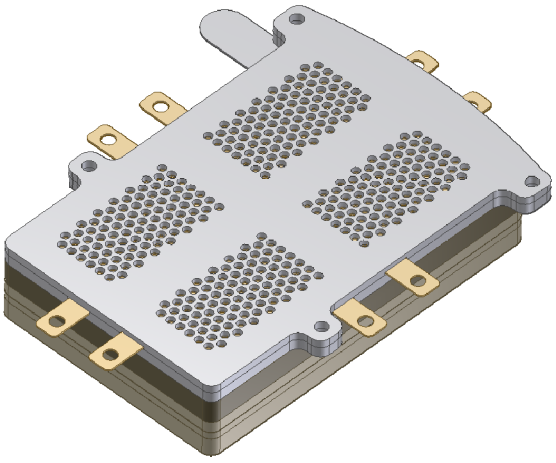

b)

Figure 5: (a) Illustration of a vDMFC cross-section and (b) complete 4-cell system assembly.

References

[1] S.K. Kamarudin, W.R.W Daud, S.L. Ho and U.A. Hasran, Journal of Power Sources, 163 (2), 743-754 (2007)

[2] J. H. Han, H. T. Liu, Journal of Power Sources, 164 (1), 166-173 (2007)

[3] A. Oedegaard, C.Hebling, A. Schmitz, S.Möller-Holst, R. Tunold, Journal of Power Sources, 127 (1-2), 187-196 (2004)

[4] J.G. Liu, T.s. Zhao, R.Chen and C.W. Wong, Electrochemistry Communications, 7 (3), 288-294 (2005)

[5] S. Eccarius, X. Tian, F. Krause, K. Beard and C. Agert, Journal of Micromechanical and Microengineering . 18, 2008

[6] S. Eccarius, B. Garcia, C. Hebling, J. W. Weidner, Journal of Power Sources, 179 (2), 723-733 (2008)

A Novel Power Generation System Based on Combination of Hydrogen and Direct Carbon Fuel Cells for Decentralized Applications

Nazim Muradov, **Franklyn Smith**, **Pyoungho Choi**, **Gary Bokerman**, University of Central Florida, USA

Abstract

Fuel cell (FC) based power generation systems are characterized by highest chemical-to-electrical (CTE) energy conversion efficiency compared to conventional power generators (e.g., internal combustion and diesel engines, turbines). Most efforts in this area relate to hydrogen-FC coupled with hydrocarbon fuel reformers (HFR). However, the overall CTE efficiency of the combined HFR-FC systems is relatively low (about 30-35%). The objective of this work is to develop a highly-efficient power generation system integrating a hydrocarbon decomposition reactor (HDR) with both hydrogen and direct-carbon FC. A unique feature of direct carbon FC is that its theoretical CTE efficiency is close to 100% and the practical efficiency could rich 80-90%. The concept of the integrated hydrogen and direct carbon FC system is discussed and the experimental data on the performance testing of a HDR coupled with PEM FC are presented in this paper.

1 Introduction

In view of dwindling resources of hydrocarbon fuels, it is imperative to substantially increase the efficiency of power generation systems. Fuel cells (FC) are considered the most efficient chemical-to-electrical (CTE) energy conversion devices. Most of R&D efforts in this area are focused on hydrogen-fuelled FC, including proton exchange membrane (PEMFC), alkaline (AFC), molten carbonate (MCFC) and solid oxide (SOFC) FC. Typically, FCs are coupled with reformation units that provide hydrogen-rich gas to the FC. Due to availability of hydrocarbon fuels and the convenience of their storage, hydrocarbon fuel reformers (HFR) are predominant type of reformers for a variety of applications. However, the overall CTE efficiency of the combined HFR-FC systems is relatively low (about 30-35%) mainly due intrinsic limitations of hydrogen-FC theoretical efficiency (70%) and significant losses (20-40%) in HFR.

FC utilizing elemental carbon as fuel (called direct carbon fuel cells, DCFC) have received relatively little attention, compared to H_2-powered FC. In DCFC, solid carbon is introduced to the anode compartment where it is electro-oxidized to CO_2 generating electricity:

$$C + O_2 \rightarrow CO_2 \qquad E^o = 1.02\ V \qquad (1)$$

Figure 1 depicts the comparison of different fuels in terms of their theoretical (maximum) and actual (or practical) efficiency (Cao et al, 2007). The actual efficiency of DCFC could be defined by the following equation:

$$\eta = \frac{\Delta \mathrm{G(T)}}{\Delta \mathrm{H}} \mu \frac{V}{V_o} = \frac{\Delta G(T)}{\Delta G + T\Delta S} \mu \frac{V}{V_o} \tag{2}$$

where, η is FC actual efficiency, ΔG, ΔH and ΔS are free energy, enthalpy and entropy of the reaction (1), μ is a fuel utilization coefficient, V and V_o are operating and open circuit voltages of FC, and V/V_o is a voltage efficiency.

Since for the reaction (1) $\Delta S \approx 0$, and assuming that for DCFC $\mu \approx 1$ (since the fuel-carbon and the product CO_2 exist in separate phases, allowing full conversion of carbon in a single pass) and $V/V_o \approx 0.8 \div 0.9$, the efficiency of DCFC could be as high as 80-90%.

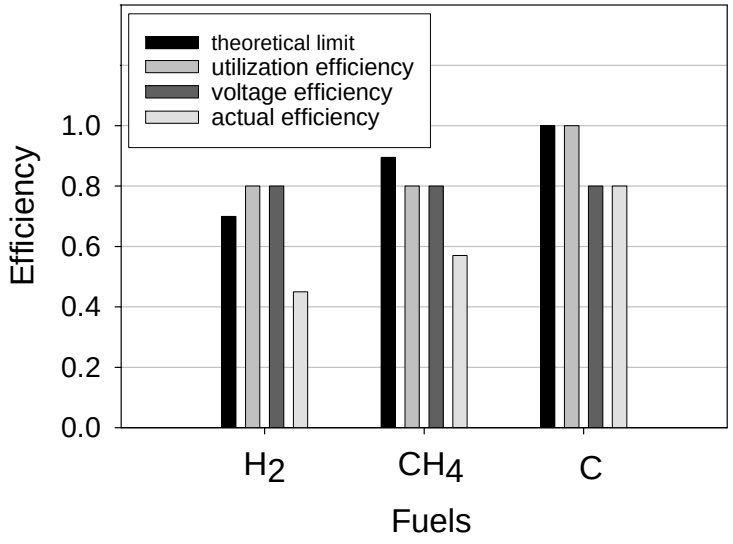

Figure 1: Comparison of efficiencies of fuel cells using different fuels.

Recently, DCFC has been under the development and efficiencies reaching 80% have been demonstrated (Cherepy et al, 2005). The objective of this work is to develop a highly-efficient electrochemical energy conversion device based on the integrated operation of hydrogen- and carbon-powered fuel cells.

2 Experimental

Methane (99.99 v.%) was obtained from Air Products and Chemicals, Inc. and used without further purification. Methane was catalytically decomposed over carbon-based catalysts at 850-900^{o}C in a hydrocarbon decomposition reactor (HDR) to produce hydrogen-rich gas. All experiments were conducted at atmospheric pressure. On-line analysis of the effluent gas was performed gas chromatographically (TCD, Ar-carrier gas, silica gel column and FID, He-carrier gas, HysepD_b column). Analysis of carbon products was conducted by X-ray diffraction (XRD, Rigaku) and scanning electron microscopic (SEM, Jeol 6400F) methods. A single and four-cell PEMFC stack was assembled from parts provided by Fuel Cell Technologies Inc. and tested using different H_2-CH_4 mixtures and the effluent gas from the HDR. An individual cell consists of a 25 cm^2 single serpentine flow field on both anode and

cathode. In measuring polarization curves, current was stepped up from zero to the maximum test current density with an increment between 10 and 100 mA cm^{-2}. A 100A Model 890B Scribner load box (Scribner Associates, Southern Pines, NC) with a built-in current interrupt resistance measurement was used for the polarization measurements.

3 Results and Discussion

The proposed concept is based on the integration of a HDR, DCFC and H_2-powered FC (PEMFC or SOFC), as shown in Fig. 2. In the HDR, hydrocarbon fuel (e.g., methane or natural gas) is catalytically decomposed (T=800-900^{o}C) to hydrogen-rich gas and carbon. The hydrogen-rich gas can be used in PEMFC or SOFC, whereas, the carbon product is withdrawn from the HDR and used in the DCFC with the efficiency of 80-90%. The combination of the HDR with SOFC is more preferable (than with PEM), because of better thermal integration of the HDR and SOFC operating in a close temperature range (850-900^{o}C). High-temperature heat generated by SOFC could be used to drive the hydrocarbon decomposition reactions (in case of methane, about 20% of the SOFC heat output would be necessary). The remaining portion of the thermal output of the SOFC (steam + CO_2) could be used to produce additional electricity via a turbine (or a Rankine cycle) with the efficiency of 30-35%.

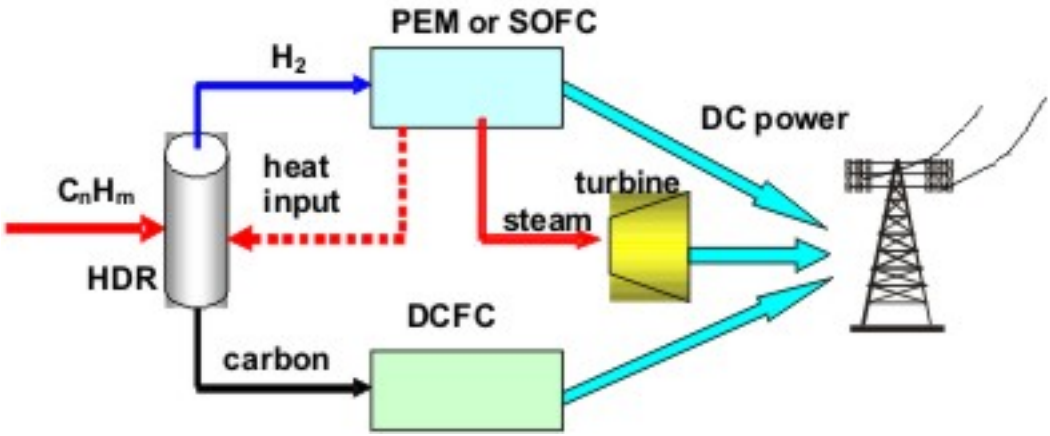

Figure 2: Simplified schematic diagram of integrated power generator.

The concentration of hydrogen in the hydrogen-rich gas depends on the nature of hydrocarbon and operating temperature in the HDR; at the temperature range of 800-900^{o}C, the hydrogen concentration is in the range of 40-80 vol%, the balance being predominantly methane along with small amounts of C_2+ hydrocarbons. If a low-temperature (80^{o}C) PEMFC is used, H_2 is consumed with the efficiency of 40-45%, while methane exits the FC intact and is used as a heat source for the HDR (e.g., via its combustion). In the case of high-temperature (900^{o}C) SOFC, both components of the H_2-CH_4 mixture are consumed as fuel with the average efficiency of 45-50%.

H_2-CH_4 mixtures with the hydrogen concentration of 40-50 vol.% were obtained by thermocatalytic decomposition of methane as a feed at 850-900^{o}C and atmospheric pressure. High-surface area amorphous forms of carbon were used as catalyst for the

process (Muradov et al., 2005, 2009). Before introducing H_2-CH_4 mixture to PEMFC, it is necessary to purify it of possible CO impurities (although there is no oxidant is present in the feed, CO could be formed in the HDR due to presence of moisture and oxygenated groups on the surface of carbon catalyst). Reduction of CO concentration in the hydrogen-rich gas down to 10 ppmv and below was accomplished via the methanation reaction by passing the gas over Ru/Al_2O_3 catalyst at 350^{o}C, as follows:

$$CO + 3H_2 \rightarrow CH_4 + H_2O \qquad (350\ ^oC)$$

Two series of experiments were conducted: with a single cell and four cell stack PEMFC. The experimental set-up for testing the four-cell stack PEMFC is shown in Fig. 3.

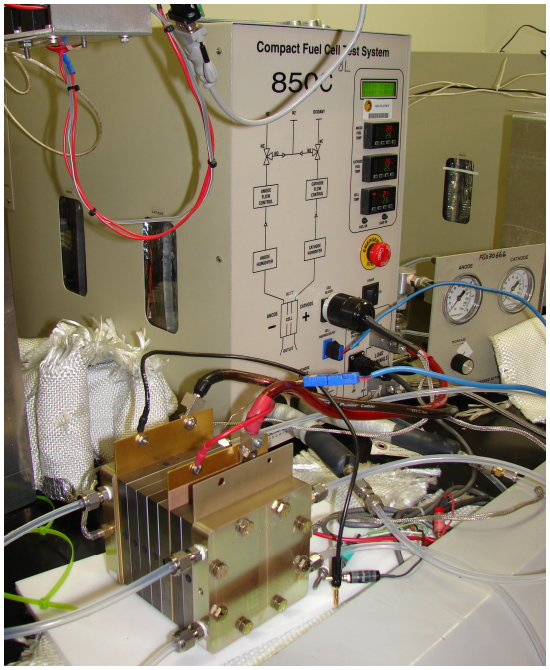

Figure 3: Experimental set-up with a four-cell PEMFC stack with an internal humidifier.

The H_2-CH_4 mixture could be directly fed to PEMFC without a need for an elaborate gas conditioning and purification systems such as water gas shift and preferential oxidation units required by conventional reformers. Figure 4 shows the results of performance testing of a single-cell PEMFC using the hydrogen-rich gas produced in the HDR. The HDR-PEMFC system ran for several hours without deterioration. These data indicate that PEMFC could be successfully operated on the H_2-CH_4 feed produced from hydrocarbon fuels.

We have conducted extensive studies on the characterization of carbon products of the process. The data indicate that carbon exhibits certain three-dimensional ordering, however, it lacks the perfect structural order characteristic of graphite (which is typical of turbostratic carbon). It has been reported that turbostratic carbon exhibited unusually high electrochemical reactivity in molten carbonate-based DCFC (Steinberg et al, 2002).

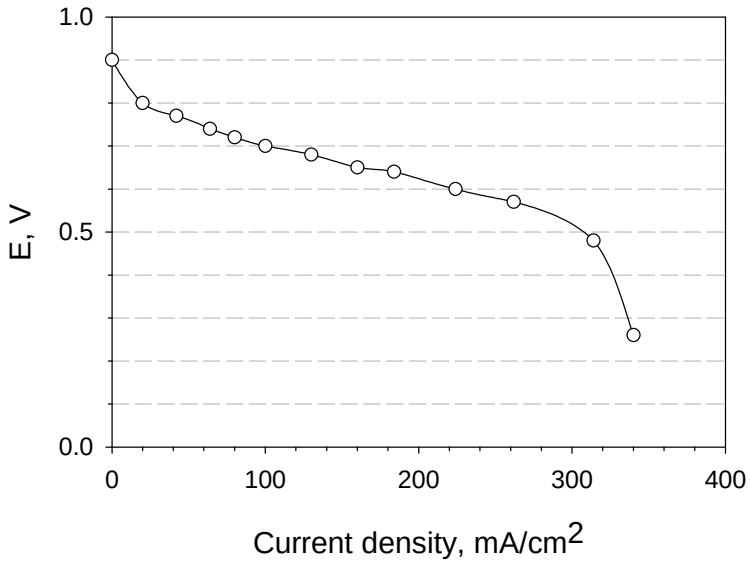

Figure 4: Performance testing of a single cell PEMFC using hydrogen-rich gas produced by hydrocarbon decomposition reactor operating on methane as a feedstock.

The overall CTE of the integrated system (including a turbine) operating on methane was estimated at 49% and 79% with PEMFC and SOFC options, respectively. Thus, the CTE of HDR-SOFC-DCFC integrated system is about two times higher than that of a conventional reformer-FC system.

Concluding, the advantages of the proposed integrated power generator over conventional reformer-FC based power generators are as follows: (1) significantly higher overall CTE efficiencies, (2) thermal integration, which simplifies the thermal management of the system, (3) the lowest amount of CO_2 emissions per kWh produced, (4) production of sequestration-ready CO_2 (since CO_2 is produced in FCFC in a concentrated form), which obviates the need for costly and an energy intensive capture of CO_2.

References

[1] Cao D. et al, J. Power Sources, 167, 250-257, 2007.

[2] Cherepy N. et al, J. Electrochem. Soc. 152, 80-87, 2005.

[3] Steinberg, M., Cooper, J., Cherepy, N. Proc. AIChE 2002 Spring Meeting, New Orleans, 2002, 2112-2127.

[4] Muradov, N., Smith, F., Raissi, A. Catalytic Today, 102-103, 225-233, 2005.

[5] Muradov, N., Smith, F., Bokerman, G. J. Phys. Chem. C, 113, 9737-9747, 2009.

Durability of MEA Prepared with PFA-g-PSSA Membrane for Direct Methanol Fuel Cell

Dong-Hyun Peck, **Segoo Kang**, **Byung-Rok Lee**, **Doo-Hwan Jung**, Fuel Cell Research Center, Korea Institute of Energy Research (KIER), Daejeon, Korea

1 Introduction

The direct methanol fuel cell (DMFC) is considered as a promising power source for portable multifunctional electronic devices and light-duty vehicles. The long-term stability of membrane materials for membrane electrode assemblies (MEAs) is of significant concern due to the degradation of cell components. The prepared sulfonic acid membranes with radiation-induced grafting method are potential substitutes for their corresponding commercial fuel cell membranes. The poly(tetrafluoroethylene-co-perfluorovinylether) (PFA) films as a polymer substrate with thermal, chemical and mechanical stabilities is used in this work. To evaluate long-term stability of the prepared MEA with radiation-grafted membrane (PFA-PSSA) for DMFC, the single cell is tested for 2000 h in a galvanostatic mode at a constant current density of 150 mA/cm^2 at 60 ^{o}C. During the long-term test, the changes in the cell performance are analyzed by the polarization curves, impedance spectra, the voltage and the output power of cell for roughly time intervals of 500 h.

2 Experimental

The polymer membrane was prepared by the simultaneous polymerization of styrene onto PFA films. Poly(tetrafluoroethylene-co-perfluorovinylether)-grafted-polystyrene sulfonic acid (PFA-g-PSSA) membranes were prepared by radiation-induced grafting method using a simultaneous irradiation technique of styrene onto PFA films with thickness of 50 μm and a subsequent sulfonation in a chlorosulfonic acid/dichloroethane mixture.

PtRu/C (HiSPEC 12100, Johnson Matthey) and Pt/C (HiSPEC 13100, Johnson Matthey) catalysts are used as the catalysts for anode and cathode, respectively. The Pt loading was 2 mg/cm^2 for the electrodes and the active area of the MEA was 9 cm^2. The MEA using PF50-SS50 membrane was fabricated by hot pressing method at 150 ^{o}C with a pressing pressure of 50 kg/cm^2 for 1 min (PFx-SSy: x = thickness of PFA film, y = DOG (degree of grafting) of polystyrene)

For long-term performance test of the MEA, a 1.0 M methanol solution (1.3 cc/min) and air (200 cc/min) were fed in the anode and cathode electrodes, respectively. The long-term performance test was carried out at a constant current density of 150 mA/cm^2 (1.35 A) for 2000 h at the temperature of 60 ^{o}C .

3 Results

SEM photographs of the cross-section of the PFA-g-PSSA films are shown in Figure 1. The thickness of PFA-g-PSSA films increased from 64 μm to 81 μm as increased the DOG of the membrane from 30 % to 80 % as shown in Fig 1. The enlarged images of Figure 1(a), 1(b)

and 1(c) are shown in Figure 1(d), 1(e) and 1(f). These SEM results confirm the incorporation of polystyrene in the pores of PFA films.

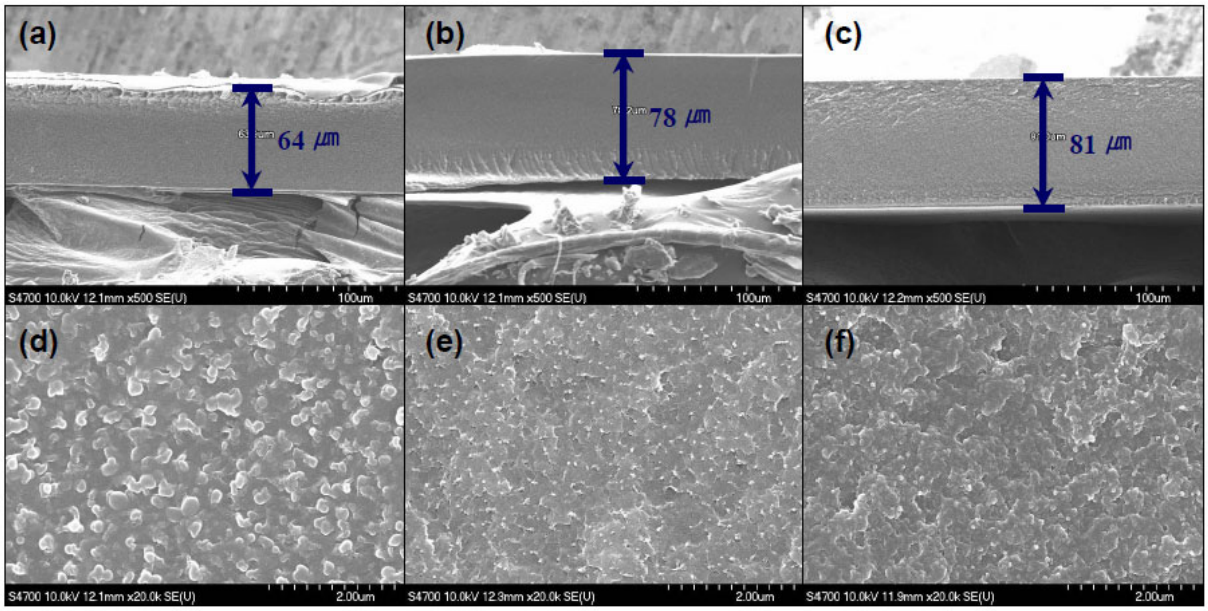

Figure 1: SEM images of the cross-section of the radiation-grafted membranes: (a, d) PF50-SS30, (b, e) PF50-SS50, (c, f) PF50-SS80.

Figure 2 shows the polarization curves of the single cells with the radiation-grafted membranes (PF50-SS30, PF50-SS50 and PF50-SS80). The power densities of the cells with the PF50-SS30, PF50-SS50 and PF50-SS80 membranes were 113, 123 and 118 mW/cm^2, respectively, at a constant cell voltage of 0.4 V. In addition, the ohmic resistance of single cell were 0.109, 0.104, and 0.105 Ωcm^2, respectively. The cell with PF50-SS50 membrane shows the highest cell performance than the other cells.

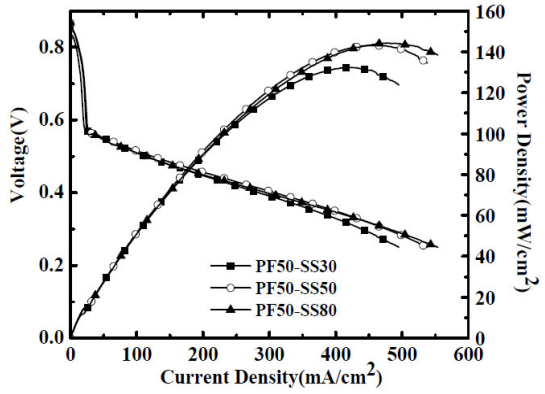

Figure 2: Polarization curves of the single cells with PFA-g-PSSA membranes at 60 °C.

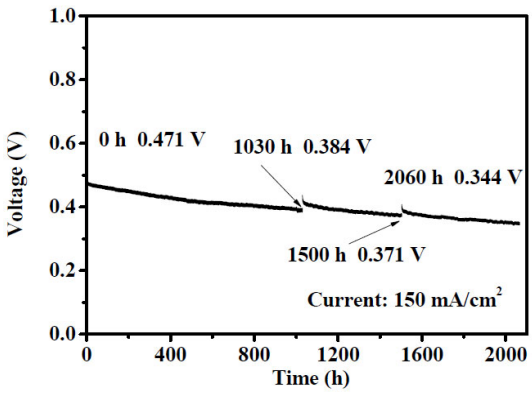

Figure 3: Long-term performance of a single cell based on the PF50-SS50 membrane at 60 °C.

Figure 3 shows the long-term performance of the cell based on the PF50-SS50 membrane for 2000 h at constant current density of 150 mA/cm^2 and 60 ^{o}C. At the beginning of the test, the cell provides 0.471 V (70mW/cm^2) of cell voltage and the cell voltage drop to 0.344 V (51.6 mW/cm^2) after 2000 h operation. The observed power density loss over the 2000 h period is about 26.2% (70 mW/cm^2 → 51.6 mW/cm^2). The decay rate of the cell voltage during 2000 h operation was determined to be about 61.6 μV/h.

In order to evaluate for MEA degradation, polarization curves were measured before and after the long-term test as shown in Figure 4. The initial peak power density of single cell was 143 mW/cm^2, and after preformed long-term test for 2000 h, the peck power density reduced to 86 mW/m^2.

Figure 5 shows the impedance spectra of the single cell at 0.4 V during the long-term test. The impedance arc increases with decreasing polarization due to increase charge-transfer resistance. On the impedance analysis results, the ohmic resistance of single cell increased from 0.101 to 0.103 Ωcm^2 after long-term operation.

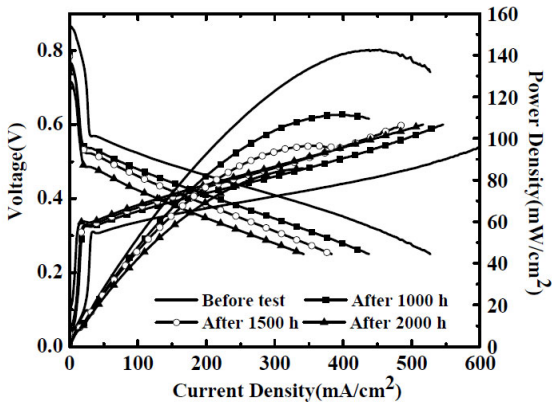

Figure 4: Polarization and power density curves of the cells before and during long-term test.

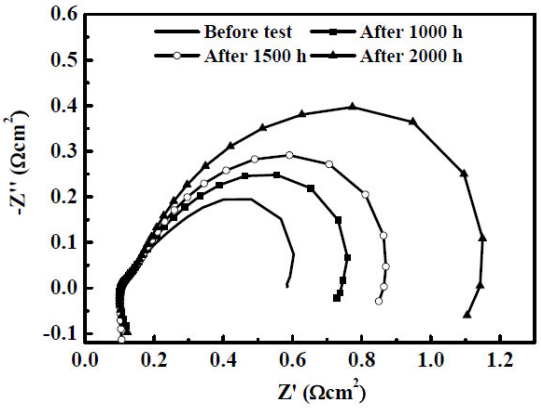

Figure 5: Impedance spectra of the cell according to polarization.

Figure 6 illustrates the powder X-ray diffraction (XRD) patterns of the anode and cathode catalysts. The XRD patterns exhibited primarily an intense diffraction peak (002) at 2θ = 26^o for carbon in the carbon paper. The characteristic peaks corresponding to Pt (111), (200) and (220) were identified from Pt and PtRu catalysts. These peaks indicated that Pt was present in the face-centered cubic (fcc) structure and the Pt (220) peak was selected to calculate the particle size of catalyst.

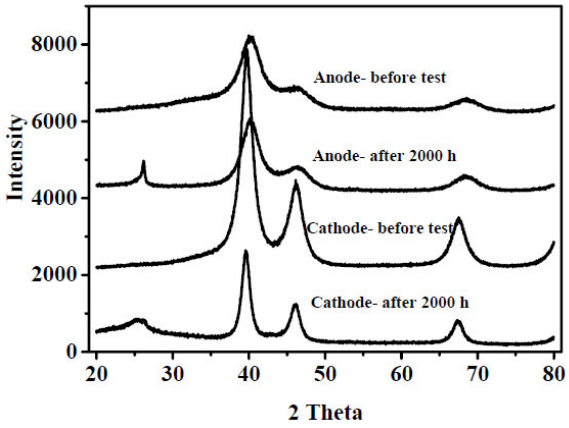

Figure 6: XRD patterns of the anode and cathode catalysts before and after long time test.

The mean particle sizes of the catalysts are summarized in Table 1. The change of particle size of the cathode and anode catalysts varied in the range of 0.5 nm and 2.0 nm, respectively. All the particle size of catalysts increased after long-term performance test and the particle size of the cathode catalyst increased much higher than the anode catalyst.

Table 1: Mean particle size of the catalysts calculated from XRD.

	Anode		Cathode	
	Before test	After 2000 h	Before test	After 2000 h
Particle size (μm)	2.0	2.5	4.1	6.1

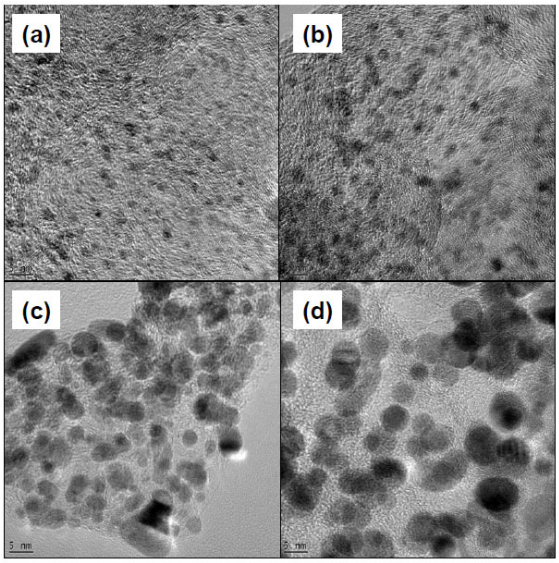

Figure 7: TEM images of anode (a,b) and cathode (c,d) catalysts before (a,c) and after (b,d) long time test.

Figure 7 illustrates the TEM images of the anode and cathode catalysts before and after the long-term test. All the particle size of catalysts increased after long-term performance test as shown in Figure 7. The particle size of the cathode catalyst increased much higher than the

anode catalyst after the long-term test (Figure 7(b) and 7(d)). Also, the morphology of the catalysts was changed to circle-like shape.

SEM images of cross-sectional of the MEA and PF50-SS50 membrane are shown in Figure 8. The PF50-SS50 membrane thickness of the initial MEA was 50 μm, and the anode and cathode catalyst layer was 25 μm and 32 μm. The thickness of PF50-SS50 membrane and anode catalyst layer remained constant after 2000 h of long-term test.

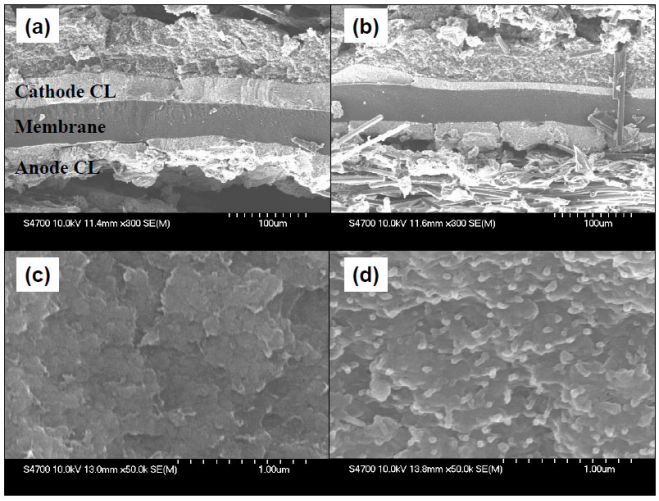

Figure 8: SEM images of cross-section of MEA (a,b) and surface of PF50-SS50 membrane (c,d) before (a,c) and after (b,d) long time test.

However, the thickness of the cathode catalyst layer decreased to roughly 15 μm. Decrease of the thickness of the cathode catalyst layer was attributed to the oxidation of the carbon support by the hydrogen peroxide, which was formed during the oxygen reduction reaction. The samall granins was formed on the surface of the prepared PF50-SS50 membrane owing to thermal decomposition of polystyrene into grafted PFA film after the long-term test for 2000 h.

4 Conclusions

In this work, the long-term performance of prepared MEA with PF50-SS50 membrane was tested with a constant load 150 mA/cm^2 for 2000 h at 60 ^{o}C. The observed power density loss over the 2000 h period is about 26.2% (70mW/cm^2 → 51.6 mW/cm^2). The decay rate of voltage for the cell operation up to 2000 h was determined to be about 61.6 μV/h. The performance loss of the single cell is considered to be due to increase of particle size of catalysts, reduction of the cathode catalyst and thermal decomposition of the PF50-SS50 membrane.

Acknowledgments

This work was supported for Collaborative Research Projects by the Korea Research Council of Industrial Science & Technology (ISTK), Korea.

References

[1] S.D. Knights, K.M. Colbow, St. Pierre, D.P. Wilkinson, “Aging mechanisms and lifetime of PEFC and DMFC”, Journal of Power Sources, 127, p.127–134 (2004).

[2] J. -H. Choi, P. -H. Kang, Y. -M. Lim, J. -Y. Sohn, J. Shin, C. -H. Jung, J. -P. Jeun, and Y. -C. Nho, “Preparation and Characterization of Poly(styrenesulfonic acid)-grafted Fluoropolymer Membrane for Direct Methanol Fuel Cell”, Korean Membrane Journal, 9, p.52-56 (2007).

[3] J. Zhang, G. Yin, Z. Wang, Y. Shao, “Effects of MEA preparation on the performance of a direct methanol fuel cell”, Journal of Power Sources. 160, p.1035–1040 (2006).

[4] E. Endoh, “Progress of Highly Durable MEA for PEMFC Under High Temperature and Low Humidity Conditions”, Fuel Cell Seminar & Exposition p.25-28 (2007)

[5] L. Gubler, S.A. Gursel, G.G. Scherer,“Radiation grafted membranes for polymer electrolyte fuel cells“, Fuel Cells, 5, p.317- 335 (2005)

[6] S.-A Kang, J. Shin, G. Fei, B.-S. Ko, C.-Y. Kim, Y.-C. Nho, P.-H. Kang, „Preparation of crosslinked polystyrene-grafted PFA films by a simultaneous irradiation method“, Journal of Industrial and Engineering Chemistry,15, p. 516-519 (2009).

Combined Local Current Distribution Measurements and High Resolution Neutron Radiography of Operating Direct Methanol Fuel Cells

Alexander Schröder, **Klaus Wippermann**, Institute of Energy Research, IEF-3: Fuel Cells, Forschungszentrum Jülich GmbH, 52425 Jülich, Germany
Tilman Sanders, Institute for Power Electronics and Electrical Drives (ISEA), RWTH Aachen University, Jägerstraße 17–19, 52066 Aachen, Germany
Tobias Arlt, Helmholtz Centre Berlin, Institute for Applied Materials, Hahn-Meitner-Platz 1, 14109 Berlin, Germany

1 Abstract

Neutron radiography allows the investigation of the local fluid distribution in direct methanol fuel cells (DMFCs) under operating conditions. Spatial resolutions in the order of some tens of micrometers at the full test cell area are achieved. This offers the possibility to study practice-oriented, large stack cells with an active area of several hundred cm^2 as well as specially designed, small test cells with an area of some cm^2. Combined studies of high resolution neutron radiography and segmented cell measurements are especially valuable, because they enable a correlation of local fluid distribution and local performance [1, 2]. The knowledge of this interdependency is essential to optimise the water management and performance respecting a homogeneous fluid, current and temperature distribution and to achieve high performance and durability of DMFCs.

2 Introduction

One of the main problems in the development of direct methanol fuel cells is the uneven fluid distribution. While CO_2 bubbles may inhibit the methanol supply on the anode side, water droplets on the cathode side block the oxygen supply. Combined with the concentration decrease of the reactants across the active area along the flow field channels, these effects lead to a pronounced inhomogeneous current distribution as well as to a power loss of the fuel cell. With the knowledge of the local distribution and transport behaviour of CO_2 bubbles and water droplets at different operation modes, investigations on the improvement of cell components and design are possible.

By means of segmented circuit boards, the currents of separate cell segments can be measured during operation of the cell. In order to investigate the effects leading to the inhomogeneous current distribution, a further measurement technique is mandatory, allowing the observation of the CO_2 and water distribution. In order to use a completely non-invasive method for the observation of CO_2 and water, we used neutron radiography, which has proved its applicability for a variety of questions [3–10]. This method is based on the high attenuation coefficient of hydrogen compared to the attenuation coefficient of most metals and carbon. The neutron beam is less affected by the solid cell components compared to liquid water which leads to a strong absorption of the beam. Thus, the distribution of

hydrogen-rich species can be observed during operation. In the test set-up, the neutron radiation is attenuated while passing the cell in through-plane direction. The transmitted radiation is converted into visible light by means of a scintillator which then can be detected by a charge-coupled device camera. Placing the scintillator close to the test cell allows for resolutions down to 70 µm. A combination of neutron radiography and segmented current distribution measurement results in an *in situ* correlation of the current and fluid distribution.

3 Experimental

3.1 Electrochemical set-up and test cell

The functional layers of the used membrane electrode assemblies (MEAs) with an active area of either 4.2 cm $\times$ 4.2 cm or 21 cm $\times$ 15 cm were prepared onto carbon cloth (Ballard). In case of the small MEAs, an untreated carbon cloth and a (standard) hydrophobised carbon cloth were used as substrate. To compare hydrophobised and untreated gas diffusion layers (GDLs) in the same cell under operating conditions, the cathode GDL was vertically split into an untreated left part and a hydrophobised right part. In case of large stack MEAs, only hydrophobised carbon cloth was used. The microporous layer consisted of 60 wt.% carbon (Cabot) and 40 wt.% PTFE. The anode catalyst consisted of 75 wt.% Pt/Ru and 25 wt.% carbon (Johnson Matthey). The Pt/Ru loading of the anodes was about 2 mg cm^{-2}. The cathode catalyst had a composition of 57 wt.% Pt and 43 wt.% carbon (Johnson Matthey) with a Pt loading of about 2 mg cm^{-2}. The anode and cathode electrodes were hot-pressed on both sides of a Nafion N-115 membrane.

Two types of flow fields were used: The first type of flow field is made of graphite and is used for the electrodes of small cells with an active area of about 18 cm^2. These flow fields have a grid design with ribs (1 $\times$ 1 mm^2 area) and channels (1 mm width and depth). The second type of flow field is made of Sigraflex (SGL Group) and applied for the electrodes of large stack cells (active area: 315 cm^2). The anode flow field has a 6-fold meander design and the cathode flow field a multi-channel design. The flow arrangement of all the flow fields was counter flow. The air feed was at the top and the methanol feed at the bottom of the cells.

All measurements were carried out at a temperature of 70 °C and ambient pressure. The anode was constantly fed by a methanol solution with a concentration of 1 mol l^{-1} and the cathode was supplied by air. The respective stoichiometric factors are indicated in the figures below.

The current distribution was measured via segmented printed circuit boards (PCBs) which were inserted between the aluminium end plate and one of the flow fields. An exploded view of the assembly used for small cells is shown in Fig. 1. A detailed description of the setup can be found in [11]. Adapted to the flow field sizes, circuit boards with either 25 segments (small cells) or 54 segments (stack cell) were used.

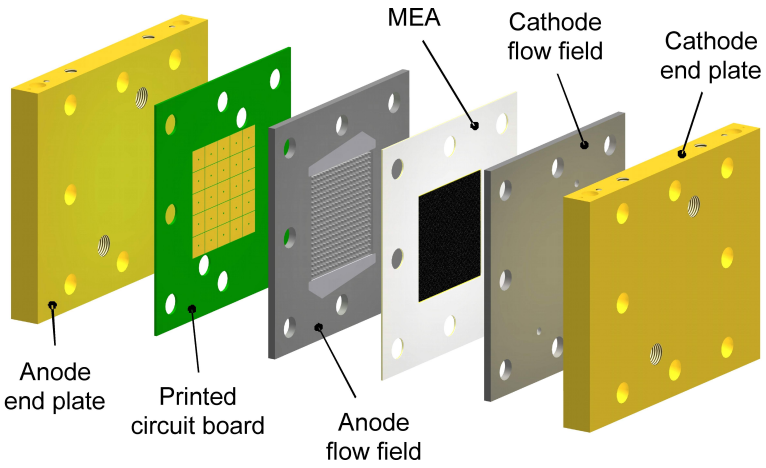

Figure 1: Exploded assembly drawing of the test cell including the adapter printed circuit board (PCB) used in [1, 2].

3.2 Neutron radiography

The radiography experiments were performed at the neutron tomography instrument CONRAD/V7 at Helmholtz Centre Berlin (formerly Hahn-Meitner Institute) in Germany. The imaging set-up is based on a pinhole geometry with a small variable aperture. The main part of the detector system is a 16-bit low-noise CCD camera (Andor DW436N with 2048×2048 pixel^2) 0. The camera is focused by a lens system on a neutron sensitive scintillator screen (mostly Gadox or LiF) which was mounted close to the fuel cells to ensure high spatial resolutions down to 70 µm in case of the small cells and 200 µm in case of the large cells.

4 Results of Combined Neutron Radiography and Current Distribution

The results obtained with a small MEA including a cathode carbon cloth splitted into an untreated part (left side of cell) and a hydrophobised part (right side of cell) are shown in Fig. 2. The left part of Fig. 2 shows the neutron radiograph and the right part the corresponding current distribution for an average current density of 300 mA cm^{-2}. Under these conditions, water droplets appear in the cathode channels over the entire left side of the cell. The flooding of cathode channels (see dark spots on neutron radiograph) corresponds to the decreased local current in this part of the cell (see blue segments): The untreated part of the cell contributes to 38 % of the total power generation only.

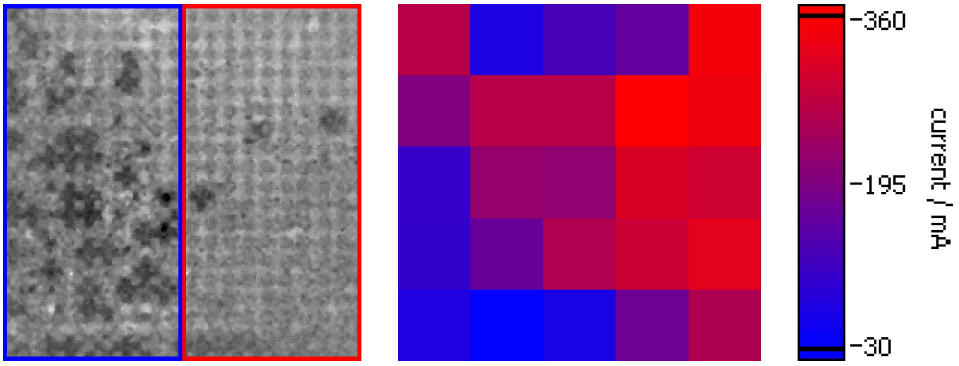

Figure 2: Normalised radiograph (left hand) and the corresponding current distribution (right hand) of a MEA with a vertically split cathode carbon cloth; T = 70°C, $\lambda_{MeOH} = \lambda_{air} = 4$, j = 300 mA cm^{-2}; dark spots in cathode grid channels indicate water droplets; light grey colour of anode grid channels reveals CO_2 evolution.

At the neutron tomography instrument CONRAD/V7 at Helmholtz Centre Berlin, a neutron beam widening allows to investigate areas up to 20 cm × 20 cm. This area is for example adequate for large single stack cells of Forschungszentrum Jülich GmbH with an area of 315 cm^2 (21 cm × 15 cm). The design of these stack cells includes a multifold-meander anode flow field and a multi-channel cathode flow field. Fig. 3 shows a first, normalised neutron radiograph of such a stack cell under DMFC operating conditions (T = 70 °C, j = 150 mA cm^{-2}, $\lambda_{air} = \lambda_{MeOH} = 4$). Though the distribution of the neutron beam intensity is locally and temporally inhomogeneous and has to be improved further, the light grey meander channels and water droplets in parts of the cathode channels can be clearly identified (left hand of Fig. 3). The current distribution shows a lower power generation of 39 % in the bottom part of the cell (right hand of Fig. 3), which is most probably caused by oxygen depletion. It is assumed, that the oxygen concentration in the bottom part of the cell is not only reduced by consumption due to Faradaic reaction, but also by partial blocking of cathode channels.

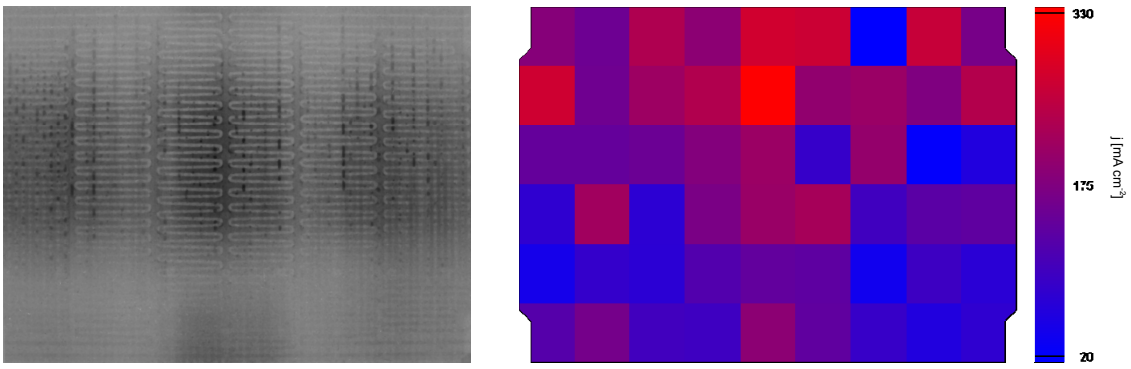

Figure 3: Normalised radiograph (left hand) and the corresponding current distribution (right hand) of a single stack MEA (active area: 315 cm^2); T = 70 °C, $\lambda_{MeOH} = \lambda_{air} = 4$, j = 150 mA cm^{-2}; dark spots in cathode straight channels indicate water droplets; light grey colour of anode meander channels reveals CO_2 evolution.

5 Conclusions

The combination of high resolution neutron radiography and simultaneous measurement of the local current distribution provides valuable information about the influence of GDL wettability on the performance of a DMFC. It turns out that hydrophobisation of the cathode carbon cloth seems to be important, as it enables a fast removal of water droplets, facilitates the oxygen transport in the cathode GDL and cathode flow field channels and thus increases the performance. It should be emphasised, that a simulation of the flow conditions in large stack cells by using small single cells is challenging. Hence, for future neutron radiography measurements in through-plane mode one should pay special attention to the investigation of practice-oriented, large stack cells. For the first time, the fluid distribution of large stack cells was measured by combined neutron radiography and current distribution measurements.

Acknowledgements

We gratefully acknowledge the financial support of this work by the German Federal Ministry of Education and Research (BMBF) under Grant No. 03SF0324.

References

[1] A. Schröder, K. Wippermann, J. Mergel, W. Lehnert, D. Stolten, T. Sanders, T. Baumhöfer, D. U. Sauer, I. Manke, N. Kardjilov, A. Hilger, J. Schloesser, J. Banhart and C. Hartnig, Electrochemistry Communications 11 (2009) 1606–1609

[2] A. Schröder, K. Wippermann, W. Lehnert, D. Stolten, T. Sanders, T. Baumhöfer, N. Kardjilov, A. Hilger, J. Banhart, I. Manke, Journal of Power Sources, Journal of Power Sources (2010), doi:10.1016/j.jpowsour.2010.02.057, in press

[3] D. Kramer, E. Lehmann, G. Frei, P. Vontobel, A. Wokaun, G. G. Scherer, Nuclear Instruments and Methods in Physics Research A 542 (2005) 52–60

[4] I. Manke, C. Hartnig, M. Grünerbel, J. Kaczerowski, W. Lehnert, N. Kardjilov, A. Hilger, J. Banhart, W. Treimer, M. Strobl, Applied Physics Letters 90, 184101 (2007)

[5] C. Hartnig, I. Manke, N. Kardjilov, A. Hilger, M. Grünerbel, J. Kaczerowski, J. Banhart, W. Lehnert, Journal of Power Sources 176 (2008) 452–459

[6] I. Manke, C. Hartnig, N. Kardjilov, M. Messerschmidt, A. Hilger, M. Strobl, W. Lehnert, J. Banhart, Applied Physics Letters 92, 244101 (2008)

[7] M. A. Hickner, N. P. Siegel, K. S. Chen, D. S. Hussey, D. L. Jacobson, M. Arif, Journal of The Electrochemical Society, 155 (4) B427–B434 (2008)

[8] P. Boillat, D. Kramer, B. C. Seyfang, G. Frei, E. Lehmann, G. G. Scherer, A. Wokaun, Y. Ichikawa, Y. Tasaki, K. Shinohara, Electrochemistry Communications 10 (2008) 546–550

[9] D. Spernjak, S. G. Advani, A. K. Prasad, Journal of The Electrochemical Society, 156 (1) B109–B117 (2009)

[10] A. Turhan, S. Kim, M. Hatzell, M. M. Mench, Electrochimica Acta 55 2734–2745 (2010)

[11] D. U. Sauer, T. Sanders, B. Fricke, T. Baumhöfer, K. Wippermann, A. A. Kulikovsky, H. Schmitz, J. Mergel, Journal of Power Sources 176 (2008) 477–483

[12] N. Kardjilov, A. Hilger, I. Manke, M. Strobl, W. Treimer, J. Banhart, Nuclear Instruments and Methods in Physics Research A 542 (2005) 16–21

FC Fuel Cell Basics

High-Temperature Fuel Cell Technology

Gael P. G. Corre and John T. S. Irvine

Abstract

This chapter reviews high temperature fuel cell technology. The two main concepts are the Solid Oxide Fuel Cell (SOFC) and the molten carbonate Fuel Cell (MCFC). SOFCs feature a solid oxide electrolyte, and operate in the range 600–1000°C, while MCFCs feature a molten carbonate electrolyte, and operate in the range 500–700°C. Due to their high temperatures, such fuel cells offer different characteristics, applications, requirements and advantages to that of low temperature fuel cells. Key advantages over low temperature fuel cells are the fuel flexibility, offering the possibility to operate with practical fuels, and an improved overall efficiency. After fuel cells principles and characteristics have been introduced, the SOFC technology is reviewed. The history, applications and materials used in SOFCs are presented. An overview of MCFCs is given as well. Finally, a study of fuel cell thermodynamics and efficiency is provided.

Evaluation of the Electrical Contact Area at the SOFC Cathode

Vincent A.C. Haanappel, I.C. Vinke, L.G.J. de Haart, D. Stolten,
Forschungszentrum Jülich GmbH, Institute of Energy Research (IEF-3), D-52425 Jülich, Germany

Abstract

In the frame of the ZeuS-III project, a model study was started on evaluation the area-specific resistances (ASRs) of various layers being used in SOFC stacks. It is well known that stack performance not only depends on cell resistance but also on the electrical conductivity of the various applied contact and protective layers. Various layers have been tested under simulated SOFC conditions, and results have shown that the lowest ASR value, about 3 mΩ.cm², was obtained for an LSM (2) contact layer. A significantly higher resistance was found for the combined contact and protective layer LCC10-Mn_3O_4, being around 37 mΩ.cm². Related to the various tests, the total ASR of an F-design stack, developed by Forschungszentrum Jülich, under ideal conditions can be estimated. In this case the ASR value was calculated as the sum of that of the LCC10-Mn_3O_4 layer and the formed oxide scale due to oxidation of Crofer22APU. Contacting resistance at the anode side was considered negligible. When differences in the ASR values occurred when compared with that from current – voltage measurements performed with real SOFC stacks, this can be explained by the limited contact area between interconnect and cathode. These results can be used to model the influence of various applied layers and different geometric contact areas on the overall ASR as determined from performance measurements with SOFC stacks.

1 Introduction

The application of protective and/or contact layers on metallic interconnects in SOFC stacks is indispensable. On one hand, to inhibit chromium evaporation at the air side, and on the other, to assure good contacting between cathode and the metallic interconnect [1-3].

Poisoning of the cathode by chromium deposition is one of the main reasons of severe degradation of SOFC performance. In order to prevent chromium evaporation from the interconnect a protective layer is needed. Such a layer has to be gas tight and to possess good electrical conductivity. The use of a contact layer is needed for assuring good electrical contact between interconnect and cathode: compensation of dimensional tolerances of the parts.

Stack performance depends not only on the cell resistance itself, but also strongly on the conductivity or resistance of the various materials being used in an SOFC stack: the higher the contact resistance between the various layers and the resistance of the individual layers being applied, the lower the output performance.

This contribution deals with a model study on evaluating area-specific resistances of various individual layers as well as various combinations of layers, used as protective and/or contact layers in SOFC stacks.

2 Experimental

Each sample consists of two metallic (platinum) sheets, one sheet with dimensions of 50 x 50 mm² and the other with a size of 40 x 40 mm². In one case, Crofer22APU was chosen as the metallic sheet (50 x 50 mm²). Before applying the layer(s) to be tested both surfaces were ground with 1200 grit and rinsed with ethanol. Two Pt-wires were attached to these sheets, one for applying a current load and the other for measuring the corresponding voltage (4 point DC). An overview of the tests including the tested layers and their deposition techniques is listed in table 1. A subdivision of the series of tests is made by the purpose of the various layers, i.e. (1) current collector (LSM(1)), (2) contact (LCC10, LSM(2)) and (3) protective (Mn_3O_4) layers. Also tests with combinations of layers were performed.

Table 1: Various tests including tested layers and their application techniques.

Application	Pt – 50 x 50 mm²	Deposition technique	Pt – 40 x 40 mm²	Deposition technique
Current coll.	LSM (1)	**SP – 70 µm	-	-
Contact	LCC10	*WPS – 130-150 µm	-	-
	LSM (2)	**SP – 70 µm	-	-
Protective	Mn_3O_4	*WPS – 10 µm	-	-
Combinations	LCC10-Mn_3O_4	*WPS – 150 µm	-	-
	LCC10-Mn_3O_4	*WPS – 150 µm	LSM (1)	**SP – 70 µm
	LSM (2)	**SP – 70 µm	LSM (1)	**SP – 70 µm
	***LSM (2)	**SP – 70 µm	-	-

*WPS: wet powder spraying; **SP: screen-printing; ***Crofer22APU as the metallic sheet forming interfacial oxide layer.

All tests were run with three samples, connected in series with each other and in such mode that no differences in current load occurred between the tested samples. Figure 1 shows the three samples with Pt as the metallic sheets coated with a current collector LSM (1) layer. All samples were isolated from each other by a thin alumina plate. On top a mechanical load was applied of 5 N/cm². The furnace was heated with a rate of 2 °C/min to 850 °C. At this temperature, the samples were exposed for about 10 h, after which the operating temperature was decreased to 800 °C. This procedure simulates the heating and conditioning procedure of SOFC stacks tested at Jülich. Before the current load was applied, current – voltage measurements were performed up to 0.75 A/cm². The constant current load was set at 0.6 A/cm². After regular intervals current – voltage plots were obtained. After

500 h of exposure, the final current – voltage plot was taken followed by cooling the furnace to room temperature.

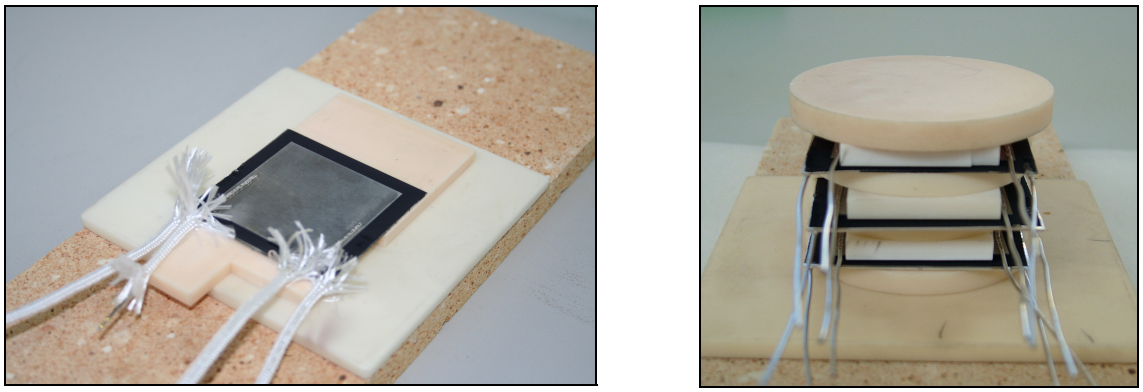

Figure 1: Left: one sample with two Pt-sheets coated with LSM (1) layer on the bottom sheet. Right: three samples "stacked" in series before testing.

3 Results and Discussion

Current collector layer: The area-specific resistances (ASRs) of three samples with Pt as the metallic sheet and an interlayer of LSM (1) being considered as the cathode current collector layer are shown in Figure 2. From this figure it can be concluded that relatively high scatter occurred between the measured ASR of the individual samples with that of sample 2 the highest and of sample 1 the lowest ASR values. Initially the ASR obviously decreased with the average value starting from about 7.7 ± 2.9 to 5.1 ± 2.6 mΩ.cm² after 500 testing hours.

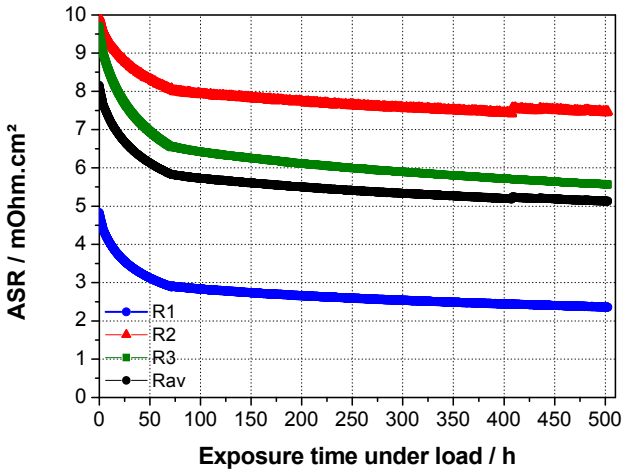

Figure 2: Area-specific resistances (ASRs) of three samples with Pt as the metallic sheets and LSM (1) as the intermediate layer being tested in air at 800 °C for 500 h. Mechanical load was set at 5 N/cm² and the applied current load at 0.6 A/cm².

The ASR values obtained after regular intervals and calculated from the current – voltage measurements are given in table 2. These values correspond well with those from Fig. 2. As such, it can be concluded that the ohmic resistance of the LSM (1) cathode current collector layer decreased with longer exposure times.

Table 2: ASR values after regular intervals of three samples with Pt as the metallic sheets and LSM (1) as the intermediate layer being tested in air at 800 °C for 500 h. Mechanical load was set at 5 N/cm² and the applied current load at 0.6 A/cm².

Specimen:	ASR (mΩ.cm²)						
	t = 0	t = 72	t = 167	t = 267	t = 339	t = 413	t = 504
1	4.38	2.86	2.68	2.54	2.47	2.41	2.33
2	9.62	8.05	7.78	7.62	7.62	7.55	7.46
3	9.04	6.54	6.21	5.96	5.96	5.71	5.59
Av.value:	7.7 ± 2.9	5.8 ± 2.7	5.6 ± 2.6	5.4 ± 2.6	5.4 ± 2.6	5.2 ± 2.6	5.1 ± 2.6

Contact layers: In the case of the contact layer type LCC10 with a thickness of about 140 µm, the ASR values showed an increase as a function of time, started at 36 ± 12 mΩ.cm² and ended, after 500 h of exposure at 48 ± 17 mΩ.cm². The ASR as a function of time is depicted in Fig. 3. A second type of contact layer is based on LSM (2). This layer showed similar features as those with the current collector layer LSM (1), as described before. In this case the average value of the ASR was about 4.6 ± 2.2 mΩ.cm² at the beginning and 3.3 ± 1.6 mΩ.cm² after about 500 h of testing.

Based on only the ohmic resistance, it would be recommended to use this type of contact layer. However, nothing can be concluded about the effectiveness of such a layer, in particular about mitigating or preventing chromium evaporation from the interlaying interconnect and thus avoiding chromium poisoning of the cathode.

Protective layer: The tickness of the protective Mn_3O_4 layer applied by wet powder spraying was only 10 µm. The measured ASR was initially about 24 ± 6 mΩ.cm² and decreased to about 17 ± 5 mΩ.cm², this as a result of densification and improved contacting between the individual grains during sintering at 800 °C.

An overview of the ASR values for the current collector, the contact and the protective layers are given in table 3. All values are average values of three samples measured simultaneously.

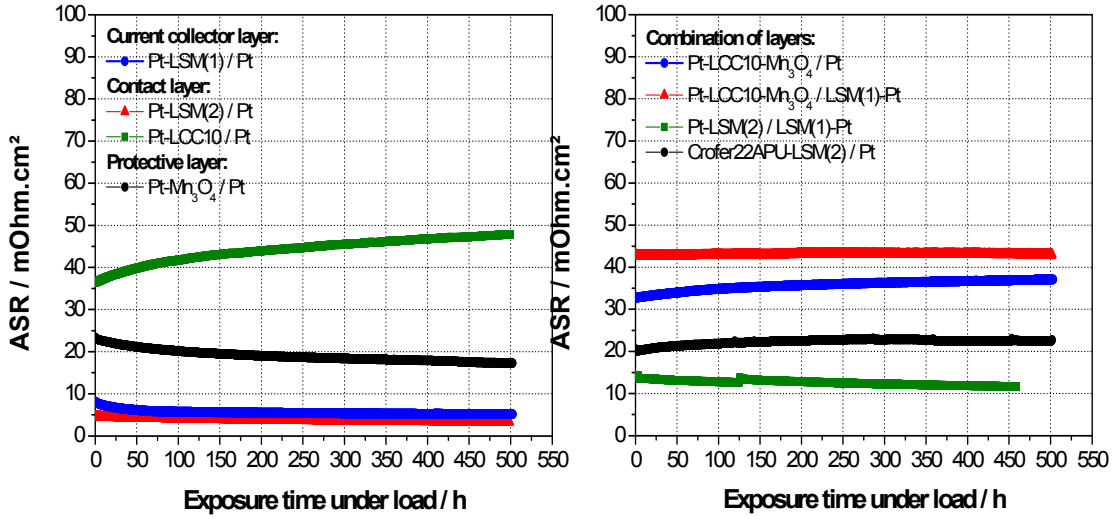

Figure 3: **Area-specific resistances of samples with (left) current collector layer LSM(1); contact layers LSM(2) and LCC10; or protective layer Mn_3O_4 as the intermediate layer, (right) combinations of layers tested in air at 800 °C for 500 h. Mechanical load was set at 5 N/cm² and the applied current load at 0.6 A/cm². All curves are average values of three samples measured simultaneously.**

Table 3: **ASR values (mΩ.cm²) of various layers with Pt as the metallic sheets being tested in air at 800 °C for 500 h. Mechanical load was set at 5 N/cm² and the applied current load at 0.6 A/cm².**

	Current collector	Contact		Protective
	LSM(1)	LCC10	LSM(2)	Mn_3O_4
t = 0 h	7.7 ± 2.9	36 ± 12	4.6 ± 2.2	24 ± 6
t = 500 h	5.1 ± 2.6	48 ± 17	3.3 ± 1.6	17 ± 5

Combination of layers: Experiments were also performed with a combination of protective and contact layer LCC10-Mn_3O_4, which is used in the Jülich-type SOFC stacks [4]. Results from the endurance tests are shown in Fig. 3 (right) depicting the ASR as a function of the testing period. The calculated ASR values from the current – voltage measurements at t = 0 and t = end are given in table 4. Based on these results, it can be concluded that the ASR slightly increased from 33 ± 10 to 37 ± 13 mΩ.cm² during exposure in air at 800 °C. The total of the individual ASR values for both layers is at t = 0 about 60 and increased slightly up to about 65 mΩ.cm², thus somewhat higher than that of those values obtained with the double layer LCC10-Mn_3O_4.

The increase of the ASR over the total exposure time was for both similar, but the absolute differences in the ASR values can be explained by differences in contacting area between the separated layers, small differences in thickness of the individual layers, or the formation of a high conductive interlayer between both layers, improving the overall conductivity of the samples.

Another combined testing was that with applying on one sheet LCC10-Mn_3O_4 and on the other LSM (1) contact current collector layer. The area-specific resistance was during the whole exposing time around 43 ± 7 mΩ.cm². The recorded ASR values for the three samples are shown in Fig. 3(right). Sum of the ASR values for the individual tested layers, measured separately, was at the beginning about 39 ± 7 mΩ.cm² and after 500 h of exposure slightly increased to values around 42 ± 8 mΩ.cm², thus with good comparison.

A combined experiment was also performed with the contact LSM (2) layer and the current collector LSM (1) layer. The ASR values as a function of the exposure time are shown in Fig. 3(right). At t = 0, the ASR value was 14.3 ± 1.2 mΩ.cm² and after about 500 h 11.7 ± 2.0 mΩ.cm². The total ASR of the individual layers, determined separately, was at the beginning 12.4 ± 2.5 and after 500h testing 8.4 ± 2.1 mΩ.cm². This means that the decrease and the sum of the ASR values of the individual tested layers are comparable with those obtained with the testing of the double layer.

Next to the contribution of the individual layers, i.e. LCC10, Mn_3O_4 and LSM (1) cathode current collector layer, the total ohmic resistance of an SOFC stack and the influence of the interconnect alloy Crofer22APU on the ohmic resistance has to be evaluated, as well.

The underlying experiment is based on the use of Crofer22APU as the metallic sheet with on one side the LSM (2) contact layer. The opposite sheet is uncoated Pt. Results from the test are summarized in Fig. 3(right). The ASR value slightly increased from 22.4 ± 6.9 to 22.9 ± 5.5 Ωm.cm² after 500 h of exposure.

Table 4: ASR values (mΩ.cm²) of various layers with Pt or Crofer22APU as the metallic sheets being tested in air at 800 °C for 500 h. Mechanical load was set at 5 N/cm² and the applied current load at 0.6 A/cm².

	Combination of layers			
	Pt – LCC10-Mn_3O_4 / Pt	Pt – LCC10-Mn_3O_4 / LSM(1) - Pt	Pt – LSM(2) / LSM(1) - Pt	Crofer22APU – LSM(2) / Pt
t = 0 h	7.7 ± 2.9	36 ± 12	4.6 ± 2.2	22.4 ± 6.9
t = 500 h	5.1 ± 2.6	48 ± 17	3.3 ± 1.6	22.9 ± 5.5

In comparison with data obtained from tests with two Pt sheets and an LSM (2) contact layer, it is clear that the calculated ASR with Crofer22APU as the metallic sheet is obviously higher, i.e. 22.9 ± 5.5 mΩ.cm². In the case of the former, the ASR decreased from 4.6 ± 2.2 to 3.3 ± 1.6 mΩ.cm². The higher ASR can be explained by the use of Crofer22APU forming a small interfacial oxide layer with relatively low conductivity. Earlier measurements revealed [5] that the ASR of Crofer22APU oxidized for 300 h at 800 °C was between 10 and 30 mΩ.cm², which corresponds well with the measurements presented here. The oxide scale, formed during the exposure period consists of an inner chromia and an outer manganese-chromium spinel layer and is thus responsible for the higher measured resistance. Taken into consideration also the ASR values measured during single cell testing with anode-supported SOFCs with LSM- or LSCF cathode, some conclusions can be drawn concerning the contribution of the various applied layers including interconnect material to

the overall ASR as determined from stack measurements. Table 5 shows the ASR values for both types of single cells, tested at Jülich [6].

Table 5: Area-specific resistances of anode-supported SOFCs with LSM or LSCF cathode as function of the operating temperature [6].

Temperature (°C)	SOFC with LSM Cathode	SOFC with LSCF cathode
	ASR (mΩ.cm²)	ASR (mΩ.cm²)
800	190 ± 6	120 ± 6
750	260 ± 11	140 ± 6
700	430 ± 10	170 ± 4

From this table it can be concluded that the ASRs of both types of SOFCs increased with lowering the operating temperature. In the case of SOFCs with LSM cathode, the calculated ASR (800 °C; 700 mV) from current – voltage measurements under standard conditions is about 190 mΩ.cm². As an example, these data can be compared with that of an SOFC stack including SOFCs with LSM cathode [4]. Such a stack is constructed of Crofer22APU (cell frames and interconnect).

Contacting the cathode with the adjacent interconnect was achieved by Mn_3O_4 LCC10 layers applied by wet powder spraying. Based on the ASR data, the following conclusion can be drawn. A rough estimation of the total ideal ASR in first approach is assumed to be the sum of the $ASR_{SOFC-LSM}$, the $ASR_{LCC10-Mn3O4}$, and the $ASR_{Crofer22APU}$: 190 + 40 + 20 = 250 mΩ.cm² (more tests are planned to verify the results in more detail). Contacting resistance on the anode side (Ni-Ni) was here neglected. In the case of an SOFC stack the ASR on average is 260 mΩ.cm² [4], which corresponds well with the sum of the individual tested layers, presented in this contribution.

Based on the geometrical factor because of the limited contact area in an SOFC stack, a larger difference was however expected. The underlying measurements showed that this additional loss was negligible or at least relatively small indicating that this contribution plays only a minor role of importance. The contribution of the formed oxide scale between the metallic interconnect and the applied protective layer is in this case more obvious.

4 Conclusions

With a simple test method the area-specific resistance of various layers was evaluated individually. Contact layers are being used in SOFC stacks aiming improved contacting between the cathode of solid oxide fuel cells and the metallic interconnect. Three specimens with various types of layers could be uniformly loaded by a constant current load.

Resistance measurements have shown that in the case of simulating SOFC stack conditions, the lowest ASR was measured for the LSM (2) contact layer. In the case of the F-design JÜLICH stack, the total ASR was calculated by the sum of that of the contact and protective layer LCC10-Mn_3O_4 and the formed oxide scale. The difference between this calculated ASR and that obtained from current – voltage measurements with a real SOFC stack was almost negligible. As a consequence, the limited contact area between the interconnect and the cathode plays only a minor role of importance.

Acknowledgements

This study was performed within the project ZeuS-III funded by the Germany ministry of Economic Affairs under contract no. 0327766. The authors would like to thank the Central Department of Technology (Forschungszentrum Jülich, GmbH, Germany), in particular Mr. A. Cramer for the preparation of the samples. In addition, the authors gratefully acknowledge Ms. Menges and Mr. Herzhof for preparation of the various applied layers.

References

[1] M.C. Tucker, H. Kurokawa, C.P. Jacobson, L.C. De Jonghe, S.J. Visco, “A Fundamental Study on Chromium Deposition on Solid Oxide Fuel Cell Cathode Materials” Journal of Power Sources 160 (2006) 130-138.

[2] M. Stanislowski, J. Froitzheim, L. Niewolak, W.J. Quadakkers, K. Hilpert, T. Markus, L. Singheiser, “Reduction of Chromium Vaporization from SOFC Interconnectors by Highly Effective Coatings” Journal of Power Sources 164 (2007) 578-589.

[3] X. Montero, N. Jordan, F. Tietz, H.P. Buchkremer, A. Ringuedé, M. Cassir, A. Laresgoiti, I. Villarreal, “Coatings on Crofer22APU Interconnect for Protecting $La_{0.8}Sr_{0.2}FeO_3$ Cathode in Solid Oxide Fuel Cells” in the Proceedings of the 8th.European Fuel Cell Forum 2008, Lucerne, Switzerland, 30 June – 4 July, 2008.

[4] L.G.J. de Haart, J. Mougin, O. Posdziech, J. Kiviaho, N.H. Menzler, “Stack Degradation in Dependence of Operation Parameters; the Real-SOFC Senstivity Analysis” Fuel Cells 6 (2009) 794-804.

[5] J. Froitzheim, G.H. Meier, L. Niewolak, P.J. Ennis, H. Hattendorf, L. Singheiser, W.J. Quadakkers, “Development of high strength ferritic steel for interconnect application in SOFC” Journal of Power Sources 178 (2008) 163-173.

[6] V.A.C. Haanappel, N. Jordan, A. Mai, J. Mertens, J.M. Serra, F. Tietz, S. Uhlenbruck, I.C. Vinke, M.J. Smith, L.G.J. de Haart, ”Advances in Research, Development, and Testing of Single Cells at Forschungszentrum Jülich”, Journal of Fuel Cell Science and Technolog 6 (2009) 021302-1-10.

Learning Curves for Solid Oxide Fuel Cells

R. Rivera-Tinoco, **K. Schoots**, Energy research Centre of the Netherlands, Policy Studies, The Netherlands
B.C.C. van der Zwaan, Energy research Centre of the Netherlands, Policy Studies; Columbia University, Lenfest Center for Sustainable Energy, The Earth Institute, New York City, NY, USA

Abstract
We present learning curves for solid oxide fuel cells (SOFCs) and combined heat and power (CHP) SOFC systems with an electric capacity between 1 and 250 kW. On the basis of the cost breakdown of production cost data from fuel cell manufacturers, we developed a bottom-up model that allows for determining overall manufacturing costs from their respective cost components, among which material, energy, labor, and capital charges. The results obtained from our model prove to deviate by at most 13% from total cost figures quoted in the literature. For the early pilot stage of development, we find for SOFC manufacturing a learning rate between 14% and 17%, and for total SOFC system fabrication between 16% and 19%. We argue that the corresponding cost reductions result largely from learning-by-searching effects (R&D) rather than learning-by-doing. When considering a longer time frame that includes the early commercial production stage, we find learning rates between 14% and 39%, which represent a mix of phenomena such as learning-by-doing, learning-by-searching, economies-of-scale and automation.

Keywords: SOFC, learning-by-doing, economies-of-scale, automation

1 Introduction

Interest in power generation with solid oxide fuel cells (SOFCs), as well as R&D dedicated to this type of technology, has considerably increased over the past few years. Among the reasons are their high efficiency relative to conventional gas and coal based power units: even in comparison to for instance an integrated gasification combined cycle (IGCC) plant their electric efficiency is typically more than 10% higher [1]. Another explanation for the increased attention for SOFCs is the possibility of effectively recovering their exhaust heat, given the high temperatures under which they operate. As with other fuel cell systems, a combined heat and power (CHP) SOFC system consists of a stack of SOFCs and a balance-of-plant (BoP). The electrochemical reaction between oxygen and the fuel – such as hydrogen, methane or (a mix of) other hydrocarbon gases – takes place in the stack of fuel cells. The BoP supports the stack, drives the fuel through the fuel cells and can recover energy from the high-temperature exhaust gas.

In spite of their high electric efficiency and ensuing economic benefits, the fabrication costs of SOFC systems, and hence their purchase prices, are still significantly higher than strategically adopted target values. As a result, the cost of electricity generation with SOFCs are today well above those of most conventional alternatives. The development of SOFCs, however, is only in the pilot stage and has not yet reached full commercial production.

Hence, progressively significant cost reductions are expected for the future when the technology transits through the various stages of maturation.

The learning curve methodology allows for estimating the cost prospects of innovative technology and allows for determining the competitive breakeven point with respect to existing technology. The developed learning curves may apply to a large range of different types of technologies and serve company strategic purposes and as a tool for public policy making. For the latter, we found information notably of energy-related technologies [2-5]. The rapidity of learning is usually expressed by the learning rate, a measure for the relative cost reduction of a good with every doubling of produced or installed capacity. A learning curve expresses graphically the cost decrease of a technology and is usually represented by a power law (see equation 1). When cost and cumulative capacity data are plotted on a double-logarithmic scale, the power law of a learning curve becomes a downward sloping straight line. The slope of this line is called the learning index (α) [6-7], which can be reformulated as the learning rate (*lr*) (see equation 2).

$$c_t = c_0 \left(\frac{P_t}{P_0} \right)^{-\alpha} \tag{1}$$

$$lr = 1 - 2^{-\alpha} \tag{2}$$

Schoots *et al*. [8] present an extensive analysis of learning phenomena for fuel cells and the present work aims to complement this recent fuel cell learning curve study, since so far no learning rates have been reported – or have been determined – for SOFCs. In our fuel cells case, the variables in equation 1 are the costs of SOFCs at time *t* (c_t), the costs of SOFCs in the first batch of production (the time of which is referred to as $t = 0$) (c_0), the cumulated production of SOFCs at time *t* (P_t), and the number of SOFCs in the first fabrication batch (hence at $t = 0$) (P_0). We express values of *P* either in number of SOFCs (typically for fuel cells) or in terms of their capacity (hence in kW, for example when referring to SOFC systems).

2 Cost Requirements for SOFCs

In the current pre-commercial production phase, planar and tubular geometries of SOFCs dominate triangular and other shapes. For all these geometries, individual fuel cells are assembled in stacks that are subsequently integrated with the BoP. An individual fuel cell consists of a multilayer device including the anode, electrolyte, cathode, and interconnects. For today's SOFC manufacture, the first three components are made of state-of-the-art ceramics, such as respectively Nickel Oxide - Yttria Stabilized Zirconia (NiO-YSZ), YSZ and Lanthanum Strontium Manganite (LSM). Interconnects are fabricated usually of high performance stainless steel alloys [9-12]. Below we will mostly investigate planar SOFCs, because data for this type are more abundant than for tubular SOFCs. An analysis of the manufacturing sequence and cost components of SOFC production, as described in the following sections, serves to estimate total fuel cell and system fabrication costs. The latter constitute the basis for our attempt to determine a learning curve for SOFCs.

Total costs

The planar SOFC are produced according to a specific sequence of steps and techniques that depend on (and determine) the manufacturing material, processing speed, production yield, and fuel cell width [13-15]. For our study we assess the most commonly used method for multilayer ceramics manufacturing, which is the tape-casting of anode and screen-printing of electrolyte and cathode. After the cutting process elementary fuel cells are formed by adding shaped interconnects to the multilayered ceramic units. A series of individual fuel cells are piled together to become an SOFC stack.

Most intricacies of SOFC manufacturing techniques and materials are well documented in the literature. However, while cost components related to the use of materials and energy are usually fairly well known, little information is often available on contributions from notably labor and capital charges. This implies that total manufacturing cost values quoted in public sources possess a high degree of heterogeneity. This complicates attempts to observe learning phenomena, and renders difficult efforts to calculate accurately learning rates. In order to determine the presence (or absence) of learning-by-doing, and develop learning curves, we have greatly endeavored to subtract heterogeneity from our data set as much as possible. For this purpose, we developed a detailed bottom-up model in which we distinguish between the four main cost components that contribute to the overall SOFC production process:

- Material costs. Total annual material costs are estimated accounting volume and price of materials purchased per year by a manufacturing facility.
- Energy costs. We assume that annual energy expenses results from the total fuel cell capacity produced by a facility per year, the energy requirements per unit of capacity [15] and the energy costs.
- Labor costs (C_{lab}). Collected data show that, when no process automation techniques are implemented, the work directly related to manufacturing and stack assembling is performed by typically five individuals full-time employed when an annual volume of 25000 fuel cells is produced [16-17]. We assume that C_{lab} is proportional to the gross Average Employment Income (*AEI*) in the country of SOFC manufacturing under consideration [18] and that, with no automation, the number of individuals employed in the plant increases linearly, β=1.0, with the fuel cell production scale, and when process becomes automated $0.2 \leq \beta \leq 1.0$: $C_{lab} = AEI\left(N_{fc}\frac{5}{25000}\right)^{\beta}$
- Capital charges. Two main types of capital charges can be distinguished as investment requirements for the construction of a fuel cell production facility: equipment costs (C_{eq}) and terrain- and building costs (C_{tr}). Both represent figures for total capital costs per annum (C_{cap}) as they are transformed from total investment values into annual capital costs through the annuities relationship for capital refunding: $C_{cap} = (C_{eq})\left[\frac{r}{(1+r)^{-T}-1}\right] + (C_{tr})\left[\frac{r}{(1+r)^{-T}-1}\right]$

  in which *r* is the interest rate (which we suppose to be 8%) and *T* the period of loan amortization (for which we assume a time frame of 10 years).

From a survey of the literature, we assume in our model that the total level of equipment costs varies linearly with the expenses related to the acquisition of furnaces, for which we suppose a dominating constant average contribution of 50% [16-17]. Aware of the latter, the model allows for estimating fuel cell manufacturing cost values under several assumptions of economies-of-scale on furnace prices.

3 Learning Curves for SOFCs

We present in this section the learning curve study for production cost of SOFCs. Available yield and cost data derives from R&D, pilot and early commercial stages for the major fuel cell manufacturers. With exemption of CFCL, because of its business plan statements, this study deals with learning phenomena for both at each stage and total lifetime of HC Starck, Versa and Topsoe facilities. As means of a tool, our cost model enables to separately study cost reductions driven by non-learning phenomena, as well as rendering cost data homogeneous, and estimating additional cost values.

3.1 Improving production yield

An important facet of the produced capacity figure is the production yield of fuel cells, that is, what is the number of SOFCs successfully manufactured per production bulk. Failure on fuel cell production takes place mainly during the sintering step, followed by the multilayer production and handling steps [13]. Our analysis show that effort on R&D and experience acquired results on 11% decrease on failure rate every doubling on cumulative capacity of fuel cells. Once early commercial production of SOFCs starts, a minimal yield rate of 80% is observed frequently.

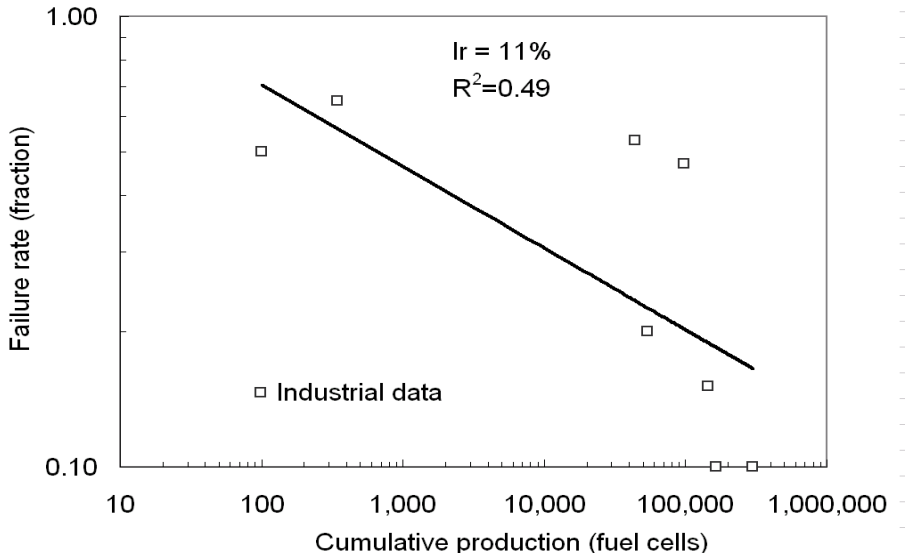

Figure 1: Learning curve for the failure rate of fuel cell production processes. Data from VERSA, Topsoe, HC Starck. [19-22].

3.2 Reducing manufacturing costs

Commencing this section with the major European manufacturer (HC Starck), we gather production cost values from R&D, pilot and early commercial production stages in the same plot (see figure 2). We include cost data and modeled cost values. Cost reduction obtained through automation and economies-of-scale are not studied in this step of the analysis.

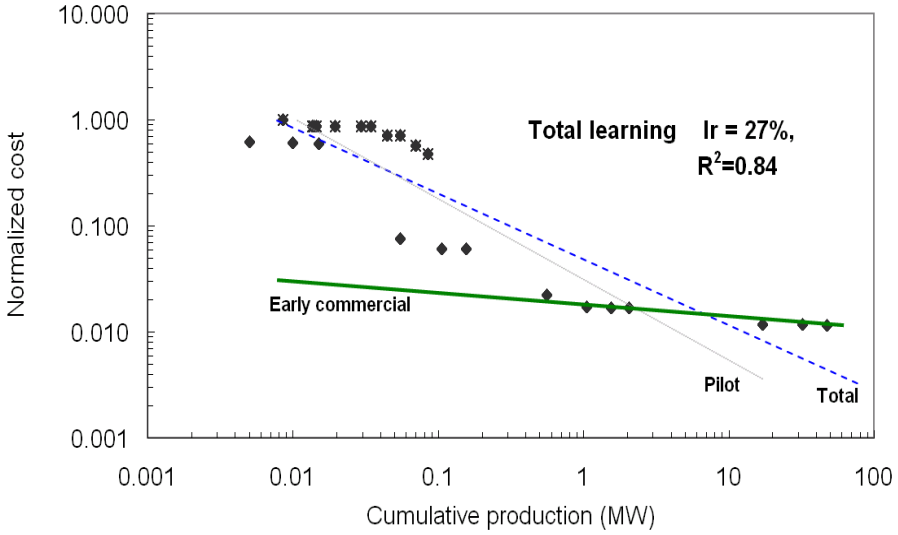

Figure 2: Learning curves for SOFC manufacturing. Data from HC Starck [16] and our model.

We estimate the learning rate value for R&D stage at 16% and for which material and labor costs remain high and are not affected for the volume of fuel cells produced. During the pilot stage, we observe that the learning rate every doubling of cumulative capacity is up to 42%. However, we estimated fuel cell production costs with our model subtracting the influence of economies-of-scale from material costs. Whether the purchase volume of powders, we assumed constant values for material costs. Learning rate results on a value of 27% and we suppose represents mainly pure learning-by-doing. Early commercial stage faces constrains against labor and capital costs, rather than material costs. The learning rate value is estimated at 5% and we suppose that learning-by-doing phenomena are mainly represented.

Accounting the relevant impact of labor and capital costs since the early commercial production stage is reached we studied further potential cost reductions driven by automation. Economies-of-scale related to material purchase volume and equipment investments are simultaneously considered. The learning rate reaches values from 35% to 39% for slightly to highly automation respectively.

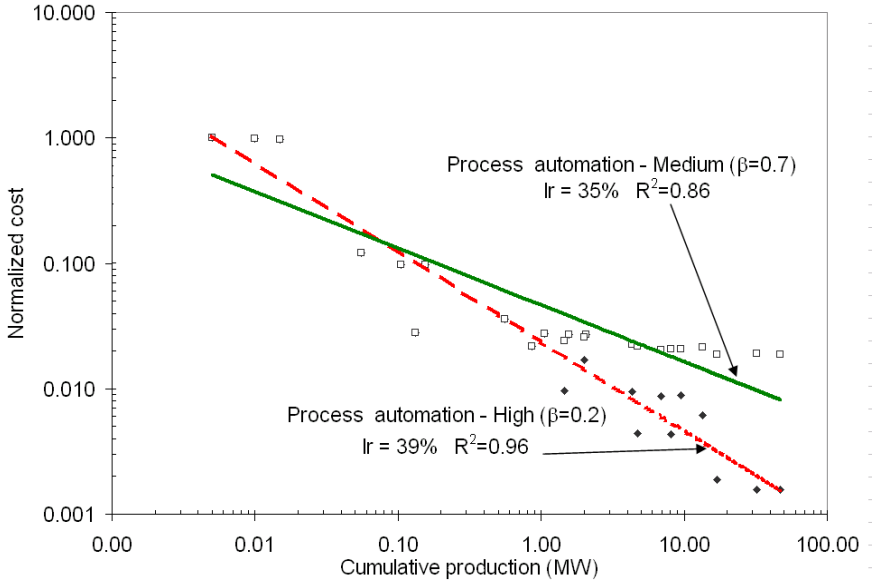

Figure 3: Modeled cost values for SOFC production under assumptions for automation and economies-of-scale effects. Data from our model and from HC Starck [16].

As our model is based on production capacity data, instead of current production capacity, and accounting that HC Starck has the highest capacity among the major fuel cell producers, we performed the sensitivity study of the impact of pilot and early commercial production capacity on cost estimations. Cost data available and estimated, only for the R&D stage, were straightly retained as they correspond to accurate values of produced fuel cells. For further production stages, we supposed a 50% load factor of the HC Starck facility. The lr results on 30% for medium automated facility (β=0.7) instead of 35% estimated with 100% load factor. This enables to estimate a maximal impact on lr values of 5% derived from uncertainties in manufacturers load factor.

Accounting facility capacity important differences, cost data from VERSA and Topsoe facilities are studied separately. Both facilities present a capacity equivalent to a R&D – semi pilot stage. Estimated fuel cell production costs deviate at most 13% of literature data. Learning rate values are found between 14% and 17%. Learning rate values from HC Starck, Versa, and Topsoe confirm that mainly learning-by-searching phenomena enable to reduce production costs by around 15%. Based on the fact that a confirmed value for learning curves is found at R&D and pilot production capacities, we will retain the costs and capacity data in order to go further with our learning curve analysis for SOFC systems.

4 Learning Curves for SOFC Systems

4.1 BoP costs

Material, energy, labor, and capital costs are included in the modeling of BoP manufacturing cost under similar assumptions than fuel cell production. The latter assumes that material and energy cost values derive from the required elements and their needed quantities to build up the BoP. As information related to labor costs (individuals needed) to produce and assemble the BoP is highly scarce and heterogeneous, the number of individuals is assumed

to be equal to the one for SOFCs manufacture. The total SOFC system labor cost would then become twice the value of fuel cell labor cost. For capital costs, we assume that they can be neglected. Indeed, the means required for these cost components are relatively small in comparison to the other contributions to overall costs.

4.2 System learning

Estimated cost values for 5 kW SOFC systems show that BoP contribution to total system manufacturing cost represents 64%. The latter fits with data provided by the consulting firm Arthur D. Little Inc. [23]. For different SOFC system capacities, the number of fuel cells contained in the stacks varies linearly with the requested power output. However, BoP would present a non-linear variation resulting on variable cost contribution, such as presented by Schoots *et al.* for PEMFC systems [8]. As the value of 64% is the only data point available for BoP contribution to SOFC system cost, we assumed that it would become the reference point for scaling contribution values for different SOFC systems presenting various power output values. The former is modeled under assumptions for an analogical behavior between PEMFC and SOFC BoP contribution to the system cost. The plot of modeled system costs based on R&D and pilot production capacities and data available derive on learning rate values for 1 to 250 kW SOFC systems between 17% and 19% (figure 4). The refunding of capital charges for both fuel cell and BoP side are not included in the costs plotted, but they would importantly increase the system cost depending on economic parameters used to discount investments.

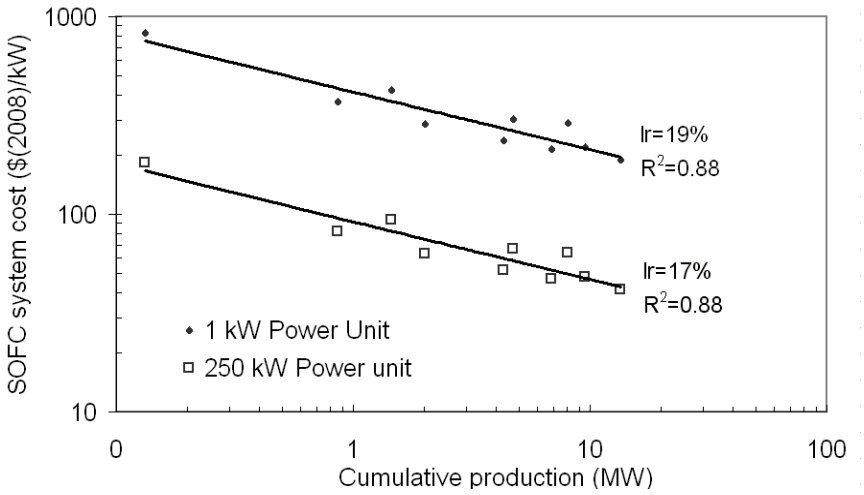

Figure 4: Learning curve for planar SOFC systems for 1 and 250 kW (electric power output). Modeled data and obtained from [23].

5 Conclusion

The learning curves for SOFCs and their systems presented in this paper are derived from modeled manufacturing costs as well as manufacturer data from the open literature. For the R&D and pilot stage of planar SOFCs, we obtained learning rates ranging from 14% to 17%. For the stages beyond, i.e. the early commercial phase, we modeled manufacturing cost

data and applied corrections in order to eliminate effects from economies-of-scale and automation. These data in combination with production capacity figures from HC Starck formed the basis of our learning-by-doing analysis. We found a learning curve characterized by a learning rate of 27 ± 15%. If phenomena of automation and economies-of-scale, as additional major drivers of cost reductions, had been taken into account, we would have obtained a learning rate of 39%. We point out that such a high rate is unsustainable. At any rate, in this and other papers, we demonstrate that the phenomenon of learning tends to decay, and gradually phase out towards zero. Based on real and modeled cost data from facilities run by VERSA and Topsoe, we find learning rates between 17% and 19% for SOFC systems with an electric output between 1 kW and 250 kW. These values correspond well with observed learning rates determined for a wide range of other energy technologies. Like with planar SOFCs, we developed a cost model for tubular SOFC systems. A lack of cost and installed capacity data, however, did not enable us to derive an accurate learning rate for such designs.

Acknowledgements

This research is funded by the Netherlands Organization for Scientific Research (NWO) under the ACTS Sustainable Hydrogen program (no. 053.61.304).

References

[1] Christou C, Hadjipaschalis Ioannis, Poullikkas Andreas. Parametric cost-benefit analysis of Integrated Gasification Combined Cycle technology. 3rd ICCCTF. Sardignia, Italy, 2007.

[2] Wright TP. Factors affecting the cost of airplanes. J Aeronaut Sci 1936;3:122-128.

[3] Joskow PL, Rose NL. The Effects of technological change, experience and environmental regulation on the construction of coal burning generation units. The Rand J. of Economics 1985;16(1): 1-17.

[4] Gruebler A, Nakicenovic N, Victor DG. Dynamics of energy technologies and global change. Energy Policy 1999;27:247-280.

[5] Söderholm P, Sundqvist T. Empirical challenges in the use of learning curves for assessing the economic prospects of renewable energy technologies. Ren. Energy 2007;32: 2559-2578.

[6] Schoots K, Ferioli F, Kramer GJ, van der Zwaan BCC. Learning Curves for Hydrogen Production Technology: an assessment of observed cost reductions. International Journal of Hydrogen Energy 2008;33: 2630-2645.

[7] Ferioli F, Schoots K, van der Zwaan BBC. Component-learning for energy technologies: the case of hydrogen production 2008

[8] Schoots K, Kramer GJ, van der Zwaan BCC. Technology Learning for Fuel Cells: an assessment of past and potential cost reductions. Energy Policy 2010; doi:10.1016/j.enpol.2010.01.022.

[9] Molin S, Gazda M, Kusz B, Jasinski P. Evaluation of 316 L porous stainless steel for SOFC support. Journal of the European Ceramic Society 2009;29(4): 757-762.

[10] Molin S, Kusz B, Gazda M, Jasinski P. Evaluation of porous 430L stainless steel for SOFC operation at intermediate temperatures. Journal of Power Sources 2008;181(1): 31-37.

[11] Smeacetto F, Salvo M, Ferraris M, Cho J, Boccaccini AR. Glass–ceramic seal to join Crofer 22 APU alloy to YSZ ceramic in planar SOFCs. Journal of the European Ceramic Society 2008;28(1): 61-68.

[12] Fontana S, Chevalier S, Caboche G. Metallic interconnects for solid oxide fuel cell: Effect of water vapour on oxidation resistance of differently coated alloys. Journal of Power Sources doi:10.1016/j.jpowsour.2008.11.041.

[13] Woodward HK. A performance based, multi-process cost model for solid oxide fuel cells.Worcester Polytechnic Inst. 2003.

[14] van Tuel M. SOFC development at ECN. Internal communication. Netherlands, December 2008.

[15] Bucheli O, Zähringer T, Bertoldi M, Herle J, Diethelm S. Customer-Oriented Design, Manufacturing and Thermal Integration of SOFC Stacks at SOFC power Srl. Lucerne Fuel Cell Forum 2008.

[16] Siewers EJ. Process Development for high volume SOFC component production. Energieonderzoek Centrum Nederlands. Confidential report. 2000.

[17] Martinez K, Nguyen T, Ihejiawu C, Diven J, Daugherty E, Treece J, Soyebo L, Ihejiawu C. Fuel Cells for Stationary Power Generation: A Comprehensive Analysis of Technology, Plant Construction, and Marketing Strategy for Small Buildings. The University of Oklahoma. Fuel Cell Corporation. 2004.

[18] International Average Salary Income Database. Worldsalaries 2008. See: http://www.worldsalaries.org/ (September 2009).

[19] Christiansen N, Hansen JB, Kristensen S, Holm-Larsen H, Linderoth S, Hendriksen PV, Larsen PH, Mogensen P. SOFC Development Program at Haldor Topsøe/Risø Laboratory – Progress. FuelCell Forum 2008.

[20] Christiansen N, Hansen JB, Holm-Larsen H, Jørgensen MJ, Kuhn TL, Hendriksen PV, Hagen A, Linderoth S. Solid Oxide Fuel Cell Research and Development at Topsø Fuel Cell A/S and Risø/DTU. Fuel Cell Forum 2008.

[21] Holm-Larsen H, Andersen CV, Jacobsen J, Primdahl S, Jørgensen MJ, Christiansen N. SOFC for m-CHP, APU and Distributed Generation-Application-Driven Development, Testing and Manufacture. Fuel Cell Forum 2008.

[22] Huiberts R, Buchner KH, Baldus HP. Commercialisation of SOFC Technology at H.C. Starck. FuelCell Forum 2008.

[23] Arthur D.Little Inc. Conceptual design of POX/ SOFC 5kW net system. Final Report. DoE - NREL. USA. January 2001.

Development of Fe-Ni/YSZ-GDC Electro-catalysts for Application as SOFC Anodes: XRD and TPR Characterization, and Evaluation in Ethanol Steam Reforming Reaction

Raigenis da Paz Fiuza*, Marcos Aurélio da Silva, Jaime Soares Boaventura, Energy and Materials Science Group, GECIM - Institute of Chemistry, Physical Chemistry Department, UFBA, 41170290, Salvador, Bahia, Brazil

Abstract

Electro-catalysts based on Fe–Ni alloys were prepared using physical mixture and modified Pechini methods; they were supported on a composite of Yttria Stabilized Zirconia (YSZ) and Gadolinia Doped Ceria (GDC). The composites had compositions of 35% metal load and 65% support (70% wt. YSZ and 30% wt. GDC mixture) (cermets). The samples were characterized by Temperature-Programmed Reduction (TPR) and X-Ray Diffraction (XRD) and evaluated in ethanol steam reforming at 650 °C for six hours and in the temperature range 300 – 900 °C. The XRD results showed that the bimetallic sample calcined at 800 °C formed a mixed oxide ($NiFe_2O_4$) in spinel structure; after reducing the sample in hydrogen, Ni-Fe alloys were formed. The presence of Ni decreased the final reduction temperature of the $NiFe_2O_4$ species. The addition of Fe to Ni anchored to YSZ-GDC increased the hydrogen production and inhibits the carbon deposition. The bimetallic 30Fe5Ni samples reached an ethanol conversion of about 95%, and a hydrogen yield up to 48% at 750 °C. In general, the ethanol conversion and hydrogen production were independent of the metal content in the electro-catalyst. However, the substitution of Ni for Fe significantly reduced the carbon deposition on the electro-catalyst: 74, 31, and 9 wt. % in the 35Ni, 20Fe15Ni, and 30Fe5Ni samples, respectively.

Keywords

Anode; Carbon deposition; Ethanol; Solid oxide fuel cell (SOFC); Fe–Ni catalyst; Ethanol Reforming; X-ray diffraction

1 Introduction

Solid oxide fuel cells (SOFC) are devices that convert the chemical energy of gaseous fuels, such as hydrogen, natural gas, and ethanol, to electricity through electrochemical processes. Due to their high efficiency, design modularity, and environmentally friendly nature, SOFCs are considered one of the most promising energy converters. In addition, the SOFC compared to other fuel cell systems offers the possibility of internal reforming of ethanol or

* Corresponding author, email: raigenis@ufba.brl

hydrocarbon fuels, which may occur directly on the anode; this provides SOFC with great flexibility in terms of fuel choice, one of its main advantages [1-5].

One of the challenges of using fuel cells as a commercial alternative for electricity generation is the fact that they usually require hydrogen as fuel. Hydrogen is predominantly produced by steam reforming reaction of natural gas or higher hydrocarbons, with carbon monoxide contents of around 100 ppm. Therefore, hydrogen production and distribution add additional levels of complexity to the overall system. However, oxidation of ethanol and hydrocarbons directly on SOFC anodes has been experimentally demonstrated by a number of authors [6-10]. It is well known that Ni–YSZ cermet anodes of SOFC have excellent catalytic properties and stability for H_2 oxidation in SOFC operation conditions [11, 12]. However, as Ni is also a good catalyst for hydrocarbon cracking reaction, the use of ethanol or hydrocarbon fuels in a SOFC with a Ni-based anode results in very fast carbon deposition, with irreversible cell degradation [13-16]. Therefore, the development of an anode material for SOFCs that operates on ethanol or hydrocarbons at lower carbon to water ratios is widely recognized to be an important technical objective [3, 7, 8, 17, 18].

2 Experimental

2.1 Sample preparation

Ni-Fe/YSZ-GDC cermets, with 35 wt. % of metal supported on YSZ-GDC (70 wt. % of YSZ), were prepared using two different methods. YSZ [$(Y_2O_3)_{0.08}(ZrO_2)_{0.92}$], surface area 6 - 9 m^2/g and particle size 0.5 - 0.7 µm, and GDC ($Ce_{0.9}Gd_{0.1}O_2$), surface area 5 - 8 m^2/g and particle size 0.3 - 0.5 µm powders, were obtained from Fuel Cell Material®.

Modified Pechini method for sample preparation started with an aqueous solution of Ni and Fe nitrate to which was added a solution of citric acid (CA). The resulting solution was stirred and heated to 60 °C when the support (YSZ-GDC) was added. Ethylene glycol (EG) was added to the solution in a molar ratio of CA/EG = 1/4, with a molar ratio of CA/metallic ion = 6/1, followed by stirring at 60 °C for one hour; the temperature was raised to 90 °C and kept at this temperature until the final volume was reduced to half its initial value. The polymeric gel formed was calcined at 350 °C, at a heating rate of 1 °C/min. Afterwards, the obtained brown solid was ground in a ball mill for 24 hours and calcined at 900 °C for three hours, with a heating rate of 5 °C/min.

Physical method for sample preparation used YSZ-GDC mixed with NiO in the presence of a small amount of ethanol; the mixture was stirred for 24 hours in a ball mill. The powder formed was calcined at 900 °C for 3 hours, with a heating rate of 5 °C/min.

2.2 Sample characterization

Sample crystallographic characterization was performed by XRD in a Shimadzu XRD 6000 equipped with Cu-Ka radiation (40 kV and 40 mA) between 10 and 80° at a rate of 0.25 °C/min[1].

TPR analysis was performed on a system consisting of a quartz reactor in a "U" shape, an oven with temperature control and a gas analysis system with thermal conductivity detector (TCD). The sample was placed in the quartz reactor, and heated from ambient temperature to about 1000 °C at a heating rate of 10 °C/min under a flow of 1.5% H_2/argon at a rate of

30 ml/min. The spectra were treated with deconvolution techniques to determine the different species present in the solids.

The measurements of specific surface area were performed in a Micromeritics ASAP 2020, using samples preheated to 300 °C for one hour under nitrogen flow.

2.3 Catalytic tests

The samples were evaluated in ethanol steam reforming in function of time on stream at 650 °C for six hours in a quartz micro-reactor. Initially the catalyst was reduced *in situ* with H_2 (10 mol%) diluted in N_2, between 30 and 800 °C with a heating rate of 10 °C/min and maintained at this temperature for 30 minutes. N_2 at a flow of 60 mL/min was the carrier gas. An ethanol aqueous solution, with a 3:1 molar ratio of water to ethanol, was injected into the reaction system through a syringe-type pump; the ethanol injection rate was 1.78×10^{-2} mol/hour. The gaseous products were analyzed by gas chromatography (SHIMADZU GC-17A), with an automatic sample injection.

3 Results and Discussion

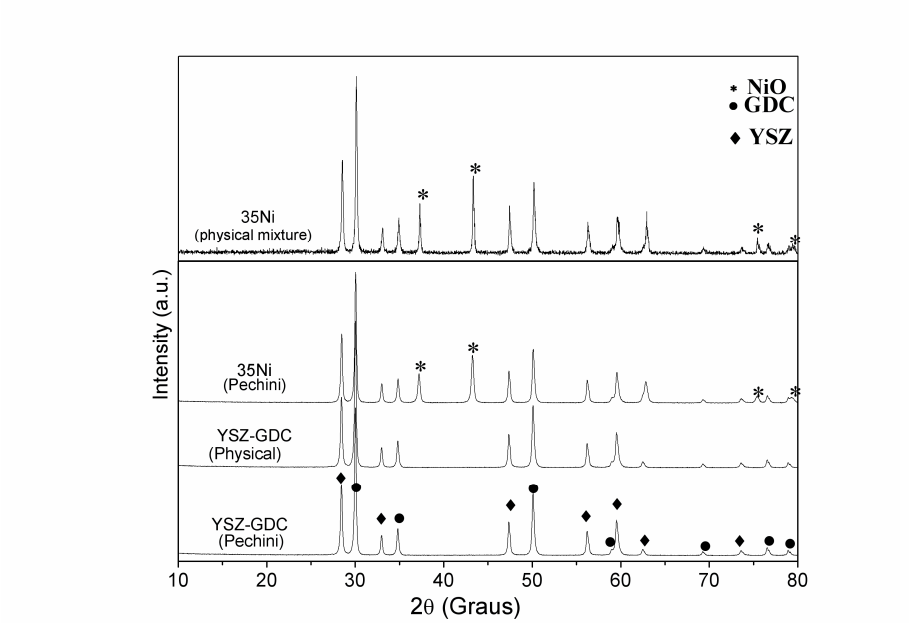

Figure 1: XRD patterns of Ni/YSZ-GDC, prepared by the physical mixture and Pechini methods and YSZ-GDC after calcination.

Figure 1 shows the XRD spectra of 35Ni, 35NiC and YSZ-GDC support. In both samples, NiO in the cubic form (JCPDS 78-0643) was formed following the calcination step; YSZ (JCPDS 82-1246) and GDC (JCPDS 75-0161) were both in the cubic form. Figure 2 shows the XRD patterns for the samples containing Fe. Only hematite in the rhombohedral structure (JCPDS 87-1166) was present in 35Fe sample. The XRD patterns of bimetallic samples indicated the coexistence of hematite and a mixed oxide of Ni and Fe ($NiFe_2O_4$), with a spinel-type cubic structure (JCPDS 74-2081). Figure 3 shows the XRD patterns of the samples after reduction in presence of H_2 at 800 °C. Ni in 35Ni sample was crystallized with

FCC structure (JCPDS 87-0712); Fe in 35Fe sample was crystallized with BCC structure (JCPDS 87-0722).

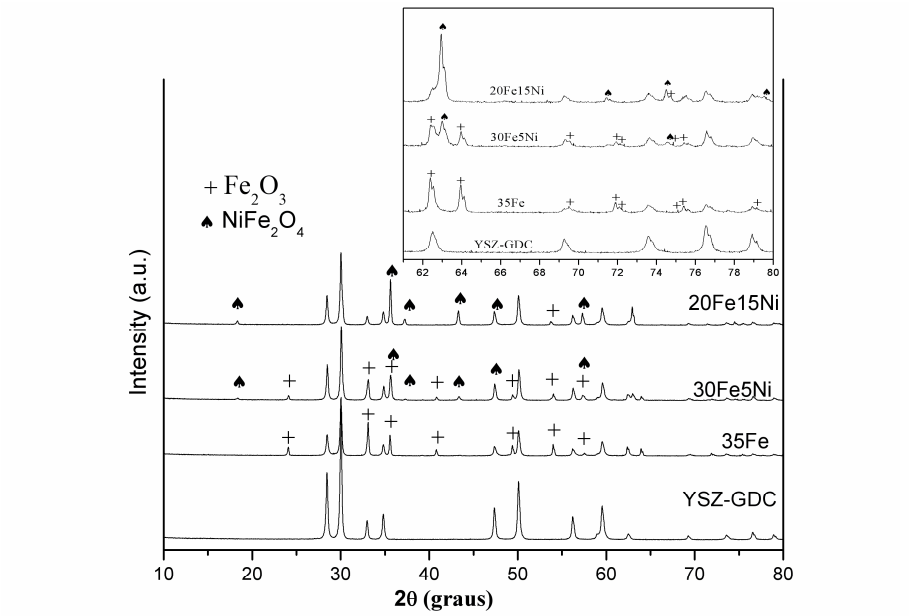

Figure 2: XRD patterns of Fe/YSZ-GDC prepared by Pechini method after calcination.

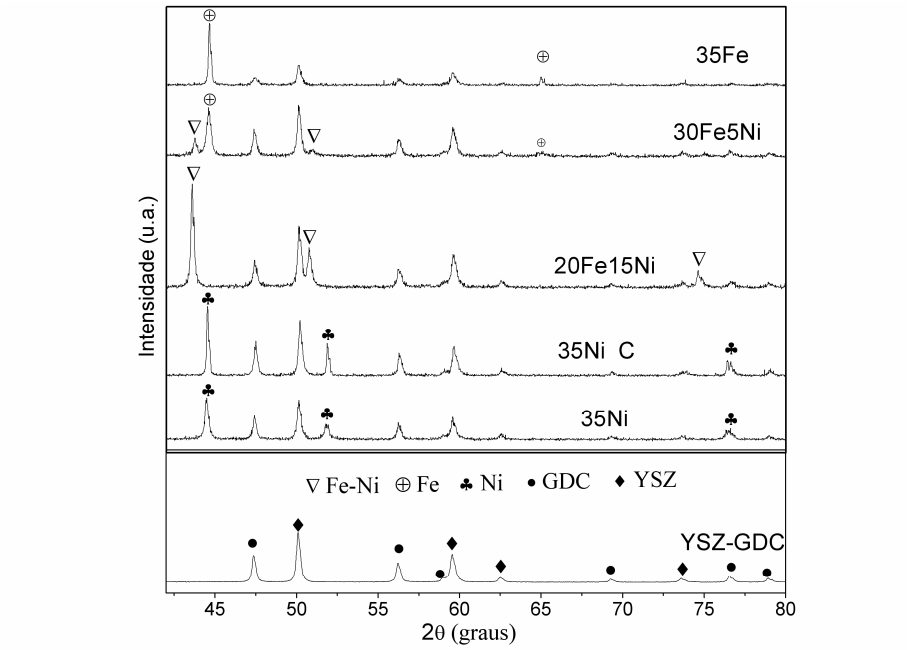

Figure 3: XRD patterns of electro-catalysts after reduction [24].

The XRD diffractogram for 20Fe15Ni (Figure 3) presented three new peaks at 2θ = 43.60, 50.84 and 74.69º, suggesting the formation of a Ni-Fe alloy (CAPES 26009) [24]; this alloy exhibited an FCC crystal structure. Similarly for 30Fe5Ni, peaks in the same positions were

observed, indicating the formation of a Ni-Fe alloy with FCC structure and suggesting that Fe replaced Ni in the unit cell. Additionally, the peaks remained in 2θ = 44.72 and 65.13º, characteristic of BCC Fe, might imply that there was phase segregation for the metallic phase of 30Fe5Ni: Ni-Fe alloy and pure Fe.

Figure 4 shows the TPR profiles for the studied materials. As the TPR curve for the support (YSZ-GDC) showed no event associated with reduction, the peaks that appeared in the sample TPR curve were attributed to the reduction of Ni and Fe species present in the composite materials. The different preparation methods for the monometallic Ni-based cermets led to solids with different resistances to reduction in hydrogen presence, observed by the differences in the areas delimited by the TPR peaks for the different materials. In these samples, the monometallic species that reduced in the temperature range of 410 - 420 °C presented weaker interactions with the support; the converse relation might also be inferred.

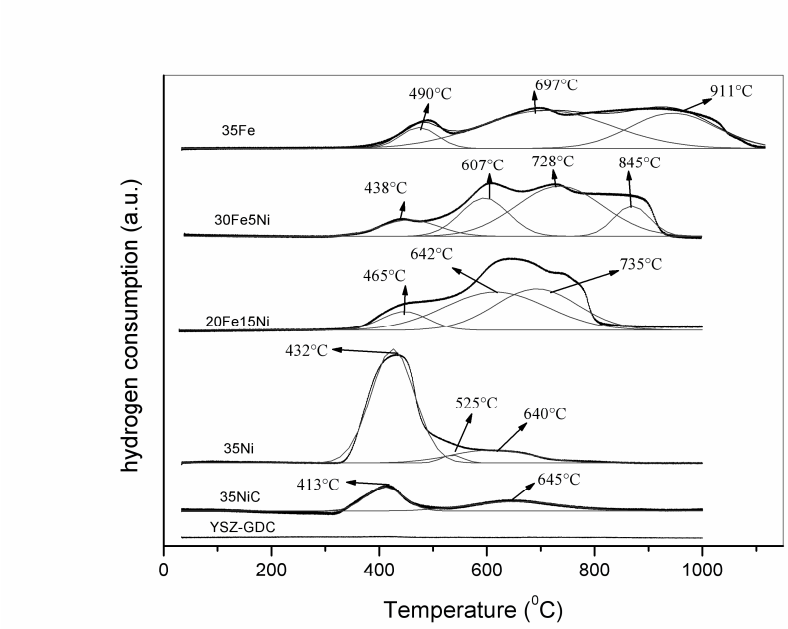

Figure 4: TPR profiles of the studied materials: (—) experimental profile; (—) Gaussian deconvolution of the TPR profiles.

Table 1 presents the quantitative data obtained from the sample TPR analyses. For the monometallic Ni samples, the stoichiometric ratio of 1:1 between H_2 and Ni was considered. For the monometallic Fe sample (35Fe), the stoichiometric relationship between molecular hydrogen and Fe was 3:2. Finally, for the bimetallic samples, the TPR hydrogen consumption was calculated as the sum of the individual consumptions for Ni and Fe species, each proportional to their concentration in the sample. The data indicate that the samples prepared using Pechini method achieved complete reduction of the metal oxides in the presence of hydrogen. In contrast, the 35NiC sample, prepared using the physical mixture method showed a low yield in the reduction of NiO with hydrogen, reducing only 14% of the oxide initially present in the sample.

Table 1: Hydrogen mol consumption obtained from the TPR analyses, the nominal molar load of sample, and the extension of metal reduction.

Samples	TPR hydrogen total consumption of (mols x 10^{-4})	nominal metal load (mols x10^{-4})			reduced metal (%)
		Ni	Fe	Total	
35 Ni	2.10	2.09	-	2.09	100
35 Ni C	0.30	2.09	-	2.09	14
35Fe	2.88		1.90	1.90	99
30Fe5NI	2.86	0.26	1.64	1.90	95
20Fe15Ni	2.64	0.72	1.01	1,72	88

Figure 5 shows the ethanol conversion for the steam reforming reaction at 650 °C for a six hour period of reaction. The results shown indicated that the electro-catalyst remained stable during the six hour period, with average ethanol conversion exceeding 80% for the samples containing Ni and prepared using Pechini method; in contrast, the average ethanol conversions for the 35NiC and 35Fe samples were respectively 43.5% and 54.8%; the average conversions presented standard deviations of less than 5%.

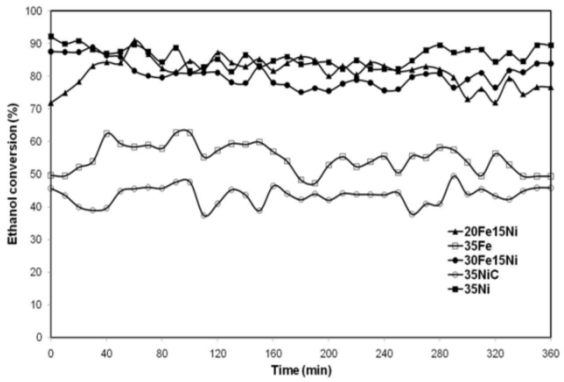

Figure 5: Ethanol conversion versus time on stream for samples prepared.

Figure 6 presents data for carbon deposition during the six hours on stream of the various electro-catalysts studied. The data are presented as carbon mass percentage by the catalyst mass after reduction. The data in Figure 6 strongly suggested that the presence of Fe in the samples significantly decreased the mass of carbon deposited on the electro-catalysts. This might be associated with the lower activity of Fe, compared to Ni, for secondary reactions that led to carbon formation, as observed by Huang et al. [3]. Studying a composite of Ni and Fe supported on ScSZ exposed to ethanol vapor for 24 hours, these authors found that carbon deposits increased as the Ni loading increased.

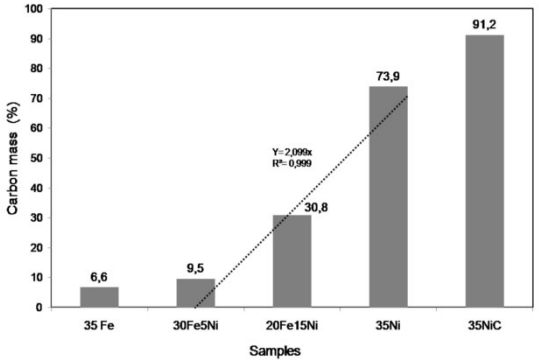

Figure 6: Carbon deposited on the electro-catalyst for ethanol steam reforming for six hours on stream, at 650 °C. Deposited carbon as percentage of electro-catalyst mass. The straight line correlates carbon formation with Ni contents.

The preparation method of the electro-catalyst also influenced its activity to catalyze reactions that led to carbon formation. The 35NiC sample prepared by physical mixture formed 17% more carbon than 35Ni sample, prepared using Pechini method. As a final important point, the samples containing Ni and prepared using the Pechini method exhibit a surprisingly linear correlation between the mass of deposited carbon and Ni content in the sample.

4 Conclusion

The Pechini method studied here for the synthesis of Ni-Fe/YSZ-GDC composites was very successfully used to produce powders with crystallographic and morphological characteristics suitable for use in SOFC anodes, whereas materials prepared using the physical method displayed limitations in particle size, reducibility, and hydrogen production.

Ni-Fe/YSZ-GDC composites are highly promising cermets for application as SOFC anode: they have a very high hydrogen yield in ethanol steam reforming reaction with a very low carbon formation. This final remark observation is especially applicable for the composites with low nickel content.

Acknowledgements

The authors gratefully acknowledge grants from the Brazilian Ministry of Science and Technology (MCT). They are especially grateful to Rede PaCOS (Grant 01.06.0901.00) and RECAT (Grant 22.02.0289.00). The authors also acknowledge FAPESB (MAS) and CNPq (RPF) for helpful scholarships.

Reference

[1] Hecht ES, Gupta GK, Zhu H, Dean AM, Kee RJ, Maier L, Deutschmann O. Appl. Catal. A: 2005;295:40.

[2] Atkinson A, Barnett S, Gorte RJ, Irvine, JTS, Mcevoy AJ, Mogensen M, Singhal SC, Vohs J. Nature Mater. 2004;3:17.

[3] Huang B, Wang SR, Liu RZ, Wen TL. J. Power Sources 2007;167:288.

[4] Douvartzides SL, Coutelieris FA, Demin AK, Tsiakaras PE. Int. J. Hydrogen Energy 2004;29:375.
[5] Hotza D, da Costa JCD. F Int. J. Hydrogen Energy 2008;33:4915.
[6] Park SD, Vohs JM, Gorte RJ. Nature 2000;404:265.
[7] Venancio SA, Gutierres TF, Sarruf BJM, Miranda PEV. Materia-Rio De Janeiro 2008;13:560.
[8] Ye XF, Wang SR, Hu Q, Chen JY, Wen TL, Wen ZY. Solid State Ionics 2009;180:276.
[9] Cimenti M, Hill JM. Asia-Pacific J. Chem. Eng. 2009;4:45.
[10] Resini C, Delgado MCH, Presto S, Luis J. Alemanyc LJ, Rianib P, Marazza R, Ramisa G, Busca G, Int. J. Hydrogen Energy 2008;33:3728.
[11] Jiang SP, Chan SH. J. Mater. Scie. 2004;39:4405.
[12] Amado RS, Malta LFB, Garrido FMS, Medeiros ME. Quimica Nova 2007;30:189.
[13] Zhao XY, Yao Q, Li SQ, Cai NS. J. Power Sources 2008;185:104.
[14] Mermelstein J, Millan M, Brandon NP. Chem. Eng. Sci. 2009;64:492.
[15] Gavrielatos I, Drakopoulos V, Neophytides SG. J. Catal. 2008;259:75.
[16] La Rosa D, Sin A, Lo Faro M, Monforte G, Antonucci V, Arico AS. J. Power Sources 2009;193:160.
[17] Baker RTK. Carbon 1989;27:315.
[18] Koh J-H, Yoo Y-S, Park J-W, Lim HC. Solid State Ionics 2002;149:157.

Electro-catalysts for Hydrogen Production from Ethanol for Use in SOFC Anodes

Marcos Aurélio da Silva, Raigenis da Paz Fiuza, Bruna C. Guedes, Luiz A. Pontes, Jaime Soares Boaventura, Energy and Materials Science Group, GECIM, Institute of Chemistry, Physical Chemistry Department, UFBA, 41170290, Salvador, Bahia, Brazil

Abstract

Nickel and cobalt catalysts, supported on YSZ, were prepared by wet impregnation, with and without citric acid; the metal load was 10 and 35% by weight. The catalyst composition was studied by XRF, XPS, and SEM-EDS. At low metal concentration, the results of these techniques presented comparables figures; at high concentration, SEM-EDS suggested a non-uniform distribution. The analysis showed that the solids were mixed oxides and formed an alloy after reduction. The surface passivation was possible under controlled conditions. The catalytic test with the steam reforming of ethanol indicated that the metal load had almost no effect on the catalytic activity, but decreased its selectivity. Afterwards, a unitary SOFC was prepared with deposition of the cathode layer. AFM and EIS were used for the characterization of SOFC components. They showed that the electro-catalyst surface was almost all covered with the metal phase, including the large pore walls of the anode. The YSZ phase dominates the material conductance of the complete SOFC assembly (anode/electrolyte/cathode). The unitary SOFC was tested with hydrogen, gaseous ethanol or natural gas; the SOFC operating with ethanol and hydrogen fuel presented virtually no over-potential.

Keywords: SOFC, ethanol, AFM, SOFC, EIS, XPS.

1 Introduction

Fuel cells are devices that directly convert the fuel chemical energy into electricity, with high efficiency and low pollutant emission. Among the several models, the solid oxide fuel cell (SOFC) attracts special interest. Because of its high operating temperature (800 – 1,000 °C) the SOFC presents high flexibility in fuel choice and the possibility of direct reform in the anode [1, 2]. The hydrogen production from the steam reforming of ethanol has attracted interest mainly for the use of bio mass in fuel cells [3]. Among transition metals, the high C–C bond-breaking activity and the relatively low cost of Ni and Co make it a suitable active phase for ethanol-reforming reactions [4]. Organic additives, including citric acid, have been added to act as a dispersant for a higher specific surface area of the support and a better distribution of active sites of the metal supported catalyst [5]. Atomic Force Microscopy (AFM) and X-ray photoelectron spectroscopy (XPS) are very well established techniques to probe the surfaces of most catalysts. [6, 7] Electrochemical impedance spectroscopy (EIS) has been extensively used to characterize fuel cells [8]. However, the simultaneous use of these three techniques has been relatively scarce [9]. Anodes prepared with nickel and cobalt supported on YSZ and with high metal load (35%) have been used in the preparation

of the solid oxide fuel cell (SOFC) [10] 4. The use of ethanol in the SOFC showed performance comparable to other fuels such as methane and hydrogen [11] 5.

2 Experimental

The wet impregnation method, with and without citric acid addition, was used for the catalyst syntheses. The support (YSZ), metal precursors (Ni and Co) and citric acid were mechanically mixed, with subsequent addition of small amounts of water for better homogenization of the mixture. The catalysts were calcined at 800 °C for two hours in air. The metallic composition of the catalysts samples were determined by XRF, SEM-EDX and XPS while the structure of the solid phase was analyzed by XRD. The AFM analyses were conduct on a transversal, clean and new surface, on non-contact mode, no prevent tip wear. EIS was made in air at variable temperature, with stainless steel contacts. The catalysts were evaluated in the ethanol steam reforming.

In the XPS experiments, the catalysts were initially calcined at 800 °C for two hours in air; afterwards the catalyst were reduced in situ with a hydrogen mixture of 10% molar in nitrogen, between 30 and 800 °C, with a heating rate of 10 °C per minute. The NiCo/YSZ catalysts were characterized by XRF, XRD, SEM-EDS, and XPS. XRF and XRD allowed to determine the bulk composition of the solids. The catalysts were characterized by SEM-EDS using a Shimdazu SS 550 model, with a 15 keV electron beam. XRD was performed in a Pananalytical X'Pert diffractometer with an Anton Paar cell for in situ treatment. The XRD analysis was in the following conditions: 16 - 90 °C, step of 0.016, 256 sec/step, time for total analysis: 2:30 h. Both catalysts were analyzed after calcination at 800 °C and exposition to air. Then the solid was exposed to a hydrogen flow, 20 ml/min, at ambient temperature, a diffractogram was registered and the temperature was increased to 250, 300, 350, 400, 450, 500 and 600 °C, using a heating rate of 2 °C/min. At each temperature it was given 30 minutes for temperature equilibration, before registration of the diffractogram. Each cycle of analysis was completed in 48 hours. After analysis under hydrogen, the solid was cooled under hydrogen flow to the ambient temperature, purged 30 minutes with N_2 flow and exposed gently to air for 12 hours. The passivation of the solid surface under controlled conditions was studied. XPS analysis was performed to determine the surface composition and the oxidation state of the elements at the surface. The spectra were obtained in an ESCALAB VG MKII using non-monochromatized Mg Kα radiation (1253.6 eV). The peak of C1s at 284.8 eV was used as reference.

3 Results and Discussion

Table 1 shows the catalyst composition measured by several techniques. The solid composition determined by XRF agreed with the nominal composition. The XPS analysis showed that the Ni surface concentration is close to its bulk concentration, but Co surface concentration was higher compared to the bulk concentration. These results agreed with the semi-quantitative XRF results for 5Ni5Co and 5Ni5Co-CA samples observed. The SEM-EDS analysis showed that the surface distribution of Ni and Co is not homogeneous, with regions with higher Ni and Co concentrations. XRD analysis [12] *in situ* showed that the catalyst after calcination formed a mixed oxide (figure 1) and that after reduction a NiCo alloy was formed. After reduction, the solid was carefully placed in contact with air. XRD analysis showed that

the alloy was preserved (figure 2), indicating that the passivation of the solid surface was successful. XPS analyses agreed with these results. The metal bulk was composed of a NiCo alloy; both oxides, Ni_2O_3 and CoO, were present at the surface. Figures 3 and 4 show the XPS spectra of the reduced samples.

Table 1: Compositions of reduced catalyst samples in mass percent, by XRF, SEM-EDS, and XPS.

Sample	XRF		SEM-EDS		XPS	
	Ni	Co	Ni	Co	Ni	Co
5Ni5Co	4.7	4.0	7.6	7.2	5.4	7.4
5Ni5Co-CA	4.9	4.2	6.4	6.0	5.4	7.3
32Ni3Co-CA	29,5	3,9	54.8	6.7	31.3	3.6

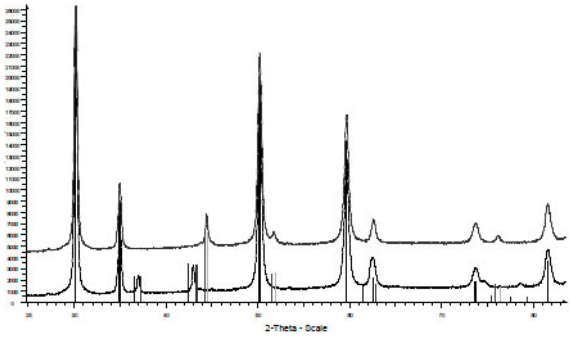

Figure 1: Diffractograms of calcined and reduced samples.

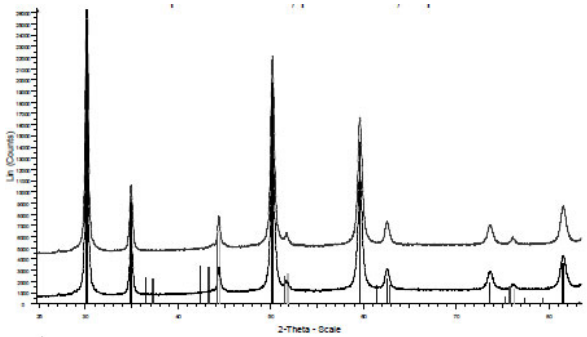

Figure 2: Diffractograms of the passivated sample.

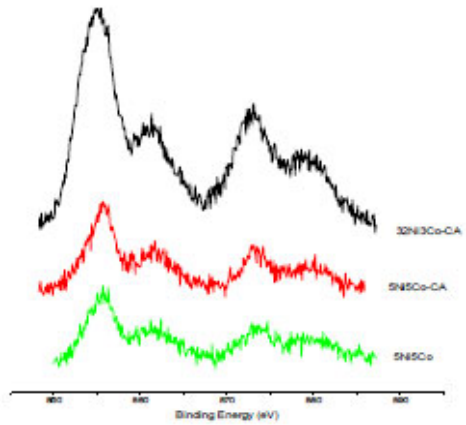

Figure 3: XPS of the calcined and reduced samples.

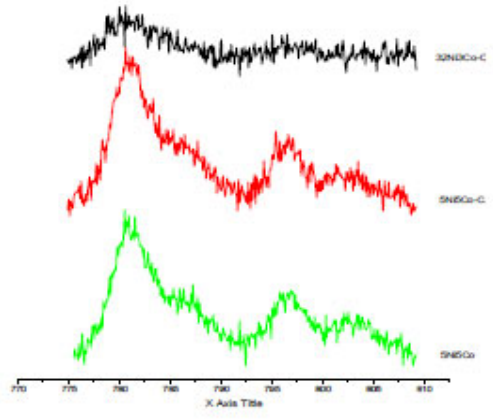

Figure 4: Diffractograms of the passivated sample.

Figure 5 showed the results of catalysts evaluation in ethanol steam reforming. Sample with higher metallic load presented slightly higher conversion of ethanol; they also showed lower selectivity for hydrogen production. Among the sample of low metallic load, the catalyst prepared with citric acid showed high selectivity. These result suggested that citric acid acted as a dispersant of metallic phase.

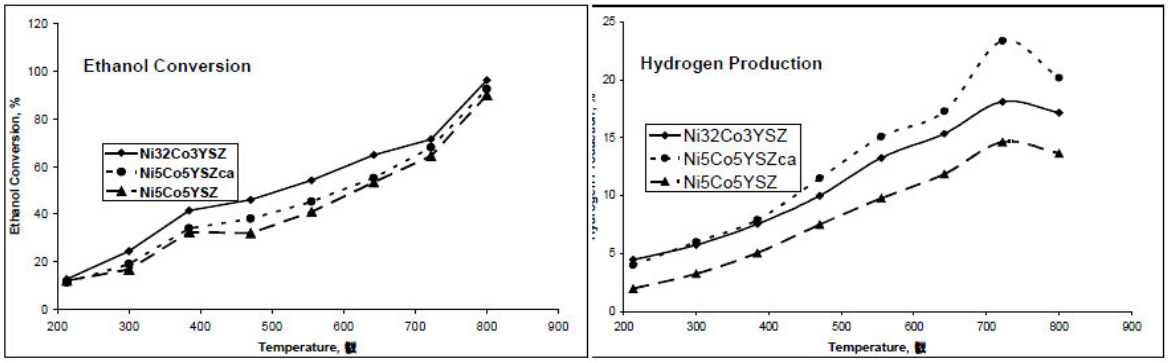

Figure 5: Ethanol conversion and hydrogen production in the ethanol steam reforming.

Figure 6 shows AFM analyses of the surface of the electro-catalyst prepared with YSZ and Ni (no Co was present). Region A (anode), surface had large holes (~1 mm) with depth exceeding 5 mm; probably the holes are vertical, since the images showed a V profile. Region B (electrolyte), the surface presented no holes, with 85 nm roughness on large scale, and 1.7 nm on small scale. Region C (cathode), the surface was very flat, with roughness of 72 nm, on a large scale, and 2 nm on small scale.

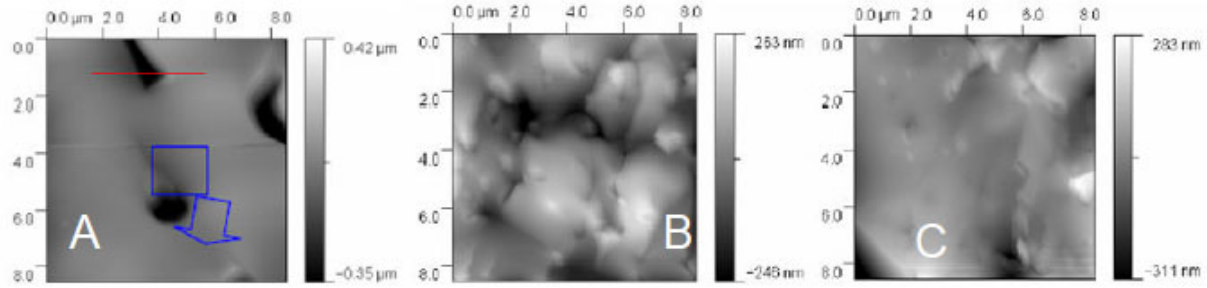

Figure 6: SOFC component AFM: a) anode (Ni/YSZ), b) electrolyte (YSZ), c) cathode (LSZ).

Figure 7 shows that the impedance decreased with increasing temperature, which indicated a raised ionic conduction for high temperatures; the impedance lowered for large frequencies. The impedance module, measure at 700 ºC and 106 Hz, was 5.1, 6.7, and 8.1 x 10^3 for the cathode/electrolyte/anode pellet, anode (Ni/YSZ) and electrolyte (YSZ) layers, respectively. From 700 to 400 ºC, the conductance activation was 0.5, 1.1, and 1.2 eV for the three materials. Apparently, for the anode and electrolyte layers, the YSZ dominated the conduction process. The electro-catalyst surface is almost all covered with the metal, including the large pore walls. The YSZ phase dominates the material conductance of the complete SOFC assembly (anode/electrolyte/cathode).

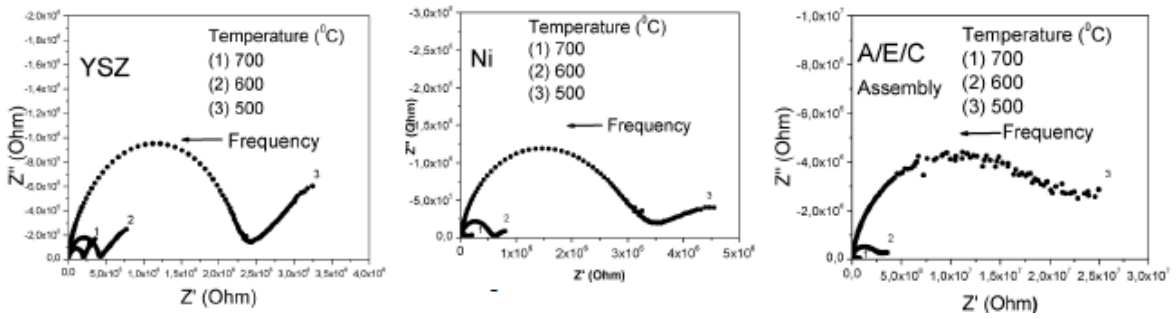

Figure 7: SOFC component EIS: a) anode (Ni/YSZ), b) electrolyte (YSZ), c) cathode (LSZ).

The unitary SOFC has been tested with hydrogen, gaseous ethanol or natural gas. The SOFC performance with the various fuels is shown in figures 8 and 9. One of the most remarkable features of the SOFC operating with ethanol and hydrogen fuel was the virtual absence of overpotential. This cell property is directly related to internal ohmic resistances, the lower the overpotential the lower the internal resistance. Therefore, the very low overpotential presented by the unitary SOFC was likely resulting from the excellent interface formed between the electrolyte and electrodes.

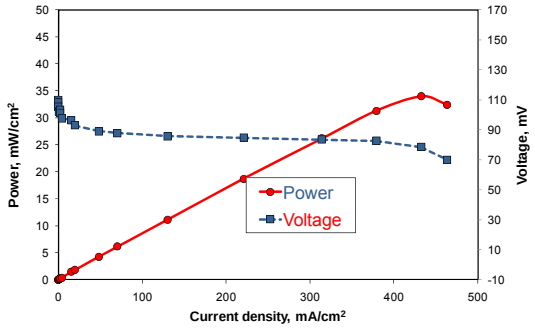

Figure 8: SOFC performance with ethanol at 800 °C (voltage and power density *versus* current density).

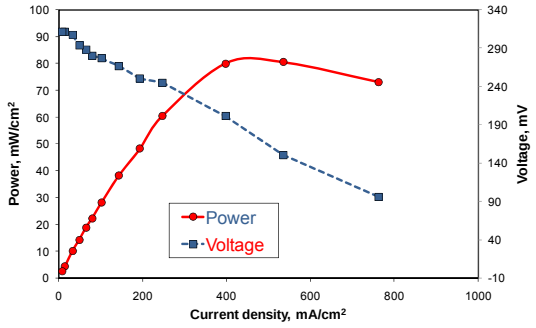

Figure 9: SOFC performance with methane at 800 °C (voltage and power density *versus* current density).

4 Conclusions

The analysis showed that the metal phase of the prepared catalysts was mixed oxides and that an alloy was formed after reduction. The surface passivation was possible under controlled conditions; after passivation the metal bulk remained as an alloy and the surface was a mixture of Ni and Co oxides. The metallic species were the active site for ethanol reforming, which explained the good activity results for these solids.

Furthermore, the metal, at low concentration, was uniformly dispersed on the catalyst support; different behavior was found for catalysts with high metal load. Nickel and cobalt formed stable alloy on YSZ, which after reduction remained as metal, even after exposure to air. The metal load had almost no effect on the catalytic activity, but decreased the

selectivity. At low metal load, the use of citric acid increased the catalytic selectivity, likely due to its dispersant effect.

Finally, AFM and EIS are very useful techniques for the characterization of SOFC components, being almost obligatory for fuel cell development. The electrocatalyst surface is virtually all covered with the metal, including the large pore walls. The YSZ phase dominates the material conductance of the complete SOFC assembly (anode/electrolyte/cathode).

References

[1] M. A. Silva, Jaime S. Boaventura, M. G. Alencar, C. P. Cerqueira, Revista Matéria, 12 (**2007**) 99

[2] S. C. Singhal and K. Kendall, “High-temperature Solid Oxide Fuel Cells: Fundamentals, Design and Applications”, Elsevier Science, UK, **2004**.

[3] T. A. Maia; J. D. A. Bellido; E. M. Assaf; J. M. Assaf, Química Nova, 30 (**2007**) 339.

[4] M. C. Sánchez-Sánchez, R. M. Navarro, J. L. G. Fierro. International Journal of Hydrogen Energy, 32 (**2007**) 1462.

[5] L. Shen, X. Zhang, Y. Li, X. Yang, J. Luo, G. Xu. Nanotechnology, 15 (**2004**) 337.

[6] T. W. Eom, H. K. Yang, K. H. Kim, H. H. Yoon, J. S. Kim, S. J. Park, Ultramicroscopy, 108 (**2008**) 1283.

[7] M. B. Pomfret, J. C. Owrutsky, R. A. Walker, Analytical Chemistry, 79 (**2007**) 2367.

[8] Y.J. Leng, S.H. Chan, K.A. Khor, S. P. Jiang, International Journal of Hydrogen Energy, 29 (**2004**) 1025.

[9] C. Guizard, A. Princivalle, Catalysis Today, 146 (**2009**) 367.

[10] M. A. Silva, M. G. Alencar, R. P. Fiúza, Fiúza, J. S. Boaventura. Revista Matéria, 12 (**2007**) 72.

[11] M. A. Silva, M. G. Alencar, R. P. Fiúza, Fiúza, J. S. Boaventura. Revista Matéria, 12 (**2007**) 99.

[12] K. D. M. Harris, M. Tremayne, Chemistry of Materials, 8 (**1996**) 2554.

Preparation of Anode-electrolyte Structures Using Graphite, Sodium Bicarbonate or Citric Acid as Pore Forming Agents for Application in Solid Oxide Fuel Cells

Raigenis da Paz Fiuza*, Marcos Aurélio da Silva, Bruna C. Guedes, Luiz A. Pontes, Jaime Soares Boaventura, Energy and Materials Science Group, GECIM, Institute of Chemistry, Physical Chemistry Department, UFBA, 41170290, Salvador, Bahia, Brazil

Abstract

Cermets based on Ni supported on YSZ or GDC were prepared for use as anode in direct reform SOFCs. $NaHCO_3$ (Na-Ni-YSZ and Na-Ni-GDC) or citric acid (Ac-Ni-YSZ and Ac-Ni-GDC) were used as pore forming agents (PFAs). The SOFC anode was also prepared using graphite (G-Ni-YSZ and G-Ni-GDC) as PFA for the purposes of comparison. The testing unitary SOFC, planar type, was made by pressing the anode-electrolyte assembly, followed by sintering at 1500 °C. After this, LSM (lanthanum and strontium manganite) paint was used for the cathode deposition. The powdered cermets were evaluated in ethanol steam reforming at 650 °C. The ethanol conversion was 84% and 32% for cermets Na-Ni-YSZ and G-Ni-YSZ, respectively and the selectivity to H_2 was 32% and 20% for the two cermets, respectively. The Na-Ni-YSZ cermet was ten times more resistant to carbon deposition than the G-Ni-YSZ cermet. SEM micrographs of the anode-electrolyte assembly showed that the use of $NaHCO_3$ as PFA created a well formed interface between layers with homogeneously distributed pores. In contrast, graphite as PFA formed a loose interface between anode and electrolyte. The performance of the unitary SOFC was evaluated using ethanol, hydrogen or methane as fuel. The cell operated well using any of these fuels; however, they exhibited different electrochemical behavior.

Keywords: SOFC, cermet, pore forming agent (PFA), YSZ, GDC, ethanol, methane

1 Introduction

In recent years, there has been a significant increase in research into new energy sources, especially focused on the production of clean energy. In this search for alternative sources, solid oxide fuel cells (SOFC) have been one of the highlights, offering an excellent option for the clean production of energy. They have therefore attracted great technological interest, especially for their capacity to handle almost any fuel. These cells can operate with pure H_2, but their cost is greatly minimized when they operate with hydrocarbon or ethanol directly reformed on the anode [1, 2].

SOFCs basically consist of three components: First, the electrolyte is composed of a dense material conductor of O^{2-} species. Second, the anode is usually made of a metallic electro-catalyst supported on the same (or similar) material used as electrolyte. Third, the cathode is

* Corresponding author, email: raigenis@ufba.brl

also an electro-catalyst of porous structure whose main task is to reduce oxygen and it usually consists of mixed oxides [3-6]. The performance of SOFCs strongly depends on the component microstructure, especially the anode structure [7], which should be well adhered to the electrolyte, making available paths for conducting oxygen ions to enlarge the boundary region of the triple phase. The anode must also have adequate porosity, around 40%, to allow a good fuel distribution, as well as a good dispersion of the metal phase on the support. The metal particle size distribution must be adequate to form a continuous metallic phase on the support, making the anode an electrical conductor [8]. This paper studies the construction and evaluation of the microstructure of an anode-electrolyte set as well as the catalytic activity of the anode, both produced using different pore forming agents (PFA): graphite, $NaHCO_3$ and citric acid. The microstructure was studied by means of scanning electron microscopy (SEM); the anode catalytic activity was evaluated for ethanol steam reforming.

2 Methodology

The preparation of anode-electrolyte set was made using graphite, $NaHCO_3$ or citric acid as PFA. The electrolyte was produced from YSZ (8 mol-% Y_2O_3 in ZrO_2) and GDC ($Gd_{0.1}Ce_{0.9}O_2$); the three PFAs were used with both materials. First, a mixture of YSZ, graphite and NiO was prepared to produce the anode [9, 10], formulate to contain 35% by weight of Ni metal and enough graphite to generate an average porosity of 40%. The electrolyte was formed with pure YSZ; a layer of the previous described mixture (as anode) and a layer of pure YSZ (as electrolyte) were put into a steel mold and pressed to produce pellets of an average thickness of one millimeter. This set based on YSZ, NiO and graphite was called G-Ni-YSZ. The same procedure was reproduced, replacing YSZ, both in the electrolyte and anode, by GDC; the set was named G-Ni-GDC. The sets were synthesized according to a careful heating program, taking into account the temperature of melting, boiling and decomposition of PFA and Na derivatives formed during the sintering in air, up to a temperature of 1500 °C for effective sintering. The samples were characterized by Scanning Electron Microscope (SEM) techniques and the average porosity was measured by water absorption.

To evaluate the effect of residual Na on the electro-catalyst, two cermets were prepared. For the first one, NiO, YSZ (8% Y_2O_3 in ZrO_2) and graphite (as PFA) were mechanically mixed and sintered at 1400 °C. This cermet was named G-Ni-YSZ. The other cermet was prepared in a similar fashion, however, the graphite was replaced by $NaHCO_3$; this cermet was named Na-Ni-YSZ. The Ni contents of both cermets were around 35% in mass. After sintering, the cermets were reduced to powder and separated in a 300 mesh sieve. They were evaluated in ethanol steam reforming at 650 °C in a quartz flow reactor and the reaction products were analyzed by gas chromatography. For the unitary SOFC preparation, the anode (Na-Ni-YSZ) and electrolyte were similarly pressed in a steel mould and sintered at 1500 °C for 3 hours. Afterwards, the cathode was prepared by adding a thin layer of LSM ink and sintered at 1200 °C for one hour. Platinum screens, set on both sides of the cell by ink platinum, were used as the electrical contact. Platinum wires were used to connect the cell terminals to the circuit test. A high temperature ceramic bond was used to fix the cell to an alumina tube

which supplied fuel and oxygen to the cell. The system was put into a controlled temperature furnace and the cell was tested at 800 °C using ethanol, methane or H_2 as fuel.

3 Results and Discussion

The dense aspect of the samples seen in the microphotographs indicated that they reached a high degree of densification, as Figure 1 shows. Additional SEM microphotographs revealed the good densification of GDC electrolyte, showing that the temperatures used were appropriate for its sintering. As noted in the literature, YSZ can be well sintered at lower temperatures, around 1350-1400 °C, however, GDC requires a higher sintering temperature, around 1450 °C [4, 9, 10]. For all the SOFCs prepared in this work, the electrolytes had an average thickness of 150 to 200 µm and the anodes were 400 µm thick, measured using SEM techniques.

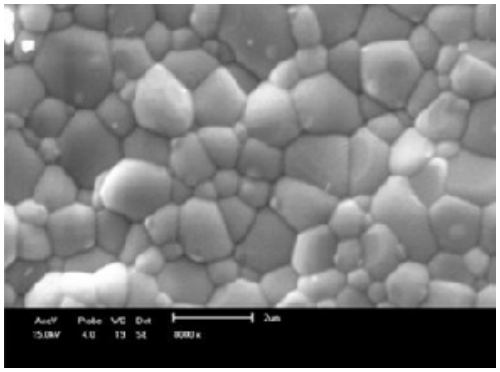

Figure 1: SEM image obtained from fracture region of AC-Ni-GDC electrolyte sample after sintering at 1500 °C.

The micrographs in Figure 2 show that the use of graphite as a PFA led to the formation of well distributed pores over the anode; they were uniform and connected to each other. However, the graphite apparently induced a separation of anode and electrolyte layers, weakening the interface and allowing these layers to come easily apart. This separation between anode and electrolyte was probably related to the lubricant action of graphite, preventing good adhesion between the anode and electrolyte layers; therefore the anode-electrolyte interface formed discontinuities during the sintering process [11]. The separation between anode and electrolyte probably reduced the number of available passes of oxygen ions [3].

The addition of $NaHCO_3$ or citric acid to the anode as PFAs led to the formation of pores with the same characteristics as observed in samples prepared with graphite, i.e. pores well distributed over the anode, uniform and connected to each other. However, excellent connectivity between anode-electrolyte, for both Na-Ni-YSZ and Ac-Ni-YSZ samples, was observed, as may be seen in Figures 3 and 4. The good adherence between anode-electrolyte layers for pellets made using $NaHCO_3$ as a PFA may be attributed to the formation of a liquid phase during heating due to the formation of sodium hydroxide and oxide [12]. This liquid phase served as a bonding agent and promoted such a good adhesion

between anode and electrolyte layers that they formed a single block. Furthermore, pellets made with citric acid as a PFA showed adherence as good as those made with sodium [13].

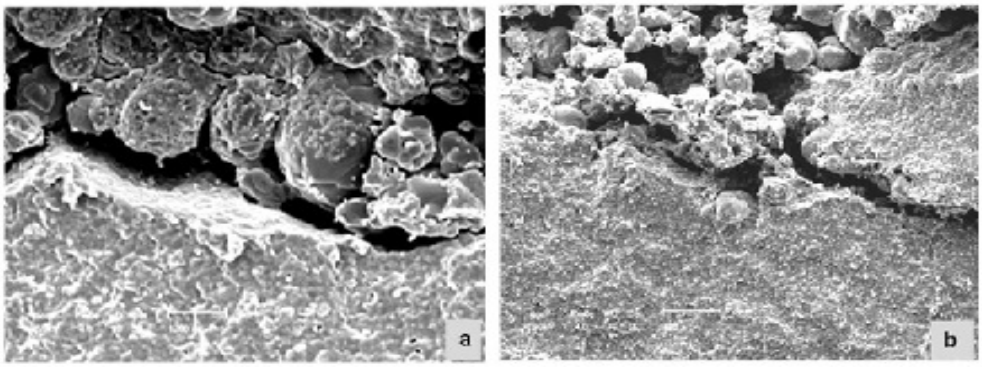

Figure 2: SEM image obtained from the electrolyte-anode interface of fractures – a) G-Ni-YSZ; b) G-Ni-GDC – both samples after sintering at 1500 °C (1220x magnification).

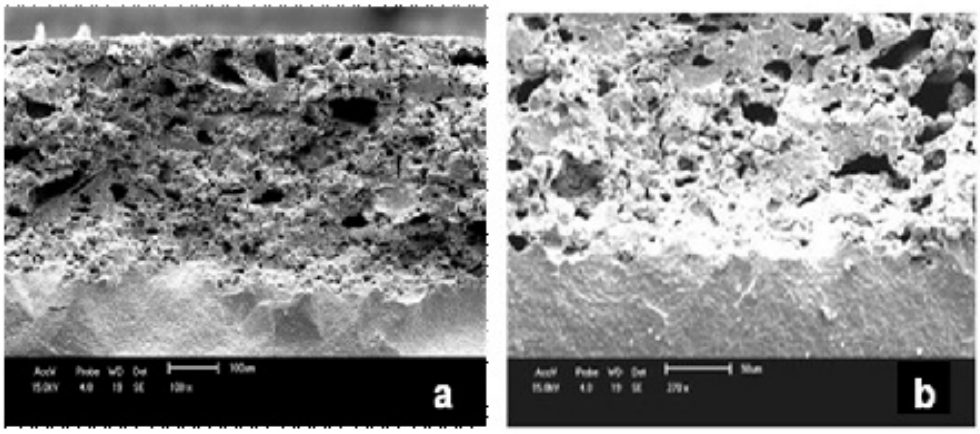

Figure 3: SEM image of the electrolyte-anode interface: a) Na-Ni-YSZ and b) Na-Ni-GDC.

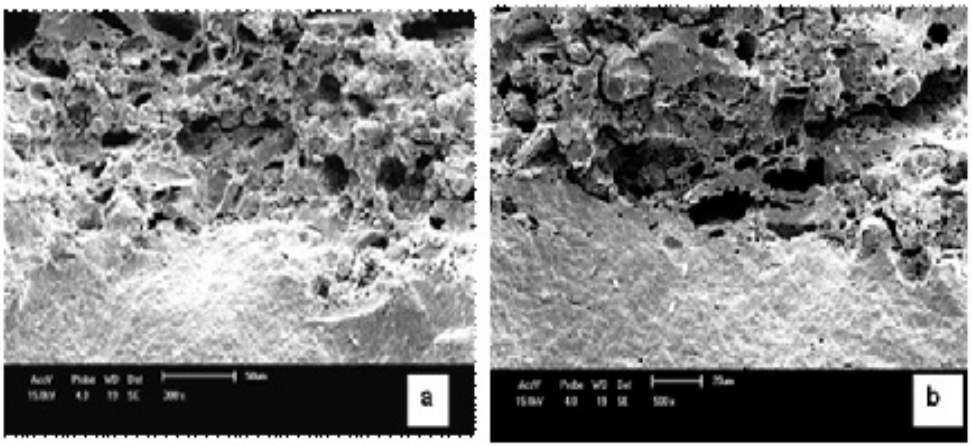

Figure 4: SEM image of the electrolyte-anode interface: a) Ac-Ni-YSZ and b) Ac-Ni-GDC.

Figure 5 shows a SEM micrograph of the anode-electrolyte-cathode assembly used for the unitary SOFC test. The anode-electrolyte-cathode interfaces were well constructed and did not present any discontinuity. Well constructed interfaces are fundamental for the performance of the cell in electricity generation [14]. Müller et al. [15], investigating electrode (cathode and anode) and electrolyte interfaces, reached the same conclusion regarding the fundamental role of interfaces on unitary SOFC performance. Furthermore, Weber and Ivers-Tiffée [16] demonstrated that the penetration of the electrolyte phase into the electrode phase significantly lowered the cell ohmic resistance. On the other hand, discontinuity regions at the interfaces drastically reduced the performance of the cell [17].

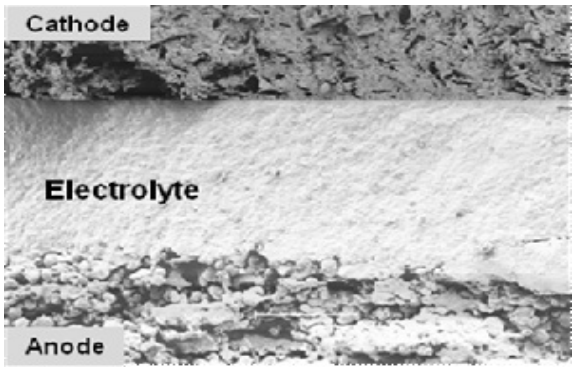

Figure 5: SEM image obtained from the cathode-electrolyte-anode interface of a fracture of Na-Ni-YSZ samples after sintering at 1500 °C.

The results of the catalytic test, carried out for the steam reforming of ethanol at 650 °C, showed that the Na-Ni-YSZ cermet was more active than the G-Ni-YSZ sample. The ethanol conversion increased by a factor of 2.5 and the H_2 production increased almost twofold. These tests also indicated that the relative amount of deposited carbon for the Na-Ni-YSZ cermet was around ten times lower than the carbon formation on the G-Ni-YSZ cermet. This significant reduction in carbon formation was attributed to the lower acidity of the Na-Ni-YSZ sample due to the basic effect of Na species formed during the cermet sintering. These results are in agreement with Haryanto et al. and Llorca et al. [18, 19]. They observed that the reduction in acidity of the catalyst was beneficially reflected in reducing the formation of carbon deposits which contributed to the deactivation of the catalyst when the cells were fed directly with gaseous ethanol. In addition to the higher activity of Na-Ni-YSZ, this electro-catalyst was more stable than the G-Ni-YSZ cermet during the studied reaction period. These results may be seen in Figure 6. The figure presents the H_2 concentration profile obtained during the test for carbon deposition. The reaction was carried out for one hour and Na-Ni-YSZ lost around 2% of its activity, while G-Ni-YSZ deactivated by around 17%. The improved stability of Na-Ni-YSZ is in agreement with results reported by Frusteri et al. [20], who noticed lower deactivation of electro-catalysts with lower acidity.

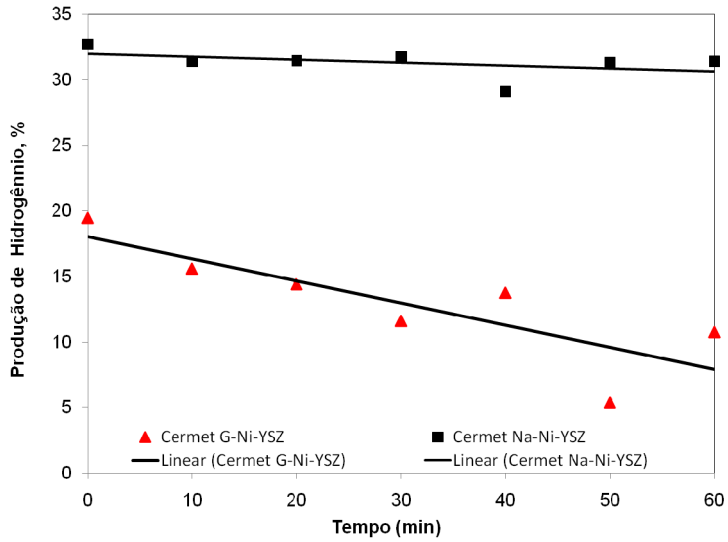

Figure 6: H_2 production from the steam reforming of ethanol at 650 °C, measured as molar concentration at the reactor outlet. The reaction was carried out for one hour.

The unitary SOFC has been tested with H_2, gaseous ethanol or methane; the performance of the SOFCs with the various fuels is shown in Figures 7 to 9. The power delivered by the cell increased with the fuel used in the following order: H_2 < ethanol < methane. The differences in the cell behavior with the various fuels may be explained on the basis of H_2 species availability on the triple phase boundary (TPB). The adsorbed H_2 species were readily available from the methane or ethanol reforming, while adsorption and dissociation steps were required for gaseous H_2. This variation in the cell performance with the fuel used may be better seen from the potential and over-potential versus current curves, shown in Figures 8 and 9, respectively. The potential curve profile for ethanol, with a steep over potential variation at low current, suggest that the anode concentration polarization was the dominant term for the ethanol cell over-potential [22, 23]. This term may arise from the lower diffusivity of gaseous ethanol. Following the low current regime, the over-potential was very closely linear to the current for all three fuels. This linearity of the over-potential has been associated with the activation and ohmic polarizations of the cell [24, 25]. The linear coefficient of the over-potential dependence on cell current increased with the fuel used as follows: ethanol < methane < H_2. This order is in agreement with the above reasoning that H_2 adsorption and dissociation were significant kinetic steps in H_2 oxidation; Ye et al. [26] made a similar observation. Furthermore, if one assumes that activation polarization are negligible for the ethanol over potential, the cell ohmic polarization was comparable to the cell activation polarization with methane and half the value with H_2 [24]. The results suggested that the cell resistance due to the electrolyte layer and its interfaces was relatively low, indicating that the $NaHCO_3$ used as PFA was an excellent alternative.

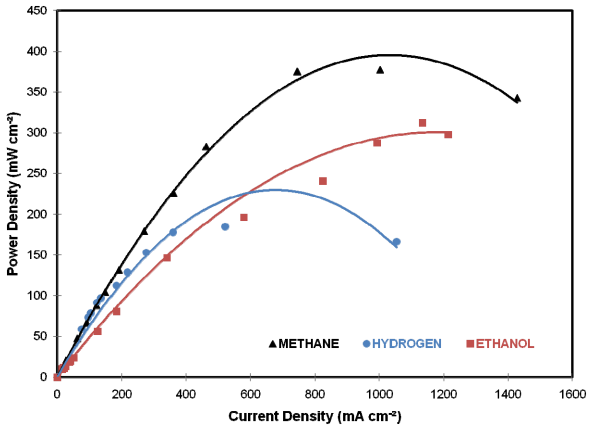

Figure 7: Performance of unitary test SOFC operating at 800 °C.

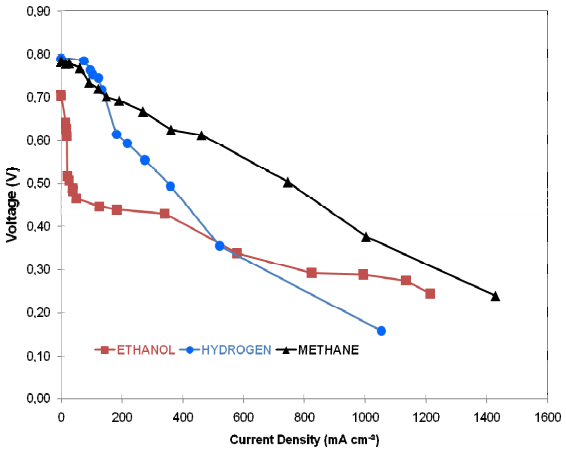

Figure 8: Cell potential versus current density for the unitary test SOFC operating at 800 °C.

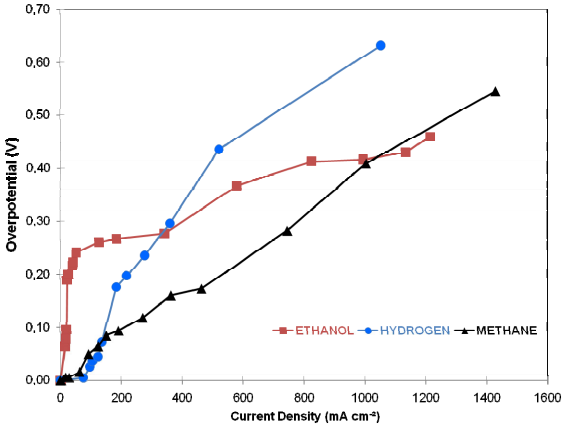

Figure 9: Cell over-potential versus current density for the unitary test SOFC operating at 800 °C.

4 Conclusion

The results show that the temperature of 1500 °C is well suited to the promoting of good sintering of GDC and YSZ pellets. Lower temperatures may sinter YSZ, but not GDC. $NaHCO_3$, citric acid and graphite have similar characteristics in the formation of coalescing, connected and well distributed pores. However, $NaHCO_3$ and citric acid, unlike graphite, enables strong adhesion of the interface between anode and electrolyte, forming a compact block which is a very important feature for high efficiency SOFCs. Furthermore, the cermets prepared with $NaHCO_3$ presented higher activity for ethanol steam reforming and around a ten times lower tendency for carbon deposition in comparison with the cermet prepared with graphite. The unitary SOFC prepared with an anode using $NaHCO_3$ as a pore forming agent shows low internal ohmic resistance for all the fuels tested (H_2, ethanol and methane),

indicating very high ionic conductance of the anode-electrolyte interface. These aspects contribute significantly to the technological advancement in the development of fuel cell components, overcoming one of the major barriers to increasing cell efficiency by the reduction of the ohmic resistance of the device.

Acknowledgments

The authors gratefully acknowledge grants from the Brazilian Ministry of Science and Technology (MCT) to support this work. They are particularly grateful to Rede PaCOS (grant 01.06.0901.00) and Rede Norte/Nordeste de Catálise (RECAT, grant 22.02.0289.00), supported by FINEP/CT-PETRO. The authors also acknowledge FAPESB (MAS) and CNPq (RPF) for their helpful scholarships.

References

[1] A. B. Stambouli, E. Traversa, Renew. Sust. Energ. Rev., 6 (**2002**) 433.

[2] A. Atkinson, S. Barnett, R. J. Gorte, J. T. S. Irvine, A. J. McEvoy, M. Mogensen, S. C. Singhal, J. Vohs, Nature Mater., 3 (**2004**) 17.

[3] D. Z. de Florio, F. C. Fonseca, E. N. S. Muccillo, R. Muccillo, Cerâmica, 50 (**2004**) 275.

[4] J. B. Goodenough, Annu. Rev. Mater. Sci., 33 (**2003**) 91.

[5] K. Chen, Z. Lü, X. Chen, N. Ai, X. Huang, B. Wei, J. Hu, W. Su, J. Alloys Compd., 454 (**2008**) 447.

[6] R. S. Amado, L. F. B. Malta, F. M. S. Garrido, M. E. Medeiros, Química Nova, 30 (**2007**) 189.

[7] J.-H. Lee, J.-W. Heo, D.-S. Lee, J. Kim, G.-H. Kim, H.-W. Lee, H. S. Song, J.-H.Moon, Solid State Ionics, 158 (**2003**) 225.

[8] R. J. Gorte, J. M. Vohs, J. Catal., 216 (**2003**) 477.

[9] M. A. Silva, M. G. F. Alencar, R. P. Fiuza, J. S. Boaventura, Revista Matéria, 12 (**2007**) 72.

[10] M. A. Silva, J. S. Boaventura, M. G. Alencar, C. P. Cerqueira, Revista Matéria, 12 (**2007**) 99.

[11] H. Yu, P. Hu, T. Shang, M. Jiang, Q. Chen, J. Wuhan Univ. Technol. - Mater. Sci. Ed., 23 (**2008**) 130.

[12] A. S. Maia, V. K. L. Osorio, Química Nova, 26 (**2003**) 595.

[13] J. Zhao, X. Liu, L. Qiang, Thin Solid Films, 515 (**2006**) 1455.

[14] A. McEvoy in S.C. Singhal, K. Kendall (Eds.). Elsevier, Netherlands, 149-171, **2003**.

[15] A. C. Müller, D. Herbstritt, E. Ivers-Tiffée, Solid State Ionics, 152 (**2002**) 537.

[16] A. Weber, E. Ivers-Tiffée, J. Power Sources, 127 (**2004**) 273.

[17] Y. L. Liu, S. Primdahl, M. Mogensen, Solid State Ionics, 161 (**2003**) 1.

[18] A. Haryanto, S. Fernando, N. Murali, S. Adhikari, Energ. Fuel., 19 (**2005**) 2098.

[19] J. Llorca, N. Homs, J. Sales, J. L. G. Fierro, P. R. de la Piscina, J. Catal., 222 (**2004**) 470.

[20] F. Frusteri, S. Freni, Chiodo L. Spadaro, O. D. Blasi, G. Bonura S.Cavallaro, Appl. Catal. A, 270 (**2004**) 1.

[21] J. R. Rostrup-Nielsen, L.J. Christiansen, Appl. Catal. A, 126 (**1995**) 381.
[22] W. Z. Zhu, S. C. Deevi, Mater. Sci. Eng. A 362 (**2003**) 228.
[23] S. H. Chan, K. A. Khor, Z. T. Xia, J. Power Sources, 93 (**2001**) 130.
[24] M. Ni, M. K.H. Leung, D. Y. C. Leung, Energy Convers. Manage., 48 (**2007**) 1525.
[25] W. G. Bessler, S. Gewies, M. Vogler, Electrochim. Acta, 53 (**2007**) 1782.
[26] X. F. Ye, S. R. Wang, Z. R. Wang, L. Xiong, X. F. Sun, T. L. Wen, J. Power Sources, 177 (**2008**) 419.

Advanced Modeling in Fuel Cell Systems: A Review of Modeling Approaches

Matthew M. Mench

Abstract

A review of fuel cell modeling approaches across various length scales is given, with special focus on low-temperature hydrogen-fed polymer electrolyte fuel cell (PEFC) systems. The overall scope of fuel cell modeling is incredibly broad, and ranges from fundamental atomistic modeling of catalytic processes and transport to nearly completely empirically based online system control models. In the first part an overview of the various scales of modeling is given, with some examples from the literature, along with a summary of the common limitations and requirements for successful predictive capabilities. In the second part, a critical analysis of the present state of polymer electrolyte fuel cell performance and water management models is given, and the inability of the existing framework of models to accurately predict the liquid water distribution and transport in the PEFC is demonstrated and discussed. Based on the discussion of the various modeling approaches and the limitations in the current framework, the needs of future research to provide precise fundamental and engineering models are discussed.

Hierarchical 3D Multiphysics Modelling in the Design and Optimisation of SOFC System Components

M. Peksen, **Ro. Peters**, **L. Blum**, **D. Stolten**, Institute of Energy Research – IEF-3
Fuel Cells Research Centre Jülich GmbH, Jülich, D-52425, Germany

Abstract

This paper presents a novel bottom-up modelling approach to aid in the design and optimisation of the Research Centre Jülich type integrated module components. The approach is demonstrated by employing the air pre-heater component. A feasibility study substituting the real design with a simplified one is introduced. Analogue design simplifications are performed to the afterburner and pre-reformer component. The integrated module, including the simplified system components is simulated in 3D, considering the multiphysics that occur within each component. The predictions of the air pre-heater component are compared to the stand-alone air pre-heater simulation results. The results are in very good agreement. The approach is proven to be useful for the optimisation of the integrated module. Moreover, the results reveal that stand-alone component analyses are feasible, and can be used for the investigation of local processes, the development and construction of models, and the structural design optimisation of each individual component.

1 Introduction

The successful optimisation of the SOFC technology depends upon a thorough understanding of the whole system components and their interactions. The optimal proportioning and structural design of each component depends upon the process conditions it is subjected to. To peruse experimentally the effects of the design and operating parameters on each system component, or on the overall integrated module performance, is prohibitive; especially, at high temperatures. Computational modelling of individual Jülich type SOFC system components together with experimental validations has been elucidated in previous studies [1-3]. The use of computational modelling is an attempt to bring mathematical optimisation into the product development mainstream. However, the design of the individual components combined with the multiphysics, is very complicated. Moreover, for a given system configuration it is difficult to determine the optimal performance, proportioning of components and subsystems that interact and work together to yield the overall system characteristics. This implies that for a reliable and cost efficient optimisation, pursuing a systematic concept is indispensable. In a previous study [2], a systematic trio approach has been introduced to develop and employ an optimisation strategy for the design and optimisation of SOFC system components. Coupling this strategic concept with the design innovation is a challenging task.

This paper presents a novel hierarchically divided bottom-up modelling approach for the design and optimisation of the integrated SOFC module, developed and tested at the Research Centre Jülich. A combinatorial multiphysics analysis considering the fluid flow, heat

transfer, chemically reacting species transport, and the thermo mechanics of the integrated module components, has been proposed.

2 Approach

The integrated SOFC module of the Research Centre Jülich is a complex system involving apart of the fuel cell, three more major components i.e., afterburner, air pre-heater and pre-reformer. Each component involves various processes contributing to the overall performance of the whole integrated module. To design and optimise the overall system performance, a hierarchically divided bottom-up approach is employed. Figure 1 depicts the general methodology.

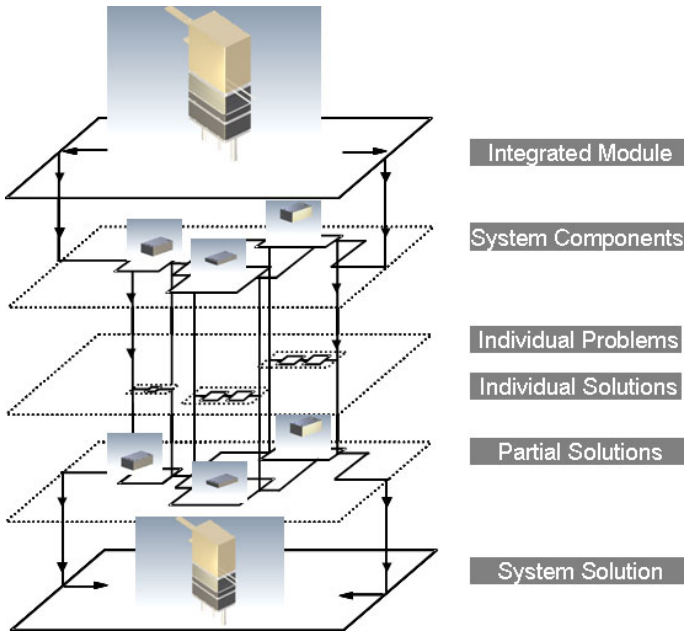

Figure 1: Schematic view of the employed bottom-up approach.

The full scale integrated module is virtually partitioned in stand-alone system components, each consisting of single unit assemblies stacked on top of each other. Each individual component comprises individual problems including additional sub components, different geometrical aspects and many different process conditions. This ensures the investigation of local processes, development and construction of models, and the structural design optimisation of each individual component. Moreover, this contributes much to a better understanding and prediction of each component's autonomous behaviour. The extrapolation of the obtained data will provide fundamental knowledge about the whole system behaviour. To verify the methodology, a feasibility study has been introduced and demonstrated on the air pre-heater component of the integrated module. The thermo fluid flow behaviour of the real air pre-heater design is compared to a simplified design. Analogue design simplifications are applied to the afterburner and the pre-reformer, mitigating the numerical difficulties associated with the geometrical and physical difficulties. In order to investigate the interaction of the air pre-heater with the peer components, the integrated module model is developed

and simulated using the simplified component designs. The air pre-heater results predicted from the whole integrated module simulation are compared to the numerical predictions performed using the stand-alone air pre-heater component.

3 Results

To test and verify the feasibility of the attempted approach, computational fluid dynamics is used to determine the thermo fluid flow behaviour of the real air pre-heater design and compare to the simplified design. The predicted results are illustrated in Figure 2.

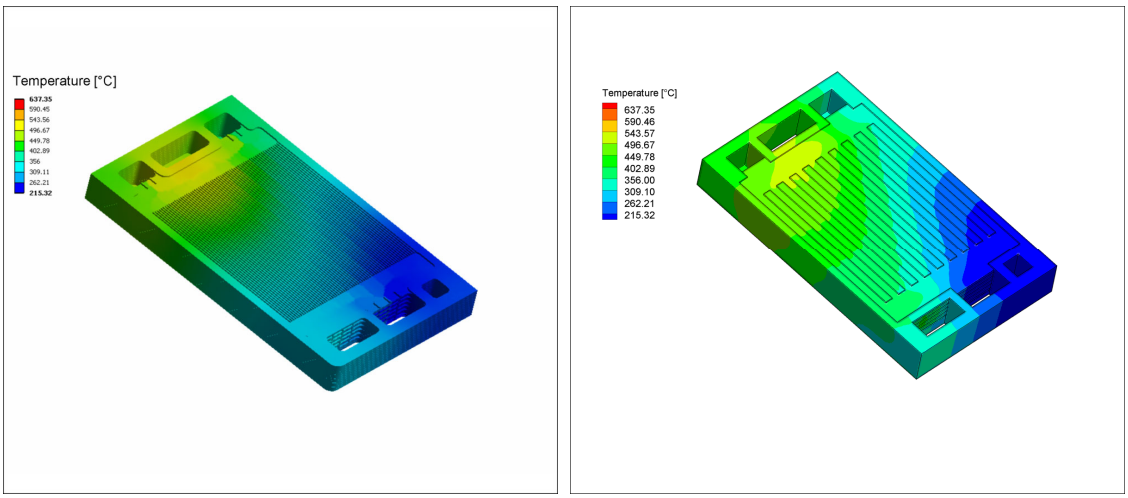

(a) (b)

Figure 2: Temperature contour plot of the real pre-heater design (a) and simplified design (b)

The results show that the simplified design depicts the temperature profile of the real design reasonable. The cooler part of the pre-heater due to the reformer fuel is well captured. The distribution also reveals that a sufficient heat exchange could be achieved with a smaller design as well. Hence, substituting the real design with the simplified one is feasible. In order to understand the limits of investigating stand-alone components compared to an analysis performed with the whole system components, the simplified stand-alone air pre-heater is compared with the results of the pre-heater simulated considering all three system components i.e. afterburner, air pre-heater and the pre-reformer together. Figure 3 illustrates the comparison.

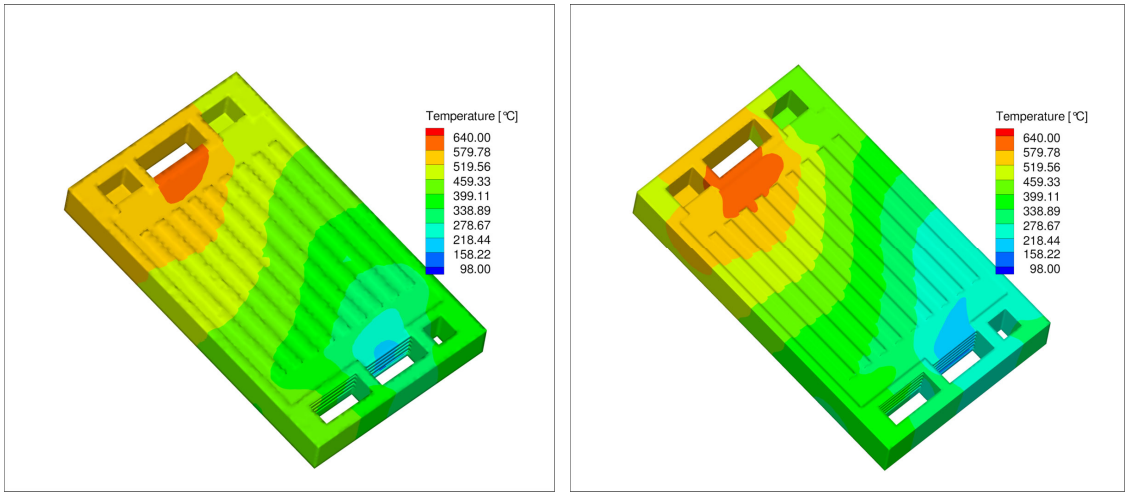

(a) (b)

Figure 3: Temperature contour plot comparison of the integrated module simulation (a) to the stand-alone component simulation (b).

The numerically predicted temperature profile obtained from the integrated module shows very good agreement with the stand-alone component. prediction. With negligible differences it can be stated that the demonstrated results of the stand-alone component are sufficient to obtain a better understanding about how each component performs within the integrated module and what impact the interaction of the components has on different physics of interest. The data provided enables to undertake an accurate design optimisation of each individual component.

4 Conclusions

A 3D bottom-up modelling approach has been proposed to design and optimise the Research Centre Jülich type integrated solid oxide fuel cell module. The feasibility to employ simplified component models has been tested and verified. The integrated module considering the whole system components i.e. afterburner, air pre-heater and the pre-reformer are considered in the model, including all physicochemical processes occurring within each component. Results predicted from the module simulation are compared to the stand-alone component simulation, being demonstrated using the air pre-heater component. Results are in very good agreement. The stand-alone component analyses enable a thorough investigation of each constituent of interest, providing detailed information about each component's autonomous behaviour. This ensures a reasonable component design optimisation Furthermore, it can be concluded that the stand-alone analyses yield to reasonable results, providing information about the component behaviour within the integrated module. The employed approach is proven to be an invaluable tool that can be used in local or global optimisations, in order to assist a rational new system design.

Acknowledgements

The technical staff of the SOFC Systems Technology Research Group, Research Centre Jülich is gratefully acknowledged.

Solid Oxide Fuel Cell and Biomass Gasification Systems for Better Efficiency and Environmental Impact

C. Ozgur Colpan, Mechanical and Aerospace Engineering Department, Carleton University, 1125 Colonel by Drive, Ottawa, Ontario, Canada
Feridun Hamdullahpur, Mechanical and Mechatronics Engineering Department, University of Waterloo, 200 University Avenue West, Waterloo, Ontario, Canada
Ibrahim Dincer, Faculty of Engineering and Applied Science, University of Ontario Institute of Technology, 2000 Simcoe Street North, Oshawa, Ontario, Canada

Abstract

In this paper, a conventional biomass fueled power production system is compared with a SOFC and biomass gasification system in terms of efficiency and greenhouse gas emissions. A heat transfer model of the SOFC and thermodynamic models for the other components of the systems are used to find the performance assessment parameters of the systems. These parameters are taken as electrical and exergetic efficiencies. In addition, specific greenhouse gas emissions are calculated to evaluate the impact of these systems on the environment. The results show that the SOFC and biomass gasification system has higher electrical and exergetic efficiencies and lower greenhouse gas emissions.

Keywords: biomass, SOFC, gasification, steam turbine, greenhouse gas, energy, exergy, efficiency

1 Introduction

SOFC is one of the high temperature fuel cells that can operate in temperatures ranging from 500 °C to 1000 °C depending on the manufacturing type, e.g., electrode-supported and electrolyte-supported. SOFCs have several advantages over low temperature fuel cells, e.g. proton exchange membrane fuel cell, such as: being simpler in design concept since there is no liquid phase, fuel flexibility, internal reformation of the gases, and integrability with other systems, e.g. gas turbine and gasifier. However, fuel containing carbon and sulphur can cause problems related to carbon deposition and sulphur poisoning, respectively. In addition, there are challenges with construction and durability due to the high operating temperature.

Biomass gasification is a thermochemical conversion technology where fuel is converted into a gas mixture called syngas, but also contaminants. The composition of this gas mixture depends on the fuel, e.g. wood and municipal solid waste, gasifier type, e.g. downdraft, updraft, and fluid bed, gasification agent, e.g. air, oxygen, and steam, and other operating parameters of the gasifier, e.g. temperature and pressure. There are two types of gasification processes: autothermal and allothermal. In autothermal gasification, heat is provided by partial oxidation that takes place within the gasifier; whereas in allothermal gasification, an external source supplies the heat needed for gasification reactions.

Studies on integrated biomass fueled SOFC systems and their analyses have increased recently. Panopoulos et al. [9][10] investigated the integration of a SOFC with an allothermal biomass gasifier using steam as the gasification agent. They found the electrical efficiency of

the system as 36% and exergetic efficiency as 32%. Cordiner et al. [7] studied the integration of a downdraft gasifier with a SOFC. They calculated the electrical efficiency of the system as 45.8%. Athanasiou et al. [2] analyzed the integrated SOFC, steam turbine and gasifier system. They found the electrical efficiency of the system as 43.3%. Omosun et al. [8] compared different gas cleanup types to be used in biomass gasification and SOFC system. Their study showed that hot gas cleanup should be selected for better performance and economical solution. Colpan et al. [5] studied the effect of gasification agent on the performance of an integrated SOFC and biomass gasification system. They found that the system in which steam is used as the gasification agent yields higher electrical and exergetic efficiencies compared to the systems in which air or enriched oxygen are used as the gasification agents. In another study by Colpan et al. [6], different technologies including the internal combustion engine, the gas turbine and the SOFC are compared in terms of performance and greenhouse gas reduction to be used in a landfill site. Their study showed that the SOFC shows higher performance and greenhouse reduction compared to the other systems studied.

In this study, a conventional biomass fueled power production system, i.e. a steam turbine system using the heat recovered from the combustion of biomass, is compared with an advanced biomass gasification and SOFC system in terms of efficiency and environmental impact. Electrical and exergetic efficiencies and specific greenhouse gas emissions are calculated for performance and greenhouse gas emission comparisons, respectively.

2 System Description

A conventional biomass fueled power production system (System-I) and an advanced biomass gasification and SOFC system (System-II) are studied for performance comparison purposes. In both of these systems, a forced drying system is used to evaporate the moisture completely in System-I and bring the moisture content to a reasonable level according to the gasifier design in System-II.

System-I consists of a dryer, a combustor, a heat recovery steam generator (HRSG), a steam turbine, a condenser and a water pump, as shown in Figure 1. In this system, the dried biomass and air enters the combustor. The gas mixture produced from this combustion process supplies heat to the HRSG where steam is produced. The gas mixture exiting the HRSG enters the dryer to supply the required amount of heat for the drying process and then it is emitted to the atmosphere. The steam produced in HRSG enters the steam turbine where the power is produced. The exit stream from the steam turbine enters the condenser and some amount of heat is rejected to the environment. The condensed liquid enters the pump and then it is sent back to the HRSG.

A schematic of the integrated biomass gasification and SOFC system is shown in Figure 2. In the gasification subsection, steam is selected as the gasification agent and external heat is supplied by the recirculation of the depleted streams from the SOFC. The gas mixture produced by gasification, i.e. syngas, has generally high level of contaminants to be used directly in the SOFC. A gas cleanup system has to be used to clean the syngas according to the SOFC impurity levels not to cause any degradation in the fuel cell. For this study, a hot gas cleanup is preferred to be compatible with the gasifier exit and SOFC inlet streams. The cleaned syngas enters the SOFC, where the electricity is generated. It should be noted that

depleted fuel stream can be recirculated to adjust the steam to carbon ratio in case there is a carbon deposition problem in the SOFC. The fuel and air streams exiting the SOFC enter the afterburner to burn the unused fuel and increase the temperature of these streams. The mixture leaving the afterburner supplies heat to the following components respectively: the blower used to supply air for the SOFC, the HRSG used to produce steam for the gasifier and the steam users, and the dryer. After exiting the dryer, this gas mixture is emitted to the environment.

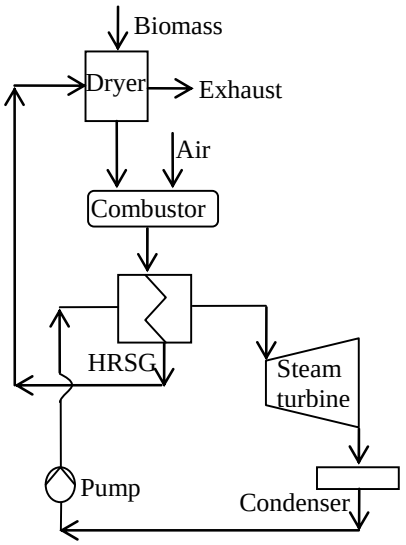

Figure 1: Schematic of the System-I (a conventional biomass fueled power production system using steam turbine).

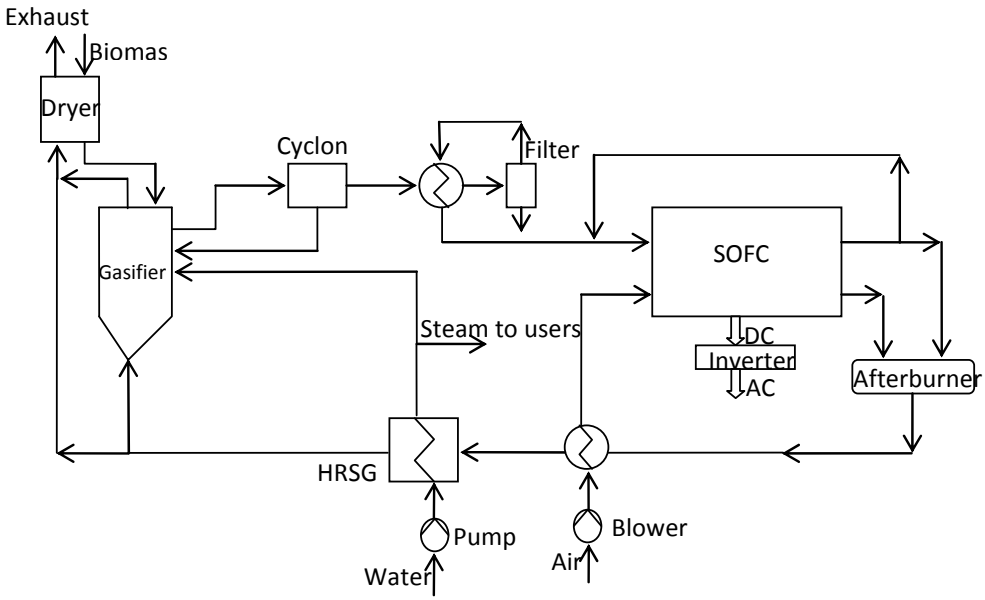

Figure 2: Schematic of the System-II (an advanced integrated biomass gasification and SOFC system).

3 Analysis

In the modeling of the conventional biomass fueled power production system, i.e., System-I, thermodynamic principles and laws are applied to the components of the system. It is assumed that complete combustion is achieved using 100% theoretical air, i.e. stoichiometric mixture. The heat recovered from the HRSG is first calculated applying an energy balance around the control volume enclosing the HRSG. Using the isentropic efficiencies of the components and the thermodynamic relations, steam produced in the HRSG is then calculated. Finally, using these finding, the power output of the steam turbine, power demand for the pump, and the net power output of the system are calculated.

For the SOFC, the transient heat transfer model developed by Colpan [4] is used. The approach and main features of this model are as follows: A control volume around the repeat element found in the middle of a planar SOFC stack is taken. It is assumed that the other repeat elements show the same characteristics with this repeat element. The solid structure, i.e. electrodes, electrolyte, and interconnects, is modeled in 2-D; whereas the air and fuel channels are modeled in 1-D. Since the gases flow with low velocity to obtain high fuel utilization, it is assumed that fully developed laminar flow conditions are achieved at the air and fuel channels. Natural convection at the heat-up stage, forced convection at the start-up stage, conduction heat transfer between the solid parts, and all the voltage losses, i.e. activation, concentration, and ohmic, are taken into account in the modeling. The input parameters of this model are cell voltage, Reynolds number at the fuel channel inlet, excess air coefficient, temperature at the air and fuel channel inlets, pressure of the cell, molar gas composition at the air and fuel channel inlets, and the geometrical dimensions of the SOFC. The output parameters are the current density, temperature, molar gas composition, and carbon activity distributions, the heat-up and start-up time, the fuel utilization, the power output and the electrical efficiency of the cell. This model is validated with IEA benchmark test [1] and Braun's model [3].

In modeling the integrated SOFC and biomass gasification system, i.e System-II, firstly, the syngas composition and the external heat needed for the gasifier are calculated by solving the set of equations derived from the thermodynamic modeling of the gasifier. These equations include three atom balances, two chemical equilibrium relations and the energy balance around the control volume enclosing the gasifier. Secondly, using the syngas composition and the heat transfer model of the SOFC, number of the SOFC stacks, molar flow rate of gases at the inlet and exit of the air and fuel channels, temperature at the exit of the air and fuel channels, and power output of the cell are found. Thirdly, combining the outputs of the gasifier and SOFC models, the molar flow rate of the dry biomass is calculated. Fourthly, applying thermodynamic principles to the components of the system, the enthalpy flow rate of all the states are calculated. Finally, using the laws of thermodynamics, work input to the auxiliary components, i.e. blower and pump, and net power output of the system are calculated.

Electrical efficiency and exergetic efficiency are selected as the performance assessment parameters. Electrical efficiency, which is shown in Eq. (1), is the ratio of the net power output of the system to the lower heating value of the fuel. In defining the exergetic efficiency, it is necessary to identify both a product and a fuel for the system being analyzed. The product represents the desired output produced by the system. The fuel represents the

resources expended to generate the product. This efficiency can also be written in terms of the total exergy destructions and losses within the system, as shown in Eq. (2).

$$\eta_{el} = \frac{(\dot{W}_{net})_{system}}{\dot{n}_{fuel} \cdot LHV} \tag{1}$$

$$\varepsilon = \frac{\dot{E}x_P}{\dot{E}x_F} = 1 - \frac{\dot{E}x_D + \dot{E}x_L}{\dot{E}x_F} \tag{2}$$

Environmental impact of these systems can be assessed calculating the specific greenhouse gas emissions, which is defined as the ratio of the GHG emission from the system to the net power output of the system. From the viewpoint of energy and environment, the lower the ratio is, the more environmentally friendly the system is.

$$\sigma = \frac{\dot{m}_{GHG}}{(\dot{W}_{net})_{system}} \tag{3}$$

4 Results and Discussion

The performance and environmental impact of the System-I and System-II were simulated for the same input data, which is given in Table 1. The results and discussion of these simulations are given in this section.

Table 1: Input data.

Environmental temperature	25 °C
Type of biomass	Wood
Ultimate analysis of biomass [%wt dry basis]	50% C, 6% H, 44% O
Moisture content in biomass [%wt]	30%
Exhaust gas temperature	127 °C
System-I	
Conditions of the steam entering the steam turbine	20 bar (saturated)
Pressure of the condenser	1 bar
Isentropic efficiency of the steam turbine	80%
Isentropic efficiency of the pump	80%
Electricity generator efficiency	98%
System-II	
Moisture content in biomass entering the gasifier [%wt]	20%
Temperature of syngas exiting the gasifier	900 °C
Temperature of steam entering the gasifier	300 °C
Molar ratio of steam to drybiomass	0.5
Number of cells per SOFC stack	50
Temperature of syngas entering the SOFC	850 °C
Temperature of air entering the SOFC	850 °C
Pressure of the SOFC	1 atm
Cell voltage	0.7 V
Reynolds number at the fuel channel inlet	1.2
Excess air coefficient	7
Active cell area	10x10 cm^2
Number of repeat elements per single cell	18
Flow configuration	Co-flow
Manufacturing type	Electrolyte-supported
Thickness of the air channel	0.1 cm
Thickness of the fuel channel	0.1 cm
Thickness of the interconnect	0.3 cm
Thickness of the anode	0.005 cm
Thickness of the electrolyte	0.015 cm
Thickness of the cathode	0.005 cm
Pressure ratio of the blowers	1.18
Isentropic efficiency of the blowers	0.53
Pressure ratio of the pump	1.2
Isentropic efficiency of the pump	0.8
Inverter efficiency	0.95

One of the most important factors affecting the performance of the System-I is the moisture content of the biomass. The more moisture content of the biomass is, the more energy demand for the dryer is. Hence, steam produced in the HRSG decreases with an increase in the energy demand of the dryer; which in turns decreases the power produced in the steam turbine and the electrical and exergetic efficiencies of the system. It is found that as the moisture content of the wood increases from 0% to 50%, electrical efficiency of the system decreases from 15.6% to 0%; whereas exergetic efficiency of the system decreases from 13.5% to 0%.

In System-II, the syngas composition is first calculated as: 2.08% CH_4, 42.75% H_2, 25.80% CO, 9.44% CO_2 and 19.93% H_2O. Using this composition and the data given in Table 1, the SOFC model is simulated. It is found the fuel utilization of the SOFC is 82%. The current density distribution is shown in 2. According to this figure, the average current density of the cell is 0.253 A/cm^2 for the cell operating voltage of 0.7 V.

As shown in Figure 3, the electrical and exergetic efficiencies of the System-I are found as 8.3% and 7.2%, respectively; whereas the electrical and exergetic efficiencies of the System-II are found as 44.9% and 41.1%, respectively.

The environmental impact of the systems studied is compared calculating the specific GHG emissions from these systems. It is found that System-I has higher GHG emissions compared to System-II. As shown in Figure 4, the specific GHG emissions from System-I and System-II are 4.564 g-CO_2.eq/Wh and 0.847 g-CO_2.eq/Wh, respectively.

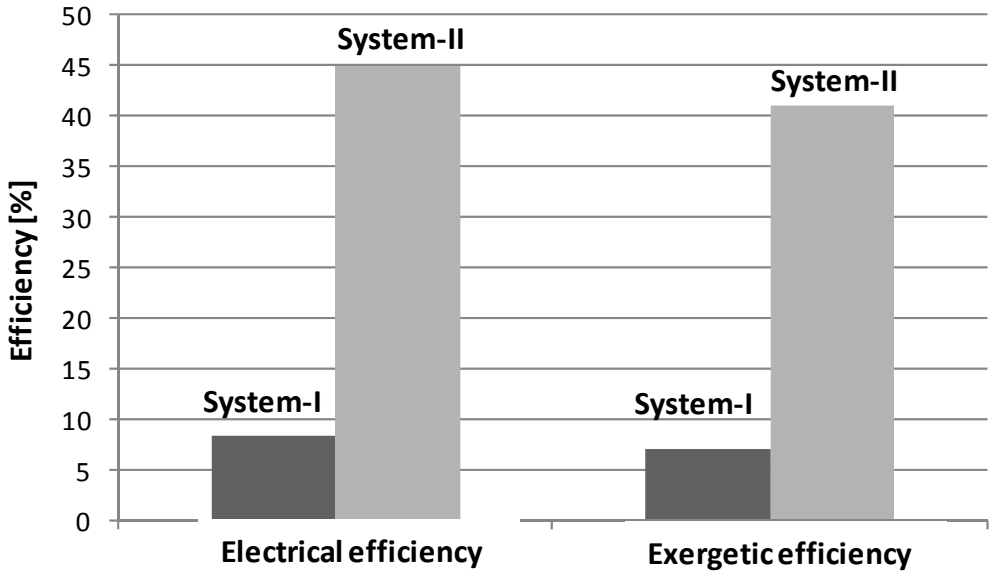

Figure 3: Electrical and exergetic efficiencies of the System-I and System-II.

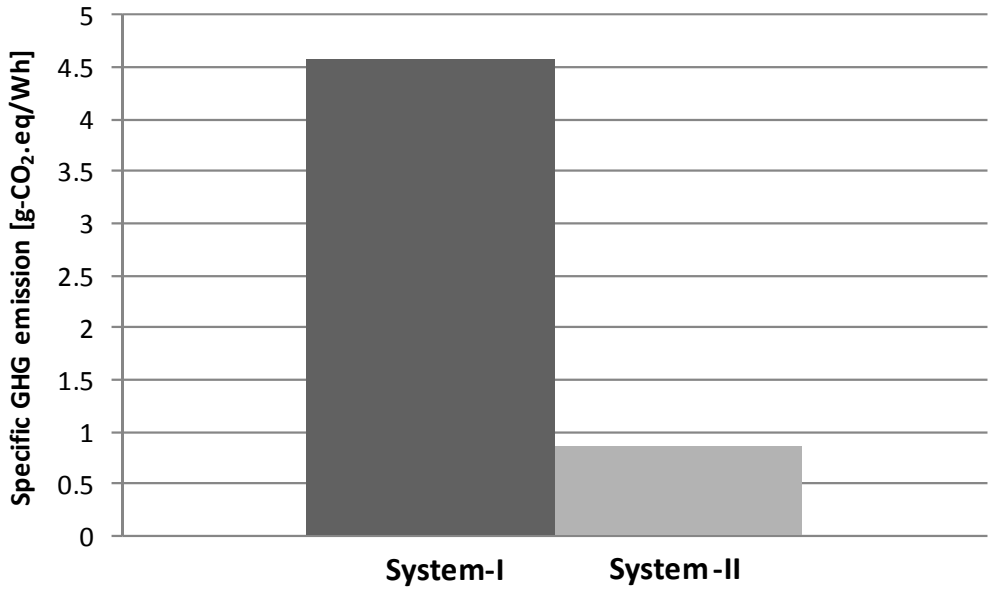

Figure 4: Specific GHG emissions of the System-I and System-II.

5 Conclusions

In this paper, the performance and environmental impact assessments of an advanced biomass gasification and SOFC system are conducted, and the results are then compared with a conventional biomass fueled power production system using steam turbine as the electricity generator. A joint model including heat transfer model for the SOFC and thermodynamic models for the rest of the components of the systems is used in the analyses. The results of the case study conducted show that the SOFC and biomass gasification system has higher electrical and exergetic efficiencies, and lower specific GHG emissions. This study has pointed out that gasifying the biomass and then using the product gas in SOFC for electricity production is a very efficient way to obtain better performance and lower GHG emissions.

References

[1] Achenbach, E., 1996, *SOFC stack modelling*, Final Report of Activity A2, Annex II: Modelling and Evaluation of Advanced Solid Oxide Fuel Cells, International Energy Agency Programme on R, D&D on Advanced Fuel Cells, Juelich, Germany

[2] Athanasiou, C., Coutelieris, F., Vakouftsi, E., Skoulou, V., Antonakou, E., Marnellos, G., Zabaniotou, A., 2007, *From biomass to electricity through integrated gasification/SOFC system-optimization and energy balance*, International Journal of Hydrogen Energy, 32, pp.337-342

[3] Braun, R.J., 2002, *Optimal design and operation of solid oxide fuel cell systems for small-scale stationary applications*, PhD thesis, University of Wisconsin-Madison

[4] Colpan, C.O., 2009, *Thermal modeling of solid oxide fuel cell based biomass gasification systems*. PhD thesis, Carleton University

[5] Colpan, C.O., Hamdullahpur, F., Dincer, I, Yoo, Y., 2009a, *Effect of gasification agent on the performance of solid oxide fuel cell and biomass gasification systems*, International Journal of Hydrogen Energy. In Press.

[6] Colpan, C.O., Dincer, I., Hamdullahpur, F, 2009b, *The reduction of greenhouse gas emissions using various thermal systems in a landfill site*, International Journal of Global Warming, 1 (1/2/3), pp.89-105.

[7] Cordiner, S., Feola, M., Mulone,V., Romanelli, F., 2007, *Analysis of a SOFC energy generation system fuelled with biomass reformate*, Applied Thermal Engineering, 27, pp. 738-747

[8] Omosun, A.O., Bauen, A., Brandon, N.P., Adjiman, C.S., Hart, D., 2004, *Modelling system efficiencies and costs of two biomass-fuelled SOFC systems*, Journal of Power Sources, 131, pp.96-106

[9] Panopoulos, K.D., Fryda, L.E., Karl, J., Poulou, S., Kakaras, E., 2006a, *High temperature solid oxide fuel cell integrated with novel allothermal biomass gasification Part I: Modelling and feasibility study*, Journal of Power Sources, 159, pp.570-585

[10] Panopoulos, K.D., Fryda, L.E., Karl, J., Poulou, S., Kakaras, E., 2006b, *High temperature solid oxide fuel cell integrated with novel allothermal biomass gasification Part II: Exergy analysis*, Journal of Power Sources, 159, pp.586-594

Systematic Assay of the Influence of Current Ripples on Polymer Electrolyte Membrane(s) in Low-Temperature Fuel Cells

M. Stark, **G. Krost**, University Duisburg-Essen, Germany
S. Gössling, **P. Beckhaus**, ZBT- Duisburg, Germany

1 Introduction

The non-linear characteristics of inverters used for feeding the electrical direct current (DC) output of fuel cells into the public alternating current (AC) based grid leads to the occurrence of current ripples both on AC and DC sides. The DC current ripples are suspected of having degrading effects on the fuel cell, which is usually counteracted by an anticipation to install filter circuits. Rather, a comprehensive analysis of coherences is still missing. On the other hand, deeper insight and authoritative evidence would allow for creating plain specifications for inverter manufacturers and fuel cell operators. The challenge of the reported project was to systematically investigate the influence of current ripples of various frequencies and amplitudes on PEM cells by long term observation and comparison with a reference cell loaded by pure DC. For the occurrence of ripples in commonly used pulse width modulation based inverters three different mechanisms are responsible:

a) Harmonics of predominantly second order result from modulation DC / grid frequency.

b) The usual inverter's switching clock frequencies are in the range of several kHz.

c) Natural frequencies of inverter circuitry, triggered by switching of transistors, are in the MHz range.

2 Test Rig for Long Term Tests

For the investigations a specific test rig was configured, allowing for simultaneous operation of three identical PEM fuel cell stacks under distinct ripple conditions.

2.1 Fuel cell stacks

The fuel cell stacks used for the different tests are composed of injection molded bipolar plates consisting of PP, carbon black and graphite, between which the membrane electrode assemble (MEA) and the appertaining seal is clamped. Bipolar plates, MEA and seals of the stacks were selected to be part of one and the same manufacturing charge in order to minimize variance. The bipolar plates are identical at both anode and cathode sides and contain a meander flow field with an active area of 50 cm^2. For cooling purposes, at the back side of the bipolar plates a second flow field is arranged in which tempered water is circulated in order to gain a homogeneously dispersed temperature across the whole cell.

2.2 Media supply

Provisioning of three PEM stacks operated in parallel with gases is shown in Figure 1. Cathode air as well as de-mineralized water needed for air humidification are supplied by mass flow controllers; the mixture is overheated in an evaporator for complete vaporization. The segment of the feeding line to the fuel cell is heated to avoid water re-condensation. At the anodic side of the fuel cell the unused hydrogen is re-circulated, which is a general practice and provides test conditions close to real supply systems. Pressure-reduced fresh hydrogen is mixed with re-circulated anode gas before re-supply to the stack; due to the re-circulation a high stoichiometry at the anode is achieved. The complete re-circulation circuit as well as the fresh hydrogen are heated to avoid water condensation. The surplus of water in the circuit is removed by a dehydrator. The high partial pressure of nitrogen at the cathode side of the fuel cell effects diffusion of nitrogen through the MEA to the anode side; the closed gas circuit at the anode side leads to increasing concentration of nitrogen. To keep the concentration of nitrogen in the anode circuit low, it is frequently purged by a valve. The cell temperature is controlled by tempered de-mineralized water flow; the conductivity of the water is steadily surveyed, and the water is changed when necessary.

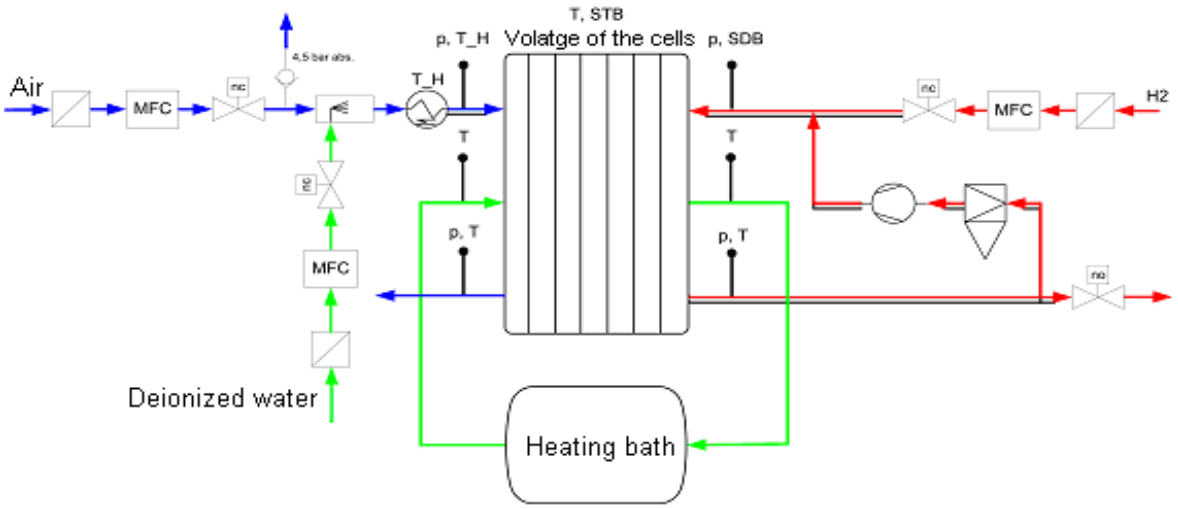

Figure 1: Media supply of test rig (one channel shown).

2.3 Electronic load

The electronic load was particularly assembled for the tests. It consists of three identical, independently controlled circuits based on power transistors (MOS FET types) used as controllable resistors, as well as appertaining control and monitoring circuits, Figure 2.

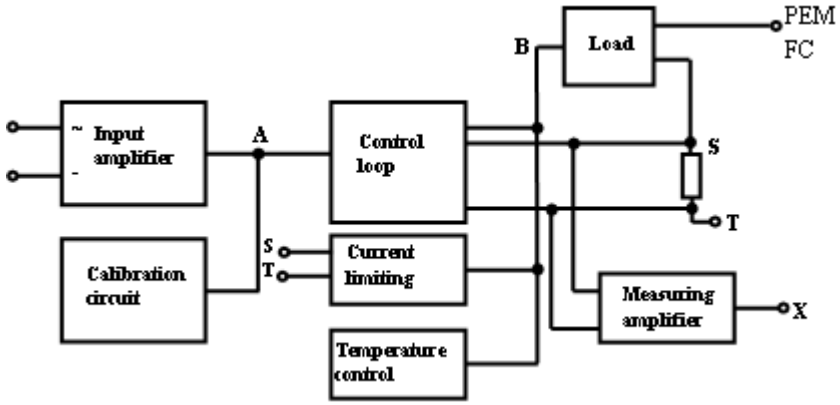

Figure 2: Block diagram of the electronic load (one channel shown).

The input signal, representing the aspired fuel cell load current, is composed by summing up the basic DC and superimposed AC constituents, and then amplified. A calibration circuit allows for adjusting the input signals or, alternatively, those of an external analogue output board for instance. The control loop, receiving the input signal from the input amplifier, actuates the power MOS FET. The actual current in the load circuit is measured by voltage drop at the shunt, followed by a measuring amplifier, which can be calibrated internally. To avoid thermal overload a temperature control was established; furthermore, a current limiting circuit cares for fault protection.

3 Measurement Methods

Terminal voltages and load currents of the stacks under investigation were steadily recorded during the long term tests. For more detailed characterization of the stack conditions, three commonly used methods for in-situ characterization of fuel cells have been applied in certain time intervals: To achieve a quick survey of the stationary behavior, the polarization curve is a well proven method. The electrochemical impedance spectroscopy (EIS) as well as the current interrupt method (CI) provide information about the frequency dependant behavior, [1], [2], [3].

4 Experimental Results of the Long Term Tests

For the first long term experiment – lasting 600 h – two 5-cell fuel cell stacks were used only. The electric parameters of the experiment are given in Table 1.

Table 1: Parameters of first long term experiment.

	DC current	AC current	Frequency
Stack 1	40 A	8 A (20%)	100 Hz
Stack 2	40 A	0 A	- (pure DC)

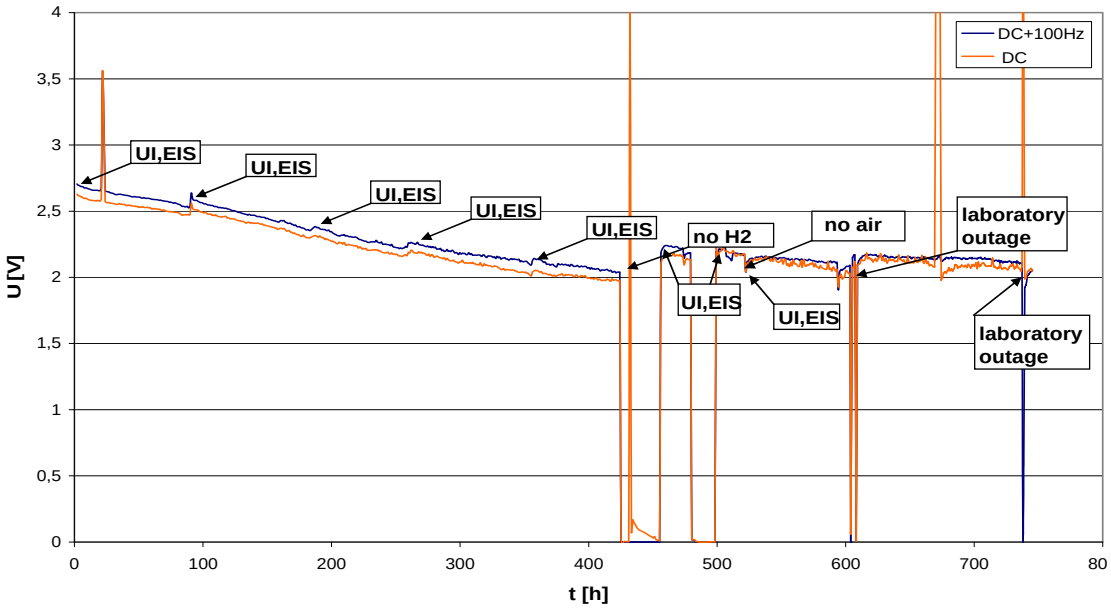

Figure 3: First long term experiment: terminal voltages of investigated stacks over time.

With 40 A basic DC current the active membrane surface of 50 cm^2 was loaded by 800 mA/cm^2 which is relatively high; the amplitude of the second harmonic (100 Hz for grid frequency of 50 Hz) at 20 % of DC was consciously chosen rather high too, in order to provoke a noticeable ripple effect on the fuel cell stack. Both terminal voltages and loading currents were recorded every 5 s, polarization curves as well as EIS curves in the frequency range 0 … 20 kHz were taken two times per week. Figure 3 shows the stack terminal voltages (5 cells) over time for the complete runtime of the experiment; for the stack exposed to ripples the RMS values, for the reference stack the average values are entered.

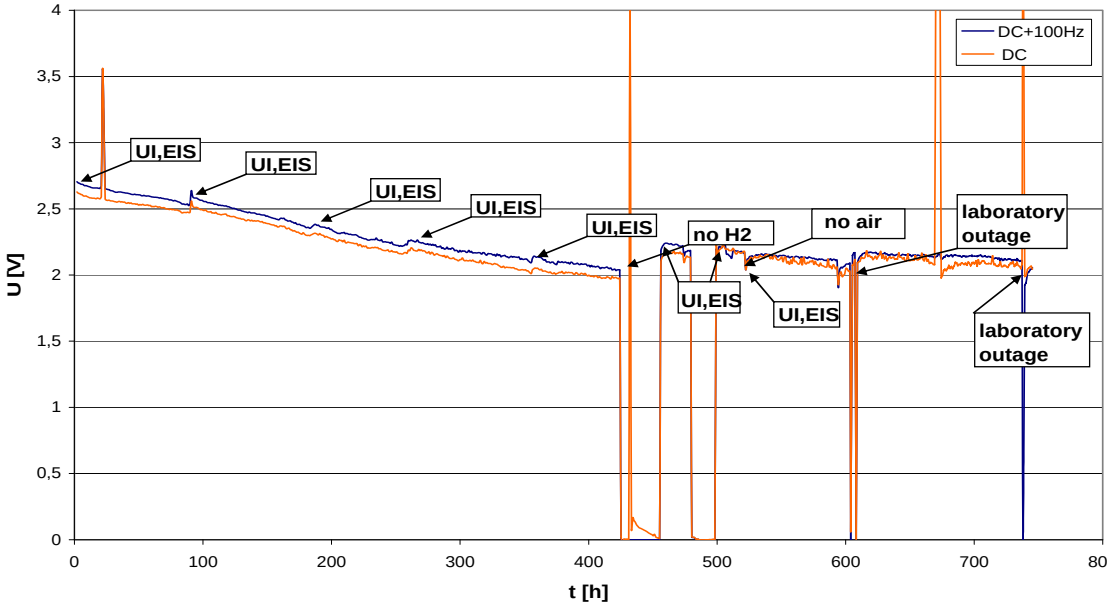

Figure 3: First long term experiment: terminal voltages of investigated stacks over time.

A significant degradation of 300 µV/h per cell on average can be observed which could be reduced to approximately 100 µV/h per cell after several interruptions of lab operation; the experiment was stopped when average cell voltages of 400 mV were reached. The appertaining polarization curves of the two stacks at the beginning and end of the experiment are shown in Figure 4.

The characteristics of the stack exposed to ripple is rather identical to that of the one loaded by pure DC (low divergence in the range of diffusion processes may be caused by slightly different temperature, humidity or load currents); obviously no noticeable impact of ripple on the static behavior of the stack can be recognized.

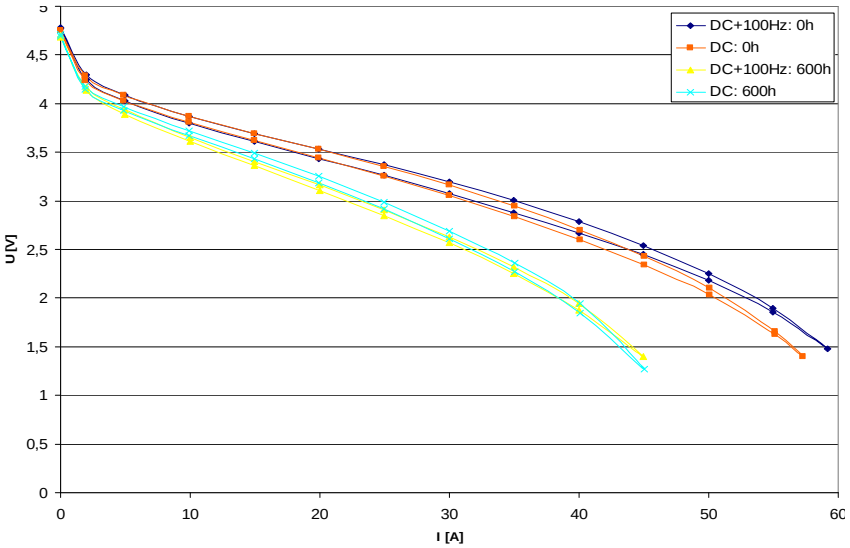

Figure 4: Polarization curves of stacks at begin and end of first long term test.

The EIS curves in Figure 5, taken at start and end of the experiment, also show the degradation over time of both stacks, in particular at the cathode bow (low frequencies). For higher frequencies the curves are approaching to each other which doesn't give any hint of ripple impact as well. After implementation of several improvements at the test rig a second long term experiment was started, investigating three identical new stacks. As a consequence of the unnoticeable ripple impact in the first experiment the basic DC load was reduced to 20 A, connected with significant increments of ripple amplitudes up to 15 A corresponding to a remarkable 75 % of basic DC. Ripple frequencies were chosen at 100 Hz and 20 kHz this time. The electric parameters are summarized in Table 2.

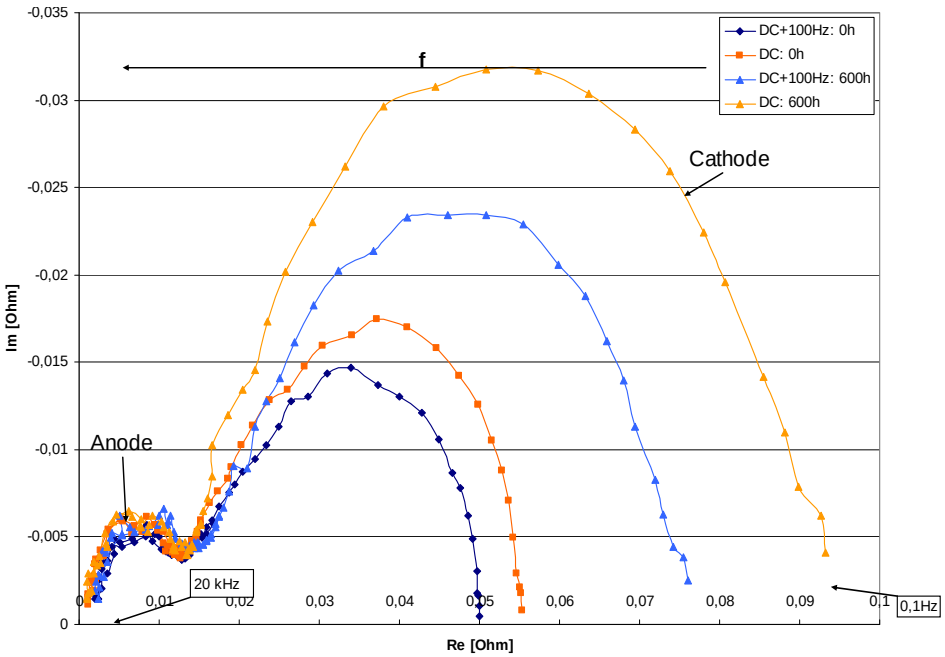

Figure 5: EIS curves of stacks at begin and end of first long term test.

The measurements were recorded just like in the first experiment, except the polarization curve which was taken every two weeks only in order to diminish the impact on steady operation (the effect of EIS measurements taken at very low currents is much lower). The total duration of this experiment was 2280 h. The consequence of several improvements at the test rig (supply of gases) was that the terminal voltage degraded much more moderately, but during this experiment several outages of lab and test rig operation happened too; the operation interruptions led to temporary recovery of the stack voltages, Figure 6.

Table 2: Parameters of second long term experiment.

	DC current	AC current	Frequency
Stack 1	20 A	0 A (0%)	- (pure DC)
Stack 2	20 A	15 A (75%)	100 Hz
Stack 3	20 A	15 A (75%)	20 kHz

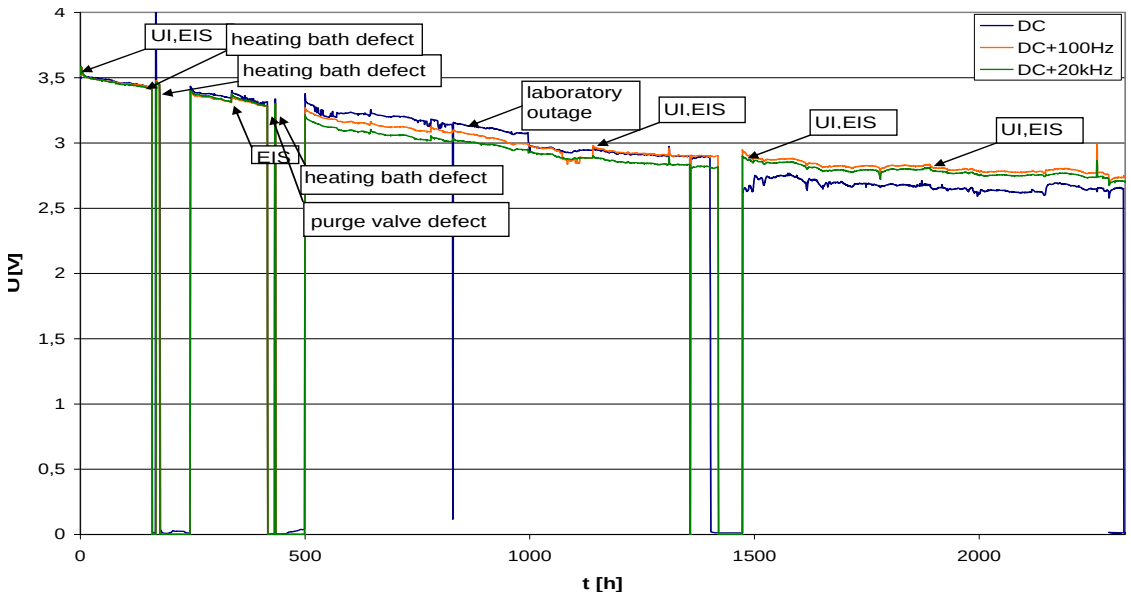

Figure 6: Second long term experiment: terminal voltages of investigated 5 cell stacks over time.

The polarization and EIS curves of the three stacks investigated, again, do not differ significantly, Figure 7 and Figure 8. The moderate distinguishable deviation of the reference stack (not impacted by ripples) could later be attributed to single cells of this particular stack, for which some drains were congested by metallic deposits. Obviously the second experiment, conducted under extreme ripple conditions, could not produce any observable impact of ripples on stack performance too.

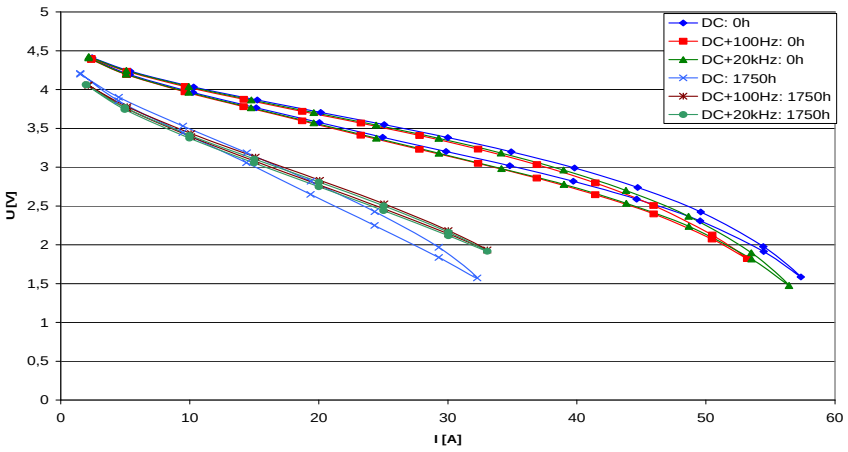

Figure 7: Polarization curves of 5 cell stacks at begin and end of second long term test.

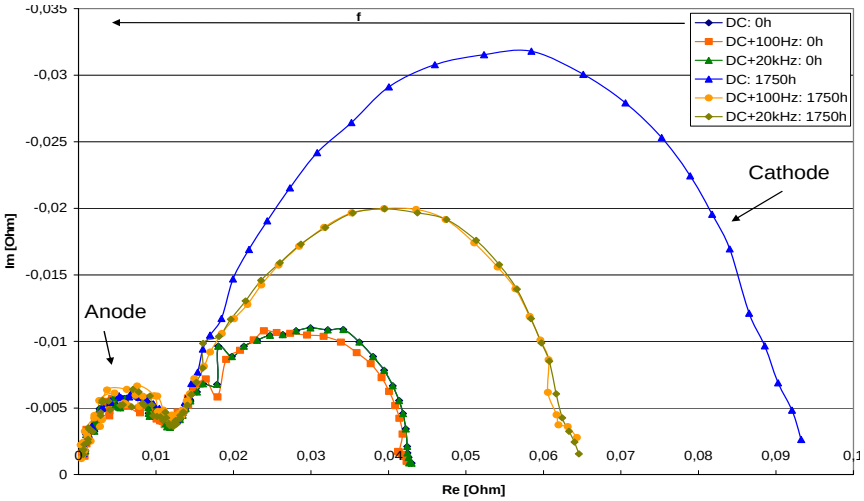

Figure 8: EIS curves of stacks at begin and end of first long term test.

In searching for further influences, stoichiometry was identified as another possible factor. For this reason in the frame of a third experiment the general stoichiometry was reduced to a value of 1.7; this should theoretically lead to short transitory undersupply (at stoichiometry of 0.97 only) during the ripple amplitude maxima. The parameters applied to this experiment, lasting 1750 h, are summarized in Table 3.

Table 3: Parameters of third long term experiment.

	DC current	AC current	Frequency
Stack 1	20 A	0 A (0%)	- (pure DC)
Stack 2	20 A	15 A (75%)	100 Hz
Stack 3	20 A	7.5 A (37.5%)	20 kHz

	Humidity	Stoichiometry
Cathode	average: 61.5% @ 74°C input: 36%, output: 85%	1.7
Anode	70% (100% @ 66°C)	-

While the general degradation over time of all stacks has very much improved in this case (Figure 9), the polarization and EIS curves (not specifically shown in this case) appeared unremarkable again with regard to ripple influences, i.e. no significant differences between ripple-loaded and reference (pure DC) stacks could be identified also in this case.

In summary for the three long term experiments the following can be stated:

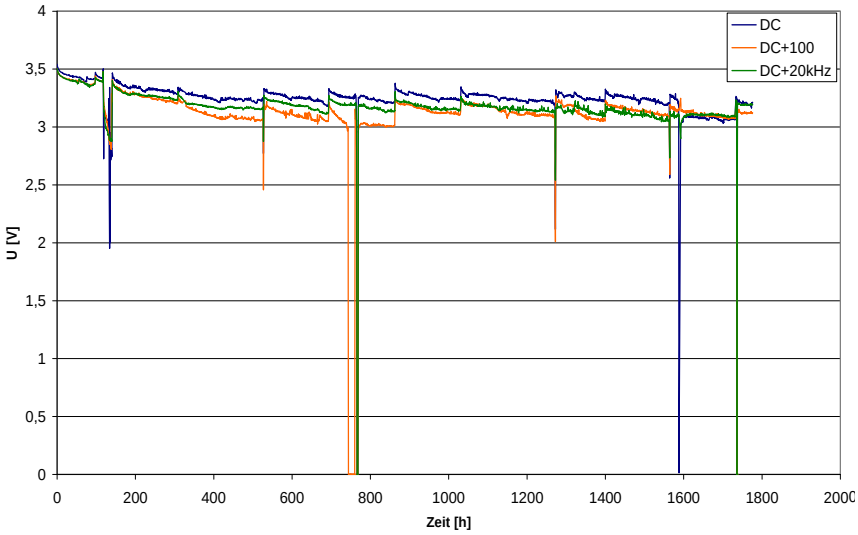

Figure 10: Third long term test: terminal voltages of investigated 5 cell stacks.

the test rig conditions could steadily be improved, finally achieving a general (not ripple-caused) cell degradation in the typical range commonly known from various literature; an impact of ripples on long term cell performance could, even in the case of extraordinary ripple amplitudes, not be observed.

5 Further Experiments

As shown in [4], current ripples have diminishing impact on the electric output power of fuel cells. This effect was further investigated in the present study by variation of ripple amplitudes at different operating points of a two-cell stack. The first experiment was conducted at 20 A DC load; ripple amplitudes of 0.1 A, 0.5 A, 1 A, 2 A, 5 A and 10 A were superimposed at frequencies of 10 Hz, 100 Hz and 1 kHz. Measurements of stack output power were taken when a stable operation point arose. The electrical output power of the stack depending on ripple amplitudes – which were set in rising order in this case – at the given frequencies is shown in Figure 10. It is conspicuous that besides the power decrement at increasing ripple amplitudes – known from, and explained by additional cell resistance in, [4] – a local power minimum occurs at very low amplitudes for all frequencies investigated. In alleviated form this phenomenon can also be observed at a lower DC operating point of 10 A, but there is no plausible explanation so far.

6 Conclusion

The influence of current ripples on long term degradation of PEM fuel cells was systematically investigated. Test stacks were exposed to synthetic current ripples of various frequencies and extraordinary amplitudes for longer time intervals. In summary it can be stated that hints to an impact of current ripples on long term degradation of stacks could not be identified. In consequence, demands to inverter manufacturers to care for strict limitation of ripples in fuel cell circuits could be re-assessed, thus sparing cost and losses of filters.

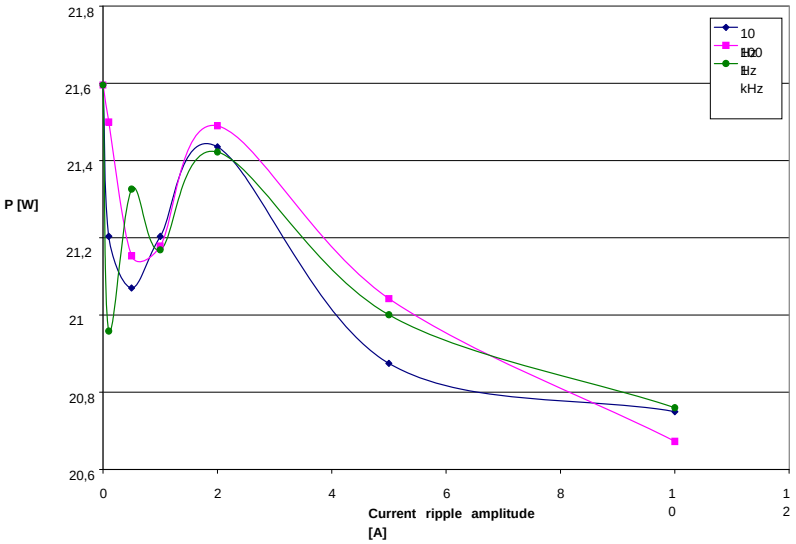

Figure 10: Stack output power depending on amplitudes of ripples at different frequencies.

Acknowledgement

Thanks to “Zentralverband Elektrotechnik- und Elektronikindustrie e.V..“(ZVEI)„“for sponsoring this project (15279 N) with allocated funds from “Bundesministerium für Wirtschaft und Technologie (BMWi)“ through „Arbeitsgemeinschaft industrieller Forschungsvereinigungen "Otto-von-Guericke" e.V. (AiF)“.

References

[1] H. Kuhn, Charakterisierung von Polymer-Elektrolyt Brennstoffzellen mittels Elektrochemischer Impedanzspektroskopie; Dissertation; University Karlsruhe, Germany, 2006.

[2] D. Vladikova, The technique of the differential impedance analysis: Part I: Basics of the impedance spectroscopy; Proceedings of the International Workshop “Advanced Techniques for Energy Sources Investigation and Testing”, 2004, Sofia, Bulgaria.

[3] B. Andreaus, Die Polymer-Elektrolyt Brennstoffzelle – Charakterisierung ausgewählter Phänomene durch elektrochemische Impedanzspektroskopie; Dissertation, École Polytechnique Fédérale de Lausanne, Switzerland, 2002.

[4] Schindele, Einsatz eines leistungselektronischen Stellglieds zur Parameteridentifikation und optimalen Betriebsführung von PEM-Brennstoffzellensystemen; Dissertation, University Karlsruhe, Germany, 2006.

Simulation of Multiphase Transport Phenomena in PEMFC Involving Water Phase Change

Munir Ahmed Khan, **Jinliang Yuan**, **Bengt Sundén**, Energy Sciences, Faculty of Engineering, Lund University, Sweden

Proton exchange membrane fuel cells (PEMFCs) are energy units that convert the chemical energy of hydrogen-oxygen reaction into electrical energy. Since the conversion process is direct, PEMFCs are considered highly efficient and also zero-emission because of water being the only product of reaction. Due to this, PEMFCs have become a prime choice for the future low power requirements especially for vehicular and mobile systems.

The candidacy of PEMFC has yet to be proven as some of the old time hurdles still persist and need to be corrected in near future. Water management is one of the old timers that still need a deep insight. Nafion™ is one of the commercially available membrane materials and the working is highly water dependant (the details can found in Larminie and Dicks (2003) [3]). Higher water content gives higher proton conduction but this advantage is not a standalone effect as higher water content may block the active sites in the catalyst layer (CL) and gas passages in the porous transport layer (PTL). Since a PEMFC is a multi-disciplinary device with many phenomena working in line, in order to understand the water management and to arrive at a conclusive point for the working point of PEMFC, all the transport mechanisms need to be simulated simultaneously.

In this study, a repeating section of cathode side with interdigitated flow field has been chosen for simulations. The interdigitated flow field has an added advantage to prevent water flooding, Nguyen (1996) [4], in PEMFCs. The reasons for selecting only the cathode side are;

1. Oxygen reduction reactions occurring at the cathode have slow kinetics and determine the overall reaction rate.
2. Water is produced at the cathode side due to electro-chemical reactions.
3. Water is used as a proton carrier in the membrane and each proton drags (electro-osmotic drag) from one to five water molecules, Zawodzinski *et al.* (1993) [8] and Ren and Shimshon (2001)[5], further aiding the flooding of cathode.

Due to the reasons explained above, cathode of PEMFC is critical in determining the overall performance and deep understanding is required for optimization if PEMFCs are to be used as alternate energy sources in near future.

As stated earlier, due to coupling of physical phenomena in PEMFC, the equations employed in this study are mass continuity and momentum, two-phase flow, two-phase temperature and two-phase current. Previously, a good number of PEMFC models have been proposed by many authors looking at different details e.g., effects of catalyst structural parameters by Sun *et al.* (2005) [6] and detailed transport mechanism and parametric optimization of fuel cell design by Yu *et al.* (2009) [7], but, both models lacked in completeness as the former model was single phase flow and the later one is isothermal model. In present study all the details of working of cathode have been modeled so that an effective conclusion can be

drawn for optimal performance of PEMFC. The model equations developed for this study were solved simultaneously and iteratively. The equations were discretized using a finite volume method (FVM) and implemented as user defined functions in commercial CFD code. The solution was considered to be convergent when the relative error in all parameters was equal to or less than 10^{-6}. More discussion on the governing equations, boundary conditions and sources terms can be referred to Khan (2009) [2].

Figure 1 shows the concentration level of liquid water in the fuel cell cathode side for the two current densities. The concentration level of liquid water at the inlet and the outlet of the domain is zero because;

1. Both inlet and outlet are considered as infinite sink for liquid water.
2. At the inlet, the partial pressure of water vapor is less than saturation pressure for condensation.

The concentration of the liquid water increases gradually in the porous transport layer by reason of more and more electro-chemical reactions which in turn increases the partial pressure of vapors for condensation and also there is influx of water at membrane/catalyst interface. The concentration for a specific current density is highest in the center of catalyst layer and this is because of the selected boundary condition types for liquid water. By comparing the saturation levels for different operating conditions i.e., current densities, the saturation level of PEMFC operating at higher current density is more as compared to low current density. This difference in saturation level is due to more electro-chemical reactions occurring and higher proton migrations.

The important parameter related to water presence (both liquid and vapor) in PEMFC is the membrane phase conductivity i.e., proton conduction of the supporting material to complete the electro-chemical reactions at the cathode. In this work, the potential difference between catalyst/membrane interface and the local potential in the catalyst layer has been considered as the driving force for proton immigration. The governing relation for the water activity incorporating both states of water is provided by He *et al.* (2009) [1] in which water activity is the product of relative humidity of gas phase and the liquid water saturation. Comparing the trends given in Figure 2, it can be observed that higher conductivity is offered for higher current density because of excess production of water, while at lower operating levels and because of less water production (rate of electro-chemical reactions is small), the conductivity is quite small and demanding the need of external provision of water to the domain. In this study the inlet humidity of 50% has been used to simulate the scenario. The power density for the fuel cell is also a function of operating currents. As the current density is increased, the power density also increases until the mass limitation effects are too much to cause a sharp decrease in the power density as can be seen in Figure 4.

Trends of higher membrane conductivity and maximum power density (Figure 4) at higher current densities suggest PEMFC operation at higher current densities. But as can be seen in Figure 3, potential wasted in deriving the electro-chemical reactions at higher current also increases depicting higher losses and also the liquid water effect (saturation) becomes more prominent as shown in Figure 4 where the present model curves deviates from the results produced by Sun *et al.* (2005) [6] which is a single phase model.

On the basis of above discussion, it can be concluded that although maximum power and membrane phase conductivity occur at higher current densities, it's not feasible to operate PEMFC at those levels because of increase in losses and water saturation effects. The only adverse effect by operating the PEMFC at lower currents is the dryness of membrane that can be effectively tackled by humidifying the inlet supply.

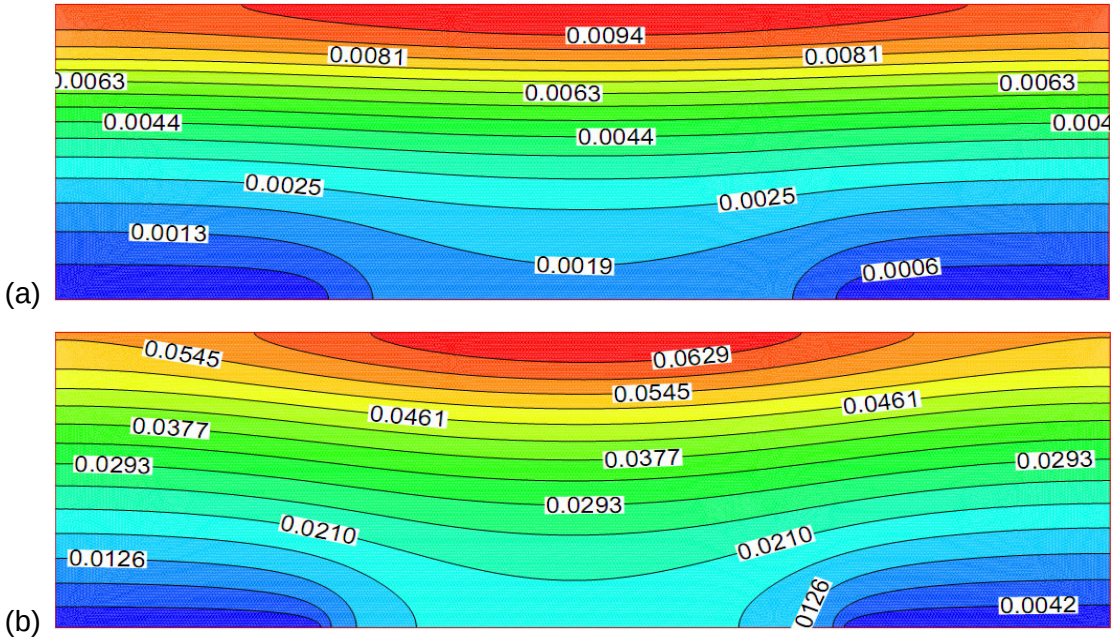

Figure 1: Liquid water saturation at (a) 0.2 and (b) 0.8 A/cm^2.

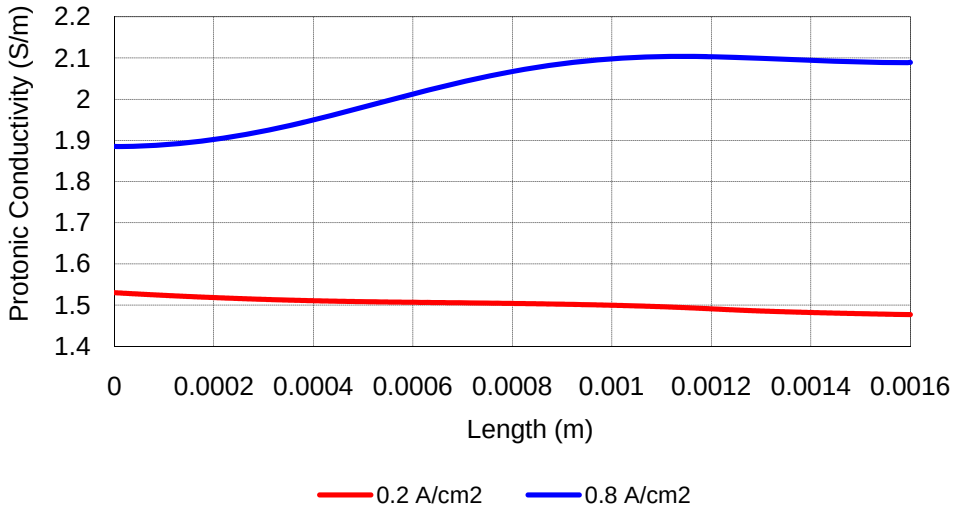

Figure 2: Membrane phase conductivity at CL/PTL interface for different current densities.

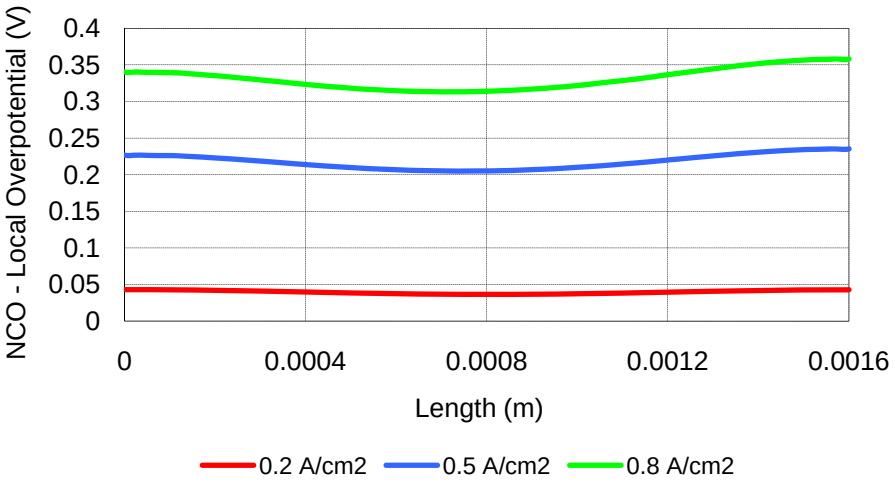

Figure 3: Driving voltage for electro- chemical reactions at CL/PTL interface.

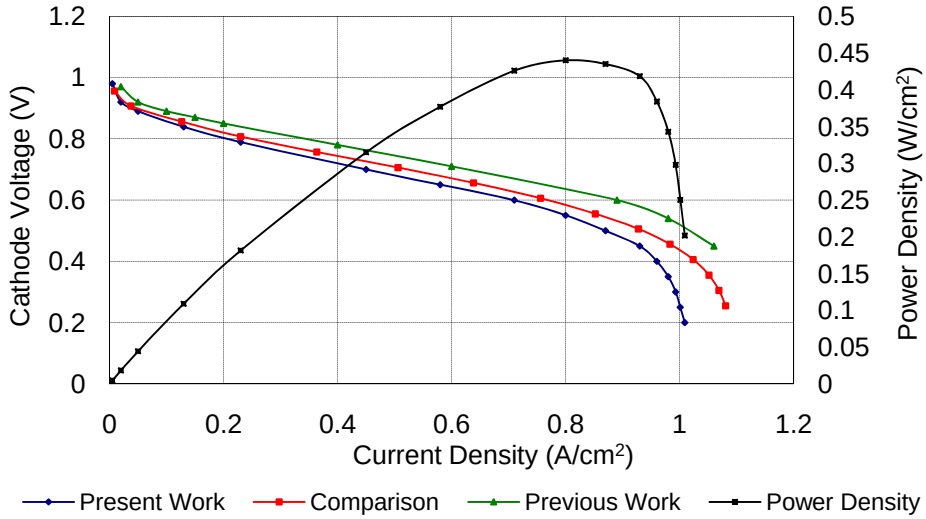

Figure 4: Polarization curve for PEMFC.

Acknowledgement

The European Research Council (ERC) partially supports the current research.

References

[1] He, G., Yamazaki, Y., Abudula, A., 2009. A droplet size dependent multiphase mixture model for two phase flow in PEMFCs. Journal of Power Sources 194, 190-198.

[2] Khan, M., 2009. Numerical simulation of multi-scale transport processes and reactions in PEM fuel cells using two-phase models, Licentiate Degree Thesis, ISRN LUTMDN/TMHP-09/7066-SE. Lund University, Lund.

[3] Larminie, J., Dicks, A., 2003. Fuel Cell Systems Explained, 2nd ed. John Wiley & Sons Ltd., West Sussex.

[4] Nguyen, T.V., 1996. A Gas Distributor Design for Proton-Exchange-Membrane Fuel Cells. Journal of The Electrochemical Society 143, L103-L105.

[5] Ren, X., Shimshon, G., 2001. Electro-osmotic drag of water in poly(perfluorosulfonic acid) membranes. Electrochemical Society, Pennington, NJ, ETATS-UNIS.

[6] Sun, W., Peppley, B.A., Karan, K., 2005. An improved two-dimensional agglomerate cathode model to study the influence of catalyst layer structural parameters. Electrochimica Acta 50, 3359-3374.

[7] Yu, L.J., Ren, G.P., Qin, M.J., Jiang, X.M., 2009. Transport mechanisms and performance simulations of a PEM fuel cell with interdigitated flow field. Renewable Energy 34, 530-543.

[8] Zawodzinski, J.T.A., Derouin, C., Radzinski, S., Sherman, R.J., Smith, V.T., Springer, T.E., Gottesfeld, S., 1993. Water Uptake by and Transport Through Nafion® 117 Membranes. Journal of The Electrochemical Society 140, 1041-1047.

Dynamic Modeling of the Water Balance in the Cathode Gas Diffusion Layer of Polymer Electrolyte Fuel Cells

Daouda Fofana, **Kodjo Agbossou**, **Yve Dubé**, **Jean Hamelin**, Institut de recherche sur l'hydrogène, Université du Québec à Trois-Rivières, 3351 boul. Des Forges, Trois-Rivières (QC), Canada

Development of PEMFC for use as a portable devices like mobile phones, computer note-books, digital cameras, etc and transport devices are receiving more coverage in recent research due to their low cost-per kW, fast start-up, lower operating temperature and zero pollution. The operation in these applications is generally dynamic. So the development of dynamic models is highly important. During fuel cell operation, management of water produced is crucial to enhance PEMFC performance. Generally, water is produced at the cathode/membrane interface due to the electrochemical reactions. Also, due to the humidification of gas at the anode and cathode inlets to supply water to the membrane, condensation takes place in the gas diffusion layer (GDL) preventing the diffusion of gas to the reactive sites. The lack of gas in the reactive sites increases diffusion loss, and leads to a decrease of the cell voltage. So its water-transport characteristics must be studied in order to reduce potential loss, flooding and enhance PEMFC performance.

The continuity equation (or mass conservation) which describes the change of mass concentration of i with respect to time at a fixed point in x direction of porous medium due to the motion of i and chemical reactions producing i is give by the concept mathematical of equation [1,2]:

$$\frac{\varepsilon_0(1-s)}{RT}\frac{\partial P_i}{\partial t}+\frac{\partial N_i}{\partial x}=R_i \tag{1}$$

The quantity $\varepsilon_0(1-s)$ represents the volume occupied by gas species in the porous medium. The source or sink terms R_i is the rate of generation or consumption of species i.

When water is present in the GDL, transport in the porous electrode is induced by capillary force and gas flow-driven shear force. The governing equation for liquid water can be expressed as [1,2]:

$$\varepsilon_0\rho_w\frac{\partial s}{\partial t}+\frac{\partial N_w}{\partial x}=-M_w R_w \tag{2}$$

Where ρ_w, M_w, N_w and R_w are density, molecular weight of liquid water, molar flux of liquid water and the interfacial mass-transfer rate of water between liquid and water vapour respectively.

The electrochemical kinetics is governed by the Voltmer-Butler equation, and since the cathode kinetics is sufficiently slow, it can be expressed by Tafel kinetics, i.e in the form [1,2]:

$$I = (1-s)\, a_c i_0 \frac{P_{cons}^{O_2}}{RT\, C_{ref}^{O_2}} \exp\left(-\frac{\alpha_c F}{RT} \eta_c \right) \quad (3)$$

Where the factor $(1-s)$ represents the reduced surface area due to liquid water that covers the active reaction sites., i_0 the exchange current density, a_c the reactive surface area, $P_{cons}^{O_2}$ the gas pressure of local oxygen, $C_{ref}^{O_2}$ the reference oxygen concentration , η the cathode overpotential and α_c the transfer coefficient for oxygen reduction.

The schematic illustration of capillary pressure P_c and gradient dP_c / ds are represented in fig.1. The capillary pressure is defined as the difference between gas and liquid-phase pressures. It interesting to note that the gradient dP_c / ds is not constant in the range of 0 and 1 of saturation. In order to bring out the variation of dP_c / ds we represented from saturation of liquid water in GDL the graph of capillary pressure P_c and the gradient dP_c / ds fig.2. The absolute valued of capillary pressure is higher at the GDL/membrane interface where saturation is higher than the GDL/ channel interface. It is interesting to note that the gradient of capillary pressure which is responsible for driving force for liquid water flow is confirmed. Furthermore, the gradient dP_c / ds which has most time taken as a constant [3-5] to reduce mathematical difficulty or to take into account the assumption of low saturation is not constant. The main conclusion of these studies is the assumption of gradient dP_c / ds constant should be used for uniform saturation or very low saturation but when saturation can be varied in the range of 0 and 0.8 this assumption can not be used.

In order to study the effect of condensation on the polarisation curve, we allowed condensation in fig.3 at pressure of 325 kPa. This figure shows the polarizations curves of fuel cell for both condensation and without condensation on GDL at 100% of relative humidity. It can be seen in this figure that the dynamic polarization curve without condensation is better than the polarisation curve with condensation before purge. When water vapour condenses in the GDL, liquid water is produced and reduces the volume available for diffusion. The concentration or pressure of reactant decreases at electrochemical reaction sites resulting in low voltage as it can be seeing in fig.3. The increase of liquid water is related to saturation increase which in return increases the activation overpotential due to relation between them.

Fig.4 presents the study state profile of cell voltage with control of condensation phase. The main reason for this decrease in performance is due to the fact that gas pressure at inlet is still constant so that the pressure or the concentration of oxygen decreases with the distance before reaching the DGL/membrane interface and also the liquid water condensed in GDL. The poor concentration of oxygen at the interface and the liquid water condensed reduce the electrochemical reaction rate and also the cell performance.

The model results reinforce some important points such as GDL, condensation effect, evaporation effect on fuel cell behaviour. The condensation of liquid water affects fuel cell

performance by reduced the voltage magnitude. The liquid water saturation level accumulates at the interface GDL/membrane is responsible for such situation than that in GDL due to the small thickness of GDL The gradient dP_c / ds depends strongly on the range of saturation. It should not be taken as a constant for large range saturation. The non-linear equation of liquid water should be resolved for dynamical model without assumption of constant gradient dP_c / ds .

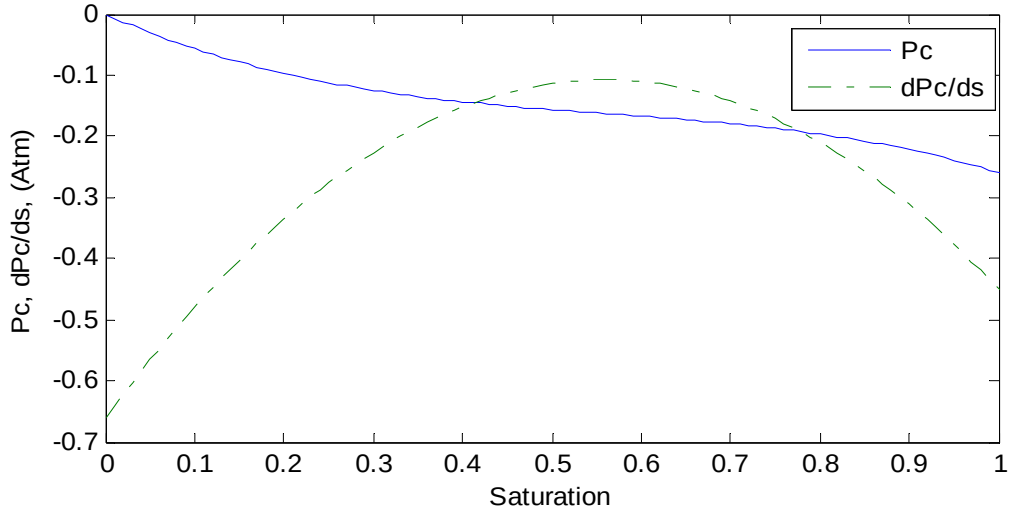

Figure 1: Graph of Capillary pressure P_c and gradient dP_c / ds .

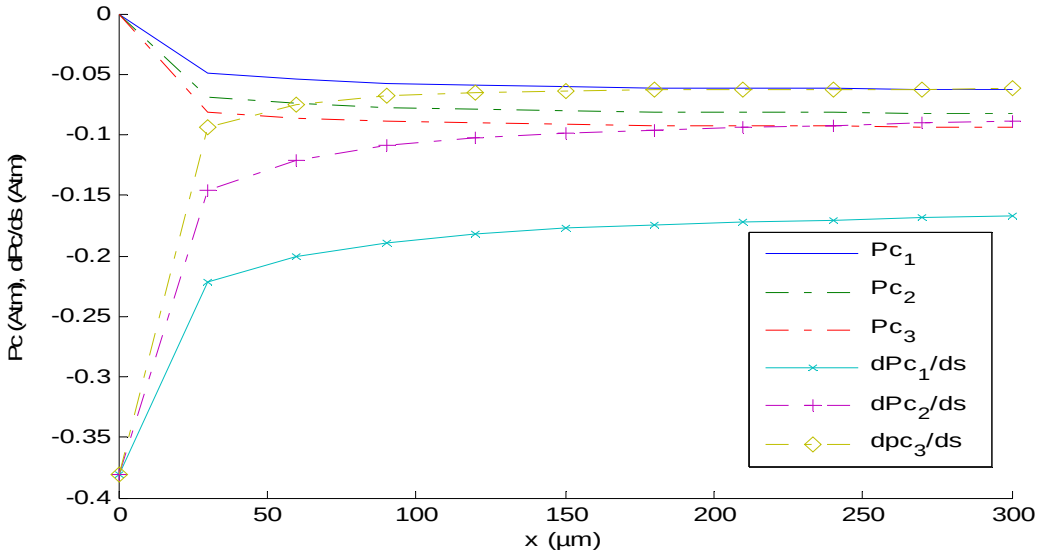

Figure 2: Schematic representation of P_c and dP_c / ds at (1):60 s,(2):100 s and (3):136 s.

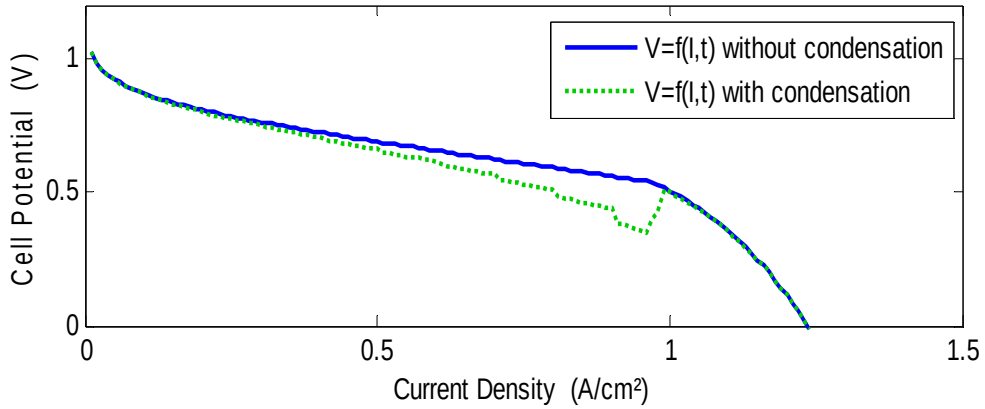

Figure 3: Effect of condensation on polarization curve of fuel cell at 325 kPa with condensation and without condensation at relative humidity (RH) of 100%.

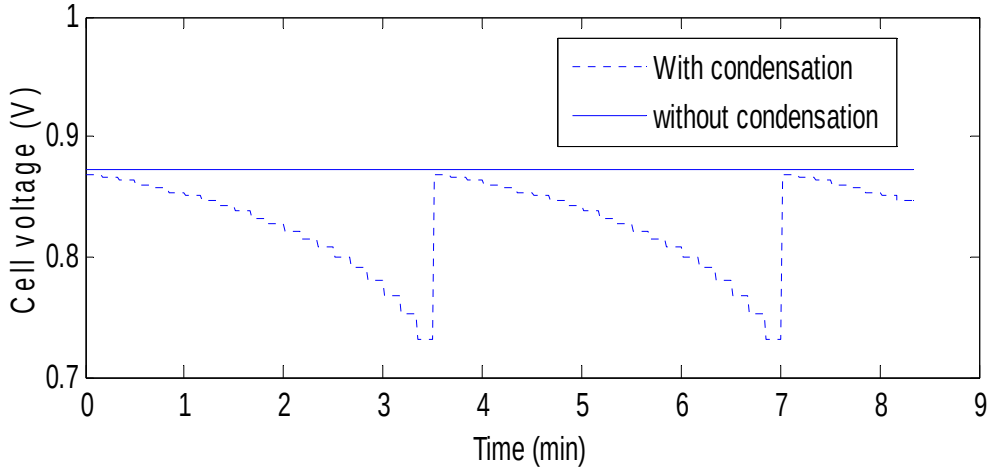

Figure 4: Steady state profile of cell voltage with condensation phase control (GDL thickness of 300 µm, 0.5A/cm²).

References

[1] D. Natarajan & T.V. Nguyen A two-Dimensional, Two-Phase, Multicomponent, Transient Model for the Cathode of a Pemfc USING CONVENTIONAL Gas distributors, journal of the Electrochemical Society, 148(12) A1324-A1335 (2001)

[2] Dilip Natarajan, Trung Van Nguyen Three-dimensional effects of liquid water flooding in the cathode of a PEM fuel cell Journal of Power Sources 115 (2003) 66–80

[3] Jin Hyun Nam 1, Massoud Kaviany Effective diffusivity and water-saturation distribution in single- and two-layer PEMFC diffusion medium International Journal of Heat and Mass Transfer 46 (2003) 4595–4611

[4] Shih-Ming Chang, Hsin-Sen Chu, Transient behavior of a PEMFC Journal of Power Sources 161 (2006) 1161–1168

[5] R. Madhusudana Rao & al. A two-dimensional steady state model including the effect of liquid water for a PEM fuel cell cathode Journal of Power Sources 173 (2007) 375-393

A Two-Fluid Model for Water Transport in a PEM Fuel Cell

Hans-Wilfried Mindt, ESI-GmbH, Germany
Kunal Jain, **Chaitanya Bapat**, ESI US R&D Inc., Huntsville, AL 35806, USA
J. Vernon Cole, CFD Research Corporation, Huntsville, AL 35805, USA

1 Introduction and Significance

Proton Exchange Membrane Fuel Cells, PEMFCs, are a promising alternative energy system for a number of applications including automotive and stationary power.

Water management in low temperature PEM Fuel Cells is highly important because of the inherent conflicts between the requirements for efficient low and high power operation. Particularly at low powers, adequate water must be supplied to establish and maintain the membrane humidification for adequate protonic conductivity or resistance losses will decrease the cell efficiency. At high power density operation, more water is produced at the cathode than is necessary for membrane hydration. This excess water must be removed effectively or it will accumulate in the Gas Diffusion Layer (GDL) and block the pathways for reactant transport to the catalysts, introducing mass transport losses and potentially "flooding" the electrode. As power density of the cells is increased to meet the needs of the transportation sector, the challenges arising from water management are expected to become more difficult to overcome simply due to the increased volumetric rate of liquid water generation. Such water management problems are critical for most PEM fuel cell applications. Thus, effectively addressing water management based issues through modeling and experimentation is a key challenge in successful application of PEMFC systems.

Despite the fact that accurate prediction of two-phase transport is critical for optimizing water management in PEMFCs, the understanding of the two-phase transport in fuel cells is still relatively poor. Wang et al. [1,2] have studied the two-phase transport in the channel and diffusion layer separately using a multiphase mixture model. The model fails to accurately predict saturation values for high humidity inlet streams. Nguyen et al. [3] developed a two-dimensional, two-phase, isothermal, isobaric, steady state model of the catalyst and gas diffusion layers. The model neglects any liquid in the channel. Djilali et al. [4] developed a three-dimensional, two-phase, multicomponent model. The model is an improvement over previous work, but neglects drag between the liquid and the gas phases in the channel. To enable model-based design and optimization of PEM fuel cells, given that proper water management is a key challenge for PEMFC systems, models must address a broad range of conditions including operation with significant liquid water in the channels as droplets or films. This work represents an effort to address the common deficiencies of previous model formulations, introducing a more general multiphase flow model that can serve as the basis for a design tool addressing water management.

2 Model Formulation

The model formulation presented is a general form for the Eulerian two-fluid model with extensions to address transport in porous media. After introducing the governing equations,

constitutive models for interphase momentum transfer are given and the discretization techniques used within this work are presented.

Governing Equations

Anderson and Jackson [5] and Ishii [6] derived the multiphase flow equations from first principles by volume averaging the point equations. The key difference between the two is the treatment of fluid-droplet traction term. van Wachem et al. [7] have shown that Anderson and Jackson's formulation [5, 8, 9] is more appropriate for a dispersed phase consisting of solid particles and that Ishii's formulation [9,10] is more appropriate for a dispersed phase consisting of fluid droplets. Since the multiphase flow in fuel cells consists of liquid droplets and films interacting with air, we have chosen Ishii's model for this work, -using averaged continuity and momentum equations in an Eulerian framework.

Fluid-Solid Momentum Transfer

The drag force exerted on a fluid phase by the solid phase of a porous media is given by a generalized form of Darcy's Law,

Fluid-Fluid Momentum Transfer

The drag force between two fluids with an interphase transfer coefficient is derived by assuming that one phase is in the form of droplets or bubbles dispersed in the continuous phase.

In this work, we used the Morsi and Alexander model for the drag function [8, 12] which is based calculated using the drag coefficient and the local value of the relative Reynolds number.

Capillary Pressure in Porous Media

Will be treated as a body force applied to the liquid phase within porous media, and the saturation will therefore correspond to the liquid phase volume fraction [13,14].

Discretization:

The discretization is based on a standard finite-volume method.

InterPhase Coupling Algorithm.

The drag force for each phase introduces a term depending on the velocity of the other phase into the momentum equations. At higher slip velocities, an implicit treatment of this term is critical for obtaining convergence. The two commonly used approaches are the Partial Elimination Algorithm, PEA, [15] and Simultaneous solution of Non-Linearly Coupled Equations, SINCE, (16). The main advantage of SINCE is the relative ease of extending the algorithm to more than two dynamic phases [17]. However, this comes at a cost of reduced implicitness/convergence. Since fuel cells can be adequately described using two dynamic phases, liquid and gas, the PEA was chosen for this work.

Continuity Equation

SIMPLE-type methods recast the continuity equation into a pressure-correction equation, the solution of which then provides corrections for velocities and pressures. This work has been

adapted to used SIMPLEC [18] algorithm. However, in the two-fluid model, the presence of two phasic continuity equations provides an additional degree of freedom and more complications. Numerical difficulties can arise in the case of large density differences between the fluids, since the continuity equation residuals of the phases would differ by orders of magnitude. The residuals of the denser fluid will then induce false, spurious, corrections in the velocity field for the low-density fluid. To address these issues, the general approach is to form a mixture continuity equation by linearly combining the phasic continuity equations using appropriate weighting factors. In our work, we will investigate using the densities of respective phases as the weighting factors.

Phase-Fraction Equation

We followed the approach of composite solution of both phase-fractions mentioned in Vaidya et al. [19]. This approach is based on Carver [20, 21] and derives an equation for the phase fraction by taking the difference of the density-weighted continuity eqations.

Solution Algorithm

The most common iterative alogrithm for solving two-phase Momentum and Mass Conservation equations in a segregated finite volume pressure-based framework is the Interphase Slip Algorithm. The algorithm is an extension of Patankar's SIMPLE algorithm [22] and can be summarized as follows:

1. Guess a pressure field P*.
2. Solve the discretized momentum equations for each phase.
3. Solve for the pressure correction equation.
4. Update the pressure and velocity components.
5. Solve the composite equation for phase volume fraction.

Steps 1-5 are repeated till convergence. The system of equations and the solution algorithm presented in the previous sections were implemented into a commercial CFD code (CFD-ACE+) [11]. The linear equations were solved using either a Conjugate Gradient or an Algebraic Multigrid solver.

3 Results and Discussion

The two-fluid model formulation has been implemented and evaluated for simulation of two-phase flows relevant to fuel cell analysis. The benchmark model cases for measuring accuracy and robustness was the predicted phase-fraction profiles obtained by Oliveira et al. [23] for the development of stratification of two fluids with different densities.

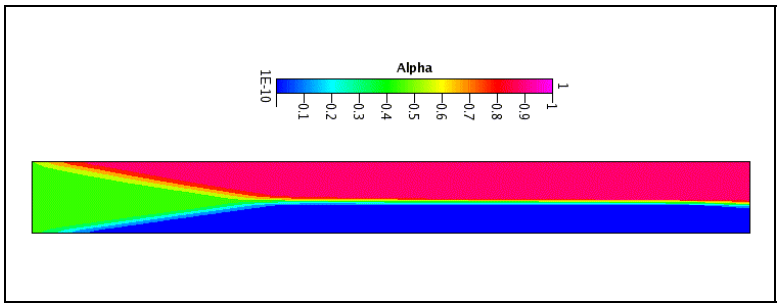

Figure 1: Alpha contours for stratification for 2d channel case.

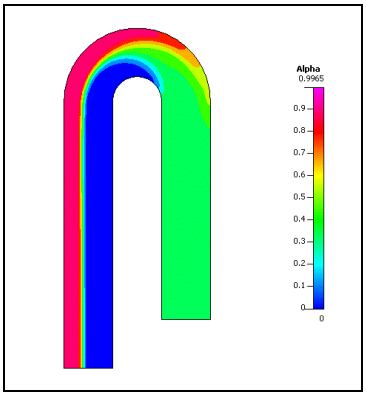

Figure 2: Liquid fraction, alpha, contours for a U-bend (2d) case.

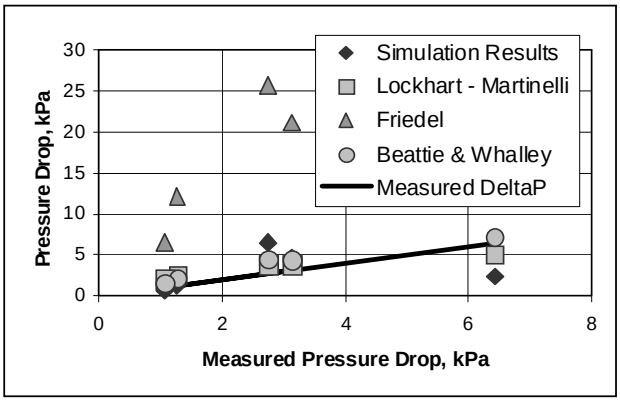

Figure 3: Comparison of predicted and measured pressure drops for two-phase flow in an annulus, documented by Dillon [24].

Two-Phase Transport in Porous Media

The fluid-solid momentum transfer implementation was verified by comparison of predicted pressure drops during one-dimensional, two-phase, flow through porous media with the corresponding analytical solutions, -described in the characterization studies of Nguyen [25].

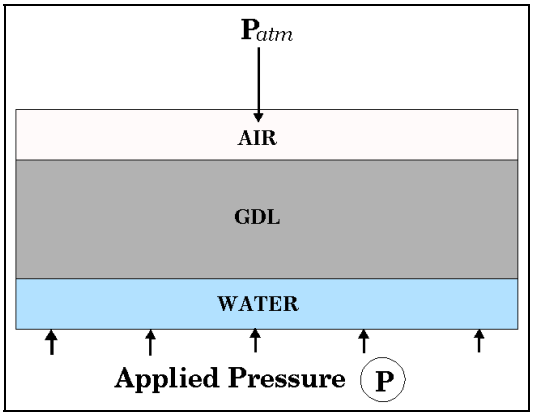

Figure 4: Schematic of model domain used to assess capillary pressure prediction.

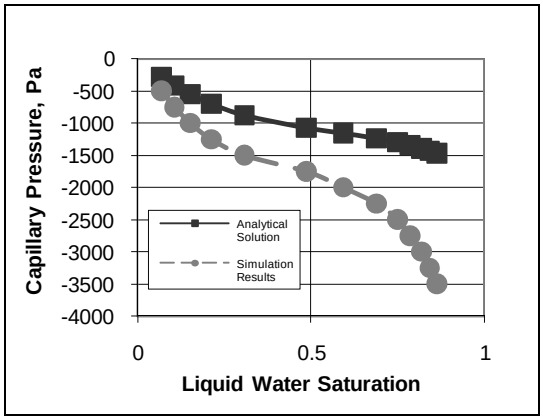

Figure 5: Comparison of predicted capillary pressure and the analytical value as a function of volume-averaged saturation.

A saturation gradient is present at the water reservoir – porous media interface, due to the unity liquid phase fraction in the water reservoir. This gradient increased the local value of the capillary pressure at that interface, and caused an over-prediction of the capillary pressure at the volume averaged saturation level. This deficiency of the implementation will be addressed in future work.

References

[1] Y. Wang, S. Basu, and C.Y. Wang, J. Power Sources, 179, 603 (2008).

[2] P.K. Sinha, and C.Y. Wang, Chem. Eng. Sci., 63, 1081 (2008).

[3] G. Lin, and T.V. Nguyen, J. Electrochem. Soc., 153, A372 (2006).

[4] T. Berning and N. Djilali, J. Electrochem. Soc., 150, A1589 (2003).

[5] T. B. Anderson, and R. Jackson, Ind. Eng. Chem. Fundam., 6, 527 (1967).

[6] M. Ishii, Direction des Etudes et Recherches d'Electricit´e de France, (1975).

[7] B.G.M. van Wachem, J. C. Schouten, C. M. van den Bleek, R. Krishna, and J. L. Sinclair, AIChE J., 47, 1035 (2001).

[8] R. Jackson, Chem. Eng. Sci., 52, 2457 (1997).

[9] R. Jackson, Chem. Eng. Sci., 53, 1955 (1998).

[10] M. Ishii, and K. Mishima, Nucl. Eng. Des., 82, 107, 1984.

[11] CFD-ACE+ Theory Manual V2007.

[12] S. Morsi, and A. Alexander, J. Fluid Mechanics, 55, 193 (1972).

[13] M.C. Leverett, Trans. AIME, 142, 151 (1941).

[14] K.S. Udell, Int. J. Heat Mass Transfer, 28, 485 (1985).

[15] D.B. Spalding, Recent Advances in Numerical Methods in Fluids, Swansea: Pineridge Press, 1, 139-168 (1980).

[16] S. Lo, and H. Karema, Computers & Fluids, 28, 323-360 (1999).

[17] D.B. Spalding, in Numerical Methodologies in Heat Transfer, Proceedings of the Second National Symposium, New York: Hemisphere, 421 (1983).

[18] J. P. van Doormaal, and G.D. Raithby, Numer. Heat Transfer, 7, 147-163, 1984.

[19] N. Vaidya, P.J. Dionne, and A.K. Singhal, ASME FED Gas Liquid Flows, 225, 179 (1995).

[20] M.B. Carver, J. Mech. Eng. Sci., 24, 221 (1982).

[21] M.B. Carver and M. Salcudean, Math. Comput. Simulation, 26, 475 (1986).

[22] S.V. Patankar, and D.B. Spalding, Int. J. Heat Mass Transfer, 15, 1787 (1972).

[23] P. J. Oliveira, and R. I. Issa, Int. J. Numer. Meth. Fluids, 43, 1177 (2003)

[24] C.M. Dillon, Two-Phase Flow within Narrow Annuli, Masters Thesis, Georgia Institute of Technology (2004).

[25] H. Ohn, T. Nguyen, D. Jacobson, D. Hussey, and M. Arif, in Proton Exchange Membrane Fuel Cells V, ECS Transactions, 1 [(6)], 481 (2005).

Hydrogen Distribution Infrastructure for an Energy System: Present Status and Perspectives of Technologies

Françoise Barbier

Abstract

Hydrogen as a clean energy carrier (its use produces no CO_2 emissions) offers effective solutions for a secure energy supply and a clean environment. To make hydrogen readily available, a hydrogen infrastructure allowing for its convenient distribution to end users is essential. The choice of relevant modes of hydrogen transport and distribution from the production plant is therefore critical. Safe, cost-effective, and energy-efficient solutions are needed. Factors such as the degree of hydrogen penetration, the environmental performance of the different pathways, and geographic parameters will influence the infrastructure deployment. Advances in delivery technologies will allow the existence of a transition infrastructure to support the commercial introduction of fuel cell vehicles and hydrogen stations. In this chapter, an overview of the distribution technologies already mastered by gas companies such as pipelines, gaseous trailers, and cryogenic trucks is given, with insights into costs, advantages or disadvantages, and advanced solutions. Further, supporting technologies such as compressors, pumps, and hydrogen quality requirements for fuel cell applications are presented. The large-scale storage to regulate hydrogen consumption and production is discussed. Finally, recent progress in refueling at filling stations is presented.

Challenges with the Largest Commercial Hydrogen Station in the World

Thomas Charbonneau, **Pierre Gauthier**, Air Liquide Canada

Abstract

This abstract's objective is to share with the participants the story of the largest hydrogen fuelling station made to this date and to kick-start the story, we will cover the challenges; first the technical ones; the operational ones; the distribution ones and; the financial ones. We will then move on to review the logistic (geographic) issues raised by the project and conclude our presentation by sharing the output values of the largest fuelling station built so far in the world.

1 The Challenges

First and foremost the challenges were linked to the transit operator technical specifications, the station needed to be installed and permitted in a city that did not have any experience with hydrogen before, it also needed to fill one transit bus (46 kgs) in less than 10 minutes, an equivalent of the time taken by current operators to fuel a diesel bus. Product quality was also important, the quality of the product at the nozzle needed to meet the SAE J2719 specifications despite the fact that the SAE specification was not going to be finalized and approved as a standard for another 4 to 5 years. The station needed to be available 99.9% of the time and provide transfers at 350 bars in a safe manner, training for operators and drivers was not to take more than 2 hours to familiarize them with the safe fuelling of a bus. Intelligent redundancy became more and more important during the design stage of the station.

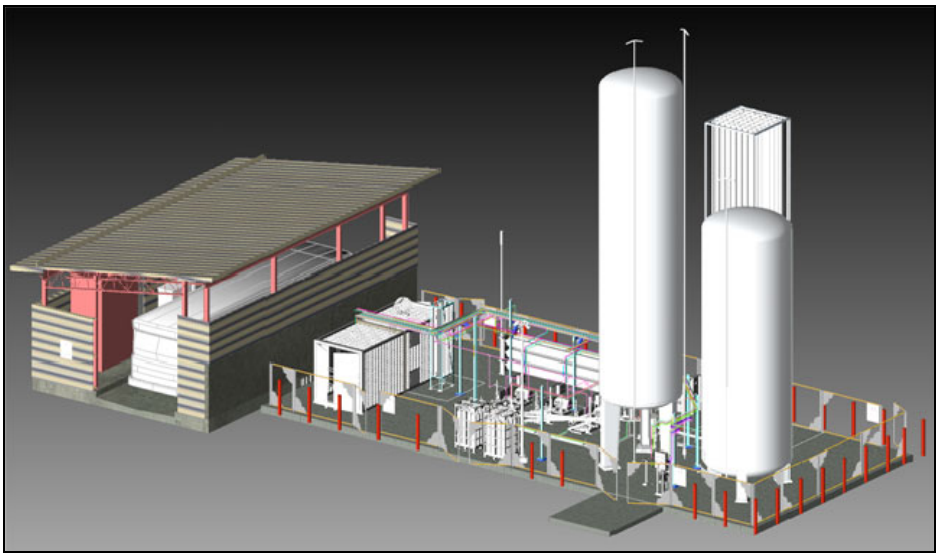

Figure 1: Whistler refuelling station design.

On the operational challenges, hydrogen as a fuel was to be as user friendly as diesel, therefore fuelling of the fleet needed to take place in any three-hour window, i.e. 18 consecutive fills in 3 hours or less. Use of the dispenser was to be as easy as any other refuelling experiences and ID verification, pre-fuelling steps and ID recognition needed to be as easy as swiping an RFID tag in front of the reader. One could appreciate the fact that moving 20 buses in a yard early in the morning or late at night could be a logistic nightmare, it is more important to ensure the flow of hydrogen vehicles going to the fuelling station is constant in order to reduce any potential product losses at the station.

Canada being a large country, we also had to solve distribution challenges as the liquid hydrogen trailer was to travel 4500 kilometres between the liquid plant and the fuelling station site. Ensuring timely deliveries, back-up plans in case of road restrictions, road accidents and weather conditions became a very important element of the fuelling station uptime. A back-up plan was carved, intelligent redundancy developed, remote monitoring and operating of the station implemented, a larger than required storage was also implemented ensuring complete autonomy for the 2010 Olympics. The Olympics and the security surrounding them added one more level of difficulty to the overall distribution issues identified, restricted access during the Olympics, additional security checks, additional volumes of passengers, unknown bus usage data, etc. all these helped produce more sleepless nights.

Figure 2: Liquid hydrogen delivery to Whistler refuelling station.

The financial challenges of the project were to ensure alignment of pre-project estimates versus the hard spent construction costs, commissioning costs, babysitting costs during the Olympics and distribution costs. The fuelling station needed to be a win-win project, allowing the transit operator to reap the benefit of the new technology and its fuel cell efficiencies while the industrial gas supplier who took a lot of risks would see the project materialize on target as to construction costs. We are all aware that operating cost is the most important element of any transit operator, in the case of hydrogen fuel cell buses, we know that the efficiency of the fuel cell bus will be double the one of the diesel bus, it is therefore important to maintain the rest of the operating costs as low as possible or as close as possible to the current ones. Fuelling time and fuelling station downtime should be better or equal to what the transit operator experienced in the past. This is what we have managed to reproduce on the west coast of Canada.

2 The Outcome

After civil work preparation has been completed, the refuelling station construction was initiated in September 2009 and lasted for 2 months. After completion of commissioning, the first liquid hydrogen delivery took place on November 13th 2009 and the first filling event with a BCT bus occurred on November 16th 2009.

Since busses were delivered to the site progressively, December and January were used to ramp up the normal operations.

The official opening ceremony took place on January 22nd 2010 with the support of Whistler's Mayor and the presence of the government of British Columbia, more than 100 people attended the event.

Figure 3: Fuel cell busses line-up at Whistler refuelling station.

Since the beginning of the project, the number of busses ramped up steadily up until a few weeks before the Olympics. During the Olympic Games, the busses were used in standard

transit operations and the users as well as the drivers enjoyed a quite ride producing zero emissions.

Mid of April, the buses had travelled more than 275,000 kilometres and more than 1350 fuelling events performed since the beginning of the project mid-November 2009.

Vehicle ID	Vehicle Odometer (Km)
1000	22404
1001	12334
1002	17717
1003	13916
1004	16066
1005	17916
1006	14482
1007	15522
1008	14770
1009	15561
1010	11636
1011	7739
1012	7665
1013	9676
1014	15271
1015	14999
1016	6454
1017	14111
1018	14668
1019	13745
TOTAL	**276652**

Month	Number Of Fills	Quantity (kg)
Apr 2010	275	7590
Mar 2010	485	13208
Feb 2010	332	7766
Jan 2010	166	2829
Dec 2009	102	1402
Nov 2009	25	482
TOTAL	**1385**	**33207**

Figure 4: Whistler refuelling station data - Updated on April, 19th 2010.

The drivers are all happy with the transition, the wash-bay operators, those who fill the buses every night do not see a huge difference between the diesel isle and the hydrogen isle in terms of speed or in terms of complexity, the buses are on the road and the passengers do not see any disadvantages, the noise level is way down in the bus, and the fleet of 20 buses will account for a reduction of green house gases in the neighbourhood of 1800 tons per year.

Buses can be filled in less than 10 minutes, the whole fleet can be filled in less than 5 hours, a normal transit operation in Whistler is now running on hydrogen, another step forward for our industry.

References

[1] Maus J & al, " Filling procedure for vehicles with compressed hydrogen tanks", International Journal of Hydrogen, Issue 33 (2008), page 4612 to 4621

[2] Yang Jiann, "A thermodynamic analysis of refueling of a hydrogen tank", International Journal of Hydrogen, Issue 34 (2009), page 6712 to 6721

[3] Kountz & al, "A new Natural Gas dispenser Control System", 1998 International Gas research Conference, November 1998

[4] Liss, W & al, “Development of a natural Gas to Hydrogen Fueling station”, Topical Report for US D.O.E, GTI-02/0193 , September 2002

[5] Farzaneh-Gord, M., "Compressed natural gas Single reservoir filling process", Gas internationalEngineering and Management, Volume 48, Issue 6, July/August 2008, page 16-18.

Polymer Pipes for Distributing Mixtures of Hydrogen and Natural Gas: Evolution of their Transport and Mechanical Properties after an Ageing under an Hydrogen Environment

Marie-Hélène Klopffer, IFP, France
Philippe Berne, CEA, France
Sylvie Castagnet, ENSMA, France
Mathilde Weber, Air Liquide, France
Gilles Hochstetter, Arkema, France
Eliane Espuche, INSA Lyon, France

Abstract

With the development of hydrogen as an energy vector, its delivery and transport from the production site to the end user remains an issue. Indeed, the key challenge to overcome is the high hydrogen permeation through existing polymer infrastructures used for natural gas distribution (Polyethylene pipes, components as connecting parts). This high flow rate of hydrogen through polymer has to be taken into account for safety and economical requirements. This 3-year project investigates pure hydrogen gas and mixtures (20% CH_4 - 80% H_2) in pipelines made of engineering polymers to develop and assess material solutions to cope with today problems for H_2 distribution. Materials such as polyethylene (PE100) and polyamide 11 (PA11) have been studied. PE100 is considered as a reference material as it is used today in natural gas distribution pipes. PA11 should allow a higher operating pressure combined with better gas-barrier performances. Test benches and protocols for testing materials in terms of mechanical and barrier properties were first developed. The materials have then been studied in terms of barrier, mechanical properties and on a microstructural point of view. The properties of the raw material and samples after ageing in presence of hydrogen in various conditions were compared to assess the long term behaviour in service. These results as well as the comparison between PA11 and PE are presented.

1 Introduction

The project called PolHYtube is relative to the development and study of innovating materials for hydrogen distribution networks and benefits from a subvention of the French Research Agency.

During this project, several engineering polymers have been characterized to assess if they are compatible with the specifications given by a major hydrogen producer, Air Liquide, set at the beginning of the project. The specifications have taken into account:

- the conditions of service of the pipes (pressure, flow of gas required for the application, temperature, …)
- the level of safety in term of hydrogen permeation through the polymer wall. In a first step, the target hydrogen permeation flow will be set equal or much lower than the

one of methane through polyethylene depending on the application. Polyethylene is indeed the reference polymer material for the distribution of a gaseous fuel

- the durability of the polymer (cost and lifetime).

In the framework of the project, the first two points have been investigated more precisely to assess materials suitable for 3 references scenarios that summarize different distribution pathways of hydrogen produced from a SMR or an electrolyser (higher service pressure) to filling stations, fuelling stations and public areas:

- High pressure (15-30 bars) and a level of hydrogen permeation equivalent to the one of methane through HDPE (high density polyethylene)
- Low pressure (4 bars) and high barrier to hydrogen (50 to 200 times lower than the one of methane through HDPE)
- High pressure (15-30 bars) and high barrier to hydrogen (50 to 200 times lower than the one of methane through HDPE).

2 Evaluation of the Materials Properties

As a technical plastics producer, Arkema participates in this project and has provided some polymer materials. In particular, Arkema shared with the other partners it's experience in developing polyamide 11 pipes for gas distribution in US. This allows the project team to well define the technical targets and specifications of the project (pipe diameter, pipe design (i.e. the thickness to diameter ratio), internal pressure). An important point to be taken into account is the extrudability of the preselected polymers and the long term property of these polymers. The aim of this work is to determine the hydrogen permeability of different polymers that could be used as alternative to PE in target pipeline and to understand their gas transport properties as a function of their structure and their crystalline morphology. The evolution of these properties after an ageing under a hydrogen environment was also studied.

Two polymers were particularly studied: a polyethylene (PE XS10B from Total Petrochemical), that has been taken as the reference material, a polyamide (PA11, Rilsan TL from Arkema).

To be representative of the target pipeline, the PA and PE samples we studied were taken from extruded sheets of 1mm thickness. The crystallinity index of each material was measured by DSC. It was equal to 60% for PE, 20% for PA11.

3 Permeation Measurements

Due to safety requirements, one of the main concerns about polymer pipes is their permeability to hydrogen, which may induce critical leakages of gaseous hydrogen. Permeation measurements were performed by IFP, CEA and INSA Lyon on unaged PE100 and PA11 material samples in various conditions of pressure, hydrogen content and temperature.

The experimental technique developed at IFP concerns gas or gas mixtures permeation through a polymer membrane or a pipe section, in a flowing stream of vector gas and detection by gas chromatography. In that kind of measurement, one or several diffusing species cross the polymer to reach an opened volume swept away by an inert gas stream.

This carrier gas fulfils its purpose by pulling the different molecules towards an appropriate detector measuring the present gas proportion. Then, it is possible to determine the intrinsic transport coefficients of each of the gases constituting the initial mixture. It allows determination of the permeability coefficients of pure gas in numerous polymers but also the permeability coefficients of gas mixtures, such as CH_4-H_2.[1, 2] Practically, many tests of permeability (> 70) were carried out during this study in order to identify the influence of four parameters: temperature (at least 3), pressure (5 and 20 bars), compositions of gases (pure CH_4, 80% H_2 – 20% CH_4, pure H_2) and polymer processing (pipe section and membrane). Most experiments have been carried out twice in order to evaluate the repeatability of the tests.

As mentioned before, some permeation experiments were also carried out on PA and PE at INSA Lyon to validate the use of the experimental device, initially developed for the study of thin films, for these thick samples. Measurements were performed for all samples at different temperatures ranging from 10 to 40°C under a pressure gradient of 5 bars. The experimental values of permeability coefficients obtained for PA11 and PE were in good agreement with those measured by the other partners of the project (IFP, CEA) showing that the INSA equipment could be used for thick samples and that the various methods used to detect and quantify the diffusing molecules through the polymer are reproducible.

As expected, permeability coefficients increase with temperature and are well represented by an Arrhenius law, that is to say that the plot of the logarithm of the permeability coefficient as a function of 1/T defined a straight line for each polymer. This is quite normal, because, in the temperature range studied, no transition temperature is associated either to the polymer or to the gases[3-5].

The H_2 permeability coefficients decreased going from PE to polyamide. These results were closely related to the cohesive energy density of the amorphous phase in each polymer. Indeed, and as previously underlined, the crystallinity was higher for PE than for PA11 whereas the barrier properties were higher for PA11 than for PE. By comparing the behaviour of the two single gases, one can see that the permeability of H_2 is larger than that of CH_4 whatever the considered temperature is and whatever the polymer is. On the other hand, no influence of the applied pressure could be detected in the studied range (5 to 20 bars). Moreover, in the case of mixtures of H_2-CH_4 either with PE or PA11, no particular interaction could be noticed that is to say no mixture effect. Consequently, for a given temperature, each gas (either H_2 or CH_4) keeps its intrinsic permeability coefficient whatever the composition of the feed mixture is.

4 Evolution of Permeability Coefficients with Ageing

CEA-Grenoble was in charge of the ageing of polymer samples under various experimental conditions, which includes the following tasks:

- ageing of polymer membranes and tubes by contact with hydrogen or with a hydrogen-methane (80-20%) mixture under controlled pressure (5 to 20 bars) and temperature (20 to 80°C) conditions,
- monitoring of the permeation coefficient during ageing of the samples,
- analysis of its variation in time.

The ageing cells have been designed to allow periodical permeation measurements during the ageing process. They comprise an upstream chamber that is continuously kept under the desired gas pressure and a downstream chamber that is normally open to the atmosphere – the sample, membrane or tube, being sandwiched between the two chambers. Permeation measurements are made on an average every second month. Whenever they are required, the downstream chamber is flushed with a neutral gas (helium or nitrogen) that transports the permeated gases to a gas chromatograph allowing detection and quantification of the hydrogen or methane flux through the sample. This technique is basically the same as the one used for the permeation measurements (previous section). It allows in situ measurement of the permeation coefficients without having to remove the samples from the ageing cells and to disrupt the experimental conditions[6]. Since the permeation coefficient has been found to be independent of pressure and gas composition, and its variation with temperature has been shown to follow Arrhenius's law, the measurements are all converted to an equivalent of pure hydrogen at 20°C to allow comparison in spite of the various experimental conditions.

A total of 17 membrane samples have been submitted to ageing and periodic monitoring for 1 year. Eight small-diameter (8 mm) and eight large-diameter (32 mm) tubes are currently under study, with the objective of also reaching a duration of 1 year.

Exploitation of the measurements on membranes has been made. The most important result is that the permeation coefficient is equal to 2.10^{-17} $Nm^3.m^{-1}.s^{-1}.Pa^{-1}$ for the PE membranes and 8.10^{-18} $Nm^3.m^{-1}.s^{-1}.Pa^{-1}$ for the PA11 membranes (at 20°C under pure H_2), and that it is unaffected by one year of ageing, whatever the experimental conditions (see Figures 1 and 2 relative respectively to PE100 and to PA11). Analysis of the available results for tube samples suggests that the same ratio exists between the permeation coefficients of PE and PA11 tubes and that they are also essentially unaltered by ageing.

5 Mechanical Measurements and Evolution during Ageing

Coupling between gas sorption and mechanics in polymers is bound to modify their mechanical properties and in-situ experiments are needed to characterize such a phenomenon and provide data for the design of industrial parts. However, when dealing with a hydrogen atmosphere, very few experimental works have been reported. Two possible effects of a hydrogen atmosphere on the tensile properties of polymers have been investigated in the present study, in polyethylene (PE), polyamide 11 (PA11): (i) a coupling effect between pressurized gas sorption and several aspects of the mechanical behaviour (tension, creep and ductile fracture), and (ii) the influence of long-term exposure to hydrogen on the tensile properties. Tensile, creep and ductile fracture tests have been carried out in a tensile testing machine fitted with a pressurized-hydrogen chamber displaying pressures from the ambient up to 400 bars. The gas chamber could be filled by nitrogen or hydrogen. Most tests were carried out at 30 bars, after thermal equilibration and gas saturation of the sample.

It can be reasonably concluded that tensile properties are not affected by H_2 diffusion into PE, even up to 100 bars. The same result stands for PA11 materials, for which the room temperature scatter appears of first importance compared to a possible hydrogen effect.

Static properties (modulus and yield stress) obviously depend on the nature of constitutive materials, but no more hydrogen effect is observed. The same conclusion stands for the creep behaviour of as-received PE and PA11. Creep tests performed at different temperatures show that the time-temperature superposition principle can be applied with similar shift factors, both in ambient air and pressurized hydrogen. In the same way, hydrogen environment was shown to have no noticeable effect on the ductile fracture of as-received PE and PA11, as estimated from a short series of tensile tests in double-notched samples.

After long-term aging up to 13 months in hydrogen atmosphere at various pressures (5 or 20 bars) and temperatures (20°C, 50°C and 80°C) ranging below and above the glass transition of PA11 and the alpha-c transition for PE, no deleterious effect was observed on the mechanical properties of PE and PA11. Differences observed for PA11 essentially result from testing temperature variability close to the glass transition temperature. Consistently with the tensile properties, no significant evolution of the crystalline microstructure after ageing into hydrogen arises from DSC experiments. Again, the clearer effect is associated with the annealing temperature in PA11.

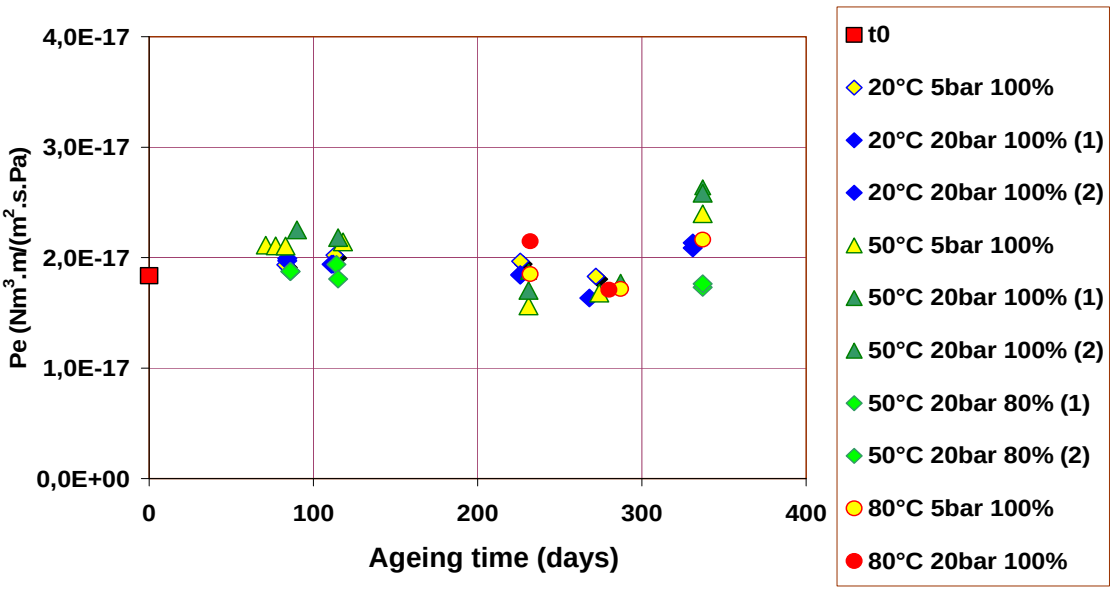

Figure 1: Evolution of the H_2 permeability coefficient in PE100 at 20°C as a function of ageing time.

6 Conclusion

On different experimental devices, the permeability coefficient of H_2 through PE100 and PA11 has been determined in different representative conditions of the pipe life (pressure, temperature, hydrogen content, geometry of the sample). It was shown that PA11 presents a lower permeability to H_2 than PE100, that the evolution with the temperature follows an

Arrhenius law and that no particular effect of the pressure or of the gas composition has to be noticed. Moreover, a good correlation of the measurements between pipe sections and discs samples was obtained which means that no influence of the polymer processing could be noticed.

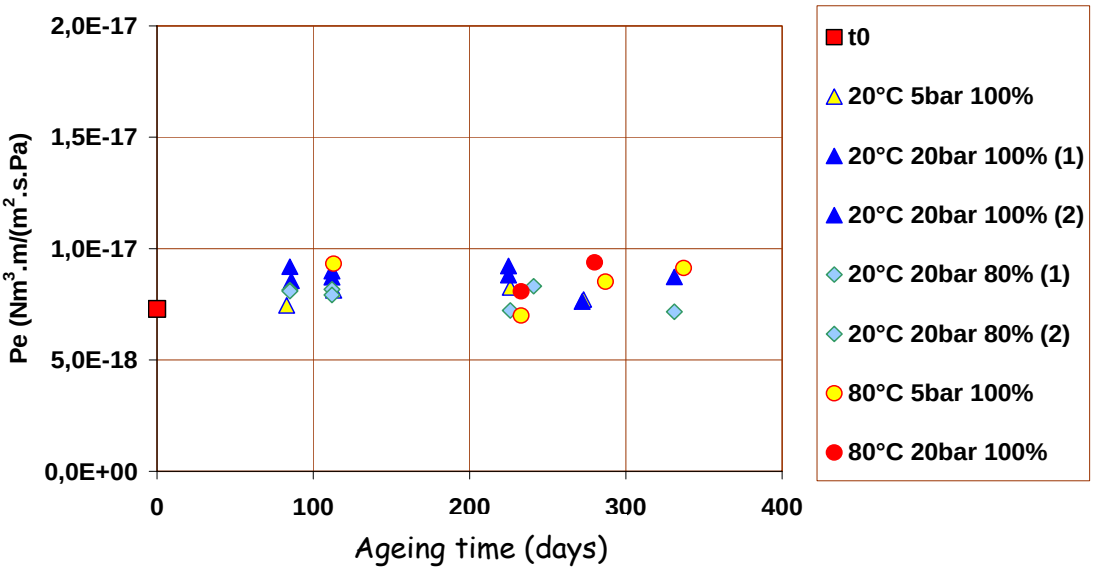

Figure 2: Evolution of the H_2 permeability coefficient in PA11 at 20°C as a function of ageing time.

But the most important point is that the effect of ageing under an hydrogen environment has also been studied. No evolution of the barrier properties of the PE100 or the PA11 system has been observed after more than one year of ageing in various conditions. The same conclusion stands for the aspects of the mechanical behaviour investigated here, i.e. tension, creep and ductile fracture, in both as-received and aged materials.

The study will be completed by an economic assessment of the solutions developed in the framework of the project.

References

[1] M.H. Klopffer, B. Flaconnèche, K. Esterlé and M. Lafontaine, *2nd European Hydrogen Energy Conference (EHEC 2005)*, 2005.

[2] M.H. Klopffer, B. Flaconneche and P. Odru, *Plastics, Rubber and Composites*, 2007, **36**(5), 184.

[3] J. Crank and G.S. Park, *Diffusion in polymers*, Academic Press, 1968.

[4] M.H. Klopffer and B. Flaconnèche, *Oil & Gas Science and Technology*, 2001, **56**(3), 223.

[5] C.E. Rogers, *Polymer Permeability*, J. Comyn, ed., Elsevier Applied Science, 1985, 11.

[6] M.P. Foulc, F. Nony, P. Mazabraud, P. Berne, M.H. Klopffer, B. Flaconnèche, G. Ferreira Pimenta, G. Müller Syring and I. Alliat, *World Hydrogen Energy Conference 16*, 2006.

Automatic Refuel Coupling for Liquid Hydrogen Tank Trailers

Michael Boersch, **Fridolin Holdener**, WEKA AG, CH-8344 Baeretswil, Switzerland

1 Distribution of Hydrogen State of Technology

Production of hydrogen is operated either directly on-site by consumers or by suppliers of industrial gases. To optimize the transportation it is required to compress or liquefy the hydrogen.

For the distribution of liquid hydrogen in medium quantities to the consumers often special tank trailers are used.

2 Current Solution in LH_2 Trailers

Normally the transfer of liquid hydrogen from a trailer to the customer tank is carried out by a manually operated and open unprotected coupling.

Such couplings are of the Johnston type principle. Design characteristics are several coaxial pipes in defined cryogenic lengths resulting in a male and female part with a vacuum insulation and a pressure-tight connection between.

However these devices are not ideal for the handling of liquid hydrogen. It is caused particularly by its limitation only to connect and disconnect the coupling in a pressureless and medium-free state. The procedure for a pressureless coupling and uncoupling with its subsequent operations (cooling, purging, warming and venting the line) requires significantly more time. This adds to the overall duration of the transfer operation from the distributors tank to the trailer and from the trailer to the customer tank.

For instance the procedure of venting the line takes about 1 to 2 hours extra time. Moreover a large quantity of valuable hydrogen is lost during these operations.

3 Approaches and Requirements of the New Design

First solutions of semi-automatic Johnston couplings are known in WEKA's standard programme since the 80th. But for application in LH_2 tank trailers several more requirements have to consider.

Most important specifications are:

- L/GH_2; 20…323 K
- Design pressure 6 barg = 0.6 MPa
- Manually connected; automatically coupling and decoupling
- Inhibit leakage of L/GH_2
- Avoid entrapped air
- Prevent impurities of medium
- Minimize heat load
- Shortest possible cryogenic length for compact design

- Disconnect without warming and venting procedure
- Protect against faulty operation
- Leakage detection

4 Development of Prototypes

In further development and as a part of several customer projects various coupling prototypes have been developed and optimized.

WEKA's technical solution allows an easy connecting and locking by hand as well as self-acting coupling and decoupling action. The automatic and compact coupling is based on the Johnston principle it is however specially designed for the use with liquid hydrogen.

So the function principle has been changed to avoid the necessity of the additional cooling and venting procedure.

In a first step the male and female part are docked and secured hermetically tight.

In the second step an actuated insert is automatically pushed in or retracted after the filling.

Main components and features of the new coupling design are:

- Pneumatic actuated ball valve on female part of the coupling opening to let pass the insert and closing just before the coupling will be disconnected and so to keep GH_2 inside.
- Shut-off valve integrated in the female part; it opens and closes only if the insert is in service position.
- Guiding and fixation unit to support easy handling and safety aspects.
- Pneumatic linear actuators for automatically operated insert.
- Control unit to assure correct activation of actuators and prevent faulty operation.
- Leak gas return to limit pressure in GH_2 filled volumes and recirculation into medium pipe.
- Connections to test tank and LH_2 feed tank.

Special focus was put in to leak tightness, prevention of impurities and avoidance of wrong handling. Therefore the coupling is designed with a double seal to medium and to ambient with O-rings, spring energized plastic seal plus metallic bellow.

The ball valve and pneumatic linear actuators are operated with a working pressure of 6 barg…10 barg.

Last but not least the optimal cryogenic length could be found with these prototypes.

5 Prototype successfully tested in LH_2 laboratory

The prototypes have been successfully tested in a specialised laboratory at customer site with LH_2 at cryogenic conditions. In result the hydrogen transfer has shown positive performance, no leakage could found and no unacceptable heat load was observed.

Tests particularly have covered:

- Cycles of coupling and uncoupling
- LH_2 endurance test
- Leakage- and functional tests

6 Further Development and Outlook

A follow-up project has been started for a coupling in DN25/PN12 however it is scalable up to DN50.

The challenge here is the development of a robust coupling system with a large nominal size of flow nevertheless still light enough to be operated by one man.

So the weight for the male part has to be less than 7.5 kg!

Several approaches to meet these requirements are pursued:

- Optimisation or substitution of metallic bellow, quick-acting closure, etc.
- Weight reduction, cost minimising
- Serial production
- …

Continuation of the development is in progress with several functional tests. Pre-serial models for the field testing are planned in 2010/11.

7 Conclusion

- Automatic fuel coupling reduces duration of LH_2 filling significantly by a higher safety level.
- Prototype with DN15 successfully tested.
- Coupling and decoupling is possible with medium inside (GH_2).
- Nominal sizes up to DN50 = NPS 2” and nominal pressure up to 12 bar feasible.
- Optimisation relating to handling, dimensions and weight still required.

icefuel® – An Infrastructure System for Cryogenic Hydrogen Storage, Distribution and Decentral Use

Georg Markowz, Evonik Degussa GmbH, Germany
Anett Dylla, Mensch-Marketing-Technik, Germany
Tom Elliger, TUEV SUED Industry Service GmbH, Germany

1 Background

The rapidly growing worldwide energy needs and the diversification of the energy mix with an increasing share of renewable energies are challenging the existing energy infrastructures. At present, central grids dominate worldwide energy supply and distribution. More flexible solutions are required, especially those that integrate renewable energies more efficiently. In the case that larger energy quantities have to be stored, hydrogen has, in spite of losses during production and reconversion to electric power, a high potential as universal and clean secondary energy source [1-3]. Numerous demonstration projects worldwide already address this kind of chemical energy storage [e.g. 4, 5]. In most cases hydrogen is stored in the gaseous state under pressure at ambient temperature and reconverted to electricity close to the point of hydrogen generation. The transition to liquid hydrogen (LH2) promises - despite the additional liquefaction effort - efficiency advantages for the storage, distribution and decentralized reconversion of the hydrogen into electricity, heat and cooling energy.

2 *icefuel*® Concept

icefuel® (integrated cable energy system for fuel and power) is a flexible system for energy storage, distribution and decentral reconversion. The concept is based on the production and liquefaction of hydrogen to buffer large quantities of excess electricity, preferentially from fluctuating renewable energies like wind and solar power, thus facilitating the equilibration of power generation and demand at high shares of renewable energies. A concept schematic is shown in Figure 1.

Thus, the *icefuel*® system should be quite easily installable in addition to existing infrastructures. To keep installations costs low, it would be favourable to apply the concept to areas with high utilization densities.

The cryogenic hydrogen (< -233 °C) is distributed through a grid of superinsulated pipes. Due to its high specific energy density and low viscosity pipes with relatively small pipe dimensions are adequate. For example, a pipe diameter of less than 20 mm is sufficient to convey an energy flux of 10 MW over a distance of 10 km (based on lower heating value - LHV - of the hydrogen). Such pipes can principally be coiled. Being equipped with an appropriate superinsulation, the pipes could be laid like conventional underground cables (see figure 2). Ideally, the insulation material and handling should be adapted to cable manufacturing processes to allow for integration of other functionalities like power and data cables or optionally for a liquid nitrogen (LN2) heat shield (see figure 3).

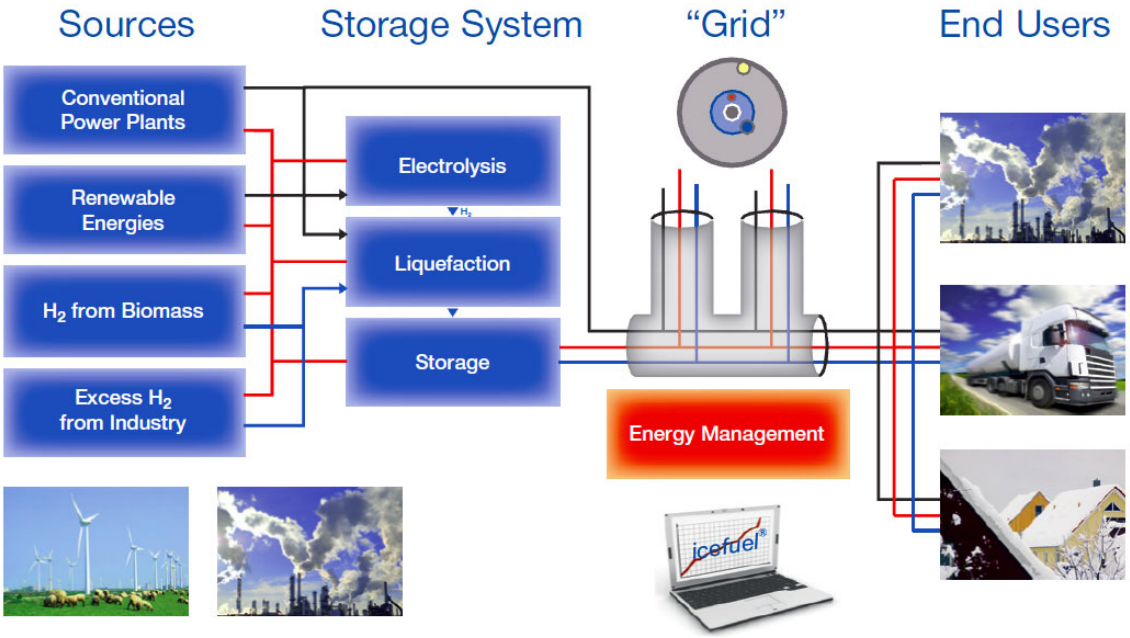

Figure 1: *icefuel*® schematic.

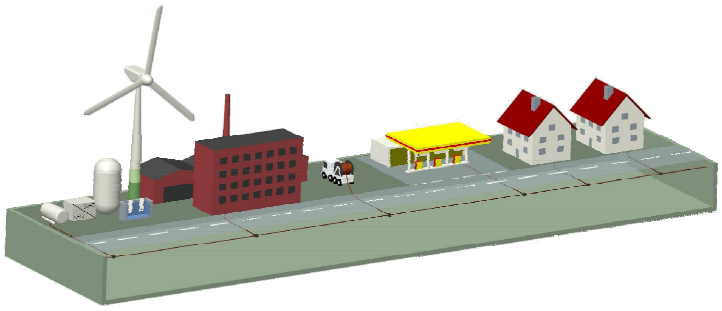

Figure 2: Vision for *icefuel*® cable laying.

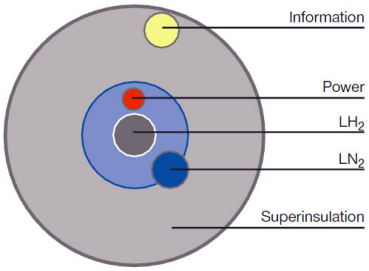

Figure 3: Example schematic for an *icefuel*® cable.

The electric efficiency of hydrogen based storage technologies (i.e. electricity via hydrogen back to electricity) is in general quite low (< 40 %). Conveying hydrogen to stationary end users enables combined heat and power production, thus, increasing the overall energetic efficiency significantly. Nevertheless, such an infrastructure concept should be combined with appropriate storage technologies covering short term charge and discharge needs. *icefuel*® is open for such a combination with other storage technologies.

3 Development project: Objectives, partners and achievements

In July 2006 a development project, funded by the Federal Ministry of Education and Research (Germany), was started. The objective was to gather fundamental and experimentally proven data about the technical feasibility of the *icefuel*® system. Since the cable is the key element in that infrastructure, the project focused on the cable design, manufacturing and testing as well as safety considerations regarding the transport of LH2 in

cables. Due to the relatively small pipe dimensions, micro system technology concepts were included to provide solutions for heat exchangers, sensors and actuators.

The following partners were involved in the development project:

- DLR (German Aerospace Institute, Cologne)
- Evonik Degussa GmbH (Hanau)
- EWE AG (Oldenburg)
- IMM (Institute for Micro Technology, Mainz)
- KIT (Karlsruhe Institute of Technology, Karlsruhe); Institute for Micro Process Engineering (IMVT)
- KIT (Karlsruhe Institute of Technology, Karlsruhe); Institute for Nuclear and Energy Technologies (IKET)
- LEONI AG (Nuremberg)
- MMT (Engineering Office, Alzenau)
- TUEV SUED Industry Service GmbH (Munich)
- ZAE (Bavarian Centre for Applied Energy Research, Wuerzburg)

3.1 icefuel® cable

To allow for transport distances of up to 10 km the unavoidable heat fluxes into the pipe during operation with LH2 should be kept below 1 $W \cdot m^{-1}$. Compared to conventional district heating pipes this requires two orders of magnitude higher insulation performance. Thus, the major development challenge for the cable and its insulation material was to combine the excellent insulation properties with a continuous processability.

After a broad screening of materials, designs and processing technologies finally a concept was identified and successfully tested on various cable samples at lengths of tens of meters. The concept allows for continuous manufacture of mechanically flexible, endless-type pipes (see figure 4). Other functionalities have not yet been realized in the cable, but could be integrated quite easily.

Figure 4: ***icefuel*® cable sample (outer diameter: ca. 40 mm; max. transport capacity: 100 – 200 kW_{LHV}; LEONI, Nuremberg).**

3.2 Infrastructure components

Micro structured heat exchangers (characteristic channel dimensions: 200 to 400 µm) generally exhibit several potential advantages for heat transfer applications with and without phase changes and especially in the context of the *icefuel*® infrastructure. First, heat transfer is very efficient which is of particular interest at low temperature gradients and very low temperatures (such as for LH2). Secondly, the hydrogen hold-up of micro heat exchangers is very low increasing the control dynamics as well as reducing potential hazards from leakages. A special challenge in the design results from the extreme physical properties of hydrogen (especially viscosity and interfacial tension) in the cryogenic state. Figure 5 shows various Micro Heat Exchangers that were developed and successfully tested on processing of hydrogen at different temperatures.

Figure 5: Various micro heat exchangers being developed for cooling, heating or other processing of hydrogen (IMVT, Karlsruhe).

Since LH2 has a specific exergy of more than 10.000 $kJ \cdot kg^{-1}$ recovering at least some of that potential technically would be worthwhile to improve energetic efficiencies as well as system economics. Different technical alternatives for exergy recovery were investigated and identified, such as liquefaction of nitrogen which could be used as a cooling shield (see figure 3). Another way is to implement thermoelectric generators into heat exchangers designed for the LH2 heat up prior to its utilization. So far, only few thermoelectrically active materials have been investigated for cryogenic applications. Figure 6 shows a micro structured heat exchanger equipped with a thermoelectric generator on the laboratory scale. The working principle has been tested and demonstrated successfully using liquefied nitrogen (-196 °C).

Figure 6: Lab scale micro heat exchanger equipped with a thermoelectric generator (DLR, Cologne and IMVT, Karlsruhe).

3.3 Miniplant

A miniplant has been designed and erected at the Institute of Micro Technology in Mainz (see figure 7). The objective is to test components that have been developed during the project, especially cable samples, on the technical scale and to provide scalable data for later field tests. Overall, four cable samples were successfully tested. Hydrogen throughputs (calculated as energy flows) are in the range of up to 30 kW_{LHV}.

The tests confirmed insulation performance results previously determined at the Bavarian Centre for Applied Energy Research (Wuerzburg) on the lab scale. Thus, specific heat inputs into the cable samples could be kept at ca. 1 $W \cdot m^{-1}$ during operation with LH2.

Figure 7: *icefuel*® miniplant at IMM (Mainz).

3.4 Safety assessment

Safety related consequences of cryogenic hydrogen releases from *icefuel*® cables were investigated both theoretically and experimentally in depth. The work focused on unconfined sonic hydrogen jets from small breaks without and with early ignition at different temperatures down to 30 K (see for example figure 8).

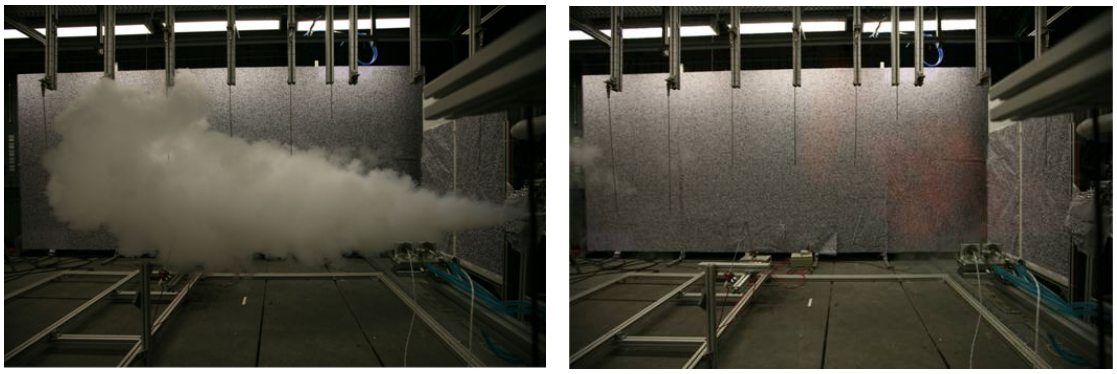

Figure 8: Pictures from cryogenic hydrogen releases before (left) and after (right) ignition (IKET, Karlsruhe).

Thermal loads, pressures as well as sound levels have been investigated for different parameters and compared to known limits for humans. All mechanical loads observed were uncritical. Investigation of thermal loads didn't show higher risk potential than for other energy carriers (e.g. natural gas, gaseous hydrogen). Overall, applying adequate technical and administrative safety measures would enable the safe operation of an *icefuel*® infrastructure.

3.5 Regulations, codes and standards

The TUEV SUED Industry Service (Munich) assessed different ways for approval of an *icefuel*® infrastructure. Currently, none of the existing regulations would be directly applicable. Based on the results in the safety investigations at IKET a newly to be defined regulation under the roof of the German Energy Industry Act is considered to be most promising. However, for the purpose of field tests, which are planned for a next development phase, existing regulations would still be applicable.

3.6 System economics

Assessment of the overall system economics at the current state of development is difficult since many system components (e.g. electrolysis, liquefaction, fuel cells) are still far from being technically and/or economically optimized. However, some qualitative statements can be made. As mentioned at the beginning, hydrogen is likely to play a major role in future energy infrastructures with high shares of renewable power despite the relatively low electric efficiency of the storage process. The questions will be how to store hydrogen and – in case of stationary utilization – how/where to reconvert it to electricity. The higher the amounts of energy to be stored (or: the longer the periods of time with excess or shortfall of renewable energy) the more attractive the storage of hydrogen as LH2 will be. Decentral utilization of hydrogen makes it easier to realize combined heat and power production. The worth of the co-generated heat depends on the alternatives for heat generation. Finally, several additional optimization potentials in an *icefuel*® system could be realized such as integration of superconducting wires into the *icefuel*® cable or utilization of the cold form the LH2 at the point of use.

4 Outlook

Based on the successful developments the project partners currently assess different alternatives for testing the *icefuel*® system on the field scale. Development activities in that context will include further hardware components such as junctions, sensors and actuators.

Acknowledgment

The scientific investigations and developments of this work have been carried out within the publicly funded research project *icefuel*® (BMBF, Bonn, FKZ 16SV2357). The authors would like to thank the German Federal Ministry of Education and Research for the support. More information: www.icefuel.eu.

References

[1] Energiespeicher in Stromversorgungssystemen mit hohem Anteil erneuerbarer Energieträger - Bedeutung, Stand der Technik, Handlungsbedarf, VDE-Studie, Dezember 2008

[2] C. Hoffmann, Design of transport and storage capacities for a future European power supply system with a high share of renewable energies, 3rd International Renewable Energy Storage Conference (IRES 2008, Berlin)

[3] H. Landinger, F. Crotogino, Large-scale underground storage of hydrogen, 3rd International Renewable Energy Storage Conference (IRES 2008, Berlin)

[4] A. Eté, Ø. Ulleberg, The Utsira wind/hydrogen demonstration system in Norway: Analysis and optimization using system modeling tools, European Wind Energy Conference and Exhibition 2008 (EWEC 2009, Marseille)

[5] D. Aklil-D'Halluin, E. Johnson, R. Gazey, B. Collard, V. Ortisi, C. Urso, M. Cherif Latreche, The PURE® project – An autonomous, hybrid and distributed wind hydrogen system for islands, European Wind Energy Conference and Exhibition 2008 (EWEC 2009, Marseille)

Enabling the Hydrogen Infrastructure – Waste Hydrogen Utilization in North Rhine-Westphalia

Boris Jermer, **Carsten Krause**, HyCologne – Hydrogen Region Rhineland, Germany

In the Rhine-Area around Cologne and other parts of NRW, big resources of hydrogen as a by-product from the chemical industry are being produced and not fully utilized [1]. A study conducted by Wuppertal Institute and Research Centre Jülich [2] focussed on assessing likely trajectories of emerging energetic demand for hydrogen in NRW, analysing the current availability of hydrogen from industrial sources, taking stock of exiting infrastructure for distribution of hydrogen and quantifying existing option for setting up a hydrogen infrastructure based on the current situation in NRW. The results of this study, which was conducted in early 2008, has shown that hydrogen which is produced in refineries or during chlorine production is commonly used in four ways: (1) chemically [fed into other chemical processes], (2) thermally [to create heat and steam], (3) sold externally [to gas industry] and (4) vented off [overcapacity which can not be used through (1,2 or 3)]. Hydrogen which is potentially available for applications can be estimated at 350M Nm3 per year. The biggest share (85%) comes from chlorine productions and offers thus a high quality (99% purity) and needs only little treatment for end users.

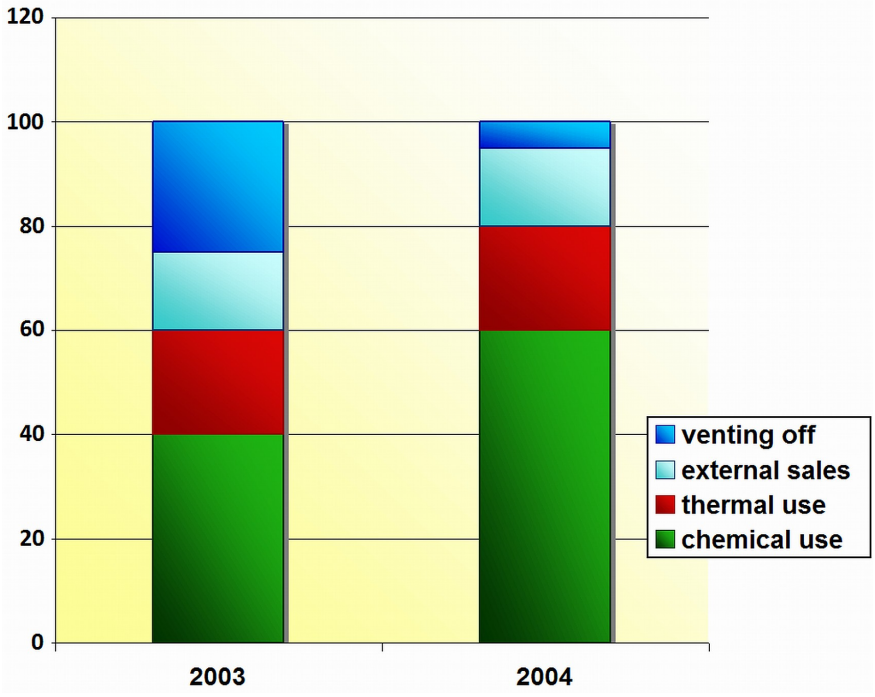

Figure 1: Example of Estimating the Availability of Hydrogen at a Chemicals Plant in NRW.

1 Available Hydrogen Sources

Hydrogen can be produced in various ways and easily be stored. In the near future the main focus will be on the production of hydrogen from renewable energy sources, but today already huge amounts of the valuable gas occur as a side-product in chemical production processes. German and international (GermanHy [3], Roads2HyCom [4]) studies show evidence that these hydrogen amounts could be made available for use in traffic & transport applications at short notice.

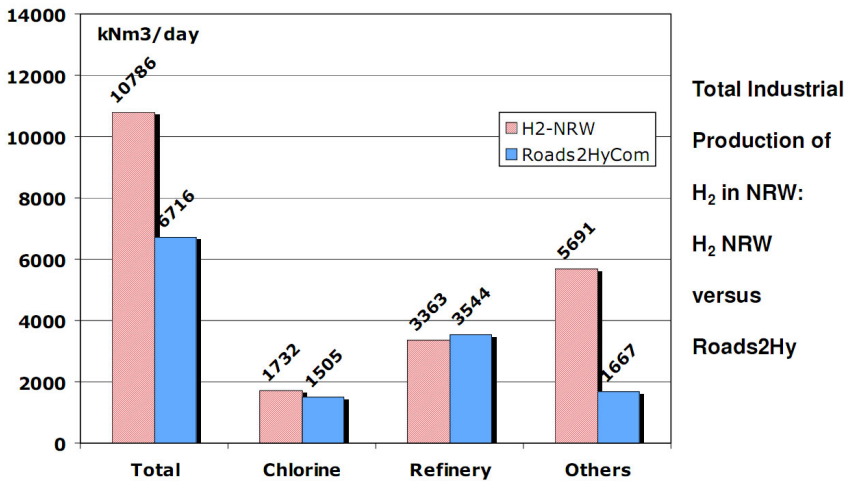

Figure 2: Total industrial Production of hydrogen – H2NRW versus Roads2Hy.

Roads2HyCom shows that German centres of activity are - among others - the Rhine-Ruhr region in Northern-Rhine-Westphalia. To keep cost for an initial infrastructure low, the existing hydrogen production could be utilized to demonstrate sustainability and provide a basis for a larger transition in the energy system.

To give a more specific example the situation in the Cologne region should illustrate the existing potential: alone in the Cologne are 6,7 billion Nm3 of hydrogen are being produced per year. Despite the fact that big parts of this hydrogen is used by various customers a share of 203.000 Nm3 per day [~18 tons H_2 per day] has been classified “available” by the producers of hydrogen [5] Available hydrogen was defined as volumes which were vented off or used for thermal applications und thus could be replaced by natural gas. The availably amount equals the energy needed to power 56.000 passenger cars (12.000 km/a, 3,5 l gasoline [eq] or 120 MJ per 100 km) or 1010 hydrogen busses (55km per year, 4kWh H2 per km or 12KG H2 per 100km). As there are approximately 1000 diesel busses being operated in the Cologne area the latter findings show clearly that (based on the available energy amount) the complete bus fleet could be replaced by hydrogen busses.

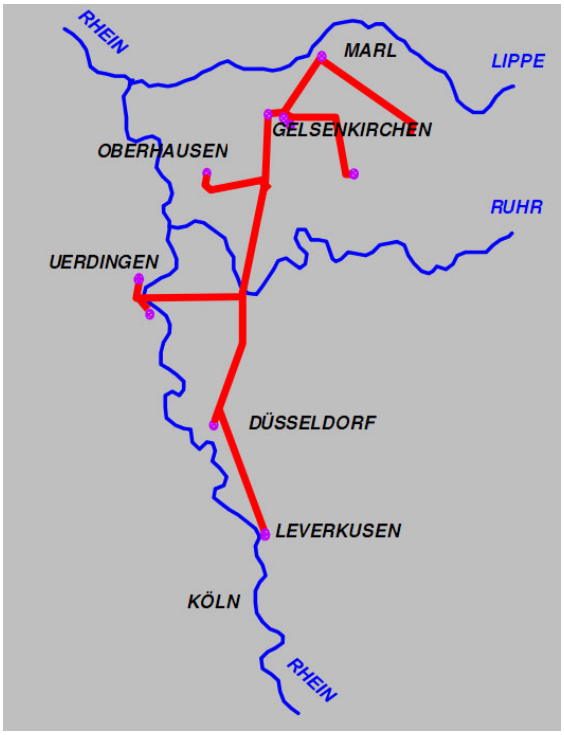

Figure 3: Pipeline-Network in NRW operated by AirLiquide.

Since 1998 the French gas company AirLiquide operates a hydrogen pipeline network in NRW which has a total length of 240 km and connects 14 production sites [6]. The total transmission capacity of the pipeline network is estimated at 250M Nm3 / year. This pipeline could be a complementary part allowing NRW to keep initial setup costs low. Depending on the level of political commitment and industry willingness the potentially available hydrogen is estimated to be sufficient for vehicle applications until 2020.

2 HyCologne as Local Network of Innovation

HyCologne focuses on using these resources and is building up a local network of innovation for hydrogen related technologies. Currently there are twenty partners organised in a cluster and two main projects initiated. Starting early 2010 HyCologne will establish a hydrogen bus fleet and built up a hydrogen powered fuel cell power plant in industrial size. Therefore a project has been set up to use the availably by-product hydrogen. The project called “Chemergy” will demonstrate clean energy solutions that make use of an existing but currently untapped source of hydrogen fuel – hydrogen emitted as the by-product of a sodium chlorate manufacturing plants. The purified hydrogen could be used to greatly reducing greenhouse gas emissions, local air pollutants, and the use of fossil fuels.

3 Utilizing Waste Hydrogen – The CHEMERGY Project

The demonstration project “Chemergy” will involve the operation of hydrogen hybrid busses and a number of fuelling stations. By making use of an existing by-product stream, the plant

significantly reduces the financial cost and energy required to provide 99.99% pure hydrogen.

The „Chemergy“ project has the purpose to open up the infrastructure of the chemical industry, which has so far been closed in, and to provide public access, so that hydrogen can be used as energy carrier. This constitutes a necessary condition to establish an optimal starting position for the commercially reasonable operation of hydrogen applications in the future.

The development of the infrastructure is clearly beneficial for the location’s and the region’s competitiveness. In parallel to the local activities the project partners examine how the findings of the Chemergy project can be transferred to other locations and how the potential resources of the industrial by-product hydrogen can be put to use in the region, in NRW and in Germany as a whole to ensure optimal results in efficiency.

References

[1] Maisonnier, G., Perrin, J., Steinberger-Wilckens, R., and Trümper, S.C. (2007) European Hydrogen Infrastructure Atlas and Industrial Excess Hydrogen Analysis, Oldenburg

[2] Pastowski, A. and Grube, Th. (2010) Scope and Perspectives of Industial Hydrogen Production and Infrastructure for Fuel Cell Vehicles in North Rhine-Westphalia, Energy Policy

[3] GermanHy, http://www.germanhy.de (accessed in March 2010)

[4] Roads2Hy, http://www.roads2hy.com (accessed in March 2010)

[5] Pastowski, A. and Grube, T. (2010)

[6] Barbier, F. (2010) Hydrogen Distribution Infrastructure for an Energy System,

Nippon Oil's Activities toward Realization of Hydrogen Society

Kojiro Nakagawa, **Junji Okazaki**, **Yoshihiro Kobori**, **Hideshi Iki**, NIPPON OIL CORPORATION, Japan

Abstract

Nippon Oil Corporation, a major Japanese energy distributor, has been devoting extensive efforts toward the establishment of hydrogen supply systems. The Council on Competitiveness-Nippon (COCN), an advisory organization which has influence on Japanese government policy, has announced that the establishment of hydrogen infrastructure should be started in 2015. By that time, we plan to have completed the development of necessary technologies for the infrastructure. It is well recognized that the storage and transportation of hydrogen is the sticking point on the path to realization of a hydrogen economy.

The scope of our research covers key technologies for hydrogen storage and transportation, including carbon fiber reinforced plastic (CFRP) tanks for compressed hydrogen gas, hydrogen storage materials, and hydrogen transportation systems which utilize organic chemical hydride (OCH). This article describes Nippon Oil's strategy for realization of the hydrogen economy.

Keywords: Hydrogen Infrastructure, Hydrogen Storage Materials, CFRP Tank, Organic Chemical Hydride

1 Hydrogen Infrastructure

The time has come to take action to curb global warming. A considerable number of studies have been conducted on ways to limit emissions of greenhouse gases such as carbon dioxide. In particular, it has been recognized that utilization of hydrogen as an energy carrier would improve the efficiency of fossil fuels and contribute to the fight against global warming.

It is very important for energy suppliers to make hydrogen available at reasonable cost at places convenient for the customer. However, at the first stage of a hydrogen economy, sales of hydrogen will not be enough to cover the huge investments required to construct new facilities, so utilization of existing facilities is highly recommended.

Experts have pointed out that oil refineries have considerable capacity for hydrogen production, and currently produce large amounts for use in hydrodesulfurization and other refining processes. However, the facilities are not always operated at full capacity, meaning that refineries have extra capacity to provide hydrogen to the market.

Having extra hydrogen production capacity on hand, oil companies have a clear incentive to study technologies for the transportation and storage of hydrogen, some of which will be mentioned below.

2 High Pressure Hydrogen Storage Tanks

Hydrogen gas has good energy density by weight, but poor energy density by volume when compared with hydrocarbon fuels. Hence, the hydrogen storage pressure in fuel cell vehicles (FCVs) must be set high enough for the vehicles to achieve a good cruising distance. A recent trend has emerged in which the pressure has doubled from 35 MPa to 70 MPa, which has enabled FCVs to drive more than 500 km on one hydrogen charge [1]. Therefore, with hydrogen station applications in mind, we have been developing a large-scale CFRP tank of 80 MPa, capable of hydrogen refilling an FCV equipped with a compressed hydrogen tank at 70MPa.

High-pressure tanks can be classified into four types (Table 1). The most commonly used are CFRP tanks such as the Type III and IV, because they offer many advantages such as high strength/stiffness-to-weight ratio.

Table 1: Types of tank.

Type	Composition
Type I	Metal tank
Type II	Metal liner with hoop lap layer of FRP
Type III	Metal liner with full lap layer of FRP
Type IV	Plastic liner with full lap layer of FRP

The filament winding (FW) fabrication process, which combines the Tow-Prepreg and liner-heating method [2-3], is a method we developed for manufacturing CFRP tanks (Figure 1). Tow-Prepreg is carbon fiber pre-impregnated with thermoset epoxy resin. It is easy to handle and has a long shelf life. One notable feature of Tow-Prepreg is its highly uniform resin content, so the FW method utilizing Tow-Prepreg makes it easy to manufacture tanks of consistent quality.

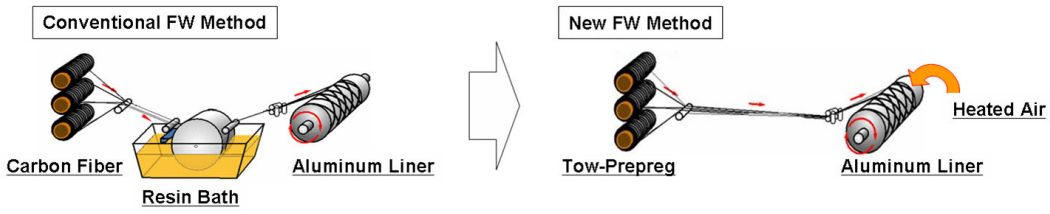

Figure 1: Filament winding fabrication processes.

Generally, the FW fabrication method requires that the dry fiber be passed through a resin bath to impregnate the fiber with resin. In the FW fabrication process utilizing Tow-Prepreg, however, the Tow-Prepreg can be directly wound over the liner. And when the liner-heating method is incorporated, the Tow-Prepreg can cure during the FW fabrication process.

In a cross-section observation of CFRP by optical microscope (Figure 2), we can see that CFRP made using the liner-heating method has fewer voids than that made using the

conventional method. This result indicates that the new liner-heating method can minimize the occurrence of voids, because the epoxy-resin effectively penetrates into the interfiber spaces.

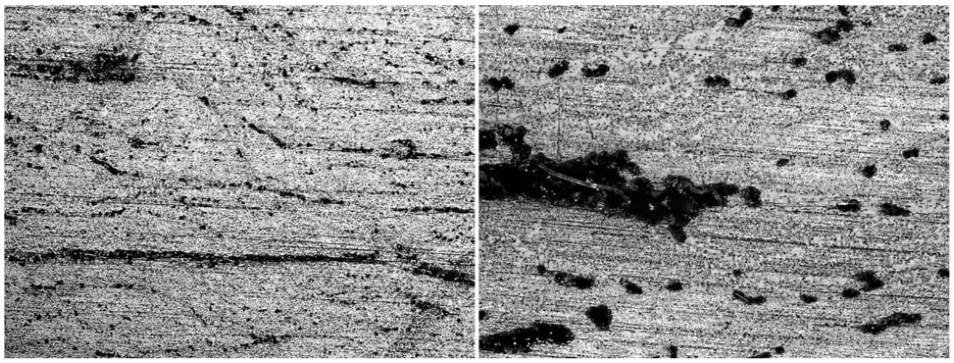

Figure 2: The Photographs of the cross-section observation of CFRP layer by optical microscope at 200-fold magnification. (Right; Conventional method, Left; Liner-heating method)

By using Tow-Prepreg combined with the liner-heating method, manufacturers could expect to achieve cost reductions, increased production efficiency and higher quality CFRP tanks.

3 Hydrogen Storage Materials

We have been developing hydrogen storage materials with the objective of increasing the amount of hydrogen that can be transported with hydrogen trailers. Our target value for hydrogen storage is 5 mass% at 35 MPa, and to achieve this target, we have been focusing on metal-organic frameworks (MOFs) due to their exceptionally high surface areas, high porosity, and chemically-tunable structures. MOFs have attracted much attention due to their potential for various applications, including gas storage materials [4]. For example, MOFs (**3**) can be obtained by synthesis of a combination of metal ions (**1**) and organic ligands (**2**) (Scheme 1).

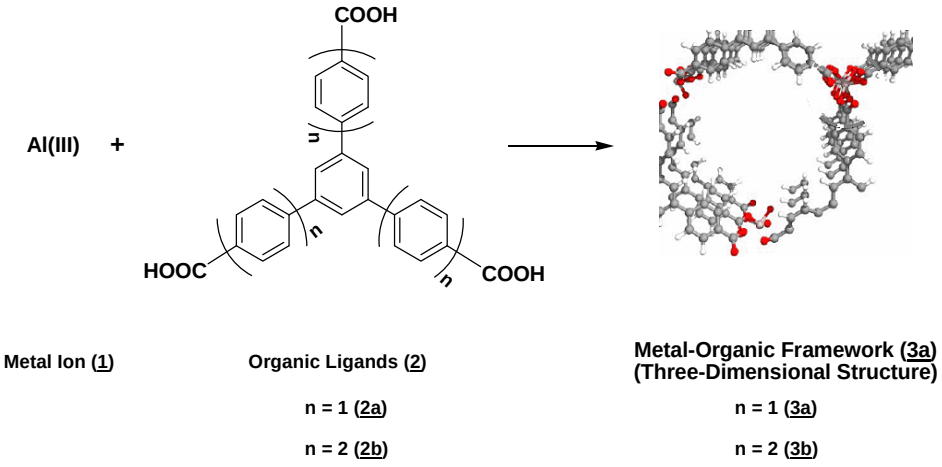

Figure 3: Synthesis of metal-organic frameworks having three-dimensional structure.

Our strategies for improving MOFs are to use light metal ions as the metal source and to enlarge the ligand size to attain a high porosity and large surface area. We were able to obtain an MOF (**3b**) which showed a hydrogen uptake of 0.94 mass% at 35 MPa, by reaction between light metal ions (**1**) and three-dimensional ligands with expanded branches (**2a**) [5].

4 Transporting Hydrogen Using Organic Chemical Hydride

The transportation of hydrogen energy as a liquid fuel is a promising option because it makes effective use of the existing network for liquid fuels. One method for transporting hydrogen energy as liquid fuel is the liquid organic chemical hydride (OCH) system [6]. The OCH system for hydrogen storage and transportation, based on a chemical reaction involving the dehydrogenation of cycloalkanes and hydrogenation of the corresponding aromatics (Scheme 2), is relatively well-established.

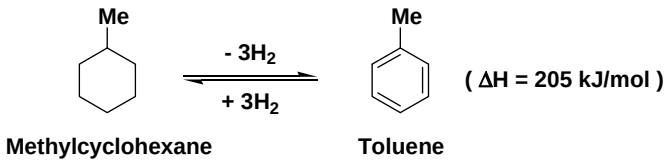

Figure 4: Organic chemical hydride system.

This system has advantages of high gravimetric and volumetric hydrogen density. We have been focusing on developing a compact hydrogen transportation system utilizing the OCH system. We have developed a concept for a hydrogen station which generates hydrogen by the OCH system. With the aim of downsizing the hydrogen feed system, we have developed a micro-channel reactor equipped with a plate-type dehydrogenation catalyst. The micro-channel reactor features a Pd-Ag membrane as the hydrogen separation membrane, which gives it the ability to generate high-purity hydrogen. A picture of the micro-channel reactor, which is a 4-layer design, is indicated in Figure 2. The micro-channel reactor can generate 2.5 L of hydrogen per minute.

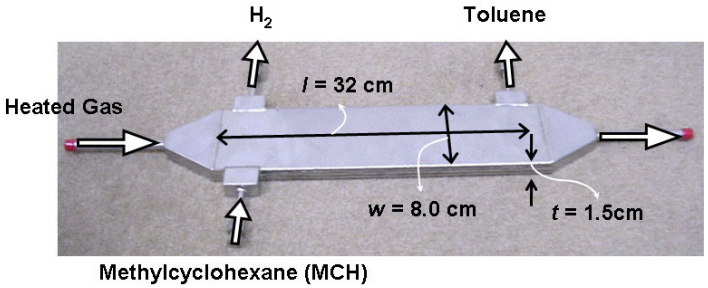

Figure 2: Picture of 4-layer micro-channel reactor.

5 Summary

As described above, we have been developing various technologies for the construction of hydrogen infrastructure, and are confident that our research will contribute to improving the hydrogen infrastructure.

Acknowledgements

This research was supported in part by funding from the New Energy and Industrial Technology Development Organization (NEDO) and the Japan Petroleum Energy Center (JPEC). We would like to thank Professor S. Kitagawa and Dr. M. Higuchi of Kyoto University for the synthesis of metal organic frameworks.

References

[1] Mori, D., and Hirose, K. *Int. J. Hydrogen Energy*, **2009**, *34*, 4569-4574.

[2] Onikura, H., and Sajima, T. *Annual report of the Faculty of Engineering, Kyushu University,* **2003**, 24-30.

[3] Onikura, H., and Sajima, T. *Annual report of the Faculty of Engineering, Kyushu University,* **2007**, 24-29.

[4] Antek, G., Wong-Foy, Matzger, A. J., and Yaghi, O. M. *J. Am. Chem. Soc.* **2009**, *28*, 3494-3495.

[5] Watanabe, D., Oshima, S., Kataoka, T., Kobori, Y., Higuchi, M., and Kitagawa, S. *Abstract. 89th CSJ Annual Meeting, Chiba, Japan,* **2009**, 2B7−47

[6] Okada, Y., Sasaki, E., Watanabe, E., Hyodo, S., and Nishijima, H. *Int. J. Hydrogen Energy*, **2006**, *31*, 1348-1356.

Chemical Hydrogen Compression by MH-NH_3 System

Takayuki Ichikawa, **Hiroki Miyaoka**, **Yoshitsugu Kojima**, Hiroshima University, Japan

In order to distribute hydrogen practically, the system of gravimetrically and volumetrically condensed hydrogen has to be developed, which should work under a moderate condition. As one of the candidates of the condensed hydrogen states, we have focused on ammonia (NH_3) because it has a high hydrogen (H_2) density of 18 mass% and is easily liquefied by compression of about 1 MPa at room temperature. Therefore, NH_3 is thought to be one of attractive hydrogen transport media. However, NH_3 is kinetically stable material because high temperature of more than 673 K is required to decompose NH_3 into nitrogen (N_2) and H_2. On the other hand, NH_3 can react with alkali metal hydrides (LiH, NaH and KH) even at room temperature by exothermic reaction, resulting that H_2 is generated. Moreover, the pressure of desorbed hydrogen from the reaction between MH and NH_3 can be increased up to at least 15 MPa because of those exothermic reactions. Here, we would like to propose the new hydrogen compression system by using MH-NH_3 reactions, which could be helpful for the hydrogen distribution.

To overcome the global challenge to the fossil-fuel depletion and the global warming, the energy sources should be distributed to the various kinds of primary energies, such as wind, photovoltaic, solar, geothermal and hydroelectric power generations. An attempt to convert from fossil-fuel to these renewable energies has been underway all over the world [1-5]. However, these fluctuating energy sources are not available anytime and anywhere. Therefore, a suitable energy storage system should be required to deal with the fluctuation and the maldistribution.

Although, the efficient battery system is quite useful and has been utilized in hybrid vehicle, laptop computer, mobile phone, etc., the energy densities of battery are too low to transport a large amount of energy. Consequently, hydrogen has been thought to be suitable energy carrier for a long distance transportation [6-11]. However, the hydrogen energy has a considerable problem to be transported, because the volumetric energy density of hydrogen is quite low whereas the gravimetric energy density of hydrogen is quite high. As shown in Figure 1, the volumetric densities of compressed hydrogen gas at 35 MPa and 70 MPa is only 2.8 and 4.7 kJ/cm^3, which are slightly low compared with liquefied hydrogen (8.4 kJ/cm^3 at 18 K) or compressed natural gas (8.8 kJ/cm^3 at 20 MPa). Although the liquefied or compressed natural gas has been circulated as a clean energy carrier in the world market, the natural gas should be primary and limited energy. Therefore, in order to establish the hydrogen based society, a suitable system to transport hydrogen as secondary energy should be required.

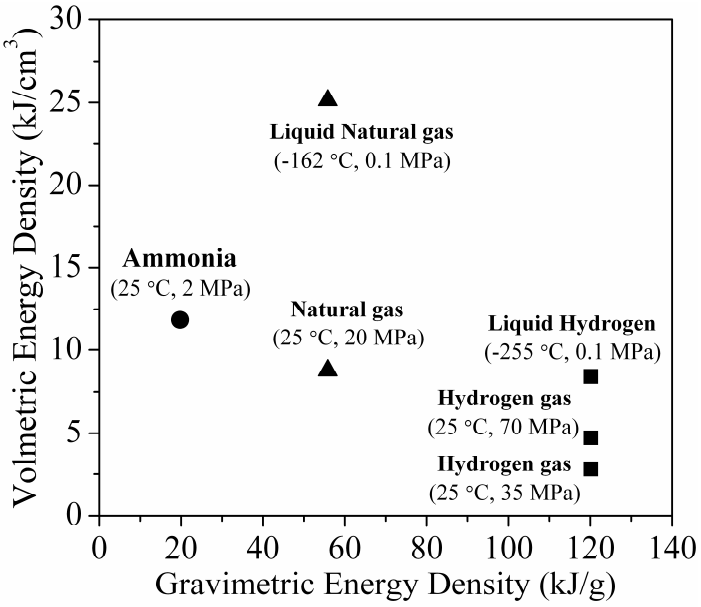

Figure 1: Comparison of various energy carriers in the volumetric viewpoint.

Recently, our group has reported on the efficient conversion from ammonia gas and metal hydride to hydrogen gas and metal amide at a room temperature [12, 13], in which ammonia can be regarded as a hydrogen carrier [14-16]. From the viewpoint as energy carrier, the volumetric energy density of ammonia is 12 kJ/cm^3 at 2 MPa at a room temperature, which is much larger than that of liquefied hydrogen as shown in Fig. 1. Therefore, we have investigated this system from various points of view. Actually, the combination of liquid ammonia and metal hydride MH could be regarded as an interesting hydrogen storage system by following reaction,

$$NH_3 + MH \leftrightarrow H_2 + MNH_2.$$

Since one mole of ammonia generates only one mole of hydrogen, we focus on the liquid state of ammonia as the original system, expecting that the generated hydrogen is high volumetric density. In this paper, we will demonstrate the chemical compression of hydrogen by means of the direct reaction between liquid ammonia and metal hydride.

In this work, commercial lithium hydride (LiH, 99.4 %, Alfa Aesar), sodium hydride (NaH, 95.0 %, Aldrich), and Ammonia NH_3 (99.999 %) were used. The properties of the liquid NH_3 and MH (LiH and NaH) systems were investigated by a following experimental procedure. Figure 2 shows an experimental system. A weighted amount of MH was packed into a reactor made by steel in a glove box (Miwa MFG, MP-P60W) filled with purified Ar gas (> 99.9999%) to avoid oxidation. The sample part of the reactor was soaked into liquid nitrogen after evacuation of the system. Then, gaseous NH_3 was introduced into the reactor, where NH_3 should be solidified in the sample part at -196 °C. Here, the molecular amount of NH_3 was adjusted in relatively lager than that of MH. After closing the VS valve, the reactor was pull out from liquid nitrogen. During an increase in temperature, inside pressure and temperature

were monitored by pressure gauge and thermocouple attached to outside of the reactor, respectively.

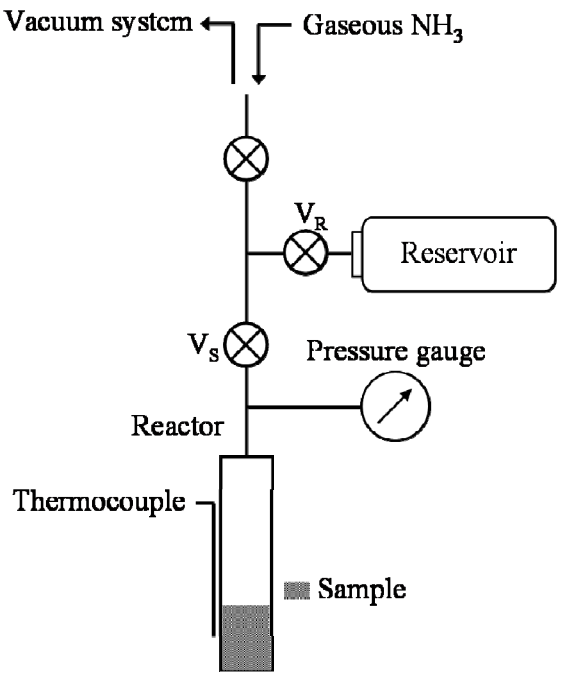

Figure 2: Experimental system.

Figure 3 shows variations of inside pressure and outside temperature of the reactor during the reaction between liquid NH_3 and LiH as a function of time. Here, since the thermocouple was attached to the outside of the reactor, the measuring temperature would be slightly different from the inside temperature. While the reactor was soaked into liquid nitrogen, the pressure was stable because the reaction between solid NH_3 and hydrides should be quite slow due to solid-solid reaction at such a low temperature. With the return of temperature to room temperature, inside pressure drastically increases. An NH_3 vapour pressure should also increase after melting. The pressure change observed during increasing temperature was compared with the variation of NH_3 vapour pressure referred from a database in NIST [17], to understand a starting temperature of the reaction. The results are shown in inset of Fig. 3. It was noteworthy that the increase in the pressure started at around -20 °C. In the case of LiH, the pressure was reached up to more than 12 MPa within 1 hour, assuming that a NH_3 vapour pressure at 25 °C is about 1 MPa [17]. Continuously, 20 MPa was obtained after 4 hours, and the maximum pressure was about 26 MPa after a month. This value was higher than the estimated maximum pressure at 25 °C, 23 MPa, obtained by the amount of liquid NH_3 (2.4 g), LiH (0.7 g), and a system volume (10 cc), which was discussed later. A similar phenomenon was confirmed for the reaction of liquid NH_3 with NaH by using the same experimental system, where the results were omitted in this paper. In this case, the pressure gain was saturated after reaching to about 12 MPa within 4 hours. This is because that the maximum pressure of this system was estimated to be about 13 MPa by a rough calculation at 25 °C from the amount of liquid NH_3 (2.4 g), NaH (1.3 g), and the system volume (10 cc).

Anyway, from these results, the reaction kinetics of NaH with liquid ammonia was thought to be much greater than LiH.

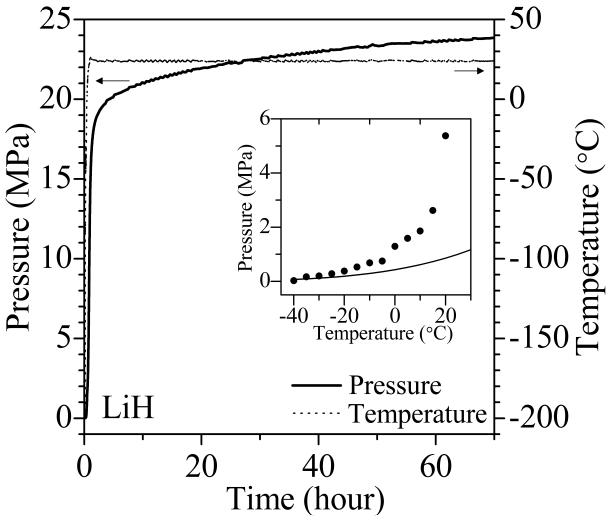

Figure 3: Variations of inside pressure and outside temperature of the reactor. Inset: Experimental pressure change and a vapour pressure of NH_3 in NIST.

In this work, we have demonstrated the production of compressed hydrogen via the direct reaction between liquid NH_3 and MH. Even below room temperature, the reaction started and more than 15 MPa of H_2 was generated within 1 hour. For the systems, the existence of NH_3 would be an essential problem for an application to a fuel cell. However, H_2 and NH_3 can be separated by using a suitable membrane. In addition, it had already clarified that metal amides as the reaction products was easily recycled back to hydrides below 300 °C under 0.5 MPa of H_2 flow condition [15], [16], [18]. Therefore, the reaction of NH_3 and MH would be a potential method as a chemical compressor of H_2 for practical use.

Acknowledgements

This work was partially supported by NEDO in Japan under “Advanced Fundamental Research Project on Hydrogen Storage Materials”.

References

[1] J.A. Turner, Science 285 (1999) 687-689.

[2] R.E.H. Sims, H.-H. Rogner and K. Gregory, Energy Policy 31 (2003) 1315-1326.

[3] D.L. Klass, Energy Policy 31 (2003) 353-367.

[4] H. Lund, Energy 32 (2007) 912-919.

[5] F.H. Sobrino, C. R. Monroy and J. L. H. Pérez, Renewable and Sustainable Energy Reviews 14 (2010) 772-780.

[6] L. Schlapbach and A. Züttel, Nature 414 (2001) 353-358.

[7] W. Grochala and P. P. Edwards, Chem. Rev. 104 (2004) 1283-1315.

[8] A. Züttel, Mitig. Adapt. Strat. Glob. Change 12 (2007) 343-365.

[9] M.B. Gorensek and C. W. Forsberg, Int. J. Hydrogen Energy 34 (2009) 4237-4242.

[10] I.P. Jain, Int. J. Hydrogen Energy 34 (2009) 7368-7378.

[11] J. Brouwer, Current Applied Physics 10 (2010) S9-S17.

[12] Y. Kojima, K. Tange, S. Hino, S. Isobe, M. Tsubota, K. Nakamura, M. Nakatake, H. Miyaoka, H. Yamamoto and T. Ichikawa, J. Mater. Res. 24 (2009) 2185-2190.

[13] H. Yamamoto, H. Miyaoka, S. Hino, H. Nakanishi, T. Ichikawa and Y. Kojima, Int. J. Hydrogen Energy 34 (2009) 9760-9764.

[14] W.H. Avery, Int. J. Hydrogen Energy 13 (1988) 761-773.

[15] T. Hejze, J. O. Besenhard, K. Kordesch, M. Cifrain and R. R. Aronsson, J. Power Sources 176 (2008) 490-493.

[16] M.R. Rahimpour and A. Asgari, Int. J. Hydrogen Energy 34 (2009) 5795-5802.

[17] NIST Chemistry WebBook. National Institute of Standards and Technology: http://webbook.nist.gov/chemistry/.

[18] S. Hino, N. Ogita, M. Udagawa, T. Ichikawa, Y. Kojima, J. Appl. Phys. 105 (2009): 023527.

Field Test of Hydrogen in the Natural Gas Grid

Henrik Iskov, Danish Gas Technology Centre A/S, Denmark
Mats Backman, Borealis AB, Denmark
Hans Peter Nielsen, FORCE Technology, Denmark

It has become ever clearer that the resource of natural gas is an energy source which will be less important in the future due to limitations in natural reserves. In order to prepare for the future the gas industry is looking at alternative gaseous fuels, one such fuel gas is hydrogen.

In order to prepare for a future use of hydrogen it became evident that very little information exists regarding the compatibility between long term exposure and transportation of hydrogen in steel gas transmission pipelines and polyethylene gas distribution pipelines. A program was therefore set to study the transportation in a small scale pilot grid at the field test facilities of the Danish Gas Technology Centre situated at the Scion-DTU research centre in Hörsholm, Denmark.

The test program included former used steel pipes from the Danish gas transmission grid and polymer pipes from the Danish and Swedish gas distribution grid.

The Project partners was Danish Gas Technology Centre, Borealis AB and FORCE Technology. Danish Gas Technology Center was project manager and responsible for operation of the field test. Borealis - one of the biggest suppliers of raw material from polyethylene for the production of pipes for e.g. pressure pipes for gas distribution - provided analytical services for the determination of compatibility problems between polyethylene pipes and hydrogen under long term exposure. FORCE Technology focused on dynamic testing and analysis of the steel pipes from the gas transmission grid.

1 Polymer Pipe Test and Analysis

A dominant part of the natural gas distribution grid consists today of polyethylene pipe due to its excellent track record as a reliable piping material with minimal maintenance. The reason for this is the inherent properties like its corrosion free nature, the possibility to create fully weldable systems, its high ductility and excellent low temperature properties.

The program was devised so that a part of the test grid was to be dug up each year and analyses were performed on the pipes. In this way any form of influence on the integrity of the polyethylene pipe would be detected. The pipes were analysed before exposure to hydrogen, then the pipes has been dug up after 1 year, 2 years, 3 years and 4 years of exposure. Some of the pipes have also previously been used in the Danish natural gas network. The oldest pipes have been subjected to natural gas for 20 years before exposure to H_2 in the pilot grid.

The analytical program was devised to detect any influence on the additivation of the polyethylene as this have an influence oxidative resistance. Furthermore the test pipes were analysed for possible degradation caused by extrusion of the material. The possible interaction between the antioxidant and hydrogen has been checked by the so called oxygen induction temperature (OIT), which shows the antioxidation effect of phenolic antioxidants.

The possible extrusion influence has been analysed by Fourier Transform Infrared analysis and a check of the carbonyl content on the inner surface of the pipes was performed.

Furthermore the study has focused on detecting possible changes in the structural composition the polyethylene. The materials for gas pipes are very high molecular weight materials, therefore rheology was chosen as this is very sensitive for changes in the high molecular weight part of the material. The rheology has been presented as a number of index, namely $\eta_{2,7\ KPa}$, $SHI_{2,7/210}$ and $\eta_{747\ Pa}$ this gives an indication of the molecular weight, the molecular weight distribution and the high molecular weight tail. The rheological analysis has been performed on an Anton Paar, Physica MCR350, in a plate/plate set up at 190 degree C. Also, Melt flow rate (MFR) and flow rate ratio (FRR) has been utilised to further detect any structural changes. The MFR analysis has been performed according to ISO 1133.

To complete the analysis the most important mechanical properties has been checked, in order to further strengthen that the analysis of the antioxidant interaction and the possible interaction to the polymer structure has been able to pick up any changes. The most important mechanical properties have been defined as: Tensile test, elongation at break, tensile modulus and slow crack growth, measured in the CTL test. Especially if changes takes place in the slow crack growth properties of the material this would be very negative as in practise the resistance to slow crack growth determines the potential life length of the pipe line system. The tensile tests and modulus has been performed according to ISO 527-2/1B and the CTL analysis has been performed according to ISO 6252-1992 fitted with a notch according to ASTM F 1473 at 60 degree C in a 10 % Igepal 720 water solution.

In this investigation two different classes of polyethylene pipes and materials have been studied, namely PE80 medium density polyethylene (MDPE) gas pipes and PE100 high density polyethylene (HDPE) gas pipes. The MDPE gas pipes have different manufacturing dates. Some of the PE80 gas pipes were manufactured in 1982. The PE100 gas pipes consist of two different pipes and materials. One pipe/pipe material is an orange single wall pipe, while the other was a two layer pipe with a natural coloured main inner pipe and a thin orange outer protective layer. The purpose of the outer layer is to provide a UV protective layer, an easy peelable layer before welding and protect the inner layer from outer damage. Also in the case of the PE100 gas pipes different manufacturing dates are present. The oldest pipe is from 2001.

Summary of the results:

In all of the pipes sampled from each of the years (no exposure, 1 year, 2 years, 3 years and 4 years) that has been analysed no surface oxidation has been found. This means that all pipes have been extruded according to industry praxis and no pre-damage has taken place.

The study of the antioxidant shows no indication of a deterioration of the stabilisation. This means that in the oxygen induction time (OIT) measurements at two temperatures we have not found any significant changes over the four years of exposure compared to a non-exposed material. The OIT values remains at a similar value throughout the 4 year test period within the accuracy of the measurement. Typical results after 1 - 4 years of exposure is approximately 22 min at 210 C and 50 min at 200 C for the PE80 samples and approximately 60 min at 210 C and 160 min at 200 C for the PE100 samples. The standard

demand in EN1555, the PE gas pipe standard, is 20 min at 200 C which is also clearly surpassed by both the PE80 and PE100 material. The interpretation is that there is no interaction between the hydrogen and antioxidants or hydrogen and material over the investigated period. The results are valid for both the PE80 and the PE100 pipes.

The structure analysis also indicates that there is no interaction between hydrogen and the Polymer. Neither in the MFR/FRR analysis nor the rheological analysis is revealing any interaction between the polymer and the transported media, hydrogen. The structure of the polymer is intact according to the analysis made after four years of exposure. This is valid for both the PE80 and the PE100 pipe materials.

The mechanical analysis shows the same. The tensile tests, elongation at break and the elastic modulus as well as the slow crack growth show that no deterioration occurred due to the exposure to pressurised hydrogen during the four years of exposure.

In summary, according to the tests performed in this study, we have found strong indications that polyethylene gas pipes PE80 and PE100 can be used for transportation of hydrogen without any adverse long-term effects on antioxidants, polymer structure or the mechanical performance of the polymer pipes. The same indications have been found for both new and old pipes that has been used in the Danish natural gas distribution network for more than 20 years.

An additional remark: The gas distribution network consists of many other components and connections. The above conclusion only applies to the tested types of pipe material. Before introduction of hydrogen in the natural gas network all components and connections must be investigated.

2 Steel Gas Transmission Pipeline Test and Analysis

The object of the steel pipe test was to see the effect on fatigue life of existing natural gas transmission lines with hydrogen gas being added to natural gas. The test and analysis focused on the effect of hydrogen on fatigue cracking in pipeline girth welds.

Full scale tests was performed using cut-out API 5L X70 pipe sections 20 inch diameter by 7 mm WT from the Danish natural gas transmission system. The pipe sections contained field girth weld made during the installation of the pipe line in eighties.

The internal test environment consisted of 100% hydrogen gas at fluctuating pressures representing the daily peak to peak variation in the gas transmission line. The maximum pressure was 70 barg and the maximum pressure amplitude used was 30 bar.

2 test series were conducted with increasing pressure amplitude from 20 barg to 30 barg.

The pressure cycle variation frequency was less than 0,0017 Hz. and each test serie was run for 15.000 or 30.000 cycles. 15.000 cycles corresponds to 40 years operation with one pressure cycle per day.

The girth welds were checked prior to test and again after the completed test cycle by ultrasonic examination. If no cracks were observed the test specimen continued in test for the next period.

Test series 1 was completed in 2008 and test series 2 was completed in 2009.

The girth welds has been dissected and subjected to metallographic examination in addition to the ultrasonic testing in order to describe possible defects and defect growth in the weld zones. The dynamic testing equivalent of 80 years with two times the maximal pressure variations found in the danish gas transmissionssystem (that is 2 x 15 bar equal to 40 to 70 bar for 30000 cycles) has shown no defect growth.

References

[1] Andersen, Paw, Celia Juhl, Lars Bo Pedersen, Asger N. Myken, Henrik Iskov: Hydrogen as an energy carrier. (In Danish with English summary only). Dansk Gasteknisk Center a/s. 1999. ISBN 87-7795-172-7.

[2] Iskov, Henrik: The suitability of the gas grid for distribution of pure hydrogen. (In Danish with English summary only). Dansk Gasteknisk Center a/s. 2004. ISBN 87-7795-253-7.

[3] Jensen, Jan K. and Iskov, Henrik: Field Test of Hydrogen in the Natural Gas Grid. World Gas Conference. 2006.

Advances in Hydrogen Refuelling Stations

Jonathan Macron, **Loic Damongeot**, **Françoise Barbier**, Air Liquide R&D, France
Thomas Charbonneau, Air Liquide Canada

Hydrogen-powered vehicles represent a promising solution to reduce overall green house gas emissions and ensure sustainable mobility.

Car manufacturers are developing prototypes with improved performances, more reliability and autonomy proving the viability of advanced technology vehicles. In parallel, the hydrogen infrastructure has to evolve to meet real-world demands and provide the required filling stations network that will enable the users to refill their cars, buses or scooters …

Air Liquide is a global leader in hydrogen fuelling and infrastructure. It has manufactured and installed more than 40 hydrogen fuelling stations in different countries, working jointly with leading vehicles manufacturers in order to design and build the future generation of filling stations.

Figure 1

These advanced stations should be able to perform fast filling on any type of vehicle.

As of today, temperature increase during filling has been causing many concerns and has prevented “blind” filling like what is performed with gasoline stations.

This paper presents innovative solutions developed by Air Liquide group to solve this issue and also to perform filling without communication, hence simplifying a lot the process. Combining modeling and advanced process control, these solutions enable to match the customer's requirements and specifications while ensuring quality and safety in the filling process. The path is now opened to moving from prototypes to industrialization.

The first step consists in implementing a control strategy to transfer hydrogen within vehicle tank taking into account the constraints given by the customer. Control scheme should enable to keep the temperature of the hydrogen inside the vehicle tank under maximum safety level while optimizing the refuelling time.

The control strategy has been built on the basis of dynamic simulations of a standard hydrogen station under Matlab/Simulink. A critical device to characterize was the actuator: at

such level of pressure (above 800 bars), linear behaviour of the actuator is no longer guaranteed hence impacting highly the dynamical efficiency of the control scheme.

The specified advanced control scheme enabled Air Liquide to perform fast filling on high pressure hydrogen-powered vehicles while maximizing the transferred mass and keeping the whole system safe. This solution has been industrialized and validated on several fuelling stations manufactured by Air Liquide (Figure 2).

The second and highly innovative step aims at defining adaptive control schemes for fast filling procedures. This means that control strategy should be used to refill any type of vehicle, with different tank volumes.

The final objective is to perform a filling in the most optimal way, as follows:

- Maximize the mass of product transferred within the tank
- Operate safely in regards to temperature variations
- Perform filling without communication with the vehicle (no information on type, tank volume and level)
- Operate a filling as fast as possible

Figure 2: Air Liquide hydrogen station.

To achieve this goal, a filling procedure coupled to a real-time soft–sensor has been designed and validated under simulation to estimate the temperature during a filling of the vehicle tank, after having estimated its volume and the remaining hydrogen quantity when the vehicle connects to the station.

To do so, the filling procedure starts with pulses of hydrogen being transferred into the vehicle tank.

Thermophysical assumptions, based on modelling of the tank and the station, lead to the estimation of the volume of the tank.

Based on the estimated parameters and constants, an advanced control scheme has been designed to perform the filling in regards to pre-described requirements.

This advanced control strategy is scheduled to be tested on pilot stations within the coming months.

References

[1] Yang Jiann, “A thermodynamic analysis of refueling of a hydrogen tank”, International Journal of Hydrogen, Issue 34 (2009), page 6712 to 6721

[2] Daney DE & al, “Hydrogen vehicle fueling station”, Advances in cryogenic Engineering, Issue 41 (1996), 1041-8

[3] Kountz Kenneth, “Modeling the fast fill process in Natural Gas vehicle storage cylinders”, American Chemical Society paper, 207th National Meeting (1994)

[4] Maus J & al, “Filling procedure for vehicles with compressed hydrogen tanks”, International Journal of Hydrogen, Issue 33 (2008), page 4612 to 4621

[5] NASA Glenn research center, “Chapter 6 – Hydrogen”, Revision of 2003

Air Liquide Roadmap for Hydrogen Energy

Eric Prades, Air Liquide, France

1 Context

Climate change, pollution, reliance on fossil energies, surging energy demand have become critical global challenges today. The energy industry is undergoing a complete transformation, and while it is essential to ensure our energy supply, it is also of the utmost importance that the new production methods are able to limit the impact of their usage on our environment. In the frame of those global challenges, hydrogen can play a key role in the development of new energy alternatives.

As a carrier that is compatible with other types of energies, it can be produced from a wide variety of sources including renewable, while presenting unique storage options and, combined to a fuel cell, efficiently produces electricity with zero direct pollution.

The presentation will illustrate how Air Liquide envisages and contributes to the raise of this new Hydrogen Energy economy.

2 Air Liquide and Hydrogen today

2.1 A challenge for committed players

New energies cannot appear without great investments, as the markets they are aiming do not exist yet. Thus, only experimented players have the expertise, the knowledge and the capacity to impulse the technologies and infrastructures needed. Air Liquide is the world leader in gases for industry, health and the environment, and is present in over 75 countries with 42,300 employees. For almost 50 years, Air Liquide has built up considerable credibility in the hydrogen field and has put every measure in place to ensure the reliability and efficiency of its equipment. In 2008, the 200 plants of the Group produced 7 billions Nm3 of hydrogen for 1.2 billion € sales for industrial applications. The Group's global hydrogen network encompasses R&D innovation, engineering development, gas production, product transport and distribution, and customer service and maintenance, covering the whole chain of application from generation to demanding end users. On this basis, the group has built a strong expertise from which it can transfer its skills and know-how to emerging markets.

3 Air Liquide and the New Economy of Hydrogen Energy

3.1 Our vision

For Air Liquide, a new sustainable economy policy requires a larger strategic approach of the environment. The Group decided to build his strategy to drive and inspire every activity in the business lines on 5 growth drivers, of which Energy & Environment:

"Our activities lie at the heart of the most important challenges facing the planet. To meet those challenges, Air Liquide develops innovative technologies and sustainable solutions,

optimizing the use of air and the planet's natural resources, enabling progress and preserving life".

When applied to our day-to-day environment, these principles naturally go along with sustainable mobility. Therefore, with the substantial progress that has been achieved in hydrogen energy technologies these past five years and, thanks to the different players in the industry including Air Liquide, financial investment decisions and technical breakthrough should allow for hydrogen vehicles to be ready for the commercialization on the market by 2015.

3.2 Innovation, starting from an existing basis

However, getting more companies to cooperate, public funding to be budgeted and technologies to reach performance and targeted costs might not be easy. If creating breakthrough technologies is a key factor to prepare the energy consumption transformation [1], it can only be done within the expected time span with a solid industrial basis. That's the reason why Air Liquide decided to increase innovations on H2 plants energy efficiency, CapEx reduction, CO_2 mitigation and H_2 transport for a global investment in 2008 of almost 300 millions €. More than 40 hydrogen filling stations are now operated around the world including the largest one in Vancouver – BC – Canada.

Moreover, preparing the new energy markets requires to design a completely new supply chain from production to end-user distribution. Transfers of knowledge and know-how from existing industry may speed up greatly the transition to a sustainable energy. As a consequence, Air Liquide has been underpinned for several years by the teams of R&D Corporate and Advanced Technologies, as well as some subsidiaries of the Group, such as Canada, together with Axane, its wholly-owned subsidiary founded in 2001 that develop and manufacture PEM Fuel Cells. Due to this specific context, Air Liquide enjoys a unique position among gas producers, and will build on this basis to better understand and anticipate hydrogen energy markets and user's expectations and offer equipment or service solutions.

4 The Foreseen Potentials of the New Hydrogen Energy Markets

As a rule of common sense, estimations of potential growths do pilot the investments decisions. In addition, if environment preservation is the goal for our society, the economic viability of a new energy is the key for its development. As early as today, several hydrogen energy markets are already accessible, thus justifying the name of "early markets". On the other hand, the mass transport market considered today as the most promising one and for which the Fuel Cell Vehicle (FCVs) brings a solution is deploying first infrastructural and social prerequisites to create the conditions of its success.

4.1 Early markets

An early market grants almost immediate access to the player who enters it. Consequently, not only for technology replacement but also for new utilizations, the hydrogen energy encompasses at the same time the possibility to promote economic growth and to improve its new technologies in real-life conditions. Finally yet importantly, such deployments are the initiation of further cost reductions by series effect.

When combined to a fuel cell, hydrogen efficiently and silently produces electricity with zero direct pollution. Air Liquide believes in fuel cell applications within four distinct early markets selected for their potential:

- Specialty vehicles: already an important market in terms hydrogen volume, hydrogen specialty vehicles and captive fleets can grant significant productivity gain to customers. Hydrogen forklift deployment in the US have already capture 4% market share of electric truck fleet in the US
- Off-grid sites: Supplying energy to isolated off-grid sites is the next biggest early markets. Hydrogen offer autonomy and preserve the environment at the point of use
- Back-up power: This market presents also a big potential, mainly conditioned by reliability and safety.
- Mobile energy: High visibility with applications amongst cinema, special events, rescue & safety and architecture design is typical for this market.

All the early markets also hold the advantage of enabling the transition towards and opening the way for future applications such as in transport. When the new mass transport market is mature enough, they will be able to follow their own way, accompanying the developments of hydrogen technology.

4.2 Mass transport market

Today, transport vehicle technology has reached its maturity. The internal combustion engine technology, known for years, shows limitations for further development.

It is penalized by low energy efficiency and only marginal improvements can be expected. On the basis of equal power supply, its consumption and therefore its emissions can only be reduced to a certain extent. Faced with demands for energy efficiency and lower emissions, car manufacturers are proposing new wheel drive alternatives, such as electric and hydrogen vehicles. Not only do higher energy yield electric engines power them both [2], but they also eliminate the need for oil-based liquid fuels since they rely on new energy carriers: electricity and hydrogen.

By using hydrogen in transport applications, greenhouse gas emissions will be reduced and city pollution levels, including noise, will be lowered.

FCVs have developed significantly over the last 5 years and several car manufacturers anticipate strongly that from 2015 onwards a quite significant number of them could be produced. This number justifies the efforts and investments needed and opens new playgrounds for technology developers. Such complex and massive market cannot be approached without a convergence of the industry players.

Moreover, to deal efficiently with the sustainable transport stakes, the hydrogen industry needs to:

- foresee the roadmap to achieve a complete “green” supply-chain [3],
- validate its technological advances in real-life conditions,
- convince society of the value of the technological innovations (social acceptance [4]),
- implement regulations and codes for daily use,
- and create an infrastructure base on which future fleets of hydrogen vehicles can rely.

The presentation will explain further how to answer those concerns within the partnerships.

5 On the Path to the New Hydrogen Energy Economy

5.1 Hydrogen biggest challenges can't be overcome alone

On the path to the new Hydrogen Energy economy, Public-Private Partnerships (PPP) are required. In Europe, the main hydrogen energy funding programs are based on a "Fuel Cells & Hydrogen" Joint Technology Initiative, launched in 2008 by the European Commission with €80 million/year [5].

Several projects in the past have initiated the demonstration of hydrogen efficiency, some of them still being active, and have prepared the path for early markets partnerships. On a longer-term basis, mass transport partnerships are gathering the key players into a convergence of means and visions.

Air Liquide subscribes to this frame and is an active actor of the following programs:

5.1.1 The Hychain project

Over the period 2006-2010, Hychain [6] is a €37 million program, which deploys in four European countries small urban vehicles: minibus, tricycles, utility vehicles and wheelchairs. The project also tests a dedicated infrastructure for exchangeable hydrogen cylinders.

5.1.2 The Horizon Hydrogen Energy (H2E) project

The Horizon Hydrogène Energie (H2E) [7] program is the latest of Air Liquide's commitment. This ambitious program represents a global investment of 190 million Euros over 7 years in research and technology development and federates 19 partners in order to implement a new industry for hydrogen energy.

H2E is a unique occasion to promote France and Europe into the implementation of a sustainable energy industry and has been tailored especially to fit the targeted early markets.

In summary, H2E is a program:

- aiming at building sustainable and competitive hydrogen energy solutions in the targeted markets
- investing in research & technology over seven years
- aiming at breakthroughs in the entire industry on electrolysis, fuel cells, hydrogen production and high pressure storage technologies
- opening early markets to ensure the transition towards and open the way for future applications such as in transport.
- deploying several thousands of systems throughout Europe by 2015 and in subsequent years
- opening early markets that, in Europe, represent a potential of several billions of Euros beyond 2015.

5.2 Mass transport partnerships

As briefly presented formerly, the sustainable mobility for mass transport implies three main stakes, namely

- to preserve the environment,
- to define a third-countries-independent and sustainable energy,
- to generate economy growth based on an affordable energy.
- and to offer the same conditions of use as today's vehicles

To reach such goal, industries and customers benefit from drivers of change which are the environment policies, the energy policies and the economical context. However, cost reduction is the major stake to influence the economical context and is the responsibility of technology makers. With fuel cells for example, Axane has been able to divide the cost of its cells by ten thanks to breakthroughs. Yet, to reach cost objectives compatible with the various markets, notably in transport, it is imperative to continue to raise the equipment performance and reach large-scale production levels.

Air Liquide decided to promote and to play a leading role in the following transport programs:

5.2.1 British Columbia Transit project

The BC Transit project in Vancouver [8] have deployed with Can$ 89 million the largest hydrogen bus fleet operating in a single location with 20 buses refuelled at the largest hydrogen station ever built today. The project has been launched on the occasion of the last Vancouver Olympics.

5.2.2 H2 Mobility Project

"*A comprehensive infrastructure for hydrogen refueling will be in place in Germany by 2015*." This statement is the origin of a three-phase plan of action. In the first phase, concepts for the expansion of new hydrogen refuelling stations should be developed by 2011 with the help of funding from Germany's economic stimulus package. In the second phase, this infrastructure will be realized, while the third phase will be marked by electric vehicles powered by fuel cell technology hitting the roads around 2015 in Germany as regional starting point.

Air Liquide decided to share his efforts with the signing manufacturers; NOW, Daimler, Linde, Air Products, Shell, Total, OMV, ENBW, Vattenfall) in order to prepare the FCVs mass market in Europe.

In a second deployment phase, similar concepts for the market penetration of hydrogen infrastructure could be developed in other regions of the world, including Europe, USA, Japan and Korea as further starting points.

6 Conclusion

Air Liquide is confident Hydrogen Energy applications will create tremendous growth opportunities. All those partnerships, combined with the development of their associated technologies, should allow for hydrogen vehicles to be ready for the commercialization on the market by 2015, contributing to the raise of the new Hydrogen Energy economy.

References

[1] Paul Miller (2005), Stratégie et marketing de l'innovation technologique, DUNOD.

[2] S. Campanari et al. (2009), Energy analysis of electric vehicles using batteries or fuel cells through well-to-wheel driving cycle simulations, J. of Power Sources 186(2009) 464-477

[3] http://www.europarl.europa.eu/sides/getDoc.do?pubRef=-//EP//TEXT+TA+P6-TA-2007-0197+0+DOC+XML+V0//FR

[4] Ricci M., Bellaby P. and Flynn R. (2008), What do we know about public perceptions and acceptance of hydrogen? A critical review and new case study evidence. International Journal of Hydrogen Energy, 33, pp. 5868-5880

[5] http://ec.europa.eu/research/fch/index_en.cfm

[6] http://www.hychain.org/

[7] http://www.planete-hydrogene.com/en/notre-engagement/the-progra-hydrogen-energy-h2e.html

[8] http://www.busonline.ca/fuelcell/

Business Case Hydrogen Infrastructure

Christoph Stiller, **Jan Michalski**, **Ulrich Bünger**, Ludwig-Bölkow-Systemtechnik GmbH, Germany

1 Introduction, Scope and Methodology

A hydrogen refuelling infrastructure is more complex than other fuel infrastructures due to the number of technology options, the site- and volume-dependent cost structure, the varying CO_2 emissions burden depending on hydrogen source and the risks and conflict of interests of the players involved. Market economics alone cannot lead to a successful breakthrough of this technology; a coordinated and concerted approach is needed for the early introduction.

A case study has been conducted to realistically simulate the build-up of hydrogen use in transportation and refuelling infrastructure in the Greater Oslo Area in Norway. The H2INVEST model was used to simulate the hydrogen infrastructure and to perform business analyses for the region. The model creates sets of refuelling sites allowing for maximum user convenience, estimates the hydrogen demand at these locations over time, and creates cost-optimum spatially and timely discrete production and distribution infrastructure to supply the hydrogen to the sites, respecting potential policy measures. [1]

Then, these results were utilized for a detailed business analysis, focussing on the five stations with highest and lowest demand, respectively.

The paper highlights key results of the case study in terms of refuelling station build-up, hydrogen supply infrastructure and subsidy models. Conclusions will be drawn on the requirement of subsidies and levelling mechanisms between high- and low-demand stations.

2 Hydrogen Demand and Refueling Station Rollout

The case study is based on modelling the spatial distribution of the infrastructure and its development over time. In 2008, the Greater Oslo Area (GOA) had about 980,000 inhabitants. It is assumed that the users of the cars live in the GOA, while they may drive to places outside; i.e. hydrogen refuelling stations can also be located outside GOA which also holds for hydrogen production locations. The analysis timespan covers 2010 to 2025 in one-year steps.

We have assumed that mass roll-out of hydrogen fuel cell vehicles commences in 2016-18 and that by 2025, about 60,000 hydrogen vehicles will be registered in the area, beside private cars also comprising about 100 public city buses and fair numbers of multi-purpose vehicles and delivery vans. A total hydrogen demand of app. 6,000 tons/year was projected for these vehicles by 2025. The vehicles were distributed over the municipalities of GOA following deployment logics at regional scale (i.e. a municipality which is connected later will

[1] For a detailed description of the methodology used to calculate demand, locate refuelling stations and optimise the hydrogen supply infrastructure in the H2INVEST model, refer to www.H2INVEST.com

gradually catch up in penetration with municipalities connected earlier). The number of refuelling stations in the area was assumed to reach a level of 20-30 by the year 2020 and then remain constant until 2025 (with the average hydrogen turnover per station continuously growing). The stations were assigned to the municipalities respecting the area and the local vehicle population. Then, to place the hydrogen stations within each municipality, a subset of conventional refuelling sites was chosen. It was distinguished between hydrogen demand for local, highway and public fleet driving. Conventional refuelling sites along high traffic roads were preferred in general while at the same time a widespread distribution of HRSs across the analysis region should be achieved.

With a set of 30 stations, an average travel distance to the next refuelling station of 3.4 km is achieved (assuming vehicles and HRS to be equally distributed over the municipalities). By reducing the number of HRS to 20, this distance increases to 4.1 km. Finally, the hydrogen demand at the stations was estimated by means of a simple distance-related traffic model and scaled by the traffic passing by each station.

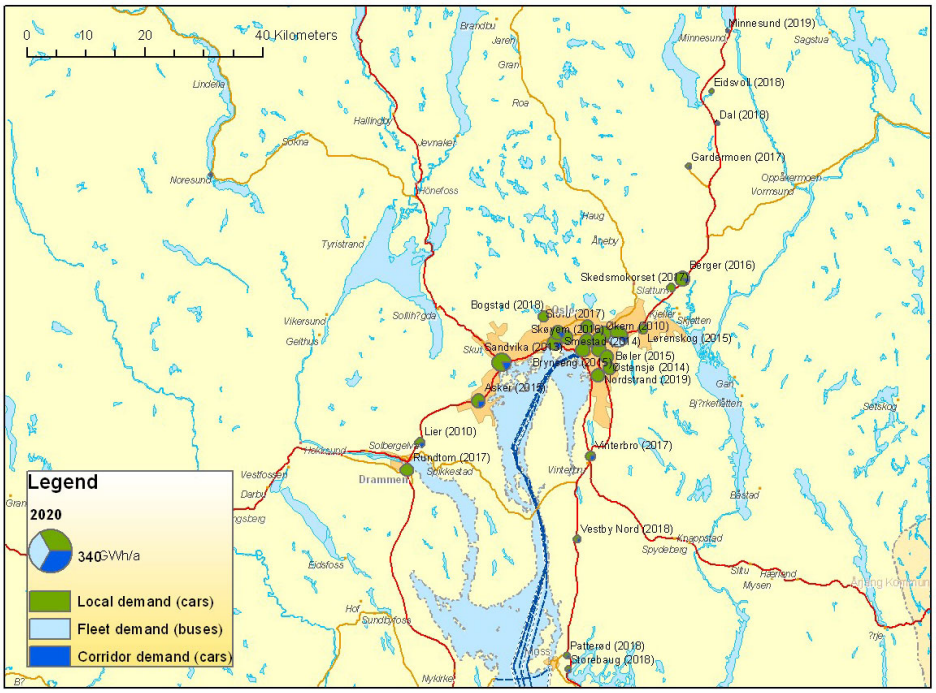

Figure 1: Selected hydrogen refuelling locations and calculated hydrogen demand 2020.

Figure 1 shows the selected hydrogen refuelling station locations and the estimated hydrogen demand at each station by 2020 (30 stations). Stations in the centre encounter the highest demand due to high traffic density than in remote locations. Four standard station equipment types were defined with capacities of 25, 300, 1,000, and 3,000 kg/day. Once the demand at a station would exceed the current capacity, the current equipment would be removed (to be installed at a new site, either within the same area or in other areas), and the next larger equipment type would be installed.

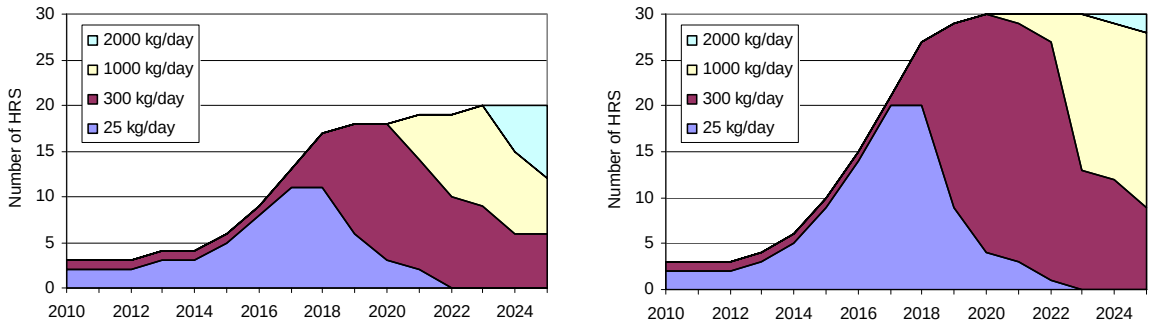

Figure 2: Split of HRS types over time (left: 20 stations; right: 30 stations).

Figure 2 depicts how the HRS type split changes over time for scenarios with 20 and 30 stations. It can be seen that 1/2 (20 HRS) and 2/3 (30 HRS) of the lowest capacity station equipment is required between 2016-18 when the hydrogen turnover is low in order to create customer convenience. For economic reasons this is unfavourable for the retailers since such stations require high investments and yield low revenues. The initial investment in small HRS is not lost as it is assumed that the equipment will be used at more remote locations later (outside the analysis region) afterwards. Yet, in order to avoid early investments in a large number of specifically costly small HRS an option is to install higher capacity equipment earlier though initially heavily underutilized. Although this would result in higher initial costs they are likely to be overcompensated by savings for avoided new installation costs after a few years.

3 Hydrogen Supply Infrastructure Build-up

With the H2INVEST model [2], cost optimized production and transport infrastructure scenarios were calculated to supply the above set of refuelling stations with the hydrogen demand estimated. Relevant hydrogen production options defined were electrolysis (central & onsite), central steam reforming of NG and biogas, and biomass gasification, and a set of industrial locations for the placement of these production plants were specified.

As hydrogen delivery options truck-based distribution of vessel bundles, tube and liquid trailers or pipeline distribution were chosen. Also, short pipelines between adjacent stations to jointly utilize onsite generation equipment were foreseen to form local clusters. The techno-economic data of the production and transport equipment were mainly taken from [3] and [4]. Data on electrolyser and refuelling equipment came from Statoil. The energy prices assumed can be seen in Figure 3. Natural gas and conventional fuel prices rely on a constraint fossil resources scenario [1].

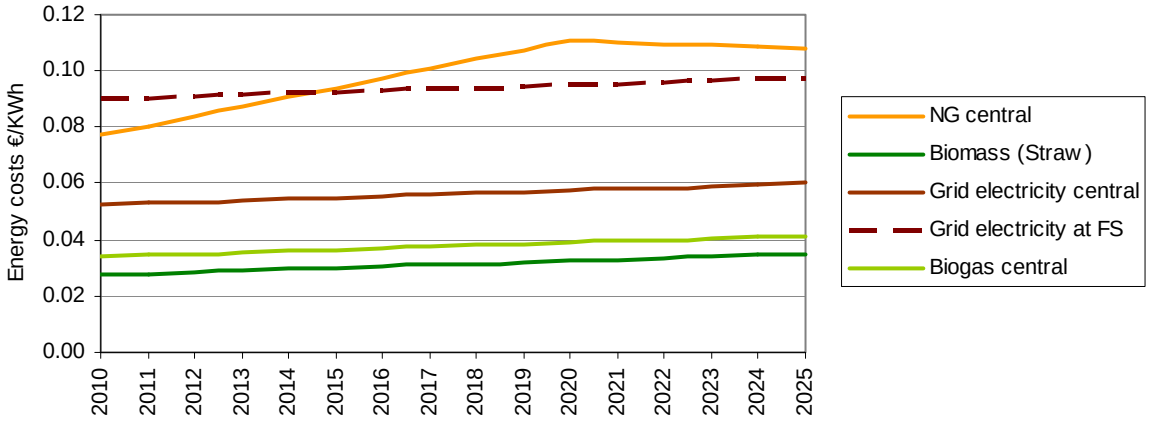

Figure 3: Energy prices assumed for scenarios.

Out of these options, the H2INVEST model calculated integrated supply infrastructure scenarios, choosing hydrogen production locations and production equipment as well as the distribution mode to the set of pre-defined hydrogen refuelling stations. The optimization objective for each time step is to supply the entire hydrogen demand at minimum annual costs. Figure 4 shows the resulting hydrogen production and distribution infrastructure by 2024.

Aggregated results of the hydrogen production and distribution in GOA for the scenario with 30 stations can be seen in Figure 5. For 2010 to 2015 the model suggests to supply most HRSs with by-product hydrogen from a nearby chlorine-alkali-electrolysis plant by tube bundle trailers, which, due to the low total demand, turns out to be the cheapest option during this phase. Only the HRS for buses has a higher hydrogen throughput and is supplied by tube trailer, representing about 80-90% of the overall hydrogen demand in that period.

By 2017, a biogas based SMR is installed, and all hydrogen is supplied from there by truck. By 2020, more biogas reformers are added, and due to the increasing hydrogen turnover, the majority of the HRS is supplied by tube trailers. By 2022, a further demand increase causes a radical shift in the infrastructure, since the limited regional biogas potential available for hydrogen is exceeded. Electrolysis is added to the production portfolio, and most central HRS locations switch to pipeline supply (see also Figure 4). Two onsite electrolysers are built.

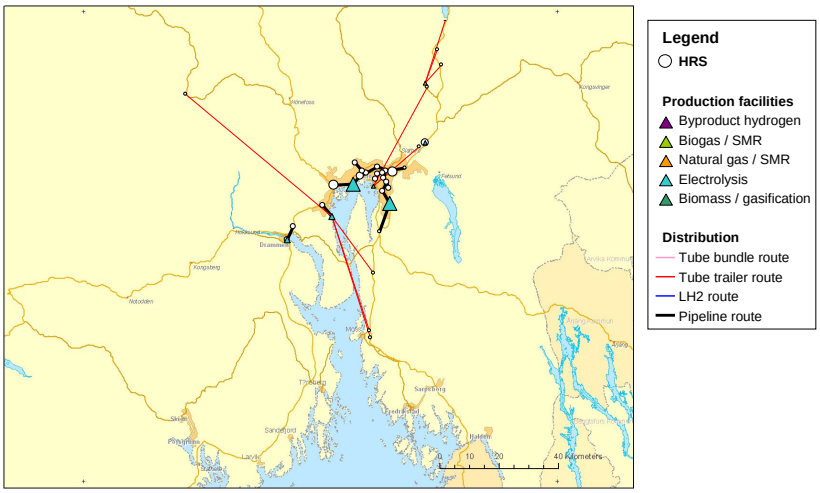

Figure 4: Production and distribution infrastructure for Oslo (30 stations; 2024).

After 2022 the infrastructure does not change further radically. The increased demand is mostly supplied by new electrolysis capacity, and the pipeline grid is expanded by a few branches towards HRS locations at the city border to replace shorter truck routes.

NG-based SMR and biomass gasification were not chosen due to the high feedstock price assumed for NG, and the low efficiency and high electricity consumption assumed for the biomass gasification plant. Likewise, LH_2 distribution is not used in any of the scenarios, since it is typically beneficial for larger distances. LH_2 had most likely become a preferred option if a larger supply region had been analysed.

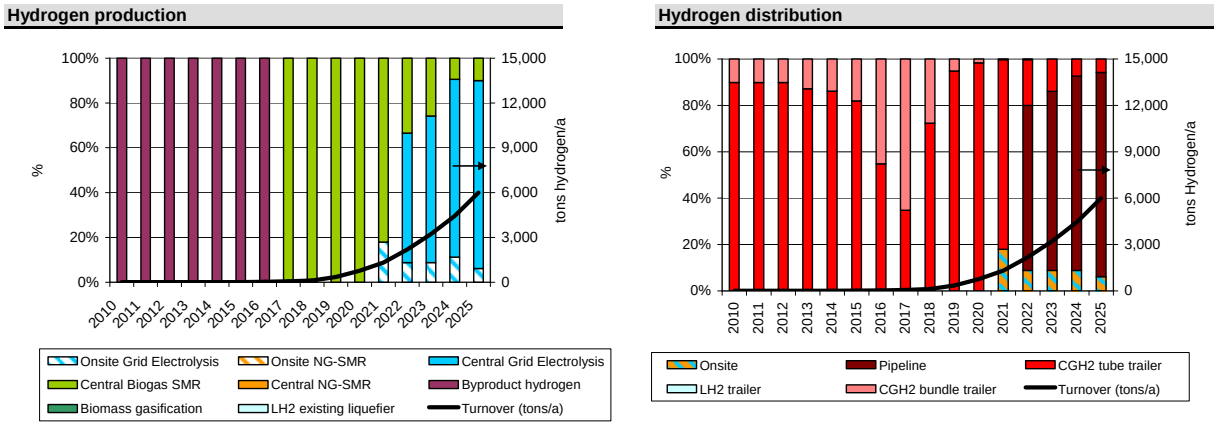

Figure 5: Aggregated hydrogen production and distribution (30 stations).

In the scenario with only 20 stations, the resulting infrastructure roll-out is very similar. However, electrolysis and pipelines are chosen about 2 years earlier than for the 30 station option (Figure 5) which results from the higher turnover per station, a major decision criterion for the hydrogen distribution type.

As a consequence from the use of biogas and electricity (which in Norway is practically greenhouse gas neutral due to the large percentage of hydropower in the electricity mix), the resulting well-to-wheel GHG emissions for fuel cell cars are very low from 2017 and onwards,

reaching a CO_2 equivalent level of below 20 g/km. The introduction of hydrogen mobility in Oslo as specified here can cumulatively save about 300,000 tons CO_2 equivalent until 2025.

4 Business Case Analysis

The simulation results from above were used for a detailed economic evaluation of the refuelling stations and the hydrogen infrastructure. In particular, the H2INVEST business tool allows for clustering single infrastructure elements into business divisions and specifying transfer prices for hydrogen between divisions and players defined. With these inputs, major economic parameters such as operating income, cash flow from investments and capital structure are calculated for each division. The clustering process can be structured by the position within the value chain (production-conditioning-distribution-refuelling), being either technology- or location-specific. Financial results can be generated for each business division.

For this study, we assumed two major types of investors. One investor (one independent business division) is responsible for the entire production and transportation of hydrogen to the HRS, regardless of the technology. Furthermore, every HRS is one business division, assuming the HRSs to be economically independent from each other. The transfer price for hydrogen deliveries between the production division and HRSs is site-specific and includes both operating costs (i.e. variable and fixed operating and maintenance costs as well as energy costs) and capital costs (i.e. debt interest and cost of equity). The consumer price at the HRS, however, is calculated as gasoline equivalent and is exempt from fuel taxation until 2020. From 2021 to 2025, we assumed taxation to ramp up to per-km parity with conventional fuel, reducing the net price received by the refuelling station. In addition we assumed the following:

- Working capital requirement for each technology is 5% of the initial investment.
- Declining balance depreciation is used for every infrastructure element.
- Debt ratio is 20% with 9.5% interest on average and 12% costs of equity for all investors.
- Division tax is 30%.
- No extra overhead for infrastructure planning and no inflation.

The profitability of the HRS was assessed based on site-specific net present values (NPV) as a sum of the corresponding discounted free cash flows. The final free cash flow at the end of the analysis timeframe contains the remaining book value of the corresponding equipment in order to account for the terminal value of each station in a conservative way. Figure 6 (left) shows the NPV results for the five HRSs with highest demand (in central, heavily travelled on areas) and five HRSs for lowest demand (in rural areas, which are required for customer convenience), respectively. It can be seen that while for the high-turnover HRSs, the NPV increases from 2020 to 2025 and two stations yield a positive result by 2025, for the low-turnover HRS the NPV decreases even further during this period. This is because the latter have higher specific hydrogen costs and through the beginning fuel taxation, the net retail price is strongly reduced.

We also calculated a case with a one-time investment subsidy upon erection of a new refuelling station of 1.5 million € for HRSs erected by 2010, reduced by 10% each

subsequent year (see Figure 6 right) in order to ensure adequate profitability for all stations. With this subsidy, the 2020 NPV is levelled out to a positive value for all HRSs. However, by 2025 the high-turnover HRSs have a high NPV, while for the low-turnover HRSs, the NPVs have decreased to a value near zero. This is also due to the specific hydrogen costs. Moreover, because the high-turnover HRSs are generally erected earlier than the low-turnover HRSs, the high-turnover HRSs receive more subsidies, and the NPV difference in 2025 is higher than without subsidies. A fair subsidising scheme must therefore not only consider the year of erection but also the site particularities (such as traffic and population density). Yet, the delay of the late stations must be taken into account; assuming a further increase in turnover, some years later also the low-turnover stations would probably yield positive NPVs.

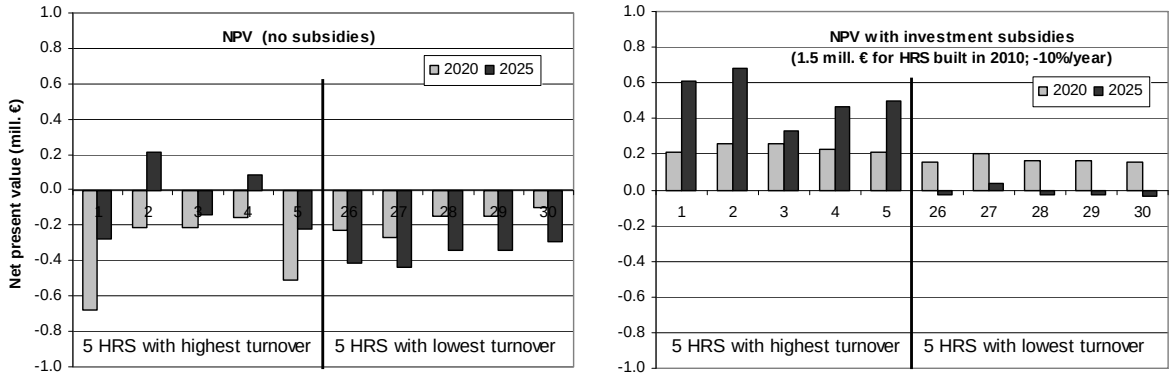

Figure 6: NPV of 5 HRS with highest and lowest turnover; w/o and w/ subsidies.

5 Conclusions

A detailed study for the hydrogen refuelling infrastructure for the Greater Oslo Area was conducted, assuming 20-30 hydrogen refuelling stations by 2025. The results suggest that over time and with increasing demand, hydrogen sources will switch from hydrogen by-product to biogas and later to electrolytic hydrogen. Hydrogen delivery is initially accomplished using vessel bundles and tube trailer trucks; later a pipeline infrastructure gradually develops to supply the most central locations. A CO_2 equivalent level of below 20 g/km is reached (well-to-wheels). A business analysis of the refuelling stations results in negative net present values by 2020 for all stations; by 2025, stations with high turnover partially achieve positive NPV. Applying subsidies, these values can be varied, but a degressive investment subsidy alone is not able to level out financial differences between stations with high and low turnover.

References

[1] GermanHy – a study addressing the question: “**Where Will the Hydrogen in Germany Come from by 2050?**”. Financed by the German Federal Ministry of Transport, Building and Urban Affairs in collaboration with the German National Organization Hydrogen and Fuel Cell Technology. 2008. Final report, August 2009, available at www.germanhy.de.

[2] Ludwig-Bölkow-Systemtechnik GmbH: **H2INVEST, the hydrogen infrastructure venture support tool**, www.h2invest.com

[3] **HyWays – an integrated project to develop the European Hydrogen Energy Roadmap**, European Commission, 6th Framework Programme (contract N° 502596), Deliverable 1.4: technology fact sheets. Ottobrunn, Germany: Ludwig-Bölkow-Systemtechnik GmbH, 2007. http://www.hyways.de

[4] The Research Council of Norway. **NorWays—providing decision support for introduction of hydrogen into the Norwegian energy system**, project 173045/S30. Trondheim, Norway: SINTEF. Report D8, “Description of / Results from Infrastructure Analysis Model”, February 2009, available at www.ntnu.no/NorWays.

Techno-Economics of Distributed Generation and Storage of Solar Hydrogen

Tim Cockerill, Marcello Contestabile, Imperial College London, UK

Abstract

For hydrogen to become a truly sustainable energy vector, low carbon generation technologies need to be developed and brought to market. Hydrogen from solar energy is a promising approach, capable, if successfully developed, of producing hydrogen from an abundant source with greatly reduced carbon emissions.

At present fundamental research on a wide range of solar hydrogen technologies is being investigated, including thermal, biological and electrochemical methods. The techno-economic properties of these technologies differ significantly. Some are best suited to large-scale centralised applications, whereas others may be employed on a smaller scale as part of a distributed energy resource strategy.

This work focuses on understanding the commercial potential of distributed generation and storage of hydrogen for stationary applications within a future energy system. Of particular interest is the combination of different generation approaches with appropriate storage technology and capacity. The choice of each depends on a number of factors, including electricity price fluctuations and the temporal mismatch between solar generation and demand profiles.

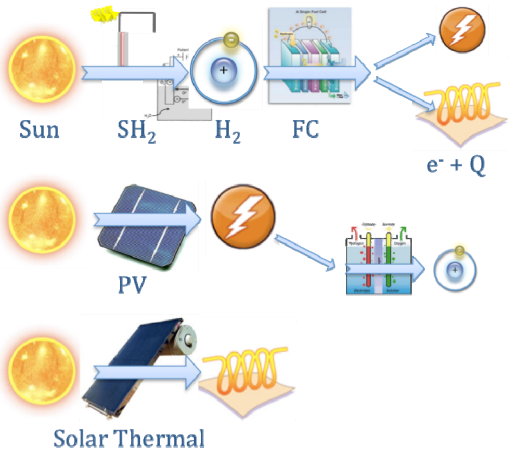

Figure 1: Conversion pathways for solar energy.

1 Energy Storage in a Low Carbon System

Low carbon energy sources tend to be either intermittent (wind, PV, wave) or inflexible (nuclear). For a future energy system this is expected to make system balancing more difficult and UK electricity prices even more volatile than they already are.

A recent Monte Carlo simulation by Pöyry on a future energy scenario has resulted in periods of high electricity prices (> 1000 £ MWh-1), as well as periods of excess electricity, which has low or even negative prices as shown in Figure 3 (Cox, 2009). The price spikes are said to be necessary for plants with low load factors to be kept on the system to meet demand peaks.

Given the potential for arbitrage between peak and trough prices, it appears interesting to question the role storage may play in such a future energy system. Despite over 3 decades of successful large scale storage applications in the UK and abroad, many of the future scenarios envisaged today do not consider storage as a significant part of the system. Instead, the ECCC recently stated that “[…] excess electricity could be channelled into domestic water and space heating thermal storage that would otherwise use gas". (ECCC, 2010)

Hydrogen storage in particular has widely been dismissed as `too inefficient'. Schaber claims, when comparing storage technologies, that “[…] if all other considerations are equal, efficiency is paramount […]" (Schaber, 2004). This is certainly true for limited and precious resources. But how important is efficiency, when we are dealing with `excess electricity', as seen in Figure 2?

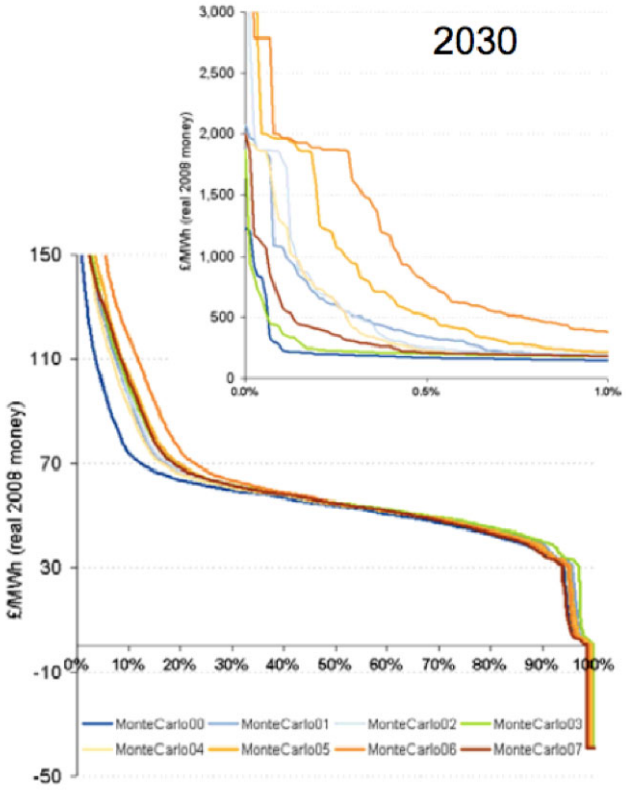

Figure 2: Monte Carlo simulation results of electricity prices in a 2030 UK energy scenario. Periods of electricity valued in excess of 1000 £/MWh contrast with negative dump load prices. (Cox, 2009)

2 Residential Storage

Distributed solar generation tends to suffer from low capacity credit, since the time of generation does not coincide with peak demand. A conveniently storable form of energy would therefore be desirable. The benefit of such a storage pathway has been modelled based on the structure shown in Figure 3. Solar energy can be converted into electricity, heat or hydrogen. A time series of storage is built up from hourly generation and demand profiles. Introducing storage raises the utilisation and adds value by displacing grid supply.

The best results have been achieved through a combination of all three forms of energy, suggesting that solar hydrogen may complement a highly renewable generation strategy. However the costs of local storage and conversion facilities are seen as prohibitive. Regional or national storage and distribution facilities are needed to support solar hydrogen generation.

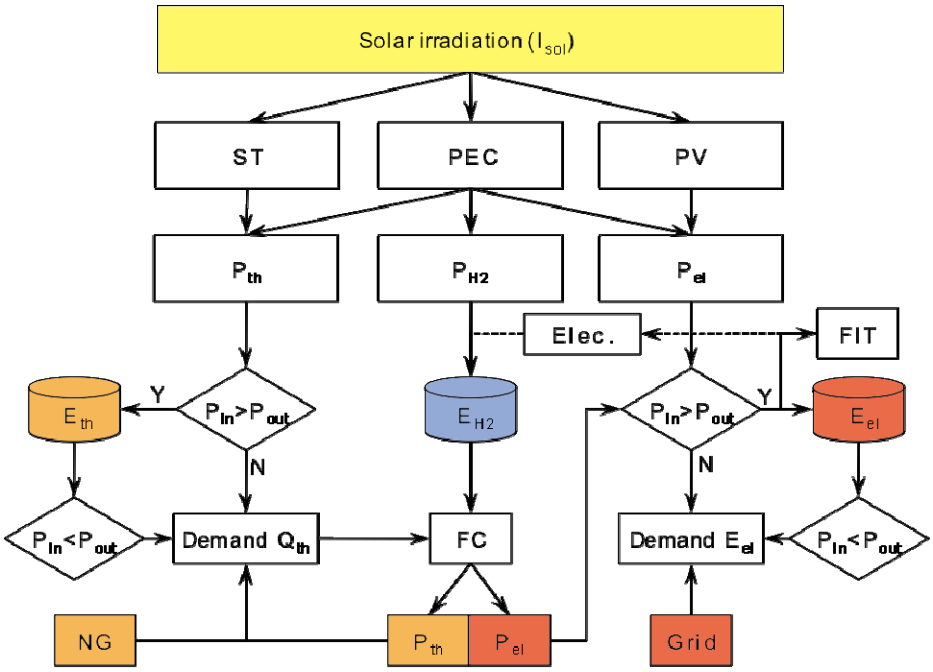

Figure 3: Model for temporally resolved energy flows in a residential application.

3 UK Storage

The model for a UK wide use of storage follows a similar basic principle to the residential model by building up a time series of generation resource and demand profiles. The choice of energy sources has been expanded to include wind, nuclear and a generic class of fossil fuel plants. Data for the wind and solar resource is based on historical data over the previous 6 years, measured mostly in 1-hour intervals and interpolated to match the 30 min resolution of the National Grid energy consumption data. (National Grid, 2010; UK Meteorological Office, 2006)

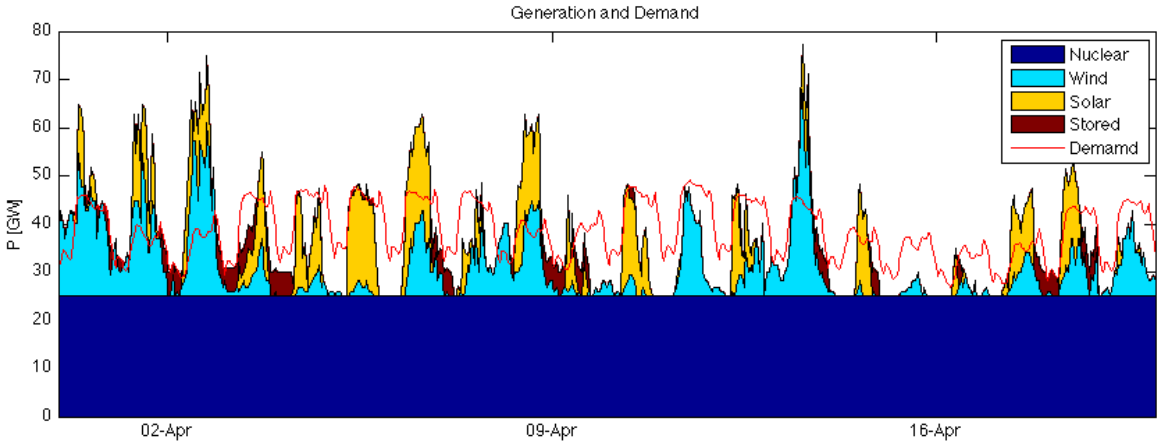

Figure 4: Extract of time series of generation and demand. At times of excess generation energy is stored. Once demand exceeds generation from the low carbon sources, stored energy is released back into the system. Data based on National Grid (2010); UK Meteorological Office (2006).

Heat demand is not considered in this model, to allow direct comparison with pure electric storage pathways, such as batteries. In practice, inclusion of CHP applications may shift the results in favour of hydrogen storage.

The dispatch order is kept deliberately simple, to avoid any technology bias arising from inaccurately estimated merit orders. Nuclear power is delivered as base load, which does not respond to demand. Solar power and wind are dispatched whenever possible or else stored, if storage is available. Should demand not be met by nuclear, wind and solar energy, stored energy is used. Fossil fuel plants only operate to meet the remaining demand (see Figure 4). In terms of merit order, this strategy could be described as highly carbon price dominated, but not necessarily economically or strategically optimal.

The resulting time series for flows in and out of storage gives an indication of the characteristics that are desirable in a large-scale storage system. If run unconstrained (i.e. infinite storage capacity and power) the power and storage capacity that would ideally be available can be estimated. Further, some typical usage patterns can be established from FFT plots and a storage duration histogram.

With the inclusion of costs for energy storage capacity and power, a solver finds the most cost effective storage configuration for any given generation mix (see Figure 5). The exact electricity prices a storage operator could negotiate in practice are the result of several complex factors that are beyond the scope of this study. Fixed electricity prices have therefore been assumed for off-peak periods and times when stored energy is released.

It has been found that large scale storage, providing arbitrage services in an energy system with more than 30 GW of renewable energy, can be economically viable. For the production of solar hydrogen to be competitive at the residential level, is more challenging. Large installations and a dynamic operation, delivering electricity, heat or hydrogen, are required, whilst meeting ambitious manufacturing cost targets of less than 1\$/W_p.

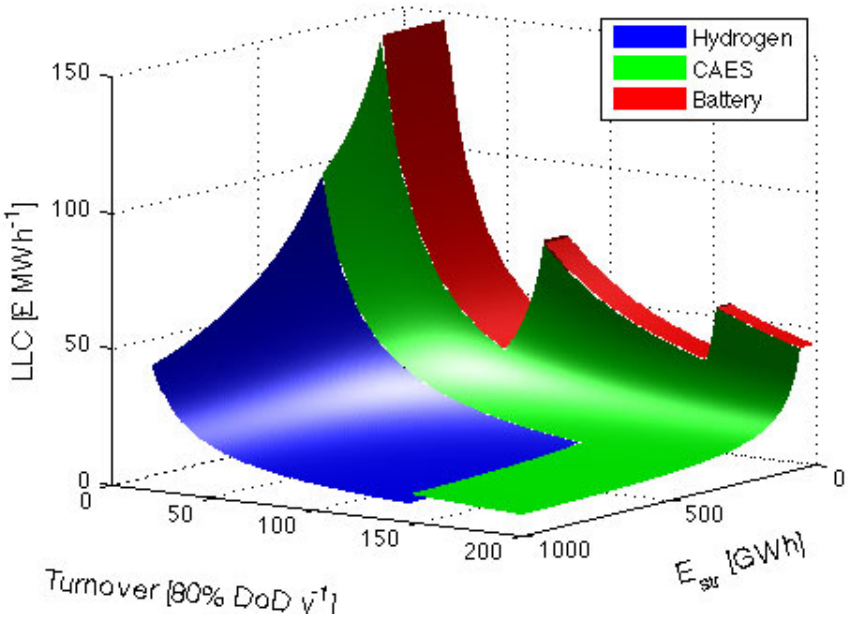

Figure 5: Example of optimum storage technologies for a range of system storage capacities and utilisation.

References

[1] J. Cox (2009). Impact Of Intermittency: How Wind Variability Could Change - The Shape Of The British And Irish Electricity Markets, Poyry Energy, Oxford. Technical Report.

[2] ECCC (2010). The future of Britain's electricity networks. HC 194-I, House of Commons, Energy and Climate Change Committee, www.publications.parliament.uk/pa/cm200910/cmselect/cmenergy/194/194.pdf. London.

[3] National Grid (2010). Metered half-hourly electricity demands. Online, Available from: www.nationalgrid.com/uk/Electricity/Data/Demand+Data/. [Accessed Jan 2010].

[4] C. Schaber, et al. (2004). 'Utility-Scale Storage of Renewable Energy'. The Electricity Journal **17**(6):21–29.

[5] UK Meteorological Office (2006). MIDAS Land Surface Stations data (1853-current), British Atmospheric Data Centre, Online. Technical Report. Available from: http://badc.nerc.ac.uk/data/ukmo-midas.

The Implementation of SAE J2601: Hydrogen Fuelling Protocol Guideline for Demonstration Projects

Jesse Schneider, Proton Motor Fuel Cell GmbH, Germany
Juergen Klugman, Adam Opel GmbH, Germany
Bob Boyd, Linde Gas Company, USA
Justin Ward, Toyota Motor Company, USA

1 Scope

The goal of this presentation is to describe the Technical Information Report SAE J2601, how it was developed and its intended implementation in hydrogen vehicle demonstration projects.

The international SAE Fuel Cell Standardization and Interface team, who created this document, consisted of cross-industry representation of most of the major automakers, energy companies, laboratories and government hydrogen and fuel cell system suppliers.

The implementation of hydrogen vehicles in the market necessitates having a universal fuelling protocol for all vehicles. The goal is to achieve a 'customer acceptable' fuelling, which means a full tank of hydrogen within a reasonable amount of time without exceeding the temperature, pressure and density (SOC) limits. However, fuelling performance may be limited by the pre-cooling capacity of the station dispenser.

2 Industry-wide Fuelling Protocol

SAE TIR J2601 establishes industry-wide fuelling protocol guidelines for the fuelling of gaseous hydrogen into on-road passenger vehicles operating with nominal working pressures (NWPs) of 35MPa and 70MPa. Fuelling stations should employ fuelling algorithms and equipment to conduct the fuelling process within these guidelines. Vehicles filled at stations using these protocols should be designed appropriately for fuelling according to these guidelines. SAE TIR J2579 provides guidance for qualifying the vehicle hydrogen storage system (HSS) for operation at specific nominal working pressures.

This document establishes safety limits and performance requirements for gaseous hydrogen fuel dispensers. The criteria include maximum fuel temperature at the dispenser nozzle, the maximum fuel flow rate, the maximum rate of pressure increase and other performance criteria based on the cooling capability of the station's dispenser.

J2601 establishes fuelling guidelines for "non-communication fuelling" in the absence of vehicle communication and guidelines for "communication fuelling" when specified information is transmitted from the vehicle and verified at the dispenser. The process by which fuelling is optimized using vehicle-transmitted information is specified. SAE TIR J2799 (fig. 2) provides details of the communication data transmission protocol.

This document applies to light duty vehicle fuelling for vehicles with storage capacity from 1kg to 10kg for 70MPa and 1kg to 7.5 kg for 35MPa. It is intended to be revised in the next two years to include separate requirements for fuelling heavy duty vehicles and motorcycles,

and also for residential hydrogen fuelling appliances. Since there is a significant difference between the onboard storage capacity of heavy-duty and light-duty vehicles, the performance specifications could be different.

Standard Designation		H35			H70		
Storage Capacity Classification		Small (motorcycle)	Light Duty (light duty 1 ~ 7.5 kg)	Heavy Duty (bus, commercial truck)	Small (motorcycle)	Light Duty (light duty 1 ~ 10 kg)	Heavy Duty (bus, commercial truck)
Fueling Connection Device		J2600 Recommended Practice			J2799 TIR (to J2600 in future)		
Vehicle-to-Station Communication		J2799 TIR (to J2601 in future)			J2799 TIR (to J2601 in future)		
Fueling Protocols	A ➔ -40C	2601 in future	J2601 TIR in 2009	2601 in future	2601 in future	J2601 TIR in 2009	2601 in future
	B ➔ -20C	2601 in future	J2601 TIR in 2009	2601 in future	2601 in future	J2601 TIR in 2009	2601 in future
Dispenser Type ➔ Cooling	C ➔ 0C	2601 in future	J2601 TIR in 2009	2601 in future	2601 in future	2601 in future	2601 in future
	D ➔ None	2601 in future	J2601 TIR in 2009	2601 in future	2601 in future	2601 in future	2601 in future
	Residential	2601 in future	2601 in future	2601 in future	2601 in future	2601 in future	2601 in future

Figure 1: Summary of fuelling interface standards and scope of current TIR J2601.

The tables based approach in this document has been simulated by vehicle auto manufacturers and validated by independent laboratory and some preliminary field results. The tables give targets for pressure levels with a given ambient temperature, for non-communications fuelling and start pressure to arrive at a high desired state of charge.

SAE J2799 Optional Communications: IrDA Wireless Communications

- IrDA Available Technology
- Transparent to customer
- Vehicle tank info for Temp. Comp.
- Real Time H2 Storage Information

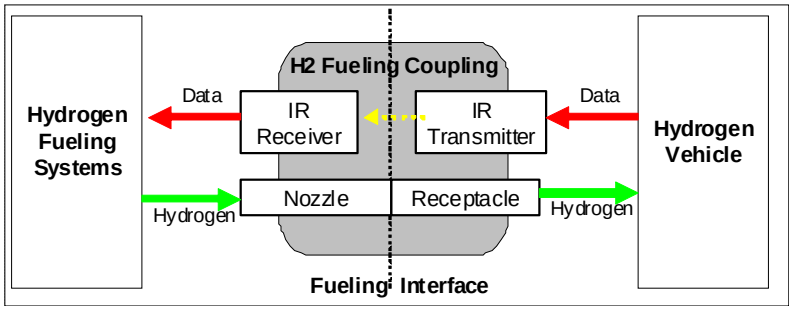

Figure 2: Overview of SAE J2799.

This document applies to fuelling using an average pressure ramp rate methodology which is to be verified with a hydrogen dispenser test apparatus as defined CSA HGV 4.3. This document includes provisions for optional alternative communications fuelling protocols and is planned to be revised in the future to include specifications for additional fuelling processes to allow more freedom than the present document. New dispenser protocol proposals would need to be verified with data and experience demonstrating the fuelling

algorithm's capability to operate within the constraints of the General Requirements for Fuel System (SAE J2579) and Interface (SAE J2600, J2799).

3 Implementation of the Hydrogen Fuelling Guideline

It is expected that this document will be used in conjunction with the CSA HGV 4.3 Hydrogen Dispenser Temperature Compensation Confirmation Report, which will to provide a test method and equipment specification for confirming that the performance of a fuel dispenser is consistent with the requirements of SAE TIR J2601.

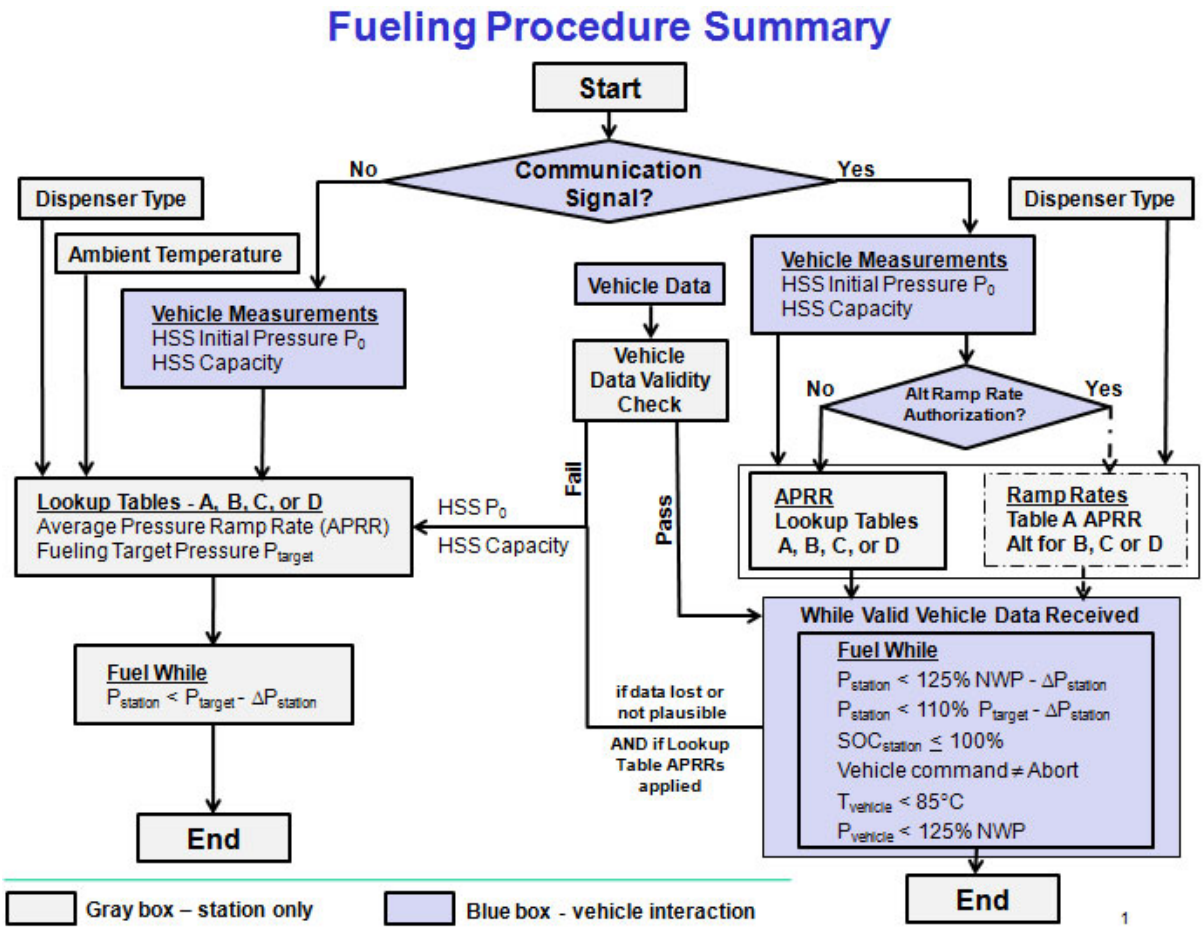

Figure 3: Flow sheet of decision tree for each fuelling procedure.

This document establishes a formal industry-wide fuelling guideline that supersedes all temporary guidelines informally established by non-ANSI-certified organizations, such as the vehicle manufacturer (OEM) document Fuelling Specification for 70 MPa Compressed Hydrogen Vehicles, Version A posted on the NextEnergy website and all CaFCP Fueling Protocols. It is understood, however, that other fuelling protocols that differ from the look-up table-based protocol specified in this document may be used when the station provider has a.) an agreement from a vehicle manufacturer that the protocol is appropriate for a particular vehicle system, and b.) a method of identifying the particular vehicle and limiting the protocol to that vehicle is utilized in the station design and operation. The intent is that developments

be brought to the SAE TIR J2601 team to enable modification of the document to allow for a more performance based approach for future revisions. The current document is table-based, providing concise performance targets and dispenser performance specifications for both communicated and non communicated fills as shown in figure 3.

This TIR is intended to evolve over time before it is standardized. The goal is to establish a protocol guideline in the initial publication and request industry to give feedback and improvement suggestions before standardizing in the 2011 timeframe.

Depending on which dispenser type is chosen (classified by pre-cooling temperature capability), a relatively quick fuelling time and SOC can be achieved. In fact, the Department of Energy fuelling goals for the year 2015 were achieved with an ‚A-Type' Dispenser.

Recommendations will be made in the presentation as to which dispenser type would give a "customer acceptable" fuelling.

References

[1] SAE J2601, Hydrogen Fueling Guideline for Light Duty Vehicles, SAE International, March 2010

[2] NHA 2005, Optimizing Hydrogen Vehicle Fueling, Schneider, J. Ward, et al.

[3] NHA 2009, 70 MPa Hydrogen Storage and Fueling Testing and Future Prospects, J. Schneider, I. Sutherland, et al.

[4] SAE Paper 2005-01-0002 "Gaseous Hydrogen Station Test Apparatus: Verification of Hydrogen Dispenser Performance Utilizing Vehicle Representative Test Cylinders", J. Schneider, J. Ward, S. Mathison, et al.

Fuel Provision for Early Market Applications

Manfred Fischedick and Andreas Pastowski

Abstract

Early market applications of fuel cells need to be supplied with hydrogen, comprising production and distribution. Production of hydrogen can be based on a multitude of processes and energy carriers and can be assessed using criteria such as systemic requirements, economic efficiency, environmental sustainability, and user acceptability. While the long-term sustainable vision is based on renewable energy, cost considerations may be prevalent for early applications. Global production of industrial hydrogen is substantial, almost entirely based on fossil fuels and generally unavailable for other use. However, excess production capacity and by-product hydrogen and also the industrial hydrogen infrastructure might be used for the supply of limited volumes of hydrogen for early applications of fuel cells. Depending on the industrial structure, potential regional supply of industrial hydrogen varies. However, with growing demand and in order to put the long-term vision into practice, new supply from renewable source will need to be set up.

Integration of Fuel Cells Systems into Chlor Alkali Plants: The Chlorine Industry Perspective

Alessandro Delfrate, UHDENORA S.p.A., Italy
Carsten Schmitt, Uhde GmbH, Germany

1 Introduction

The chlor alkali industry has always been considered an important target for the fuel cells industry, mainly because it is an energy intensive process that produces big amount of high purity hydrogen as a side product. While fuel cells manufacturer have provided over the time their strategies on how to approach the chlorine market, few information are available from the chlorine industry perspective on the specific conditions that will facilitate the application of fuel cell systems in such specific industry. In this article, the specific characteristics of the chlor alkali industry will be discussed, highlighting the potential for fuel cells applications from the perspective of one of the most important engineering companies active in the field.

2 The Chlor Alkali Industry

The chlorine – caustic soda industry in one of the corner stone of the world chemistry, being those chemicals, directly or as intermediates, involved in more than 50% of the chemical industry. Chlorine, caustic soda and hydrogen are produced simultaneously throughout the electrolysis of a concentrated solution of sodium chloride, using three different technologies that have evolved with time: mercury cells, diaphragm cells and ion exchange membrane cells, being the latter the only technology commercialized today (Figure 1). The chlorine industry is a highly specialized industry, with very few technology licensors: UHDENORA of Milan, a joint venture between Uhde GmbH of Dortmund, Germany, and Industrie De Nora, Milan, Italy is one of the relevant players in this market.

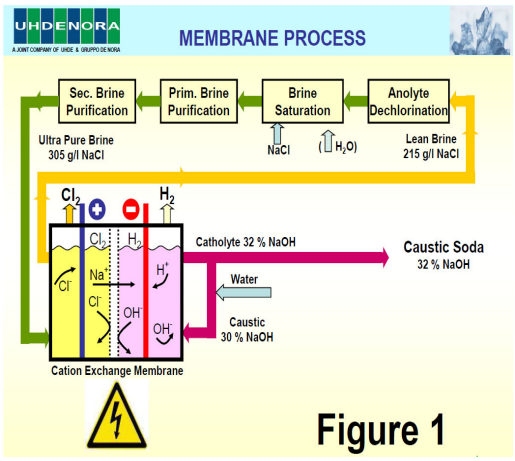

Figure 1

2.1 The numbers of the chlor alkali industry

On a world basis, a capacity of approximately 68 million ton per year of chlorine production is today installed, achieved by a total of about 550 chlorine plants. Main chlorine producers are China (24 MTPY), Asia (11 MPTY), North and South America (13 MTPY) and Europe (10 MTPY).

Considering a 90% plant utilization factor, the associated hydrogen production is equal to approx 216 ton/h, for a total theoretical potential of approx. 3.2 GW electricity production. The total accessible market, however, is to be considered much smaller, since only the hydrogen that is vented to the atmosphere, thus at zero value, will be of interest during the initial phase of fuel cells applications; this market can be estimated at 400 MW – 600 MW, depending from the characteristics of the fuel cells considered. The hydrogen used as a chemical will never be accessible for other uses, while the hydrogen that today is burnt to produce steam may became available to fuel cells if the overall system price will allow interesting paybacks [1,2].

2.2 The importance of fuel cells for the chlorine industry

Electricity consumption is the key parameter to measure the competiveness of a chlorine plant, being electricity up to 60% of the variable production costs. With the most up to date electrolysis technologies, the electricity consumption can be considered close to the thermodynamic limit, leaving only a small space for further power savings. The two possible breakthrough toward the reduction of power consumption for the electrolysis are both related to the use of the hydrogen available in the plant: the first is through the so called Oxygen Depolarized Cathode technology, where additional oxygen is fed to the cathode and H_2 is reduced to water inside the membrane electrolysers, with 30% of potential energy reduction, the second through the conversion of the hydrogen into electricity using fuel cells, with a 20% of potential electricity reduction[3]. To be underlined that the recovery of hydrogen through ODC technology is already used by UHDENORA and Uhde for the electrolysis of aqueous solution of hydrochloric acid to chlorine, with a demonstrated energy saving of approx 30% with respect to the standard diaphragm electrolysis and a licensed capacity of more than 330.000 ton of chlorine per year.

2.3 Fuel cells for Integration in C/A plants

UHDENORA, as system integrator, does not develop any proprietary fuels cells technology, rather is selecting from the industry the most promising products for this application. With the term “Integration”, we intend a fuel cell system that is completely embedded into the electrolysis process, installed inside or close to the cell room, built in full compliance with the safety regulations and with customers technical standards, with a balanced tradeoff between the maximum system simplification and its safe performances. Other approaches are possible, such as the installation of fuel cells running on purified hydrogen form the chlorine plant, and feeding the AC power to the grid, that can be considered a valid solution for some applications, but that will not allow the full exploitation of the available market.

For an effective integration, the main characteristics requested to fuel cells are the following:

1. Capability to operate on a 24/7, 320-350 days per year.

2. Base load operation, with slow load following capabilities (30% - 100%)
3. Able to operate with industrial grade hydrogen
4. Good resistance to sudden shut down
5. Easy monitoring of main parameters
6. Minimum balance of plant provided by the fuel cell supplier for the integration into the system
7. High quality heat for possible CHP use (low pressure steam generation the best)

All those characteristics have a direct impact with the overall system design, thus with the fuel cell system cost. As an example, few data are available on long term fuel cells performances in presence of the contaminants typical of the hydrogen from the chlorine plants (i.e. caustic soda or mercury). As a consequence, very high purity hydrogen is sometime requested, increasing the cost for the hydrogen purification section. A second example is the determination of the consequences of the number of shut down on the fuel cells durability: if complex systems are requested to properly manage such critical situations, the system complexity increases, as well as its costs.

3 System Characteristics

In the last four years, UHDENORA had designed and demonstrated a proprietary technology for the integration of fuel cells stacks and minimum balance of plant inside the electrolysis circuit of electrochemical plants, with direct connection to the DC bus bars of the electrolysers [4]. The pilot system has the following main characteristics (Figure 2):

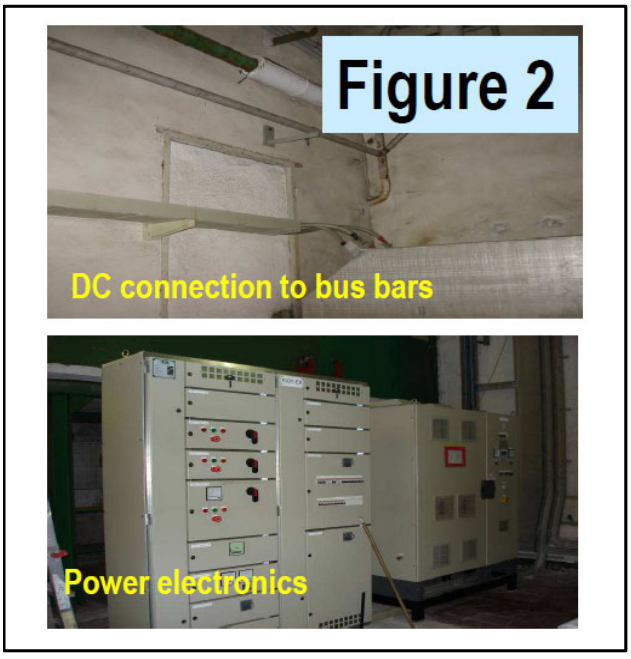

Figure 2

1. Modular configuration to fit different plant sizes, capable to accommodate different fuel cells technologies
2. Usage of DC power from fuel cells to reduce electrolysis power consumption
3. Installation and maintenance without perturbing the chlorine plant production cycle
4. Designed for installation inside electrolysis room
5. Remote control and monitoring capabilities in environments characterized by strong EM noise

It is to be underlined that most of the chemical companies have internal standards for equipment and materials, and all the fuel cell system equipment must be supplied accordingly. While standardization of performances is possible for most of the plants, standardization of equipment is more difficult to be achieved, and specific know how and experience is requested [5].

4 Value Proposition and Cost Targets

The payback time of the fuel cell system depends from the end use of the electricity generated:

- DC power from fuel cells is directly used to reduce the DC power consumption for the electrolysis process. Main variables to be considered for the payback are the hydrogen value and the grid electricity price.
- DC power from fuel cells is used to increase the chlorine plant capacity. This is of particular importance in areas where the grid capacity is already at the upper limit. Payback time depends also from the value of the extra production.
- DC power from fuel cells is converted to AC and sent to the grid. Main variables are the hydrogen value and the grid electricity price.

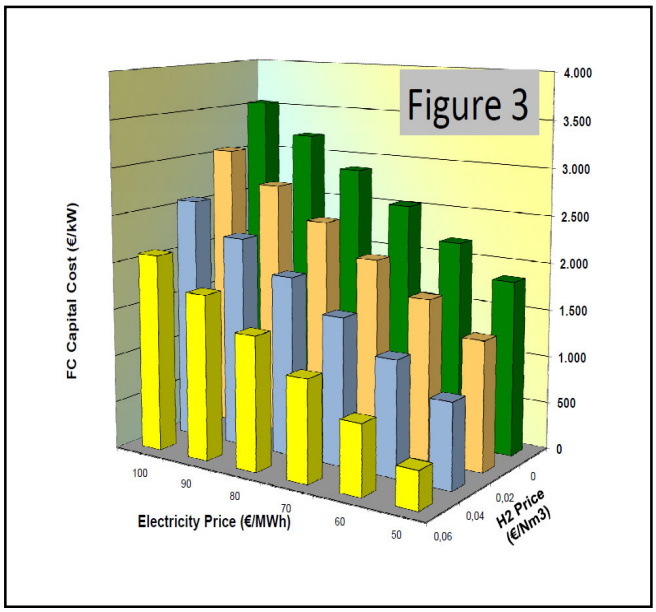

Figure 3

In Figure 3 the sensitivity analysis between fuel cell system capital cost versus price of grid electricity and hydrogen value is reported (Simple payback: 5 years, fuel cells system net efficiency 45%, heat recovery partially considered). It is to be noted that results can be substantially different depending from the technology considered (i.e. low temperature Vs high temperature fuel cells), in particular considering the associated operating costs. No subsidies or feed in tariffs have been considered in the calculations, since there are strongly dependant from the local supporting policies.

As a reference, for investment in energy saving equipments, the average requested payback is approx. 3 years; only for particular projects that may involve additional advantages, such as green image or achievement of CO_2 reduction targets, payback can be extended to over 5 years.

5 Commercialization

As previously anticipated, the integration of fuel cells into chlorine plants presents unique advantages for an early adoption, such as:

- Hydrogen is already available and with high purity
- Fuel cells and chlorine industry speaks the same electrochemical language (low acceptance barriers)
- Energy reduction is paramount to this highly competitive industry and the energy produced with fuel cells is 100% CO_2 free, generating additional advantages for green image and plant eco efficiency.

In spite of a such positive characteristics, only few demonstration projects have been deployed in the field in the last 10 years. This consideration alone should indicate that the market is not as easily accessible as it could be anticipated.

To our knowledge, the majority of the fuel cells applications located into chlorine plants are based on the use of the available hydrogen to produce AC electricity to be fed to the grid. Some of these applications use the hydrogen available to test on a large scale fuel cells technologies for transportation, or to improve fuel cells performances and for cost reduction.

We believe that for a successful fuel cells application, a deep knowledge of the chlorine industry needs and the associated dynamics is necessary: ignoring the rules of this market is very dangerous, and companies who have tried different approaches have already disappeared.

From a system integrator perspective, a number of information are still missing from the fuel cells industry, such as performances in presence of specific contaminants (both at the anode and at the cathode side), and durability data under the typical operating conditions of a chlorine plant. All those issues can be technically resolved at balance of plant level, but the associated increase of complexity will increase the overall costs, further limiting the total accessible market.

A second important step to commercialization will be the availability of commercial guarantees from fuel cell system suppliers. Today, depending from the fuel cells technology, it is still difficult to consider guarantees in line with industrial expectations. As an example, the electrolysers membranes can have a typical guarantee of 4 years, and fuel cell components must have guarantees in line with those values.

6 Conclusions

1. The chlorine industry is a real opportunity for fuel cells, upon satisfaction of the specific industrial requirements for the application.
2. The chlorine industry is not the “Nirvana” for fuel cells applications, but is a tough market that needs specific competence to be approached.
3. In the last years, the fuel cells industry seems to focus mainly on small size systems, far from the megawatt size and ruggedized applications needed for the chlorine industry.
4. The chlorine industry represents an unique application, where the energy savings opportunities are linked to CO_2 emissions reduction, making the application interesting for corporate and policy makers.

References

[1] Roads2HyCom, Fuel Cells and Hydrogen in a Sustainable Energy Economy. Doc. N. R2H8500PU.6. 8 April 2009.

[2] EuroChlor, Chlorine Industry Review, 2008-2009, http://www.eurochlor.org/upload/documents/document352.pdf

[3] John Moorhouse, Modern Chlor Alkali Technology, Vol 8, Blackwell Science Ltd, ISBN 0-632-05559-6

[4] R.L. Santorelli, A. Schervan and A. Delfrate Energy Production from Hydrogen Co-Generated in Chlor Alkali Plants by the Means of PEM Fuel Cells Systems, CHEMICAL ENGINEERING TRANSACTIONS, Volume 12, 2007, ISBN ISBN 88-901915-4-6

[5] Uhde Chlor Alkali Technical Brochure http://www.uhde.eu/cgi-bin/byteserver.pl/archive/upload/uhde_brochures_pdf_en_10.00.pdf

Hydrogen Refuelling Station Hamburg HafenCity

Daniel Hustadt, **Oliver Weinmann**, Vattenfall Europe Innovation GmbH

1 Project Concept and Objectives

Decoupling the growing road traffic and the related greenhouse gas emissions demand a major effort by research, OEMs as well as oil and energy companies. Above all the reduction of CO2-emissions is a growing need for climate protection. Bio fuels can help to reach those targets, however the available sources are not sufficient to guarantee a sustainable supply. Battery Electric Vehicles are today limited technically with regards to range and weight and will most likely be used in metropolitan regions.

In this project the necessary infrastructure to refuel buses and cars of a bigger fleet will be installed. Doing so the prerequisite for using fuel cell based cars and buses as an alternative way of mobility is developed. The capability of new components for the productions, storage and distribution of larger amounts of hydrogen is shown. Additionally still existing potential optimizing on a technical and operational level shall be made available. Ultimately the possibilities of using electrolysers for levelling alternating feed in from wind power will be looked at in a first step.

2 Description of the Project

The project Hydrogen Refuelling Station HafenCity Hamburg is a joint project between Vattenfall Europe and a competent partner with knowledge on the field of hydrogen refuelling and retailing. Being part of the lighthouse project Clean Energy Partnership (CEP) this station has been granted funding within the National Innovation Program hydrogen and Fuel Cell Technology (NIP).

The HafenCity Hamburg is one of the biggest inner city development projects in Europe. Already today the HafenCity project is internationally recognized with regards to urban development and quite popular with tourists. The planning standards to be fulfilled by the constructors conform to highest standards and the energetic concept of the area is unique. Amongst others Vattenfall operates the district heating plant and a molten carbonate fuel cell in the heart of HafenCity Hamburg.

The Hydrogen Refuelling Station will be located at the east entry of the HafenCity Hamburg and face to face with the new headquarter of the publisher Spiegel. This place guarantees a high visibility and attractiveness for the relatively new hydrogen application for transport purposes. Also the place is a good choice, because of the good accessibility for third users within the city centre.

The project is divided into two phases. In phase one it is projected to service 10 buses and 10 cars. In the second phase from 2013 onwards the number of buses will be increased to 20 and the number of cars to more than 20.

The main properties of the new supply infrastructure are the following components and services:

- A daily capacity of max. 750kg
- At least 50% of the hydrogen will be produced by on-site electrolysis. The electrolysers will produce hydrogen in a high purity to be consumed in the vehicle's fuel cells. The used electricity is from proven renewable sources provided by Vattenfall. In this case it is possible to service the cars and buses of the first phase only with the hydrogen produced by the electrolysis.
- A special challenge is the fact that the station is located at a highly frequented place and in an urban zone. The station is a part of a small group of public stations in the world. To have a supply guarantee the production plant is build on in a modular structure with multiple electrolysers and two state of the art compressors. This system allows servicing a part of the bus fleet during a malfunction of a component.
- The rest of the hydrogen demand will be delivered from external sources yet to be determined by tendering. This could be by-product hydrogen or green hydrogen form wind-power in dedicated projects. The demand for delivered hydrogen is about approx. 120,000 kg annually when reaching peak load in 2013. The mixture between on-site electrolysis and delivered hydrogen ensures high flexibility and also test the daily delivery of hydrogen to a station.
- A special feature of this pure hydrogen refuelling station is location of the production and conditioning of the hydrogen. It will be located in a two story building covering all the existing ground area. Future hydrogen refuelling stations which will be integrated stations might benefit from the experiences gained at this project. A technical challenge is the interacting of the components in a limited space.
- A major aim is to adjust the hydrogen production according to a certain level of power production from wind. For this purpose, the hydrogen refuelling station will be applied with wind power profiles to gain experiences from the alternating production properties of the electrolysers and the whole system. The electrolyser will have to follow a wind power profile of generated electricity by wind power in dedicated tests. This feature plays a big role in integrating fluctuating wind power in the energy system. Through this regulation the transmission net can be relieved and more wind power can be integrated. For this purpose the control system of the plant is designed in a way so it is possible to upload real wind profiles into the system and adjust the performance of the electrolyser.

Table 1: Technical data.

Hydrogen production by electrolysis	Approx. 355 kg/day (equal with 14,8 kg/ hour)
Delivered hydrogen	Approx. 355 kg/day when fully expanded (20 buses 2013)
Total hydrogen demand	Max. 750 kg/day
Storage capacity tanks (gaseous)	Medium pressure tanks: max. 500 kg, High pressure tanks: max. 300 kg: Σ: max. 800 kg
Production hydrogen	3 electrolysers with 60 Nm³/h each
Compression on storage pressure	2 ionic compressors from Linde
Number of buses Beginning from end of 2010	10
Number of buses 2013	20
Number of cars 2011	20+
Number of cars 2013	40+
Planned operating time	2010 to 2017

- The storage of hydrogen for the refuelling of the buses takes place in pressure vessels in several pressure stages. The highest pressure stage works at around 900 MPa. This pressure allows that the hydrogen can overflow to the buses. The same applies for cars which can be refuelled at 35 or 70 MPa.
- The station will be one of the first stations offering the SAE standard for refuelling of 70 MPa-vehicles. A -40° C precooling will be available for the 70 MPa-refuelling of passenger cars.
- The hydrogen refuelling station is designed as a self service station. A card-reader-system allows that all CEP-members can use the station. The station has a video monitoring and a remote monitoring system to guarantee the technical and operational safety.
- The cost of total € 7.5 Mio are funded with 48% within the NIP program.
- The commissioning of the hydrogen station HafenCity is planned for the second quarter of 2011.

Figure 1: Artist view of the hydrogen station HafenCity Hamburg.
(Copyright: www.dilight.com)

The Hydrogen Valley within the Ruhr Metropolis

Volker Lindner, **Emanuel Grün**, **Frank Nosczyk**, **Jens W. Kuhlmann**,
h2-netzwerk-ruhr, Germany

1 The Ruhr Metropolis

The Ruhr Metropolis is due to the organically grown energy-technical and chemical structures from the past as a mining location the first address for fuel cells and hydrogen. And it is in demarcation of the mining past just the focus on the regenerative, the renewable, the lasting that characterizes this metropolitan area in Europe.

The region has about 5.2 million inhabitants and a population density of 1.220 inhabitants per km². About 60 million people are accessible in the vicinity of a three-hour driving time; in the vicinity of 500 kilometers 40 percent of the EU population are living. No other region in Germany is traffic-technically so systematically accessible like the Ruhr Metropolis.

Figure 1: The Ruhr Metropolis – central metropolitan area in Europe.

A large part of the electricity and heat consumed in Germany is generated in the Ruhr Metropolis. Due to the necessity to move the energy supply of the future towards climate friendly technologies, the Ruhr Metropolis is therefore in a forerunner position. Since the production of regenerative electricity is increasing and more and more included in the world's energy supply structure and so the electric energy changes from a secondary energy source to a primary energy source, one must also think about suitable storage procedures. One of the possibilities favored at present is the electrolysis of water and the storage of the produced hydrogen.

2 The Energy Carrier Hydrogen

Today hydrogen in the Ruhr Metropolis is produced primarily by steam reformation of natural gas (“brown hydrogen”), one of the biggest reformers in Europe is located in the chemical park Marl in the north of the Ruhr Metropolis. As actual sources for by-product hydrogen large-scale technical chlorakali electrolyses are available in the Ruhr Metropolis in Marl and Rheinberg.

Figure 2: Chemical park Marl – location of one of Europes biggest reformers and starting point of 230 km pipeline network.

The discontinuation of hydrogen production from fossil energy sources by climate protection purposes and also the shortage of resources will make new sources for the entry into a hydrogen economy necessary, the first projects are already in place in the Ruhr Metropolis: So-called “green hydrogen” is won by the use of regenerative electricity in combination with water electrolysis, the gasification of biomass, the reformation of digester gas and the hydrogen production by algae.

There are projects in which green hydrogen is produced in Bottrop (waste water treatment plant of the Emschergenossenschaft) and Herten (wind power electrolysis in the Application Centre and biomass gasification in the Blue Tower) complemented with research in the areas of algae and chemical cyclic processes.

In the waste water treatment plant in Bottrop the originating digester gas which contains primarily methane is fed into a steam reformer after cleaning and the produced hydrogen is used in a nearby school in a hydrogen CHP unit.

The electrolysis which will be operated in the Application Centre H2Herten uses locally generated wind power for the splitting of water in hydrogen and oxygen. The so won very pure hydrogen is very well suitable for the application in fuel cells, as for example in the project HYCHAIN MINI-TRANS, a demonstration project of small vehicles in the northern Ruhr Metropolis.

Figure 3: Waste water treatment plant in Bottrop – source of green hydrogen.

The Blue Tower, presently under construction in Herten, is a gasification plant in which locally harvested biomass is converted to a hydrogen rich gas.

With hydrogen production through algae different research groups in the Ruhr Metropolis are dealing. At the university of Bochum a research department purely on this topic has lately been established, but also at the university Duisburg-Essen and the university of applied science in Bottrop academic groups are working on this topic.

In company research another way of regenerative hydrogen production is under development: AEI Europe in Herten deals with chemical cyclic processes which generate hydrogen from water by use of iron oxides.

Generally it is assumed that in 2030 “green hydrogen” will overtake "brown hydrogen" in production.

The Ruhr Metropolis already today has an exceptionally dense and variable regenerative hydrogen production structure and is worldwide competitive here.

3 Distribution of Hydrogen

Because of the grown structures between coal, steel and chemistry in the Ruhr Metropolis big experiences in dealing with technical gases like hydrogen are already present. All big gas providers like Air Liquide, Air Products and Linde are of course residents here.

The distribution of hydrogen is guaranteed in the complete Ruhr Metropolis. This happens with industrial customers by the use of a pipeline network which branches out from the northern Ruhr Metropolis on a total length of 230 km. The supply of smaller end users is done through hauling. There are hydrogen filling stations in the Ruhr Metropolis in Bottrop, Gladbeck and Herten.

The filling station in Bottrop will be able to deliver filling pressures of 200 and 350 bar and will be the first in Germany at which vehicles can be refueled with locally generated regenerative hydrogen.

4 Stationary Fuel Cell Applications

Stationary applications like UPS, storage and reconversion of regenerative energy and CHP-units are produced and operated in the Ruhr Metropolis.

b+w Electronic Systems from Oberhausen and Idatech from Herten are active for a long time already in the field for stationary UPS for mobile communication systems.

This is one of the areas which are looked at as "Early Market", so as an entrance market for the introduction to the mass market.

5 Mobile Fuel Cell Applications

"HYCHAIN-MINI TRANS" is one of the leading projects of the European Union in which 24 European partners take part. The purpose of the project is the introduction of hydrogen as an alternative fuel on the base of innovative fuel cell vehicles. The northern Ruhr Metropolis is as well as the regions of Rhônes-Alpes (F), Emilia Romagna (I) and Castilla y Léon (E) to four European model regions in which the fuel cell technology is developed and tested in five vehicle types. Since May 2009 the first vehicles are already on the roads here.

Figure 4: Fuel cell midibus in the project HYCHAIN-MINI TRANS.

The northern Ruhr Metropolis serves not only as a region in which the hydrogen vehicles are tested, but also two vehicle suppliers as well as the hydrogen supplier for the whole project are seated here: In Gladbeck Hydrogenics which equips electric coaches with a modern fuel cell drivetrain has its seat, in Herten Masterflex Brennstoffzellentechnik develops and produces innovative load bicycles, so-called Cargobikes, and Air Liquide Deutschland has established a worldwide unique hydrogen-filling station in the chemical park in Marl for the high-pressure (up to 700 bar) cartouches with which a large part of the vehicles is equipped.

Hydrogenics also equips forklift trucks and other carrier vehicles with fuel cell drivetrain. This is also one of the areas which are looked at as "Early Market".

6 Science and Research

Workgroups at the universities Bochum, Dortmund and Duisburg-Essen as well as at the universities of applied science of Bochum, Dortmund and Gelsenkirchen are active in the area of fuel cell and hydrogen technology in the Ruhr Metropolis. This research density is raised even further by the activities of renowned Fraunhofer-, Leibniz- and Max-Planck-Institutes.Apart of basic research this dense network also covers all adjoining subject fields - from hydrogen production to application.

With the centre for fuel cell technology (ZBT) in Duisburg another hotspot of the national research scenery is located in the Ruhr Metropolis. The Duisburg institute, settled directly on the university campus, is continuously developing since its foundation in 2001 and herewith documents its steady competence increase.

A technical center was opened in 2008 for production and inspection engineering at the ZBT. Currently more than 70 employees devote themselves comprehensively in all relevant fields of research to the subject fuel cell and hydrogen.

These fields of research are Gas process technology, Fuel cell and system technology, Electrochemistry and layer technology, Quality assurance and inspection, Microsystems and fluid mechanics, Hydrogen and batteries and Production engineering. The PBT at the ZBT is also the only German accredited testing laboratory for fuel cells and components.

Already in 2001 the energy institute of the university of applied science of Gelsenkirchen, which also deals with the future subject hydrogen, was founded. It serves as a partner and interchange for the collaboration between science and industry. The purpose of the work in Gelsenkirchen is the optimisation of modern energy systems taking into account a eco-friendly energy use. In this context the future technologies around hydrogen play of course a central role.

7 h2-netzwerk-ruhr

The Ruhr Metropolis wants to take a central role for the fuel cell and hydrogen technology for the future and distinguishes itself along the whole value added chain by enterprises and research.

The h2-netzwerk-ruhr is the umbrella which stretches over all these activities and represents the Ruhr Metropolis nationwide and internationally in strong partnership with North Rhine-Westphalia, Germany and the EU.

Feel invited to participate in our future!

Revamping of Existent Chlor-alkali Plants for Conversion of Hydrogen to Electricity, Hydrogen Community Germination Step

Iordache Ioan, **Patularu Laurentiu**, **Iordache Mihaela**, The National R&D Institute for Industrial Ecology – ECOIND, Rm. Valcea, ROMANIA
Alessandro Delfrate, UHDENORA SpA, Italy

Abstract

The transition towards hydrogen becoming widespread in future energy systems and may be one of the greatest social and technical challenges facing society. A wide range of stakeholders will need to work together over extended periods of time to make the sustainable hydrogen “vision” a reality. Community-based projects are seen as a route to stimulate the start of the transformation, leading to more widespread early adoption of these new technologies.

Valcea have premises to develop some local projects in order to become a Hydrogen Community. This “Community” fulfils both an economic-technical background and a scientifically potential.

1 Hydrogen Community

Hydrogen is an indispensable co-product of the chlorine production process. Hydrogen can convert chlor-alkali technology into a more efficient one and may save a certain amount of energy. EU-27 chlorine producers know as Euro Chlor, want to increase recycling and re-use of hydrogen gas from 80% (2001) to 95% by 2010, difficult to achieve, into the opinion of many. The companies improved their utilization rate, others however did not, and this has had a negative influence on the consolidated result [1]. The fuel cell stationary applications are one of the additional efforts necessary in order to achieve 2010’s goal.

A Hydrogen Community refers to an early adopter of Hydrogen and Fuel Cell technologies, having the potential to lead to a coordinated, larger-scale adoption of such technologies within a coherent end-user grouping. Although, the specific costs of current prototype PEMFCs are still high, large cost reduction potentials are expected during the next years which shall enable mass penetration of this technology into several markets. Various small and large industrial enterprises worldwide are developing commercial PEMFC systems and preparing their market introduction. First prototype applications are tested in pre-commercial applications together with prospective future customers [2].

Revamping of existent chlor-alkali plants (92 into Europe) for conversion of hydrogen to electricity is a germination step in order to growth up a Hydrogen Community.

In practice, other types of hydrogen communities could be regions, cities, remote locations (such as islands), self-contained entities (airports, seaports, industrial complexes, etc), or distributed entities (hydrogen highways, etc).

In a Hydrogen Community, hydrogen plays a significant role in the community as an energy vector. A Hydrogen Community may evolve out of, or in parallel to, large demonstration projects. Possible cluster activities within the Community can include fundamental or applied research and demonstration projects that feed new technology into the Community.

For a lot of East European country where exists regions with a strong technology or manufacturing base, but with declining industries, a chlor-alkali plant could regenerate itself by becoming a centre for hydrogen technology. This could create jobs and bring money into the local economy. In the longer term, it could allow the region to establish itself as a major innovator/manufacturer of hydrogen technologies. As a technology that is new, and is expected to become very significant, hydrogen represents an attractive option for regional growth.

Existent chlor-alkali plants with municipalities and authorities form an important base of Hydrogen Community early adopters. The revamping of existent chlor-alkali plants project will represent an useful tool as early adopter: establishing a database of potential technology demonstrations; characterizing these early adopters in terms of their drivers and capacities, enabling conclusions to be drawn regarding key success factors; studying relevant policy measures, and drawing conclusions on critical points for the future in terms of general policies and regional cluster development in hydrogen and fuel cells; give an overview of the technologies, planning establishing and running a project, monitoring its success, financing and exploitation, etc.

For the commercialization of hydrogen and fuel cells, it is essential that the immature technologies are able to be demonstrated in real world conditions. This is also crucial from the point of view of the technologies gaining public acceptance. Developing of this type of revamping project, for example, could be national or on a private individual basis. The concept of a community, as an end user, is very promising.

Communities can support hydrogen and fuel cell industries. Hydrogen and fuel cells is novel developing technologies and many regions are interested in claiming some value in the area of the technology supply chain – from research to manufacturing and distribution.

Communities are trying to develop ‘clusters’ where a number of hydrogen technology-related organizations are geographically localized, and are able to benefit from being close to one another. This is seen as a way to promote regional innovation, and contributes to the development of hydrogen technologies.

Depending on its specific circumstances, there are a number of reasons why communities could be stakeholders in hydrogen projects. Expertise in cutting-edge technologies like H_2&FCs might improve the competitiveness of local firms, or generate new high value organizations. New clusters combining competences on energy, transportation and services may emerge. Aside from business and economic growth the community as a whole would benefit via learning processes and strengthened cooperation between different actors in the field of high-technology (universities, research institutes, public actors etc.). The community would acquire eco-innovative credentials which later on could attract new investments and funding.

Some towns, cities or regions have a strong economic dependency on industries that are now in clear decline. Engaging with a growth industry like hydrogen can offer a chance to re-

invigorate a local economy. This could mean manufacturing hydrogen technologies, producing hydrogen from a local energy source, or expanding research facilities. Apart from providing platforms for new industries in hydrogen and fuel cell technologies, these technologies could affect existing industries. In the first place they could replace older technologies such as batteries and small combustion engines. Services are also likely to be needed to facilitate the introduction of a hydrogen economy. These include specialized financial services, insurance, logistics, shipping, truck transportation, retail, surveillance and overhaul and maintenance. Furthermore, hydrogen and fuel cell technologies can be the technological platform for developing totally new services such as energy storage. Some regions might prefer to promote such service industries instead of traditional industrial manufacturing.

2 Premises for a Hydrogen Community at Rm. Valcea, Romania

1. In November 2004, the Romanian Ministry of Education and Research promoted the Sectorial Plan of Research & Development which aims are the support of Romanian economy competitiveness and the preparing of integrating in the European research space and accessing EU. Developing a Hydrogen and Fuel Cells R&D Integrated Platform was one of the Sectorial Plan projects. The financial support, of 325,000 euro, is provided by the Ministry of Education and Research 250,000 Euro, and by the partners themselves 75,000 euro. The platform, managed by National R&D Institute for Cryogenics and Isotopic Technologies ICIT Rm. Valcea, it is networking nine R&D organizations acting in the area of Hydrogen and Fuel Cells in Romania, in order to develop the Romanian capabilities in this domain and to reach the level permitting the connection with the European HFP. Leader of the Consortium: ICSI Ramnicu Valcea H2-FC (PEMFC) RD&D, members: National R-D Institute for Electrical Engineering-Advanced Research, ICPE-CA, Bucharest, National R-D Institute for Materials Physics, Bucharest-Magurele, National R-D Institute for Isotopic and Molecular Technologies - ITIM, Cluj-Napoca, National R-D Institute of Technical Physics - IFT, Iasi, Petroleum and Gas University, Ploiesti, University Politehnica Bucharest, ZECASIN SA Bucharest, ICEMENERG SA Bucharest.
2. OLTCHIM is one of the biggest Romanian chemical companies end one important chlor-alkali east-European producer, established in 1966 with the name of Chemical Works Ramnicu Valcea, by Minister Council Decision 1046/26.05.1966. The erection has begun in July 1966. The first plant, Mercury Cells Electrolysis, was commissioned on 28 July 1968. In 1990, by Government Decision 1213/20.11.1990, based on the Law 15/1990, the Chemical Works Ramnicu Valcea turned into a joint-stock company, called OLTCHIM S.A.
3. Ministry of Industry (now Economy) from Romania and World Bank has done a study that explores six Romanian companies where it could be located fuel cell plants. Consulting firm, hired by above mentioned institutions, concluded that the most attractive location is a OLTCHIM S.A., it can produce hydrogen for capacities greater than 3MW [3].

4. The integration of fuel cells into electrochemical plants is a method for the direct connection of fuel cells to electrolysers of electrochemical plants producing hydrogen as a by-product. The by-product hydrogen is fed to the fuel cells and the electric energy thereby produced is transferred to the electrolysers, with the consequent saving of the overall energy consumption. The direct coupling avoids the need for DC/AC converters or voltage adjusters and may be affected either in series or in parallel. In the latter case the fuel cell are assembled in modules, the number and voltage of which is regulated by means of interrupters activated by a computerized control and supervision system. As an alternative, the voltage of the modules may be varied by varying the pressure of the air fed to the fuel cells.

One of the earliest markets applications are using of fuel cells for recovering hydrogen from industrial chlor-alkali processes (electrolysis process) [4].

UHDENORA and OLTCHIM SA have contacts for the installation of the first industrial fuel cell plant at the OLTCHIM's chlor-alkali production site at Ramnicu Valcea, Romania. One similar application, 120 kW, was installed at a sodium chlorate production plant, Caffaro Chimica, Brescia, Italy. This industrial installation represents a successful step in the development and commercialization of the green energy [5].

The goal of this project was to produce clean electricity by using the hydrogen co-generated in the electrolytic process [6].

Fuel cell reality premise:

- around 84 stationary fuel cell systems with hydrogen have been installed all over the world. Some of them have an high installed power, 125 or 250 kW, but the biggest majority provide power between 1 and 5 kW,
- Uhdenora and Caffaro have installed and started up of the first industrial fuel cell system for electricity production and savings in the electrochemical industry, Caffaro Chimica, Brescia, Italy.
- Chlor-alkali reality premise:
- the recycled or re-used hydrogen produced by the chlor-alkali plants was less than 90% in 2006 and the target will not exceed 95% in 2010,
- at each tone of chloride is produced 28 kg (310 Nm^3) of hydrogen,
- the world chloride capacity was estimated to approximate 60 million metric tons.

3 Conclusions

The term 'Hydrogen Community' refers to early adopters of hydrogen and fuel cell technology, who have the potential to become large scale adopters. Cities, regions, islands, and industrial zones are examples of potential hydrogen communities.

Communities are important for the commercialization of H_2&FC technologies: providing willing consumers, developing H_2 infrastructure, developing production of H_2.

Communities may be interested in adopting H_2&FC technology, as it can offer: innovation and growth, publicity, prestige, branding, a solution to local air quality, reduced CO_2 emissions, and practical advantages over existing technologies.

The aim of this presentation is to point out some ideas about research state of the art and trends into, hydrogen, fuel cell and chlor-alkali, and the possibility utilizes both, technical improvements for environmental protection and European scientifically mechanisms, in order to develop a Hydrogen Community at Rm. Valcea, Romania.

References

[1] Chlorine Industry Review, Euro Chlor, 2008-2009.

[2] Roads2HyCom, Hydrogen and Fuel Cells - A Handbook for Communities Volume A, October 2007, www.roads2hy.com.

[3] Ionescu Constantin, Fuel Cells Brochure, Romanian Ministry of Education and Research, Ed. Universul Energiei 2005, 119-133.

[4] Faita et al., U.S. Patent 6423203, 23 July 2002,

[5] Adrian Schervan, Alessandro Delfrate, H2_FUEL_CELLS_MILLENIUM _ CONVERGENCE, September 21st, 2007, Bucharest,

[6] Iordache Ioan, Adrian Schervan, Alessandro Delfrate, Iordache Mihaela, First Regional Symposium on Electrochemistry of South-East Europe Crveni Otok, Rovinj, Istria, Croatia, May 4-8, 2008.

1. **Einsatz von multispektralen Satellitenbilddaten in der Wasserhaushalts- und Stoffstrommodellierung – dargestellt am Beispiel des Rureinzugsgebietes**
von C. Montzka (2008), XX, 238 Seiten
ISBN: 978-3-89336-508-1

2. **Ozone Production in the Atmosphere Simulation Chamber SAPHIR**
by C. A. Richter (2008), XIV, 147 pages
ISBN: 978-3-89336-513-5

3. **Entwicklung neuer Schutz- und Kontaktierungsschichten für Hochtemperatur-Brennstoffzellen**
von T. Kiefer (2008), 138 Seiten
ISBN: 978-3-89336-514-2

4. **Optimierung der Reflektivität keramischer Wärmedämmschichten aus Yttrium-teilstabilisiertem Zirkoniumdioxid für den Einsatz auf metallischen Komponenten in Gasturbinen**
von A. Stuke (2008), X, 201 Seiten
ISBN: 978-3-89336-515-9

5. **Lichtstreuende Oberflächen, Schichten und Schichtsysteme zur Verbesserung der Lichteinkopplung in Silizium-Dünnschichtsolarzellen**
von M. Berginski (2008), XV, 171 Seiten
ISBN: 978-3-89336-516-6

6. **Politikszenarien für den Klimaschutz IV – Szenarien bis 2030**
hrsg.von P. Markewitz, F. Chr. Matthes (2008), 376 Seiten
ISBN 978-3-89336-518-0

7. **Untersuchungen zum Verschmutzungsverhalten rheinischer Braunkohlen in Kohledampferzeugern**
von A. Schlüter (2008), 164 Seiten
ISBN 978-3-89336-524-1

8. **Inorganic Microporous Membranes for Gas Separation in Fossil Fuel Power Plants**
by G. van der Donk (2008), VI, 120 pages
ISBN: 978-3-89336-525-8

9. **Sinterung von Zirkoniumdioxid-Elektrolyten im Mehrlagenverbund der oxidkeramischen Brennstoffzelle (SOFC)**
von R. Mücke (2008), VI, 165 Seiten
ISBN: 978-3-89336-529-6

10. **Safety Considerations on Liquid Hydrogen**
by K. Verfondern (2008), VIII, 167 pages
ISBN: 978-3-89336-530-2

11. **Kerosinreformierung für Luftfahrtanwendungen**
    von R. C. Samsun (2008), VII, 218 Seiten
    ISBN: 978-3-89336-531-9

12. **Der 4. Deutsche Wasserstoff Congress 2008 – Tagungsband**
    hrsg. von D. Stolten, B. Emonts, Th. Grube (2008), 269 Seiten
    ISBN: 978-3-89336-533-3

13. **Organic matter in Late Devonian sediments as an indicator for environmental changes**
    by M. Kloppisch (2008), XII, 188 pages
    ISBN: 978-3-89336-534-0

14. **Entschwefelung von Mitteldestillaten für die Anwendung in mobilen Brennstoffzellen-Systemen**
    von J. Latz (2008), XII, 215 Seiten
    ISBN: 978-3-89336-535-7

15. **RED-IMPACT**
    Impact of Partitioning, Transmutation and Waste Reduction Technologies on the Final Nuclear Waste Disposal
    SYNTHESIS REPORT
    ed. by W. von Lensa, R. Nabbi, M. Rossbach (2008), 178 pages
    ISBN 978-3-89336-538-8

16. **Ferritic Steel Interconnectors and their Interactions with Ni Base Anodes in Solid Oxide Fuel Cells (SOFC)**
    by J. H. Froitzheim (2008), 169 pages
    ISBN: 978-3-89336-540-1

17. **Integrated Modelling of Nutrients in Selected River Basins of Turkey**
    Results of a bilateral German-Turkish Research Project
    project coord. M. Karpuzcu, F. Wendland (2008), XVI, 183 pages
    ISBN: 978-3-89336-541-8

18. **Isotopengeochemische Studien zur klimatischen Ausprägung der Jüngeren Dryas in terrestrischen Archiven Eurasiens**
    von J. Parplies (2008), XI, 155 Seiten, Anh.
    ISBN: 978-3-89336-542-5

19. **Untersuchungen zur Klimavariabilität auf dem Tibetischen Plateau - Ein Beitrag auf der Basis stabiler Kohlenstoff- und Sauerstoffisotope in Jahrringen von Bäumen waldgrenznaher Standorte**
    von J. Griessinger (2008), XIII, 172 Seiten
    ISBN: 978-3-89336-544-9

20. **Neutron-Irradiation + Helium Hardening & Embrittlement Modeling of 9%Cr-Steels in an Engineering Perspective (HELENA)**
by R. Chaouadi (2008), VIII, 139 pages
ISBN: 978-3-89336-545-6

21. **in Bearbeitung**

22. **Verbundvorhaben APAWAGS (AOEV und Wassergenerierung) – Teilprojekt: Brennstoffreformierung – Schlussbericht**
von R. Peters, R. C. Samsun, J. Pasel, Z. Porš, D. Stolten (2008), VI, 106 Seiten
ISBN: 978-3-89336-547-0

23. **FREEVAL**
Evaluation of a Fire Radiative Power Product derived from Meteosat 8/9 and Identification of Operational User Needs
Final Report
project coord. M. Schultz, M. Wooster (2008), 139 pages
ISBN: 978-3-89336-549-4

24. **Untersuchungen zum Alkaliverhalten unter Oxycoal-Bedingungen**
von C. Weber (2008), VII, 143, XII Seiten
ISBN: 978-3-89336-551-7

25. **Grundlegende Untersuchungen zur Freisetzung von Spurstoffen, Heißgaschemie, Korrosionsbeständigkeit keramischer Werkstoffe und Alkalirückhaltung in der Druckkohlenstaubfeuerung**
von M. Müller (2008), 207 Seiten
ISBN: 978-3-89336-552-4

26. **Analytik von ozoninduzierten phenolischen Sekundärmetaboliten in *Nicotiana tabacum* L. cv Bel W3 mittels LC-MS**
von I. Koch (2008), III, V, 153 Seiten
ISBN 978-3-89336-553-1

27. **IEF-3 Report 2009. Grundlagenforschung für die Anwendung**
(2009), ca. 230 Seiten
ISBN: 978-3-89336-554-8

28. **Influence of Composition and Processing in the Oxidation Behavior of MCrAlY-Coatings for TBC Applications**
by J. Toscano (2009), 168 pages
ISBN: 978-3-89336-556-2

29. **Modellgestützte Analyse signifikanter Phosphorbelastungen in hessischen Oberflächengewässern aus diffusen und punktuellen Quellen**
von B. Tetzlaff (2009), 149 Seiten
ISBN: 978-3-89336-557-9

30. **Nickelreaktivlot / Oxidkeramik – Fügungen als elektrisch isolierende Dichtungskonzepte für Hochtemperatur-Brennstoffzellen-Stacks**
von S. Zügner (2009), 136 Seiten
ISBN: 978-3-89336-558-6

31. **Langzeitbeobachtung der Dosisbelastung der Bevölkerung in radioaktiv kontaminierten Gebieten Weißrusslands – Korma-Studie**
von H. Dederichs, J. Pillath, B. Heuel-Fabianek, P. Hill, R. Lennartz (2009), Getr. Pag.
ISBN: 978-3-89336-532-3

32. **Herstellung von Hochtemperatur-Brennstoffzellen über physikalische Gasphasenabscheidung**
von N. Jordán Escalona (2009), 148 Seiten
ISBN: 978-3-89336-532-3

33. **Real-time Digital Control of Plasma Position and Shape on the TEXTOR Tokamak**
by M. Mitri (2009), IV, 128 pages
ISBN: 978-3-89336-567-8

34. **Freisetzung und Einbindung von Alkalimetallverbindungen in kohlebefeuerten Kombikraftwerken**
von M. Müller (2009), 155 Seiten
ISBN: 978-3-89336-568-5

35. **Kosten von Brennstoffzellensystemen auf Massenbasis in Abhängigkeit von der Absatzmenge**
von J. Werhahn (2009), 242 Seiten
ISBN: 978-3-89336-569-2

36. **Einfluss von Reoxidationszyklen auf die Betriebsfestigkeit von anodengestützten Festoxid-Brennstoffzellen**
von M. Ettler (2009), 138 Seiten
ISBN: 978-3-89336-570-8

37. **Großflächige Plasmaabscheidung von mikrokristallinem Silizium für mikromorphe Dünnschichtsolarmodule**
von T. Kilper (2009), XVII, 154 Seiten
ISBN: 978-3-89336-572-2

38. **Generalized detailed balance theory of solar cells**
by T. Kirchartz (2009), IV, 198 pages
ISBN: 978-3-89336-573-9

39. **The Influence of the Dynamic Ergodic Divertor on the Radial Electric Field at the Tokamak TEXTOR**
von J. W. Coenen (2009), xii, 122, XXVI pages
ISBN: 978-3-89336-574-6

40. **Sicherheitstechnik im Wandel Nuklearer Systeme**
von K. Nünighoff (2009), viii, 215 Seiten
ISBN: 978-3-89336-578-4

41. **Pulvermetallurgie hochporöser NiTi-Legierungen für Implanat- und Dämpfungsanwendungen**
von M. Köhl (2009), XVII, 199 Seiten
ISBN: 978-3-89336-580-7

42. **Einfluss der Bondcoatzusammensetzung und Herstellungsparameter auf die Lebensdauer von Wärmedämmschichten bei zyklischer Temperaturbelastung**
von M. Subanovic (2009), 188, VI Seiten
ISBN: 978-3-89336-582-1

43. **Oxygen Permeation and Thermo-Chemical Stability of Oxygen Permeation Membrane Materials for the Oxyfuel Process**
by A. J. Ellett (2009), 176 pages
ISBN: 978-3-89336-581-4

44. **Korrosion von polykristallinem Aluminiumoxid (PCA) durch Metalljodidschmelzen sowie deren Benetzungseigenschaften**
von S. C. Fischer (2009), 148 Seiten
ISBN: 978-3-89336-584-5

45. **IEF-3 Report 2009. Basic Research for Applications**
(2009), 217 Seiten
ISBN: 978-3-89336-585-2

46. **Verbundvorhaben ELBASYS (Elektrische Basissysteme in einem CFK-Rumpf) - Teilprojekt: Brennstoffzellenabgase zur Tankinertisierung - Schlussbericht**
von R. Peters, J. Latz, J. Pasel, R. C. Samsun, D. Stolten
(2009), xi, 202 Seiten
ISBN: 978-3-89336-587-6

47. **Aging of ^{14}C-labeled Atrazine Residues in Soil: Location, Characterization and Biological Accessibility**
by N. D. Jablonowski (2009), IX, 104 pages
ISBN: 978-3-89336-588-3

48. **Entwicklung eines energetischen Sanierungsmodells für den europäischen Wohngebäudesektor unter dem Aspekt der Erstellung von Szenarien für Energie- und CO_2 - Einsparpotenziale bis 2030**
von P. Hansen (2009), XXII, 281 Seiten
ISBN: 978-3-89336-590-6

49. **Reduktion der Chromfreisetzung aus metallischen Interkonnektoren für Hochtemperaturbrennstofzellen durch Schutzschichtsysteme**
von R. Trebbels (2009), iii, 135 Seiten
ISBN: 978-3-89336-591-3

50. **Bruchmechanische Untersuchung von Metall / Keramik-Verbundsystemen für die Anwendung in der Hochtemperaturbrennstoffzelle**
von B. Kuhn (2009), 118 Seiten
ISBN: 978-3-89336-592-0

51. **Wasserstoff-Emissionen und ihre Auswirkungen auf den arktischen Ozonverlust**
Risikoanalyse einer globalen Wasserstoffwirtschaft
von T. Feck (2009), 180 Seiten
ISBN: 978-3-89336-593-7

52. **Development of a new Online Method for Compound Specific Measurements of Organic Aerosols**
by T. Hohaus (2009), 156 pages
ISBN: 978-3-89336-596-8

53. **Entwicklung einer FPGA basierten Ansteuerungselektronik für Justageeinheiten im Michelson Interferometer**
von H. Nöldgen (2009), 121 Seiten
ISBN: 978-3-89336-599-9

54. **Observation – and model – based study of the extratropical UT/LS**
by A. Kunz (2010), xii, 120, xii pages
ISBN: 978-3-89336-603-3

55. **Herstellung polykristalliner Szintillatoren für die Positronen-Emissions-Tomographie (PET)**
von S. K. Karim (2010), VIII, 154 Seiten
ISBN: 978-3-89336-610-1

56. **Kombination eines Gebäudekondensators mit H2-Rekombinatorelementen in Leichwasserreaktoren**
von S. Kelm (2010), vii, 119 Seiten
ISBN: 978-3-89336-611-8

57. **Plant Leaf Motion Estimation Using A 5D Affine Optical Flow Model**
by T. Schuchert (2010), X, 143 pages
ISBN: 978-3-89336-613-2

58. **Tracer-tracer relations as a tool for research on polar ozone loss**
by R. Müller (2010), 116 pages
ISBN: 978-3-89336-614-9

59. **Sorption of polycyclic aromatic hydrocarbon (PAH) to Yangtze River sediments and their components**
by J. Zhang (2010), X, 109 pages
ISBN: 978-3-89336-616-3

60. **Weltweite Innovationen bei der Entwicklung von CCS-Technologien und Möglichkeiten der Nutzung und des Recyclings von CO_2**
Studie im Auftrag des BMWi
von W. Kuckshinrichs et al. (2010), X, 139 Seiten
ISBN: 978-3-89336-617-0

61. **Herstellung und Charakterisierung von sauerstoffionenleitenden Dünnschichtmembranstrukturen**
von M. Betz (2010), XII, 112 Seiten
ISBN: 978-3-89336-618-7

62. **Politikszenarien für den Klimaschutz V – auf dem Weg zum Strukturwandel, Treibhausgas-Emissionsszenarien bis zum Jahr 2030**
hrsg. von P. Hansen, F. Chr. Matthes (2010), 276 Seiten
ISBN: 978-3-89336-619-4

63. **Charakterisierung Biogener Sekundärer Organischer Aerosole mit Statistischen Methoden**
von C. Spindler (2010), iv, 163 Seiten
ISBN: 978-3-89336-622-4

64. **Stabile Algorithmen für die Magnetotomographie an Brennstoffzellen**
von M. Wannert (2010), ix, 119 Seiten
ISBN: 978-3-89336-623-1

65. **Sauerstofftransport und Degradationsverhalten von Hochtemperatur-membranen für CO2-freie Kraftwerke**
von D. Schlehuber (2010), VII, 139 Seiten
ISBN: 978-3-89336-630-9

66. **Entwicklung und Herstellung von foliengegossenen, anodengestützten Festoxidbrennstoffzellen**
von W. Schafbauer (2010), VI, 164 Seiten
ISBN: 978-3-89336-631-6

67. **Disposal strategy of proton irradiated mercury from high power spallation sources**
by S. Chiriki (2010), xiv, 124 pages
ISBN: 978-3-89336-632-3

68. **Oxides with polyatomic anions considered as new electrolyte materials for solid oxide fuel cells (SOFCs)**
by O. H. Bin Hassan (2010), vii, 121 pages
ISBN: 978-3-89336-633-0

69. **Von der Komponente zum Stack: Entwicklung und Auslegung von HT-PEFC-Stacks der 5 kW-Klasse**
von A. Bendzulla (2010), IX, 203 Seiten
ISBN: 978-3-89336-634-7

70. **Satellitengestützte Schwerewellenmessungen in der Atmosphäre und Perspektiven einer zukünftigen ESA Mission (PREMIER)**
von S. Höfer (2010), 81 Seiten
ISBN: 978-3-89336-637-8

71. **Untersuchungen der Verhältnisse stabiler Kohlenstoffisotope in atmosphärisch relevanten VOC in Simulations- und Feldexperimenten**
von H. Spahn (2010), IV, 210 Seiten
ISBN: 978-3-89336-638-5

72. **Entwicklung und Charakterisierung eines metallischen Substrats für nanostrukturierte keramische Gastrennmembranen**
von K. Brands (2010), vii, 137 Seiten
ISBN: 978-3-89336-640-8

73. **Hybridisierung und Regelung eines mobilen Direktmethanol-Brennstoff-zellen-Systems**
von J. Chr. Wilhelm (2010), 220 Seiten
ISBN: 978-3-89336-642-2

74. **Charakterisierung perowskitischer Hochtemperaturmembranen zur Sauerstoffbereitstellung für fossil gefeuerte Kraftwerksprozesse**
von S.A. Möbius (2010) III, 208 Seiten
ISBN: 978-3-89336-643-9

75. **Characterization of natural porous media by NMR and MRI techniques: High and low magnetic field studies for estimation of hydraulic properties**
by L.-R. Stingaciu (2010), 96 pages
ISBN: 978-3-89336-645-3

76. **Hydrological Characterization of a Forest Soil Using Electrical Resistivity Tomography**
by Chr. Oberdörster (2010), XXI, 151 pages
ISBN: 978-3-89336-647-7

77. **Ableitung von atomarem Sauerstoff und Wasserstoff aus Satellitendaten und deren Abhängigkeit vom solaren Zyklus**
von C. Lehmann (2010), 127 Seiten
ISBN: 978-3-89336-649-1

78. **18th World Hydrogen Energy Conference 2010 – WHEC2010 Proceedings**
Speeches and Plenary Talks
ed. by D. Stolten, B. Emonts (2010)
ISBN: 978-3-89336-658-3

78-1. **18th World Hydrogen Energy Conference 2010 – WHEC2010 Proceedings**
Parallel Sessions Book 1:
Fuel Cell Basics / Fuel Infrastructures
ed. by D. Stolten, T. Grube (2010), ca. 460 pages
ISBN: 978-3-89336-651-4

78-2. **18th World Hydrogen Energy Conference 2010 – WHEC2010 Proceedings**
Parallel Sessions Book 2:
Hydrogen Production Technologies – Part 1
ed. by D. Stolten, T. Grube (2010), ca. 400 pages
ISBN: 978-3-89336-652-1

78-3. **18th World Hydrogen Energy Conference 2010 – WHEC2010 Proceedings**
Parallel Sessions Book 3:
Hydrogen Production Technologies – Part 2
ed. by D. Stolten, T. Grube (2010), ca. 640 pages
ISBN: 978-3-89336-653-8

78-4. **18th World Hydrogen Energy Conference 2010 – WHEC2010 Proceedings**
Parallel Sessions Book 4:
Storage Systems / Policy Perspectives, Initiatives and Cooperations
ed. by D. Stolten, T. Grube (2010), ca. 500 pages
ISBN: 978-3-89336-654-5

78-5. **18th World Hydrogen Energy Conference 2010 – WHEC2010 Proceedings**
Parallel Sessions Book 5:
Stategic Analysis / Safety Issues / Existing and Emerging Markets
ed. by D. Stolten, T. Grube (2010), ca. 530 pages
ISBN: 978-3-89336-655-2

78-6. **18th World Hydrogen Energy Conference 2010 – WHEC2010 Proceedings**
Parallel Sessions Book 6:
Stationary Applications / Transportation Applications
ed. by D. Stolten, T. Grube (2010), ca. 330 pages
ISBN: 978-3-89336-656-9

Schriften des Forschungszentrums Jülich
Reihe Energie & Umwelt / Energy & Environment

78 Set (7 Bände)

18th World Hydrogen Energy Conference 2010 – WHEC2010 Proceedings
eb. by D. Stolten, T. Grube, B. Emonts (2010)
ISBN: 978-3-89336-657-6

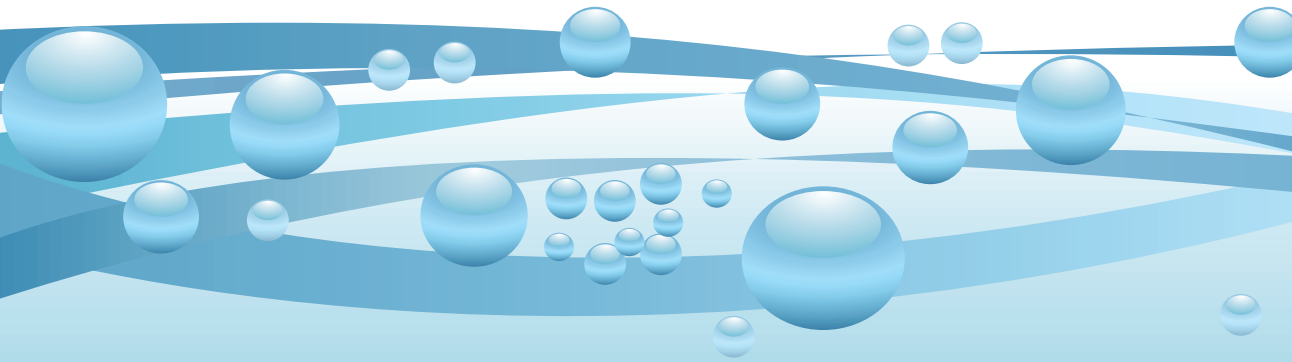

Energy & Environment
Volume 78-1 Book 1

Vol. 78 ISBN 978-3-89336-658-3
Vol. 78-1 Book 1: ISBN 978-3-89336-651-4
Vol. 78-2 Book 2: ISBN 978-3-89336-652-1
Vol. 78-3 Book 3: ISBN 978-3-89336-653-8
Vol. 78-4 Book 4: ISBN 978-3-89336-654-5
Vol. 78-5 Book 5: ISBN 978-3-89336-655-2
Vol. 78-6 Book 6: ISBN 978-3-89336-656-9
Vol. 78 Set (complete book series): ISBN 978-3-89336-657-6

JÜLICH
FORSCHUNGSZENTRUM